UNIVERSIDADE
BEIRA INTERIOR

Alternative Liquid Fuels for Aviation Gas Turbines: Experiments and Modelling

Inês Alexandra dos Santos Ferrão

Tese para obtenção do Grau de Doutor em
Engenharia Aeronáutica
(3º ciclo de estudos)

Orientador: Prof. Doutor André Resende Rodrigues Silva
Co-orientador: Prof. Doutora Ana Sofia Oliveira Henriques Moita
Co-orientador: Prof. Doutor Miguel Abreu Almeida Mendes

junho de 2025

UNIVERSIDADE
BEIRA INTERIOR

Alternative Liquid Fuels for Aviation Gas Turbines: Experiments and Modelling

Inês Alexandra dos Santos Ferrão

Tese para obtenção do Grau de Doutor em
Engenharia Aeronáutica
(3º ciclo de estudos)

Orientador: Prof. Doutor André Resende Rodrigues Silva
Co-orientador: Prof. Doutora Ana Sofia Oliveira Henriques Moita
Co-orientador: Prof. Doutor Miguel Abreu Almeida Mendes

Júri:
Prof. Doutor Jorge Manuel Martins Barata
Prof. Doutor Pedro Jorge Martins Coelho
Prof. Doutor Rafael de Camargo Catapan
Prof. Doutor Daniel Cardoso Vaz
Prof. Doutor Miguel Rosa Oliveira Panão
Prof. Doutor Leandro Barbosa Magalhães

8 de maio de 2025

Declaração de Integridade

Eu, Inês Alexandra dos Santos Ferrão, que abaixo assino, estudante com o número de inscrição $d2575$ do Curso 3° Ciclo em Engenharia Aeronáutica da Faculdade de Engenharias, declaro ter desenvolvido o presente trabalho e elaborado o presente texto em total consonância com o **Código de Integridades da Universidade da Beira Interior.**

Mais concretamente afirmo não ter incorrido em qualquer das variedades de Fraude Académica, e que aqui declaro conhecer, que em particular atendi à exigida referenciação de frases, extratos, imagens e outras formas de trabalho intelectual, e assumindo assim na íntegra as responsabilidades da autoria.

Universidade da Beira Interior, Covilhã 31/10/2024

Inês Alexandra dos Santos Ferrão

Dedicatória

I wish to dedicate this entire work to two individuals that started this journey with me and left so unexpectedly…

Professor Mário Costa, thank you for the support during this project and for sharing your passion for research. I hope I accomplished everything you envisioned. As you asked me so many times, yes, the combustion chamber is in the combustion laboratory.

Vó, minha Isabelita. Partiste mesmo na reta final desta jornada de forma tão inesperada… É com tristeza que chego a este momento por não conseguir partilhar contigo. Obrigado por teres acreditado em mim, em todos os momentos da minha vida e teres me dado a força para continuar. Tenho saudades tuas Vó.

Acknowledgments

I would like to thank my supervisor, Professor André Resende Rodrigues da Silva, for the opportunity to work with him, who followed me throughout this process of encouragement, support, and guidance at the University of Beira Interior. I also acknowledge my Instituto Superior Técnico co-supervisors, Professor Mário Costa, Professor Miguel Mendes, and Professor Ana Moita. Professor Mário Costa, thank you for your invaluable guidance and support on my PhD journey. His wisdom, encouragement, and passion for knowledge remain a constant source of inspiration for my growth as a research scientist. I also express my deepest gratitude to Professor Miguel Mendes for your optimistic perspective and fruitful discussions. I am thankful for your mentorship and help supporting the combustion team in a challenging moment. I would also like to thank Professor Ana Moita for all the support and guidance from the beginning of my PhD journey. Thank you so much for your dedication, enthusiasm, and knowledge.

I would like to express my gratitude to Professor Jorge Barata for the opportunity to participate in AEROG initiatives and to improve scientific research. I sincerely also thank Professor Miguel Panão for the valuable discussions concerning the spray analysis. This work would not have been possible without the assistance of Ana Rita Sousa, Professor Ilídio Correia, Flávia Morais, Francisco Costa, Duarte Diogo, Professor Viriato Semião, Professor Sohel Murshed, Professor Ana Paula, Uxía Calvinho, Diogo Roque that assisted me with the physical properties measurements and supplied the essential tools for the experiments.

I would like to extend particular thanks to Manuel Pratas, who has been very helpful in the combustion laboratory and has kept an extremely positive and encouraging attitude throughout this experience. I am also thankful to Rita Maia and Sandra Dias for providing me with all the support.

Throughout my PhD experience, I had the chance to work closely with the master students: Tomás Mendes, Francisco Dias, Ricardo Santos, Ana Sofia Ladino, Maria Alice Martins, and Leonardo Silva. It has truly been a pleasure to collaborate with each of you.

I wish to express my gratitude to all my colleagues and friends in the AEROG, IN^{+}, and combustion laboratories for all the good times presented in every stage of this project. In particular, a special thanks to my friends Daniela and Rodrigues, who have always been by my side during the good and bad moments. Rodri, no words describe your help during the last years. Thank you for all the calls you have made to help along this path and for being a source of positivity and laughter in the most hard times.

I wish to extend my thanks to my friend Dr. Teresa Constantino, who accompanied me through the various challenges and achievements of my PhD journey. Your support was essential for me to reach this objective.

Lastly, I would like to take this opportunity to express my gratitude to my family, especially to my parents and brother, who have always inspired me with their unconditional support throughout the last difficult years. Thank you, Gonçalo, for always being by my side during this long and challenging journey and for your patience and invaluable support.

Funding

The research project was supported by Fundação para a Ciência e Tecnologia through the PhD scholarship with the reference SFRH/BD/144688/2019 and partially through projects JICAM/0003/2017, PTDC/EME-SIS/2017 and PTDC/EMETED/7801/2020. The present work was performed under the scope of the Laboratório Associado em Energia, Transportes e Aeronáutica (LAETA) and Laboratório de Robótica e Sistemas de Engenharia (LARSyS) activities through the projects UID/EMS/50022/2019, 10.54499/UIDB/50022/2020, 10.54499/UIDP/50022/2020, 10.54499/UIDB/50009/2020, 10.54499/UIDP/50009/2020 and 10.54499/LA/P/0079/2020, 1018P.03201.1.01.

Abstract

Air transport plays a crucial role in globalization, connecting people and businesses worldwide. Nonetheless, its reliance on fossil fuels significantly contributes to greenhouse gas emissions and pollution. The continuous growth of this sector, alongside the environmental issues and the depletion of fossil fuels, has promoted the investigation of alternative and sustainable energy sources that could supply the aviation industry. Biofuels, drop-in fuels, are considered a promising alternative since they can offer carbon neutrality and substantially further reduction of pollutant emissions, leading to an attractive replacement for conventional jet fuel. Besides reducing dependence on fossil fuel and offering cleaner combustion, many challenges remain regarding biomass availability, process cost, and fuel properties like energy content, viscosity, and volatility. One of the ways to improve the performance of biofuels could be the addition of nanoparticles. This new fuel generation is noted as nanofuels centered on dispersing nanoparticles stably suspended in conventional liquid fuels. In particular, metallic nanoparticles have shown increased fuel energy density, enhancements in combustion rates, reduced ignition delay and fuel consumption, and decreased emissions.

According to the previous discussion, the present study investigates the influence of metallic particles on sustainable aviation fuel. This fundamental study initially focuses on nanofuel preparation and stability to address its potential use in real applications. Several preparation approaches are suggested to maintain the stability of nanofuels, particularly for high particle concentrations. Following this, both experimental and numerical investigations are conducted on the combustion of a single droplet, exploring several furnace temperatures, particle sizes, and concentrations. In light of this, the droplet size evolution, disruptive burning phenomena, and potential mechanisms that affect nanofuel combustion are discussed. The experiments conducted in a drop tube furnace suggest that nanoparticle addition promotes the appearance of disruptive burning phenomena regardless of the furnace temperature and particle and size concentrations. In addition, a departure from the D^2-law is noticed, affecting the droplet burning rate. Based on this, the addition of nanoparticles to a liquid fuel is numerically studied. Subsequently, an experimental analysis of the spray under non reacting conditions is performed. An experimental facility was developed using a commercial air-assisted atomizer with external mixing to ease the operation of nanofuels. Imaging and Phase-Doppler Interferometer techniques were used to understand the breakup length, spray cone angle and droplet size, and velocity distributions for several air-fuel ratios. The findings suggest that in terms of single droplet combustion, the addition of nanoparticles possesses a beneficial role, whereas, in atomization, an adverse impact is observed, particularly when the particle concentration is increased. Finally, the development of a laboratory combustion chamber for liquid fuels is discussed. An experimental setup was designed and constructed, which plays a significant role in researching alternative and sustainable fuels.

Keywords

Nanofuel, Single Droplet, Spray, Combustion, Alternative Jet Fuel

Resumo

O transporte aéreo desempenha um papel relevante na globalização apresentando vantagens a nível social, económico, entre outros. Porém depende substancialmente de combustíveis fósseis que contribuem para a emissão de gases com efeito de estufa e poluentes. Consequentemente, é necessário identificar fontes de energias alternativas e sustentáveis viáveis para o setor da aviação. Os biocombustíveis surgem como uma alternativa promissora para a substituição do combustível convencional de modo atingir a neutralidade carbónica e redução nas emissões de poluentes. Embora apresente benefícios, existem algumas preocupações relativas à disponibilidade da matéria-prima, custos de produção, e às suas propriedades referente à densidade energética, viscosidade e volatilidade. De modo a melhorar o desempenho destes biocombustíveis, uma solução em análise é a adição nanopartículas. Estes combustíveis são tipicamente designados de nano combustíveis, envolvendo a adição de nanopartículas a um combustível líquido convencional. Especificamente, o uso de partículas metálicas nestes combustíveis tem produzido um aumento na densidade energética e taxa de queima do combustível assim como uma redução no atraso à ignição, consumo e emissões.

Assim sendo, este estudo investiga fundamentalmente a influência da adição de partículas metálicas a um biocombustível. Numa fase inicial a preparação e estabilidade do nano combustível foi estudada para avaliar o seu potencial uso em aplicações convencionais. Neste contexto, diversos modos de preparação foram explorados para garantir que o nano combustível permanece estável, principalmente a altas concentrações. Posteriormente, realizou-se uma análise experimental e numérica à queima de gota isolada explorando diversas temperaturas do forno assim como diferentes tamanhos e concentrações de partículas. Desta forma, a evolução temporal do diâmetro da gota, fenómenos de queima disruptiva e potenciais mecanismos que afetam a queima de nano combustíveis foram discutidos. Os resultados provenientes do estudo experimental num forno de queda livre indicam que a adição de nanopartículas promove o aparecimento de fenómenos de queima disruptiva independentemente do tamanho e concentração das partículas assim como da temperatura do forno. Adicionalmente, verifica-se um desvio da Lei do D^2 afetando também a taxa de queima. Dando ênfase a estes resultados, a influência da adição de nanoparticulas a um combustivel líquido foi avaliada através de uma abordagem numérica. Subsequentemente explorou-se a dinâmica do spray em condições não reativas. Para tal, desenvolveu-se uma instalação experimental, recorrendo ao uso de um atomizador comercial assistido a ar de mistura externa para facilitar no uso de nano combustíveis. Nesta análise duas técnicas, nomeadamente a aquisição, tratamento de imagens e interferometria laser foram utilizadas de modo a concluir uma investigação dedicada ao comprimento da fragmentação, o ângulo de cone do spray e também a distribuição do diâmetro e velocidade das gotas para diferentes razões de ar e combustível. De um ponto vista geral, os resultados sugerem que a nível da queima da gota isolada a adição de nanopartículas possui um efeito benéfico, enquanto, na atomização verifica-se um impacto negativo principalmente quando ocorre um incremento da concen-

tração de partículas. Por fim, desenvolveu-se uma câmara de combustível para combustíveis líquidos desde o seu conceito até à sua construção contribuindo assim para investigações futuras dedicadas a combustíveis alternativos e sustentáveis.

Palavras-chave

Nano combustíveis, Gota Isolada, Spray, Combustão, Jet Fuel Alternativo

Resumo alargado

O transporte aéreo desempenha um papel relevante na globalização apresentando vantagens a nível social, económico, entre outros. Porém, esta indústria depende substancialmente de combustíveis fósseis que contribuem para a emissão de gases com efeito de estufa e poluentes. Nos últimos anos este sector tem experienciado um aumento significativo, o que suscita uma preocupação relativa à escassez dos combustíveis fósseis assim como para os problemas ambientais. Consequentemente, é necessário identificar fontes de energias alternativas e sustentáveis viáveis para o sector da aviação. Neste contexto, os biocombustíveis surgem como uma alternativa promissora para a substituição do combustível de aviação convencional de modo atingir a neutralidade carbónica e redução nas emissões de poluentes. Apesar dos biocombustíveis apresentarem benefícios na redução do uso de combustíveis fósseis e a nível das emissões, existem algumas preocupações relativas à disponibilidade da matéria-prima, custos de produção, e às suas propriedades referente à densidade energéticas, viscosidade e volatilidade. De modo a melhorar o desempenho destes biocombustíveis, uma solução que tem vindo a ser estudada é a adição nanopartículas. Estes combustíveis são tipicamente designados de nano combustíveis, envolvendo a adição de nanopartículas a um combustível líquido convencional. Especificamente, o uso de partículas metálicas têm reportado um aumento na densidade energética do combustível, aumento da taxa de queima, redução no atraso à ignição e consumo de combustível assim como em emissões. Porém, a evaporação e combustão destes nano combustíveis é um processo bastante complexo e multifásico que requer uma investigação mais aprofundada para compreender o seu impacto em aplicações práticas.

Assim sendo, este trabalho avalia de uma forma fundamental a adição de nanopartículas de alumínio a um biocombustível de um ponto de vista experimental e numérico. Para a seleção das nanopartículas, alumínio foi o material escolhido devido à sua densidade energética, abundância e relativamente baixo custos de produção. Adicionalmente o biocombustível puro e um combustível convencional de aviação (Jet A-1) foram testados para fins de comparação. Diversos objetivos para este trabalho foram estabelecidos de modo a abordar tópicos dedicados à estabilidade, combustão e atomização dos nano combustíveis. A primeira abordagem centrou-se na preparação e estabilidade dos nano combustíveis para altas e baixas concentrações utilizando processos físicos e químicos. Desta análise verificou-se que para altas concentrações de partículas é necessário o uso de um surfactante para garantir que o nano combustível permanece estável durante os ensaios experimentais sobre a queima da gota isolada e dinâmica do spray. A estabilidade de um nano combustível com uma concentração de 4.0 wt.% foi alcançada pelo menos para um período de 4 horas. Concluiu-se que um aumento do tamanho e concentração promove uma redução na estabilidade. Após esta preparação, foi efetuada uma caracterização dos combustíveis confirmando que adição de nanopartículas e surfactante não tem um impacto significativo na tensão superficial e na densidade. Contrariamente, um incremento de cerca 20% na viscosidade foi observado quando uma concentração de 4.0 wt.% de nanopartículas de alumínio e 4.0 wt.% de surfac-

tante são adicionados ao HVO.

Após a conclusão da preparação e caracterização dos combustíveis, o foco do trabalho centrou-se na queima de gota isolada. Nesta fase, um estudo experimental e numérico foi desenvolvido, avaliando-se a influência do tamanho, e concentração das partículas. O trabalho experimental foi realizado num forno de queda livre presente no Instituto Superior Técnico. Esta instalação experimental permite a recolha de imagens provenientes de uma câmara de alta velocidade para posteriormente analisar-se a queima das gotas. Gotas com um diâmetro inicial de 250 μm foram inseridas no forno e a sua queima foi avaliada para temperaturas de 600, 800, 1000, 1100 °C. Desta forma, a evolução temporal do diâmetro da gota, fenómenos de queima disruptiva e potenciais mecanismos presenters na queima de nano combustíveis foram discutidos. Os resultados revelam que o HVO e o Jet A-1 apresentam um comportamento semelhante, seguindo a lei do D^2 sem qualquer ocorrência de fenómenos de queima disruptiva. Contrariamente quando nanopartículas são adicionadas ao biocombustível, independentemente do seu tamanho e concentração verifica se um desvio da lei do D^2 e a ocorrência de micro-explosões. Relativamente aos fenómenos de queima disruptiva, os resultados experimentais indicam que um aumento da concentração e da temperatura promove um aumento da intensidade destes eventos. Uma melhoria na taxa de queima foi verificada quando nanopartículas são adicionadas ao biocombustível aumentando também com o aumento da temperatura do forno. Devido a isto, foi desenvolvido um modelo dedicado à queima da gota isolada de nano combustível. O modelo prevê o diâmetro final da gota antes da ocorrência de micro-explosões indicando que um aumento da concentração resulta num aumento do diâmetro da gota. Para trabalhos futuros é necessária uma avaliação sobre os efeitos da emissões da queima de nanopartículas de alumínio assim como o impacto das micro-explosões em motores.

Na fase seguinte desenvolveu-se uma instalação para acoplar duas técnicas experimentais para o estudo do spray em condições não reativas. Assim sendo, dinâmica do spray foi estudada através da aquisição e tratamento de imagens e da técnica interferometria laser. O comprimento da fragmentação, o ângulo de cone do spray e também a distribuição do diâmetro e velocidade das gotas para diferentes razões de ar e combustível, aproximadamente de 1 até 16 foram avaliadas. Um atomizador assistido a ar foi usado nesta fase do trabalho e algoritmos para o processamento de imagens foram desenvolvidos assim como uma correlação para comprimento da fragmentação do spray. Os resultados demonstram que um aumento da concentração de partículas promove um aumento do diâmetro das gotas presentes no spray. Adicionalmente a dinâmica do spray do HVO e do Jet A-1 são muito similares, evidenciando o potencial uso de biocombustíveis no sector aeronáutico. De um ponto vista geral, o spray avaliado produz gotas mais pequenas com um maior grau de uniformidade para razões de ar combustível mais elevadas. Preferencialmente, as gotas mais pequenas estão localizadas no interior do spray, enquanto as gotas de maior diâmetro e menor velocidade estão presentes na periferia. A distribuição do tamanho das gotas foi avaliada considerando funções matemáticas de probabilidade onde o Log-normal produziu os resultados mais favoráveis. De um ponto vista geral, os resultados sugerem que a nível da queima da gota isolada a

adição de nanopartículas possui um efeito benéfico, enquanto, na atomização verifica-se um impacto negativo principalmente quando ocorre um incremento da concentração de partículas.

Tendo por base todas estas observações referentes ao uso de nano combustíveis, o desenvolvimento de uma câmara de combustível para combustíveis líquidos foi realizado desde o seu conceito até à sua construção. O projeto teve em consideração o desenvolvimento da câmara ou do componente onde a combustão irá ocorrer, *annular axial swirl* e do *swirl burner*. Uma análise mais detalhada sobre o sobreaquecimento do combustível no interior do atomizador, limites de flamabilidade, e sistema de exaustão foi realizada. O desenvolvimento da câmara de combustão foi alcançado com sucesso, garantindo segurança e uma operação eficaz. A este respeito, não foi relatado qualquer sobreaquecimento do combustível durante a avaliação preliminar. Nesta avaliação foi ainda possível testar a instalação experimental com Jet A-1. O objetivo é proporcionar uma experimental ferramenta que permita avaliar de uma forma mais geral a queima destes combustíveis abordando a sua viabilidade contribuindo assim para investigações futuras de combustíveis alternativos e sustentáveis.

Contents

Acknowledgements . . . vii
Abstract . . . xi
Resumo . . . xiii
Resumo alargado . . . xv
List of Figures . . . xxiii
List of Tables . . . xxxi
Nomenclature . . . xxxiii

1 Introduction **1**
1.1 Motivation . . . 1
1.2 Objectives . . . 6
1.3 Contributions . . . 7
1.4 Overview . . . 11

2 Literature Review **13**
2.1 Introduction . . . 13
2.2 Aviation Fuels Contextualization . . . 13
2.2.1 Jet Fuel Composition . . . 15
2.2.2 Jet Fuel Emissions . . . 18
2.2.3 Strategies To Address Aviation Environmental Concerns . . . 21
2.2.4 Sustainable Aviation Fuels - Biofuels . . . 27
2.2.5 Additional Alternative Technologies for Sustainable Aviation . . . 35
2.2.6 Sustainability in Aviation: Alternatives Comparison . . . 41
2.3 Single Droplet . . . 43
2.3.1 Overview . . . 43
2.3.2 The Addition of Particles in a Liquid Fuel . . . 59
2.4 Spray . . . 79
2.4.1 Overview . . . 79
2.4.2 Atomizers . . . 81
2.4.3 Factors Impacting the Atomization . . . 83
2.4.4 Primary and Secondary Atomization . . . 86
2.4.5 Spray Combustion . . . 101

3 Fuels preparation and characterization **109**
3.1 Jet Fuel and Pure Biofuel Characterization . . . 109
3.2 HVO and Aluminum Particles . . . 113
3.2.1 Fuel Preparation and Stability Study . . . 114
3.3 Summary . . . 122

4 Single Droplet Combustion **125**
4.1 Introduction . . . 125

4.2 Experimental Methodology . . . 126
4.2.1 Experimental Setup . . . 126
4.2.1.1 Drop Tube Furnace (DTF) . . . 126
4.2.1.2 Injection Apparatus . . . 128
4.2.1.3 Image Acquisition System . . . 129
4.2.2 Operating Conditions . . . 131
4.2.3 Image Data Processing . . . 135
4.3 Single Droplet Combustion: Experimental Results . . . 139
4.3.1 Visualization and Description of Pure Fuels Combustion . . . 140
4.3.2 The Addition of Particles to an Alternative Jet Fuel . . . 146
4.3.3 Disruptive Burning Phenomena . . . 162
4.4 Numerical Methodology . . . 169
4.4.1 Hexadecane as a Surrogate Fuel . . . 170
4.4.2 Incorporation of the Convective Effects . . . 171
4.4.3 Incorporation of Nanoparticles in a Liquid Droplet . . . 174
4.4.4 Sensitivity Analysis . . . 181
4.5 Single Droplet Combustion: Mathematical Model Results . . . 182
4.5.1 Pure Fuels . . . 183
4.5.2 Nanofuels . . . 184
4.6 Summary . . . 187

5 Spray: Non Reacting Conditions 189
5.1 Introduction . . . 189
5.2 Experimental Methodology . . . 190
5.2.1 Experimental Setup - Imaging Technique . . . 190
5.2.2 Experimental Setup - Phase-Doppler Interferometer . . . 192
5.2.3 Operating Conditions . . . 194
5.2.4 Image Data Processing . . . 197
5.2.4.1 Breakup Length . . . 198
5.2.4.2 Spray Cone Angle . . . 200
5.3 Experimental Results . . . 202
5.3.1 Visualization . . . 203
5.3.2 Breakup Length . . . 207
5.3.3 Spray Cone Angle . . . 212
5.3.4 PDI Results . . . 214
5.3.5 Summary . . . 230

6 Spray: Reacting Conditions 233
6.1 Introduction . . . 233
6.2 Initial Design Considerations . . . 234
6.2.1 Operating Conditions . . . 237
6.3 Preliminary Setup Challenges . . . 240
6.3.1 Target Temperature for Liquid Fuel Operation . . . 241

6.3.2 Swirl Burner Design 242
6.3.3 Combustion Chamber Design 254
6.4 Final Design of Combustion Chamber 258
6.5 Summary 264

7 Closure **267**
7.1 Work Summary and Main Conclusions 267
7.2 Suggestions for Future Work 270

Bibliografia **273**

Appendix **311**

A Biofuels - Conversion Process **311**

B Drop Tube Furnace - Injector **313**

C Air Properties **315**

D SCA - Calibration **317**

E Spray: Operating Conditions **319**

List of Figures

1.1 Distribution of carbon dioxide emissions produced by the transportation sector worldwide in 2022, by sub-sector. . . . 2
1.2 Nanoscience and nanotechnology in science and engineering. . . . 4
1.3 Thesis document outline. . . . 12

2.1 World passenger traffic evolution, 1945–2022 . . . 14
2.2 By-products of fractional distillation . . . 15
2.3 Pratt and Whitney PW4084 turbofan, the jet engine used to power Boeing 777 aircraft . . . 18
2.4 Emissions from an aircraft engine underneath ideal and real conditions . . . 19
2.5 ICAO Global environmental trends on CO_2 emissions and contribution of measures for reducing international aviation net CO_2 emissions . . . 22
2.6 Contribution toward achieving Net Zero Carbon by 2050 . . . 22
2.7 A nominal ASTM D4054 evaluation process . . . 25
2.8 CO_2 life cycle comparison between: a) Fossil fuels; b) Sustainable biofuels. . . . 27
2.9 Biofuel generations . . . 29
2.10 Conceptual design for a full electric aircraft . . . 38
2.11 Strengths and challenges of alternatives for aviation . . . 42
2.12 Schematic of the simplified droplet combustion model and its temperature and species profiles. . . . 45
2.13 Schematic of the mass flow relationships at the flame reaction sheet. Note that the net mass flow in both the inner and outer regions is equal to the fuel mass flow rate, $\dot{m}_F$ . . . 47
2.14 Schematic of the surface energy balance at the droplet liquid-vapor interface . 49
2.15 Schematic of the surface energy balance at the flame reaction sheet . . . 50
2.16 Illustration of experimental techniques used to study the evaporation and combustion of single droplets. . . . 54
2.17 Porous sphere combustion experiment under normal gravity and forced convection conditions: a) Sphere with envelope flame; b) Sphere with wake flame. 55
2.18 Ignition delay as a function of the droplet diameter for several ambient temperatures . . . 56
2.19 Evolution of the: a) Square of the normalized droplet diameter with normalized time for single-component fuel; b) Mean burning rates (left, blue) and normalized combustion duration (right, red) with four single-component n-alkane droplets . . . 57
2.20 Disruptive burning events: a) Puffing; b) Micro-explosions. . . . 58
2.21 Applications of nanofluids/nanofuels. . . . 61
2.22 Overview of the parameters that affect the nanofluids/nanofuels preparation. 62
2.23 Preparation methods: a) Single-step; b) Two-step . . . 63
2.24 Stability evaluation methods. . . . 65

2.25 Sedimentation behaviours in nanofluids, where t indicates time and $t_0 < t_1 < t_2 < t_3$ 66
2.26 Comparsion between liquid and solids fuels: a) per kg; b) per L 68
2.27 Nanofuel surface tension with different particle size and temperatures: a) CNT; b) CeO_2; c) Co_3O_4. 70
2.28 Human health implications due to nanomaterials exposure. 71
2.29 D^2-law illustration of a nanofuel and a conventional fuel. 72
2.30 Schematic of the typical nanofuel droplet dynamics compared to conventional fuel droplets. 73
2.31 Illustration of atomization process. Representation of the two distinct regions: the spray formation region and the spray region. The initial region involves primary and secondary atomization, whereas, in the subsequent region, the spray is typically fully developed, with the majority of droplets being spherical. 80
2.32 Atomizers Categorization: a) Pressure atomizers; b) rotary atomizers; c) twin-fluid atomizers. 82
2.33 Fragmentation of a liquid jet discharged into a stagnant gas: a) Dripping; b) Rayleigh-Plateau; c) First wind-induced; d) Second wind-induced; e) Schematic stability curve relating the average liquid core length to the Weber number (We), increased from a) to d) by increasing the liquid flow rate here. D_L corresponds the liquid nozzle inner diameter 87
2.34 Breakup regimes for air-assisted cylindrical jets: a) Rayleigh-type breakup; b) Membrane-type breakup; c) Fiber-type breakup 89
2.35 Secondary breakup regimes. 93
2.36 Spray cone angle. 95
2.37 Radial SMD distribution of the spray at various fuel supply pressures and air flowrates: a) 40 SLM; b) 80 SLM; c) 120 SLM 99
2.38 Planar distributions of the axial velocity at different axial distances: a) Z = 45 mm; b) Z = 75 mm; c) Z = 120 mm; d) Z = 135 mm. 100
2.39 Variation of flammability limits as a function of temperature. 103
2.40 Combustion Regime: a) Heterogeneous; b) Homogeneous. 104
2.41 Flame Stabilization: a) Bluff body; b) Swirl Vanes. 105

3.1 Jet A-1 chemical composition. 110
3.2 HVO production process. 110
3.3 Properties measurements equipment: a) Portable density/specific gravity meter DA-130N, from Kyoto Electronics Manufacturing; b) Optical tensiometer Theta; c) Viscosimeter DV3T, from AMETEK Brookfield. 112
3.4 Distillation curve for Jet A-1 and HVO. 113
3.5 SEM images of aluminum particles: a) 40 nm; b) 70 nm; c) 5 μm. 114
3.6 Procedure employed in preparing nanofuels using the 2^{nd} approach. 115
3.7 Temporal evolution of particle sedimentation. 116
3.8 Temperature analysis of the HVO + 0.5% Al during and after sonication, using and not using an ice bath. 117

3.9 Temperature analysis of the HVO + 1% Al for two sonication power. 117
3.10 Qualitative stability study criteria. 118
3.11 Procedure employed in preparing HVO and Oleic acid mixture. 119
3.12 Sedimentation evolution for two nanofuels, where surfactant was added before (upper) and after (lower) sonication. 120
3.13 Procedure employed in preparing nanofuels using the 4^{th} approach. 120
3.14 Temperature analysis regarding the addition of surfactant to HVO with aluminum nanoparticles in a size of 40 nm at different particle concentrations. . 121

4.1 Schematic of the experimental setup for single droplet combustion. 126
4.2 Interior view of the drop tube furnace. 127
4.3 Furnace temperature inside the quartz tube as a function of the vertical distance for the respective wall temperature conditions (P∞ = 1 atm). The injector tip is located at x = 0 cm. 128
4.4 Equipment for generating and injecting droplets into the drop tube furnace. . 129
4.5 a) CR600x2 high-speed camera with a magnifying lens Zoom 6000®; b) Photron FASTCAM mini UX50 with 1.3 Megapixel. 130
4.6 Schematic of the arrangement employed for the image acquisition. 131
4.7 Drop tube furnace injector. 132
4.8 Schematic view of the MDG-100. 134
4.9 Data acquisition method. 135
4.10 Illustration of the droplet flame image analysis using data processing. 135
4.11 Single droplet combustion: droplet inter-spacing. 136
4.12 Illustration of the image analysis procedure utilizing ImageJ for data processing. 137
4.13 Analysis of burning rate as a function of the sample size. 137
4.14 Illustration of the image data processing for micro-explosions. 138
4.15 Images obtained in image data processing for micro-explosions: a) Number of fragments, b) Position identification of initial fragments. 139
4.16 Jet A-1 and HVO combustion at T_∞ = 800 °C: a) Droplet size evolution; b) Visualization of single droplet combustion. 141
4.17 Jet A-1 and HVO combustion at T_∞ = 1000 °C: a) Droplet size evolution; b) Visualization of single droplet combustion. 142
4.18 Droplet velocity as a function of the normalized droplet diameter at a) T_∞ = 800 °C; b) T_∞ = 1000 °C. 144
4.19 Droplet Reynolds Number as a function of the droplet squared ratio at furnace temperatures of T_∞ = 800 °C and T_∞ = 1000 °C. 144
4.20 Temporal evolution of burning rate and final burning rate for the Jet A-1 and pure HVO: a) T_∞ = 800 °C; b) T_∞ = 1000 °C. 145
4.21 Average burning rate of pure HVO and Jet A-1 for $D^2/D_0^2 > 0.2$. 146
4.22 Sequence of instantaneous images of pure HVO and nanofuels at a furnace temperature at T_∞ = 1100 °C. 147
4.23 Droplet size evolution of pure HVO and nanofuel at T_∞ = 1100 °C. 148
4.24 Droplet lifetime of pure HVO and nanofuels at T_∞ = 1100 °C ($D_0 = 250\mu m$). . 150

4.25 Sequence of instantaneous images of HVO + 40 nm + 0.5% Al and HVO + 5 μm + 0.5% Al at T_∞ = 800 °C and T_∞ = 1000 °C. 151
4.26 Droplet size evolution of pure HVO and HVO with nano and micron particles: a) T_∞ = 800 °C; b) T_∞ = 1000 °C. 152
4.27 Temporal evolution of the burning rate of HVO with nano and micron particles: a) T_∞ = 800 °C; b) T_∞ = 1000 °C. 153
4.28 Sequence of instantaneous images of HVO + 4% OA and nanofuels at a furnace temperature of $T_\infty = 800$ °C. 156
4.29 Sequence of instantaneous images of HVO + 4% OA and nanofuels at a furnace temperature of $T_\infty = 1000$ °C. 157
4.30 Droplet size evolution of pure HVO, HVO with the addition of 4.0 wt.% of OA: a) $T_\infty = 800$ °C; b) $T_\infty = 1000$ °C. 159
4.31 Droplet size evolution of pure HVO, HVO with the addition of 4.0 wt.% of OA and the different nanofuels studied for: a) $T_\infty = 800$ °C; b) $T_\infty = 1000$ °C. . . . 160
4.32 Average droplet burning rate for the steady-state combustion phase ($D^2/D_0^2 > 0.3$) of pure HVO, HVO with the addition of 4.0 wt.% of OA and the different nanofuels with a particle size of 40 nm studied as a function of the furnace temperatures T_∞ = 800 °C and T_∞ = 1000 °C. 161
4.33 Disruptive burning phenomena for HVO + 40 nm (1.0 wt.%) at T_∞ = 800 °C, where t = 0 ms corresponds to the beginning of the micro-explosion. 163
4.34 Disruptive burning phenomena for HVO + 40 nm (1.0 wt.%) at T_∞ = 1000 °C, where t = 0 ms corresponds to the beginning of the micro-explosion. 164
4.35 Number of fragments as a quantification method for micro-explosion intensity at different furnace temperatures for HVO + 40 nm (1.0 wt.%). 165
4.36 A relation between the number of fragments with the micro-explosion duration different furnace temperature for HVO + 40 nm (1.0 wt.%). 166
4.37 Number of fragments at each region of interest after the micro-explosion for HVO + 40 nm (1.0 wt.%). 167
4.38 Number of fragments as a quantification method for micro-explosion intensity as a function of the particle concentration at different furnace temperatures. . 167
4.39 Micro-explosions at $T_\infty = 800$ °C for different nanofuels: a) HVO + 1% OA + 1% Al; b) HVO + 2% OA + 2% Al; c) HVO + 4% OA + 4% Al. 168
4.40 Micro-explosions at $T_\infty = 1000$ °C for different nanofuels: a) HVO + 1% OA + 1% Al; b) HVO + 2% OA + 2% Al; c) HVO + 4% OA + 4% Al. 169
4.41 Extrapolation of hexadecane a) Gas thermal conductivity; b) Gas heat capacity. 171
4.42 Comparison of temperature and species profiles with and without forced convection. Theoretical film thicknesses are indicated by δ_T (temperature) and δ_M (species) 173
4.43 Droplet Nusselt Number as a function of the droplet squared ratio at furnace temperatures of T_∞ = 800 °C and T_∞ = 1000 °C. 174
4.44 Schematic of a liquid bridge between two particles. 179

4.45 Schematic of the numerical approach to obtain volume fraction profile of nanoparticles inside the droplet. 180
4.46 Flowchart of the model solution algorithm. 181
4.47 Influence of the fuel gas thermal conductivity in the average droplet burning rate for: a) $T_\infty = 800$ °C; b) $T_\infty = 1000$ °C. 182
4.48 Influence of the fuel gas heat capacity in the average droplet burning rate for: a) $T_\infty = 800$ °C; b) $T_\infty = 1000$ °C. 182
4.49 Comparison between experimental and numerical results for the droplet size evolution of pure HVO and HVO with the addition of 4.0 wt.% of OA: a) $T_\infty = 800$ °C; b) $T_\infty = 1000$ °C. 183
4.50 Comparison of average burning rate for experimental and numerical approaches at both furnace temperature: $T_\infty = 800$ °C; $T_\infty = 1000$ °C. 184
4.51 Comparison between experimental and numerical data for the droplet size evolution of: a) HVO + 1% OA + 1% Al ($T_\infty = 800$ °C); b) HVO + 1% OA + 1% Al ($T_\infty = 1000$ °C); c) HVO + 2% OA + 2% Al ($T_\infty = 800$ °C); d) HVO + 2% OA + 2% Al ($T_\infty = 1000$ °C); e) HVO + 4% OA + 4% Al ($T_\infty = 800$ °C); f) HVO + 4% OA + 4% Al ($T_\infty = 1000$ °C). 185
4.52 Solid volume fraction at: a) $T_\infty = 800$ °C; b) $T_\infty = 1000$ °C. Shell thickness and droplet radius ratio at: c) $T_\infty = 800$ °C; d) $T_\infty = 1000$ °C. 186

5.1 Illustration of the experimental setup for spray visualization. 191
5.2 SCHLICK Two-Substance Nozzle Model, 0/2 atomizer a) side view, b) liquid nozzle front view, c) liquid nozzle side view. 191
5.3 Illustration of the experimental setup for spray visualization 192
5.4 Illustration of the experimental setup for PDI measurements. 193
5.5 Illustration of radial and axial positions considered for the PDI measurements. 193
5.6 Rotameter calibration for alternative and conventional jet fuel: ■ - HVO, HVO + 0.5% Al, HVO + 1% Al; ● - Jet A-1 195
5.7 Illustration of the image data processing for breakup length. 198
5.8 Image data processing for breakup length: a) Original image; b) Cropped image; c) Identification of the breakup length. 198
5.9 Influence of the number of frames in the breakup length analysis: a) HVO; b) Jet A-1. Three different air flowrate are considered using 4^{th} fuel operating conditions. 199
5.10 Influence of the threshold value in the breakup length analysis for HVO in the 4^{th} conditions under two air flowrates. 200
5.11 Illustration of the image data processing for spray cone angle. 200
5.12 Visualization of the binarization of the spray using several frames. 201
5.13 Illustration of the parameters relevant for the SCA analysis. 201
5.14 Influence of the a) threshold value and b) number of frames in the SCA analysis. 202
5.15 Sequence of images of HVO equally spaced 1.5 ms under the following conditions: 1^{st} fuel condition, $\dot{m}_a$ = 0.11 g/s. 203

5.16 Sequence of images of HVO equally spaced 1.5 ms under the following conditions: 5^{th} fuel condition, $\dot{m}_a$ = 0.11 g/s. 204
5.17 Sequence of images of HVO equally spaced 2.25 ms under the following conditions for 4^{th} fuel condition: a-c) $\dot{m}_a$ = 0.11 g/s; d-f) $\dot{m}_a$ = 0.22 g/s; g-i) $\dot{m}_a$ = 0.33 g/s. 206
5.18 Sequence of images equally spaced 2.25 ms under the following conditions for 5^{th} fuel condition and $\dot{m}_a$ = 0.22 g/s for: a-c) HVO; d-f) Jet A-1; g-i) HVO + 1% Al. 207
5.19 Influence of liquid Reynolds Number on the normalized mean breakup length, considering $\dot{m}_a$ = 0.11 g/s. 208
5.20 Influence of We_a in the normalized mean breakup length and breakup events for: a) HVO; b) Jet A-1. 209
5.21 Normalized mean breakup length as a function of momentum flux (M) for: a) HVO; b) Jet A-1; c) HVO + 0.5 wt.% Al; d) HVO + 1.0 wt.%. Al. 210
5.22 Normalized mean breakup length correlations. 211
5.23 Influence of the AFR in the spray cone angle (SCA) for: a) HVO; b) Jet A-1. . 212
5.24 Half spray angle concerning the central line at the 4^{th} condition for HVO and Jet A-1. 213
5.25 Jet A-1 calibration parameters at AFR = 7.9 for a) data rate; b) spherical validation. For an AFR = 15.7: c) data rate; d) spherical validation. 215
5.26 Influence of the axial distance for HVO: a) axial velocity; b) Sauter mean diameter. 216
5.27 Influence of the axial distance (Z) for Jet A-1: a) axial velocity; b) Sauter mean diameter. 217
5.28 Histogram of droplet axial velocity for HVO at AFR $\approx$ 8 in the following positions: a) X = 0 mm, Y = 0 mm, Z = 5 mm; b) X = 6 mm, Y = 6 mm, Z = 5 mm; c) X = 0 mm, Y = 0 mm, Z = 15 mm; d) X = 10 mm, Y = 10 mm, Z = 15 mm. . 218
5.29 Droplet diameter histograms for HVO considering several axial distances at an AFR $\approx$ 8: a) central region; b) boundary region. 219
5.30 Influence of the fuel and air mass flowrate for HVO: a) axial velocity; b) Sauter mean diameter. 220
5.31 Influence of the fuel and air mass flowrate for Jet A-1: a) axial velocity; b) Sauter mean diameter. 220
5.32 HVO and Jet A-1 comparison in terms of SMD for a constant fuel flowrate and different air flows: a) $\dot{m}_{air} \approx$ 0.22 g/s; b) $\dot{m}_{air} \approx$ 0.33 g/s; c) $\dot{m}_{air} \approx$ 0.55 g/s. . 221
5.33 Contour of the Sauter mean diameter for X and Y radial distances for HVO: a) AFR = 2.6; c) AFR = 3.9; e) AFR = 6.5. For Jet A-1: b) AFR = 2.6; d) AFR = 3.9; f) AFR = 6.4. 222
5.34 Contour of the axial velocity for X and Y radial distances for HVO: a) AFR = 2.6; c) AFR = 3.9; e) AFR = 6.5. For Jet A-1: b) AFR = 2.6; d) AFR = 3.9; f) AFR = 6.4. 223

5.35 Pure HVO and HVO + 0.5% Al comparison in terms of a, c, e) Sauter mean diameter and b, d, f) axial velocity. In addition, a, b) corresponds to Z = 5 mm, c, d) corresponds to Z = 10 mm and e, f) corresponds to Z = 15mm. 225
5.36 HVO + 0.5% Al and HVO + 1.0% Al comparison regarding a, c) Sauter mean diameter and b, d) axial velocity. In addition, a, b) corresponds to Z = 10 mm and c, d) corresponds to Z = 15 mm. 226
5.37 Probability density function of HVO, HVO + 0.5 wt.% and HVO + 1.0 wt.% at different radial and axial distances for an AFR $\approx$ 8. 227
5.38 Probability density function of HVO, HVO + 0.5 wt.% and HVO + 1.0 wt.% at different radial and axial distances for an AFR $\approx$ 16. 228
5.39 Log-normal and Gamma distributions fitting for HVO, HVO + 0.5% Al and Jet A-1 for an AFR $\approx$ 8. 230

6.1 Spray combustion chamber and fuel and air delivery system. 234
6.2 Combustion chamber design. 235
6.3 Swirl burner design. 236
6.4 Total air mass flow rate for HVO and Jet A-1, considering an AFR = 2. 239
6.5 Volumetric flow rates of the secondary air: a) HVO; b) Jet A-1. 239
6.6 Heating power requirements for secondary air for HVO and Jet A-1, considering an AFR = 2. 240
6.7 Auto-ignition, final boiling point, and 10 vol% distillation temperatures for Jet A-1 and HVO. 241
6.8 Swirl parameters: a) Hub and outer diameter; b) Angle (θ). 243
6.9 Swirl vane angle (θ) for 0.6 < S_N < 0.78. 243
6.10 General heat transfer problem of the swirl burner: a) Illustration; b) Thermal circuit. 244
6.11 Temperature distributions for a parallel-flow heat exchanger. 246
6.12 An approach of the heat transfer problem for the swirl burner: a) Illustration; b) thermal circuit. 247
6.13 Swirl blade: a) Angle (α); b) Dimensions. 251
6.14 Axial swirler velocity representation. 251
6.15 Reynolds number at the swirler exit: a) Function of insulation thickness for two temperatures; b) Insulation thickness influence in percentage. 252
6.16 Reynolds Number considering several blades number: a) HVO; b) Jet A-1. . . 253
6.17 Evaluation of LFL. 257
6.18 Flammability limits for: a) HVO; b) Jet A-1. 258
6.19 Overall dimensions of the combustion system. 259
6.20 Combustion chamber: a) Technical drawing (units in mm); b) Top view. . . . 260
6.21 A technical schematic of the air swirler with 8 blades (units in mm). 260
6.22 Swirl burner: a) Side view; b) Front view. 261
6.23 Thermocouple arrangement for temperature evaluation. 262
6.24 Temperature measurements of thermocouples 1 and 2 considering preheating of secondary air at 400 $^{\circ}C$ and 500 $^{\circ}C$. 263

6.25 Temperature measurements of thermocouples 1, 2, and 3 considering preheating of secondary air at 500 $^{\circ}C$. 263
6.26 Flame images for 6 kW power output: a) ϕ = 0.47 and AFR = 2; b) ϕ = 0.47 and AFR = 2.5. 265

A.1 Biofuels approved conversion processes 311

B.1 Injector technical draw (units in mm). 313

C.1 Air density as a function of temperature. 315
C.2 Air kinematic viscosity as a function of temperature. 315

D.1 The influence of frame number on the SCA for Jet A-1 under different AFR conditions: a) 1000 images; b) 2000 images; c) 3000 images; d) 4000 images; e) 5000 images; f) 6000 images. 317
D.2 Comparsion of SCA for Jet A-1, a) AFR = 2.6, b) AFR = 3.9, c) AFR = 7.8. . . 318

List of Tables

2.1 Factors that contribute to aviation emissions 21
2.2 Minimum proportions of alternative aviation fuels required in ReFuelEU by years. 26
2.3 SAF approved conversion processes 31
2.4 Assumptions made in the simplified model for single droplet combustion . . . 44
2.5 Nanoparticles types and their applications 67
2.6 Summary of nanofuel studies presented in the literature. 75
2.7 Regime map of a liquid jet breakup discharged into a quiescent environment. 88
2.8 Regime map of a liquid jet breakup exposed to a co-flowing air stream. 90
2.9 Correlations for the characteristic length of air-assisted/airblast atomization. . 90
2.10 Criteria for the secondary breakup droplet, at Oh < 0.1. 93
2.11 Table of the mean diameters with their application. 98
2.12 Experimental operating conditions of laboratory burners presented in the literature. 107

3.1 Jet A-1 and HVO properties 112
3.2 Bulk properties of aluminum 114
3.3 Initial procedures for nanofuel preparation. 115
3.4 Visual inspection results considering a particle concentrations up to 1.0 wt.%. 118
3.5 Sedimentation analysis of HVO with 2.0 wt.% of aluminum nanoparticles using a surfactant-to-nanoparticle mass ratios of 1:2 and 1:1. 120
3.6 Sedimentation analysis of HVO with 2.0 wt.% and 4.0 wt.% of aluminum nanoparticles using a surfactant-to-nanoparticle mass ratios of 1:1. 121
3.7 Density, viscosity, and surface for HVO with the addition of surfactant and several particle sizes and concentrations. 122

4.1 Airflow conditions for each furnace temperature. 132
4.2 Furnace temperatures considered on single droplet combustion for liquid fuels. 133
4.3 Furnace temperatures considered on single droplet combustion for HVO with aluminum particles. Study cases are considered with a check mark. 133
4.4 Estimated magnitude order from experimental results. 172
4.5 Continued estimated magnitude order from experimental results. 180

5.1 High-speed camera conditions for breakup length and spray cone angle measurements. 192
5.2 PDI Measurement Configuration. 194
5.3 Operating conditions employed in the experiments related to the imaging technique. Based on that, experiments are dedicated to the breakup length (BL), and spray cone angle (SCA). 196

5.4 Axial (Z) and radial distances (Rx and Ry) employed in the experiments related to the Phase-Doppler Interferometry measurements. 197
5.5 Operating conditions employed in the experiments related to the Phase-Doppler Interferometry measurements. 197
5.6 Pixel size concerning the breakup length experiments for all the fuels. 199
5.7 Pixel size concerning the spray cone angle measurements for all the fuels. . . . 202

6.1 Delivery components specifications. 237
6.2 Fuel and primary air flowrate for several power outputs. 238
6.3 Summary of the design specifications. 240
6.4 Heat exchanger results for L_1 = 0.2 m, L_2 = 0.35 m and L_3 = 0.6 m. 250
6.5 Summary of the swirl burner dimensions. 253
6.6 Summary of the combustion chamber design specifications. 256
6.7 Values of LHV, M_{fuel} and ΔH_c for HVO and Jet A-1. 257
6.8 Operating conditions of preliminary tests. 265

E.1 Fuels operating conditions and the corresponding dimensionless numbers. . . 320

Nomenclature

A	Area	$[\mathrm{m}^2]$
a	Inner Shell Radius	$[\mathrm{m}]$
Al	Aluminum	$[-]$
b	Outer Shell Radius	$[\mathrm{m}]$
$B_{o,q}$	Spalding Heat Transfer Number	$[-]$
C_r	Heat Capacity Ratio	$[-]$
C_1, C_2	Integration Constants	$[-]$
c_p	Specific Heat	$[\mathrm{J\,kg^{-1}\,K^{-1}}]$
D	Droplet Diameter	$[\mathrm{m}]$
$\mathcal{D}$	Mass Diffusivity Coefficient	$[\mathrm{m^2\,s^{-1}}]$
d_j	Laminar Jet Diameter	$[\mathrm{m}]$
E	Emissive Power	$[\mathrm{W\,m^{-2}}]$
f	Excitation Frequency	$[\mathrm{s^{-1}}]$
G	Irradiation	$[\mathrm{W\,m^{-2}}]$
g	Gravitational Acceleration Constant	$[\mathrm{m\,s^{-2}}]$
Gr	Grashof Number	$[-]$
h	Convection Coefficient	$[\mathrm{W\,m^{-2}\,K^{-1}}]$
h	Enthalpy	$[\mathrm{J\,kg^{-1}}]$
h_f^o	Enthalpy of Formation	$[\mathrm{J\,kg^{-1}}]$
h_{fg}	Latent Heat of Vaporization	$[\mathrm{J\,kg^{-1}}]$
J	Radiosity	$[\mathrm{W\,m^{-2}}]$
k	Thermal Conductivity	$[\mathrm{W\,m^{-1}\,K^{-1}}]$
k_B	Boltzmann Constant	$[\mathrm{J\,K^{-1}}]$
K_c	Burning Rate Constant	$[\mathrm{m^2\,s^{-1}}]$
L	Characteristic Length	$[\mathrm{m}]$
$\overline{L}$	Mean Breakup Length	$[\mathrm{m}]$
L_L	Principal Radius of the Liquid Meniscus	$[\mathrm{m}]$
LFL	Lower Flammability Limit	$[-]$
LHV	Low Heating Value	$[\mathrm{J\,kg^{-1}}]$
M	Momentum Flux	$[\mathrm{m}]$
m	Mass	$[\mathrm{kg}]$
$\dot{m}$	Mass Flow Rate	$[\mathrm{kg\,s^{-1}}]$
$\dot{m}''$	Mass Flux	$[\mathrm{kg\,m^{-2}\,s^{-1}}]$

$\dot{m}'''$	Mass Production Rate per unit Volume	$[\mathrm{kg\,m^{-3}\,s^{-1}}]$
MW	Molecular Weight	$[\mathrm{kg\,kmol^{-1}}]$
N	Blade Number	$[-]$
P	Pressure	$[\mathrm{Pa}]$
Pe	Péclet Number	$[-]$
Pr	Prandtl Number	$[-]$
Q	Volumetric Flow Fate	$[\mathrm{m^3\,s^{-1}}]$
q	Heat Transfer Rate	$[\mathrm{W}]$
$\dot{Q}$	Heat Transfer Rate	$[\mathrm{W}]$
R	Specific Gas Constant	$[\mathrm{J\,kg^{-1}\,K^{-1}}]$
r	Radius, Radial Coordinate	$[\mathrm{m}]$
R_u	Universal Gas Constant	$[\mathrm{J\,kmol^{-1}\,K^{-1}}]$
Re	Reynolds Number	$[-]$
Ri	Richardson Number	$[-]$
S_N	Swirl Number	$[-]$
Sh	Sherwood Number	$[-]$
T	Temperature	$[\mathrm{K}]$
t	Time	$[\mathrm{s}]$
U	Axial Velocity	$[\mathrm{m\,s^{-1}}]$
UFL	Upper Flammability Limit	$[-]$
v_r	Bulk Flow Velocity	$[\mathrm{m\,s^{-1}}]$
We	Weber Number	$[-]$
X	Mass Fraction	$[\mathrm{kg\,kg^{-1}}]$
x	X Coordinate	$[\mathrm{m}]$
y	Y Coordinate	$[\mathrm{m}]$
Z	Axial Distance	$[\mathrm{m}]$
Z_F	$1/\left(4\pi\rho_g\mathcal{D}_{F,Pr}\right)$	$[\mathrm{m\,s\,kg^{-1}}]$
Z_T	$c_{pg}/\left(4\pi k_g\right)$	$[\mathrm{m\,s\,kg^{-1}}]$

Greek Symbols

α	Absorptivity	$[-]$
α_h	Half-filling Angle	$[^\circ]$
β	Coefficient of Thermal Expansion	$[\mathrm{K^{-1}}]$
χ	Mole Fraction	$[\mathrm{kmol\,kmol^{-1}}]$
Δh_c	Enthalpy of Combustion	$[\mathrm{J\,kg^{-1}}]$
Δr	Thickness of the Radial Shell	$[\mathrm{m}]$

Δt	Time Interval	$[\mathrm{s}]$
μ	Dynamic Viscosity	$[\mathrm{Pa\,s}]$
ν	Kinematic Viscosity	$[\mathrm{m^2\,s^{-1}}]$
ν_{of}	Oxidizer-to-Fuel Stoichiometric Mass Ratio	$[\mathrm{kg\,kg^{-1}}]$
ϕ	Equivalence Ratio	$[-]$
ρ	Density	$[\mathrm{kg\,m^{-3}}]$
σ	Surface Tension	$[\mathrm{N\,m^{-1}}]$
σ_B	Stefan-Boltzmann Constant	$[\mathrm{W\,m^{-2}\,K^{-4}}]$
σ_m	Mechanical Stress	$[\mathrm{Pa}]$
θ	Contact Angle, Vane Angle	$[^\circ]$
ε	Effectiveness	$[-]$
ε	Shell Porosity	$[-]$
ε_d	Emissivity	$[-]$

Subscripts

0	Initial
1	Gaseous Region Inside the Flame Front
2	Gaseous Region Outside the Flame Front
∞	Furnace
ψ	Tangential Direction
a	Aerodynamic
af	Airflow
air	Air, Ambient
$boil$	Boiling Point
c	Cold
$chamber$	chamber
$conv$	Convection
d	Droplet
eff	Effective
F	Fuel
f	Flame
g	Gas
h	Hot, Hub Diameter
I	Inter-spacing
i	Interface, Inlet, Inner
inj	Injection

ins	Insulation
int	Interior, internal
l, liq	Liquid
max	Maximum
min	Minimum
nf	Nanofluid
np	Nanoparticle
o	Outlet, Outer
Ox	Oxidizer
p	Particle
Pr	Combustion Products
$prim$	Primary
r	Ratio
r, y	Radial Direction
rad	Radiation
ref	Reference
s	Shell, Droplet Surface, Swirl, Outer Diameter
sat	Saturation
sec	Secondary
$steel$	Steel
$stio$	Stoichiometric
T	Temperature
$totalair$	Total air for combustion
$tube$	Quartz Tube of the Drop Tube Furnace
v, vap	Vapor
w	Wall
x	Axial Direction

Acronyms and Abbreviations

AFIR	Alternative Fuels Infrastructure Regulation
AFR	Air-Fuel Ratio
AHRJ	Heterotrophic Algae
APU	Auxiliary Power Unit
ASTM	American Society for Testing and Materials
BL	Breakup Length
CAAFI	Commercial Aviation Alternative Fuels Initiative

COP	United Nations Climate Change Conference
CR	Confinement Ratio
DAC	Direct Air Capture
DLS	Dynamic Light Scattering
DTF	Drop Tube Furnace
EASA	European Aviation Safety Agency
EU	European Union
FAA	Federal Aviation Administration
FOM	Figures of Merit
FT	Fischer-Tropsch
FT-SPK/A	Fischer-Tropsch Synthetic Kerosene with Aromatics
FTIR	Fourier Transform Infrared Spectroscopy
GHG	Greenhouse Gas
HEFA	Hydroprocessed Esters and Fatty Acids
HLB	Hydrophilic-Lipophilic Balance
HVO	Hydrotreated Vegetable Oil
IATA	International Air Transport Association
ICAO	International Civil Aviation Organization
IEA	International Energy Agency
IEP	Isoelectric Point
IRZ	Inner Recirculation Zone
LBO	Lean Blowout
LTO	Landing-Take Off
MDG	Monosize Droplet Generator
MFC	Mass Flow COntroller
MOD	British Ministry of Defence
NTU	Number of Transfer Units
OA	Oleic Acid
ORZ	Outer Recirculation Zone
PDF	Probability Density Function
PDI	Phase-Doppler Interferometer
PIV	Particle Image Velocimetry
ROI	Region of Interest
SAF	Sustainable Aviation Fuels
SCA	Spray Cone Angle
SEM	Scanning Electron Microscope

SMD	Sauter Mean Diameter
TEM	Transmission Electron Microscopy
TRL	Technology Readiness Levels
UV	Ultraviolet Radiation

Chapter 1

Introduction

The present study is devoted to the investigation of conventional and alternative jet fuel, with particular attention to the addition of metallic particles. The work mainly concerns fuel characterization, stability, atomization, and combustion, employing several experimental techniques and numerical approaches developed at Instituto Superior Técnico, Lisbon. This chapter provides an overview of the context and motivation behind this research topic and outlines the objectives of this study. Furthermore, it discusses the contributions of the research project to the scientific community, particularly focusing on the publications that emerged during the development of this thesis. Lastly, it provides a summary of the PhD thesis document.

1.1 Motivation

The modern world is heavily dependent on cargo and passenger transportation due to the prompt industrial development and the improvement of the living standards of society [1]. As a result, there is a current demand for a consistent energy supply while the consumption of fossil fuels persists. In this scenario, the transportation sector mainly relies on petroleum fuels, being around 19% of worldwide energy usage, leading ro approximately 23% of greenhouse gas emissions [2]. Excessive dependence on fossil fuels leads to its depletion, global warming, and air pollution, causing irreversible consequences to the environment in which we currently live. Energy production, industrialization, and agricultural practices are human actions that promotes the release of high greenhouse gas emissions into the atmosphere. The consequences rely on an expected increase of 2°C above pre-industrial levels in the global temperature, influencing humanity and the ecosystem. From this viewpoint, storms, floods, and the extinction of faunal and floral species have become more common, posing serious implications for the biodiversity of our planet. There is a worldwide agreement on restructuring the energy sectors to promote sustainability and ensure long-term energy security [3].

Liquid fuels provided by petroleum are the main source for the transportation sector due to their high energy density, ease of transport and storage, and the extensive global infrastructure established over the past century to maintain this system [1]. However, burning fossil fuels affects global warming due to carbon pollution. In particular, greenhouse gases such as CO_2, CH_4, NO_2, as well as soot, among other pollutants, are daily delivered into the atmosphere, harming the planet. More specifically, in the last years, CO_2 emissions have increased at the most significant reported rates, being the major responsible for global warming. Figure 1.1 shows the distribution of carbon dioxide emissions produced by the trans-

portation sector worldwide in 2022 by sub-sector where road transportation presents the highest greenhouse gas emissions. Aviation also significantly contributes to carbon dioxide (CO_2) emissions into the atmosphere. This sector helps develop employment, promotes commerce, supports tourism, and fosters sustainable development worldwide, resulting in substantial yearly growth. The rapid expansion of this industry, along with its heavy reliance on fossil fuels, leads to considerable greenhouse gas emissions. In contrast to the ground emission sources, aircraft exhaust is released directly into the upper troposphere and stratosphere, leading to a more pronounced greenhouse effect, as previously stated by [4, 5].

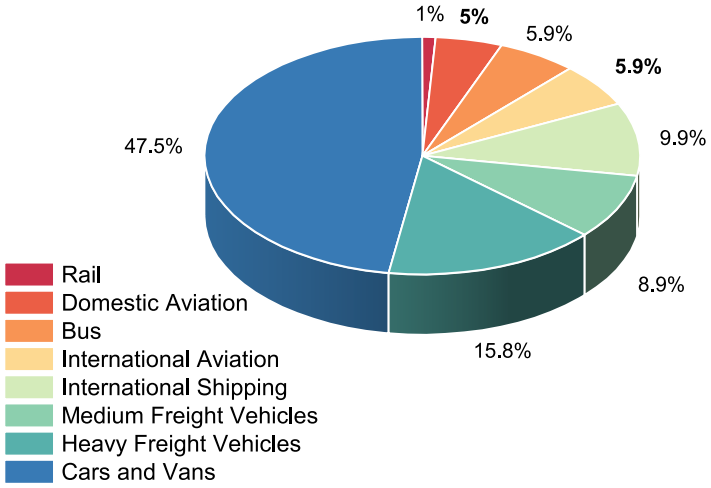

Figure 1.1: Distribution of carbon dioxide emissions produced by the transportation sector worldwide in 2022, by sub-sector. Adapted from [6].

Despite the considerable benefits of air transportation, this industry is responsible for more than 2% of all anthropogenic CO_2 emissions worldwide [7]. Furthermore, emissions related to a non-CO_2, such as water vapor and soot, are also released, increasing environmental concerns, such as radiative forcing from aircraft-induced clouds or aerosol emissions [8]. Consequently, the consumption of fossil fuels should be reduced. Accordingly, more severe measures are imperative to regulate and limit CO_2 emissions from transportation and other energy-related sectors into the atmosphere.

In the current perspective, the world is in a vulnerable condition due to the prolonged effects of the COVID-19 pandemic and Russian - Ukraine conflict. The energy sector, specifically emphasizing the transportation sector, was noticeably affected by the COVID-19 pandemic. The pandemic impact was primarily due to worldwide travel restrictions. During the early phase of the shutdown, restrictions on international air travel and industrial activities led to a substantial reduction in CO_2 emissions [1]. Besides that, the decrease in road, air, and maritime transportation also played a relevant role in the oil demand. However, deactivating the transportation sector is not a viable solution to address environmental issues and mitigate fossil fuel depletion. On the other hand, it can provide valuable insights regarding the influence of the transportation sector on environmental conditions and air quality, as well as the adaption of environmentally friendly transportation systems. More recently, the Russian-Ukraine conflict that was disrupted in February 2022 has threatened the global en-

ergy supply chain and promoted rapid fluctuations in energy prices within a short period of time, presenting significant challenges in ensuring energy security. Several sanctions were applied to the Russian energy supply, resulting in long-lasting, profound, and extensive impacts on the global energy economy [9]. Following the International Energy Agency (IEA), aviation fuel accounts for 6.3% of the total amount of oil consumed [10].

As mentioned earlier, political actions have been implemented to safeguard the global energy economy, supply, and security in the contemporary situation. The first World Climate Conference occurred in 1979, alerting technical and scientific specialists to climate change and future impacts and risks. In the subsequent years, the Kyoto Protocol established emission reduction responsibilities for developed countries from 2008 to 2012, introducing policies, monitoring, and reporting systems [11]. In 2015, the Paris Agreement focused on restricting global temperature increase to 2°C by 2100 and pursuing efforts to limit the increase to 1.5°C. Recently, COP27 and COP28, aligned with the aforementioned, have been dedicated to ambitious targets to mitigate greenhouse gas emissions. Concerning this, it is important to emphasize that there is no definitive solution or clearly defined roadmap for addressing climate change. However, the implementation of all available strategies and technologies is required to solve this current world problem [12].

Therefore, to mitigate global environmental issues and meet the energy requirements of contemporary society, the incorporation of alternative and sustainable energy sources into our daily basis is mandatory. Promising renewable and green energy sources are being intensively investigated, especially in air transportation. The alternatives to the aviation sector can be classified into drop-in and non drop-in fuels. The former corresponds to fuels that can be used as direct substitutes or as a mixture with conventional jet fuel, such as biofuel. The non-drop-in fuels correspond to alternatives that require modifications in aircraft and infrastructure. An example that has been studied is the implementation of hydrogen. In this context, drop-in fuels emerge as the most promising solution in the short/mid-term to address the CO_2 emissions in aviation. In particular, drop-in fuels present a higher technological readiness, possessing a similar energy density to conventional fossil, requiring minor adjustments to the aircraft and its propulsion system [13]. However, from the perspective of long-term investment decisions, it is unclear which option offers the greatest overall environmental performance or whether alternatives are more sustainable or superior to fossil-derived kerosene [14]. Biofuels are a renewable energy source derived from sustainable feedstock and are considered potential carbon-neutral fuels that reduce pollutant emissions. These fuels can be obtained from firewood, animal fats and oils, animal dung, and vegetable oils. Using alternative fuels reduces the risk of scarcity with the variability of energy sources and reduces oil dependence, being a finite natural source [15, 16]. However, a primary challenge remains the availability of a sustainable biomass source to address the aviation demand alongside its costs [13]. Moreover, concerns regarding low energy content, high viscosity, and lower volatility properties are also reported.

As mentioned earlier, liquid hydrocarbon fuels have been indispensable for transportation

for decades, and several alternatives are actively being investigated to address aviation concerns. However, the energy content of liquid hydrocarbons has nearly achieved its theoretical limit, creating further enhancements through chemical methods challenging [17,18]. The expansion of the aviation industry, coupled with the limited volume of engines in the current fleet and increasing concerns about fossil fuel, disrupts the attention to novel solutions. An emerging solution is the addition of nanoparticles to a liquid fuel. This new fuel generation is noted as nanofuels centered on dispersing energetic or inert nanoparticles, i.e., particles in size between 1 nm and 100 nm, stably suspended in conventional liquid fuels [19]. In the 1980s, nanotechnology disrupted attention in the scientific community. Following this, nanotechnology emerged as a research focus for basic and applied sciences due to its potential to address scientific, engineering, and industrial challenges [20]. The nanomaterials possess different physicochemical properties from the bulk material, which inherently depends on their size and shape [21]. Figure 1.2 shows the areas in which nanoscience and nanotechnology are being explored. From a mechanical engineering point of view, the addition of nanoparticles to a liquid fuel has been explored in the transport sector.

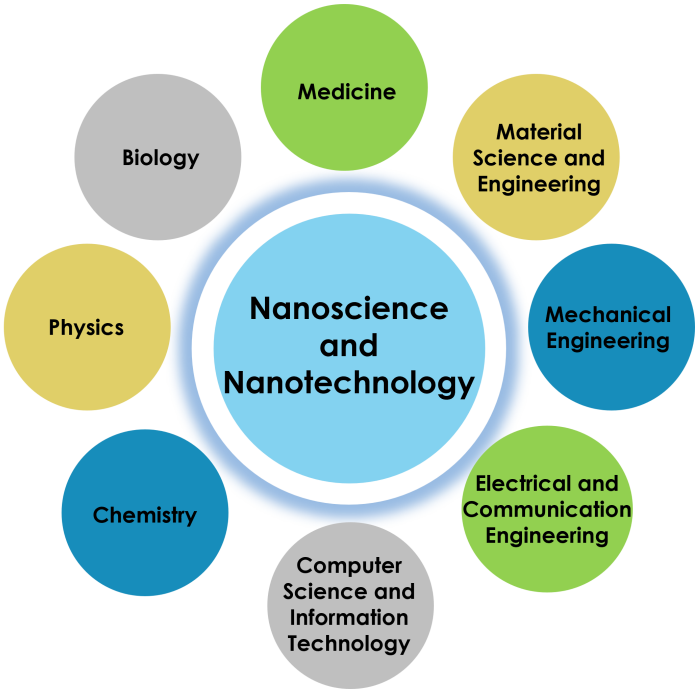

Figure 1.2: Nanoscience and nanotechnology in science and engineering. Adapted from [21].

In particular, metallic nanoparticles, such as aluminum, magnesium, and boron, can exhibit higher volumetric and gravimetric energy densities that potentially enhance the fuel reactivity [18]. Due to the increased reactive surface area allied with the improved thermal and mass transport characteristics of nanomaterials, the high heat of formation of these metallic fuels affects the combustion behavior. Incorporating metal nanoparticles into liquid fuels has a catalytic effect, improving the combustion rate, reducing ignition delay and fuel consumption, and lowering emissions [22]. Nanoparticles exhibit a substantially higher surface-area-to-volume ratio, providing a larger contact surface area during the rapid oxidation process [23]. Consequently, for a fixed combustor volume, as in aircraft, adding metal

particles to a liquid fuel can enhance the energy released during combustion [24]. For this reason, adding nanoparticles to biofuel is a noteworthy research subject that enhances fuel combustion performance to mitigate their inherent concerns. In this context, several investigations dedicated to the addition of nanoparticles to alternative fuels are presented in the literature, addressing different fields of research [17, 19, 25–28]. Despite their potential, nanofuels present certain challenges, particularly regarding emissions from the combustion of solid particles and long-term stability. To establish nanofuels as feasible future fuels, it is essential to comprehend the combustion mechanisms and implement methods to minimize particle aggregation.

In the transportation sector, liquid fuel is injected into the combustion chamber. In this practical spray system, liquid droplets are injected either with high momentum or into a strongly accelerating flow field after primary atomization. In both cases, the aerodynamic shear at the interface between the droplet and the flow field induces disintegration (i.e., secondary atomization) [29]. This secondary atomization of liquid fuel increases its interfacial area with air, which in turn improves the evaporation and mixing of fuel with air. Finally, when mixed properly, ignition can occurs. The characteristics of a fuel spray, such as liquid phase penetration, atomization, air entrainment, and mixture formation, play a crucial role in controlling the combustion process, where investigations dedicated to single droplets are also crucial. As a result, experimental and numerical studies are valuable in advancing scientific knowledge. Experimental research enables the examination of theoretical hypotheses by providing data regarding phenomena through diverse empirical methods. This improves the accuracy of models and serves as a useful tool for numerical research. Nevertheless, conducting experimental studies can present challenges related to substantial resources, such as time, funding, and equipment. Thus, numerical work reduces the cost of equipment and materials and enables the analysis of complex phenomena in cases where analytical solutions are difficult to acquire or evaluate experimentally. In this respect, it is essential to investigate the entire process comprehensively, from the initial stages of their preparation and characterization, to discover methods that could improve the stability of nanofuels is essential. Following that, and considering that single droplet combustion is a prerequisite to understanding spray combustion, experimental and numerical approaches are required to understand nanofuel combustion mechanisms. In light of this, the addition of nanoparticle particles also impacts the atomization process, requiring a detailed understanding of their effects on primary and secondary atomization. Consequently, it affects spray combustion in terms of performance and emissions. Finally, the development of laboratory-scale burners is essential for research progress, allowing a representation of real combustors with a simpler design and well-defined and optically accessible configurations to enable detailed data acquisition and facilitate modeling.

1.2 Objectives

Research on alternative fuels to address fossil fuel dependency and environmental concerns is a critical issue. It is imperative to change the paradigm of the current world. Understanding the factors and repercussions of our actions is a path to finding solutions. In particular, aviation has notorious implications for globalization, operating on a conventional fuel derived from finite fossil fuels and responsible for high pollutants and greenhouse gas emissions. Consequently, identifying solutions to fulfill aviation fuel requirements and mitigate environmental issues is essential. Recently, nanoparticles have started to be perceived as a promising means to improve the quality of so-called alternative fuels that can be used in actual engines, allowing for a smooth transition to other more disruptive propulsion technologies.

The main objective of this PhD thesis is to evaluate fundamentally the potential use of the addition of nanoparticles to a liquid alternative fuel in terms of stability, atomization, and combustion. To accomplish this purpose, a comparative analysis of conventional fuel, pure alternative fuel, and nanofuels (liquid fuel containing nanoparticles) is performed. To attain the main objective of this study, several specific goals should be addressed in terms of:

- Selection and characterization of the fuels and particles, followed by the identification of physical and chemical methods to improve the stability of nanofuels, particularly for higher particle concentration. The stability of different particle sizes and concentrations is evaluated through visual inspection.

- Adaptation of the experimental setup to evaluate nanofuel single droplet combustion in a droplet tube furnace using a high-speed camera and image data processing. The influence of furnace temperatures, particle sizes, and concentrations is investigated concerning droplet size evolution and disruptive burning phenomena. This includes a detailed analysis of the micro-explosions nanofuels droplet combustion. Additionally, conventional jet fuel, pure biofuel, and nanofuels are compared.

- Development of a simplified macroscopic model focused on single droplet combustion of a multi-component fuel to a surrogate fuel, as well as the influence of adding nanoparticles to a liquid fuel. The purpose is to compare numerically the combustion behavior of a single droplet involving pure biofuel and biofuel with nanoparticles.

- Evaluation of the atomization process for conventional and alternative jet fuel. The influence of nanoparticles in primary and secondary atomization is addressed. Spray visualization under different operating conditions allied with measurements on the spray cone angle is conducted. Additionally, the measurements concerning the breakup length lead to the development of a correlation and comparison with the literature. The Phase-Doppler interferometer technique is adopted to compare fuels droplet diameter and velocity distribution.

- Development of a laboratory combustion chamber to evaluate the spray combustion of liquid fuels.

1.3 Contributions

The present work examines alternative fuels in the aviation context using experimental and numerical approaches. In light of this, a literature review concerning the challenges of this industry in terms of solutions to address fossil fuels and environmental concerns was carried out. For a short/mid-term solution, biofuels present the most acceptable alternative. Besides their noticeable benefits, concerns regarding the demand for aviation fuels require further investigation. Recent advancements in nanotechnology have enabled innovative research using nanoparticles. These nanoparticles typically range from 1-100 nm and possess properties different from those of bulk material. Investigations dedicated to enhancing biofuel performance using nanoparticles are a novel and relevant subject, offering solutions to the issues arising from biofuel applications. Due to this, the research topic of this PhD thesis centers on adding aluminum nanoparticles to an alternative aviation fuel. The objective is to complement and fill the gaps highlighted in the literature discussed by the scientific community. A significant issue related to the application of nanofuels is their stability. The present work investigates diverse approaches established to guarantee the stability of the nanoparticles in alternative fuels for long periods and address the potential use of nanofuel in real applications. This part of this work proved that physical and chemical procedures are essential to ensure a stable nanofuel for long periods, particularly for higher particle concentrations. Moreover, in terms of fuel characterization, major deviations from the pure fuel were noticed as an influence of the particle concentration. This observation was incorporated into the subsequent phases of the research, particularly in the atomization and combustion experiments. A specific procedure regarding the nanofuel preparation was established to guarantee their stability during the experiments.

Following the nanofuel preparation and characterization, experiments on single droplet combustion were performed. This is an essential task in the field of fuel combustion, acting as a preliminary step. In the available literature, most of the publications focus on nanofuel single droplet combustion experiments using a supporting fiber method. However, this technique significantly affects the combustion process. In particular, for nanofuels, the supportive fiber can act as a nucleation site that influences the disruptive burning phenomena. An experimental setup presented in the Instituto Superior Técnico was modified to guarantee safety and control during the nanofuel combustion. In contrast to the majority of existing literature concerning nanofuel droplets, the experimental setup used in the present study focuses on the falling droplet method, allowing high environment temperatures to promote an acceptable compromise between experimental and practical conditions. This technique is more complex and requires a more profound understanding of processing the acquired data. The findings acquired from the single droplet combustion experiments were processed and analyzed using developed in-house algorithms. Enhancement of the burning rate and the occur-

rence of disruptive burning phenomena, as previously highlighted in the literature, prove the benefit in terms of nanofuel use for the transportation sector. To address the gap in knowledge concerning disruptive phenomena, a detailed analysis was conducted to understand the influence of particle concentration and furnace temperature in these events. Moreover, a study comparing alternative and conventional jet fuels was undertaken to determine the viability of these emerging solutions in the preliminary stages. A simplified macroscopic model was developed to better understand the improvement in the combustion process due to the addition of metallic particles to liquid fuels, employing a surrogate fuel to facilitate the multicomponent behavior of a biofuel already tested in aviation gas turbines. This simplification enables further research and advancements in related areas of study. Current investigations dedicated to nanofuels focus on individual aspects during the evaporation and combustion, discarding their complex interconnections. Consequently, the present work explored and implemented in the model the most relevant mechanism that must be considered in nanofuel combustion for different furnace temperatures and particle concentrations, contributing to the studies in the nanofuel field.

Considering the benefits and considerations acquired in single droplet combustion findings, evaluating the spray combustion is indispensable to fully understand the potential use of nanofuel. Due to this, understanding the atomization of a nanofuel was prioritized as the first step in designing a laboratory combustion chamber to evaluate spray combustion performance and its emissions. Studies involving primary and secondary atomization in nanofuels are relatively rare due to their novelty. Thus, the present study explored the spray characteristics of conventional and alternative jet fuel. Their inherent properties affected by the particle concentration and different operating conditions were considered for deeper comprehension. To accomplish this purpose, an experimental setup was developed to employ two techniques: imaging and a Phase Doppler Interferometer. Measurements dedicated to the breakup length, spray cone angle, droplet diameter, and velocity profiles for conventional and alternative jet fuel are discussed, addressing the existing gaps in knowledge related to this subject. A correlation regarding the breakup length, including the nanofuels, is presented and compared with the literature available. Moreover, the influence of the physical properties and air-fuel ratio are examined in the remaining spray characteristics. The study culminates in one of its most significant objectives: developing a combustion chamber for liquid fuels. The purpose was to design and build a modular burner for liquid fuels, considering the most relevant findings during the progression of this study. The knowledge of fuel properties, single droplet combustion, and spray provided insight to address the difficulties in developing a burner. In particular, attention to fuel injection, potential harmful emissions, and flame stability, among other aspects, were considered, and preliminary experiments were carried out to validate the laboratory combustion chamber. The advancement of the burner is fundamentally important, as it offers an experimental framework for evaluating alternative fuels in aviation and other sectors that require the use of liquid fuels. The present research serves as a benchmark in nanofuel stability, characterization, atomization, and combustion. Throughout this PhD thesis, several publications have been performed, exchanging knowledge with the scientific community. The contributions are presented below.

Journal Publications

1. Ferrão, Inês; Vasconcelos, Daniel; Ribeiro, Daniela; Silva, André; Barata, Jorge. "A study of droplet deformation: The effect of crossflow velocity on jet fuel and biofuel droplets impinging onto a dry smooth surface". Fuel 279, 118321 (2020). http://dx.doi.org/10.1016/j.fuel.2020.118321

2. Ferrão, Inês; Silva, André; Moita Ana; Mendes Miguel; Costa, Mário. "Combustion characteristics of a single droplet of hydroprocessed vegetable oil blended with aluminum nanoparticles in a drop tube furnace". Fuel, 302, 121160 (2021). https://doi.org/10.1016/j.fuel.2021.121160

3. Ferrão, Inês; Mendes, Miguel; Moita, Ana; Silva, André. "The addition of particles to an alternative jet fuel". Fuels, 3(2), 184-206 (2022). https://doi.org/10.3390/fuels3020012

4. Ferrão, Inês; Mendes, Tomás; Mendes, Miguel; Moita, Ana; Silva, André. "Influence of aluminum nanoparticles in alternative fuel: Single droplet combustion experiments and modeling". Fuel, 379, 132850. (2025) https://doi.org/10.1016/j.fuel.2024.132850

5. Ferrão, Inês; Panão, Miguel; Mendes, Miguel; Moita, Ana; Silva, André. "How different are conventional and biofuel sprays applied to aviation? An infodynamic comparative analysis". Experiments in Fluids, 66(6), 1-31. (2025) https://doi.org/10.1007/s00348-025-04042-9

Conference Publications

1. Ferrão, Inês; Ribeiro, Daniela; Barata, Jorge; Silva, André. "A Study of a Single Droplet Impinging onto a Sloped Surface: Jet-Fuel and Biofuel Mixtures" 29^{th} European Conference on Liquid Atomization and Spray Systems - Paris, France (2-4 September 2019).

2. Ferrão, Inês; Vasconcelos, Daniel; Ribeiro, Daniela; Silva, André R. R; Barata, Jorge. "Jet Fuel and Biofuel Droplets Impinging onto a Dry Surface: Effect of Crossflow Variation" 14^{th} International Conference on Energy for a Clean Environment - Madeira, Portugal (8-12 September 2019).

3. Ferrão, Inês; Silva, André; Moita, Ana; Mendes, Miguel; Costa, Mário. "Single Droplet Combustion of Aluminum Nanoparticles added to a Biofuel" 21^{st} Annual Conference on Liquid Atomization and Spray Systems - Zhenjiang, China (23-26 October 2020)-

4. Ferrão, Inês; Mendes, Miguel; , Moita, Ana; Silva, André. "The Influence of Aluminum Particles in a Hydroprocessed Vegetable Oil combustion" 10^{th} European Combustion

Meeting - Naples, Italy (14 - 15 April 2021).

5. Ferrão, Inês; Mendes, Miguel; Moita, Ana; Silva André. "Single Droplet Combustion of Aluminum Nanoparticles added to a Biofuel: Effect of Particle Concentration and Ambient Temperature" ICLASS 2021 - 15^{th} Triennial International Conference on Liquid Atomization and Spray Systems - Edimburgo, United Kingdom, (29 Aug. - 2 Sept. 2021).

6. Dias, Francisco; Ferrão, Inês; Mendes, Miguel; Moita, Ana; Silva, André. "Mathematical Approach for Modeling a Single Droplet Combustion of Jet-A1 and Alkanes" 5^{th} Meeting of the Young Researchers of LAETA - Lisboa, Portugal (5 - 6 May 2022).

7. Ferrão, Inês; Mendes, Miguel; Moita, Ana; Silva, André. "How do nanoparticles affect the combustion of a biofuel?" 5^{th} Meeting of the Young Researchers of LAETA - Lisboa, Portugal (5 - 6 May 2022).

8. Dias, Francisco; Ferrão, Inês; Mendes, Miguel; Moita, Ana; Silva, André. "Numerical Analysis of a Single Droplet Combustion of Jet-A1 and Alkanes" AIAA Aviation Forum - Chicago, EUA (27 June – 1 July 2022).

9. Ferrão, Inês; Mendes, Miguel; Moita, Ana; Silva, André. "Experimental investigation of disruptive burning phenomena on nanofuel droplets" 20^{th} International Symposium on Application of Laser and Imaging Techniques to Fluid Mechanics - Lisboa, Portugal (11-14 July 2022).

10. Mendes, Tomás; Ferrão, Inês; Mendes, Miguel; Moita, Ana; Silva, André. "The Impact of High Particles Concentration in a Biofuel Droplet Combustion" 31^{st} Conference on Liquid Atomization and Spray Systems - Virtual, Israel, (6-8 September 2022).

11. Ferrão, Inês; Mendes, Miguel; Moita, Ana; Silva, André. "Spray dynamics of conventional and alternative jet fuel" 32^{nd} Conference on Liquid Atomization & Spray Systems - Napoli, Italy (4-7 September 2023).

12. Ferrão, Inês; Mendes, Miguel; Moita, Ana; Silva André. "An Experimental Analysis of the Air-Liquid Interaction of Conventional and Alternative Aviation Fuel" ICLASS 2024 - 16^{th} Triennial International Conference on Liquid Atomization and Spray Systems, Shanghai, China, (June 23-27, 2024).

13. Panão, Miguel; Ferrão, Inês; Moita, Ana. "Is biofuel HVO an alternative in aviation? An Infodynamic Comparative Analysis" 21^{st} International Symposium on Application of Laser and Imaging Techniques to Fluid Mechanics - Lisboa, Portugal (8-11 July 2024).

14. Ferrão, Inês; Mendes, Miguel; Moita, Ana; Silva André. "Insights on Liquid Jet Breakup and Spray Formation of an Air-Assisted Atomizer: Conventional and Alternative Jet Fuel" 21^{st} International Symposium on Application of Laser and Imaging Techniques to Fluid Mechanics - Lisboa, Portugal (8-11 July 2024).

1.4 Overview

This PhD thesis document is organized into seven chapters, as shown in Figure 1.3. **Chapter 1** includes the motivation and context, main objectives, and contribution of the present study. The **Chapter 2** is dedicated literature review, focusing firstly on aviation fuel contextualization, followed by droplet and spray background. This includes the main findings in both experimental and numerical approaches regarding single droplet combustion and the latest advancements in the nanofuels field. Moreover, the concept and practical applications of sprays are discussed, addressing the most relevant subject in this topic. Subsequent to the introduction and literature review of the present research, **Chapter 3** is devoted to fuel preparation, characterization, and study focus on the nanofuel stability. Following the fuel preparation and characterization, **Chapter 4** is dedicated to a single droplet combustion study involving experimental and numerical approaches. The methodology adopted, operating conditions, and image data processing for the experimental work are presented. The experimental results are subsequently compared with the numerical findings related to a simplified macroscopic model. In this context, the influence of adding nanoparticles to a liquid fuel is evaluated numerically, where the numerical methodology is described. **Chapter 5** is dedicated to the study of spray under non-reacting conditions and highlights the two experimental setups employed, as well as the methodology, operating conditions, and image processing. In addition, the results are discussed centered on the visualization, breakup length, spray cone angle, and distribution of the droplet diameter and velocities. **Chapter 6** focuses on the discussion of developing a combustion chamber for liquid fuels. The design and build of the burner are presented, including the preliminary experiments to validate the experimental setup. Finally, **Chapter 7** outlines the most relevant conclusions of this study and suggests future work.

Figure 1.3: Thesis document outline.

Chapter 2

Literature Review

2.1 Introduction

The current chapter provides an overview of conventional liquid fuels in current times and their reliance on the aviation industry. From this point of view, aviation fuel composition, global emissions, and their environmental impact are outlined. Strategies to mitigate the concerns regarding using a renewable energy source are also presented. Subsequently, a detailed review of topics pertinent to the research focus of this thesis dedicated to droplets and sprays is presented. Fundamental concepts, practical applications, and the factors that affect their dynamics will be discussed. The advancement in the nanofuel field is presented, addressing their advantages and disadvantages to better understand their viability in practical application. Investigations concerning the experimental and numerical studies of single droplet combustion are also outlined. In addition, the understanding of mechanisms related to the breakup and atomization of liquid fuels, considering pure fuels and fuels with nanomaterials, is addressed as being essential in the area of combustion and propulsion systems.

2.2 Aviation Fuels Contextualization

Air transport has a relevant impact on globalization, connecting people and businesses worldwide. In this context, the aviation industry has allowed a favorable correlation between travel time and distance. From an economic perspective, it has generated numerous jobs, promoted the development of the tourism industry, and facilitated international trade. This emphasizes the disruption of the general interest in safety and an increasing desire for enhancements in the aviation industry. In terms of social development, it has promoted educational opportunities, cultural exchange, and fast response during disasters, allowing the delivery of food, medical, and rescue services [30]. Consequently, the growth of air transport has been notorious in the last decades. Figure 2.1 shows the world passenger traffic evolution from 1945 to 2022. As evident, its development has been noteworthy until the appearance of the coronavirus (COVID-19) pandemic. The appearance of COVID-19 posed one of the most critical challenges in aviation history. The global lockout caused an unprecedented decline in world passengers in recent years to prevent the virus from spreading. Despite the challenges due to the pandemic, it is predicted that there will be continuous growth in the aviation sector, with passenger miles expected to double by 2050, compared to 2010 [31]. Apart from this period of travel restrictions, air transport remains essential for the global economy and society and should operate sustainably and efficiently in the near future.

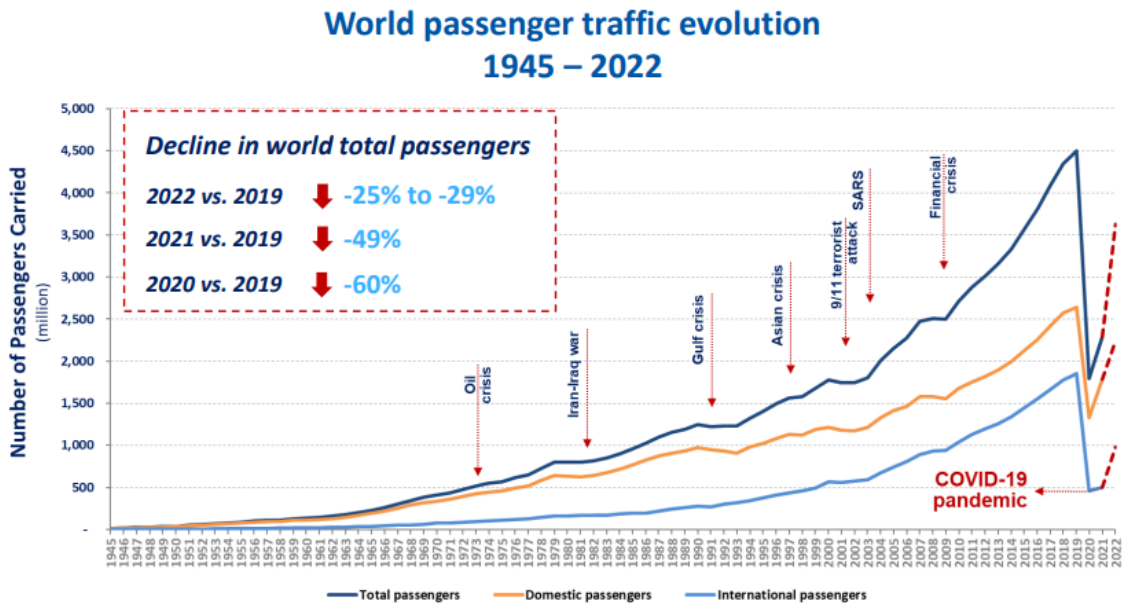

Figure 2.1: World passenger traffic evolution, 1945–2022, adapted from [32].

Due to this, fuel consumption is a crucial element of the expansion of the aviation industry. This means that an increase in air traffic requires an increase in energy usage. Jet fuel is a specialized aviation fuel that is precisely prepared for the propulsion of aviation gas turbine engines, being one of the highest operating costs for the aviation industry [33]. According to Edwards et al. [34], fuel costs have increased and account for approximately 32% of global operating expenses for airlines in 2014, five times greater than in 2003 values [35]. In recent decades, aviation fuel costs have exhibited substantial fluctuations directly related to the variation in petroleum global supply [36].

Aviation fuel, a petroleum-derived fuel utilized for aircraft propulsion, considers rigorous quality standards compared to fuels employed in road transportation. Jet fuel supplies an energy source for propulsion and performs other functions for the proper operation of aircraft, such as a hydraulic fluid and cooling medium in aircraft engines [37,38]. Conventional aviation fuel is provided by kerosene, produced from crude oil, a finite and non-renewable energy source [39]. In particular, coal, oil, and gas are the three most recognized primary fossil fuels [40]. Fossil fuels containing carbon are a product of geological processes from the remains of microscopic organisms hundreds of millions of years ago under high pressure and temperature and are safely stored underground. Crude oil or petroleum has been crucial in promoting the industrial world and improving living standards. This mixture of hydrocarbons provides a valuable energy source for transportation, heating, and industrial purposes. To acquire aviation fuel from crude oil, refinery processes, such as distillation, hydro treatment, and catalytic reforming, are necessary [41]. The refining process involves separating various components through atmospheric and vacuum fractional distillation. The process begins with heating the crude oil, causing the components to boil at different temperatures, transforming them into gases. These gases are subsequently recondensed into liquids. Figure 2.2 shows the refining process, initiating from the heating phase and concluding with

acquiring various products used in quotidian applications.

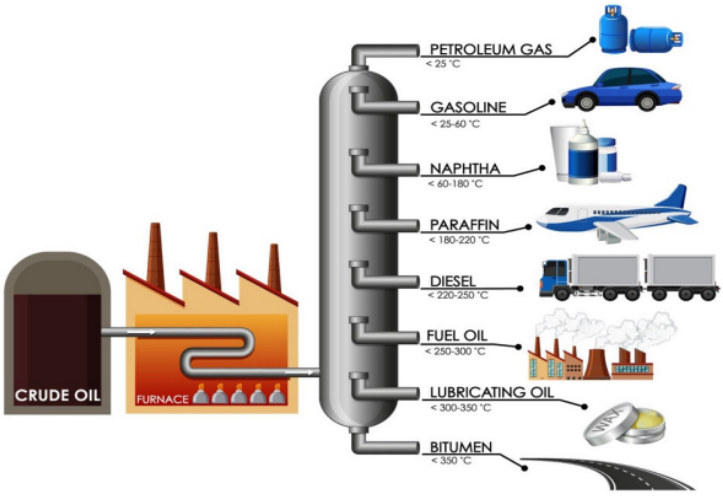

Figure 2.2: By-products of fractional distillation, derived from [42].

The lowest boiling fractions are obtained from the top of the distillation column, while the residual fraction or bottom fractions can operate as a source of heavy boiler fuel [10]. Jet kerosene is commonly distilled between a boiling point range of 150 °C to 300 °C. Subsequently, it combined high-octane streams and additives to satisfy the performance criteria required for aviation fuel [39]. Presently, the majority of removed jet fuel is derived from the middle distillates of crude oil, specifically the kerosene fraction, which distills between the gasoline and diesel fractions.

In 1939, aviation gasoline (avgas) fuelled the first successful aircraft. Gasoline was chosen due to its wide accessibility during that period, being the primary fuel for all piston-engine aircraft. A few years later, Frank Whittle used ”illuminating kerosene” as fuel for a turbojet engine that demonstrated a higher tolerance for various fuel properties than piston engines [43]. Concerns regarding gasoline use were mainly due to its high volatility and poor lubricity, leading to wear and reducing the life of metering pumps [44]. Consequently, in the early stages, it became evident that modifications would be necessary for avgas to operate effectively in jet-powered aircraft. Thus, the requirement for increased power has disrupted the attention for aviation gas turbines powered by kerosene, leading to further advancements and modifications in the conventional aviation fuels named jet fuel [45]. The selection of liquid fuel as an energy source for the aviation sector was mainly based on petroleum advantage. In this respect, liquid fuels possess a higher energy content per unit volume than gases, which are more manageable and suitable for handling and distribution than solids. Among the liquid options available, liquid hydrocarbons present an ideal balance for energy content, availability, and price [45].

2.2.1 Jet Fuel Composition

Conventional jet fuel, typically denoted as jet fuel, is a complex fuel composed of several components, featuring a carbon chain length ranging from C_8 to C_{16}. Hydrocarbon compounds

in jet fuel can be classified into four groups: n-alkanes, isoalkanes, cycloalkanes, and aromatics [46, 47]. The predominant components are branched and linear paraffins and naphthenes (cycloalkanes), commonly representing more than 70% of the components by volume. Paraffins present a high hydrogen to carbon ratio, leading to a substantial heat release per unit weight and cleaner combustion compared to other hydrocarbons [48]. Cycloparaffins exhibit a lower hydrogen-to-carbon ratio, which generates less heat per unit weight while contributing to the fuel increased density. However, their advantage relies on the reduction of the fuel freeze point essential for high altitude flights [49]. Aromatics enhance the fuel lubricity and guarantee that seals and O-rings operate as intended to prevent fuel leakage [50], and should not exceed 25% in jet fuel composition. According to Blakey et al. [49], there is a minimum value for the aromatic content of 8% in jet fuel due to the aging seals in the aircraft and engine potentially leaking.

The fuel composition affects its physical properties and should comply with the specifications established for each transportation sector [38]. For the aviation industry, the initial fuel specifications emerged in 1943 in the UK and 1944 in the US [43, 51]. Therefore, many changes were performed over the years, primarily driven by safety and security considerations [49]. Civil aviation fuel specifications are regulated by the American Society for Testing and Materials (ASTM) International and the British Ministry of Defence (MOD). In this respect, ASTM D1655 Standard Specification for Aviation Turbine Fuels and MOD Defence Standard 91-91 are the specifications for jet fuel supported by an extensive knowledge of the production and utilization of aviation fuels derived from conventional sources [52]. In general, the fuel requirements and considerations rely on [33, 49, 50]:

- High heat content for maximum range or payload
- High specific energy to decrease take-off weight
- Good atomization
- Rapid evaporation
- Good burning characteristics, including relight capability at altitude
- Low freezing point and viscosity in cold temperatures to promote safe operation at cruising altitudes
- Maximum allowable sulfur and aromatics content to ensure correct O-ring seal and prevent fuel leakage
- Minimum fuel electrical conductivity
- Minimum allowable flash point to ensure safety operations due to the fire-hazard consideration
- Low explosion risk
- High specific heat capacity
- Free from contaminants
- Minimum carbon formation
- Low viscosity and high lubricity

- High thermal stability that prevents the chemical decomposition of the fuel within the gas turbine engine
- Wide availability and acceptable cost
- Products of combustion acceptable environmentally
- Good ground storage and handling characteristics

The main fuels employed in civil aviation are Jet A and Jet A-1. Jet A is used in the United States, whereas Jet A-1 is employed throughout the rest of the world. The main difference between these fuels is the freezing point. For Jet A, the freezing point is -40 °C while the Jet A-1 presents -47 °C. The lower freezing point of Jet A-1 is more appropriate for long-haul flights, especially on polar routes during the winter [45]. Considerations regarding fuel cost and accessibility influence the use of Jet A, especially in the US. The typical fuel for military purposes is JP-5 and JP-8, specifically developed for high-performance requirements. The main distinction between civil and military fuel is the use of additives dedicated to the prevention of water in fuel, fuel pump failure, corrosion, icing inhibitors, as well as incidents due to static discharge during fuelling procedures and acidity level [38, 44, 53].

In aviation gas turbines, power generation occurs by converting the fuel chemical energy into mechanical energy. It is essential to understand how a gas turbine operates and the mechanisms behind its function. An aviation gas turbine is an internal combustion engine responsible for aircraft propulsion for air transportation. This complex engine has several systems and subsystems that should operate simultaneously [54]. As previously stated, the objective of this engine is to supply propulsive energy to propel the aircraft during its mission with the suitable attainment of performance, efficiency, and security [54]. The fundamental ideas regarding the operation of a gas turbine rely on the intake and compression of the air, combustion, and finally, expansion and exhaust, where the transformed energy is employed.

Shortly and in-depth, thrust is generated by the propulsion engine to propel an aircraft through the air. Firstly, the engine captures the incoming air, and the air intake duct must ensure the engine receives unrestricted and clean airflow. A portion of this incoming air flows through the fan, proceeding into the core compressor. Subsequently, it enters the combustion chamber, where it combines with fuel, leading to combustion. The combustion area controls the combustion process between air and fuel, releasing heat that allows the expansion and acceleration of air. The combustion chamber should efficiently burn fuel across various operational conditions while guaranteeing stable combustion to prevent flame blow-out [55]. Moreover, the gases escaping the combustion chamber must be suitably cooled by mixing with air to protect the turbine blades from damage. Generally, the fuel is introduced in the combustion area as a well-atomized spray in combustors. The decrease in droplet diameter is directly related to an increase in the evaporation rate. The spray quality is relevant for combustion efficiency, stability limits, and pollutant emission. There are three combustor types: tubular, tuboannular, and annular [55]. Thereafter, the hot exhaust passes through the core and fan turbines before ultimately leaving through the nozzle. A large amount of air should

be supplied to the turbine to generate the required power. The conversion of the gaseous energy of the air and burned fuel mixture out of the combustor into mechanical energy is performed by the turbine that drives the compressor (which might incorporate an additional fan or propeller). A shaft connects the turbine and compressor units, as the turbine provides the power needed to operate the compressor. The purpose of the fan is to significantly increase the amount of air moving through the engine, thereby increasing the engine thrust. In conclusion, the gas flow exiting the turbine is pushed to the atmosphere in an exhaust nozzle to generate thrust or propulsion power. The remaining incoming air moves through the fan and bypasses the engine. The proportion of air that goes around the engine compared to the air passing through the core is denominated as the bypass ratio. Thrust is produced by air flowing through the fan (bypass air) and the gas generator. High-bypass ratios are desired in civil aviation for satisfactory fuel efficiency and low noise [56]. Currently, turbofan engines power most commercial aircraft [13], as depicted in Figure 2.3.

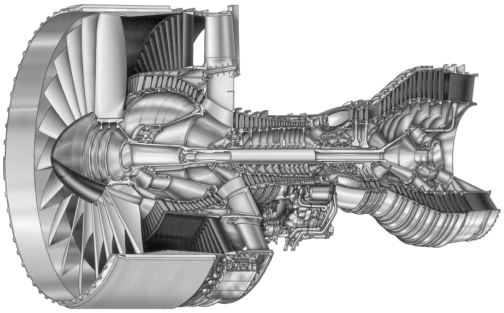

Figure 2.3: Pratt and Whitney PW4084 turbofan, the jet engine used to power Boeing 777 aircraft, adapted from [57].

2.2.2 Jet Fuel Emissions

As noted earlier, the fuel combustion occurs in the combustion chamber. The fuel is atomized, breaking into multiple smaller droplets, increasing its surface area. This atomized liquid fuel is mixed with pressurized air, leading to ignition and combustion that releases gaseous and non-gaseous species at ground level, such as at the airport and flight level, which may impact the local air quality and the climate [58]. Due to the complex chemical composition of aviation fuel, greenhouse gases, and pollutants are released into the atmosphere when they react with air under specific conditions that are inherently related to the composition of the fuel. According to the literature, the emissions are also associated with the temperature and pressure of the combustion chamber, air-fuel ratio, and the efficiency of the atomized liquid fuel [56, 59]. Moreover, engine technology, model, and thrust additionally affect the emissions expelled by the aircraft. The air quality is impacted by high-altitude emissions as well as by ground emissions in the vicinity of large airports [60]. Considering the complete and ideal combustion of hydrocarbons, the products released are CO_2 and water without any pollutants. Nevertheless, the combustion in real engines is never ideal, leading to the formation of additional pollutants [61]. The burning of jet fuel emits carbon dioxide (CO_2), water vapor (H_2O), carbon monoxide (CO), unburned hydrocarbons (HC), sulfur oxides (SO_x), soot particles (C_{soot}), nitric oxide (NO), and nitrogen dioxide (NO_2), where NO and NO_2 to-

gether are expressed as NO_x [36]. Figure 2.4 shows the emissions produced from jet fuel combustion and its impact on the environment and society. The emissions can impact the development and duration of contrails, which have implications on climate through radiative forcing [61]. Emissions consist of a component of the airworthiness certification process

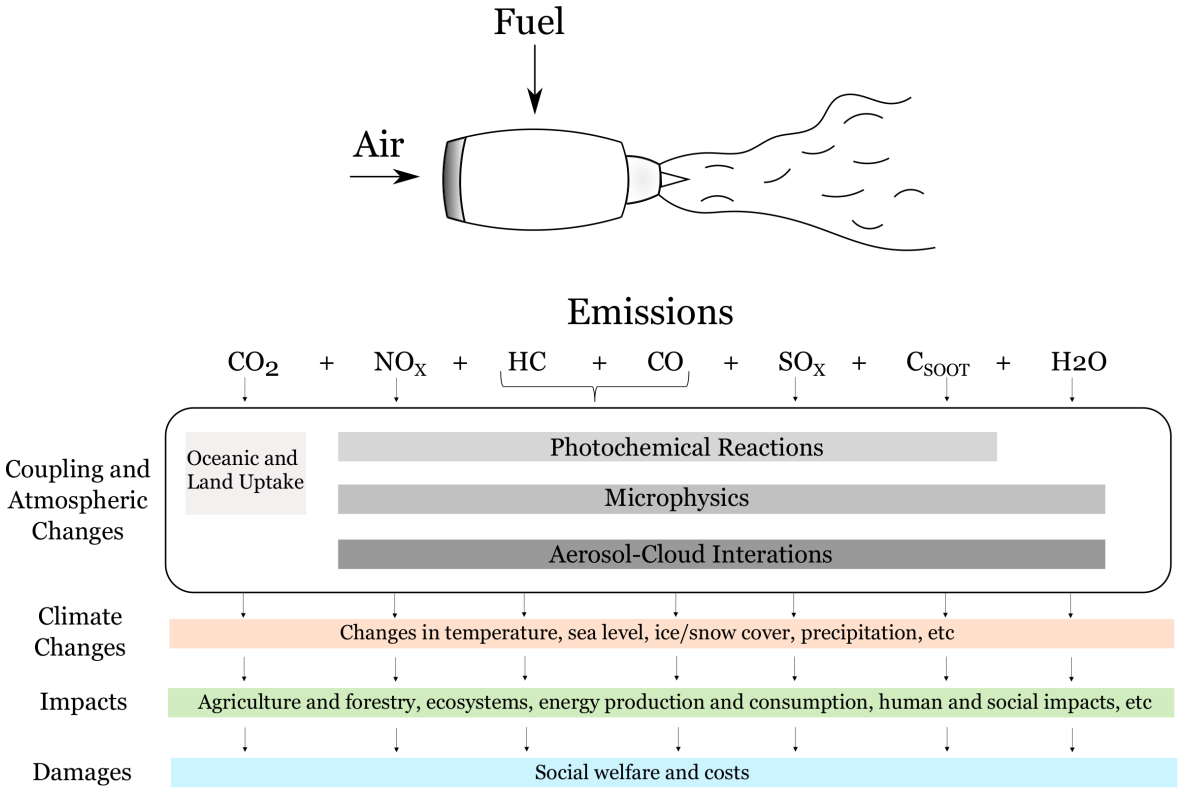

Figure 2.4: Emissions and effect of air transportation, based on [36, 62].

under the oversight of a national aviation regulatory authority [63]. The International Civil Aviation Organization recommended emission regulations for civil aircraft requiring certification during the Landing-Take Off (LTO) phases when aircraft operate at altitudes below 3000 feet [64]. The examination averages jet engine loads and duration at several load conditions simulating scenarios in the vicinity of and at an airport [60]. The LTO cycle involves power configurations such as taxi, approach, climb, and takeoff, relating to 7, 30, 85, and 100% thrust, respectively [61]. At high altitudes, the effects are related to the possibility of contrail formation, impacts on the aerosol radiative effects, and lifetimes for emissions above the cloud deck [65].

Generally, air transportation emissions have two primary impacts, including local air quality, particularly in the proximity of airports, and global climate [63]. Based on this, a detailed overview of each emission released by the aviation sector will be provided. Carbon dioxide (CO_2) is the predominant gas responsible for the greenhouse effect that, in excess, leads to global warming. The emissions of CO_2 are directly related to jet fuel combustion and correspond approximately to 72% of total combustion products [56]. The emissions of CO_2 can be decreased by increasing the fuel hydrogen/carbon ratio, which can be applicable to possible alternative fuels in the air transportation industry [66]. Furthermore, the Earth tempera-

ture rise can also be influenced by the non-CO_2 emissions, more specifically nitrogen oxides (NO_x), water vapor, and soot, as will further be explained [7]. Nitrogen oxides (NO_x) are generally significant during the climb and cruise, particularly when combustion temperatures are higher, through the thermal oxidation of atmospheric N_2 [49]. These emissions are susceptible to the combustion chamber pressure, temperature, flow rate, and geometry [56]. To address this issue, efforts towards new engine designs have been made to guarantee rapid and complete combustion, resulting in uniform combustion temperatures and a subsequent decrease in NO_x emissions. [45]. These influence the environment by altering the levels of atmospheric ozone (O_3) and methane (CH_4), both critical greenhouse gases resulting in an influence on the Earth radiative balance [36]. More precisely, NO_x emissions result in further microphysical reactions that locally cause an increase in ozone (O_3) formation. This commonly occurs in tropopause cruise altitudes of commercial aircraft. Besides that, NO_x also affects the lifetime of methane (CH_4) at tropopause altitudes [36]. This suggests that interactions with NO_x emissions have been related to a decrease in the lifetime of methane at tropopause altitudes. Consequently, there is a marginal reduction in radiative forcing due to the local decrease in CH_4. The increase in radiative forcing impact caused by O_3 is commonly identified as outweighing any reduction in radiative forcing due to methane concentration decrease, leading to an overall warming effect that particularly varies with altitude [36]. More specifically, the aviation emissions of NO_x at low altitudes contribute to ozone formation, concerning human health and local air quality. Conversely, at high altitudes, NO_x ozone depletion leads to an increase at the surface level of Ultraviolet radiation (UV) [63]. Water emissions are also released by hydrocarbon combustion, which tends to condense into clouds of ice crystals that induce the appearance of contrails or aviation-induced cloudiness [36]. Regarding the CO emissions, Blakey et al. [49] stated that are higher when the air in the combustion chamber is at the lowest temperature and pressure at the lower power idle conditions where jet fuel combustion is incomplete and less efficient. This occurs when an engine operates in a fuel-rich condition caused by an insufficient supply of oxygen required to complete the reaction into CO_2. Additionally, CO emissions are related to fuel injectors and increase with the decrease of the thrust [56]. The effects of CO emissions on human health rely on reducing the capacity of the blood to absorb oxygen and, in high concentrations, can cause asphyxiation and even death [55]. Sulfur oxides (SO_x) appear as a consequence of the combustion of sulfur content present in aviation fuel in low concentrations that may contribute to aerosols and particulate formation [45]. The sulfur oxides are toxic, leading to the reduction in turbine blade life and the formation of sulfuric acid in the atmosphere [63]. Particulates and unburned hydrocarbons are emitted due to incomplete combustion of jet fuel and are noticed as smoke or soot expelled from the engine. Moreover, these emissions are also related to poor fuel atomization, insufficient reaction rates, the localized extinguishing of the flame, or a combination of all of these conditions [63]. The main influencing factors for unburned hydrocarbons and CO emissions are similar. Soot emissions are related to the aromatic content in jet fuel and negatively impact the environment and human health. In this context, the presence of soot particles at the surface level significantly contributes to the deterioration of urban air quality, creates haze and smog, and can be harmful if inhaled. Soot emissions have

a significant impact on contrail characteristics and the formation of cirrus clouds, influencing the Earth Radiative Forcing constant [61]. Table 2.1 summarizes aviation factors related to emissions, previously discussed in Braun-Unkhof et al. [61].

Table 2.1: Factors that contribute to aviation emissions [61].

Emissions	**Factors**
CO_2 and H_2O	Proportional to fuel combustion
H_2O	The higher the H/C ratio, the higher the amount of water released
SO_x	Proportional to amount of sulfur (S) within the fuel
UHC, NO_x, CO	Dependent on the combustion parameters (Temperature, pressure, among others)
CO and UHC	High at idle and taxi
NO_x, Soot	High at take-off, climb

2.2.3 Strategies To Address Aviation Environmental Concerns

Reflecting on the impacts of emissions, it is concluded that introducing sustainable alternatives in the aviation sector is imperative. According to the International Air Transport Association (IATA), sustainability is a term that refers to something that can be constantly sourced consistently with economic, social, and environmental goals [67]. The main objective is to maintain an ecological equilibrium by preventing the depletion of natural resources. However, the decarbonization and application of the term sustainability in aviation is quite challenging compared to other transportation sectors. As indicated above, high requirements are crucial for reliability and security in aviation. Air transportation demands specific power and energy characteristics under various operational circumstances. Besides that, a sustainable alternative for the future of aviation should also include considerations on direct CO_2 and non-CO_2 emissions, life cycle emissions, cost and scalability, material properties, safety, toxicity, and fuel handling requirement societal impact and public perception [36]. Therefore, any proposed alternative aviation fuel must meet international standards, including criteria dedicated to thermal stability, acceptable cold flow characteristics, and a low freezing point [68]. In 2010, a starting point to change the aviation sector paradigm was developed. To address the CO_2 emissions, the following objectives were established [69]:

- An average improvement in fuel efficiency of 1.5% per year between 2010 and 2020
- A cap on net aviation CO_2 emissions from 2020
- A reduction in net aviation CO_2 emissions of 50% by 2050 relative to 2005 levels

Furthermore, the International Civil Aviation Organization (ICAO) aims to achieve an annual 2% fuel efficiency, followed by carbon-neutral growth beyond 2020 [39]. To address the CO_2 emissions, in 2016, ICAO introduced the Carbon Offsetting and Reduction Scheme for International Aviation (CORSIA). CORSIA is a global market-based measure scheme for international aviation with a baseline initially focused on an average of 2019 and 2020 emissions. Nevertheless, the COVID-19 pandemic changed the aviation perspective, significantly declining the air transport market to less than half of the levels reported in 2019, leading

to a revision of the CORSIA baseline. In June 2020, the ICAO Council adopted the 2019 emissions exclusively as the baseline for CORSIA from 2021 to 2023 [70]. CORSIA will be executed in three stages: a pilot phase from 2021 through 2024, a first phase from 2024 through 2026, and a second phase from 2027, where the offsetting requirements will apply to all global flights [70]. The aviation sector centers the emissions reductions through improvements in airframe and engine technologies, more efficient aircraft and ground operations, and sustainable aviation fuels (SAF) [71]. Figure 2.5 shows the strategies specified by ICAO to stabilize net emissions in the air transport sector.

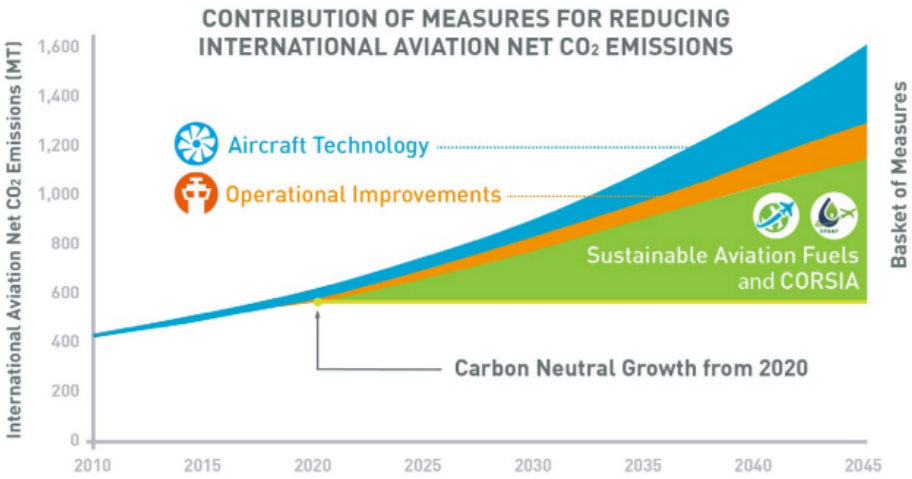

Figure 2.5: ICAO Global environmental trends on CO_2 emissions and contribution of measures for reducing international aviation net CO_2 emissions, adapted from [69].

Relying solely on operating improvements and innovative technologies cannot directly resolve the decarbonization of the aviation industry. Instead, it should be part of a comprehensive set of strategies where numerous actions must be taken in the aviation industry to attain the objectives of ICAO, as shown in Figure 2.6.

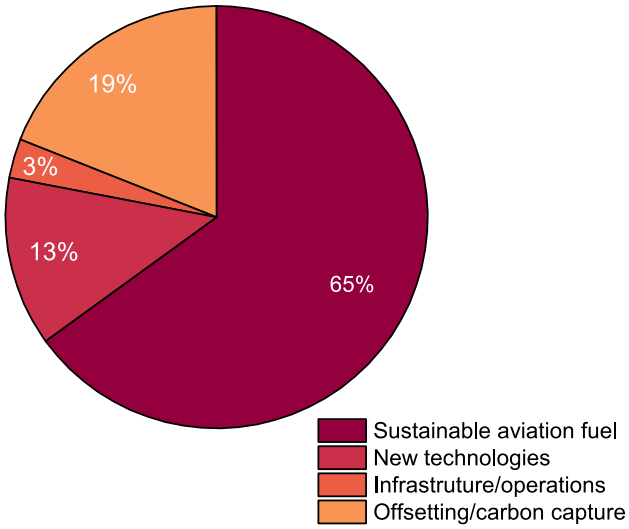

Figure 2.6: Contribution toward achieving Net Zero Carbon by 2050, adapted from [72].

These efforts and adaptations require the comprehensive development of society, entities, and governments worldwide, being intensified in recent years. In 2021, to address and revise the long-term goal for 2050, at the 77^{th} Annual General Meeting, the IATA approved a resolution for the global air transport industry. The goal is to achieve net-zero carbon emissions by 2050, aligning with the Paris Agreement goal for global warming not exceeding 1.5 °C. To achieve net-zero carbon emissions, the aviation sector must reduce emissions at the highest possible level at their origin. The net-zero carbon emissions target can be achieved by utilizing sustainable aviation fuels (SAF), adopting innovative propulsion technologies, and various efficiency enhancements, including improvements in air traffic navigation, as previously stated [69].

Investigations dedicated to aerodynamics and structural solutions have focused on using new materials, lighter airplanes with additive manufacturing components, novel wing or aircraft concepts, and new energy-powered aircraft in order to increase efficiency [73]. Concerning alternative fuels, the IATA defined sustainable aviation fuel as a main term for nonconventional aviation fuel [72]. This designation has already been accepted by the Federal Aviation Administration (FAA) and the European Aviation Safety Agency (EASA) [74]. Aviation fuels could be considered drop-in or non-drop-in fuels. The expression drop-in corresponds to a fuel that can be used as a direct substitute or blend for conventional jet fuel (typically Jet A or Jet A-1) without demanding any adaptation to the aircraft engines or fuel infrastructure [7]. The chemical and physical properties of these fuels display similarities to conventional jet fuel, promoting easy blending and enabling its application in the current systems. Conversely, non-drop-in aviation fuels are alternative fuels that are not interchangeable with conventional jet fuel and require engine modifications, fuel systems, or infrastructure [7]. Sustainable aviation fuel depends mainly on feedstock and can be divided into biofuels and synthetic aviation fuels. SAF biofuels are related to biomass-based fuels, solid, liquid, and gaseous waste-based fuels. Conversely, synthetic aviation fuels, termed e-fuels, are associated with green hydrogen and captured CO_2 that are converted into alternative fuel via a Fischer-Tropsch process [75]. Commonly, biofuels refer to fuel resulting from biological resources. Yet, advancements in technology allow the production of fuels from non-biological resources (e.g., hydrogen and e-fuels) [76]. As a result, the term SAF comprehensively encloses all these alternative aviation fuels. IATA has recognized the production of drop-in sustainable liquid fuels (SAFs) as the most favorable strategy, particularly in the short term, to mitigate the environmental impact of the aviation sector. Consequently, enhancing industrialization and optimizing the production of SAF seems to be the most efficient approach to address decarbonization in the aviation industry, where prioritizing procedures to accelerate production, incentivizing adoption, and minimizing costs should be a central focus [73]. This implementation is the main practical fuel alternative for larger, long-range aircraft without significant new designs and is expected to remain unchanged until the year 2050 [75, 77].

According to Cracknell et al. [75], using SAF not only decreases CO_2 emissions throughout its life cycle. It is also important to reduce non-volatile particulate matter and contrails. These factors contribute to radiative forcing and, consequently, global warming. To align with the

term suitability, SAF feedstock should avoid conflicting with food crops or production and prevent the need for additional resource usage, such as water or land clearing. Additionally, it is recommended to avoid deforestation, soil productivity, or biodiversity loss. During fuel production, it is essential to maintain human rights, labor rights, and the rights of land and water use. As a drop-in, SAFs are mixed with jet fuel in different percentages depending on the conversion technology, as will be further discussed. The introduction of SAF not only benefits in terms of emissions but also has the potential to produce economic and social advantages by developing new industries and creating new jobs. Moreover, adopting SAF can mitigate the risks associated with supply chain disruptions in jet fuel due to price volatility and geopolitical concerns [53]. Sustainable aviation fuels presently face high production costs, being not economically competitive. Hence, a significant path exists to produce renewable aviation fuels that are economically feasible. The aviation industry, government, and biofuel companies, among others, require effort toward an optimal strategy that utilizes the most adequate feedstock sources to promote the widespread use of this alternative source [33]. Furthermore, novel technologies such as electric (battery-driven) and hydrogen have been explored besides integrating sustainable fuels, whether biofuels or synthetic fuels. These innovations demand significant modifications in aero-engine configurations and infrastructures for further application, as will be further discussed [14].

Implementing SAF in the aviation industry must satisfy specific criteria to be categorized as drop-in fuels. In light of this, SAF must meet ASTM standards to guarantee safety, operability, and optimal performance within the current aircraft fleet [31]. To control the production and quality of sustainable aviation fuels, an expansion of D1655 was created to include fuel specifications required for SAF blending [33]. In 2009, this expansion was formalized as ASTM Specification D7566 (Standard Specification for Aviation Turbine Fuel Containing Synthesized Hydrocarbons), which requires a rigorous testing and approval process focused on assuring the safety compliance of SAF. If SAF agrees with the requirements of ASTM D7566, the properties of SAF and jet fuel blend must satisfy the ASTM D1655 standard [50]. In this respect, ASTM 7566 mandates that sustainable aviation fuel must be mixed with a minimum of 50% jet fuel [7]. The sector has been performing active efforts to attain compatibility with 100% SAF. However, significant actions within the industry remain indispensable to guarantee the certification and widespread implementation of 100% SAFs [75]. Combining conventional and sustainable aviation fuel aims to guarantee the composition of paraffin and aromatics [53]. In particular, the lack of aromatic content due to the absence in the SAF composition can difficult seal compatibility. Therefore, a minimum of 8% of aromatic content is required to more closely resemble the composition of jet fuel derived from petroleum [2,41]. This reference value is an active research topic that demands more investigation for the 100% SAF implementation and to minimize the soot emissions [31]. Compared with jet fuel, reducing aromatic content in SAF is an advantage since their capacity to reduce soot formation can positively affect aircraft emissions. As a primary step, new turbine engine fuel additives and blend components must be certified to ASTM D4054 (Standard Practice for Qualification and Approval of New Aviation Turbine Fuels and Fuel Additives). These new elements required a separate specification with more stringent criteria due to the lim-

ited experience in employing new processing techniques to convert feedstock such as plant oils, woody biomass, or coal into liquid fuels [74]. ASTM D4054 is an iterative and meticulous procedure that instructs fuel developers to perform examinations of fuel samples. This certification was conceived to qualify and approve new fuels and additives for gas turbine engines dedicated to commercial and military aviation purposes [43]. The fuel examination explores how the candidate fuel or additive affects fuel specification, fit-for-purpose properties, fuel system materials, turbine materials, other approved additives, and engine operability [43,78]. In this respect, investigations dedicated to the fuel in terms of physical properties (e.g., density as a function of temperature) and ground handling considerations, including factors such as flammability limits and autoignition temperature, are explored [58]. Following the successful completion of the ASTM D4054 certification, the fuel is included in the two essential standards: ASTM D1655, summarizing specifications for Jet A-1 petroleum jet fuel, and ASTM D7566, specifying additional biofuel requirements [2]. In compliance with ASTM D4054, there are two ways of certification: Tiered Test (normal way) or Fast Track Programs (accelerated way) [2, 37]. Figure 2.7 shows the Tiered Testing Program, evidencing the estimated costs and durations for several of the steps [37].

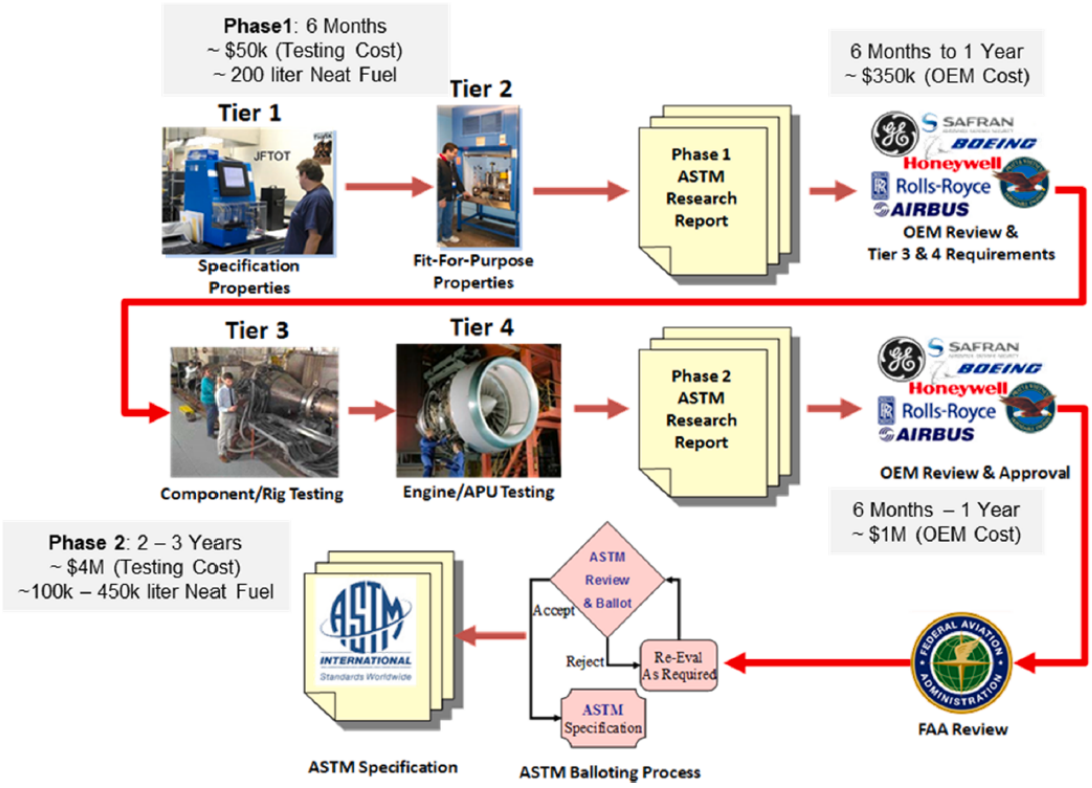

Figure 2.7: A nominal ASTM D4054 evaluation process, adapted from [37].

In general, three phases describe this certification process. The first step focuses on the physical properties of the fuel. Then, the fuel is tested on stands, the components of the fuel system, and a real engine. The final step is dedicated to the vote and approval of changes to ASTM normative documents [2]. The information produced during the D4054 process is crucial to the ASTM International subcommittee members for evaluating the new fuel to compare with the established properties and characteristics of conventional jet fuel [78]. The

purpose of the accelerated way is to minimize the duration and costs involved in the certification process. If the fuel effectively passes the certification process in an accelerated path, a maximum of 10% can be blended with conventional jet fuel. The assessment procedure refers to the FAA-approved operating limits established according to ASTM fuel specifications.

Recently, the European Commission presented the "Fit for 55" package to reduce greenhouse gas emissions by 55% in 2030 compared to 1990 levels. A sequence of recommendations was released that intended to align climate, energy, land use, transportation, and taxation policies in the European Union to mitigate greenhouse gas emissions [76]. The "Fit for 55" package initiative will impact various sectors, focusing on energy and transport. The aviation sector was dedicated to revising the EU emissions trading system for aviation, developing the ReFuelEU aviation proposal to accelerate the uptake of SAF, and revising the alternative fuels infrastructure regulation (AFIR). Table 2.2 specifies the minimum proportions of biofuels and synthetic aviation fuels required in ReFuelEU by years.

Table 2.2: Minimum proportions of alternative aviation fuels required in ReFuelEU by years. Adapted from [76].

Effective Dates	**Biofuels**	**Synthetic Aviation Fuels**
January 1, 2025	2%	
January 1, 2030	6%	
January 1, 2030 – December 31, 2031		Average share of 1.2%, with a minimum share of 0.7% in each year
January 1, 2032 – December 31, 2034		Average share of 2%, with minimum shares each year of 1.2% from January 1, 2032, until December 31, 2033, and 2% from January 1, 2034, to December 31, 2034
January 1, 2035	20%	5%
January 1, 2040	34%	10%
January 1, 2045	42%	15%
January 1, 2050	70%	35%

The quota for synthetic aviation is less than for biofuels due to technological advancement constraints compared to biomass fuel production. Renewable fuels of non-biological origin are typically noted as RFNBOs or e-fuels [76]. These synthetic fuels represent renewable liquid and gaseous transport fuels from renewable energy origins distinct from biomass. RFNBOs are hydrocarbons that are synthesized using hydrogen (H_2) and carbon dioxide (CO_2). Green hydrogen is produced by water electrolysis or steam reforming of natural gas that uses renewable energy. Carbon dioxide can be captured from the combustion of fossil fuels produced by both industrial sources or directly from the air [79, 80]. The effectiveness of these alternative fuels in mitigating climate change remains largely uncertain [80]. The production of synthetic liquid fuels, based on H_2 and CO_2, can be acquired through two distinct methods: Fischer-Tropsch (FT) and methanol synthesis [79, 81]. However, productions of RFNBOs are constrained due to available renewable electricity generation capabilities and the large-scale infrastructure for material inputs, such as hydrogen from water electrolysis and CO from CO_2 reduction [82–84]. The successful introduction of synthetic fuels relies on

supportive policy frameworks. Most of these alternatives exist in the demonstration phase and possess industrial challenges. As previously stated, regarding the renewable fuels from biomass, wide production methods and sustainable, cost-effective feedstock pathways will be essential to significantly contribute toward the CO_2 reduction. As established by ReFuelEU, the proportions of biofuels in aviation fuel must achieve a quota of 70% in 2050. This prompts the question of whether enough SAF is available to achieve this prerequisite [85]. Besides the fact that sustainable production of biomass is a fundamental pillar in enabling the decarbonization process through the use of SAF, it has encountered criticism due to issues over induced land use change when transforming high-carbon stock land into agricultural and plantation use [31].

2.2.4 Sustainable Aviation Fuels - Biofuels

SAF biofuels are assumed to be nearly carbon-neutral over their life cycle [67]. In order to understand how these alternatives achieve carbon neutrality, a summary of the carbon life cycles of jet fuel and biofuel is presented. Figure 2.8 shows a comparison between CO_2 life cycle of jet fuel and sustainable aviation fuel (SAF). It is important to note that life cycle CO_2 emissions of SAF depend on the feedstock and conversion pathway [85].

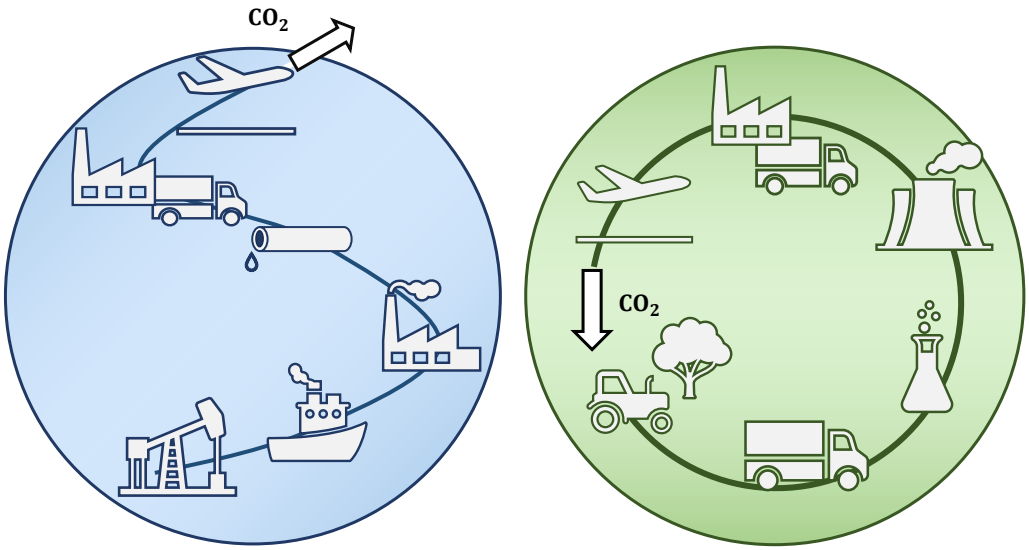

Figure 2.8: CO_2 life cycle comparison between: a) Fossil fuels: b) Sustainable biofuels. Adapted from [86].

Jet fuel is a fossil fuel derived from the decomposition of microscopic organisms hundreds of millions of years ago under high pressure and high temperature. When jet fuel burns, it releases CO_2 to the atmosphere without recycling. On the other hand, for biofuel, the CO_2 is absorbed by plants during its growth of biomass, being approximately identical to the amount of carbon dioxide released to the atmosphere by the combustion of aero-engines, leading roughly a carbon-neutral over its life cycle [67]. Biomass is a range of organisms developed through photosynthesis, including plants and microorganisms.

Drop-in biofuels generally refer to fuels derived from biomass sources acquired from biologi-

cal, thermal, and chemical conversion methods [13]. The use of biomass to obtain sustainable liquid fuel is among the most favorable candidate feedstocks required for the road and aviation sector [13, 87]. In fact, aviation is challenged by the comparative environment with the road transport sector regarding policy support, availability, and price of feedstock and supply chain. The biofuel production for each sector can utilize the same production facilities and supply chain. However, the costs related to aviation biofuel are higher depending on the feedstock and the additional advanced refining processes compared with road transportation. Additional costs are also associated with the testing and certification of sustainable fuels for aviation [39, 88]. Introducing biofuels in aviation has been challenging due to its costs, generally about 2 to 3 times the price of kerosene [73]. Furthermore, the unique characteristics of jet fuel and the available alternative fuels employed in road transport, such as biodiesel, cannot be applied in the aviation industry. Sustainable aviation fuels derived from biomass must possess properties suitable for low temperatures and high energy density to meet the energy requirements of long-haul flights, which contradicts biodiesel properties, as will be elaborated further [1]. Aviation fuels must be in the absence of oxygenated hydrocarbons and other non-heteroatom-free hydrocarbons that are adverse to fuel performance and safety [88].

The approval certification for biofuel and jet fuel blends under specific ratios depends on the producing pathways. Currently, ASTM D7566 specifies the blending proportion depending on the fuel and the production pathways [66]. The pathways are influenced by the feedstock employed in the conversion process, which includes lignocellulosic biomass, vegetable oils, starchy materials, sugars, industrial waste materials, and triglycerides [7, 66]. The production pathways of biofuels involve several stages. Initially, the produced feedstock is collected. Once the feedstock acquisition is completed, a series of pretreatment procedures specific to the feedstock type are conducted to achieve the characteristics for the conversion process. The procedure is completed when the conversion process is finalized, and the fuel is prepared for transportation and usage [86]. SAF biofuel production pathways are commonly classified into four categories: gas to jet fuels, oil to jet fuel, sugar to jet fuel, and alcohol to jet fuels [7]. Each category requires distinct pretreatment methods and is appropriate for specific types of conversion processes [86]. The use of edible crops for biofuel production is expensive and is identified as a critical competition between food and energy. Moreover, to fulfill the sustainability criteria established by the aviation industry, edible crops are not considered viable alternatives for future implementation [86]. Consequently, to produce biofuel from non-edible matter that is economically viable, it is crucial to find acceptable and feasible materials or crops [68]. The feedstock can be categorized into four groups, as illustrated in Figure 2.9. First generation biofuels are purely derived from edible feedstocks. These biofuels are food-based and related to plants and animals intended for human consumption, which include cereal crops, vegetable oils, sugarcane, and sugar beets [42, 89] and are typically used in road transportation [90]. As previously stated, not all biofuels are compatible for use in the aviation sector due to lower energy density and higher freezing points compared with conventional jet fuel [86]. The biofuels dedicated to ground transportation can include oxygen-containing fuels. However, the presence of oxygen tends to reduce the fuel

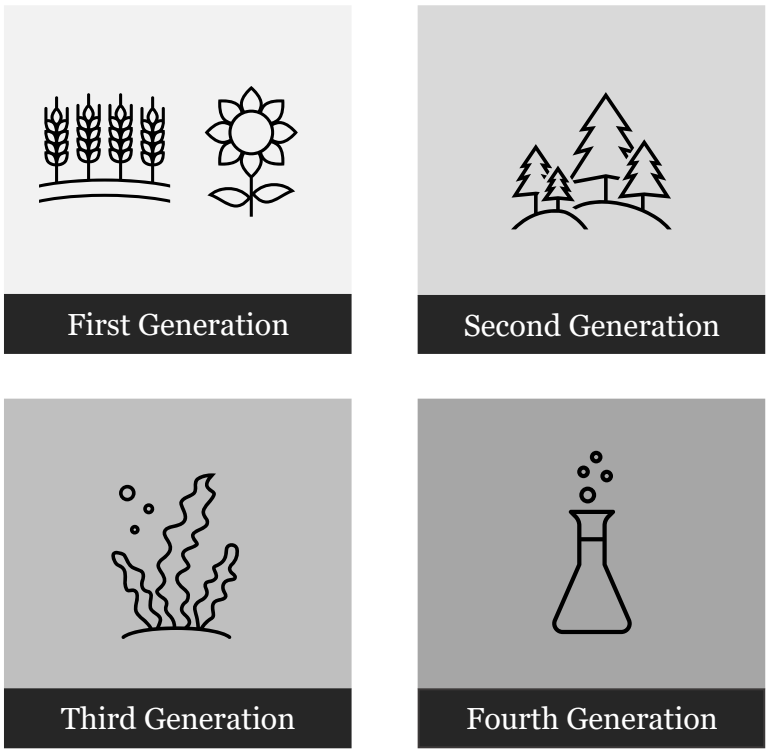

Figure 2.9: Biofuel generations, derived from [42].

energy density and stability, affecting the fuel properties and leading to consequences for aero-engines [78]. There are several disadvantages to this biofuel generation, which relies on sustainability concerns, including adverse impacts on food prices, high water, nutrient demands, and alterations in local environments due to pesticide use and other substances [86]. Conversely, advantages in terms of simplicity of the process and lack of intense pretreatment are reported in [91]. However, this production technology plays a significant role in the circular economy due to the relatively mature state of the first generation SAF market [88]. Furthermore, production expansion is crucial to attaining the pre-defined objectives, possessing a substantial technical challenge, requiring the construction of additional infrastructure [92]. Biodiesel and ethanol are considered first generation biofuels since they are commonly obtained from corn, sugarcane, sorghum, and sunflower [93]. Alternatively, bioethanol is not solely considered first-generation biofuels. Relying on the feedstock and production strain, bioethanol can also be viewed as second or even third generation biofuel [91]. Subsequently, a summary of the remaining generations will be presented.

The second generation involves feedstock from non-edible biomass resources, hence does not possess energy and food competition issues, allowing waste stream valorization (circular economy) [91]. Essentially, these second generation biofuels are produced from wood, straw, lignocellulosic feedstocks to municipal solid wastes, and all the other remaining parts of harvested crops after removing their edible parts that do not compete with edible crops [42, 94]. The drawbacks of the second generation are mainly the technical barrier and its high costs due to the requirements of intense pretreatments required in complex feedstocks [89, 91]. The third generation is typically known as algae biofuels. Algae are attractive to produce al-

ternative fuel since these possess no food value, offer high yields without substantial land needs, and have relatively low-cost requirements [89]. Additionally, it can grow in environments not recommended for consumption, such as polluted water or water unsuitable for agriculture [89]. Algae has the ability to fix CO_2 as a means of extracting CO_2 from flue gases emitted, for example, by power plants, reducing greenhouse gas emissions [1]. Nevertheless, the advancement of this biofuel generation is restricted as large-scale production is still in progress, presenting high downstream costs [42]. The drying process for these biofuels can also be highly energy intensive. These are mainly derived from microalgae and cyanobacteria biomass that can generate alcohols and lipids to convert into biodiesel or other high energy fuel products [91]. Besides all of these challenges, alternative fuels derived from microalgae are currently considered as one of the most promising sources of biofuels [88]. Lastly, the fourth generation involves genetic engineering to enhance desired traits in organisms utilized for biofuel production [91]. Examples of organisms that are genetically modified are typically microalgae, cyanobacteria, fungi, and yeast. In this respect, the purpose is to increase oil and/or sugar yields and exhibit carbon-negative capabilities [89]. This method is still in the research process, requiring further investigations in terms of potential health and environmental risks posed by these organisms. Second, third, and fourth generation biofuels are also termed advanced biofuels due to their perceived advantages over first-generation fuels. However, more research and development are required since these biofuels are still undergoing and have not yet achieved their full commercial potential [1].

Following the introduction of biofuel generations, an examination of the conversion pathways approved by ASTM International is presented. Table 2.3 shows the current approved conversion processes or annexes incorporated into D7566 for SAF biofuel production, initial release in 2009. The feedstock and maximum blend ratio for each conversion process are also displayed in Table 2.3. Each annex comprises details regarding the conversion process, feedstock, and composition of the alternative fuel, coupled with properties that the alternative fuel must meet [95]. Each pathway exhibits distinct characteristics, benefits, drawbacks, cost-effectiveness, and environmental impact. Moreover, they are specified with reaction pathways, feedstock, and catalyst requirements that are essential to understanding how these conversion processes can potentially reduce carbon emissions and affect the energetic transition for a more sustainable air transportation sector [7, 92]. An overview of the biofuel conversion processes is detailed and provided in Appendix A.1.

- **Fischer-Tropsch hydroprocessed synthesized paraffinic kerosene (FT)**

The development of alternative aviation fuel started with the approval of Sasol Fischer-Tropsch (FT) coal-to-liquid (CTL) semi-synthetic jet fuel in 1999 as a result of jet fuel scarcity coupled with its increasing demand [74]. Around the mid-1990s, with the UK AFC and ASTM International specification writing organization, Sasol disrupted the effort to incorporate this alternative fuel in jet fuel specifications [74]. The FT synthesis was originally developed by the German researchers Franz Fischer and Hans Tropsch in 1922. The purpose was to produce liquid fuels from coal [38, 86].

Table 2.3: SAF approved conversion processes [96].

Conversion process	Abbreviation	Feedstocks	Maximum Blend Ratio
Fischer-Tropsch hydroprocessed synthesized paraffinic kerosene	FT	Coal, natural gas, biomass	50%
Synthesized paraffinic kerosene from hydroprocessed esters and fatty acids	HEFA	Bio-oils, animal fat, recycled oils	50%
Synthesized iso-paraffins from hydroprocessed fermented sugars	SIP	Biomass used for sugar production	10%
Synthesized kerosene with aromatics derived by alkylation of light aromatics from non-petroleum sources	FT-SKA	Coal, natural gas, biomass	50%
Alcohol to jet synthetic paraffinic kerosene	ATJ-SPK	Biomass from ethanol, isobutanol or isobuthene	50%
Catalytic hydrothermolysis jet fuel	CHJ	Triglycerides such as soybean oil, jatropha oil, camelina oil, carinata oil, and tung oil	50%
Synthesized paraffinic kerosene from hydrocarbon - hydroprocessed esters and fatty acids	HC-HEFA-SPK	Algae	10%
co-hydroprocessing of esters and fatty acids in a conventional petroleum refinery	co-processed HEFA	Fats, oils, and greases (FOG) co-processed with petroleum	5%
co-hydroprocessing of Fischer-Tropsch hydrocarbons in a conventional petroleum refinery	co-processed FT	Fischer-Tropsch hydrocarbons co-processed with petroleum	5%
co-hydroprocessing of biomass	co-processed biomass		5%

As mentioned earlier, the pathways are classified into four categories. Fischer-Tropsch falls within the gas-to-jet classification. This process converts biomass into liquids. According to Gunerhan et al. [97], the fundamental steps to obtain this alternative fuel rely on syngas production, gas purification, FT synthesis, and product upgrading. Firstly, the biomass is pre-treated and converted to syngas by the gasification process, succeeded by the syngas improvement [13]. Syngas predominantly include carbon monoxide (CO) and hydrogen (H_2), serving as the primary constituents for producing FT liquid hydrocarbons [98]. The biofuel produced from the FT reaction possesses a mixture of hydrocarbons with carbon numbers 9–15 [38, 98]. The resulting product composition and ratio depend on the reactor and catalyst type [99]. Typically, coal and natural gas are feedstocks for the synthesis of FT. However, coal and natural gas, being non-renewable sources, are unsuitable for producing SAF [99]. The sources for this process are predominantly woody biomass, such as municipal solid waste, agricultural wastes and forest, and energy crops [100]. The first synthetic jet fuel pathway FT synthesis process (FT-SPK), listed as Annex A1 of D7566, was approved in September 2009, allowing a maximum blend ratio of 50%, as shown in Table 2.3. The biofuel obtained from this process is non-toxic and commonly sulfur-free. It contains very few aromatics

compared to diesel and gasoline, promoting lower emissions in aviation engines, possessing a TRL of 7 [8, 101]. The disadvantages of its conversion process are mainly related to the economic viability of feedstocks regarding the gasification technology and syngas clean-up [98]. Furthermore, the collection facilities from different areas, relatively low heat value, and unstable fuel quantity and quality will also produce extra costs and uncertainties in the process [38,102]. However, the FT process remains an appealing option for biomass utilization as a gasification product (syngas) and solid by-product (biochar), which can be relevant in diverse applications [38].

- **Synthesized kerosene with aromatics derived by alkylation of light aromatics from non-petroleum sources (FT-SKA)**

The absence of aromatics content in the alternative fuels can develop fuel leakage concerns caused by the inadequate swelling of the elastomer seals [38]. Therefore, in 2015, Fischer-Tropsch synthetic kerosene with aromatics (FT-SKA) was certified by ASTM, listed as Annex 4 [97, 98]. This alternative fuel is a variation of the Fischer-Tropsch process, where a small portion of light aromatic hydrocarbons is added [92]. Similar to the FT process, the blend limited is 50% [98]. This value can be increased in the following years or even be certified for 100% conventional fuel replacement [86, 92]. According to Shehab et al. [92], FT-SKA positively influences the fuel cold-weather performance. The aircraft engines are subjected to low temperatures, which may lead to solidification and increased viscosity, potentially impacting the fuel flow characteristics and affecting the aircraft propulsion system [92].

- **Synthesized paraffinic kerosene from hydroprocessed esters and fatty acids (HEFA)**

Concerning the category of oil to jet, HEFA is a common method to obtain alternative jet fuels from oils [97]. Hydroprocessed Esters and Fatty Acids (HEFA), or Hydroprocessed Renewable Jet (HRJ), converts oil from lipids to hydrocarbons using hydrotreatment and isomerization [66, 86]. According to Cabrera and Sousa [86], the biogenic material is initially purified, followed by the deoxygenation stage employing a chemical reaction using hydrogen and catalysts, where the undesired molecules are removed. Subsequently, the remaining hydrocarbons are cracked and isomerized. Ultimately, distillation occurs, separating final products, resulting in the HEFA biofuel [86]. UOP Honeywell developed this biofuel production in 2009, which consists of the hydrogenation, deoxygenation, isomerization, and selectively hydrocracking of the feedstock to produce paraffinic hydrocarbons possessing 9 to 16 carbon atoms and a high iso/normal ratio [38, 103]. Moreover, it has been recognized as a promising technology for manufacturing biofuels in road and air transportation. The feedstock employed for this conversion process is based on vegetable oils and animal fats containing triglycerides (palm, jatropha, canola, soybean, and grease) [97, 99]. This process was the second approved and listed as Annex 2, receiving its certification by ASTM in 2011 with a maximum blending of 50% [86]. As noted in the Fischer-Tropsh process, blending with conventional jet fuel is required to incorporate the normal paraffin, cycloparaffins, and

aromatics lacking in HEFA [95]. HEFA alternative fuels have already been tested in several airlines in passenger flights [101]. This is supported by the Commercial Aviation Alternative Fuels Initiative (CAAFI) through the Readiness Level, where the HEFA process shows a TRL of 9. HEFA conversion process is a fully commercialized and mature technology with fewer processing steps producing high volumes of SAF, resulting in biofuels exhibiting high thermal stability, high cetane numbers, and low greenhouse gas emissions [89, 98, 104]. However, there are concerns regarding the feedstock since it employs the similar feedstock as biodiesel production, potentially affecting the cost of edible oil, increasing land use change, and imposing strain on environmental resources. Compared with biodiesel, HEFA biofuel presents a higher cetane number, heating value, and lower oxygen content [38].

- **Synthesized iso-paraffins from hydroprocessed fermented sugars (SIP)**

Hydroprocessed Fermented Sugars to Synthetic Isoparaffins (HFS-SIP) is a pathway approved in June 2014, presented in Annex A3 of D7566, allowing a maximum blend ratio of 10%. As noted earlier, the blend ratio value is lower than FT and HEFA, due to the fuel viscosity, an essential parameter in the atomization process affecting the performance of the engines [38, 105]. The higher viscosity of SIP fuel can influence the combustion rate and fuel emissions. Before the certification, it was denoted as DSHC (direct sugar to hydrocarbons) [86]. Currently, the HFS-SIP fuel is produced through the fermentation of sugars obtained from renewable sources such as corn and sugarcane to obtain ethanol or butanol [92]. Amyris and Total developed this conversion process and employed an advanced fermentation technique to convert sugars into unsaturated hydrocarbon molecules (farnesene). Then, farnesene is upgraded into jet fuel through hydroprocessing, leading to the alternative fuel, which is a paraffinic hydrocarbon with the empirical formula $C_{15}H_{32}$ [92]. FT and HEFA are developed based on thermochemical processes, whereas SIP uses a combination of biological or enzymatic conversion of feedstocks into alcohols or farnesene before proceeding with subsequent thermochemical conversion stages [106]. Moreover, the biological routes for this process require the engineering of enzymes and microorganisms metabolism to be produced on a large scale to compete with the traditional fuels in transportation [107]. SIP presents high production costs due to the complexity and low efficiency of converting lignocellulosic sugars into fuels [101].

- **Alcohol to jet synthetic paraffinic kerosene (ATJ-SPK)**

Alcohol to jet synthetic paraffinic kerosene (ATJ-SPK) is a biochemical conversion process approved by ASTM in April 2016 for isobutanol and in June 2018 for ethanol, allowing a blend limit of 30%. ATJ-SPK converts alcohols into alternative fuel through chemical reactions—dehydration, hydrogenation, oligomerization, and hydrotreatment. Finally, distillation or separation occurs to obtain the desired biofuel. The feedstock employed for this process is mainly bio-alcohols (ethanol or isobutanol) produced from starch, sugars, and lignocellulosic biomass (e.g., corn stover) [38]. ATJ-SPK routes are attractive due to their wide range of bio-based feedstock [92, 101]. Moreover, the processes involved are already com-

mercially demonstrated, reducing the risk scale-up challenges for the pathway [100]. The economic feasibility of this process is affected by low conversion yields and high raw material prices [38]. In light of the previous conversion process, for ATJ-SPK and HFS-SIP, the conversion of sugar/starch is further advanced (TRL 7 to 8) compared to the feedstock lignocelluloses (TRL 5 to 6) [8].

- **Catalytic hydrothermolysis jet fuel (CHJ)**

In 2020, Catalytic-Hydrothermolysis-Synthesized Kerosene (CHJ) was certified, allowing a maximum blending ratio of 50%. This Annex A6 conversion process involves heating water and biomass to high temperatures and pressures using a catalyst [92]. This catalyst disintegrates the complex organic molecules in the biomass into less complex hydrocarbons. This leads to the resulting liquid that is then refined and blended to create a fuel that can be used as a sustainable aviation fuel [92]. The feedstock employed in the CHJ process is mainly triglyceride-based feedstocks such as soybean, jatropha, camelina, carinata, and tung oils, being similar to the resources used in the HEFA process [86, 97]. Since this fuel is currently under the demonstration stage, it presents a TRL of 3-4 [8].

- **Synthesized paraffinic kerosene from hydrocarbon - hydroprocessed esters and fatty acids (HC-HEFA-SPK)**

In 2020, another conversion process was approved, the HC-HEFA pathway listed as ASTM D7566 Annex 7. The HC-HEFA process uses waste oils, fats, and algae, and the feed is converted to hydrocarbons by treating the feedstock with hydrogen, removing oxygen and other less desirable molecules. Subsequently, the hydrocarbons undergo cracking and isomerization, producing a synthetic jet fuel suitable for blending [92]. This pathway differs from the HEFA pathway in terms of raw material source. However, based on the certification of ASTM, the only source approved is a special algae species (Botryococcus braunii) [97]. The feedstock generated by the Botryococcus braunii algae is an oil rich in unsaturated hydrocarbons called botryococcenes that differs from the triglycerides or fatty acids produced by other algae species. D4054 Fast Track initially approved the HC-HEFA process, due to this, a maximum blending of 10% is allowed, and it is currently at the pilot demonstration technological level [38, 68].

- **Co-processing**

The minimum value permitted for the blend ratio corresponds to the co-processing. Co-processing is not recognized as a biofuel production method certified under ASTM D7566 specifications. Nevertheless, it is acceptable under ASTM D1655 Annex A1 [97]. The purpose is to expand the proportion of renewable fuels in the final product, decrease the carbon footprint of the refinery, and create a great volume of sustainable aviation fuel [92]. Currently, three co-processing methods have been approved, as displayed in Table 2.3.

As discussed earlier, advancements regarding the use and production of alternatives have been notorious in recent years, having already been tested in real aviation gas turbines. The first flight operating with sustainable aviation fuel was in February 2008, performed by Virgin Atlantic. This flight was carried by a Boeing 747 without passengers to comprehend the viability of biofuels in air travel [9, 108]. A few years later, in June 2011, KLM Airlines carried out the first commercial flight with 171 passengers between Amsterdam Schiphol Airport and Paris Charles de Gaulle Airport, operating with a 50% SAF blend [53, 72]. The viability of SAF in aviation was proved between 2011 and 2015, with over 2500 commercial passenger flights of 22 different airlines using SAF with blends of up to 50%, using jatropha, cooking oil, camelina, and sugarcane feedstock [53, 72]. The production of SAF biofuels around 2019 was approximately 1% of the total global jet fuel demand [38, 109]. Besides the fact that several pathways are already approved, only HEFA-SPK is produced by several companies at an industrial scale [8]. Over time, additional biofuel pathways received approval, and in 2021, the SAF production tripled to 300 million liters from 100 million liters [72]. According to Cui and Chen [9] in December 2021, United Airlines executed a successful demonstration flight operating with 100% SAFs in one of its engines. Rony et al. [68] summarized biofuel production and test research in the aviation industry dedicated to test and commercial flights. To date, strategies to improve the production of SAF are being developed to ease the energy transition of the aviation sector.

2.2.5 Additional Alternative Technologies for Sustainable Aviation

Overall, the production of biofuels is constrained by the availability of feedstock, and expanding production could lead to competition with food crops that are also required for other means of transport. Therefore, it is crucial to identify the most promising and sustainable feedstocks based on their life cycle assessment to enhance their use and improve the widespread production of SAF. Coupled with this, the current production capacity is insufficient, and its costs are higher than those of conventional jet fuel. Reducing jet fuel usage is essential to achieve the criteria for carbon neutrality. Hence, initiatives to explore and research new alternatives for aviation have been developed. After introducing the conversion process to obtain biofuels, additional alternative technologies for the decarbonization of aviation will be further explored. In this respect, synthetic fuels, electric propulsion, and the use of hydrogen in aviation will be discussed.

- **E-Fuels**

The limited accessibility of biogenic feedstock for biofuel production has prompted the development of synthetic fuels from non-biogenic sources [8]. Synthetic fuels, e-fuels, or power-to-liquid are hydrocarbon fuels produced from hydrogen (H_2) and carbon dioxide (CO_2). In this scenario, this developing category of carbon-neutral corresponds to liquid fuels that have similar properties to jet fuel. These fuels are considered candidates that can be implemented with minimal adjustments to conventional aviation engines and employ the current fuel distribution and refuelling infrastructure [110]. Consequently, its environmental impact

depends on several factors, such as the source of CO_2, the technology for H_2 production, the electricity mix, and the electrolyzer efficiency [80].

The production of synthetic fuels requires highly energy-intensive processes related to H_2 production from water electrolysis and obtaining CO_2, requiring renewable electricity to offer substantial potential for reducing emissions. In this respect, one of the main challenges for the large production of these fuels is the availability of green electricity that compromises its application [110]. As noted in Table 2.2, the availability of non-biogenic fuels may expand in the near- to mid-term, being presently limited to experimental phases that can positively contribute to long international flights [8, 92, 111]. Moreover, the production cost of this method is about 5 times higher than kerosene [73]. To address the issue concerning renewable electricity, an alternative is to use solar or wind power [92,110]. The H_2 can be produced via electrolysis of water, while CO_2 can be obtained from biomass combustion, industrial processes (e.g., flue gases from fossil oil combustion), biogenic CO_2, and CO_2 captured directly from the air [80, 101].

The methodology for acquiring CO_2 was described in Ballal et al. [80]. The authors stated that capturing CO_2 can be achieved by employing direct air capture (DAC). This process uses ventilators, heat exchangers, adsorbents, and a vacuum system to capture the atmospheric CO_2 using a temperature-vacuum swing process in an adsorption–desorption cycle. From the biogenic point of view, the obtained CO_2 relies on the biomass-to-liquid conversion process. In this technique, about 45% of biomass carbon is released from the system as CO_2 subsequent to gasification and syngas purification [80]. Following this step, the CO_2 can be combined with hydrogen derived from electrolysis technologies to generate e-fuels, consequently improving the carbon conversion efficiency of the biomass-to-liquid process [80, 112]. The use of biogenic carbon presents the most considerable potential advantages in both present and future instances. However, its true potential for emissions mitigation compared to fossil jet fuel remains significantly reliant on the electricity mix [80]. Alternatively, the CO_2 can be provided from a fossil-fueled power plant based on natural gas [80]. In this context, a common capture method enables the passage of treated flue gas through a chemical adsorption column. Consequently, an amine-based solvent captures the CO_2 in the flue gas and releases it as a purified stream. Instead of storing CO_2 it can be considered a carbon source for producing e-fuels [80]. The production of e-fuels should rely on a renewable transformation of power energy into chemical energy that allows for the long-term use of alternative fuels and easy transportation. E-fuels are derived from the synthesis of H_2 and CO_2, and then produced through two distinct methods: Fischer-Tropsch (FT) synthesis and methanol synthesis that corresponds to catalytic reactions to produce liquid hydrocarbon fuels [14, 79, 110]. However, only the FT method is certified by the ASTM [14]. In this context, renewable electricity is employed to produce H_2 and capture CO_2 to acquire SAF. Subsequently, the transformation into syngas occurs, leading to hydrocarbon synthesis through the Fischer-Tropsch (FT) process [113]. Comparing the costs, the Fischer-Tropsch (FT) process for producing e-fuels is higher than those sourced from biogenic feedstocks due to the substantial requirement for renewable or "green" electricity [8]. Besides this, e-fuels from non-biogenic feedstock exhibit

higher availability but limited production capacities [8].

- **Electric Aircraft Propulsion**

Electric vehicles in ground transportation have attracted notable interest in recent years. Currently, the development of electric batteries or fuel cell vehicles has promoted remarkable advancements in the operational capabilities and storage characteristics [36,109]. Electric vehicles do not promote direct emissions, which can be relevant in addressing climate change. Moreover, advantages in terms of low noise and operating cost reduction have been mentioned [114]. Concerning the emissions from conventional jet fuel, the electrification of aircraft has been explored. Compared to ground transportation, there are several limited prospects for long-distance commercial passenger flights and larger air vehicles [31]. Despite the benefits of electric propulsion systems for aircraft, considering the current low energy density of battery technology, achieving a medium-range flight exclusively powered by electric propulsion within the next decade seems impractical [115]. Several projects for electric aircraft have been developed that should be adapted for their purposes, meaning that different aircraft types require distinct levels of specific energy and specific power to be viable. In light of this, Dahal et al. [116] stated that batteries can propel short-range planes with fewer seats, which is insufficient for single- and twin-aisle aircraft. The ongoing advancements in battery technologies offer the possibility of significant improvements in specific energy. This remains a challenge in determining an exact value for the enhancement, which is required for the design and development of electric aircraft [117]. Additionally, using batteries results in a consistent performance in aircraft performance throughout the flight since batteries do not significantly reduce mass during discharge, as conversely occurs in typically aero-engine, which exhibits weight reduction as fuel is consumed [36]. The aircraft weight remains approximately constant as the energy is consumed, implying that there is no effect on the aircraft center of gravity, offering increased adaptability in aircraft design. Unfortunately, it had a negative effect on the landing performance and substantially increased the energy requirements [73,86]. It is also important to highlight that batteries not only serve as propulsion systems. These elements are essential to aircraft power services such as the flight control system, cabin environmental control system, or the auxiliary power unit (APU) [14].

Despite being one of the most promising energy sources for propulsion, batteries face several limitations that must be overcome for their widespread use in aviation, as previously highlighted. Issues related to high costs and insufficient development of lighter and high-energy-density batteries lead to maximum range limitations, reliance on scarce critical elements, and require further developments in infrastructures and aircraft [13, 14]. The development of batteries consists of energy-intensive processes which have an adverse effect on the environment. Additionally, the production requires scarce and critical materials with diverse social risks and unsatisfactory working conditions, as previously stated by Barke et al. [117]. Li-ion batteries are becoming increasingly relevant for electric aircraft development due to their higher specific energy and demonstrated success in portable electronic devices and the automobile industry [114]. Currently, the gravimetric energy density of lithium-ion (Li-ion)

battery technology is approximately 300 to 400 Wh kg^{-1} whereas jet A-1 presents approximately 12000 Wh kg^{-1} [14]. Moreover, concerns regarding battery material extraction, exposure of occupational toxins to workers and surrounding communities, and soil erosion, as discussed in [36]. Policy interventions are necessary to neutralize these effects, such as producing batteries using alternative materials and extensive recycling capacities for lithium-ion batteries to make these systems viable and fully sustainable [36].

According to Dahal et al. [116], three different electric propulsion configurations are being evaluated: all-electric, turbo-electric, and hybrid-electric. All-electric propulsion systems depend exclusively on the battery or fuel cell as the energy source, while hybrid electric propulsion systems use batteries or fuel cells and gas turbine engines powered by jet fuel. These systems are presently in development and offer the potential to deploy in short-range air travel [50]. Nevertheless, the energy density of batteries should be at least triple to enable all-electric short-haul flights, as reported by [13]. Adopting hybrid electric propulsion in aviation offers a pertinent solution to mitigate the limitations resulting from the relatively low energy density of batteries in fully electric aviation. Hybrid electric propulsion explores the benefits of both systems and will also be crucial in advancing electric aircraft technology [86, 115]. An additional benefit of hybrid propulsion is using SAFs or H_2, amplifying environmental benefits [86]. However, to implement these systems, the aviation infrastructures should be adapted, especially in terms of recharge cycles [111]. The turbo-electric combines a gas turbine with an electric generator to convert the chemical energy from a fuel into electrical power to drive the electric propulsor, either entirely or partially [116, 118, 119]. In a generic sense, for an electric propulsion system, power and thrust for the aircraft are provided through electric motors driven by a generator, which receives its energy from liquid or gaseous fuels (e.g., kerosene or hydrogen) and/or batteries [119]. In an all-electric aircraft, propellers generate thrust, electric motors drive them, and batteries store energy [117]. Figure 2.10 shows a conceptual design for a fully electric aircraft.

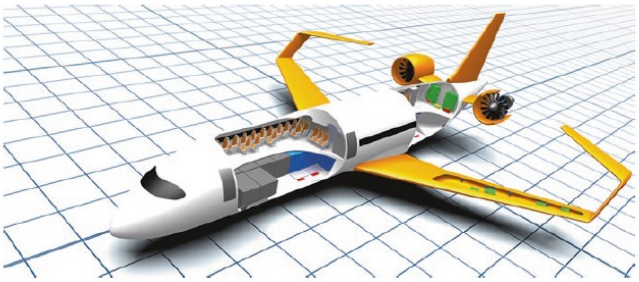

Figure 2.10: Conceptual design for a full electric aircraft [74, 120].

Similar to the e-fuels, energy requirements for the electrification of aviation would require a considerable expansion of the electrical grid [36]. Particularly, the impact on environmental sustainability mainly relies on the energy production methods of the electrical grid. Due to this, the ability to decrease emissions through adopting battery-electric aircraft also depends on expanding renewable energy sources [36]. If electric aviation uses electricity generated by renewable sources, direct CO_2 emissions are negligible throughout the usage phase [13]. Be-

sides its advantages in reducing aviation emissions, adopting electric aircraft is challenging and complex since it faces several technological and regulatory challenges that hinder energy transition in aviation [114]. Furthermore, investigation into hybrid and electric aircraft has been developed. For long-haul flights, it will depend more on SAF due to the challenges in currently introducing other options [109]. To enable both short/medium and long-haul flights through electrification, the mass of the battery required to store the necessary energy leads to a take-off weight increase of 1.7 and 3.8 times the maximum acceptable take-off weight of the entire aircraft, respectively [50]. The introduction of electric aircraft is not feasible in the immediate future. As noted by Cabrera and Sousa [86], large battery-powered aircraft are not expected to perform flight distances of 500km even by 2050. Presently, advancements in fully electric aircraft designed to transport 2–9 passengers have already been performed through the NASA X-57 program, Pipistrel Velis Electro aircraft, and Eviation Alice aircraft, enforcing the purpose of scaling these developments to larger transport-class applications [36].

- **Hydrogen**

The implementation of hydrogen in the aviation sector has disrupted attention in academia and industry [121]. This renewable energy source stands apart from biofuels due to its absence of food security or sourcing, does not emit greenhouse gases from petroleum, and does not present the storage limitations experienced by batteries [122]. Compared to batteries, it provides higher energy-to-mass [50]. Several methods to produce hydrogen are categorized according to their impact on sustainability [73]. If hydrogen is obtained from coal, it is termed ”black”, when derived from natural gas through steam methane reforming, it is identified as ”gray”, whereas if generated from natural gas with carbon capture, it is named ”blue”. Green hydrogen emerged when its production relies on renewable energy [122]. More specifically, it is obtained from the electrolysis of water employing electricity derived from sustainable energy sources, such as wind power, hydroelectricity, or solar power, as noted by Ficca et al. [73]. This method also produces synthetic fuel, presenting relatively minimal conversion losses from electricity to hydrogen through electrolysis [86, 111]. Hydrogen is also required to hydrogenate aviation biofuels [14]. Hydrogen can potentially operate as an energy source for aircraft through combustion as fuel or in fuel cells. Hydrogen combustion can be employed as a substitute for liquid fuel. However, engine configuration adjustments are also necessary, as in airport infrastructures [86]. The hydrogen fuel cell produces electrical power through an electrochemical reaction involving hydrogen and oxygen. Similar to hydrogen combustion, hydrogen fuel cells employ hydrogen as their primary fuel [73]. This system emits lower or zero emissions compared to traditional engines; specifically, they are environmentally friendly and noiseless and generate water vapor as exhaust [73]. Nevertheless, their viability in the aviation sector is also restricted by range limitations [86].

In simple terms, hydrogen combustion, either liquid or gaseous, should burned in a modified turbofan or turboprop engine to produce propulsion [73]. One of the main challenges in hydrogen propulsion is hydrogen storage. In contrast with jet fuel, a liquid fuel, hydrogen

is a gas that requires pressurized tank storage to minimize its volume [73]. Due to this, it requires cryogenic hydrogen, also defined as liquid hydrogen, that demands specific equipment for its storage [14, 73]. Moreover, to liquefy hydrogen, it is essential to decrease its temperature to -253 °C at ambient pressure to convert it into a liquid, which influences the volumetric energy density and displays limitations on the combustor and fuel system of aircraft [110]. Cryogenic tanks are larger and heavier than conventional systems and, due to this, are incompatible with storage in aircraft wings as conventional jet fuel. As a result, fuel tanks may have to be incorporated into the aircraft fuselage, influencing the seating capacity and available space [110, 111]. It also raises more difficulties regarding the complex pressure and thermal requirements [75]. Hydrogen possesses a gravimetric energy density three times greater than conventional kerosene. However, it presents lower volumetric energy density than jet fuel, approximately four times requiring more volume of hydrogen, [14, 73, 75]. According to Gray et al. [50], an aircraft under jet fuel operation accounts for 9% and 20% of the aircraft maximum allowable take-off weight for short and long haul flight, whereas an aircraft using cryogenic hydrogen would contribute to 32% and 71% of maximum allowable take-off weight for short and long-haul flights, respectively. There are several prototypes in development for the use of hydrogen in aviation. H_2 fuel cell aircraft is exclusively for short-range flights, while hydrogen turbine aircraft are predicted to be capable of flying longer distances, it is not expected that they will be able to perform long-distance flights due to their limited energy density [86, 123].

Despite the several advantages of mitigating conventional jet fuel emissions, using hydrogen remains an engineering challenge. To implement hydrogen, it is mandatory to redesign and build new aircraft and additional infrastructures for production, distribution, and refuelling to address fuel storage and safety [50, 86, 111]. Regarding aircraft fuelled by hydrogen, it is essential to develop new materials to reduce the tank weight, and as previously mentioned, the cryogenic tank is unsuitable for the current aircraft wings. Consequently, during the design phase, the location of hydrogen tanks should be taken into account during the preliminary concept to ensure the passengers safety and aircraft operation [14]. Ling-Chin et al. [124] provide several designs for the use of hydrogen by regional, short-, medium- and long-range aircraft. Additionally, airports must reinforce the infrastructure to store, liquefy, and transport hydrogen to aircraft. This requires updated safety procedures due to the use of cryogenic temperature and should consider the longer refuelling times for aircraft related to the increased volume needed [73]. As previously indicated, hydrogen combustion does not emit CO_2 emissions. On the other hand, it is responsible for the NO_x and water vapor, which results in contrails at high altitudes [73, 75, 121]. Regarding its combustion, it possesses a higher stability range, peak combustion temperature, and a higher burning velocity leading to smaller flame fronts, [75]. As discussed, there is still a long way to go for introducing hydrogen, and this alternative may not be fully available before 2050 to attain the prerequisites imposed by the ICAO, being the first commercial aircraft expected by 2035 [111]. However, the research and development process is crucial where improvements in the supply chain and production process are imperative [13]. Additionally, it is expected that, as time evolves, the technology reaches a level of maturity suitable for aircraft application through decreasing

costs and increasing the availability of green hydrogen sources to become a competitive and sustainable option for this industry [73].

2.2.6 Sustainability in Aviation: Alternatives Comparison

As highlighted earlier, there are several relevant alternatives to address the environmental challenges in the aviation sector. All of these alternatives can play a pertinent position in addressing the environmental concerns of aviation. Renewable feedstock, such as biomass, implies that the carbon released in its operation is reintroduced into the atmosphere, whereas e-fuels, electric aircraft, and hydrogen are predominantly influenced by the primary fuels or energy carriers utilized in their production processes [116]. The alternatives can be categorized as drop-in and non-drop-in fuels. Biofuels and synthetic fuels are sustainable aviation fuels (SAF) or drop-in aviation fuels that can be relevant in mitigating aviation emissions in the near to medium term [50]. These liquid fuels possess almost identical chemical and physical characteristics, allowing their implementation in the current fleet and not demanding alterations and adjustments in the traditional fuel systems, such as fuel distribution network [101]. Biofuels have been extensively researched as alternative fuels in recent years. As noted in Table 2.3, several pathways are already approved. To avoid dependence on biomass and to reduce the difficulties associated with biofuel land use, synthetic fuels or e-fuels have emerged as sustainable aviation fuels. These fuels can be relevant to achieving goals in the medium and long term, mainly for long-haul flights [79,113]. Its production relies on hydrogen (H_2) from water electrolysis and industrial or atmospheric CO_2, as previously stated [8, 14, 113].

Sustainable aviation fuels (synthetic fuels and biofuels) can be stored and transported similarly to conventional fossil fuels, being more resilient in light of disruptions and quickly mitigating greenhouse gas and pollutant emissions [42]. Moreover, SAFs are drop-in fuels with a limited blend with conventional jet fuel previously tested and approved for aero-engines. There are some challenges to the widespread implementation of SAFs, for example, due to high costs and renewable electricity [9]. In this respect, new technology options are also being investigated in the aviation industry. The non-drop alternatives are carbon-free fuels mainly focused on electric and hydrogen-powered aircraft. However, aviation relies on prolonged lifecycles of infrastructures, aircraft, and engine technologies, coupled with an extremely restricted scope of new technology applications [125]. Due to this, these alternatives present specification/legal constraints that require more technological adaptations in terms of aviation systems, including fuel and airport infrastructure. Furthermore, it involves the costly and time-consuming processes of developing and certifying new aircraft technology, which makes it difficult to transition to alternative low-carbon energy sources in the near future [8, 85]. The success of their implementation depends on collective efforts from airlines, airports, air navigation service providers, manufacturers, and substantial government support [73]. Moreover, electric aircraft and hydrogen-powered aircraft are new technologies that will take 20 years or even from conceptualization to achieve operational maturity [74, 125]. Its development should also consider risk and safety concerning distinct

combustion properties of hydrogen and hydrogen blends compared to conventional fuels and explosion hazards due to the possibility of thermal runaway and combustible gases released by batteries [75]. Additionally, batteries present a low energy density and high weight, whereas liquid hydrogen storage requires more volume than conventional kerosene propulsion systems, adaption in aircraft structure for the cryogenic tank [119]. The low energy density of these alternatives reduces the aircraft range and diminishes the extent of adaptability regarding its applicable routes, a disadvantage for airline operations [8]. These new technologies should initially be implemented in smaller aircraft categories before expanding their use to larger segments, as stated by Ficca et al. [73]. The potential of prioritizing a change towards hydrogen instead of a drop-in fuel pathway would probably affect the defined goal for the aviation sector decarbonization in 2050. Consequently, Scheelhaase et al. [125] stated that e-fuels can effectively present higher costs but are more propensity to global carbon reduction efforts sooner than those originating from a hydrogen trajectory. Similarly, aircraft powered by all-electric or hybrid modes can address environmental concerns. However, due to the energy storage limitations, it is not expected to be applicable for long-distance applications currently [101]. Figure 2.11 shows an overview of the alternatives for aviation regarding its strengths and challenges.

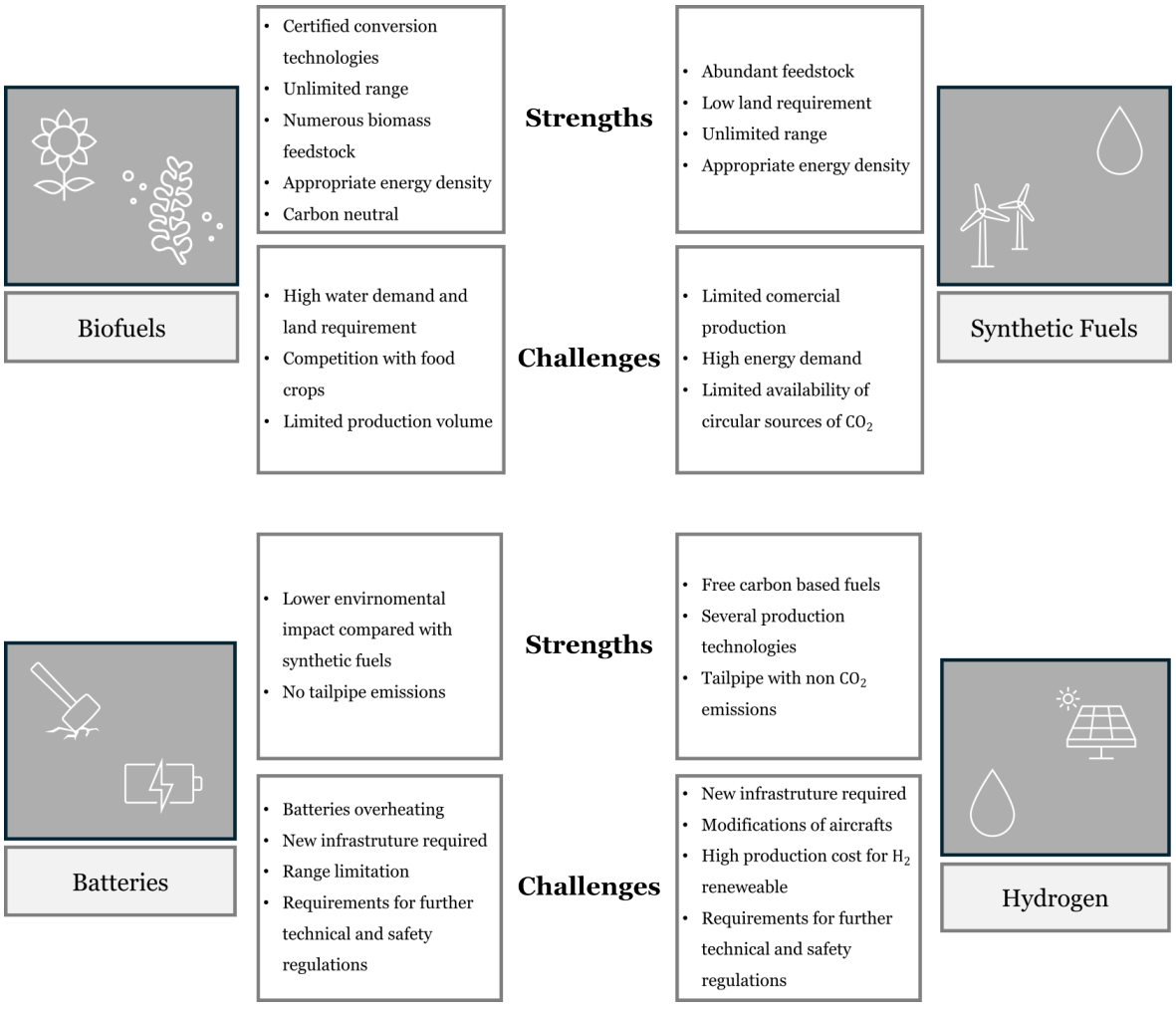

Figure 2.11: Strengths and challenges of alternatives for aviation [1, 14, 126].

2.3 Single Droplet

The relevance of liquid fuels in our society has already been discussed. In combustion systems, the study of droplets and spray is fundamental to developing our understanding of how to improve engines. Moreover, the limited availability of conventional fuel supplies, as well as the environmental concerns, provides a strong incentive to utilize alternative sources. The focus of research and development of future alternatives is a requisite to widen the potential fuel in practical applications, which initially require a fundamental study in terms of droplet evaporation/combustion, spray atomization, combustion, and its emissions. In light of this, the present section provides an overview of single droplet evaporation/combustion in terms of theoretical, experimental, and numerical approaches. In addition, the use of particles in a liquid fuel is presented, addressing its advantages and disadvantages. Additionally, the current advancements in this field and the preparation methods are outlined.

2.3.1 Overview

The spray is composed of individual droplets that constitute the dispersed phase surrounded by a gas medium that corresponds to the continuous phase [127]. Diesel, rocket, and gas-turbine engines, as well as oil-fired boilers, furnaces, and process heaters, incorporated spray combustion in their operations [128]. However, spray combustion is a complex multidimensional aerothermochemical process that involves different physical and chemical processes interacting simultaneously [127]. Due to this, the initial step involves investigating single droplet evaporation and combustion to understand the spray process in a large-scale system. Preliminary studies were dedicated to single droplet evaporation concerning dilute sprays. Frössling [129] evaluated droplet evaporation of water, nitrobenzene, and aniline suspended in air, and a dimensionless analysis was derived based on the relationship for the Sherwood number as a function of the Reynolds and Schmidt number [127]. The vaporization of a droplet is a multidisciplinary topic that involves heat and mass transport, fluid dynamics, and chemical kinetics [130]. Generally, the process of droplet evaporation consists of two main phases. The first concerns the detachment of molecules from the surface of the droplet into gas in the immediate vicinity of the droplets. Afterward, the vapor diffuses from the droplet surface into the environment [131]. In addition, studies developed by Williams [132] and Ranz and Marshall [133] were essential as introductory research for the more complex study of the ignition and combustion of fuels [134]. Over the past few decades, the evaporation and combustion of droplets have been extensively investigated and reported in the literature [135–139]. Significant advancements have been achieved in theoretical progress for liquid fuel droplet evaporation and combustion, including the establishment of physical models. In this context, the classic combustion theory for isolated liquid fuel droplets was first proposed by Godsave [140] and Spalding [141] and is typically known as the D^2-law for droplet combustion. The model was developed based on an isolated, pure-component droplet burning in an oxidizing environment. Additionally, the convective effects can be easily included using the film theory, as will be further discussed. The classic D^2-law, derived by assuming spherical symmetry, quasi-steadiness, and flame-sheet combustion, predicts

the decrease of the square of the droplet diameter linearly with time. The model assumes constant average properties for the gas phase. While there can be significant variations in these properties from the droplet surface to the ambient surroundings, careful selection of mean values enables reasonably accurate predictions. To facilitate the comprehension, Table 2.4 displays the assumptions that yield a simplified model for single droplet combustion while preserving the essential physical processes.

Table 2.4: Assumptions made in the simplified model for single droplet combustion [128].

No.	Assumption
1	A spherical burning droplet, surrounded by a spherically symmetric flame, is located in an infinite medium.
2	Combustion process is quasi-steady. This means that the process can be described as in a steady state at any instant in time.
3	Fuel is mono-component with zero solubility for gases, and phase equilibrium prevails at the liquid-vapor interface.
4	Pressure is constant and uniform.
5	The gaseous phase consists only of fuel vapor, oxidizer, and combustion products.
6	Fuel and oxidizer react in stoichiometric proportions at the flame front. Chemical kinetics are assumed to be infinitely fast, resulting in an infinitesimally thin flame reaction sheet.
7	Lewis number, Le, defined as the ratio of thermal diffusivity to mass diffusivity, is unity.
8	Radiative heat transfer is negligible.
9	Liquid fuel is the only condensed phase, i.e., no soot or liquid water is present.

Figure 2.12 shows a schematic of the spherically-symmetric droplet combustion model based on the previous assumptions presented in Table 2.4. The temperature and species profiles are displayed through the inner region between the droplet surface and the flame, $r_s \leq r \leq r_f$, and through the outer region beyond the flame, $r_f \leq r < \infty$. The flame represents a sink for the outwardly transported fuel vapor and inwardly transported oxidizer gas. A detailed description of the theoretical formulation for the simplified droplet combustion model is provided below, which can also be found in Turns [128].

Focusing on the mass conservation in the gas phase and assuming a quasi-steady burning, the total mass flow rate is constant

$$\dot{m}(r) = \dot{m}_F = \rho_g v_r 4\pi r^2 = constant\,, \quad \textbf{(2.1)}$$

where $\dot{m}_F$ is the fuel mass flow rate, ρ_g is the gas density and v_r is the bulk flow velocity. The total mass flow rate remains identical to the fuel mass flow rate throughout the combustion process, corresponding to the burning rate, which is relevant in the application of species conservation, as will be discussed.

In the inner region, designated by region 1 presented in Figure 2.12, Fick's law can be applied

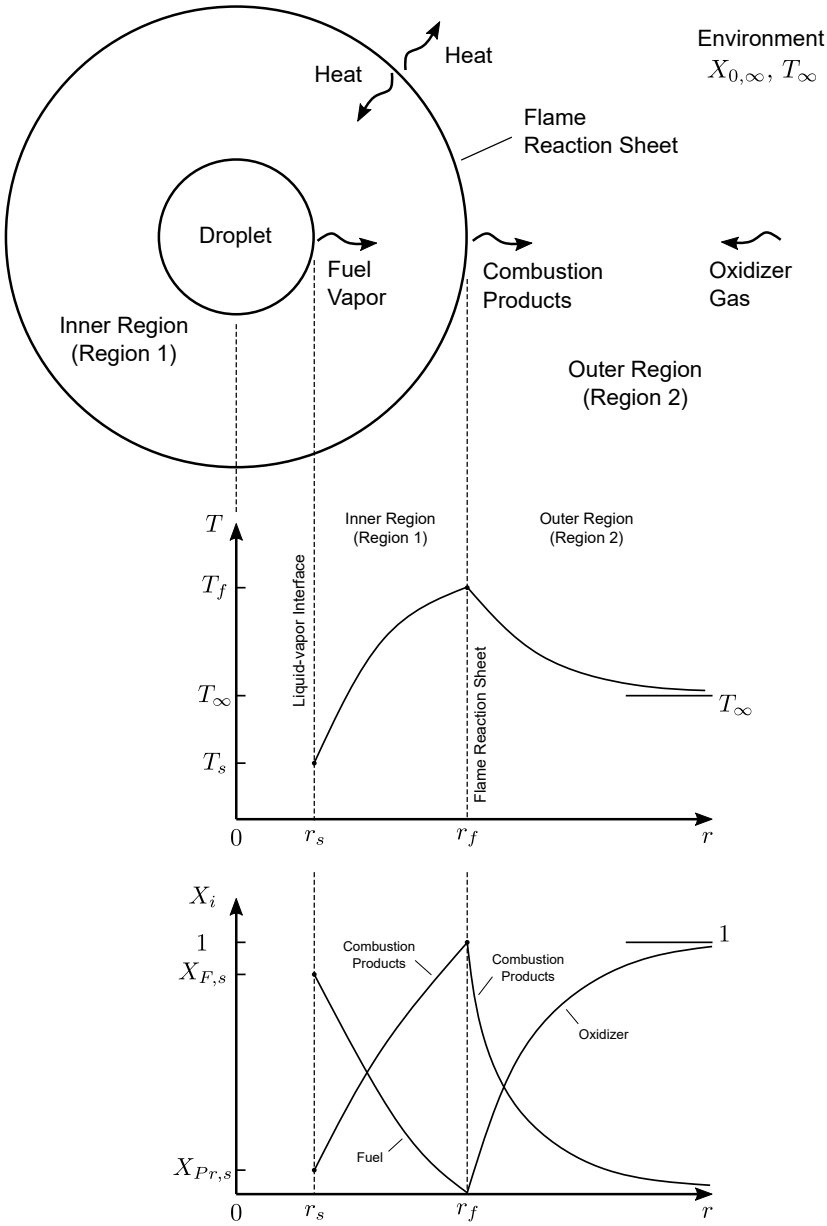

Figure 2.12: Schematic of the simplified droplet combustion model and its temperature and species profiles, adapted from [128, 142].

$$\dot{\mathbf{m}}''_F = X_F \left(\dot{\mathbf{m}}''_F + \dot{\mathbf{m}}''_{Pr} \right) - \rho_g \mathcal{D}_g \nabla X_F \,, \quad (2.2)$$

where $\dot{\mathbf{m}}''_F = \dot{m}_F / 4\pi r^2$ is the mass flux of fuel vapor, $\dot{\mathbf{m}}''_{Pr} = 0$ is the mass flux of combustion products, X_F is the mass fraction of fuel vapor and $\mathcal{D}_g$ is the mass diffusivity coefficient for gases. In spherical coordinates where the only variations occur in the radial direction, the ∇-operator becomes $\nabla() = d()/dr$. Therefore, Equation (2.2) yields

$$\dot{m}_F = -4\pi r^2 \frac{\rho_g \mathcal{D}_g}{1 - X_F} \frac{dX_F}{dr} \,. \quad (2.3)$$

Equation (2.3) has to satisfy two boundary conditions: one at the droplet surface, $r = r_s$, in which liquid-vapor equilibrium prevails

$$X_F(r_s) = X_{F,s}(T_s), \quad (2.4)$$

where $X_{F,s}$ is the fuel vapor mass fraction at the droplet surface at surface temperature, T_s; and another at the flame front location, $r = r_f$, where the fuel vanishes

$$X_F(r_f) = 0. \quad (2.5)$$

Integrating Equation (2.3), defining $Z_F \equiv 1/(4\pi\rho_g\mathcal{D}_g)$ and applying the boundary condition defined by Equation (2.4), the following expression for the fuel vapor mass fraction is obtained

$$X_F(r) = 1 - \frac{(1 - X_{F,s})\exp(-Z_F\dot{m}_F/r)}{\exp(-Z_F\dot{m}_F/r_s)}. \quad (2.6)$$

Applying the flame boundary condition given by Equation (2.5), one gets the following expression for the fuel vapor mass fraction at the droplet surface

$$X_{F,s} = 1 - \frac{\exp(-Z_F\dot{m}_F/r_s)}{\exp(-Z_F\dot{m}_F/r_f)}. \quad (2.7)$$

To fully resolve the species conservation in region 1, the mass fraction of combustion products can be expressed as follows. However, this step is not required to achieve the main objective.

$$X_{Pr}(r) = 1 - X_F(r). \quad (2.8)$$

In the outer region, denoted by region 2, the oxidizer and fuel combine stoichiometrically at the flame front according to

1 kg fuel + ν_{of} kg oxidizer = (ν + 1) kg combustion products,

where ν_{of} is the oxidizer-to-fuel stoichiometric mass ratio and includes non reacting gases that may constitute the oxidizer stream, e.g., nitrogen. This relationship is depicted in Figure 2.13. The mass flux vectors in Fick's law are, then, $\dot{\mathbf{m}}''_{Ox} = -\nu_{of}\dot{\mathbf{m}}''_F$ and $\dot{\mathbf{m}}''_{Pr} = +(\nu_{of}+1)\dot{\mathbf{m}}''_F$. Thus, the Fick's law in region 2 is

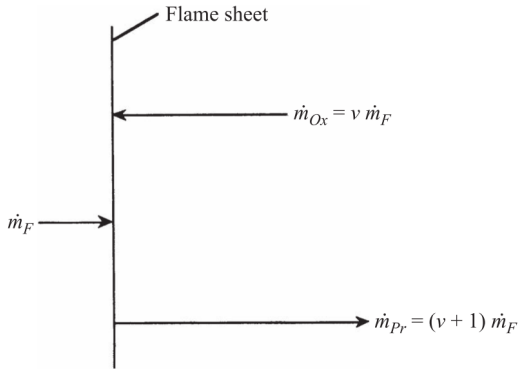

Figure 2.13: Schematic of the mass flow relationships at the flame reaction sheet. Note that the net mass flow in both the inner and outer regions is equal to the fuel mass flow rate, $\dot{m}_F$ [128].

$$\dot{m}_F = +4\pi r^2 \frac{\rho_g \mathcal{D}_g}{\nu_{of} + X_{Ox}} \frac{dX_{Ox}}{dr}\,, \quad \textbf{(2.9)}$$

where X_{Ox} is the mass fraction of oxidizer. The boundary conditions that Equation (2.9) must satisfy are

$$X_{Ox}(r_f) = 0\,, \quad \textbf{(2.10a)}$$
$$X_{Ox}(r \to \infty) = X_{Ox,\infty} = 1\,. \quad \textbf{(2.10b)}$$

Integration of Equation (2.9) and application of the flame boundary condition described by Equation (2.10a), yields

$$X_{Ox}\,(r) = \nu_{of} \left[\frac{\exp\left(-Z_F \dot{m}_F / r\right)}{\exp\left(-Z_F \dot{m}_F / r_f\right)} - 1 \right]\,. \quad \textbf{(2.11)}$$

Applying the boundary condition at $r \to \infty$ given by Equation (2.10b), one obtains the following equation

$$\exp\left(+Z_F \dot{m}_F / r_f\right) = \frac{\nu_{of} + 1}{\nu_{of}}\,. \quad \textbf{(2.12)}$$

To complete the species conservation in region 2, the distribution of combustion products mass fraction can be expressed as follows

$$X_{Pr}(r) = 1 - X_{Ox}(r)\,. \quad \textbf{(2.13)}$$

A brief explanation of energy conservation in the gas phase is discussed. With the assumption of a unity Lewis number, the one-dimensional spherical Shvab-Zeldovich form of the energy equation is suitable for describing gas-phase energy conservation [128]

$$\frac{1}{r^2}\frac{d}{dr}\left[r^2\left(\rho_g v_r \int c_{pg}dT - \rho_g \mathcal{D}_g \frac{d\int c_{pg}dT}{dr}\right)\right] = -\sum h^o_{f,i}\dot{m}'''_i\,, \quad (2.14)$$

where c_{pg} is the gas specific heat and $h^o_{f,i}$ and $\dot{m}'''_i$ are, respectively, the enthalpy of formation and mass production rate per unit volume of component i. As chemical reactions are limited to the boundary or flame front, the reaction rate term in Equation (2.14) is zero in the flame inner and outer regions. Moreover, with the assumption of constant properties, Equation (2.14) can be reformulated and expressed as

$$\frac{d\left(r^2\frac{dT}{dr}\right)}{dr} = Z_T\dot{m}_F\frac{dT}{dr}\,, \quad (2.15)$$

where $Z_T = c_{pg}/(4\pi k_g)$ was defined for convenience and k_g is the gas thermal conductivity. The parameter Z_F, defined in the species conservation analysis, equals Z_T when the Lewis number is unity, as in that case $c_{pg}/k_g = \rho_g\mathcal{D}_g$. The boundary conditions applied to Equation (2.15) are the following: for the inner region,

$$T(r_s) = T_s\,, \quad (2.16a)$$
$$T(r_f) = T_f\,, \quad (2.16b)$$

where T_f is the droplet flame temperature; and for the outer region,

$$T(r_f) = T_f\,, \quad (2.17a)$$
$$T(r\to\infty) = T_\infty\,, \quad (2.17b)$$

where T_∞ is the environment temperature. The general solution of Equation (2.15) is

$$T(r) = \frac{C_1\exp\left(-Z_T\dot{m}_F/r\right)}{Z_T\dot{m}_F} + C_2\,, \quad (2.18)$$

and, in region 1, the temperature distribution resulting from the implementation of Equations (2.16a) and (2.16b) is expressed by

$$T(r) = \frac{(T_s - T_f)\exp\left(-Z_T\dot{m}_F/r\right) + T_f\exp\left(-Z_T\dot{m}_F/r_s\right) - T_s\exp\left(-Z_T\dot{m}_F/r_f\right)}{\exp\left(-Z_T\dot{m}_F/r_s\right) - \exp\left(-Z_T\dot{m}_F/r_f\right)}\,, \quad (2.19)$$

for $r_s \leq r \leq r_f$. In region 2, the adoption of Equations (2.17a) and (2.17b) to Equation (2.18), leads to

$$T(r) = \frac{(T_f - T_\infty)\exp\left(-Z_T \dot{m}_F / r\right) + T_\infty \exp\left(-Z_T \dot{m}_F / r_f\right) - T_f}{\exp\left(-Z_T \dot{m}_F / r_f\right) - 1}\,, \quad (2.20)$$

for $r_f < r < \infty$. Figure 2.14 shows the conductive heat transfer rates and enthalpy fluxes present at the surface of the evaporating droplet.

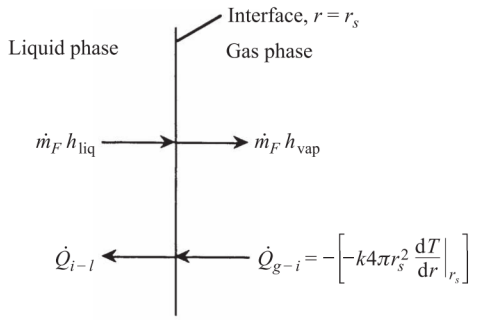

Figure 2.14: Schematic of the surface energy balance at the droplet liquid-vapor interface [128].

Thermal energy is conducted from the flame to the surface of the droplet, where part of it is used to vaporize the fuel, and the rest is transferred into the droplet interior. This process leads to the following mathematical expression:

$$\dot{Q}_{g-i} = \dot{m}_F \left(h_{vap} - h_{liq}\right) + \dot{Q}_{i-l} \quad (2.21)$$

or

$$\dot{Q}_{g-i} = \dot{m}_F h_{fg} + \dot{Q}_{i-l}\,, \quad (2.22)$$

where $\dot{Q}_{g-i}$ is the heat conducted into the droplet surface, $h_{fg} = h_{vap} - h_{liq}$ is the latent heat of vaporization, and $\dot{Q}_{i-l}$ represents the heat conducted into the interior of the droplet. $\dot{Q}_{i-l}$ can be addressed using various approaches. Additional details can be found in Turns [128]. The simplest approach to determine $\dot{Q}_{i-l}$ is to assume that the droplet quickly heats up to a steady temperature, T_s. This means that the droplet thermal inertia is negligible, $\dot{Q}_{i-l} = 0$. Moreover, Fourier's law can evaluate the conductive heat transfer from the gas phase, $\dot{Q}_{g-i}$. Replacing in Equation (2.22), results

$$-\left[-k_g 4\pi r^2 \frac{dT}{dr}\right]_{r_s} = \dot{m}_F h_{fg}\,, \quad (2.23)$$

where the temperature gradient at the droplet surface, $(dT/dr)_{r_s}$, can be obtained by differentiating the temperature distribution in region 1, defined by Equation (2.19). Evaluating the heat-transfer rate at $r = r_s$, by reorganizing and incorporating the definition of Z_T in

Equation (2.23), the following expression can be established

$$\frac{c_{pg}(T_f - T_s)}{h_{fg}} \frac{\exp\left(-Z_T \dot{m}_F / r_s\right)}{\exp\left(-Z_T \dot{m}_F / r_s\right) - \exp\left(-Z_T \dot{m}_F / r_f\right)} + 1 = 0\,. \quad (2.24)$$

Figure 2.15 depicts the correlation of the various energy fluxes at the flame reaction sheet.

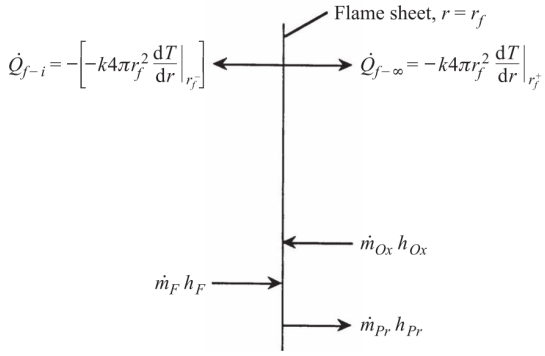

Figure 2.15: Schematic of the surface energy balance at the flame reaction sheet [128].

Considering the flame temperature is the highest temperature present in the system, heat conduction occurs both into the droplet, $\dot{Q}_{f-i}$, and towards the surrounding environment $\dot{Q}_{f-\infty}$. Chemical energy release is addressed by employing standardized enthalpy fluxes for the fuel, oxidizer, and combustion products. Thus, the surface energy balance at the flame reaction sheet can be expressed as

$$\dot{m}_F h_F + \dot{m}_{Ox} h_{Ox} - \dot{m}_{Pr} h_{Pr} = \dot{Q}_{f-i} + \dot{Q}_{f-\infty}\,. \quad (2.25)$$

The definitions of the enthalpies are expressed as

$$h_i \equiv h^o_{f,i} + c_{pg}(T - T_{ref}), \quad (2.26)$$

for $i = F,\, Ox,\, Pr$, where T_{ref} is the reference temperature. The heat of combustion per unit mass of fuel, Δh_c, is expressed as

$$\Delta h_c(T_{ref}) = (1)h^o_{f,F} + (\nu_{of})h^o_{f,Ox} - (1 + \nu_{of})h^o_{f,Pr}\,. \quad (2.27)$$

Despite the presence of combustion products in the inner region, there is no net flow of these products occurs between the droplet surface and the flame front. Thus, all the combustion products flow radially outward away from the flame. The mass flow rates of fuel, oxidizer, and combustion products are stoichiometrically related. Considering this, Equation (2.25)

becomes

$$\dot{m}_F \left[h_F + \nu_{of} h_{Ox} - (\nu_{of} + 1) h_{Pr}\right] = \dot{Q}_{f-i} + \dot{Q}_{f-\infty} \,. \quad (2.28)$$

Replacing Equations (2.26) and (2.27) into Equation (2.28), yields

$$\dot{m}_F \Delta h_c + \dot{m}_F c_{pg} \left[(T_f - T_{ref}) + \nu_{of}(T_f - T_{ref}) - (\nu_{of} + 1)(T_f - T_{ref})\right] = \dot{Q}_{f-i} + \dot{Q}_{f-\infty} \,. \quad (2.29)$$

Considering that c_{pg} is constant, Δh_c is independent of temperature; thus, the flame temperature can be chosen as a reference state to simplify Equation (2.29). Repeatedly, relying on Fourier's law to evaluate the conductive heat transfer terms, $\dot{Q}_{f-i}$ and $\dot{Q}_{f-\infty}$, it follows

$$\dot{m}_F \Delta h_c = k_g 4\pi r_f^2 \left.\frac{dT}{dr}\right|_{r_f^-} - k_g 4\pi r_f^2 \left.\frac{dT}{dr}\right|_{r_f^+} , \quad (2.30)$$

in which Equation (2.19) is differentiated to evaluate the temperature gradient at $r = r_f^-$, and Equation (2.20) is differentiated to evaluate the gradient at $r = r_f^+$. By applying these substitutions and rearrangements, the energy balance at the flame reaction sheet can be expressed as

$$\frac{c_{pg}}{\Delta h_c} \left[\frac{(T_s - T_f)\exp\left(-Z_T \dot{m}_F / r_f\right)}{\exp\left(-Z_T \dot{m}_F / r_s\right) - \exp\left(-Z_T \dot{m}_F / r_f\right)} - \frac{(T_\infty - T_f)\exp\left(-Z_T \dot{m}_F / r_f\right)}{1 - \exp\left(-Z_T \dot{m}_F / r_f\right)}\right] - 1 = 0 \,. \quad (2.31)$$

Finally, it is assumed that liquid-vapor equilibrium exists at the droplet surface. The Clausius-Clapeyron equation is incorporated for conditions close to the fuel normal boiling point, resulting in the following expression for the fuel vapor partial pressure at the droplet surface

$$P_{F,s} = P \exp\left[\frac{h_{fg}}{R}\left(\frac{1}{T_{boil}} - \frac{1}{T_s}\right)\right] , \quad (2.32)$$

where $P = 1$ atm is the atmospheric pressure, $R = R_u / MW$ is the specific gas constant, R_u is the universal gas constant, MW is the molecular weight and T_{boil} is the fuel normal boiling temperature. The fuel partial pressure can be related to the fuel mole fraction and mass fraction as follows

$$\chi_{F,s} = \frac{P_{F,s}}{P} \quad (2.33)$$

and

$$X_{F,s} = \chi_{F,s} \frac{MW_F}{\chi_{F,s} MW_F + (1 - \chi_{F,s}) MW_{Pr}} . \quad (2.34)$$

Substituting Equations (2.32) and (2.33) into Equation (2.34), yields the following expression

$$X_{F,s} = \frac{P \exp\left[\frac{h_{fg}}{R}\left(\frac{1}{T_{boil}} - \frac{1}{T_s}\right)\right] MW_F}{P \exp\left[\frac{h_{fg}}{R}\left(\frac{1}{T_{boil}} - \frac{1}{T_s}\right)\right] MW_F + P\left[1 - \exp\left[\frac{h_{fg}}{R}\left(\frac{1}{T_{boil}} - \frac{1}{T_s}\right)\right]\right] MW_{Pr}} . \quad (2.35)$$

Consequently, the mathematical formulation for the classic single droplet combustion theory is completed as presented in Turns [128]. The solution to the problem has been attained, resulting in five equations (2.7), (2.12), (2.24), (2.31) and (2.35); for five unknowns: $\dot{m}_F$, r_f, T_f, T_s and $Y_{F,s}$. The system of nonlinear equations can be significantly simplified if T_s is treated as a known parameter. Considering that the chemical effects often dominate over thermal effects, particularly when the surrounding environment is cold, making T_∞ approximately equal to T_s. As a result, the precise value of T_s is usually not required. Additionally, considering that the droplet is expected to be near its boiling point during steady-state combustion under intense heating, it is proper to assume that $T_s = T_{boil}$ [143], thereby implying $Y_{F,s} = 1$. Solving Equations (2.12), (2.24) and (2.31) for $\dot{m}_F$, r_f and T_f, the analytical solution for the fuel mass flow is achieve. Considering that the theoretical model focuses on predicting combustion characteristics, such as droplet size evolution and constant burning rate, the analytical solution for the fuel mass flow rate is given by the following expression [128]:

$$\dot{m}_F = \frac{4\pi k_g r_s}{c_{pg}} \ln\left(1 + B_{o,q}\right), \quad (2.36)$$

where the Spalding heat transfer number, $B_{o,q}$, is defined as

$$B_{o,q} = \frac{\Delta h_c / \nu_{of} + c_{p,g}\left(T_\infty - T_s\right)}{h_{f,g}}, \quad (2.37)$$

where Δh_c is the enthalpy of combustion, ν is the kinematic viscosity and $h_{f,g}$ is the latent heat of vaporization. It is assumed that the fuel droplet temperature is at its boiling point, $T_s = T_{boil}$ [143]. For very small droplets, the initial heating from ambient temperature up to boiling temperature happens rapidly and hence can be neglected. Consequently, the burning rate, K_c, is shown by the subsequent equation:

$$\frac{dD^2}{dt} = -K_c = \frac{8 k_g}{\rho_l c_{p,g}} \ln\left(1 + B_{o,q}\right), \quad (2.38)$$

where k_g is the thermal conductivity of the gas, ρ_l is the liquid density and $c_{p,g}$ is the specific

heat. The inclusion of the convective effects in D^2-law was previously reported by [128]. In this way, for a quiescent medium, Nu_d = 2, however, taking into account the convection effects, the burning rate can be defined as:

$$K_c = \frac{4k_g Nu_d}{\rho_l c_{pg}} \ln\left(1 + B_{o,q}\right). \quad (2.39)$$

Given that, the simplified basis of the D^2-law for droplet combustion represented in Equation (2.40) states that the square of the droplet diameter decreases linearly with time as evaporation proceeds [143]. Considering the initial condition $D(t = 0)$ = D_0, the D^2-law is represented by:

$$D^2 = D_0^2 - K_c t. \quad (2.40)$$

To summarize, the phenomena of single droplet combustion initiate when a droplet is inserted into a high-temperature environment, and heat transfer from the gas phase leads to an increase in the droplet surface temperature. The energy is conducted on the droplet until it reaches its boiling temperature. As heat is conducted inward, the droplet interior temperature increases, leading to a substantial loss of droplet mass. As the fuel is evaporated into the gas phase and forms a combustible mixture, the diameter decreases following the D^2-law. This occurs when the droplet reaches thermal equilibrium, balancing heat conduction with surface evaporation, resulting in a steady evaporation rate. Subsequently, the mixture ignites and burns as a spherically symmetric laminar non-premixed flame. After the ignition delay, the gas-phase combustion is initiated, and the presence of a flame significantly heats the droplet, which in turn increases the evaporation rate [144, 145]. The ignition delay corresponds to the time required for the mixture of fuel and oxidizer to react under a certain temperature and pressure. It can be defined as a time interval in which a droplet is exposed to a high temperature until a visible flame is spotted. Following a review of the classical droplet combustion theory, the subsequent discussion is focused on studies regarding experimental and numerical approaches for single and multi-component single droplets. Thus, the influence of the fuel composition, ambient conditions, and convection effects are explored.

Different techniques have been developed to experimentally evaluate single droplet evaporation/combustion in terms of droplet size evolution and flame structure. In this context, four methods can be encountered in the literature: suspended droplet, free-falling droplet, levitated droplet, and porous sphere. Figure 2.16 shows the most common experimental approaches for evaluating single droplet evaporation/combustion. The advantages and disadvantages can be identified depending on the purpose of the experiment based on the study objective and the technique employed.

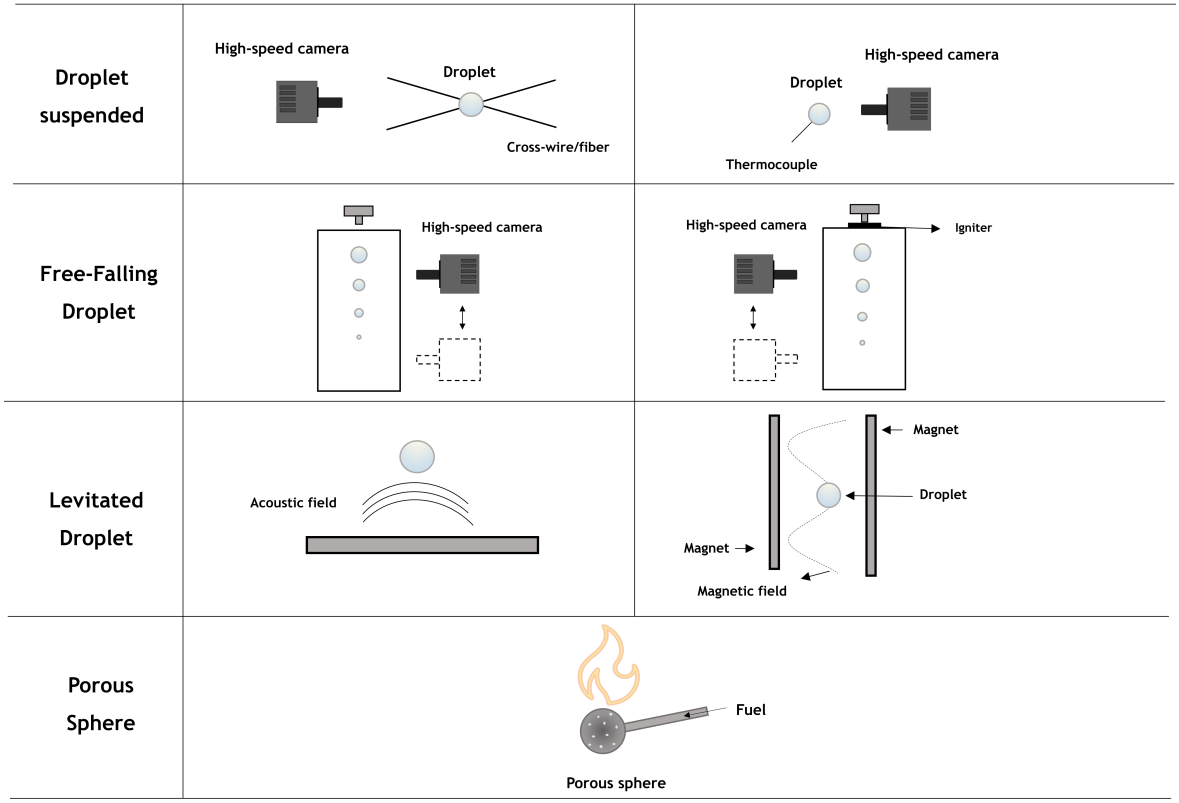

Figure 2.16: Illustration of experimental techniques used to study the evaporation and combustion of single droplets.

Wang et al. [146] reported the recent progress observed in the experimental investigations on fuel droplet evaporation. In addition, the authors described the advantages and limitations of the majority of experimental setups displayed in Figure 2.16. The droplet suspended technique is mainly used for its simplicity in measuring the droplet parameters. However, using a supportive fiber does not allow the study of a relatively small droplet size. The typical droplet diameters in this experimental setup are around 1 mm, which is considerably higher than droplets produced by liquid fuel atomization. Moreover, the thermal conductivity of the supportive fiber influences the burning rate and disruptive burning phenomena as reported by [29] and [147]. In contrast with the droplet suspended, the free-falling droplet method allows the study of droplets on a micrometer scale, and no foreign elements/filaments are presented in the experimental arrangement. In this respect, the droplet enters the combustion chamber, becoming subject to higher temperatures and pressures to recreate the operating conditions of practical engines [148]. However, regarding the limitations of this experimental method, Wang et al. [146] reported that the measurement of droplet characteristics is difficult due to droplet motion, being the process of tracking more complex. In addition, the droplet-air interaction affects the evaporation/combustion since the droplet is presented in a convective environment. In the levitated droplet method, the droplet parameters are easy to acquire, and there is no influence of fiber or thermocouples. Nevertheless, it is not suitable for higher ambient temperatures. Brenn et al. [149] evaluated experimentally with the acoustic levitator the evaporation of multi-component droplets. The experimental results were further compared with a theoretical model, and a good agreement was reported. The

porous spheres are used to examine the flame insights studied by Parag and Raghavan [150]. This technique consists of injecting the liquid fuel into the porous sphere, which can be relatively large and difficult to recreate the spray conditions. Regardless of the experimental technique used, to fully capture with detail the evaporation/combustion characteristics, a high-speed or IR camera is required, as noticed in several studies of [25, 26, 151].

Furthermore, experiments carried out in the presence of gravity can be affected by buoyancy effects. In particular, experimental setup related to free-falling droplet technique are affected by forced convection. In the study of single droplet combustion, buoyancy and forced convection can influence burning rates due to increased transport rates and distortion of flame shape from the spherical symmetry described in classical droplet combustion theory. According to Law [152], if the droplet diameter is relatively small in a range of 50 and 300 μm, buoyancy effects are generally negligible in free-falling droplet experiments conducted under normal gravity conditions. To avoid the influence of the buoyancy effect, experiments under microgravity have been performed [153]. Figure 2.17 shows two flame configurations: envelope and wake flame. The observation of the images indicates that for a relatively small droplet Reynolds number, Re_d, where no forced convection or weak forced convection is presented, an envelope flame is spotted in Figure 2.17 a). On the other hand, for stronger forced convection and higher values of droplet Reynolds number, the flame may detach from the droplet, resulting in combustion occurring exclusively in the wake region, referred to as a wake flame.

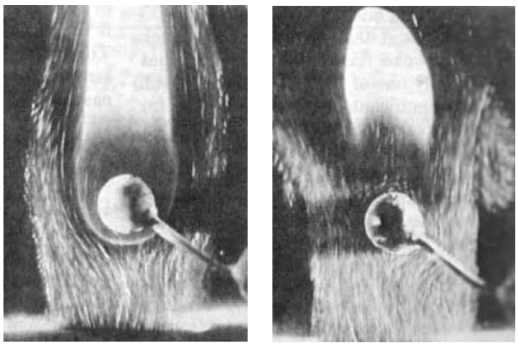

(a) (b)

Figure 2.17: Porous sphere combustion experiment under normal gravity and forced convection conditions: a) Sphere with envelope flame; b) Sphere with wake flame [154].

When forced convection is considerably intense, the droplet flame can be ”blown off,” and a transition occurs from combustion to exclusive droplet evaporation. As mentioned earlier, the convection effect not only affects the flame configuration but also impacts the droplet lifetime and the ignition delay caused by the increase of the mass and heat transfer between both phases. Chen et al. [155] performed an experimental analysis of droplet evaporation characteristics under forced convection. To accomplish this purpose, the authors suspended droplets of n-decane, toluene, and butanol that were subjected to different convection velocities. The results reveal that the droplet evaporation rate increased with the increase in the convection velocity. This result may be attributed to the increase of Reynolds number as

convection velocity increases, which leads to a higher intensity and an increase in the mass diffusion coefficient. In addition, the authors stated that the increase of the convective velocity has a minimal influence on the increase of the evaporation rate compared with the ambient temperature. The incorporation of the convective effect in the classic combustion theory for isolated liquid fuel droplets will be detailed and examined in Chapter 4.

The environment temperature surrounding the droplet also has a significant impact on its evaporation and combustion process. The relevance of the ambient temperature was previously discussed by Lefebvre [156], and several studies highlight similar conclusions indicating that increasing the ambient temperature leads to an increase in the evaporation and combustion rates [157–159]. Figure 2.18 shows the influence of the ambient temperature in the ignition delay. The experimental findings of Saitoh et al. [160] indicate that high ambient temperatures enhance droplet combustion by increasing heat transfer to the droplet surface, increasing the evaporation rate. In addition, higher initial droplet temperatures result in more rapid ignition as the droplet diameter increases.

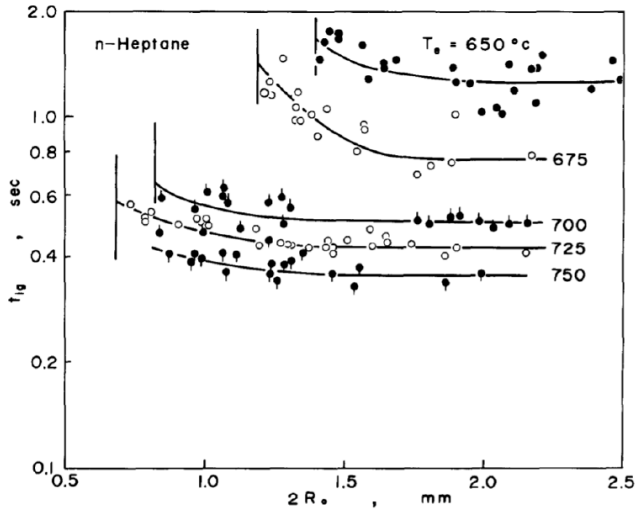

Figure 2.18: Ignition delay as a function of the droplet diameter for several ambient temperatures [160].

The influence of the ambient temperature was also investigated in numerical work. Awasthi et al. [161] investigate numerically the impact of the ambient temperature and initial diameter in droplet combustion. The study considered an n-heptane single droplet in a transient numerical simulation. The authors reported that the D^2-law agreed with the results. The findings also reveal that an increase in the ambient temperature leads to an increase in the droplet burning rate and a decrease in the droplet lifetime.

Another key aspect that affects the evaporation and combustion of a single droplet is fuel composition. The fuel can be classified into single-component and multi-component. The former corresponds to a fuel that is only composed of one component, such as ethanol fuel and n-hexadecane fuel. In contrast, a multi-component fuel possesses several components, such as kerosene, widely used in aerospace [146]. In particular, the majority of the transportation sector employs multi-component fuels that include diesel, gasoline, and Jet A-1.

Single-component fuels typically possess a well-defined boiling point. However, in multi-component fuels, the components may present very different volatilities, having different boiling points affecting the evaporation and combustion of the droplets. This observation is more predominant in fuel mixtures when both are multi-component fuels, as will be further discussed. To better understand the distinct behavior of single and multi-component fuel droplets, Shang et al. [162] performed an experimental study at room temperature and atmospheric pressure under normal gravity using n-octane, n-dodecane, n-tetradecane, and n-hexadecane and their blends in different proportions. Figure 2.19 reveals that all the fuels follow the D^2-law. Increasing the number of carbon atoms in the fuel chain is a noted reduction in the burning constant and an extension of the heating phase. This result suggests a relation between the fuel carbon content and the droplet lifetime. Fuels with lower carbon numbers present shorter lifetimes due to their lower boiling points and higher vapor pressures. Furthermore, the burning rate is slightly higher than the experiments conducted in low or microgravity due to buoyancy, forced convection, and/or natural convection.

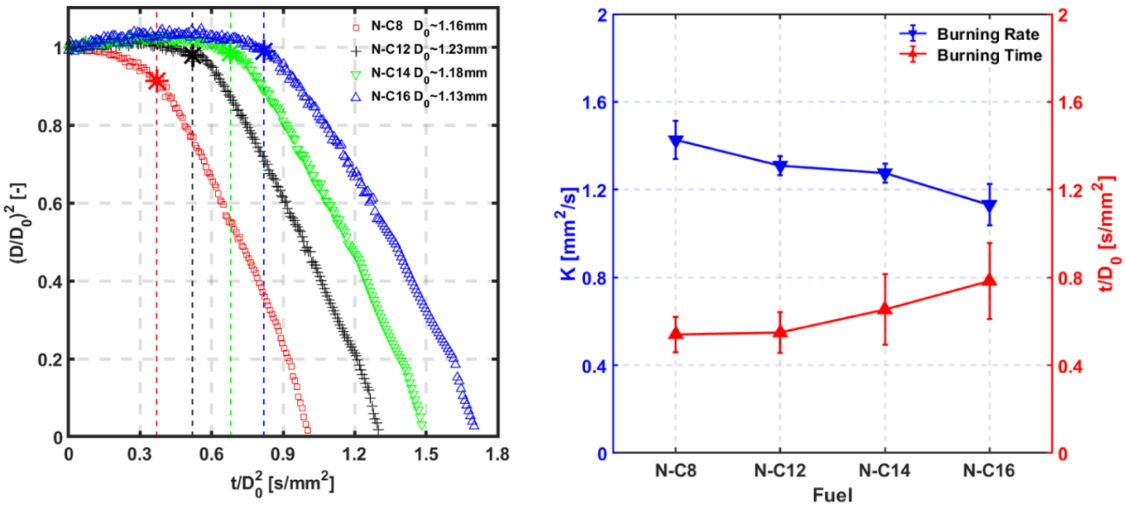

(a) (b)

Figure 2.19: Evolution of the: a) Square of the normalized droplet diameter with normalized time for single-component fuel; b) Mean burning rates (left, blue) and normalized combustion duration (right, red) with four single-component n-alkane droplets [162].

Concerning multi-component fuels, Law [143] highlighted three factors that should be considered. First, the relative concentrations and volatilities of the liquid components potentially lead to specific behaviors that were not identified in the gasification process of single-component fuels. The miscibility of the liquid components and the ideality of the mixture that affect the phase change behavior and surface vapor pressure characteristics. Finally, the rate of liquid-phase mass diffusion, droplet surface regression, and internal movement within the droplet significantly influence the rate at which liquid components are transported to the surface for evaporation. Xu et al. [163] conducted an experimental study on mixtures of two multi-component fuels. The investigation explored the droplet-burning characteristics of a renewable jet fuel derived from algae, and three AHRJ/Jet-A blends were compared to conventional aviation fuel (Jet-A). Besides its relevance to multi-component fuels, this study also evaluates alternative fuels for aviation purposes, where a mixture of biofuel and Jet A-

1 are experimentally considered. Spherical droplets under a free-fall environment of pure jet fuel, pure algae-derived biofuel, and blends containing 25%, 50%, and 75% algae biofuel were examined. From the experimental results, AHRJ and AHRJ/Jet-A mixture droplets have burning rates that are higher than Jet-A. The results also suggest that the soot emissions are related to the aromatic content, where Jet A-1 possesses the highest soot emission. As mentioned above, Shang et al. [162] also evaluated the multi-component fuels and observed micro-explosions. According to Wang et al., [146], when the droplet temperature is higher than the boiling points of light components while remaining below the boiling points of the heavy components, the light components evaporate inside the droplet, resulting in bubble formation. Once the internal bubble pressure exceeds the droplet surface tension and ambient pressure, bubbles inside the droplet burst, causing its fragmentation [29]. This leads to an increase in surface area, enhancing evaporation and reducing the droplet lifetime, which is crucial for improving fuel atomization and combustion efficiency. During the combustion of multi-component droplets with substantial, large volatility, the differential may undergo spontaneous disruptive burning events, resulting in a partial fragmentation noted as puffing or complete droplet disintegration, referred to as micro-explosion. Figure 2.20 shows a schematic of the two disruptive burning events: a) puffing and b) micro-explosions.

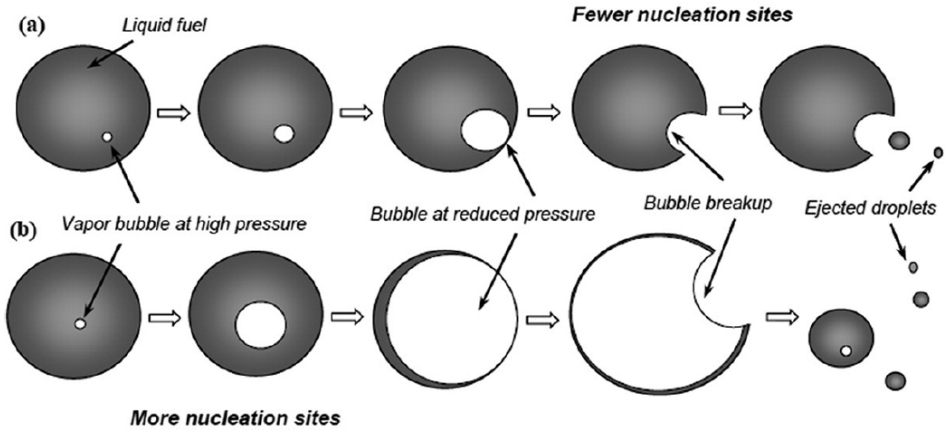

Figure 2.20: Disruptive burning events: a) Puffing; b) Micro-explosions from [164].

The phenomenon initiates when small gas bubbles nucleate inside the droplet, and the pressure inside the vapor bubble becomes higher than the ambient pressure. The small gas bubbles coalesce, resulting in a larger bubble due to the internal circulation inside the droplet. The nucleation site is highly dependent on the proportion of higher volatile compounds. A lower concentration of these components leads to fewer nucleation sites and consequently reduces the coalescence of small bubbles. Eventually, the bubbles reach a limit and can not go further, expand, break, and release several small secondary droplets. This description corresponds to puffing. In addition, when the breakup of the inner gas bubble leads to the complete disintegration of the droplet that releases smaller secondary droplets and volatile, a micro-explosion is spotted. The disruptive burning events were previously studied numerically by Shinjo et al. [165]. The authors reported that multiple puffing events can result in micro-explosions, increasing the degree of the breakup. Each explosion starts as an independent puffing event. As a result, the total disintegration of the droplet occurs due to these

interactions.

The conventional fuels employed, in particular in the transportation sector, are multi - component fuels that possess hundreds to thousands of hydrocarbon species. Consequently, understanding the underlying mechanisms of combustion can be challenging due to their complexity. In numerical approaches, the fuel composition can be simplified to a single component surrogate fuel to simulate and replicate the desired behavior and specific characteristics of a more complex fuel. Due to the restricted number of chemical reactions and physical interactions, numerical simulations can be carried out efficiently [145]. Surrogate fuels are required to replicate the physical and chemical properties of conventional fuels, as well as their injection, vaporization, mixing processes, and combustion behavior. According to Ra and Reitz [166], multi-component fuel models are categorized into continuous multi-component models and discrete multi-component models. In the former, the fuel composition is represented as a continuous distribution function involving aspects such as the molar mass, boiling point, and number of carbon atoms. Thus, it is possible to reduce computational complexity while predicting the complex vaporization behavior of multi-component fuels. However, additional assumptions and simplifications can restrict the accurate representation of multi-component fuel characteristics, complicating the modeling of individual component consumption. The discrete multi-component models focus on a finite number of compounds. A common approach involves the selection of different parts of the distillation curve. The model tracks individual fuel components during the evaporation process and allows for the integration of their reaction kinetics. Besides its high computational costs, recent advancements in computational capacity have made this approach more accessible [166].

Focusing on multi-component fuel, mixtures of liquid-liquid have already been described. In this context, the following subsection is dedicated to multi-component fuels involving solid-liquid mixtures. An overview dedicated to adding particles to a liquid will be explored. Different types, sizes, and concentrations are considered, and their advantages and disadvantages are presented. Furthermore, preparing these fuels is also addressed to better understand how they can be further implemented in real applications. An assessment of the most recent progress in single droplet combustion of liquid fuels with nanoparticles is also provided.

2.3.2 The Addition of Particles in a Liquid Fuel

The growing global energy demands require solutions to address fossil fuel depletion and environmental concerns. It is essential to develop technologies capable of enabling long-term clean energy storage, transportation, and trade on a global scale. In the aviation field, possible alternatives have already been discussed, presenting different stages of development. Following the statement of Gupta et al., [167], the energy content of liquid hydrocarbon fuels has nearly reached its upper limits, and additional improvements in energy value through chemical methods are significantly difficult. In particular, aviation demands significant fuel volumes, which poses a challenge for alternative fuels in this sector. Moreover, the limited energy density of conventional hydrocarbon fuels restricts the improvement of spe-

cific thrusts of rockets and aircraft [17]. Consequently, an emerging solution is to disperse particles in conventional hydrocarbon fuels. Initial investigations were dedicated to slurry fuels. According to Choudhury [168], slurry fuels are colloidal suspensions of fine particles of solid fuel dispersed in liquid hydrocarbons. The size of the particles depends on the applications and can range from submicron size to hundreds of microns. Reports concerning the use of slurry fuels have presented benefits [169]. The findings highlight that for flight propulsion, the addition of metals can offer the possibility of more flight range and thrust than can be obtained with conventional hydrocarbon. However, the study suggests that further modifications in the fuel system and combustors were required to compensate for the difference in flow properties between jet hydrocarbons and slurry fuels. Specifically, ramjet operating with magnesium slurry was flown successfully, requiring improvement in the combustors and fuel systems. The advantage of using this type of fuel relies on the high energy density, and slurry fuels were considered ”liquid fuel extenders” [168]. However, the combustion of slurry fuels involving micron-sized particles in several applications showed issues regarding clogging, rapid settlement, poor stability, and agglomeration, low combustion efficiency [23]. The minimization of these effects was achieved by the use of nanoparticles. In the 1980s, the development of nanotechnology pioneered a new field of study worldwide [20]. Micro-scale and nano-scale additives possess characteristics of high energy density or a significant surface-to-volume ratio, which enhances their reactivity in thermochemical reactions. Nonetheless, based on their respective sizes, different outcomes can be achieved. In this context, nanoparticles have shown beneficial effects on fuel performance, particularly regarding thermophysical properties [170].

The concept of nanofluids was initially introduced by Choi and Eastman [171]. The authors proposed this new class of heat transfer fluids involving the use of nanoparticles in conventional heat transfer fluids, where an enhancement in thermal conductivity was reported. This potentially contributes to new industrial technologies, addressing micro- and nanoelectromechanical systems, power electronics, and light-emitting diodes (LEDs) [172]. Nanofluids consist of nano-sized particles of 1- 100 nm dispersed in a liquid. Considering the thermophysical properties, nanofluids have improvements regarding thermal conductivity, thermal diffusivity, viscosity, and convective heat transfer coefficients relative to their base fluids, indicating their promising applicability in several sectors [173]. Nanomaterials are an emerging area of interest in the combustion research community aimed at improving the burning characteristics of liquid fuel droplets, particularly in the form of nanofluids, commonly referred to as ”nanofuel”. Metal, metal oxide, and carbon-based nanoparticles have been extensively investigated in a variety of hydrocarbon-based fuels [174]. The type of nanoparticles commonly used will be further discussed. Figure 2.21 illustrates the wide range of applications where nanofluids/nanofuels can be employed. This includes desalination processes, carbon dioxide capture, aerospace applications, oil recovery methods, automotive radiators, refrigeration systems, boilers, electronic equipment cooling, component lubrication, heating and cooling of buildings, medical processes, and any liquid-based heat exchanger [175]. In the combustion field, nanofuels are shown to increase the ignition probability or enhance fuel reactivity and improve the energy density of the liquid fuel [29].

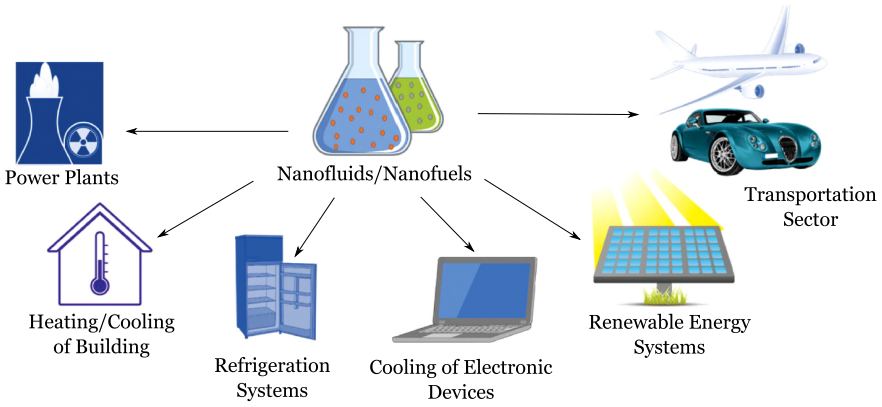

Figure 2.21: Applications of nanofluids/nanofuels. Adapted from [175].

Besides the fact that nanofuel can possess several benefits to overcome the limitations of hydrocarbon fuels, significant barriers remain, including concerns regarding fuel stability, The rates of corrosion and erosion of the materials in contact with them, relatively high cost of production, combustion efficiency, and environmental impacts due to particle combustion. Therefore, several investigations have been carried out to mitigate these weaknesses [17]. Notably, the preparation is one of the most essential steps in studying nanofluids/nanofuels. The purpose is to guarantee long-term quality stability to attain reliable results that would not affect the thermophysical properties, atomization, and combustion of nanofluids/nanofuels. This is a critical parameter that is affected over time and for different particle concentrations that should be evaluated before their practical application. Following Sezer et al. [176] colloid chemistry suggests that when a particle reaches a critical size, it remains stable, and no sedimentation is spotted. However, the high surface energies and subsequent nanoparticle interactions can result in agglomeration, cluster formation, and increased settling rates. The collisions between particles, driven by Brownian motion and strong van der Waals forces, lead to cluster formation, negatively impacting nanofluid/nanofuel stability. Van der Waals forces are primarily influential over short distances and are not caused by covalent bonding or the electrostatic forces between ions. When combined with the Brownian motion of nanoparticles, frequent collisions are induced, leading to instability in the nanofluids. In this scale, gravity possesses a minor significance [177]. On the other hand, considerably large clusters of particles are influenced by gravity. Nanoparticles constantly collide due to Brownian motion caused by their large surface areas having high activity. An increase in the Brownian motion is related to smaller particle size, lower viscosity, and temperature increment, which should be considered during the nanofluid/nanofuel preparation. Increasing the particle concentration results in a reduction of the interparticle distance, which enhances the Van der Waals attractive potential. Consequently, this increases the Van der Waals attractive potential, leading to more agglomeration and less stability [178]. In this respect, the stability depends on the balance of repulsive and attractive forces between the particles. To achieve a stable nanofluid/nanofuels, the repulsive force must be larger than the attractive force between the particles [179].

The synthesis of these nanofluids/nanofuels is influenced by diverse factors ranging from the nanoparticles utilized to the techniques employed, which inevitably leads to inconsistent outcomes. An overview of each parameter is displayed in Figure 2.22. The first step relies on the preparation method, which can be classified into single-step and two-step methods. The former consists of synthesizing nanoparticles and dispersing them in the base fluid simultaneously. Since this method avoids the stages of drying, storage, transportation, and dispersion of nanoparticles, the agglomeration of nanoparticles due to their large surface area to volume ratio and their high surface energy is minimized, enhancing the stability.

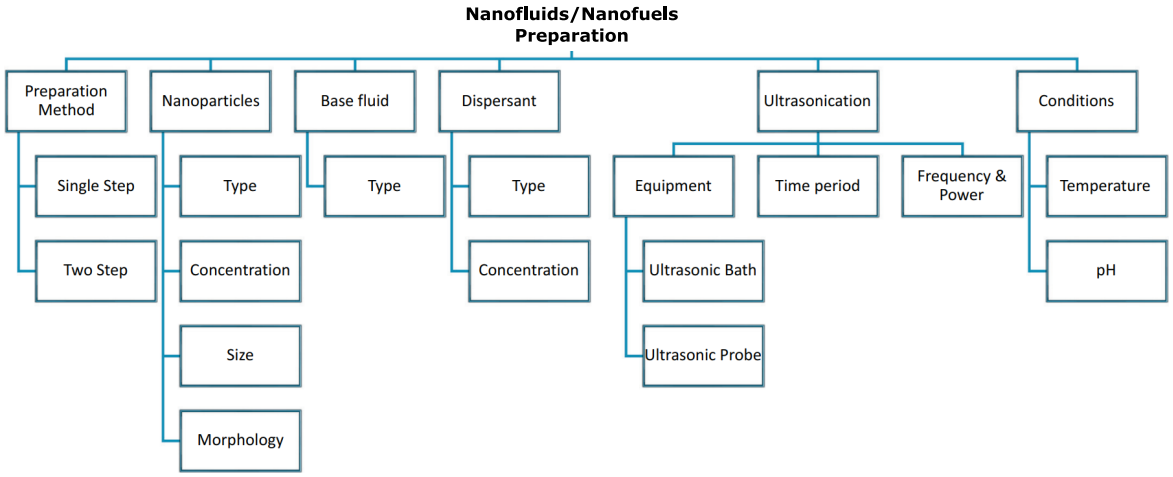

Figure 2.22: Overview of the parameters affecting nanofluids/nanofuels preparation. Adapted from [176].

However, the single-step method possesses relatively higher production costs and limitations to low vapor pressure base fluids. It operates in batch mode, limiting the control of relevant parameters, such as particle size [176, 180]. In contrast to the single-step method, the two-step method is more commonly used, particularly for industries producing large scales. This methodology primarily involves the manufacturing of nanoparticles as dry powders through chemical and physical processes. Subsequently, the nanoparticles are dispersed into a base fluid using different approaches. The advantages of the two-step method rely on increased production capacity and reduced costs, as the synthesis of nanopowders has already been scaled up to industrial production levels. However, in terms of long stability, a single step presents a better result [180]. An illustration of the two preparation methods is presented in Figure 2.23.

The synthesis of nanofluids usually requires strategies to enhance their stability, increasing the repulsive forces that contribute to long-term stability. Several physical procedures can be employed to mitigate aggregation, such as magnetic stirring, ultrasonication, high shear-rate mixing, and ball milling. Additionally, chemical treatments, such as incorporating surfactants, pH adjustment of the sample, or surface modification, can also be applied. The most commonly used are dispersants and sonication. The former corresponds to surface active agents that enhance the interaction between a liquid and a solid surface, a characteristic often referred to as wettability. The purpose of this agent is to reduce the surface energy and enhance the dispersibility of particles. Surfactants are an easy and economical method

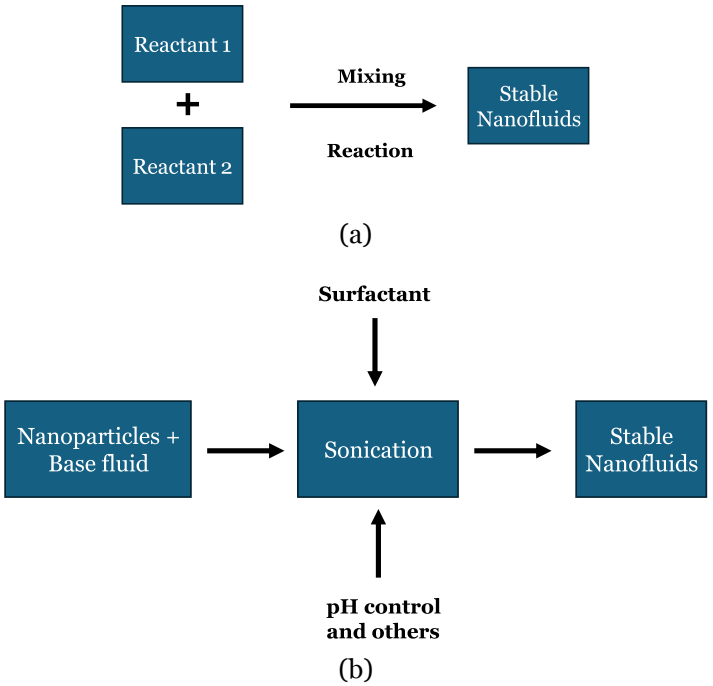

Figure 2.23: Preparation methods: a) Single-step; b) Two-step [180].

to improve stability, but there are a few drawbacks. Two considerations must be considered regarding the surfactant selection: the type of surfactant employed and its concentration. The solubility of the surfactant in a base fluid is a crucial factor in the surfactant selection, which is generally addressed by the hydrophilic-lipophilic balance (HLB) value. A lower HLB value indicates it is more soluble in oil, whereas a higher HLB value is more soluble in water [173]. Furthermore, the concentration of surfactant significantly impacts the uniformity of suspension. A larger concentration can have a negative influence on the properties, such as density and viscosity of these fuels [177]. Consequently, affecting processes such as heat transfer, atomization, and combustion.

The sonication process is considered the most effective method for breaking large clusters of nanoparticles into smaller clusters or even individual nanoparticles [181]. The purpose is to apply high sound energy on fuels to break down nanoparticle clusters and disperse the nanoparticles. This physical method is commonly performed by a probe or bath devices. However, differences in terms of process capabilities and effectiveness are reported. In comparing the two equipment, probe sonication has proven to be more effective and powerful than ultrasonic baths in the dispersion of nanoparticles. Nanofluids/nanofuels preparation using an ultrasonic bath device is affected by cavitation randomly distributed across the fluid, leading to a lower intensity and irregular distribution of ultrasonication. Sonication with probe devices is a more intense and focused process that can be controlled and reproducible. Although sonication is widely used to stabilize nanofluids/nanofuels, no standard process is still established. Consequently, it is essential to determine the optimal parameters for sonication. Several factors should be considered: duration, amplitude, continuous or pulsed modes of sonication, sample volume, sample temperature, particle size, material, and con-

centration [181]. Sonication can be performed at power and frequency for periods. According to Urmi et al., [180], the time of sonication may be dependent on the type, size, shape, concentration, and mixing ratio of nanoparticles and base fluid and also on the preparation method. There is no ideal duration for sonication, which can provide contradictory results, as highlighted in the review by Asadi et al. [181]. However, careful attention regarding the relation between the sonication duration and nanofluid temperature should be considered. During the sonication process, the temperature of the sample must be controlled at low temperatures. Ensuring low temperatures can be achieved by applying low amplitude or shorter sonication times. At high temperatures, degradation of nanoparticles and stability are reported. A common strategy to address this issue is using external cooling or submerging the sample in an ice bath during the sonication period [182, 183]. Amrollahi et al. [184] evaluated the effect of the sonication time and particle concentration on the stability of nanofluid composed of carbon nanotubes and ethylene glycol. The authors mentioned that increasing the sonication time results in a better dispersion of the particles. For higher particle concentrations, random collisions among nanoparticles occur at a higher rate, resulting in lower stability in comparison with low particle concentrations. Sonication can be applied in both continuous and discontinuous forms. In this respect, applying the continuous pulses leads to the fragmentation of clusters into smaller sizes, leading to a more uniform particle size than the results achieved by applying the discontinuous pulses [181]. The sonication can also be accompanied by a magnetic stirrer.

Following this overview of strategies to enhance the stability of nanofluids, a discussion concerning the approaches to evaluate their stability is presented. Figure 2.24 shows the most common methods for evaluating nanofluids/nanofuel stability. Zeta potential measures the electrical potential (degree of repulsion) between small van der Waals forces and dispersed particles [177]. High values, whether positive or negative, are considered stable nanofluids. On the contrary, low values of zeta potential correspond to unstable nanofluids. Zeta potential values around 25 mV possess a critical threshold for distinguishing between low- and high-charged surfaces concerning stability. Values ranging from 40 to 60 mV indicate good stability, whereas excellent stability is assumed for valuer higher than 60 mV [176, 185].

Zeta potential values are affected by the pH of the nanofluids. In addition, surfactants significantly impact the zeta potential. Zeta potential increases as surfactant concentrations increase [177]. The pH measurements are also commonly used to evaluate the stability of nanofluids. Controlling the pH allows for the improvement of nanofluid stability since the surface charge is related to the pH values. Measurements concerning the pH indicated that values far from the isoelectric point (IEP) enhance the stability of nanofluids. The isoelectric point is defined as the state at which the surface charge of the particles and the corresponding zeta potential is equal to zero [180]. To prevent corrosion of heat transfer surfaces and dissolution of nanoparticles, the pH values are usually required to be kept around neutral [176]. Spectral absorbance and transmittance are indicators of stability to measure the absorbance peak using a UV–VIS spectrophotometer. This method relies on absorbing light across both the visible and ultraviolet frequency ranges where unstable nanofluids display low values

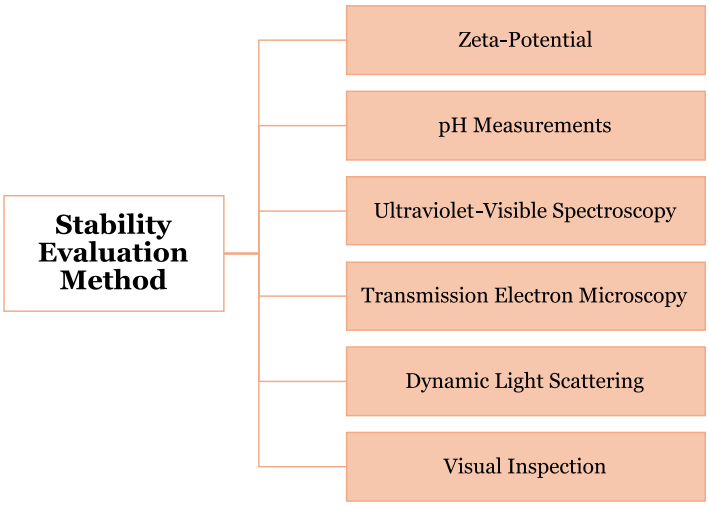

Figure 2.24: Stability evaluation methods.

of observance. The observance and transmittance can be determined by Equation 2.41 and Equation 2.42, respectively.

$$A = log_{10}\frac{I_0}{I} = \alpha l c\,, \quad \textbf{(2.41)}$$

$$T = \frac{I}{I_0}\,, \quad \textbf{(2.42)}$$

where I_0 is the intensity of incident laser light, I is the intensity of the laser light beam after passing through the colloidal suspension, α is the absorptivity, l is the length of the light path, and c is the concentration of particles. This method allows quantitative analysis with respect to particle concentration, where several findings indicate that the absorbency ratio of nanoparticles is proportionately related to the concentration of nanofluid [180].

Transmission electron microscopy (TEM) is also a method to evaluate the stability of nanofluids/nanofuels. This technique allows the characterization of the structure and agglomeration size of nanoparticles [181]. Dynamic light scattering (DLS) technique evaluates the particle size distribution of particles and agglomerates [26]. However, similar to the zeta potential technique, DLS involves equipment with a significant cost. Finally, the visual inspection or sedimentation technique is presented. This method is the simplest and most extensively used method to analyze the stability of nanofluids/nanofuels. It is a widely adopted approach that is easy, cost-effective, non-contact, and non-intrusive to the nanofluids. In addition, it does not require special equipment, and only a small volume of samples is necessary. However, this method can be subjective. The stability is evaluated by tracking the sedimentation by observing nanoparticle clustering and sedimentation driven by gravitational forces within the nanofluids/nanofuel [26]. After the preparation, the nanofluids become unstable, and three sedimentation behaviors can be observed. The dispersed sedimentation occurs when

sediment height gradually increases as the samples become clearer. Contrarily, in flocculated sedimentation, the sediment height reduces over time, and the mixed sedimentation is a combination of all behaviors occurring simultaneously, as displayed in Figure 2.25. A stable nanofluid/nanofuel is identified when the fluid concentration remains consistent with time [180].

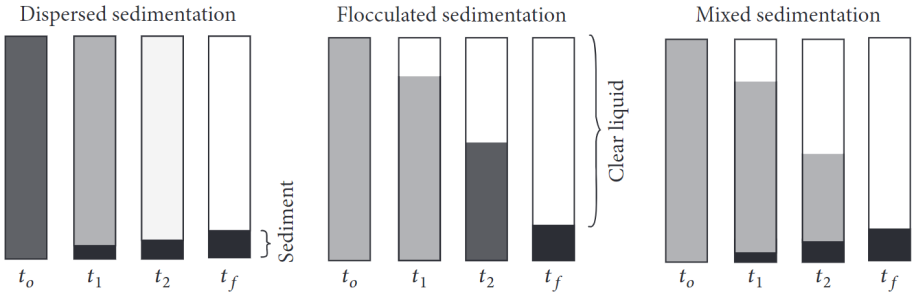

Figure 2.25: Sedimentation behaviours in nanofluids, where t indicates time and $t_0 < t_1 < t_2 < t_3$ [186].

As noted in Figure 2.22, the nanoparticles present different types, concentrations, sizes, and morphologies, which are critical factors influencing the stability and thermophysical properties of nanofluids/nanofuels. A few considerations were already discussed previously. Each of these parameters is chosen with careful consideration of the application or the field of study. As outlined by Parveg and Rather [187], the particle concentration can be classified into low, medium, high, and ultra-high particle concentration. Low particle concentration corresponds to $\leq$ 0.1 wt.%, medium particle concentration between 0.1 and 1 wt.% and, high from 1 wt.% to 5 wt.% and ultra-high from 5 wt.% to 10 wt.%. To distinguish nanofuel from slurry fuels, in the combustion studies, the latter possess particle concentrations higher than 10 wt.%. For simplification purposes, the present work adopted low particle concentration until 1 wt.% and high particle concentration above 1 wt.%. Concerning the types of nanoparticles, Taylor et al. [188] summarized the available nanoparticles and their corresponding application, as shown in Table 2.5. Considering the investigation of nanofuels, which can be classified into energetic and non-energetic [189]. Energetic nanoparticles act as reactants in exothermic reactions, contributing to an increase in the total energy released. Two notable examples are carbon and metallic nanoparticles.

Metallic nanoparticles present benefits for propulsion applications, where enhancing the volumetric energy density of the base fuel is crucial. In contrast, carbon nanoparticles can be used in applications to enhance heat transfer properties. Comparing the two types of nanoparticles, carbon additives offer a cost-effective alternative to metal-based fuel. The selection of the nanoparticle type generally depends on the specific application demands, taking into account performance trade-offs, emissions, and environmental concerns [187]. Reactive metals such as aluminum, magnesium, and boron have attracted widespread interest in various energy applications, including propulsion systems, explosives, gun powders, propellants, and pyrotechnics, among others, due to higher volumetric and gravimetric energy densities [190]. In terms of additives, metal nanoparticles are being used in nanofuels research due to their increased reactivity and energy properties, which result in shorter ig-

Table 2.5: Nanoparticles types and their applications [188].

Particle types	**Applications**
Noble metals (Pd, Pt, Ag, Au)	Catalysts, plasmon resonance, heat transfer enhancement
Magnetic (Fe, Ni, Co)	Heat transfer, biomedical imaging, flow control, microwave absorbers
Semiconductors, quantum dots (Si, CdS, CdSe, ZnS, ITO)	Fluorescence, light trapping, LEDs, optical memory
Core-shell (metal, semiconductor, or polymer core and/or shell)	Biomedical, fluorescence, solar absorbers, sensors, optoelectronics, catalysts
Metal-oxide nanoparticles (Al, Ti, Zn, Cu, etc.)	Heat transfer, catalysts, optoelectronics
Polymer nanoparticles	Biomedical (drug delivery), conductive optoelectronics

nition delays and enhanced combustion rates, as well as the catalytic effect. Furthermore, it enhances thermal conductivity and ignition probability, contributing to a greater overall energy release, reducing fuel consumption, and addressing environmental concerns [29, 190].

Figure 2.26 shows the energy density of liquid and solid fuels. Boron exhibits the highest volumetric heat of reaction in oxygen, reaching up to 138 kJ $cm^{-}3$. However, the ignition of boron particles is notably delayed due to a B_2O_3 oxide layer. Regardless of particle size, the ignition temperatures of boron particles in oxygenated environments range between 1500 and 1950 K [191]. Beryllium is particularly appealing for various applications. However, its extreme toxicity presents significant risks to humans and animals, even in minimal concentrations [192]. Moreover, it is relatively scarce and presents high costs. Magnesium has also been considered in engineering applications. Nevertheless, concerns regarding instability in the presence of water and humid air production costs, flame temperature, and material availability reduce the attractiveness of this material for widespread use. Compared to the heat of combustion, magnesium and zirconium possess a lower value in terms of mass and volume than aluminum. In particular, aluminum is a viable option for an energy carrier possessing relevant characteristics that are most important for a sustainable energy carrier: high energy density, abundance, and recyclability, and it is anticipated that the alumina-reduction process will soon be free of carbon emissions.

In addition, aluminum has high thermal conductivity, excellent surface absorption, and low melting/ignition temperatures [23]. It is considered safe for storage and transportation, and advancements in production and recycling technologies to reduce greenhouse gas emissions are currently being implemented [194]. Aluminum is also the most abundant metal in the Earth crust [191]. The use of aluminum nanoparticles in combustion systems can pose challenges due to the emissions of nano oxides and their separation from hot exhaust gases, as well as their collection for recycling [194]. Aluminum has been one of the most used additives due to the increased overall heat release of the reacting system through the increase of the flame temperature and heat of combustion. Considering effects on the thermal conductivity, an increase in this property has shown aluminum-based nanofuels have also shown a ben-

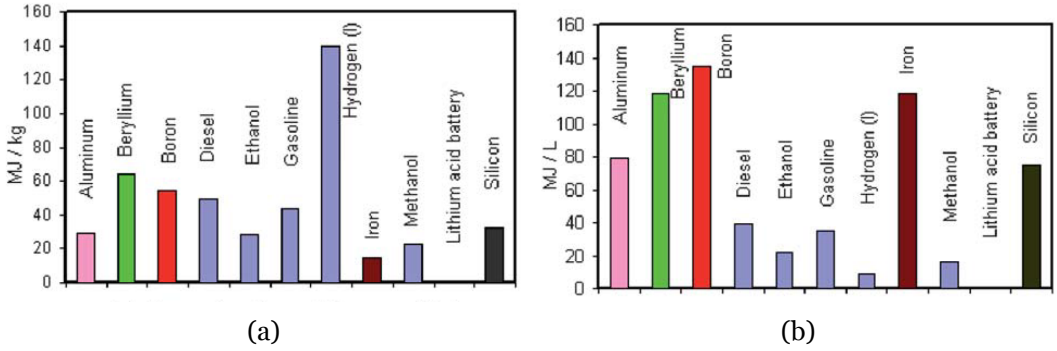

(a) (b)

Figure 2.26: Comparsion between liquid and solids fuels: a) per mass; b) per volume [193].

efit to droplet burning [195]. Aluminum is a relatively cheaper metal than other materials such as boron, silicon, and magnesium [196]. Aluminum is often used as an additive in solid propellants to optimize combustion processes in rocket engines [197, 198]. The production processes for aluminum nanoparticles are typically classified into vapor phase condensation and liquid phase chemistry as described in [199]. When exposed to air, aluminum particles create a natural oxide (Al_2O_3) layer on their surface. This layer is typically uniform and amorphous, with a thickness of 2–5 nm [200]. The evaluation focused on aluminum combustion disrupted the 1960s. Preliminary studies indicated that the combustion of a metal particle was similar to the combustion of a hydrocarbon droplet. However, the ignition was assumed to occur after melting of the oxide shell of Al_2O_3, while steady combustion was assumed to be reached on exceeding the aluminum boiling point [201]. Regarding reactivity, aluminum nanoparticles exhibit greater reactivity compared to micro-sized aluminum, being influenced by both particle size and the type and thickness of the passivation layers [202]. In terms of temperature ignition, micron-sized aluminum particles have an ignition temperature very close to the melting point of the oxide shell (2300 K), while aluminum nanoparticles have been experimentally observed to ignite closer to the melting temperature of aluminum (930 K) [200]. Concerning the nonenergetic nanoparticles, practically all metal-oxide comprise this class. Several examples corresponds to such as Al_2O_3, CeO_2, CuO, SiO_2, TiO_2, among others. These nanoparticles can contribute to the decrease in the activation energy required for chemical reactions and the fuel oxidation temperature possessing benefits in terms of radiative heat transfer and mass transfer characteristics along with enhancing the thermal exchange between fuel droplets and the ambient air [189]. As noted by Lv et al. [203], copper oxide (CuO), aluminum oxide (Al_2O_3) and titanium dioxide (TiO_2) have shown advantages in thermal conductivity, strong catalytic function, high oxygen content, more free radicals and fast combustion rate, which are conducive to reducing fuel consumption, improving thermal efficiency and further improving emission pollution.

Regardless of the type employed, particle size and concentration also significantly affect the nanofluid / nanofuels stability and thermophysical properties. According to Javed et al., [204] comparing nano and micron size particles, the former presents a higher surface volume to ratio, allowing more fuel to be in contact with the oxidizer, consequently resulting

in higher combustion efficiency. The size of the agglomeration is reduced, positively influencing the stability. The enhancement of the stability with the decrease of the particle size was also reported by [205, 206]. Moreover, in terms of combustion field, nanoparticles oxidize more fully and quickly than micrometer-scale and larger particles [207]. To address the influence of nanoparticles on the thermophysical properties, Alktranee and Bencs [177] provided a review that highlighted the impact of reducing the particle size and increasing the concentration has contributed to the improved thermal conductivity of nanofluids. Concerning the particle shape, cylindrically shaped nanoparticles demonstrate a reduced impact on the thermal conductivity of nanofluids when compared to spherical nanoparticles [177]. According to Arshad et al. [208], there are two reasons for enhancing the thermal conductivity in the nanofluids, which relies on the Brownian motion and liquid layering at the liquid-particle interface. Concerning the Brownian motion, the nanoparticles move through the liquid, leading to potential collisions that allow direct solid-solid heat transport between particles, resulting in increasing the thermal conductivity of the nanofluid. Alternatively, the thermal conductivity in nanofluids is affected since the liquid molecules closed to the solid nanoparticles form nanolayered structures that can act as a thermal path between the solid nanoparticles and bulk liquid molecules [208].

For systems involving the atomization process, the influence of nanoparticles on the viscosity and surface should be evaluated with careful attention. An increase in the viscosity has been reported when nanoparticles are added to a base fuel. Furthermore, increasing the particle concentration also leads to an increase in the viscosity [205, 209]. Regarding the influence of particle size on viscosity, there is a discrepancy in the results provided in the literature. Moreover, the influence of particle size is dependent on its shape, where nanoparticles with similar size or diameter and different shapes, such as spherical or cylindrical, result in variations in viscosity and other related properties [210]. A detailed analysis of the surface tension, dedicated to the addition of nanoparticles and surfactant to a hydrocarbon fuel liquid, was conducted by Mei et al. [211]. Nanoparticles of CNT, CeO_2 and Co_3O_4 with different sizes and mass concentrations were dispersed in diesel using CTAB as a surfactant. The purpose is to determine experimentally at 10–140 °C based on the pendant drop method and the effects of mass concentration, particle size, nanoparticle types, and temperature on the surface tension of nanofuel. The results for this analysis are provided in Figure 2.27. Concerning the addition of surfactant, CTAB was used to form a thin layer between nanoparticles and surrounding liquid fuel molecules to increase the potential of nanoparticles and the repulsive force between them. Through this approach, it is possible to enhance the stability of nanofuels so that they can be used in practical applications. The effect of the particle size is also presented in Figure 2.27.

Increasing the particle size leads to a higher surface tension since separating diesel molecules is more difficult for larger nanoparticles than smaller ones. Additionally, the surface tension of all fuels decreases nearly linearly as temperature increases, where the surface tension of nanofuels is higher than that of diesel at each temperature. Regarding the type of nanoparticle, the addition Co_3O_4 to diesel exhibits the most significant surface tension changes as

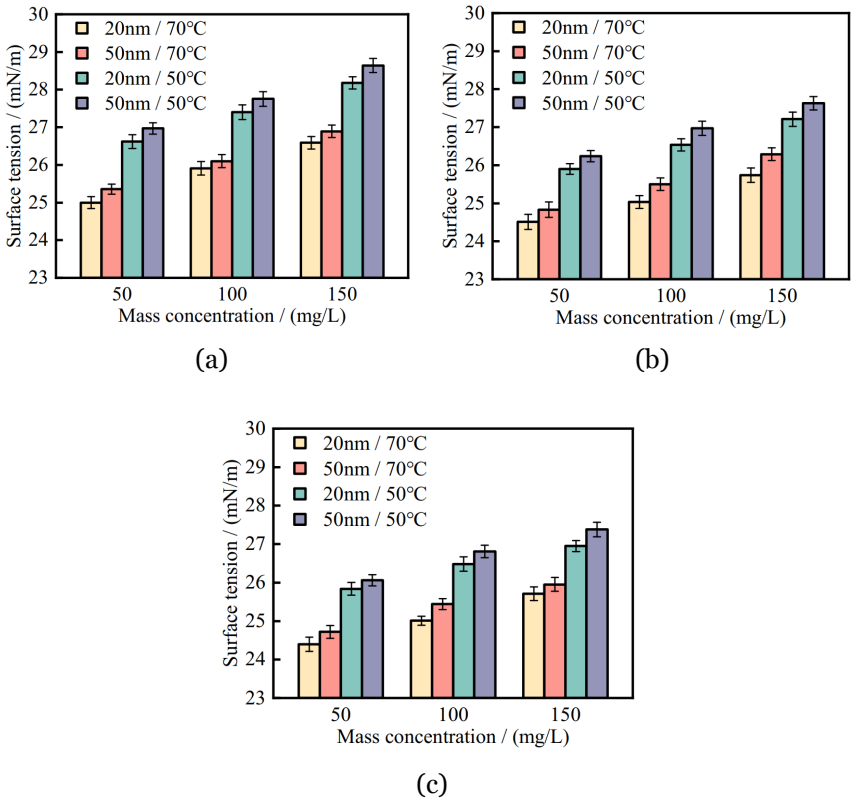

Figure 2.27: Nanofuel surface tension with different particle size and temperatures: a) CNT; b) CeO_2; c) Co_3O_4. Adapted from [211].

temperature increases, particularly at lower mass concentrations and with smaller particle sizes. The effect of the particle concentration is also evaluated by Mei et al. [211]. With the increase of the particle concentration, the distance between particles is reduced, and the van der Waals force increases, resulting in a higher surface tension than the base fuel. Moreover, the surface tension is only marginally affected for low particle concentration since the inter-particle distance is sufficiently large, even at the liquid/gas interface [212]. Similar observations were reported by [24, 27]. The increase of the viscosity and surface tension should be considered in the droplet formation, which will negatively affect the atomization process and, consequently, the combustion performance, as will be discussed in the spray background. In light of this, a slight increase in the density is expected as the particle concentration increases due to the higher density of the nanoparticles compared to the base liquid [209].

Besides the influence of the nanoparticles in the thermophysical properties, there is a concern regarding their use in the transportation sector. Issues related to nanoparticle toxicity and human exposure to nanomaterials are also reported. The latter is due to a possible dermal absorption and inhalation, resulting in organ damage and diseases, cellular and genetic effects, and biochemical changes [189, 213]. Figure 2.28 shows the implications in human health caused by using nanomaterials. Furthermore, using nanofuels as fuels for transportation during the exhaust, nanomaterials are released, which may interact with air, soil, and water through various mechanisms [189]. A detailed description of the nanoparticles influence in air, soil and, water is provided in [189, 214]. It should be highlighted that the impli-

cations for human and environmental health are also impacted by the type of nanomaterials employed.

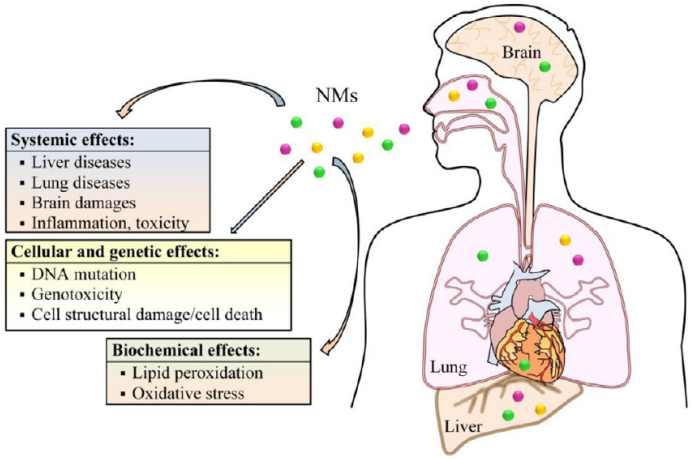

Figure 2.28: Human health implications due to nanomaterials exposure, adapted from [189].

After summarizing the most relevant details about the use of nanoparticles, it is clear that further research is essential to overcome all of these concerns since the benefits in terms of combustion systems have been discussed. In particular, the addition of nanoparticles encompasses a diverse array of applications within the field of engineering due to their potential as a working fluid instead of conventional liquids due to their outstanding performance [177]. Consequently, it is essential to prioritize the investigation of the combustion characteristics at the droplet scale, as these form the fundamental basis for any combustion system that employs liquid fuel spray. In this respect, Table 2.6 presents several studies focusing on nanofuel evaporation/combustion, illustrating the contemporary advancements in this area. The purpose is to provide a chronological point of view of the studies presented in the literature in both experimental and numerical approaches and the influence of adding nanoparticles. preliminary study involving the use of nanoparticles in conventional fuel was developed by Tyagi et al. [215]. The study aimed to improve the ignition properties of diesel, adding aluminum and aluminum oxide nanoparticles in different particle sizes (15 and 50 nm) and volume fractions (0%, 0.1%, and 0.5%). Results demonstrated that the ignition probability of diesel increases when nanoparticles are added. To understand the effect of particle size, Gan and Qiao [206] performed an experimental study to evaluate the burning characteristics of fuel droplets containing nano and micron-sized aluminum particles [216]. Based on the conducted literature review, the predominant finding is that the evaporation and combustion of nanofuel droplets do not follow the classical D^2-law related to the single droplet evaporation and combustion. Figure 2.29 shows the square droplet size evolution for a nanofuel and a conventional fuel droplet.

After the initial heating phase, observations indicate that the evaporation and combustion rates of nanofuel droplets do not remain constant. In contrast, gradually decreases [218]. As noted in Figure 2.29, the heating and steady-stage are presented in nanofuel and conventional fuel combustion. However, the addition of nanoparticles leads to a dry-out stage,

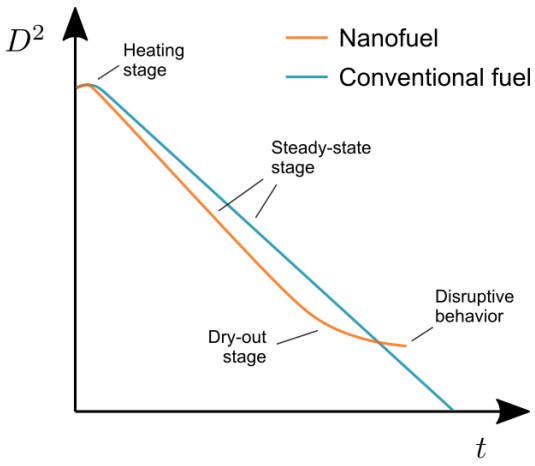

Figure 2.29: D^2-law illustration of a nanofuel and a conventional fuel, adapted from [16, 217].

where the droplet diameter decline rate is significantly reduced, which finishes when the disruptive behavior stage occurs due to the occurrence of puffing and micro-explosions [16, 206, 218, 219]. In other words, The dry-out phase corresponds to the last stage of the nanofuel droplet lifetime, where residual nanoparticles can be detected at the end of the steady-state phase or disruptive burning events [220]. A more comprehensive illustration of these stages is provided in Figure 2.30, highlighting the presence of disruptive burning phenomena at the end of the nanofuel lifetime. The presence of disruptive burning phenomena in nanofuel combustion has been highly reported, regardless of particle size and concentration, leading to the partial or total disintegration of the primary droplet, smaller fragments, and enhanced combustion process. [219, 221–223]. The deviation of the D^2-law was reported in multiple researches [206, 219, 221, 224–227]. To address this, Wang et al. [228] performed a numerical study on the evaporation rate of a copper–water nanofluid droplet. The authors reported that the D^h-law is influenced by the nanoparticles used in the study. For a pure liquid, the exponent h is about 2. However, this exponent will be less than 2 for lyophilic nanoparticles (i.e., attracting the liquid) and greater than 2 when lyophobic nanoparticles (i.e., repelling the liquid) are added. These results also confirm the decrease in the average evaporation rate of the nanofluid droplet at the end of droplet evaporation due to the aggregation of the nanoparticles on the surface.

The evaporation/combustion of nanofuels is a highly complex, multi-phase phenomenon in which several processes occur simultaneously [229]. The main mechanisms that influence the droplet evaporation and burning rate when nanoparticles are added to liquid fuels have already been identified but not clearly understood [17, 220, 225, 227, 229, 230]. Those are nanoparticle radiation absorption and particle accumulation at the droplet surface. In addition, the effect of adding nanoparticles can also increase the thermal conductivity, influencing droplet evaporation and combustion. Nevertheless, an excessive particle concentration in liquid fuels could cause aggregate formation, potentially affecting the thermal conductivity of the fuel either positively or negatively [223]. In this context special attention will be given to the radiation absorption and particle aggregation. The former provides an addi-

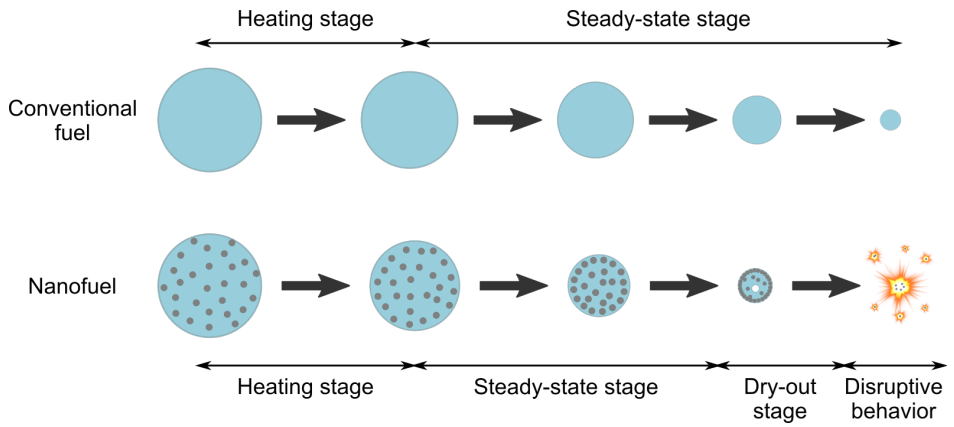

Figure 2.30: Schematic of the typical nanofuel droplet dynamics compared to conventional fuel droplets, adapted from [16, 218].

tional energy budget, accelerating the heating and enhancing the evaporation/burning rate of the droplet, thus allowing a greater heat release rate [19, 231]. As previously mentioned, studies concerning droplet combustion are typically neglected, as most liquid fuels are nearly transparent to the radiation emitted by the flame. However, when nanoparticles are added, the optical properties are affected [232]. In addition, the presence of nanoparticles inside a liquid fuel can behave as a strong absorber, and localized convection may occur between particles and the surrounding fluid due to temperature differences and the Brownian motion of nanoparticles [230]. Conversely to the radiation absorption, particle aggregation at the droplet surface creates a resistance to the evaporation of liquid fuel, suppressing the evaporation/burning rate [19]. As shown in Figure 2.30, as the liquid fuel evaporates, the nanoparticles typically remain inside the droplet until disruptive burning phenomena occur. Although the time scales differ significantly, this phenomenon is similar to droplet drying for solid particle formation, commonly employed in the pharmaceutic industry [233]. In this respect, due to slow particle diffusion, nanoparticles accumulate near the droplet surface as the surface recedes, eventually leading to a shell of particles [226, 234]. This shell creates a mass resistance that hinders the evaporation of the liquid fuel. Following Maurice et al. [235] at this point, the first drying stage concludes and begins the transition to the second drying stage. As evaporation proceeds, the shell gets thicker, and the evaporation rate is reduced. Eventually, the resistance of the shell becomes greater than the compressive capillary forces applied to its surface, and the shell reaches an approximately constant diameter [217, 236]. At this stage, the droplet transited into the second phase of the drying process occurring the dry-out phase. This can generate the nucleation of liquid fuel that remains trapped inside the droplet, leading to an increase in the pressure inside the droplet [237]. Under conditions, a disruption of the droplet occurs, leading to the formation of puffing or a micro-explosion, as shown in Figure 2.30. The occurrence of micro-explosions reduces the droplet lifetime and enhances complete combustion by dispersing the solid fuel contained within the droplet [16]. As noted in Table 2.6, most studies involve the droplet suspension technique. However, this serves as a bubble nucleation affecting the nanofuel droplet behavior. Due to this, investigations concerning different techniques should be considered [29]. Concerning disruptive burning events, Javed et al. [219] investigated the micro-explosion phenomenon in dense

concentrations of aluminum nanoparticles added to kerosene. A droplet suspended method was used to evaluate the evaporation and micro-explosions for dense concentrations. The authors stated that micro-explosions were detected when aluminum nanoparticles were added to the kerosene. The micro-explosion intensity increases with the ambient temperature and particle concentration. Ittoo et al. [238] investigated single droplet combustion of diesel and nanofuels composed of multiwalled carbon nanotube. Micro-explosions were identified, and their intensity depended on the particle concentrations.

However, these two mechanisms compete against each other to dominate the change in evaporation rate [227], where the influence of the particle concentration possesses a relevant role, as noted by Nam and Kim [17]. In this context, a question remains whether there is any optimal particle concentration that no longer enhances evaporation or burning rate by the radiation absorption. The increase in particle concentration also improves the particle accumulation rate at the droplet surface, reducing the evaporation/burning rate [229, 239]. The study of higher nanoparticle concentrations can be related to the increase in the energy density of nanofuel, being a benefit for applications where the volume of engines is limited. Conversely, the nanofuel stability is negatively affected [19]. Similar findings were reported by Yadav et al. [198], and Li et al. [240], suggesting that a burning rate enhancement can be achieved until a specific particle concentration. Further increase of nanoparticle concentration in a droplet causes a higher agglomeration, negatively influencing the combustion process.

To improve the understanding of the behavior and dynamics of nanofuels, visualizing and identifying the motion of nanoparticles within the droplet during evaporation and combustion would be relevant to gain insights into these processes. However, cost, safety, time constraints, and challenging operating conditions can limit experimental studies. In this way, mathematical models can ease the phenomenological understanding of complex systems and predictions of the relevant processes. Consequently, developing numerical/analytical models capable of predicting the dynamics of liquid conventional fuels and nanofuels addressing the different mechanisms previously mentioned is essential. In addition, the atomization process and spray combustion should be analyzed to introduce these fuels in real-world applications. Consequently, the subsequent subsection will be dedicated to the spray dynamics.

Table 2.6: Summary of nanofuel studies presented in the literature.

Reference	Article Type	Experimental Setup	Base Fuel	Nanoparticles	Operating Conditions	Key Findings
Tyagi et al. [215]	Experimental	Hot-plate single droplet ignition	Diesel	Al (50 nm + 1.5 nm Al (50 nm + 1.5 nm passive oxide layer; 0, 0.1 and 0.5 vol.%) and Al_2O_3 (15 and 50 nm; 0, 0.1 and 0.5 vol.%)	T: hot-plate temperature range 688-768 °C (increments of 20 °C); P: 1 atm	• Ignition probability was much higher with the addition of nanoparticles. • The hypothesis is that adding nanoparticles improves the radiative and heat/mass transfer fuel properties.
Gan and Qiao [206]	Experimental / Theoretical	Suspended single droplet combustion	Ethanol and N-decane	Al (80 nm, 5 and 25 μm + 2-8 nm passive oxide layer; 10 wt.%)	T: Room temperature; P: 1 atm	• Nanosuspensions present higher stability than micron suspensions. • Nanofuel droplets present a micro-explosion behavior. • Theoretical analysis shows that particle collision and aggregation are dominated by the Brownian motion for nanoparticles and dominated by fluid motion for micron-sized particles.
Gan and Qiao [224]	Experimental / Numerical	Suspended single droplet evaporation	Ethanol and N-decane	Al (80 nm; 0.5, 2.5 wt.%)	T: 300, 320, 330 and 380 K; P: 1 atm	• A departure from the D^2-law was observed for nanofuels. • Results from a model based on the population balance equation suggest that particle aggregation may cause the d^2-law deviation.
Gan and Qiao [230]	Experimental	Suspended single droplet evaporation	Ethanol	Al (80 nm + 2-8 nm passive oxide layer; 0.1, 0.5 and 5 wt.%) and Al_2O_3 (25 nm; 0.1, 0.5 and 5 wt.%)	T: Room temperature; P: 1 atm	• Radiation absorption can be significantly enhanced by nanoparticles. • The strong absorption of radiation energy increases the nanofluid droplet temperature and enhances the droplet evaporation rate.
Javed et al. [219]	Experimental	Suspended single droplet evaporation	Kerosene	Al (70 nm; 2.5, 5.0 and 7.0 wt.%)	T: 400-800 °C; P: 1 atm	• Distintive stages identified in the evaporation of nanofuel droplets beyond the steady-state phase. • Micro-explosion behavior occurred and was more intense for higher particle concentration and ambient temperature. • The addition of nanoparticles increased the evaporation rate for higher temperatures and decreased it for lower temperatures.

Table 2.6 Continued: Summary of nanofuel studies presented in the literature.

Reference	Article Type	Experimental Setup	Base Fuel	Nanoparticles	Operating Conditions	Key Findings
Gerken et al. [234]	Experimental / Numerical	Suspended single droplet evaporation	Ethanol	Al (40-60 nm; 0.1, 0.27, 1.0 and 3.06 wt.%)	T: Room temperature; P: 1 atm	• Gradual decrease of the evaporation rate with increasing nanoparticle concentration. • Surface tension unaffected with the concentrations of nanoparticles added. • Model developed to describe the evaporation of nanofluid droplets.
Javed et al. [221]	Experimental	Suspended single droplet combustion	N-heptane	Al (70 nm; 0.5, 2.5 and 5.0 wt.%)	T: 600-850 °C; P: 1 atm	• Nanofuel droplets exhibited disruptive burning behavior and did not obey the d^2-law. • Nanoparticles were ejected from the droplets via microexplosions, which were more intense at higher temperatures and concentrations. • The addition of nanoparticles increased the burning rate for higher temperatures and decreased it for lower temperatures.
Tanvir and Qiao [225]	Experimental / Theoretical	Droplet stream combustion	Ethanol	Al (80 nm; 0.1, 1.0, 2.0, 3.0 and 5.0 wt.%)	T: Room temperature; P: 1 atm	• Adding nanoparticles significantly increases the thermal conductivity, while viscosity and surface tension remain nearly unchanged. • Adding nanoparticles significantly increases the droplet burning rate, and a deviation from the d^2-law was observed. • A theoretical analysis showed that radiation absorption by the nanoparticles from the stream flame is an important mechanism of energy transfer in nanofuels.
Kim et al. [241]	Experimental	Suspended single droplet ignition	Kerosene	Al (70 nm; 0.1 and 1.0 wt.%)	T: 400-800 °C; P: 0.1-2.5 MPa	• The addition of nanoparticles reduces the droplet ignition delay.
Tanvir and Qiao [229]	Experimental / Numerical	Droplet stream combustion	Ethanol	Graphite (50 and 100 nm; 1.0 and 3.0 wt.%)	T: Room temperature; P: 1 atm	• Droplet burning rate increases with particle concentration. • Model developed based on Monte Carlo algorithm to estimate droplet radiation absorption from stream flame. • Radiation absorption enhances droplet burning rate and is located near the droplet surface, promoting localized boiling at the surface.

Table 2.6 Continued: Summary of nanofuel studies presented in the literature.

Reference	Article Type	Experimental Setup	Base Fuel	Nanoparticles	Operating Conditions	Key Findings
Wei et al. [226]	Numerical	-	-	-	-	• Model developed to predict the evaporation behavior of nanofluid droplets for the stage prior to particle shell formation. • Model predicts the deviation from the d^2-law.
Tanvir et al. [227]	Experimental / Numerical	Suspended single droplet evaporation	Ethanol	Graphite (50 nm; 1.0, 3.0 and 5.0 wt.%)	T: Room temperature; P: 1 atm	• The addition of nanoparticles results in a deviation from the d^2-law. • Two competing mechanisms control evaporation rate: (a) radiation absorption, which enhances evaporation, and (b) particle aggregation, which suppresses evaporation. • Model developed based on Monte Carlo algorithm coupled with Mie theory and Beer-Lambert law to predict the evaporation behavior of nanofluid droplets exposed to radiation prior to particle shell formation.
Ghamari and Ratner [239]	Experimental	Suspended single droplet combustion	Jet A-1	CNPs (100 nm); MWCNTs (8-15 nm x 0.5-2 μm); Graphene (width 5 μm, thickness 6-8 nm) Concentration: 0-3.0 wt.%	T: Room temperature; P: 1 atm	• The addition of nanoparticles, nanotubes, and nanoplatelets increases the droplet burning rate. • For each particle type, a concentration was found at which the maximum burning rate was achieved. • Beyond this concentration, the burning rate is reduced, possibly due to higher particle agglomeration.
Pandey and Basu [231]	Experimental / Theoretical	Acoustic levitated single droplet evaporation	Ethanol and N-dodecane	CeO_2 (25 nm; 0.1, 0.25 and 0.5 wt.%)	T: room temperature; P: 1 atm	• Nanofuel droplets showed enhanced vaporization due to radiation absorption. • Nanofuel droplets exhibit internal boiling induced atomization, and a time scale analysis was performed to elucidate the mechanism.
Pandey et al. [242]	Experimental	Free-falling single droplet combustion	N-dodecane	Al_2O_3 (40 nm; 0.5, 1.0, 5.0, and 10.0 wt.%)	T: Room temperature; P: 1 atm	• Flame shape regimes varying with the droplet Reynolds number, Re_d.

Table 2.6 Continued: Summary of nanofuel studies presented in the literature.

Reference	Article Type	Experimental Setup	Base Fuel	Nanoparticles	Operating Conditions	Key Findings
Mosadegh et al. [223]	Experimental	Suspended single droplet combustion	Ethanol	Graphene oxide (GO) (0.01 and 0.1 wt.%)	T: Room temperature; P: 1 atm	• Atomization phenomenon could occur for all fuels with GO. • The addition of graphene oxide into ethanol and increasing the loading concentration from 0.01 to 0.1% improves the overall burning rate.
Yang et al. [243]	Experimental	Suspended single droplet combustion	JP-10	Al (50 nm; 1.0, 2.5, 5.0 wt.%)	T: 300, 400, 500, and 600°C; P: 1 atm	• The evaporation rate decreases with the increasing concentrations of oleic acid and Al nanoparticles. • At high temperatures of 400°C or above, the droplets undergo obvious microexplosion after adding oleic acid and Al nanoparticles.
Noh et al. [28]	Experimental	Suspended single droplet combustion	Ethanol	Aluminum (Al - 100 nm; 2.5, 5.0 wt.%) and nickel-coated aluminum (Ni-Al-2.5, 5.0 wt.%)	T: Room temperature; P: 1 atm	• Ni-Al demonstrated a diminished burning rate in contrast to its Al counterpart. • Nanofuels containing Ni-Al possess elevated energy potential relative to those with Al, albeit with an expected increase in total combustion duration.
Nam and Kim [17]	Experimental	Suspended single droplet combustion	Ethanol	Boron (70 nm; 2.0, 4.0, 6.0 wt.%)	T: Room temperature; P: 1 atm	• The average burning rate increased when the boron concentration was at 2 wt.%, attributed to the enhanced thermal conductivity. However, the rate decreased as the boron concentration rose further due to particle aggregation within the droplet.

2.4 Spray

The current section focuses on the current developments in spray research. First, an introduction dedicated to the principles and application of sprays is provided. Subsequently, a summary dedicated to the atomization process, including primary and secondary atomization, as well as spray characteristics, is also considered. Finally, a survey concerning the current evolution of the spray combustion field is addressed to understand the physical processes and their consequences on combustion.

2.4.1 Overview

Atomization occurs due to the breakup of the liquid jet or sheets near the atomizer nozzle, and the subsequent interaction between droplet and air plays a critical role in many applications. Consequently, its efficiency is related to the control of the spray characteristics, such as the droplet size distribution, the spray spatial spreading, or the droplet production frequency [244]. In this respect, selecting appropriate droplet sizes and uniformity in different spray systems depends on their application. Atomization is required in agriculture, coatings, gasification, pharmaceuticals, metal powder production, 3D printing, spray drying, fire extinguishing, cooling, and, more specifically, gas turbines, industrial furnaces, and rocket engines [245]. In medical systems, droplets may be considerably small, with a few micrometers allowing them to travel through small airways and reach the lungs. However, agricultural or fire suppression applications require large droplets to maintain sufficient momentum, avoiding dispersion by the wind stream [246]. Concerning the combustion perspective, the atomization process allows the conversion of bulk liquid fuels into smaller droplets, enhancing the fuel surface area and playing a relevant role in droplet vaporization. The fuel atomization quality is directly related to combustion efficiency and emission performance [247]. Furthermore, the highest combustion efficiency coupled with reduced pollutant emissions is achieved when the fuel spray rapidly disperses and evaporates to yield a homogeneous mixture of fuel and air [248]. On the other hand, large droplets are obtained from poor atomization, resulting in localized fuel-rich combustion that produces soot and nitric oxides [249]. As noted, depending on the applications and different specifications, lying solely on the mean droplet diameter may not provide sufficient information. Moreover, a spray possesses a large quantity of droplets, so accurately determining the size and velocity of each droplet is extremely difficult. Experiment studies have been conducted using imaging techniques to obtain the spray cone angle, ligament breakup characteristics, and droplet formation. Furthermore, Phase-Doppler Interferometry (PDI) is commonly employed to evaluate droplet diameter and velocity distribution to understand the spray dynamics. As a result, a full understanding of the droplet distribution is essential, and statistical analysis emerges as a practical tool for understanding the atomization process, as will be further discussed [246].

Lefebvre [250] stated that atomization refers to the process of converting bulk liquid into a dispersion of small droplets from submicron to several hundred microns in diameter. Consequently, a spray can be intended as a flow of individual liquid droplets in a surrounding

gaseous medium, where each droplet possesses a distinct diameter and velocity and may experience collisions and coalescence [251]. The atomization process is a competition between stabilizing forces, primarily surface tension and viscosity, and disruptive forces exerted by both internal dynamics and external forces. Liquid turbulence, nozzle cavitation, and aerodynamic interactions with the surrounding environment are essential in this procedure. Atomization occurs when the disruptive forces overcome the surface tension forces [156]. The atomizer size, geometry, and the physical properties of both the liquid and the gaseous medium profoundly impact the spray characteristics. The spray formation can be classified into two phases. The first phase, or the initial disintegration, is denominated by primary atomization and is characterized by the disintegration of a liquid jet into ligaments or fragments. When a liquid jet is released from the nozzle as a continuous cylindrical body, oscillations and perturbations emerge due to the imbalance between cohesive and disruptive forces on its surface. When amplified under specific conditions, these oscillations can cause the jet fragmentation into droplets. During this process, bag-like structures and ligaments can be spotted. On the other hand, secondary atomization involves the disintegration of droplets into smaller droplets. If the larger droplets produced during the primary atomization are subjected to an ambient flow field moving at a relative velocity, aerodynamic forces may induce deformation, resulting in its fragmentation into smaller droplets, evidencing the secondary atomization. Commonly, the primary atomization occurs near the nozzle, and secondary atomization arises downstream [252]. An illustration of the atomization process is shown in Figure 2.31.

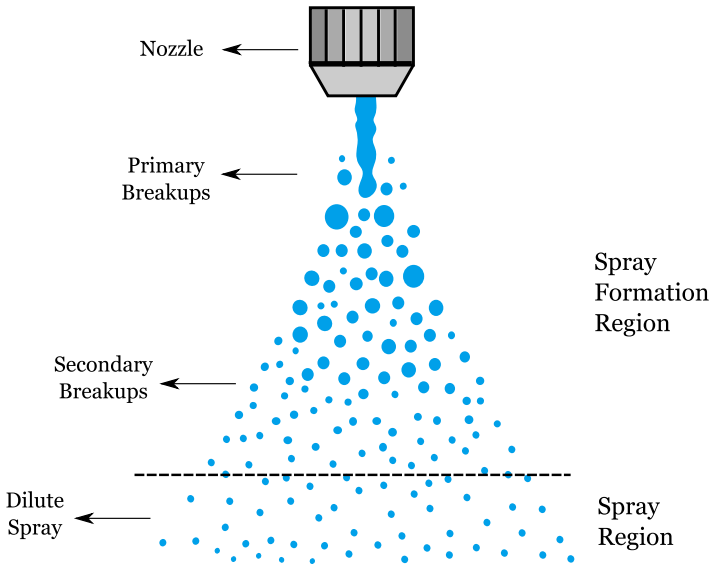

Figure 2.31: Illustration of atomization process. Representation of the two distinct regions: the spray formation region and the spray region. The initial region involves primary and secondary atomization, whereas, in the subsequent region, the spray is typically fully developed, with the majority of droplets being spherical.

The spray breakup is influenced by four key forces: inertial force, viscous force, surface tension, and aerodynamic forces acting on the jet. To achieve proper atomization, aerodynamic, centrifugal, or pressure forces must overcome surface tension forces. As previously highlighted, the primary objective of breaking a bulk liquid jet into a spray is to maximize the liquid surface area while minimizing the breakup length, thereby enhancing subsequent heat and mass transfer processes [253]. Understanding the breakup and atomization processes

of liquid jets is essential for addressing issues related to two-phase flow in combustion and propulsion systems. Focusing on the combustion systems, liquid fuels are atomized before the combustion process, producing small droplets that allow a higher surface area, reducing the vaporization time and leading to better air-to-fuel mixing, significantly impacting combustion emissions, performance, and flame stability. Since liquid atomization is crucial for engine performance and subsequent emissions, investigations focused on comparing alternative and conventional fuels are vital to advancing the implementation of sustainable fuels in the modern world. For a better understanding of how the variation properties of alternative fuels impact atomization, diverse and valuable theoretical, experimental, and numerical investigations have been reported, as will be addressed in the following subsections.

2.4.2 Atomizers

Atomizers or spray nozzles typically consist of nozzle orifices, where the liquid jet is released and atomized, producing droplets due to its kinetic energy or as a consequence of interaction with a high-speed gas flow. A crucial factor for the atomization of the injected liquid is the high relative velocity between the liquid and the surrounding air or gas [246]. Depending on the fuel properties and specific applications, several atomizers can be selected. Additionally, the design differences in practical atomizers enable the enhancement of a specific process under diverse liquid flow rates and operating conditions, producing different droplet size distributions [246]. An ideal atomizer should exhibit the following characteristics [254]:

- Good atomization over a wide range of liquid flow rates
- Immediate adjustment to the variation in liquid mass flow rate
- Stability in flow dynamics
- Lower power requirement
- Design flexibility, capable of scaling
- Cost-effective, lightweight, and simple to service.

The atomizers are divided into pressure atomizers, rotary atomizers, and twin-fluid atomizers, as shown in Figure 2.32. For each category, several configurations are encountered. The performance of any atomizer depends on the nozzle geometry, the operating conditions, and the physical properties of the dispersed and continuous phases [252, 255].

Pressure atomizers release liquid at high pressure through a small orifice into the surrounding atmosphere in a relatively slow stream of gas. Consequently, the pressure energy is converted into the kinetic energy, [255]. Pressure atomizers in internal combustion engine systems may have disadvantages related to their structure and working stability [256]. Typically, pressure nozzles require much higher injection pressures than two-fluid nozzles to

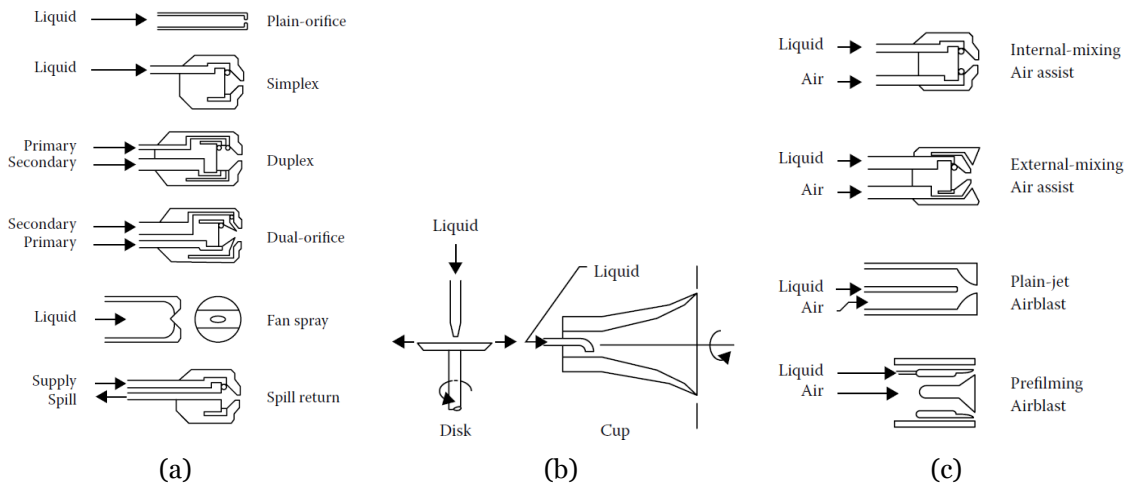

Figure 2.32: Atomizers Categorization: a) Pressure atomizers; b) Rotary atomizers; c) Twin-fluid atomizers. Adapted from [255].

achieve suitable atomization quality [246]. The key parameter in pressure atomizers is the orifice geometry, which is responsible for the energy conversion and the shape of the spray. From this orifice, a pressure atomizer can produce a jet-like spray, a flat one produces a fan spray, and adding a swirl allows a full cone or hollow cone spray structure [257]. Ensuring the design quality of these atomizers is critical since these devices operating under high pressure can cause damage over time and reduce the overall efficiency of the device [258]. Moreover, an increase in the injection pressure increases the influence on the atomization of the liquid fuel, which will be substantially reduced [259]. Due to this, a different design nozzle should be employed to operate with high viscous fuels and low pressures.

Regarding twin-fluid atomizers, they operate the relatively slow-moving liquid to a high-velocity airstream. Thus, atomizing air acts as the energy source, which is transformed into surface energy to produce the spray droplets. Typically, the momentum flux of a high-velocity gas stream is equal to or greater than the liquid jet [260]. These atomizers can be subclassified into air-assist and air-blast, where the main difference is the values of airflow velocity [254]. In this context, the air-blast atomizer uses a high amount of air at a limited velocity and can be divided into plain jet and prefilming. The air-assisted atomizer employs a low amount of air at a high velocity and is divided into internal and external mixing. In contrast to pressure atomizers, twin-fluid atomizers require low injection pressures. Pressure atomizers release high-pressure liquid into a slow-moving environment, causing a lot of soot formation. A common arrangement in twin-fluid atomizers, the liquid is released in the central zone and presents a high-speed co-flowing annular air stream, evidencing reducing emission characteristics [261]. Twin-fluid atomizers are widely used in practical applications, especially in combustion systems [262]. This configuration occurs when the gas and liquid phase moves in the same direction or when the time scale of the breakup process is relatively long. Thus, the liquid disrupts in a classic method, giving sufficient time for wave instabilities to emerge [263]. Coaxial atomizers possess significant importance in aero-gas

turbines, allowing a high level of fuel atomization and an entrance air co-flow with enough swirling motion to promote a central recirculation zone that is responsible for aiding the fuel and air mixing and flame stabilization [264]. Moreover, reduced pollutant emissions are reported due to the prevention of rich mixtures, as the air employed in atomizing the liquid enables thorough mixing and more efficient atomization, being an appropriate equipment for cold and viscous fuels [265]. The air-assisted atomizer can be used with internal or external mixing. For external mixing, the liquid and gas phases are mixed outside of the nozzle exit with the external mixing atomizer. This type of atomizer can independently control the air and liquid flow rates, avoiding liquid-blocking phenomena characteristic of internal mixing atomizers. However, external mix atomizers, compared to internal mix atomizers, require higher atomizing airflow rates to achieve the same levels of atomization. Regarding the internal mix atomizers, the mixing of the liquid and air occurs inside the atomizer body. In typical twin-fluid atomizers, compressed air is used for atomizing the liquid, while the liquid can be delivered by pressure feed, gravity feed, or the siphon principle [266].

A rotary atomizer possesses a high-speed rotating disk with a mechanism for introducing liquid at its center. The liquid flows radially outward across the disk and is expelled at high velocity from its periphery with the aid of vanes or slots. For this configuration, small disks at high rotational speeds and low flow rates produce sprays with relatively homogeneous droplet sizes [255]. Rotary devices offer the advantage of enabling independent control of the atomization quality and flow rate and are typically employed in spray drying and fire extinguishing systems [246]

2.4.3 Factors Impacting the Atomization

The atomization process is related to the nozzle design, the physical properties of the liquid and the ambient gas environment, as well as the operating conditions. A brief explanation regarding the atomizers employed is discussed above. The surrounding ambient where the spray is released is also a relevant parameter that can vary widely in pressure and temperature, which is highly pertinent in combustion systems. In this context, diesel engines operate under critical and supercritical pressure and temperature conditions, and in gas turbine combustors, fuel sprays are introduced into highly turbulent, swirling flows of reacting gases. Similarly, in industrial furnaces, fuel is injected into high-temperature flames formed by recirculating combustion products [255]. Regarding the environmental conditions and nozzle design, the density of the air is one of the most relevant parameters. In air-assist airblast atomizers, increasing the air density enhances atomization efficiency due to the increase in the Weber number. In this context, the aerodynamic interactions promote smaller diameters and longer breakup lengths. For pressure-swirl atomizers, however, droplet size initially increases with increasing ambient air density until reaching a critical value decreases as air density continues to rise [255]. Numerous studies have been carried out dedicated to the influence of pressure and temperature on different systems, as will be addressed in detail below in the spray combustion.

Liquid density possesses a minimal effect on the atomization process. A preliminary study focused on the density effect was performed by [267]. The authors stated that, for a thin-sheet atomizer, the average diameter of the droplets increases with the density up to a value around 1500 Kg m^{-3}. Above this value, any increase in density causes a decrease in the SMD (Sauter Mean Diameter). Later, Lorenzetto and Lefebvre [268] using an air-assisted atomizer, reported that the quality of atomization was always improved by increasing the density of the liquid, contracting the results obtained by Rizkalla and Lefebvre [267]. This discrepancy reveals the relevance of considering the influence of liquid density separately for each type of atomizer. Additionally, It should be noted that the density effect is attenuated by the fact that most liquids present only slight variations in the value of this property [255].

Surface tension is defined as the energy per unit area at the interface between two fluids. Higher surface tension acts as a consolidating force, resisting any disturbances or irregularities on the liquid surface [246]. Surface tension has a qualitatively negative effect on atomization quality since it represents a consolidation force and counteracts any distortion of the liquid surface. Thus, an increase in the surface tension delays the formation of ligaments and droplets, leading to larger droplet sizes [156]. Lorenzetto and Lefebvre [268] validated these findings by noting that the adverse effect of surface tension decreases at higher air velocities. A similar finding is observed with viscosity, which suggests that the two properties should be analyzed in parallel.

Similar to surface tension, viscosity is a significant factor negatively impacting atomization quality. An increase in viscosity leads to a reduction in the Reynolds number, hindering the natural formation of instabilities that are essential for jet breakup. In detail, increasing liquid viscosity results in an increase in the length of the undisturbed liquid sheet, as well as an increase in jet penetration, hindering wave formation decreases the break-up rate of distortions or droplets, reduces turbulence, and consequently produces coarser sprays [246].

The Reynolds number is the ratio between the inertial and viscous forces, defined by the following expression:

$$Re = \frac{\rho U L}{\mu}, \quad (2.43)$$

where ρ is the fluid density, U the velocity and L characteristic length. Lorenzetto and Lefebvre [268] showed that any increase in viscosity promotes an increase in the average diameter of the droplets, which is related to the increase in viscous forces that tend to oppose the disintegration of the liquid into droplets. However, this effect can be attenuated at higher air velocities due to the increased energy availability for atomization [255, 268]. The relation between the atomizer orifice and viscosity is relevant. The influence of the liquid orifice diameter on the average droplet size is inconsistent, as it depends on the viscosity of the liquid, as reported by Lorenzetto and Lefebvre [268]. The authors found that for low viscous liquids

(≅1 mPa.s), Sauter mean diameter (SMD) changes slightlywith different orifice diameters. On the other hand, for highly viscous liquids (≅ 36 mPa.s), SMD significantly depends on the orifice diameter. Additionally, Rosa et al. [269] conducted a detailed comparison between liquids with low and high viscosity and found that with identical operating parameters, the more viscous liquid produces sprays with larger droplets. Notably, the primary difference between the two jets was the significant number of large drops in the center of the spray formed by the higher viscosity liquid. Another significant aspect is the relative velocity between the gas and liquid, as well as the air-fuel ratio (AFR). An increase in the air velocity, maintaining a liquid velocity, results in a higher relative velocity, which results in the formation of wave instabilities on the liquid surface. Consequently, the mean droplet size is inversely proportional to the relative velocity, and the air velocity does not exceed sonic speeds [268, 270]. In particular, Lorenzetto and Lefebvre [268] performed a study using water and kerosene varying the air velocity through the use of holes of different dimensions for a constant AFR. The results reveal a considerable decrease in the average droplet diameter with increasing air velocity, particularly for low-viscosity liquid. For small AFR values, the amount of air may not be sufficient to break the aggregating forces of viscosity and surface tension, while for high AFR values, part of the injected air is too far away from the liquid to play an active role in atomization. Thus, increasing the amount of air for a constant liquid mass flow rate ($\dot{m}$) enhances atomization. The air-fuel (AFR) is the mass ratio between the air and liquid flows, and its increase tends to benefit the atomization quality. Similar findings are reported by Rizkalla and Lefebvre [267], which enables the identification of the optimal range of air-fuel ratio (AFR) values for each atomizer that maximizes the effects of the mixture between air and fuel. Thus, for each atomizer, it is necessary to determine the AFR for which the average droplet diameter stabilizes and try to operate in that regime. Thus, it is important for each atomizer to find the AFR for which the average droplet diameter stabilizes and try to operate in that regime.

An additional significant aspect of the atomizers is the presence of the swirl. This feature affects the spray structure and the droplet movement. Swirl enhances the liquid jet fragmentation, and when the atomizing gas transfers angular momentum to the liquid droplets, centrifugal forces significantly influence the radial transport of the droplets [271,272]. Moreover, swirl atomizers provide liquid sheets and droplets, leading to higher surface contact area with the environment, as well as a higher surface-to-volume ratio than any other form of jet, planar, or cylindrical [273]. A higher swirl intensity leads to increased radial distribution from centrifugal momentum, which reduces the Sauter Mean Diameter (SMD), enhancing the atomization process [274]. According to Presser et al., [275], the swirl allows the transport of smaller droplets from the downstream to upstream near the nozzle. In the context of combustion, it permits the recirculation of combustion products, influencing the droplet/air mixing. Swirling flows are commonly used in practical combustors, characterized by velocity components in axial and azimuthal directions, producing topological structures different from non-swirling jets. Moreover, the presence of swirl axial velocity components in both the positive and negative streamwise directions are identified [276]. Further details of the influence of swirl on the atomization process are discussed in [244, 272, 277].

2.4.4 Primary and Secondary Atomization

As previously mentioned, atomization results from the interaction between the liquid and surrounding air due to several deformation mechanisms. As the liquid jet leaves the atomizer in a cylindrical shape, it becomes subjected to cohesive and disruptive forces that produce oscillations and disturbances. Under favorable conditions, the oscillations are amplified, and the liquid, initially in the form of a cylinder, disintegrates into individual large droplets and ligaments in a process known as primary atomization. The jet breakup has been intensively studied using theoretical and experimental approaches. Prior to the introduction, which is dedicated to the breakup of the liquid jet by a high-speed annular air jet employed in a twin-fluid atomizer, a brief elucidation regarding droplet formation in a static regime is provided. The most basic atomization process is the formation and release of droplets from a tube. Rayleigh [278] developed a pioneering study. The author defined a laminar jet with an initial diameter of d_j, released by a circular orifice and influenced by surface disturbances. The results reveal that symmetric disturbances, defined by an optimal wavelength of $\lambda_{opt} = 4.15 d_j$, tend to amplify over time, leading to the breakup of the jet into ligaments that eventually originate spherical droplets with a diameter $D_0 = 1.89 d_j$, obtained from the following expression:

$$\lambda_{opt} \frac{\pi}{4} d_j^2 = \frac{\pi}{6} D_0^3 \,. \quad (2.44)$$

Weber extended Rayleigh theory using the Ohnesorge number to include the effect of liquid viscosity. This dimensionless number represents the ratio of an internal viscous force to a surface force resulting from surface tension:

$$Oh = \frac{\mu}{\sqrt{\rho \sigma L}} \,, \quad (2.45)$$

where μ is the liquid dynamic viscosity, σ the surface tension, ρ is the liquid density and L is the characteristic length. Thus, following Weber's theory, the optimal unstable wavelength is given by [279]:

$$\lambda_{opt} = \sqrt{2} \pi d_j (1 + 3Oh)^{0.5} \,, \quad (2.46)$$

where the characteristic length in the Ohnesorge number is defined by d_j. The previous theories described conducted by Rayleigh and later refined by Weber proposed that liquid jet breakup occurs as surface perturbations grow and propagate, with the wavelength of maximum growth rate producing droplets larger than the jet diameter, being applicable under laminar flow conditions in the liquid phase. However, this study does not consider the influence of gravity and aerodynamic shear [280].

The properties of the fluid influence the breakup of an injected liquid, the diameter of the jet, and the corresponding outlet velocity [278]. For a comprehensive understanding of the primary breakup mechanism, the behavior of cylindrical liquid jets discharged into a quiescent environment should be addressed. Furthermore, the liquid jet breakup can be classified into five regimes: the Dripping, the Rayleigh regime, the first wind-induced regime, the second wind-induced regime, and the atomization regime. Figure 2.33 shows a sequence of images regarding the fragmentation of a liquid jet discharged into a stagnant gas in the dripping, Rayleigh-Plateau, first wind-induced, and second wind-induced regimes. Additionally, the evolution of the average length of the liquid jet until break-up in respect to the velocity [281]. The breakup length is the length of the jet that is still connected to the nozzle, normalized by the nozzle diameter $\overline{L}/D_l$.

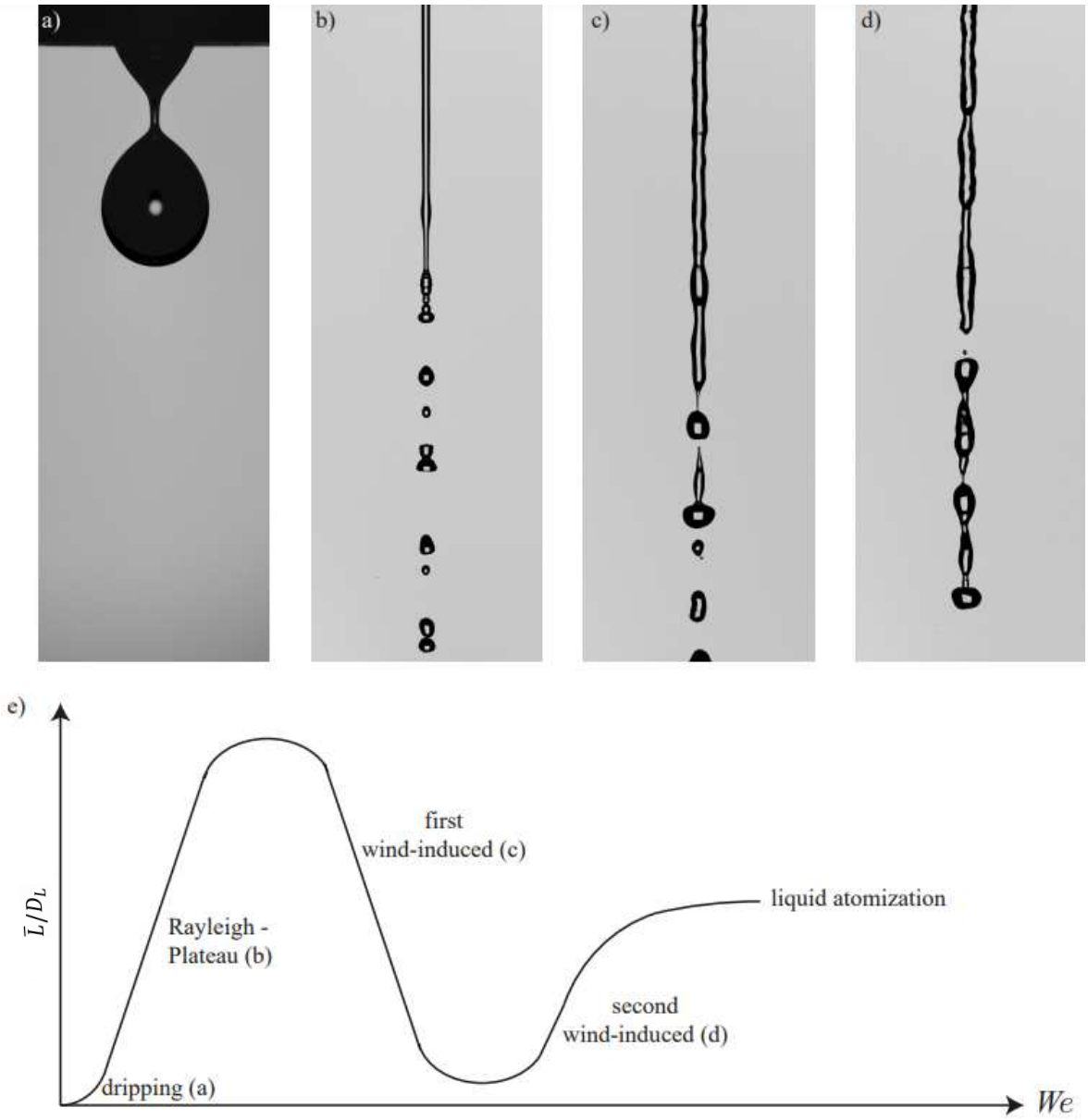

Figure 2.33: Fragmentation of a liquid jet discharged into a stagnant gas: a) Dripping; b) Rayleigh-Plateau; c) First wind-induced; d) Second wind-induced; e) Schematic stability curve relating the average liquid core length to the Weber number (We) increased from a) to d) by increasing the liquid flow rate here. D_L corresponds to the liquid nozzle inner diameter [281].

The transition between regimes is determined by the corresponding Weber numbers. The Weber number (We) is the ratio between inertial (or aerodynamic) and surface tension forces and can be expressed by the following expression:

$$We = \frac{\rho U_l^2 L}{\sigma}, \quad (2.47)$$

ρ is the density of the liquid, σ the surface tension, U_l velocity of the liquid jet, L is the characteristic length of the liquid flow more concretely the jet diameter. In the dripping regime, due to the significantly low outlet velocity, the liquid accumulates at the nozzle tip until it eventually detaches and drips. The Rayleigh regime is associated with the formation of droplets with uniform sizes higher than the nozzle outlet diameter when the air velocity is considerably low. Consequently, by increasing the air velocity, the influence of the aerodynamic force on jet breakup becomes relevant [282]. In the first wind-induced regime, droplets are formed at a considerable distance from the nozzle exit and exhibit diameters comparable to the nozzle outlet diameter. In the second wind-induced regime, atomization is enhanced, resulting in reduced breakup lengths and smaller droplet diameters. The atomization regime corresponds to a droplet diameter characterized by significant droplet diameters significantly smaller than the nozzle diameter [283, 284]. Table 2.7 shows the limits of each regime, defined by the Weber number already presented in Equation (2.47), the Ohnesorge number displayed in Equation (2.45) and gas Weber number defined by:

$$We_g = \frac{\rho_g U_l^2 L}{\sigma}, \quad (2.48)$$

ρ_g is the density of the gas, σ the surface tension, U_l velocity of the liquid jet, L is the characteristic length of the liquid flow more concretely the jet diameter.

Table 2.7: Regime map of a liquid jet breakup discharged into a quiescent environment, adapted from [285–287].

Regimes	**Criteria**
Dripping Regime	$We < 8$
Rayleigh Regime	$We > 8$ $We_g < 0.4$ or $1.2 + 3.41Oh^{0.9}$
First Wind-Induced Regime	$1.2 + 3.41Oh^{0.9} < We_g < 13$
Second Wind-Induced Regime	$13 < We_g < 40.3$
Atomization Regime	$We_g > 40.3$

In general, increasing the fluid viscosity delays the liquid jet breakup due to the suppression of internal fluid turbulence and instabilities. At high Weber and Reynolds numbers, viscosity has a minor effect on the primary breakup. However, its impact remains influential on the secondary breakup [288]. There are atomizer configurations where a round liquid jet is exposed to a co-flowing air stream. This configuration is named an air-assisted cylindrical jet. Farago and Chigier [289] developed a morphological classification of disintegrating coaxial using air-water jets. Three atomization regimes were identified: the Rayleigh-type breakup, the membrane-type breakup, and the fiber-type breakup [251]. Figure 2.34 shows

the regimes of round liquid jets exposed to a co-flowing air stream.

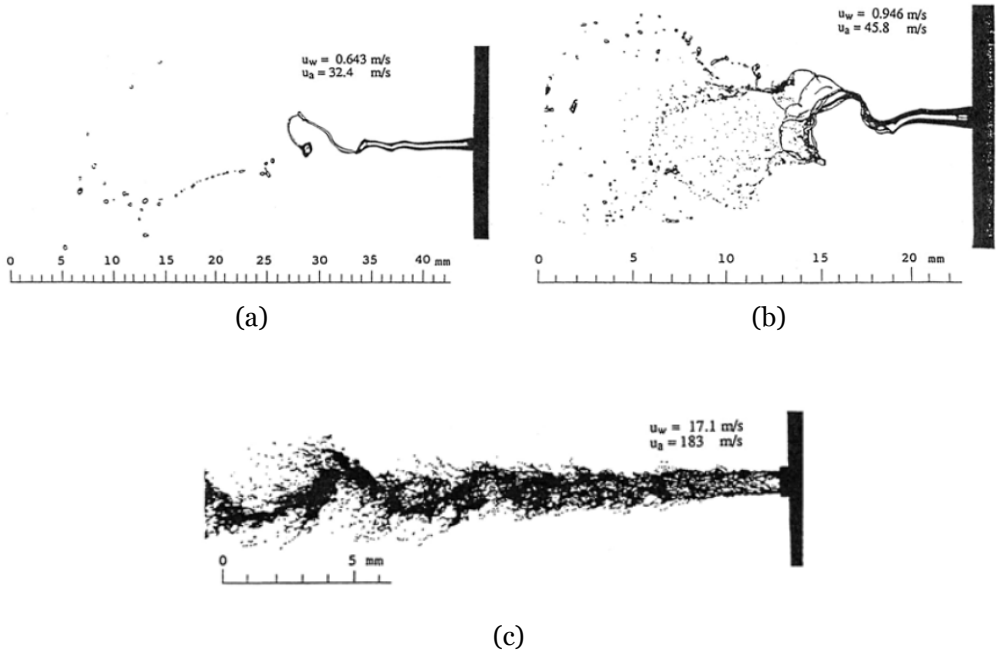

Figure 2.34: Breakup regimes for air-assisted cylindrical jets: a) Rayleigh-type breakup; b) Membrane-type breakup; c) Fiber-type breakup [289].

The Rayleigh-type regime is detected when the liquid jet directly breaks into droplets instead of forming ligaments, membranes, or fibers. The droplets released have a diameter in the order of the jet diameter. Rayleigh breakup can be categorized into sub-regimes depending on the Weber number: axisymmetric and non-axisymmetric breakup. Axisymmetric regime occurs when accelerating liquid core, and the co-flowing air causes the liquid jet to form a spiral structure as it progresses at an aerodynamic Weber number $We_a < 15$. On the other hand, non-axisymmetric breakup appears at $15 < We_a < 25$, where the high-speed velocity of the air reduces the liquid jet diameter. The membrane-type breakup is evident due to the development of thin liquid sheets or membranes. The aerodynamic forces induce Kelvin-Helmholtz instabilities on the membrane, resulting in droplets with diameters much smaller than those observed in the previous regime. Finally, the fiber-type breakup is spotted when thin liquid fibers peel off the jet and disintegrate via a mechanism identical to the non-axisymmetric regime at low relative velocities. Farther downstream, the liquid core undergoes wave formation that breaks into ligaments, peeling off smaller fibers, producing droplets that are initially tiny and increase with the downstream distance. The identification of each regime can be defined using the aerodynamic Weber Number (We_a), as displayed in Table 2.8. The aerodynamic Weber Number (We_a) presented in Table 2.8 can be defined by the following expression:

$$We_a = \frac{\rho_a (U_a - U_l)^2 D_l}{\sigma} \quad (2.49)$$

where U_l and U_a is the liquid and air velocity, respectively. σ surface tension and D_l is the

bore liquid diameter.

Table 2.8: Regime map of a liquid jet breakup exposed to a co-flowing air stream, adapted from [285–287].

Regimes	**Criteria**
Rayleigh-type Breakup	$We_a < 25$
Membrane-type Breakup	$25 < We_a < 70$
Fiber-type Breakup	$100 < We_a < 500$

Regarding the liquid jet under a coaxial airflow, two instabilities induce its fragments. The primary is denominated as Kelvin–Helmholtz instability, and the latter is denoted as Rayleigh–Taylor instability [290]. Kelvin–Helmholtz instability arises at the liquid–gas interface in coaxial atomization due to the shear between the gas and liquid phases, being responsible for the formation of ligaments or thin films [276]. Consequently, these elements are stretched in the air stream, reducing their diameter and eventually becoming droplets.

A detailed review dedicated to primary atomization, in particular, to air-assisted atomization, was performed by Dumouchel [251]. The author provided a comprehensive of all the regimes presented above. Additionally, insights regarding the breakup length are supplied. Understanding the physical phenomena of primary atomization plays a relevant role in determining the connection between the design of the nozzle and the consequent droplet size, which requires further investigations [273, 291]. In this context, studies dedicated to the breakup length can provide valuable insight into the atomization quality. As previously mentioned, the instabilities on the liquid jet surface are caused by the interaction with surrounding high-speed gas intensify as they progress downstream, eventually causing the jet to disintegrate [292]. The breakup length represents the continuous portion of the liquid jet or sheet attached to the nozzle. It is defined as the length at which the liquid jet is completely broken into drops and ligaments [244]. A comprehensive understanding of the dominant forces that control the disintegration of the liquid jet and affect the behavior of the primary atomization has practical importance in many applications [280]. Thus, the development of a correlation is useful to knowledge of this subject. Several authors proposed a correlation as a function of dimensionless numbers to better understand the breakup length, as shown in Table 2.9. These correlations are related to the mean breakup length and are mainly obtained through shadowgraph measurements.

Table 2.9: Correlations for the characteristic length of air-assisted/airblast atomization.

Authors	**Correlations**
Eroglu et al. [293]	$\overline{L}/D_l = 0.66 We_a Re_l^{0.6}$
Leroux et al. [294]	$\overline{L}/D_l = \frac{10}{M^{0.3}}$
Zhao et al. [295]	$\overline{L}/D_l = 5.2(\frac{A_l}{A_{air}})^{-0.17} M^{-0.28}$
Kumar and Sahu [296]	$\overline{L}/D_l = \frac{5.45}{M^{0.22}}$

Eroglu et al. [293] developed an experimental study on breakup length measurements in coaxial airblast atomizers under the following conditions: Re_l = 1100–18000 and We_a =

13–267. As displayed in Table 2.9, Eroglu et al. provided an empirical correlation for the breakup length based on the Weber number at the nozzle exit and the Reynolds number of the liquid jet. Their measurements were carried out on membrane-type and fiber-type regimes using a limited number of images and a poor temporal resolution, leading to considerable statistical uncertainty. Moreover, through the Eroglu et al. [293] correlation, it is possible to understand that continuously decreasing liquid core length occurs when the gaseous relative Weber number increases or when the liquid Reynolds number decreases, representing a crucial preliminary investigation [251, 297].

A few years later, Leroux et al. [294] conducted a study using a coaxial liquid jet of five different liquids produced by nine different nozzles, considering operating conditions of Re_l = 45–1000, We_a = 1–1000 and M = 0.17–60. The correlation indicates that the breakup length exhibits a power law relation with the momentum flux ratio (M). According to Lasheras and Hopfinger [244], stated that the momentum flux ratio represents the most pertinent parameter in assessing the breakup of an unbroken liquid core. The momentum flux (M) is represented by the Equation 2.50.

$$M = \frac{\rho_a U_a^2}{\rho_l U_l^2} \quad (2.50)$$

where ρ_a and ρ_l is the air and fuel density, respectively. U_a and U_l are related to the air and fuel velocity. In alignment with [244, 283], if M $\ll$ 1, the liquid jet governs the breakup. On the other hand, if M$\gg$ 1, the breakup length is determined by the gas jet, whereas for considerably high M values, the length is very short. Zhao et al. [295] analyzed the influence of the atomizer exit area ratio on the breakup morphology of water-air jets in the presence of the following conditions Re_l = 783–35000, We_a = 8.8–455 and M = 0.011–620. The results indicated that for low We_g, the jet breakup occurs in the membrane-fiber regime, which is considered an intermediate phase between the bag-type and fiber-type breakup modes of the liquid jet. Moreover, for a constant air flowrate, increasing the liquid flowrate provides a longer liquid core [296]. Recently, Kumar and Sahu [296] stated that the mean jet breakup length was found to follow a power law relation. The authors evaluated the primary atomization experimentally through the measurements of the fluctuations of the jet breakup length and the flapping instability. The results also reveal that the fluctuations of the jet breakup length first decrease and then increase with the momentum flux ratio. The operating of Kumar and Sahu [296] are Re_l = 3000–5000, We_a = 80–300 and M = 1.1–8.3.

In addition to the studies that provided breakup length correlations, Sikka et al. [298] evaluated the primary atomization and stated that an increase in the air to liquid momentum relation leads to a reduction in the liquid core length and a consequent decrease in the spray cone angle. Thus, the breakup length decreases as the AFR increases. As the air velocity increases, the aerodynamic effects promote a decrease in the length and diameter of ligaments. This results in a higher number of ligaments being governed by surface tension, causing them

to assume a spherical shape [299,300]. Moreover, the swirl flow field also affects the breakup length, promoting a reduction in the jet breakup length. This outcome improves the fuel-air mixing and promotes vaporization, thereby stabilizing the combustion of liquid fuel [260].

The process subsequent to the primary atomization is denominated as secondary atomization and occurs downstream caused by the disruption of these ligaments and large droplets [301]. In detail, these fragments move with a relative velocity in relation to the surrounding environment, undergo deformation, and eventually disintegrate into smaller droplets and additional fragments due to the influence of aerodynamic forces [302]. The liquid breakup near the atomizer exit influences the atomization process, followed by the droplet-air interaction further downstream. In particular, the final droplet diameter produced in the atomization is highlighted as relevant in various scientific and engineering applications. Concerning combustion systems, the main purpose of atomization is to provide small droplets to increase the surface area of the fuel. This enhances the evaporation and mixing rates, playing a relevant role in the combustion performance in terms of flame stability, as well as emissions [254, 301].

When a droplet is exposed to an airflow, it moves with a relative velocity, which induces deformation from the initial spherical shape due to the non-uniform distribution of pressure and shear stress. In this case, the surface tension and viscosity oppose the deformation. However, the droplet enters the fragmentation phase if aerodynamic forces become sufficiently strong. The droplet breakup from primary to secondary atomization occurs until the droplet stabilizes at a critical equilibrium size governed by the relative air and liquid interaction [301]. This means that droplets or ligaments with local Weber numbers higher than critical Weber number fragments produce smaller droplets or ligaments. A comprehensive review of the critical Weber number is provided in [303]. Since this process is dependent on the physical properties of the fluids and environmental conditions, dimensionless numbers can be used to identify the different breakup regimes, as previously noted in the primary atomization. Secondary atomization is a phenomenon characterized by the competition between the aerodynamic and surface tension forces; the aerodynamic Weber number is typically employed to distinguish the different breakup regimes. The definition and expression regarding the aerodynamic Weber number (We_a) was already provided in Equation 2.49. This suggests that a higher aerodynamic Weber number implies a potential for fragmentation. Furthermore, the viscosity also influences the deformation process since it dissipates energy supplied by aerodynamic forces [301]. Consequently, the use of the Ohnersorge number is also relevant in this field, as it represents the ratio of droplet viscous forces to the surface. The Ohnorsege number was displayed in Equation 2.45, where characteristic length corresponds to the initial droplet diameter. For very values of the Ohnersorge number, the effect of liquid viscosity becomes minor, and the transition between various regimes can be accurately described using only the aerodynamic Weber number. The secondary breakup regimes are displayed in Table 2.10 governed by the aerodynamic Weber number, considering an Oh < 0.1 for Newtonian fluids. Guildenbecher [301] provided a comprehensive description of each regime. Thus, a summary of the regimes is presented here. The first regime is named vibrational and is characterized by oscillations at the natural frequency of the droplet.

Table 2.10: Criteria for the secondary breakup droplet, at Oh < 0.1, adapted from [301]

Regime	Criteria
Vibrational	$We_a < 11$
Bag Breakup	$11 < We_a < 35$
Multimode	$35 < We_a < 80$
Sheet Thinning	$80 < We_a < 350$
Catastrophic Breakup	$We_a > 350$

The breakup of the primary droplet releases droplets with sizes comparable to those of the parent droplet. The bag breakup corresponds initially to a deformation of the primary droplet to a structure similar to a bag. This phenomenon comprises a thin hollow bag attached to a thicker toroidal rim. Firstly, the bag disintegrates, producing a large amount of small fragments, followed by the rim. In comparison with the bag, the rim releases large fragments. A similar disintegration process is noted in the multimode breakup, the main difference in the appearance of a stamen. In this outcome, the bag first disrupts, followed by the rim and the stamen, releasing several fragments of a variety of sizes. In Sheet Thinning, a thin film is consistently removed from the droplet surface. This thin film rapidly fragments, producing considerably small droplets compared to the parent droplet. Furthermore, the liquid core can remain, possessing dimensions comparable to the original droplet. Catastrophic breakup appears at higher aerodynamic Weber numbers, and in this event, the droplet surface becomes highly corrugated due to the formation of large amplitude waves with long wavelengths. Eventually, it produces a small number of large fragments that, in turn, break into even smaller ones. The identification of this regime is limited in practical applications due to the high velocities. It is essential to highlight that the magnitude of each critical threshold is not consistent throughout the available literature [304]. The visualization of the secondary breakup regimes is shown in Figure 2.35.

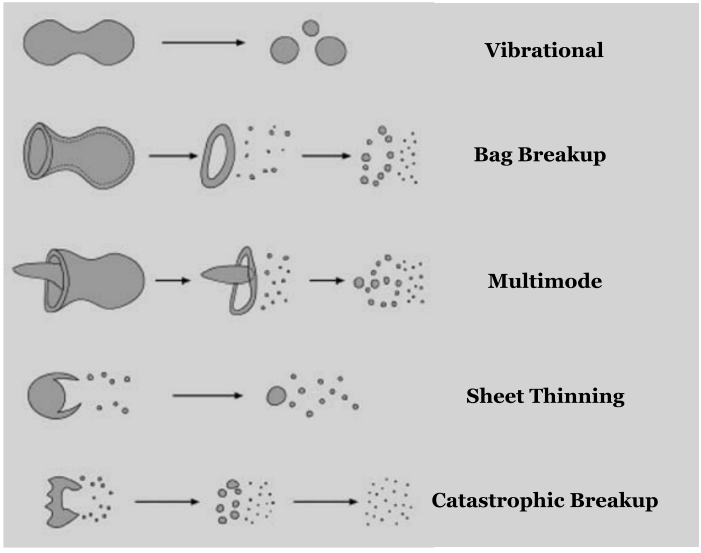

Figure 2.35: Secondary breakup regimes. Adapted from [301].

The regimes described are related to low numbers of Oh < 0.1. For values higher than 0.1, the

effect of viscosity became pronounced, and the critical Weber numbers that distinguish the different regimes may change. More detailed information regarding the regime transitions as a function of both We and Oh numbers can be found in [301, 303].

Lefebvre [156] that stated for a better understanding of the spray dynamics, characteristics such as mean drop size, drop size distribution, cone angle, patternation, and penetration should be profoundly explored. These characteristics focus on the different regions of atomization previously described, and several experimental techniques are used for their evaluation, which play a valuable role in validating and improving the available physical models [305]. Several techniques are applied depending on the objectives of the study. The most frequently employed optical methods are visualization/imaging techniques and PDI/PDA, Phase Doppler interferometer, and anemometry for measurements of global length scale parameters of the spray, such as spray cone angle and breakup length. The primary atomization section already discussed evaluations dedicated to the breakup length. The analysis of these characteristics is mainly performed using visualization techniques since the conditions near the nozzle preclude the transmission of light, which makes the use of laser interferometric techniques difficult [297]. It is a non-intrusive technique, with ease of setup and requiring equipment readily available in typical laboratory settings. However, it may possess certain limitations based on the intensity of atomization, which can be addressed through temporally resolved measurements [306]. Concerning the combustion applications, breakup length and spray cone angle (SCA) assess fuel distribution inside the combustion chamber [307]. The spray cone angle is associated with the dispersion characteristics of the spray. Due to this, ensuring proper spray dispersion is crucial, particularly during the pilot injection phase, to ease the fuel and air mixing that affects the combustion efficiency and pollutant emission [308]. In particular, Dai et al. [309] stated that for gas turbines, the spray cone angle is particularly beneficial, as small spray angles generally promote efficient light-up and lean blowout performance, evident under conditions of low fuel flow and injection pressure. On the other hand, at high fuel injection pressures, usually of high power levels, a wider spray angle is desired to mitigate soot production and exhaust smoke, allowing for greater air entrainment, which enhances atomization as well higher rates of heat and mass transfer [310]. However, careful attention should be paid to the large spray angle as it could lead to losses due to fuel impingement on the cylinder walls [308]. The selection of the proper spray cone angle value in combustion systems is influenced by the geometry of the combustion chamber and the initial air and fuel mixing characteristics [311]. Besides its relevance in combustion application, it contributes substantially to cooling and metallurgy [312]. According to Sikka et al., [298], the spray cone angle is related to the aerodynamic interaction of liquid droplets with the surrounding air, which impacts the downstream droplet size distribution. The factors that influence the spray cone are the nozzle dimensions, injector pressure differential, the liquid fuel properties (density and viscosity) as well, and the density of the environment into which the fuel is sprayed [308]. In the literature, the spray cone angle is defined as the angle formed by the atomizer nozzle until a given distance, displayed in Figure 2.36 [55, 313, 314].

Mao et al. [265] conducted an experimental study on mean drop size (SMD), size distribu-

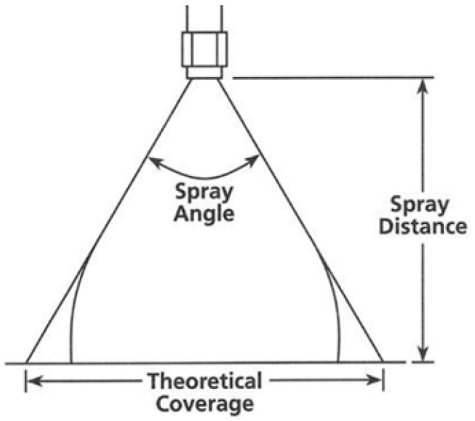

Figure 2.36: Spray cone angle. Adapted from [315].

tion, obscuration, and contour maps of spray patterns using a Malvern instrument at various axial and radial locations in the spray for an air assist swirl atomizer sprays. The conical form of the spray is caused by the radial velocity components in the flow, it is expected that the components of axial to radial velocities also increase. For a pressure-swirl nozzle, Dai et al. [309] stated that an increase in the spray cone angle results in a finer spray since it reduces the thickness of the conical sheet formed at the nozzle exit. In particular, for pressure nozzle applications, the spray cone angle affects the ignition probability [22]. Karnawat and Kushari [316] used a twin-fluid internally mixed swirl atomizer and reported that for constant liquid pressure, increasing the air-fuel ratio leads to a decrease in the spray cone angle. The increase in AFR causes the air in the outer annular region to force the liquid in the inner region, enhancing the axial velocity of the liquid and thereby restricting its radial expansion after leaving the atomizer orifice, promoting a reduction in the spray cone angle. The results provided by the experimental study of Karnawat and Kushari [316] indicate that increasing the liquid pressure leads to a higher spray cone angle at low values of AFR. According to Shafaee et al., [311] in the twin-fluid atomizer, the spray cone angle is influenced by two primary parameters: the liquid flow rate and the gas jet velocity. Consequently, the spray cone angle can be analyzed using the momentum flux ratio M for different values of We_a, as highlighted by Poozesh et al. [313]. The observations indicate that the spray angle initially decreases sharply as the air velocity increases, followed by a gradual asymptotic reduction. Nevertheless, Gad et al. [317] reported that the spray cone angle of an airblast atomizer increases with increasing atomizing AFR and swirler angle. Similar findings were noticed [318]

The impact of the nozzle, air, and fuel flowates on the spray cone angle has already been addressed. As indicated by Asibor et al. [308], the physical properties also have a relevant influence on the spray angle. Davanlou et al. [319] experimentally evaluated the breakup characteristics using a hollow cone hydraulic injector nozzle induced by pressure swirl. The purpose was to understand how the variation of properties, such as surface tension and viscosity, impact the atomization process. The results reveal that reducing the surface tension of the liquids increases the growth rate of the most unstable modes, promoting an earlier sheet breakup. The surface tension also influences the size of the droplet. Lower surface

tension and lower droplet size presented in the same spatial location enhance the centrifugal dispersion due to the lower inertia, causing a wider spray cone angle. Several studies have been performed exploring the influence of viscosity on the spray cone angle [299, 320, 321]. The findings suggest that an increase in viscosity leads to a reduction in the spray cone angle. This evaluation was dedicated especially to alternative fuels, such as vegetable oils and butanol, to compare their atomization characteristics with conventional fuels. In particular, vegetable oils possess a higher viscosity, promoting poor atomization and inefficient mixing with air for combustion purposes [320]. The authors indicated that reducing viscosity decreases the viscous damping of the tangential momentum, leading to a higher tangential velocity and a wider spray cone angle. Basak et al. [320] reported the influence of fuel temperature in its viscosity and consequences on the spray cone angle that the liquid viscosity decreases with the increase in temperature, and the spray cone angle also increases with the increase in liquid temperature. The physical properties of the addition of nanoparticles have already been discussed. The investigation of the spray characteristics is relatively limited. Kannaiyan and Sadr [22] evaluated the effects of aluminum nanoparticle addition in an alternative gas-to-liquid (GTL) jet fuel on the atomization characteristics and reported that the liquid sheet breakup length decreases with an increase in the nanoparticle concentration in the base fuel and presents a spray cone angle value of approximately 85° for all the cases. Alumina nanoparticles were also added to water for concentrations varying between 0.5% and 2 wt.% in an experimental study conducted by Malý et al. [209]. The authors documented an increase in viscosity followed by an increase in alumina concentration that resulted in a small decrease in the cone angle of the spray and in the diameter of the atomized droplets. It was possible to conclude that the liquid viscosity is a key factor in determining the spray characteristics of nanofluids/nanofuels, particularly influencing the primary breakup. Conversely, surface tension plays a dominant role in the secondary breakup process. Analogous conclusions were reported by Asibor et al. [308]. Thus, an increase in the nanoparticle concentration leads to a lower spray cone angle.

In combustion systems, global large-scale characteristics impact the distribution of fuel in the combustion chamber. On the other hand, the combustion characteristics of the fuel are related to droplet diameter and velocity distributions. A significant parameter affecting fuel conversion and evaporation rate is the droplet size distribution, which also governs heat and mass transfer [322]. Small droplets are related to faster evaporation, which can promote complete combustion inside the combustor. Conversely, large droplets require more time to evaporate, influencing the heat release zone and potentially leading to undesired pollutants formation [323]. Similar to the breakup length and spray cone angle, the fuel physical properties also have a relevant role in droplet distribution [307]. A spray is characterized by a two-phase flow involving the interaction of liquid droplets with a continuous gas phase. Its dynamics are controlled by complex stochastic and often nonlinear interactions where simultaneous, rather than sequential, measurements are crucial for understanding processes such as internal nozzle flows, liquid breakup, and the transfer of heat, mass, and momentum between phases [324]. Droplet characteristics such as droplet diameter, velocity, and number density, have been investigated using various advanced laser diagnostic techniques,

such as particle image velocimetry (PIV), phase Doppler interferometry (PDI) (also called phase Doppler anemometry) [325]. An overview dedicated to the techniques employed near and far field on a spray is provided in [324]. One of the most used techniques dedicated to quantitative spray measurements is the phase Doppler interferometry. This method was developed in the 1980s to determine droplet size and velocity simultaneously. It consists of a non-intrusive method pointwise measurement technique for droplet size, velocity, and volume flux at rates up to tens of thousands of measurements per second that rely on light scattered from two intersecting, coherent laser beams [272, 324].

Initial liquid fragmentation releases ligaments and large droplets that undergo secondary atomization. Typically, spherical droplets with different sizes are released depending on liquid properties, the atomizer type, and the breakup process. A non-uniform spray is characterized by a wide range of droplet sizes, whereas a monodisperse spray is considered perfectly uniform. However, investigations have shown that non-uniform drop-size distributions exhibit faster evaporation during the initial phase than uniform sprays with the same mean diameter due to the higher number of small droplets [326]. Since a spray possesses multiple droplet sizes and velocities, managing the complete dataset of droplet sizes and velocities presents significant challenges. Thus, organizing the data in statistical histograms is the most common way [327]. For combustion and mass transfer calculations to simply instead of using the complete drop size distribution, it is more practical to work with an average or mean droplet diameter [260]. In the literature, different expressions for the mean diameter are expressed depending on the application. Consequently, for a spray consisting of a total number of N droplets, the mean diameter is generally defined by the following equation:

$$D_{ab} = \left(\frac{\sum_{i=1}^{N} d_i^a}{\sum_{i=1}^{N} d_i^b} \right)^{\frac{1}{a-b}} \quad (2.51)$$

where d corresponds to the size of each droplet in the sample, and a and b possess values of 0, 1, 2, 3, or 4. Table 2.11 shows the mean diameters and their corresponding field applications. Arithmetic mean diameter assumes that all droplets have an average size equivalent to the diameter D_{10}. At a specific location, an increase in its value implies more droplets of larger sizes [327]. In addition to the arithmetic mean diameter, several other mean diameters provide valuable information, including the surface area mean diameter, D_{20}, the volume mean diameter, D_{30}, and the Sauter Mean Diameter (SMD), D_{32}, as shown in Table 2.11 [328]. In particular, for combustion applications where the phenomena of heat and mass transfer occur in the droplet surface area, the Sauter Mean Diameter is employed. For cooling applications, D_{43}, the average of a volume-weighted probability distribution is commonly used [327]. In terms of numerical investigations, the prediction of the droplet diameter and velocity distribution over the spray is a valuable tool. The identification of the corresponding mean diameter is essential to further compare experimental and numerical investigations and where the droplet distribution functions obtained from droplet statistics have significant implications for the prediction and calibration of spray models in computational fluid

dynamics [329].

Table 2.11: Table of the mean diameters with their application, adapted from [330].

Definition	Mean diameter	Field of application
D_{10}	Arithmetic mean diameter	Evaporation rate
D_{20}	Surface area mean diameter	Monitoring surface applications
D_{21}	Area-length mean diameter	Absorption studies
D_{30}	Volume mean diameter	Hydrology and mass flux applications
D_{31}	Mean evaporative diameter	Evaporation and diffusion applications
D_{32}	Volume/surface mean diameter or Sauter mean diameter	Evaporation, Mass transfer and reaction
D_{43}	Mean diameter over volume or De Broukere diameter	Combustion equilibrium

The overall distributions of droplet size and velocity can be represented mathematically to ease the comparison between the numerical and experimental findings. Previous studies have explored the following distributions for the mathematical representation of the collected data: Rosin-Rammler, Nukiyama-Tanasawa, Gamma, and Log-Normal distributions and are detailed in [260, 331]. The authors typically employ probability mathematical functions to understand their data, as noted by Roudini and Wozniak [332] using a Log-Normal distribution to describe their experimental results of droplet diameters along the spray central line. In addition, Wu et al. [326] stated that the probability density function (PDF) of the droplet diameter distribution can be represented by a Log-Normal distribution. In contrast, the PDF of the droplet axial velocity is close to the Normal distribution [326]. An analysis of the fragment size distribution of ligaments indicates that they can be effectively distributed by the gamma distribution [333].

In terms of evaluation in detail of the droplet diameter and velocity distribution using an air assist swirl atomizer, Mao et al., [265] noticed that for a constant fuel injection pressure, an increase of airflow rates normally leads to a decrease in SMD. However, the reduction in SMD is also detected, increasing the air flowrate until a certain value. Similar observations were also reported by [316, 334]. The authors affirm that this conclusion is attributed to the increase in the kinetic energy of the liquid due to its interaction with the atomizing air, enhancing the atomization process. In addition, the shear force acting on the liquid extracts smaller droplets from the primary liquid flow, leading to more effective atomization. Pereira et al. [335] conducted an experimental study using an air-assisted atomizer and reported that the spray quality significantly enhanced until AFR increased up to around 0.5, beyond which the improvements in spray quality are marginal, regardless of the water mass flow rate. The impact of the AFR and liquid pressure was previously explored by [252, 334], indicating that an increase in the liquid supply pressure leads to a reduction in the Sauter mean diameter. In addition, Roudini and Wozniak [252] highlighted that for an air blast, the liquid

flow rate has a weaker effect on the spray performance. The radial and the axial distribution of the liquid characteristics were analyzed by Urban et al. [312]. The results revealed that peripheral droplets were highly stable, and intense secondary atomization was confined to the spray center. Kumar et al. [299] stated that regardless of the operating condition used in the study, the Sauter mean diameter increases monotonically from the injector centre-line toward the spray boundary. Zhao et al. [318] evaluated the atomization process using a pressure swirl atomizer with external mixing. Figure 2.37 shows the results regarding the radial distribution in terms of SMD for several pressure and air flowrates. Increasing the air flowrate leads to a reduction of SMD in the central with minor variation in the outer region of the spray. Moreover, as the spray develops downstream, the SMD gradually increases, reaching its maximum value at the position of Z/L = 10 and then remains unchanged.

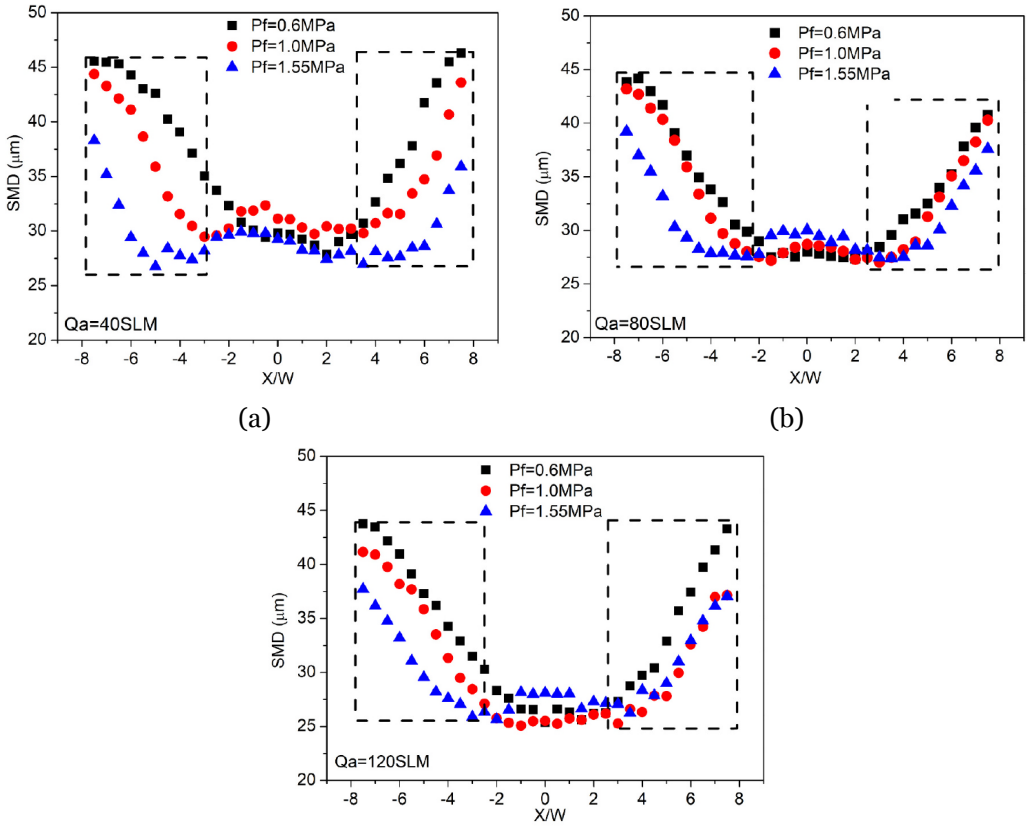

Figure 2.37: Radial SMD distribution of the spray at various fuel supply pressures and air flowrates: a) 40 SLM; b) 80 SLM; c) 120 SLM [318].

Chinnaraj and Sadanandan [336] reported a similar observation, where large droplets are placed at the periphery of the spray, and the smaller droplets are closer to the axis of the spray which is affected by the velocity distribution. Consequently, as the distance from the nozzle increases and droplet velocity reduces, an increase in SMD is spotted. In this context, Kumar et al. [299] stated that the droplet velocities are inversely correlated with the size, being in agreement with the observations that large droplets are in the spray boundary and smaller droplets in the central region. Additionally, investigations in the numerical field have been developed. Chaussonnet et al. [337] compare experimentally and numerically the

air-assisted atomization of a water jet. The results indicate that an optimal ambient pressure (6 bar in this case) exists to obtain the smallest SMD influenced by the concentration of momentum of the gas impacting the liquid jet. Xia et al. [338] provided planar distributions of the axial velocity at different axial distances, as depicted in Figure 2.38. The results reveal that the higher droplet velocities are presented in the central region of the spray and gradually reduce for the periphery. Furthermore, the central region is marked by smaller droplets and a larger liquid volume flux.

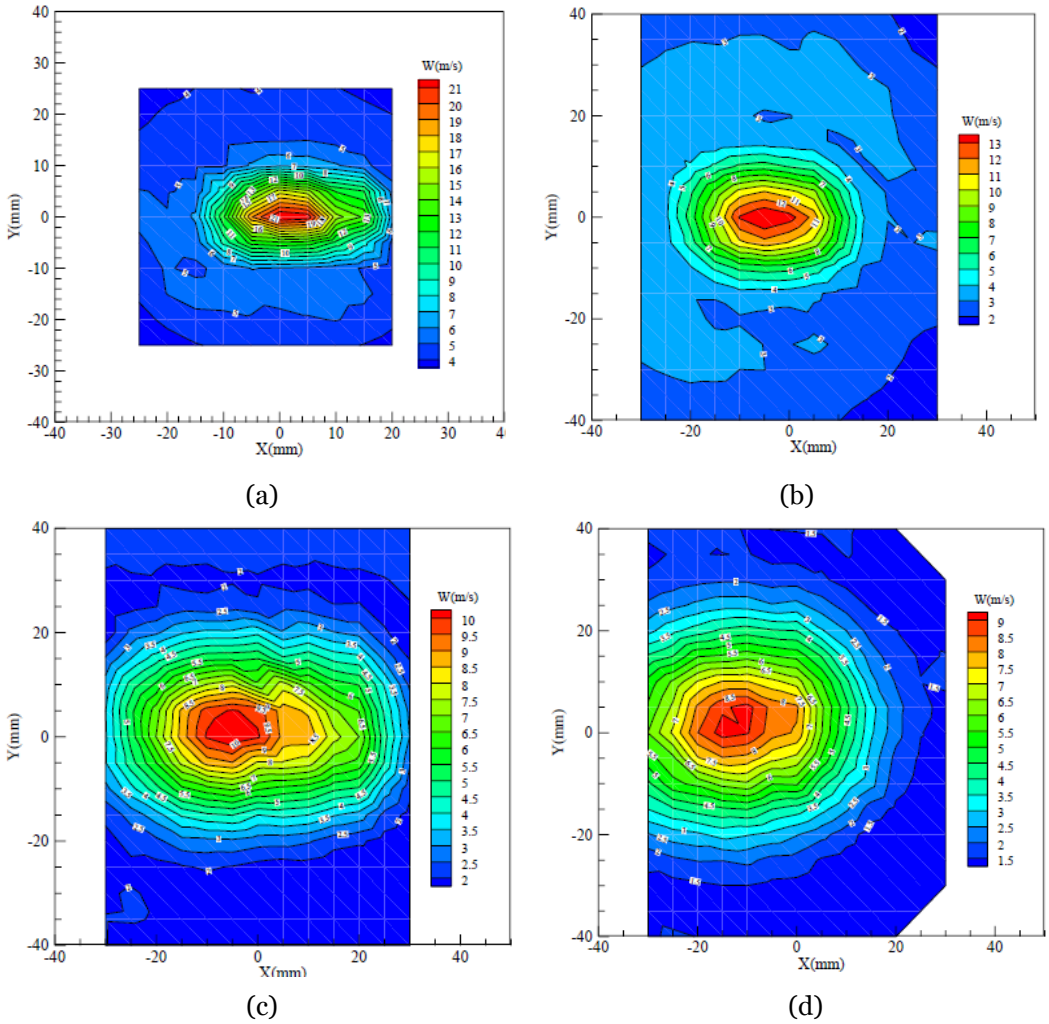

Figure 2.38: Planar distributions of the axial velocity at different axial distances: a) Z = 45 mm; b) Z = 75 mm; c) Z = 120 mm; d) Z = 135 mm [338].

Zhao et al. [318] stated that the droplet axial velocity reduces as the radial distance increases, which can be attributed to the large droplet that possesses a large inertia in the outer region. Moreover, as the distance from the nozzle increases, the droplet velocity diminishes due to the reduction in airflow. Comparable results were observed by Roudini and Wozniak [332] where the maximum is presented at the center with a symmetric planar distribution in different locations. This distribution is also affected by the swirl, as reported by [305, 339]. Sanadi et al. [305] noticed that in the far-field region, SMD increases along the centerline and decreases along the spray boundary with increased swirl strength. However, in the near field, increasing swirl strength had no significant effect on SMD. With respect to the radial

distributions, with the increase in the swirl intensity, the radial resultant velocity of droplets changes its direction and generates radial droplets at the far field.

This section has previously discussed the role of physical properties in atomization characteristics. Kumar et al. [299] explored several fuels under various operating conditions and noted that butanol has the highest SMD, whereas it is the lowest for butyl butyrate. Regarding the Jet A-1, no significant differences in the droplet distribution were noticed compared to butanol since there is a minor variation in the physical properties. On the other hand, Jet A-1 produces larger droplets when compared with the P–N–Ar blend, which produces droplets with a slightly smaller SMD [340]. The addition of nanoparticles was also explored in the studies [22, 341, 342]. According to Sun et al., [342], aluminum nanoparticles possess a relevant role in fragmentation, which promotes the disintegration of large droplets near the spray center, especially under high rotational speeds. In the droplet presented in the spray boundaries, this effect is not pronounced, and the fragmentation is affected by rheological properties. The authors concluded that the low viscosity and high rotational speed can promote the spray quality. A reduction in the droplet size of nanofuel compared to the base fuel was also reported by Kannaiyan et al. [341]. The authors highlighted that this result was only detected at higher injection pressure. Thus, At lower injection pressure, the difference in Sauter mean diameter between the base fuel and the nanofuel is marginal. A possible explanation for this outcome is the longer time available for secondary atomization, which results in the faster disintegration of the liquid sheet for the nanofuels. In addition, the mean axial droplet velocities of nanofuels were found to be higher than those of the base fuel due to the higher momentum of small droplets of nanofuels [341]. Furthermore, the nanofuel spray presents a smaller mean droplet diameter in most of the radial locations due to the shorter sheet breakup length for the nanofuels, which, in turn, provides a longer distance/duration for secondary atomization when compared to that of the base fuel. The authors also highlighted that the spray performances in the near nozzle regions are more affected by the presence of nanoparticles than the downstream regions.

2.4.5 Spray Combustion

The combustion of liquid fuel sprays is widely used in applications such as gas turbines, internal combustion engines, industrial furnaces, and boilers [247]. The characteristics of a fuel spray, such as liquid phase penetration, atomization, air entrainment, and mixture formation, play a crucial role in controlling the combustion process. These phenomena occur on a longer time scale than chemical reactions [343]. The performance of the fuel combustion is highly dependent on the atomization. The first step is fuel atomization, being responsible for fuel droplet size distribution, trajectories, and velocities and thus can control the degree of fuel/air mixing ahead of the chemical energy conversion step [344]. Specifically, liquid fuels are atomized before the combustion process, producing small droplets that allow a higher surface area, reducing the vaporization time and leading to better air-to-fuel mixing, significantly impacting combustion emissions, performance, and flame stability. Inadequate atomization can produce portions of the fuel that may remain unburned, requiring additional

energy to vaporize and ignite larger droplets [274]. As previously stated by Watanawanyoo et al. [263], increasing the air supply leads to a smaller droplet and a larger number of droplets. Thus, increased swirl and turbulence that enhance fuel dispersion, which may cause better oxidation, leading to higher thermal efficiency.

Flame characteristics, such as size and heat release rates, are closely related to the spatial distribution of fuel droplets relative to the flame front. Flames are generally classified into premixed and diffusion flames. The flame classification depends on operating conditions and the fuel employed. If the fuel pre-evaporates before entering the reaction zone, it originates a flame with characteristics similar to premix flames. In other words, the fuel and the oxidizer are mixed before the combustion reaction takes place. In a diffusion flame, the fuel and oxidizer remain initially separated before the combustion process occurs. Laminar diffusion flames are affected by the rate of mass transfer, while laminar premixed flames are limited by chemical kinetics [345]. As previously mentioned, in spray combustion, the fuel is atomized and injected into the combustion chamber, where it vaporizes before reacting with the oxidizer in the gas phase. The vaporization process allows the presence of the liquid droplets in the flame region to form a non-premixed flame structure, where fuel vapor diffuses from the droplets to the flame front.

The ignition of a fuel and air mixture by a heat source depends on the fuel concentration, which should be in accordance with the specific fuel flammability limits. A fuel and air mixture is flammable when the fuel concentration is between the upper and lower flammability limits. Consequently, the lower flammability limit (LFL) is the lowest fuel concentration in air that sustains flame spread. In contrast, the upper flammability limit (UFL) is the maximum fuel concentration beyond which the mixture cannot ignite due to a lack of oxygen [346]. Flammability limit is typically defined as the percent of fuel by volume or fuel/oxidizer mass ratio. It depends on several factors, such as temperature, pressure, type of fuel and oxidizer, ignition source, and apparatus. Flammability limits differ from ignitibility limits, where the latter increases with increasing spark energy until a point where further increases in energy no longer affect the range [347]. Figure 2.39 shows the variation of flammability limits as a function of temperature. The flammability range typically expands with increasing temperature [348, 349]. Figure 2.39 also depicts the autoignition and flash point temperature. The former corresponds to the lowest temperature at which a material will spontaneously burn in air without an external ignition source, whereas the flash point refers to the lowest temperature at which a liquid produces sufficient vapor to form an ignitable mixture with air [348]. The flammable region corresponds to the range in which the mixture ignites when an external ignition source is introduced, whereas, in the autoignition region, flame propagation occurs without the need for an ignition source. A spray is composed of liquid droplets with several diameters dispersed in a gas ambient. Consequently, an examination of its combustion is rather complex. According to Coelho and Costa [350] there are two distinct theories have been developed to explain the underlying mechanisms of spray combustion. The first theory relies on the hypothesis that spray combustion can be interpreted as the combustion of a group of isolated droplets.

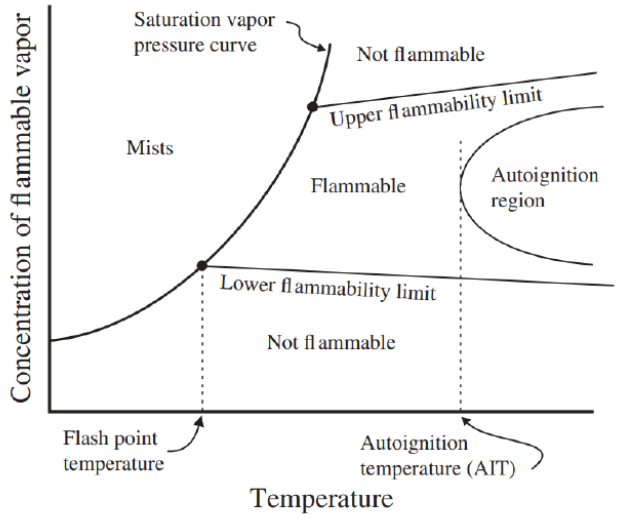

Figure 2.39: Variation of flammability limits as a function of temperature, adapted from [348, 351].

On the other hand, the second theory indicates that not all droplets burn with a flame surrounding them. Hence, a flame surrounds the spray, originating from the fuel vapor formed with droplet evaporation. Thus, spray combustion should not be considered as the combustion of a collection of isolated droplets. On the other hand, the evaporation rate of the droplets present in a spray may be analyzed using the principles of isolated droplet combustion [350]. As noted above, the droplet distributions impact the spray combustion phenomena.

In this context, Williams [352] divided into heterogeneous and homogeneous combustion, as shown in Figure 2.40. In the homogeneous combustion regime, the fuel droplets completely evaporate prior to mixing with the oxidizer and igniting. Regarding the heterogeneous combustion regime, individual droplets burn surrounded by diffusion flames. Figure 2.40 a) shows a heterogeneous combustion regime where moderate to large droplets with a diameter higher than 100 μm tend to partially vaporize as they near the flame zone. Commonly, heterogeneous flames display a yellow color. When the droplet evaporation is completed, the surrounding flame is extinguished, leading to the formation of a homogeneous combustion zone further downstream, Figure 2.40 b) [350, 353]. In the homogeneous combustion regime, droplets with considerably reduced diameter rapidly vaporize due to heat transfer as they approach the flame zone. Due to this, only vapor mixed with air reaches the combustion zone. In this case, no individual diffusion flames surround the droplets, and the resulting blue flame is similar to a premixed flame for small droplets, which fully vaporize before combustion [350, 353]. Since the spray is characterized by a droplet size distributed that possesses large and small droplets. The spray does not always suggest the characteristics of a dilute spray, and consequently, both heterogeneous and homogeneous reaction zones are present. Due to this, the combustion of the spray is not uniform [353]. The influence of droplet size distribution in the context of spray combustion has been previously examined.

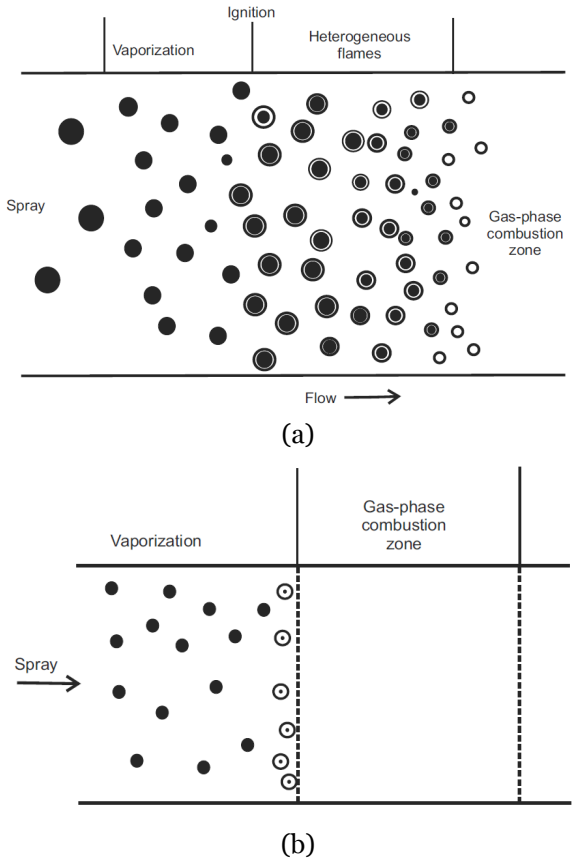

Figure 2.40: Combustion Regime: a) Heterogeneous; b) Homogeneous [353].

Furthermore, devices such as diesel or gas turbines employ fuels that present high boiling points, leading to a heterogenous combustion process, which can result in high emissions of NO_x and particulate. Subsequently, in order to address the flame stability, the influence of the swirl will be explored. In a spray combustion system such as in gas turbine combustors, a swirling air stream is often added to the combustion of the liquid fuel spray. Turns [128] stated that when the flame speed equals the local mean velocity, a flame is locally stabilized, resulting in a stationary flame at the specific location and is resistant to blowoff, flashback, and liftoff. Consequently, swirl stabilization is a method that allows controlling both flame stability and combustion intensity that can be performed through geometric configurations such as vane swirl, mechanical rotation, or by injecting the flow tangentially for aerodynamic control [354]. An illustration of the swirls typically employed is displayed in Figure 2.41.

According to Dunand et al., [271], for a certain degree, swirl promotes a central recirculation zone, enhances mixing efficiency, and allows a hot flow of recirculated combustion products and a reduced velocity region where flame speed and flow velocity can be matched. The analysis of the swirl is mainly performed based on the swirl number, which is given by the ratio of the momentum of the azimuthal velocity component to the momentum of the axial velocity component. If the swirl number is less than 0.4, it is denominated as a low swirl, whereas a high swirl possesses a value higher than 0.6, and the swirl is strong enough to create a toroidal reversal flow along the axis of the flow [353].

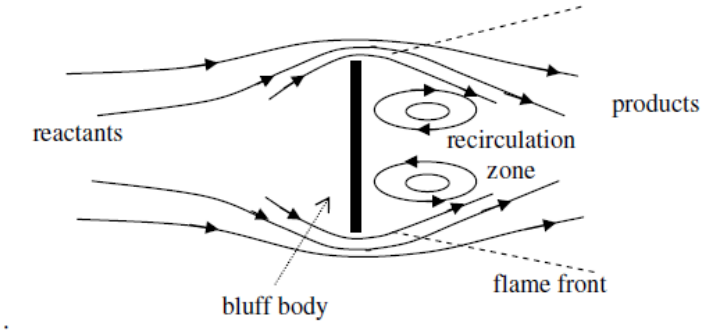

(a)

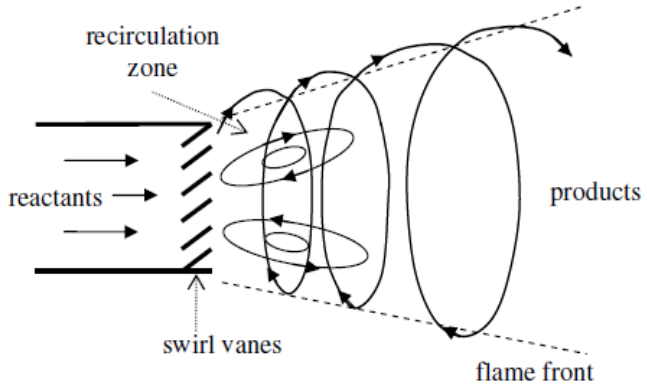

(b)

Figure 2.41: Flame stabilization: a) Bluff body; b) Swirl Vanes [345, 355].

The swirl number can be expressed by:

$$SN = \frac{2}{3}\left[\frac{1-(\frac{D_h}{D_s})^3}{1-(\frac{D_h}{D_s})^2}\right] tan\theta\,, \quad (2.52)$$

where D_h and D_s represent the swirl hub diameter and the swirl diameter, respectively, and θ is the angle of the swirl blade from the centreline [356]. The authors [271] point out that for swirl numbers equal to or higher than 0.6, radial and axial pressure gradients are enough to produce internal recirculation zones (IRZs), as mentioned by Gupta [355]. In these zones, the flame stability is enhanced by entraining droplets and recycling hot combustion products, which leads to a significant decrease in the flame length as well as the stabilization distance from the burner. Regarding emissions, ideal combustion releases CO_2, water (H_2O). However, in a real combustion process, the complexity and rate-dependent nature of flame chemistry release various reaction by-products, releasing carbon monoxide (CO), unburned hydrocarbons (HC), nitrogen oxides (NO_x), sulfur oxides (SO_x), and particulate matter (PM) [357]. A brief description of the factors that affect the emissions has already been provided.

There are several types of liquid fuel burners, including wick, pre-vaporizing, vaporizing, porous, and atomizing burners, that are employed depending on the application [353]. In particular, aero engines require an injection system that ensures efficient atomization, typically using airblast or air-assisted injectors, also using swirling air co-flow that promotes a central recirculation zone for enhanced fuel-air mixing and flame stabilization. [264]. Consequently, the development of laboratory-scale burners is essential for research progress. In this context, it is representative of real combustors with a simpler design and well-defined and optically accessible configurations to enable detailed data acquisition and facilitate modeling. The experimental and numerical findings can contribute to the advancement of novel combustor design and the reduction of emissions, particularly for future green fuel applications [264, 354]. An overview of the laboratory burners operating with atomized liquid fuels in the field of aero engines is provided in Table 2.12. The primary study present was performed by Bulzan [358]. The author conducted an experimental investigation of a reacting spray in a swirl stabilized using an air-assisted atomizer. The purpose is to understand the droplet size and velocity distributions under-reacting environments. The results indicate that gas-phase axial velocities increase in reacting conditions due to thermal expansion. However, the mean droplet velocities remain slower, with smaller droplets exhibiting a minimal velocity difference compared to the gas phase. McDonell and Samuelsen [359] evaluated the methanol spray under reacting and non reacting conditions also dedicated to three modes of injection: No atomization air, non-swirling air, and swirling air. It was possible to observe that swirling air increased spray width, and droplets remained in reacting conditions. Gas-phase velocities are significantly influenced by atomizing air, leading to distinct variations in vapor concentrations along the centerline. The authors [247, 360, 361] employed the same burner possessing an air and fuel supply system, a heating unit for the main air, a plenum, an atomizer, a swirler, a combustion chamber, and an exhaust system. Moreover, it presents a relevant investigation into the comparison of alternative and conventional fuels. The results reveal that the smaller droplets are in the central region, whereas the large droplets are present in the spray boundaries outside of the flame reaction zone, where the alternative and conventional fuel possess relatively similar spray flame [247]. Chong and Hochgreb [361] also evaluated the spray characteristics of rapeseed oil methyl ester and reported that it possesses similar spray combustion as the diesel whereas containing higher droplet concentration and volume flux, indicating a longer evaporation time scales. In addition, the alternative fuel, palm biodiesel, releases lower NO_x emissions and higher CO emissions per unit of energy than Jet-A1 [360]. Chong et al. [362] also explored liquid fuel combustion using a burner with the same compounds as the previous one using air heated air and reported higher NO emission, while CO correspondingly decreased. Belal et al. [363] and El-Zoheiry et al. [364] employed a partially premixed pre-vaporized combustion system. Several differences from the previous burners are noticed from the alignment within the plenum, design, and placement of the atomizer as displayed in Table 2.12.

Table 2.12: Experimental operating conditions of laboratory burners presented in the literature.

Authors	**Atomizer**	**Fuels**	**Power (kW)**	ϕ	**Swirl**	$\mathbf{T}_{heating(C)}$
Bulzan [358]	Simplex air-assisted	Heptane	N/A	N/A	45^{o} vanes	No
McDonell and Samuelsen [359]	Air-assisted	Methanol	N/A	N/A	Tangential air	No
Chong and Hochgreb [247]	Air blast	Jet A-1 and Rapeseed Oil Methyl Ester	6	0.47	SN=0.78	350
Chong and Hochgreb [360]	Air blast	Jet A-1 and Palm Methyl Ester	6	0.47	SN=0.78	350
Chong and Hochgreb [361]	Air blast	Diesel, Rapeseed Oil Methyl Ester and Rapeseed Oil Methyl Ester/Diesel Mixture	6	0.47	SN=0.78	350
Chong et al. [362]	Air blast	Diesel, Sunflower Methyl Ester and Sunflower Methyl Ester/Diesel Mixture	9.3	0.65	SN=0.84	30, 150 and 250
El-Zoheiry et al. [363]	Pressure	Jet A-1 and Jet A-1/Jojoba Methyl Ester Mixture	15.5	0.87-0.95	SN=0.78	170
Belal et al. [364]	Pressure	Jet A-1	14.6	0.75	SN=0.55	250
Kumar and Karmakar [365]	Air blast	Jet A-1 and Butyl Butyrate (BB)/Jet A-1 Mixture	5.36	0.5	SN=0.78	0, 100 and 200

More recently, Kumar and Karmakar [365] reported that Jet A-1 emits higher NO_x emissions compared to butyl butyrate and their mixtures and increases as the temperature of the swirling air increases. This observation of the NO_x emissions with respect to the swirling air was noticed for all the fuels tested. Moreover, pure butyl butyrate and their mixtures with Jet A-1 exhibit considerably lower CO emissions than Jet A-1, regardless of preheating. The development of these systems also involves the acquisition of valuable insights related to the introduction of alternative and sustainable fuels essential in the transportation sector. In this respect, various studies are being conducted to address the potential use of nanoparticles in liquid fuels. In light of this, adding nanoparticles to a liquid fuel influences the fuel physical properties, which potentially will affect the atomization, combustion, and emissions characteristics in a combustion chamber [27]. However, studies concerning the use of nanofluids in laboratory combustion chambers are scarce and require further investigation. Pourhoseini and Ghodrat [366] investigated the addition of Al_2O_3 nanoparticles to 20 % blend of palm oil biodiesel with diesel fuel in terms of the flame characteristics, radiation, temperature, and pollutant emissions in an oil burner. The results indicate that higher nanoparticle concentrations result in a significant enhancement in radiation heat flux. Moreover, nanofuels produce higher CO emissions. The addition of particles to a liquid fuel was also explored by Gupta et al. [167]. The authors experimentally investigated the combustion characteristics of boron/Jet A-1 slurry fuel spray in a swirl-stabilized combustor. The experiments were carried out using a slurry suspension prepared with 10 wt.% boron and surfactant. The results reveal that higher loading of boron is always desirable for positive thermal contribution. To summarize, in spray combustion, droplets with various diameters and velocities are presented in a combustion chamber. Consequently, the evaporation of each droplet is highly dependent on its diameter, relative velocity, and the burner operating condition. The fuel vapor is subsequently mixed with an oxidizer, and if the temperature exceeds the temperature of autoignition, the mixture ignites, and a flame is spotted. The spray penetration is related to the droplet velocity and their evaporation process. Spray combustion is a complex phenomenon that involves dynamics at multiple spatiotemporal scales, and due to their complexity, a statistical approach is commonly employed.

Chapter 3

Fuels preparation and characterization

This section provides a comprehensive overview of the liquid fuels used in the present work. Firstly, aviation fuel and biofuel are compared in terms of physical properties and outcomes emerging from their application. Parallel to this, a novel approach to enhancing the combustion characteristics of liquid fuels will be scrutinized. This approach involves the addition of metallic particles to a liquid fuel. A comprehensive examination of its preparation, fuel stability, and influence on the physical properties to understand its potential application in real engines will be explored. Additionally, different particle sizes and concentrations are also investigated.

3.1 Jet Fuel and Pure Biofuel Characterization

Two pure liquid fuels were evaluated in the present work. A conventional jet fuel employed in aviation gas turbines, denoted as Jet A-1, was investigated and used for comparison purposes. Jet fuel for aircraft engines differs from traditional fuel combustion engines, mainly in their physicochemical properties, due to restrictions imposed by the aeronautical industry to guarantee reliability, safety, security, and other aspects. Moreover, it requires a high-energy content, good flow characteristics, and thermal stability [49]. In contrast with Jet A, Jet A-1 possesses a lower maximum freezing point, which is appropriate for long international flights, especially on polar routes during the winter. Due to this, Jet A is mainly used in the United States, while Jet A-1 is employed worldwide. This parameter ensures that jet fuel moves properly from the fuel reservoirs in the wings to the engine through the aircraft fuel system without wax crystals forming [45]. Aviation fuel is a primary energy carrier and is also relevant for heat exchange mechanisms and weight equilibrium, which is particularly crucial given the extreme conditions experienced involving ground and high altitude conditions [58]. This fuel is a mixture of many different hydrocarbons mainly composed of n-paraffins, branched iso-alkanes (iso-paraffins), cyclic alkanes (naphthenes), and aromatics with an average chemical composition of $C_{11}H_{21}$ [39,367,368]. Jet fuel is a multicomponent fuel, with each component displaying distinct physical and chemical properties depending on the carbon length and degree of branching [368]. Consequently, jet fuel properties are determined by the characteristics of all fuel constituents [368]. Aviation fuel may contain less than 3000 ppm sulfur levels and additives, such as antioxidants, to improve fuel quality for proper functioning during flights [58]. For a better understanding, Figure 3.1 shows the chemical composition of Jet A-1.

Conventional jet fuels are provided from kerosene produced from crude oil, a finite source

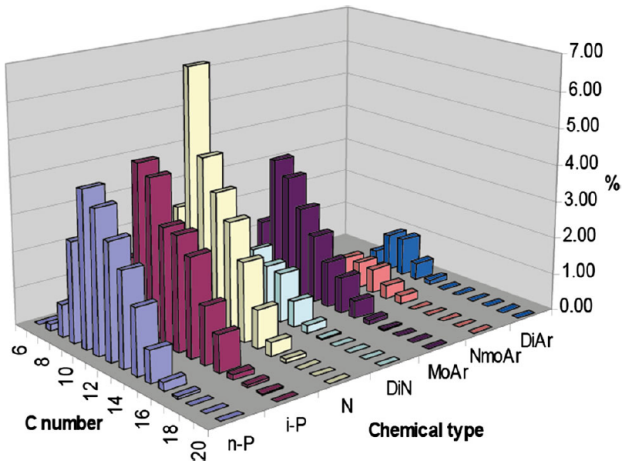

Figure 3.1: Jet A-1 chemical composition, adapted from [61].

with a broad distribution of paraffins. The content and variety of paraffin are impacted by the crude and the processing/refining techniques to obtain jet fuel [369]. Fossil fuels are the main energy source globally and have limited resources. Besides the considerations regarding energy efficiency and local environmental concerns such as noise and air quality, the aviation industry is also confronted with a profound and persistent long-term impact of its emissions on the global climate [370]. Thus, the aviation issues regarding the depletion of fossil fuels, allied with the accelerated growth of this sector and consequent emissions, have forced more ecological and sustainable solutions. A potential pathway to solving these issues is the employment of biofuels due to their sustainability and the possibility of their implementation in aero-engines. Consequently, the present work explores a HEFA biofuel, more concretely, a hydrotreated vegetable oil (HVO), an aviation drop-in fuel. This alternative fuel was acquired from Neste Oil Corporation and is commonly referred to as renewable diesel, with the commercial name NExBTL (next-generation bio-to-liquid), which has disrupted interest in road, aviation, and marine transportation. This biofuel is a mixture of straight chain and branched alkanes, with typical carbon numbers ranging from C_{15} to C_{18}, and features negligible amounts of sulfur, oxygen, and aromatics, with a chemical composition C_nH_{2n+2} [371]. According to Gong et al. [372], HVO is composed of 18.1% Pentadecane $C_{15}H_{32}$, 31.1% Hexadecane C_16H_{34}, 25.5% Heptadecane $C_{17}H_{36}$ and 25.3% Octadecane $C18H_{38}$. Moreover, it has a low freezing point, preventing wax formation in the fuel supply system [373]. HVO is a biofuel from 2^{nd} generation mainly obtained from vegetable oils or animal fat that is subsequently subjected to a pretreatment process to extract impurities and contaminants. The feedstock selection is a process that should guarantee sustainability [374]. The feedstock undergoes a series of processes, such as hydrotreatment and isomerisation, as displayed in Figure 3.2. The feedstock is decomposed during the process, and oxygen and sulfur molecules are eliminated through the use of hydrogen under high temperatures and pressures [375].

Figure 3.2: HVO production process.

Additionally, the improvement of cold properties and fuel quality is achieved by the isomerization process [371, 375]. In terms of operating logistics, NExBTL exhibits comparable behavior to jet fuel, as it demonstrates good stability during storage and high performance under cold weather [376]. Additionally, it presents stable storage, resistance to microbial growth and does not form engine deposits. Several investigations have reported positive outcomes from utilizing HVO biofuel in engines [373, 377–379]. Chan et al. [377] carried out a comparison investigation on the CF700-2D-2 turbofan engine using jet A-1 and biofuels. The results reveal that a blend of HVO and Jet A-1 can reduce the NO_x emissions. Regarding the emissions of soot and sulfur oxide emissions, observed a reduction in comparison with JP-8 due to the absence of aromatics and sulfur in the biofuel composition [378]. The work was developed on a T63 turbine engine operated on camelina and tallow with different blends to evaluate the engine performance and emissions. Additionally, a reduction in the number, density, and size of particulate matter was noticed in a TRS-18 engine when JP-8 and HVO blended instead of Jet A-1, regardless of the altitude and engine speed [379].

Conventional and alternative jet fuels present similar compositions since both comprise hydrocarbons. Nonetheless, substantial variations in the amount and type of hydrocarbons are evidenced. Thus, the chemical composition of each fuel influences both the behavior and combustion characteristics, being an essential study to understand single droplet and spray combustion [58]. Since liquid fuels are responsible for providing energy for aero-engines it is important to know the energy density to predict the fuel volume required on each flight to guarantee safety and operability. Allied with this, alternative aviation fuel should present high H/C and low O/C atomic ratios, an indicator of the fuel energy density [38]. As previously discussed by Afonso et al. [13], fuels that exhibit higher H/C ratios possess higher specific energy when bond strain is absent. Properties related to fuel evaporation, flammability (e.g., flash point, freeze point distillate temperature), viscosity, and surface tension that will affect the spray dynamics are valuable for developing studies in this field requiring a more attentive analysis [13]. Thus, Table 3.1 shows the properties and chemical composition of Jet A-1 and HVO. The ASTM D1655 limits are also presented in Table 3.1.

Most properties displayed in Table 3.1 are already presented in the literature. As the current study relies on the behavior of single droplets and sprays, measurements focused on density, viscosity, and surface tension were performed. A brief description of the equipment employed for these measurements is provided. The density was measured at room temperature (20 ± 2 °C) and atmospheric pressure using a portable density/specific gravity meter DA-130N, produced by Kyoto Electronics, as shown in Figure 3.3. The surface tension was determined at room temperature and atmospheric pressure with an optical tensiometer Theta, from Attention, shown in Figure 3.3. The pendant drop method was adopted to obtain the surface tension. The drop shape is optically analyzed in this method, and the surface tension is acquired based on integrating the Young-Laplace equation [388]. To attain good accuracy of the results, a total of 20 measurements were performed for each fuel. The viscosity of the fuel was determined at room temperature and atmospheric pressure using a viscosimeter DV3T, manufactured by AMETEK Brookfield. This device is exhibited in Figure 3.3.

Table 3.1: Jet A-1 and HVO properties adapted from [45, 380–387].

	Specification	ASTM D1655	Jet A-1	HVO
Distillation Temperature (°C)	Density at 15 °C (Kg m^{-3})	775–840		
	Density at 20 °C (Kg m^{-3})		798	780.6
	Viscosity at −20 °C (mm^2 s^{-1})	Max. 8.0		
	Viscosity at 25 °C (mm^2 s^{-1})		1.40	4.33
	Surface Tension at 20 °C (N m^{-1})		0.0247	0.0265
	Flash Point (°C)	Min. 38	38	77
	Freezing Point (°C)	Max. −47	-51	−54.4
	Aromatics (vol.%)	Max. 25	13.8	0
	Sulfur (wt.%)	Max. 0.3	0.054	0
	10% Recovered	Max. 205	170	262
	50% Recovered		189	279
	90% Recovered		219	291
	Final Boiling Point	Max. 300	237	308
	Low Heating Value (MJ kg^{-1})	Min. 42.8	43	43.9
	Smoke Point (mm)	Min. 25.0	24.2	-
	Cetane Number		45	74
	H/C Ratio		1.91	2.18
	A/F_{stio}		14.5	15.2
	Refractive Index		1.44	1.43

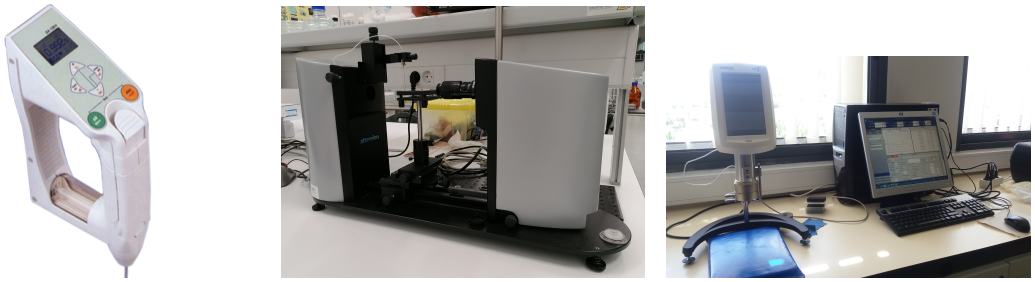

(a) (b) (c)

Figure 3.3: Properties measurements equipment: a) Portable density/specific gravity meter DA-130N, from Kyoto Electronics Manufacturing; b) Optical tensiometer Theta; c) Viscosimeter DV3T, from AMETEK Brookfield.

The measurements indicate negligible density and surface tension disparity when comparing Jet A-1 with HVO. The predominant distinction pertains to viscosity, which is higher for biofuel. These findings are essential to understand further how adding metallic particles will influence the fuel properties, considering different particle sizes and concentrations.

The distillation profile is pertinent to fuel volatility, a critical parameter since the fuel must undergo vaporization before combustion [45]. Considering that both jet fuel and biofuel are identified as multicomponent fuels, each component exhibits a distinct distillation temperature. Figure 3.4 shows the distillation curve for the biofuel (HVO) and the conventional jet fuel (Jet A-1). The HVO presents a higher boiling point when compared to the Jet A-1. Additionally, it also displays a narrow boiling point range. This observation can be attributed

to the fact that HVO biofuel consists mainly of saturated hydrocarbons having 15 to 18 carbon atoms in their molecules [389]. On the other hand, aviation fuel comprises C_8 to C_{16} hydrocarbon molecules, reflecting a broad distillation curve.

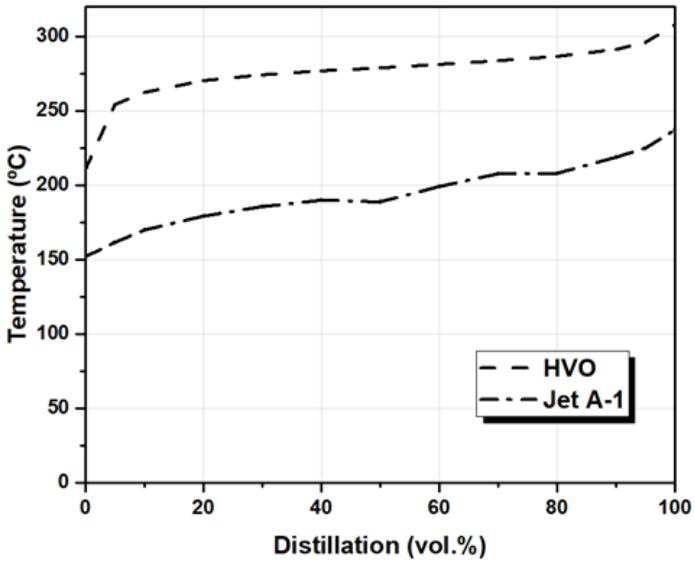

Figure 3.4: Distillation curve for Jet A-1 and HVO.

3.2 HVO and Aluminum Particles

The present section is dedicated to adding metallic particles to biofuel. Initially, an analysis of the particle selection for this study is presented. In light of this, the particle type, shape, size, and concentration are discussed. Subsequently, a detailed investigation of the fuel preparation is carried out. The specific procedure to guarantee a stable nanofuel for different particle sizes and concentrations is explored using physical and chemical processes. The evaluation of the nanofuel stability is performed through a visual inspection. Finally, the fuels composed of HVO and metallic particles are characterized in terms of density, surface tension, and viscosity.

There has been recent interest in adding energetic particles to fuels. The emphasis on metal additives in solid propellants has demonstrated advantages in increasing combustion enthalpies and quality. This observation is related to the enhancement of the specific impulse of propellants due to the addition of reactive metal particles, such as aluminum (Al), magnesium (Mg), boron (B), and zirconium (Zr), among others [23, 390]. Incorporating energetic particles allows a high volumetric enthalpy of combustion, extending the flight range and possibly increasing the payload, bringing benefits for propulsion systems constrained by volume limitations [391]. In the last decades, studies have primarily been based on micron-sized particles. Particles in micron size tend to display ignition delays, slow burn rates, and incomplete combustion of large metal particles [23]. However, with recent advancements in nanotechnology, nanoscale particles have been explored, addressing issues related to micron-size particles. The use of micron-size particles in several applications showed problems re-

garding clogging, rapid settlement, poor stability, and aggregation [23]. Minimization of these effects is noticed with the addition of nanoparticles. Thus, the present work mainly focuses on adding aluminum nanoparticles to HVO. Aluminum is a suitable additive to hydrocarbons due to its abundance, high density, high heat release during oxidation, relatively low cost, safe to use, and abundance in Earth [392]. The bulk properties of aluminum are displayed in Table 3.2.

Table 3.2: Bulk properties of aluminum, adapted from [393].

Parameter	**Value**
Density (Kg m^{-3})	2700
Melting point (°C)	660
Boiling point (°C)	2519
Heat of combustion (MJ/kg)	31.1

Spherical aluminum particles, 99.995% pure, metal basis, with an average diameter of 40 nm, 70 nm, and 5 μm were purchased from Nanografi. Aluminum micron-size particles were also considered for comparison purposes. It is essential to distinguish low from high particle concentrations. In the present work, a low particle concentration corresponds to < 1.0 wt.%, whereas particle concentration is related to > 1.0 wt.%. Scanning electron microscopy (SEM) was employed to determine the structural morphology of the aluminum particles, as shown in Figure 3.5. The visualization indicates that the particles possess a smooth surface and spherical shapes.

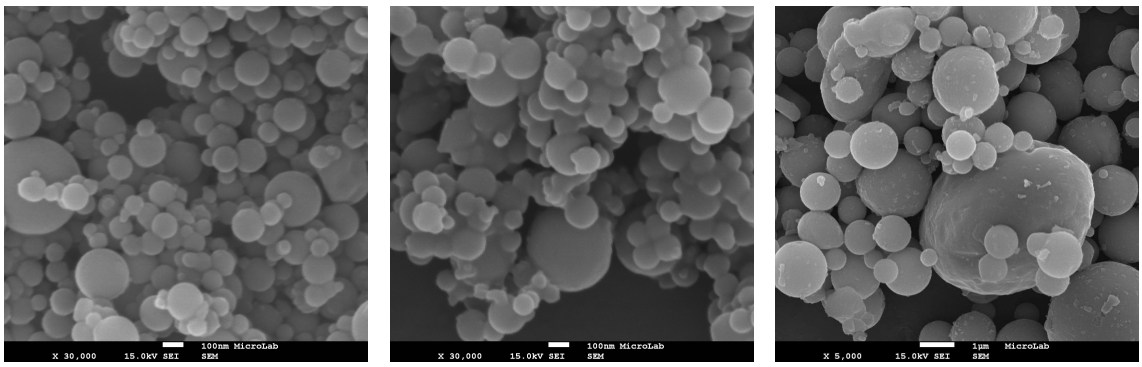

(a) (b) (c)

Figure 3.5: SEM images of aluminum particles: a) 40 nm; b) 70 nm; c) 5 μm.

3.2.1 Fuel Preparation and Stability Study

Before conducting nanofuels experiments, a precise and appropriate procedure should be executed to ensure fuel stability. The purpose is to obtain homogeneous, long-term stable suspensions with a low level of particle agglomeration [206], guaranteeing experimental accuracy and a proper evaluation of the physical properties. In this respect, Wang et al. [394] reported that Brownian motion and nanoparticle aggregation are fundamental mechanisms in nanofluids, contrasting with micron-sized suspensions. Regardless of the particle size employed, the formation and growth of agglomeration and clogging can alter the physical

properties of the fluid [208]. As discussed in chapter 2, methods such as sonication and surfactant addition are generally employed in nanofuel preparation to improve stability. Table 3.3 highlights the different approaches considered in the present study for nanofuel preparation. It is important to note that the addition of aluminum particles in HVO was prepared using a two-step method. Firstly, to obtain the desired mass fraction of the liquid fuel and nanoparticles, a weighing scale is employed. The nanofuel was stored in a 20 mL glass container to avoid interaction with polymers. As displayed in Table 3.3, the first approach merely focuses on using a magnetic stirrer to mix the nanoparticles into the HVO for 10, 30, and 45 minutes. Regardless of the particle size and concentration, it was observed that nanofuel does not remain stable for more than an hour. Consequently, the sonication process was added to enhance the stability.

Table 3.3: Initial procedures for nanofuel preparation.

	Procedure
1^{st} Approach	Magnetic Stirrer
2^{nd} Approach	Magnetic Stirrer → Sonicator
3^{rd} Approach	Magnetic Stirrer → Sonicator using an Ice Bath
4^{th} Approach	Magnetic Stirrer → Sonicator using an Ice Bath → Surfactant

To suspend the nanoparticles in the HVO and disintegrate any agglomerates, a probe sonicator UP200Ht, manufactured by Hielscher, was used. Additionally, continuous sonication was applied, given its effectiveness over the discontinuous [181]. The procedure employed in preparing nanofuels using the 2^{nd} approach is displayed in Figure 3.6. To obtain the desired particle concentration, aluminum nanoparticles were first added to HVO on a weighing scale. Subsequently, the HVO and the nanoparticles were vigorously stirred for 20 min using a magnetic stirrer, followed by the sonication process.

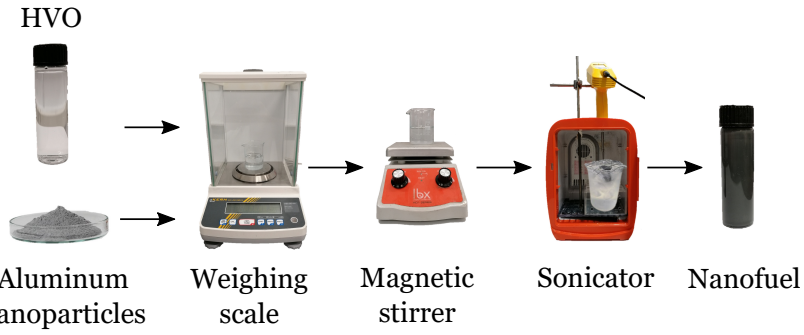

Figure 3.6: Procedure employed in preparing nanofuels using the 2^{nd} approach.

The initial analysis used a particle size of 40 nm and a particle concentration of 0.5 wt.%. A sonication power of 8, 18, 32, and 52 W and a sonication time of 20, 30, and 40 minutes were considered. For the lowest sonication power and time, the nanofuel remains stable. However, the findings did not fulfill the essential criteria for subsequent studies where the nanofuel should remain for at least four hours. Due to this, the nanofuel was placed in an ice bath (3^{rd} approach) during the sonication process to maintain its temperature. Adding

an ice bath provided satisfactory results in cases where the nanofuel is maintained for over a day. Before presenting and discussing the results regarding the 3^{rd} approach, a detailed analysis of the power and time of sonication is outlined. This investigation considered a particle size of 40 nm, 70 nm, and 5 μm and a particle concentration of 0.5, 1.0, and 2.0 wt.%. The results indicate that for a particle concentration of 2.0 wt.%, regardless of the power and time applied in the sonication process, the nanofuel cannot remain stable where the particle sedimentation is identified at the tube bottom. Thus, an addition of de surfactant to the nanofuel preparation procedure will be discussed later to enhance its stability. The stability analysis was carried out in the present study by a visual inspection. Therefore, the nanofuel was analyzed as time evolved, and a set of images was acquired for further comparison. Figure 3.7 shows the temporal evolution of particle sedimentation for a better understanding of the stability study. Typically, the nanofuel is stable after the sonication process without showing any evident sediment. However, particle sedimentation appears at the bottom of the tube as time progresses, highlighted by the dashed red line. On the top, transparency is evident, indicating the deposition of particles on the bottom. This effect becomes more pronounced as time evolves, clearly indicating that the nanofuel is unstable.

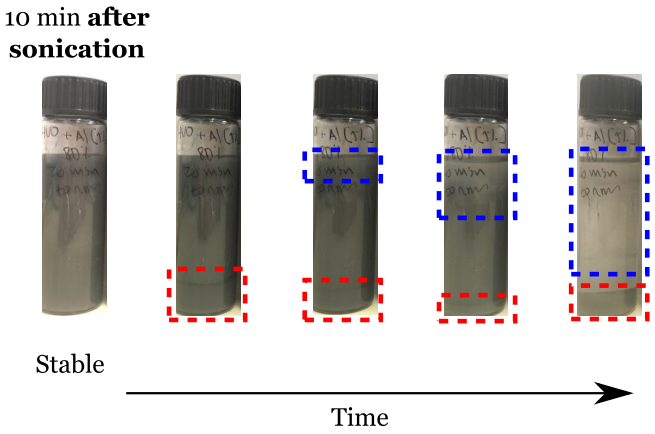

Figure 3.7: Temporal evolution of particle sedimentation.

A particle concentration of 0.5 and 1.0 wt.% are explored for the three particle sizes to define the optimal parameters in the sonication process. A sonication power of 8, 18, 32, and 52 W and a sonication time of 20, 30, and 40 minutes were considered. The results show that increased power sonication does not enhance fuel stability. In other words, for a power sonication of 32 and 52 W, the nanofuel stability reduces. A similar observation was achieved for a sonication time of 40 min. A possible explanation for this observation is the increment of the fuel temperature during the sonication process. According to Buonomo et al. [182], increasing the power and time of the sonication increases the nanofuel temperature and decreases the stability. Based on that, the temporal evolution of temperature during and after sonication, using and not using an ice bath. The measurements are performed using a thermocouple placed in the sonicator probe. Figure 3.8 shows the temporal evolution of the temperature HVO + 0.5% Al. The analysis was performed for a sonication process for 30 min, considering a power of 18 W. Adding an ice bath guarantees that the nanofuel remains at a low and stable temperature during the sonication process. On the other hand, when no

ice bath is employed in the sonication, the nanofuel increases significantly in temperature. Therefore, using an ice bath during sonication was incorporated into the nanofuel preparation process to enhance stability and prevent overheating.

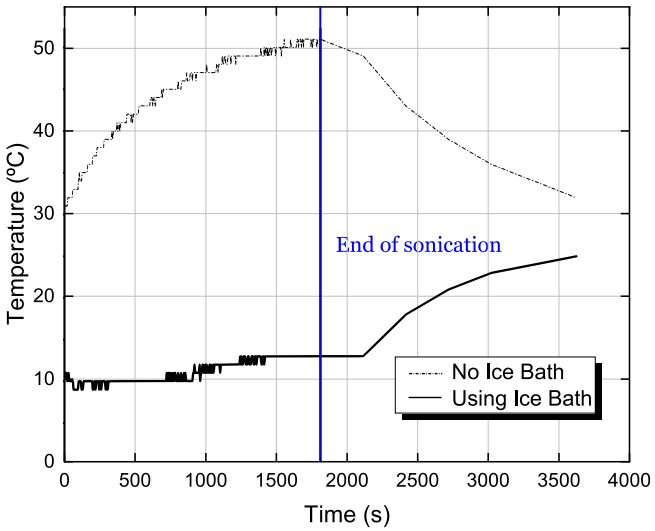

Figure 3.8: Temperature analysis of the HVO + 0.5% Al during and after sonication, using and not using an ice bath.

Following this, the influence of the sonication power on the nanofuel temperature is addressed. For this examination, 18 W and 32 W sonication power were evaluated. Figure 3.9 shows the influence of the sonication power on the temperature of HVO + 1% Al during and after the sonication process for 30 minutes. The results indicate that increasing the sonication power increases nanofuel temperature during the sonication process. Therefore, it is verified that increasing the sonication power increases the nanofuel temperature, resulting in lower stability.

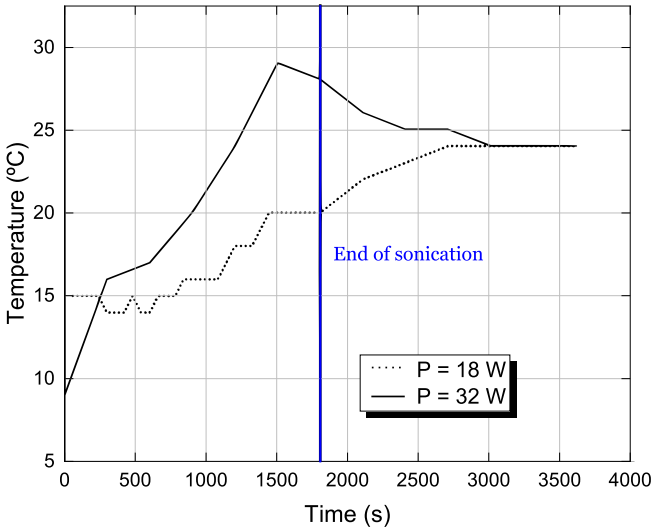

Figure 3.9: Temperature analysis of the HVO + 1% Al for two sonication power.

Considering the earlier observations, the recommended preparation method should include the sonication process with an ice bath at a power setting of 18 W for 30 minutes, especially for particle concentrations lower than 2 wt.%. After defining the optimal parameters for the

nanofuel preparation, a more detailed stability study is performed through visual inspection. In this context, a qualitative evaluation of the nanofuel stability is carried out, categorizing sedimentation into various levels, as illustrated in Figure 3.10.

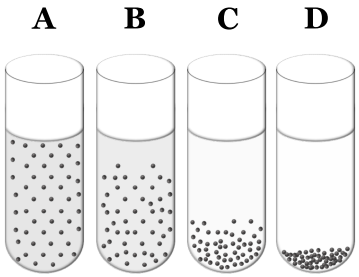

Figure 3.10: Qualitative stability study criteria.

Based on the visual inspection, four sample levels were considered. Level A corresponds to a stable nanofuel with no obvious sedimentation. Levels B and C correspond to two intermediate cases when the nanofuel is partially and highly sedimented, respectively, and level D indicates a fully unstable nanofuel when all the nanoparticles remain at the bottom of the test tube. It is important to note that nanofuels must maintain stability for at least 4-5 hours to guarantee stability during the experiments. Table 3.4 shows the results concerning the stability study for the nanofuels with particle concentrations up to 1.0 wt.% for three particle sizes.

Table 3.4: Visual inspection results considering a particle concentrations up to 1.0 wt.%.

	4-5 hours	1 day	2 days	1 week	
0.2 wt.%	A	A	A	B	40 nm
0.5 wt.%	A	A	B	C	40 nm
	A	B	C	C	70 nm
	A	B	C	D	5 μm
1.0 wt.%	A	B	C	C	40 nm
	A	B	C	C	70 nm
	B	C	D	D	5 μm

The findings indicate that increasing the particle size and concentration reduces the nanofuel stability. In this context, it is observed that increasing the particle size from the nano to micron scale reduces stability. Yetter et al. [395] reported that micron-size particles, after the dispersion, settle very quickly when compared with nano-size particles. Thus, nanoparticles present small mass, diameter, and specific surface area, allowing the suspension for a considerable amount of time under certain conditions.

As previously mentioned, for particle concentrations above 1.0 wt.%, the current procedure does not guarantee stability. The non-polar and hydrophobic properties of HVO components contribute to challenging stability, particularly for high particle concentrations. Consequently, a chemical process was added to enhance the stability, as highlighted in Table 3.3. In the present study, pure oleic acid (OA), pharma grade, procured from PanReac AppliChem ITW Reagents, was chosen to stabilize aluminum nanoparticles in HVO. The oleic

acid volatility is close to the volatility of the base fuel, i.e., the boiling point of OA (360 °C) is close to the final boiling point of HVO (308 °C), a relevant characteristic for the following studies concerning the single droplet combustion. In addition, oleic acid has antifoaming properties and a hydrophilic-lipophilic balance (HLB) number around 1. The lower the HLB number, the more oil-soluble the surfactants [173, 396, 397]. Besides the potential advantages of adding a surfactant to nanofuel in terms of stability, oleic acid can influence the combustion behavior. Due to this, it is essential to evaluate mixtures of HVO and OA for comparison purposes, where the understanding of effects regarding the addition of aluminum nanoparticles on combustion behavior would be more clear and precise. In contrast to nanofuels, the procedure for preparing the mixture of HVO and OA is straightforward. OA was first added to HVO on a weighing scale to obtain the desired mass fraction of each liquid. Then, the fuel mixture was vigorously mixed for 10 min using a magnetic stirrer, as displayed in Figure 3.11.

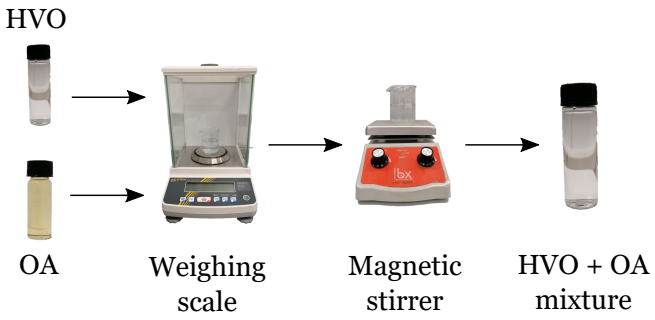

Figure 3.11: Procedure employed in preparing HVO and Oleic acid mixture.

Regarding the nanofuel preparation for high particle concentration, there is no consensus in the literature on whether the surfactant should be added before or after the sonication process. Therefore, the two approaches were tested for a nanofuel considering a particle size of 40 nm, a particle concentration of 2.0 wt.%, and an amplitude of 40% (P = 18 W) for 15 minutes. A surfactant-to-nanoparticle mass ratio of 1:1 was used, and after adding the surfactant, the fuel was vigorously stirred for an additional 10 minutes. The visual inspection is presented in Figure 3.12.

The observed sedimentation behavior from both procedures appears similar. In addition, it is verified that the addition of surfactant can enhance the stability of a nanofuel for a particle concentration of 2.0 wt.%. Thus, in the present study, surfactant was added after the sonication process, and a schematic illustrating the preparation steps for the nanofuels in this study is shown in Figure 3.13.

The procedure of high particle concentration follows the previously discussed method, where the nanoparticles and HVO are initially mixed in a magnetic stir, followed by the sonication process using an ice bath. The final step is dedicated to the addition of surfactant. Following this, a surfactant-to-nanoparticle mass ratio was evaluated to determine the optimal quantity of surfactant. According to the literature, surfactants are typically added to the mixture at surfactant-to-nanoparticle mass ratios of 1:2, 1:1, and 2:1, where the latter was discarded

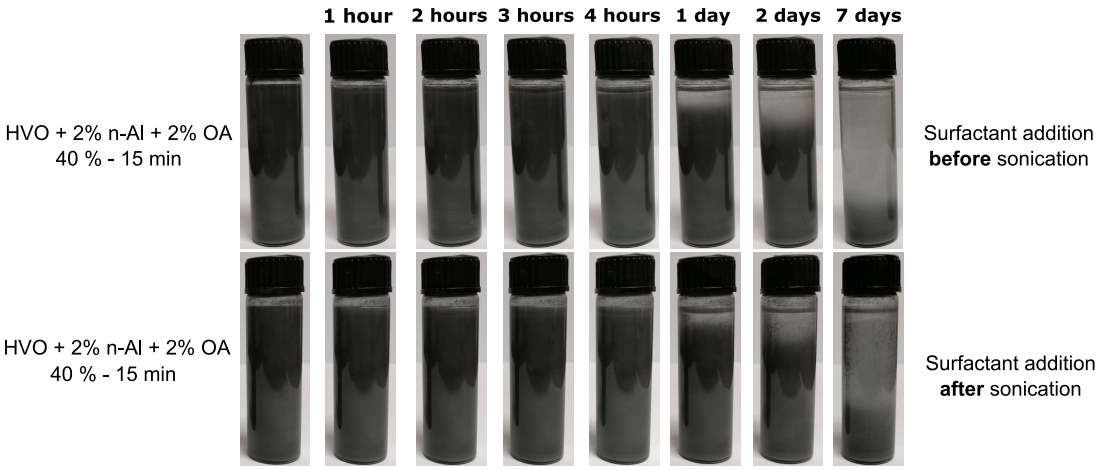

Figure 3.12: Sedimentation evolution for two nanofuels, where surfactant was added before (upper) and after (lower) sonication.

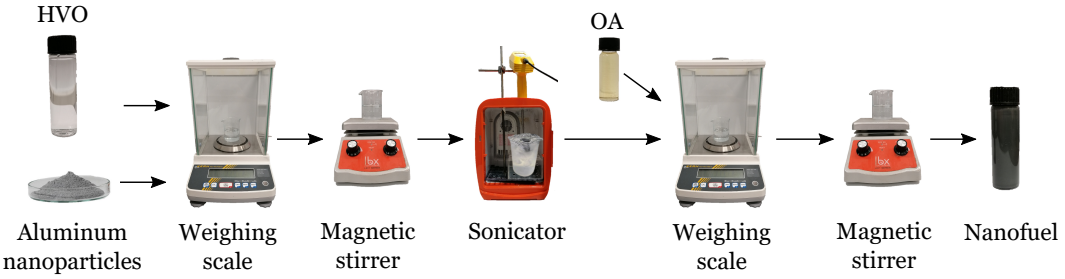

Figure 3.13: Procedure employed in preparing nanofuels using the 4^{th} approach.

in the present analysis since a high surfactant concentration significantly impacts the fuel properties. Thus, only the 1:2 and 1:1 ratios were explored, considering similar sonication configurations previously tested without surfactant. Table 3.5 shows the results for the visual inspection dedicated to a nanofuel with a particle size of 40 nm and a concentration of 2.0 wt.%. For this analysis, the power and time of the sonication process are explored, as well as surfactant-to-nanoparticle mass ratios of 1:2 and 1:1.

Table 3.5: Sedimentation analysis of HVO with 2.0 wt.% of aluminum nanoparticles using a surfactant-to-nanoparticle mass ratios of 1:2 and 1:1.

	5 min	1 hour	2 hours	3 hours	4 hours	1 day	2 days	7 days
HVO + 2% n-Al + 1% OA (P = 18W; 15 min)	A	A	A	A	A	B	C	D
HVO + 2% n-Al + 1% OA (P = 18W; 30 min)	A	A	A	A	A	B	B	D
HVO + 2% n-Al + 1% OA (P = 32W; 30 min)	A	A	A	A	A	B	C	D
HVO + 2% n-Al + 2% OA (P = 18W; 15 min)	A	A	A	A	A	B	B	D
HVO + 2% n-Al +2% OA (P = 18W; 30 min)	A	A	A	A	A	B	B	D
HVO + 2% n-Al + 2% OA (P = 32W; 30 min)	A	A	A	A	A	B	C	D

The results suggest that the nanofuel stability is enhanced with the surfactant, and the sonication configurations may become less relevant to the stability of the nanofuels. Despite the qualitative similarity of results shown in Table 3.5 for both surfactant ratios, the nanofuels prepared with the 1:1 ratio exhibited visually slightly better stability for 4 hours. Consequently, the 1:1 surfactant-to-nanoparticle mass ratio is adopted for further experiments involving higher particle concentrations. The temporal evolution of the temperature during the sonication process was also examined for the addition of surfactant. Figure 3.14 shows the influence of OA to nanofuel for different particle concentrations. The addition of surfactant of nanofuel indicates that the temperature does not increase significantly, which can also be responsible for enhancing the stability. The influence of the surfactant on the nanofuel temperature is beyond the scope of the present research.

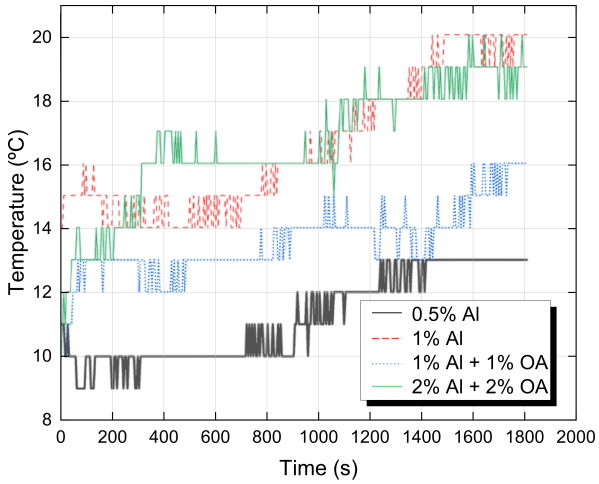

Figure 3.14: Temperature analysis regarding the addition of surfactant to HVO with aluminum nanoparticles in a size of 40 nm at different particle concentrations.

For single droplet experiments, the highest particle concentration corresponds to 4 wt.%, and the stability analysis is provided in Table 3.6. The results indicate that using the surfactant and the optimal sonication parameters already discussed, it is possible to evaluate a nanofuel with a particle concentration of 4 wt.% since the fuel remains stable for at least four 4 hours.

Table 3.6: Sedimentation analysis of HVO with 2.0 wt.% and 4.0 wt.% of aluminum nanoparticles using a surfactant-to-nanoparticle mass ratios of 1:1.

	5 min	1 hour	2 hours	3 hours	4 hours	1 day	2 days	7 days
HVO + 1% n-Al + 1% OA (P = 18W; 30 min)	A	A	A	A	A	B	B	C
HVO + 4% n-Al +4% OA (P = 18W; 30 min)	A	A	A	A	A	B	C	D

Subsequent to the nanofuel preparation method and optimal parameters, the physical properties of the fuel are characterized. Table 3.7 shows the density, viscosity, and surface tension of HVO by adding surfactant and several particle sizes and concentrations. The procedure and material employed for this analysis were already described in Figure 3.3. The results show that an increase in the particle concentration leads to an increase in the density regardless of the particle size. Furthermore, it is evident that adding aluminum nanoparticles

and OA at concentrations up to 4.0 wt.% results in only minor density variations, with a maximum variation of less than 3.5%. Similar observations are reported for the surface tension. The addition of aluminum does not promote a significant increase in the surface tension compared with the pure HVO, as displayed in Table 3.1. Concerning the effect of adding oleic acid in HVO, it was found that aluminum nanoparticles are primarily responsible for the slight increase in surface tension instead of oleic acid. The maximum variation compared to the base fuel is approximately 3.0% at a particle concentration of 4.0 wt% for both nanoparticles and oleic acid. In contrast to the density and surface tension, the effect of adding OA and aluminum particles in the viscosity is more pronounced. Increasing the particle and oleic acid concentration results in an increase in the viscosity. Adding concentrations of up to 4.0 wt% for aluminum nanoparticles and oleic acid produces a notable increase, with the highest variation of 20.0% compared with pure HVO. The evaluation of the fuels physical properties is relevant for the investigation of further studies regarding the spray behavior and droplet combustion, as will be discussed in the following chapter. Concerning the spray analysis, the refractive index of HVO with a particle concentration of 0.5 and 1.0 wt.% was analyzed. In this respect, the values for HVO + 0.5% Al and HVO + 1.0% Al are 1.44 and 1.68, respectively.

Table 3.7: Density, viscosity, and surface for HVO with the addition of surfactant and several particle sizes and concentrations.

	Density ($Kg\ m^{-3}$)	**Dynamic Viscosity (mPa.s)**	**Surface Tension ($N\ m^{-1}$)**
HVO + 40 nm (0.2 wt.%)	778.6	3.46	
HVO + 40 nm (0.5 wt.%)	779.15	3.49	26.71
HVO + 40 nm (1.0 wt.%)	781.95	3.50	26.88
HVO + 70 nm (0.2 wt.%)	779.3	3.46	
HVO + 70 nm (0.5 wt.%)	780.05		26.72
HVO + 70 nm (1.0 wt.%)	782.25		26.93
HVO + 5 µm (0.2 wt.%)	778.05	3.44	
HVO + 5 µm (0.5 wt.%)	778.75	3.48	26.75
HVO + 5 µm (1.0 wt.%)	781.6	3.55	26.94
HVO + OA (0.5 wt.%)	776.9	3.44	
HVO + OA (1.0 wt.%)	778.1	3.48	26.79
HVO + OA (2.0 wt.%)	778.7	3.51	26.82
HVO + OA (4.0 wt.%)	780.15	3.71	26.92
HVO + OA (0.5 wt.%) + 40 nm (0.5 wt.%)	779.2	3.52	
HVO + OA (1.0 wt.%) + 40 nm (1.0 wt.%)	782.5	3.56	27.01
HVO + OA (2.0 wt.%) + 40 nm (2.0 wt.%)	788.4	3.71	27.22
HVO + OA (4.0 wt.%) + 40 nm (4.0 wt.%)	802.8	4.11	27.55

3.3 Summary

This chapter describes the fuel preparation and characterization. It briefly describes the Jet A-1 and HVO composition, highlighting the main differences between the fuels. Regarding the addition of particles, aluminum was selected due to its energy content, abundance, and relatively low production costs. Compared to micron-size particles, aluminum nanoparticles

present a lower melting point and better dispersion in liquids due to their size reduction. As noted, adding particles to liquid fuel can be challenging due to the fuel stability, especially for higher particle concentrations. The increment of aluminum particle concentration increases the energy content of the fuel, a desired outcome for the mobility industry where a stable fuel is essential for its implementation in real applications. A specific procedure was established for low and high particle concentrations, and optimal power and sonication time parameters were defined. In the current study, a sonication process involving an ice bath, a sonication power of 18 W, and a time of 30 min provided the most satisfactory results. Particle concentration equal to or higher than 2.0 wt.% requires the addition of surfactant in a surfactant-to-nanoparticle mass ratio of 1:1 to ensure that the nanofuel remains stable during the experimental investigations regarding the single droplet combustion and spray behavior. Pure fuels, such as HVO and Jet A-1, are essentially transparent fluids. However, when aluminum particles are added to the base fuel, it is perceived that the sample becomes dark and opaque, potentially affecting the radiation absorption. In terms of physical properties, adding surfactant and aluminum nanoparticles does not substantially affect the surface tension and density relative to pure HVO (relative variation <5%). In contrast, adding oleic acid and aluminum increases the viscosity with the highest variation of 20.0% compared with pure HVO for a concentration of up to 4.0 wt% of aluminum nanoparticles and surfactant.

Chapter 4

Single Droplet Combustion

4.1 Introduction

In several technological processes, an immediate or controlled evaporation and, in certain instances, combustion of a liquid mass in a gaseous medium is required. Heat and mass transfer efficiency between a liquid and a gaseous medium depends on the interfacial area. Due to this, a typical approach to enhance the overall evaporation rate involves dispersing the liquid into multiple fragments, significantly increasing the total surface area compared to the original liquid mass. This process, denominated as spraying or atomization, is essential in many practical applications, such as gas turbines, diesel engines, and furnaces. The multiple fragments released by the atomization process contract under surface tension, forming nearly spherical droplets. Since the spray is much more complex than a sum of droplets, understanding the phenomena related to the evaporation and combustion of isolated liquid droplets is an essential prerequisite to comprehending the overall spray behavior. In fact, single droplets have been a usual topic evaluated in the combustion field.

In this context, the current chapter explores single droplet combustion in experimental and modelling approaches. The aim is to understand how the operating parameters can impact the droplet burning rate as well as disruptive burning phenomena for conventional jet fuel and alternative fuels concerning pure biofuel and biofuel with aluminum particles. In particular, the combustion of liquid fuel with metallic particles is a recent topic that needs more detailed attention dedicated to its behavior and dynamics to understand if they are viable for real-world applications. Furthermore, the development of numerical/analytical models capable of predicting the dynamics of single droplet combustion under different conditions is fundamental. Regarding the experimental study, falling droplet combustion experiments are conducted in a drop tube furnace at different furnace temperatures using a high-speed camera coupled with a high magnification lens to investigate the droplet size evolution as well as a disruptive burning phenomena. A detailed description of the experimental setup is provided, as well as the operating conditions and image data processing employed in this investigation to elucidate how the measurements are carried out. Focusing on the addition of particles to liquid fuel, a few models have been developed that explain the phenomena occurring during the evaporation/combustion of this type of fuel. In fact, mathematical models can ease the phenomenological understanding of complex systems and predictions of the relevant processes. Thus, a simplified theoretical model was developed in Python programming language to predict the burning behavior of single droplet combustion. The model estimates the droplet size evolution and burning rate, integrating several factors, e.g., convective ef-

fects. This comprehensive approach provides valuable insights for designing, developing, and operating more efficient and less pollutant practical devices.

4.2 Experimental Methodology

Firstly, the experimental methodology described the setup employed to evaluate the falling single droplet combustion. The operating conditions, diagnostic characteristics, and data process procedure are also described in detail. The present section discusses the influence of furnace temperature, particle size, concentration, and surfactant addition based on the experimental measurements.

4.2.1 Experimental Setup

The experimental facility to evaluate the single droplet combustion experimentally comprises a drop tube furnace, injection apparatus, and image acquisition system. A detailed description is also mentioned in [16, 19, 216]. Figure 4.1 shows the experimental setup employed for a single droplet combustion study, evidencing the drop tube furnace and the auxiliary equipment. Thus, the following subsections describe each equipment used in this experimental investigation.

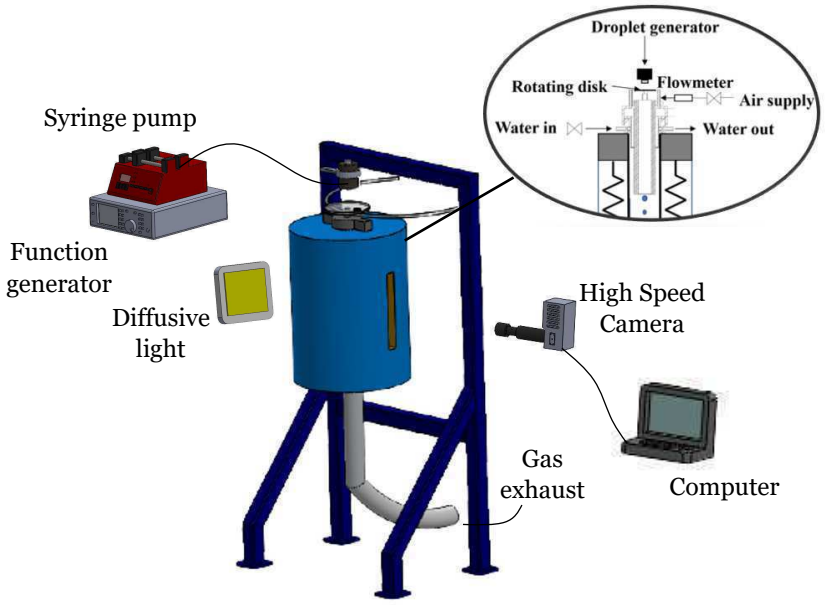

Figure 4.1: Schematic of the experimental setup for single droplet combustion.

4.2.1.1 Drop Tube Furnace (DTF)

An experimental arrangement was adopted to assess the combustion of falling droplets. In this context, an injector placed at the top of the drop tube furnace facilitates the introduction of single droplets into a high-temperature environment. The injector for liquid fuels was developed, incorporating an air supply for the oxidizing ambient and water-cooling system, as depicted in the Appendix B.1. The water-cooling presents two purposes: preventing the

equipment from potential damage and droplet ignition within the injector. The dimensions of the injector are carefully designed to evaluate the single droplet combustion. Particularly, the injector diameter is sufficiently large to prevent fuel contact with the walls. On the other hand, the injector length is kept minimal to reduce droplet heating and to prevent droplet ignition inside the injector. Regarding the air supply, a series of screens and nets were applied in the injector to align the flow and reduce the maximum eddy diameter. A net with 50 μm diameter and a honeycomb with 0.6 cm diameter and 6 cm length was used. The air supply was 5.7 L/min with a precision error of ±2%. When the air enters, the quartz tube is heated, generating a proper environment for the droplet autoignition. It is important to highlight that the air enters the quartz tube before the droplet injection from a different inlet. Figure 4.2 shows the interior of the drop tube furnace. The injector is placed at the top of the drop tube furnace, fitting the quartz tube, where the droplet combustion occurs. The vertical quartz tube has an inner diameter of 6.6 cm and a length of 82.6 cm, surrounded by electrically heated coils of the drop tube furnace. For the visualization of single droplet combustion, the DTF possesses two rectangular windows, with 2 cm width and 20 cm height, in the heating zone, which is 30 cm long. The drop tube furnace is capable of achieving wall temperatures up to 1200 °C, being controlled by two type-S thermocouples. Different furnace temperatures are considered to evaluate the single droplet combustion. In this context, temperature profiles inside the DTF were performed. The data were acquired using a 76 μm diameter fine wire platinum/platinum: 13% rhodium (type-R) thermocouple, placed on an appropriate probe. The probe is coupled to a mechanism that enables the thermocouple to move along the central axis of the quartz tube with a positioning accuracy of ± 1 mm.

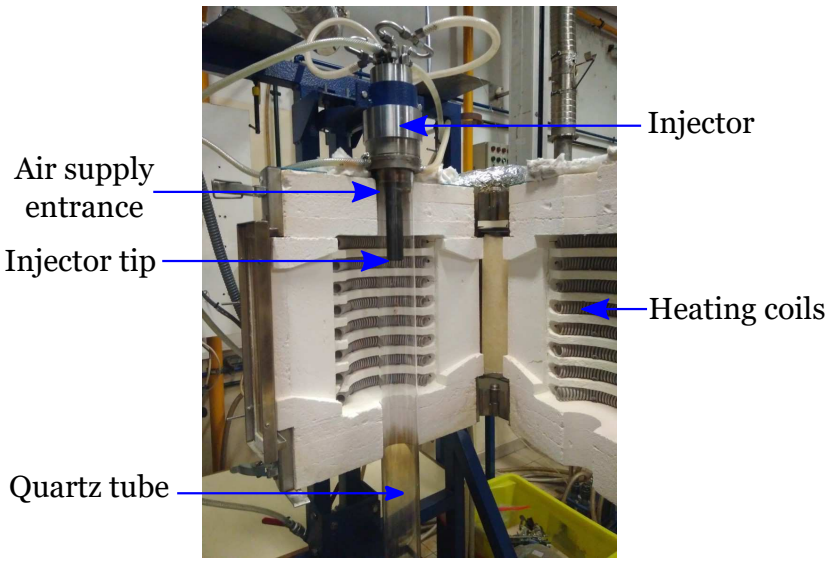

Figure 4.2: Interior view of the drop tube furnace.

Temperature measurements were collected using a data acquisition board connected to a computer. Figure 4.3 shows the temperature profile measurements inside the quartz tube.

Different furnace temperatures were considered from 600 °C to 1100 °C for the single droplet combustion investigation displayed in the present thesis. Near the injector tip (x = 0 cm), air

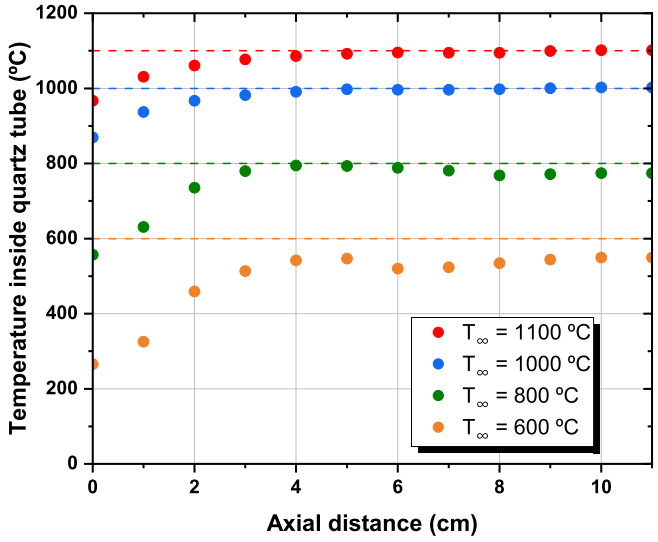

Figure 4.3: Furnace temperature inside the quartz tube as a function of the vertical distance for the respective wall temperature conditions (P∞ = 1 atm). The injector tip is located at x = 0 cm.

temperature is lower than in regions further down. This is due to the interaction of the hot air with the water-cooled injector tip, which is more evidence for the lower furnace temperatures.

4.2.1.2 Injection Apparatus

The droplets were generated and injected into DTF using the equipment presented in Figure 4.4. A monosize droplet generator (MDG), specifically the MDG100 produced by TSI, was positioned above the inlet of the DTF injector and aligned with its central axis. The production of monosize droplets is based on a piezoelectric device derived from applying a constant periodic excitation to a laminar liquid jet, which causes surface waves to form and grow as the jet slows down. Subsequently, the disintegration into a single droplet per surface wave period happens. The monosize droplet generator displayed in Figure 4.4 a) is connected to a function generator PM5136, provided by Fluke, enabling square waves with amplitudes of up to 20 Vpp and frequencies ranging from 0.1 MHz to 5 MHz, suitable for MDG specifications. A 50 mL glass syringe is connected to a syringe pump, specifically, the NE-1000 produced by New Era Pump Systems, allowing a constant fuel flow rate, as shown in Figure 4.4. The experiments were carried out using a pinhole with a diameter of 200 µm to the MDG tip under operational parameters of approximately 2.1 kHz and a flow rate of 1.3 mL/min. This droplet generation technique enables the study of droplets with smaller initial diameters remaining spherical. Moreover, it is possible to avoid the interference of a supporting filament in the droplet combustion behavior. The droplet suspended technique is mainly used for its simplicity in measuring the droplet parameters. However, using a supportive fiber does not allow the study of a relatively small droplet. The typical droplet diameters in supportive fiber setup are around 1 mm, considerably higher than droplets produced by liquid fuel at-

omization. Moreover, the thermal conductivity of the supportive fiber influences the burning rate and disruptive burning phenomena as reported by Basu and Miglani [29] and Wang et al. [147]. In contrast with the droplet suspended, the free-falling droplet method allows the study of droplets on a micrometer scale, and no foreign elements/filaments are presented in the experimental arrangement. In this respect, the droplet enters the combustion chamber and can achieve, in some cases, higher temperatures, and pressures to recreate the operating conditions of practical engines [148].

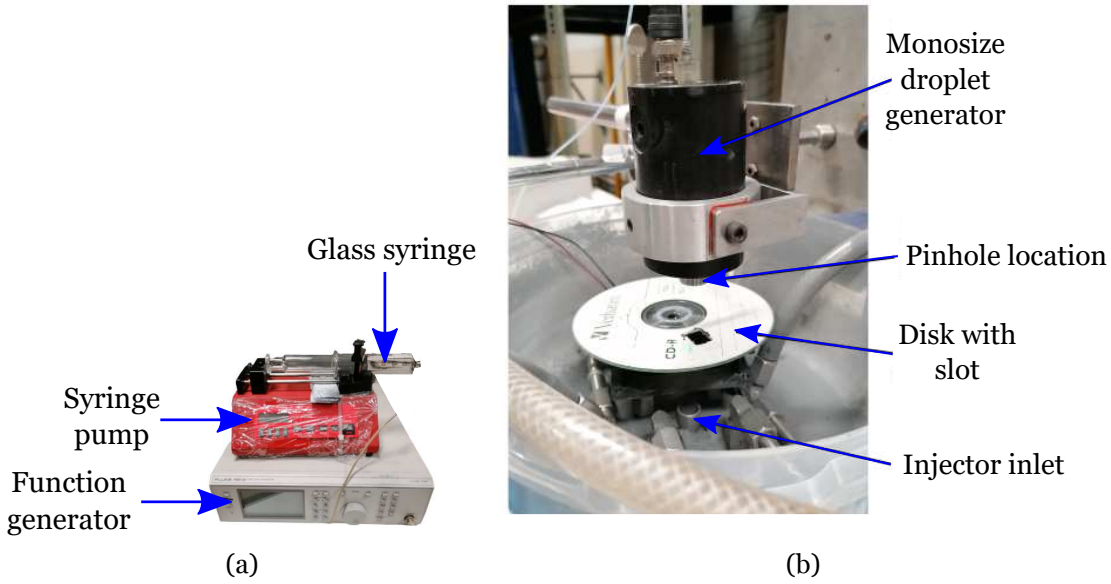

Figure 4.4: Equipment for generating and injecting droplets into the drop tube furnace.

The above description of the injection system presents numerous advantages for single droplet combustion; however, the stream created by the MDG does not guarantee enough spacing between droplets, leading to the droplets interaction. This impedes a precise analysis of single droplet combustion. Consequently, to address this issue, a rotating disk featuring a slot was positioned between the MDG and the injector entrance as displayed in Figure 4.4 b). The rotating disk possesses a diameter of 12 cm, and the slot dimensions are 1 x 1 cm attached to an electric motor. The electric motor is connected to a DC power supply of 2 A with an adjustable voltage between 3 and 12 V. In the experiments, the power supply voltage was set at 3 V, setting a rotational speed of 1200 rpm to the disk. Based on this approach, the droplets that pass through the disk slot enter the DTF, ensuring an inter droplet spacing of at least 50 droplet diameters. Therefore, no interaction between neighboring droplets occurs, and the phenomenon of single droplet combustion is guaranteed.

4.2.1.3 Image Acquisition System

As previously mentioned, an image acquisition system was employed to visualize the evaporation/ combustion of single droplets. This system is composed of a high-speed camera and an illumination set. Figure 4.5 depicts the high-speed cameras used for the single droplet behavior in terms of the temporal evolution of droplet size reduction and b) disruptive burning phenomena. For temporal evolution of droplet size reduction, a CR600x2 from Optronis

was used. The CMOS camera provides images in RGB format that were further treated for the grayscale. It can record with a maximum resolution of 1280 x 1024 px at 500 fps. Throughout the experiments for the droplet size evolution, a resolution of 1280 x 500 px, allowing for a frame rate of 1000 fps, and an exposure time of 1/12000 s and 1/13000 s were used. These respective exposure time values were determined to be optimal for capturing moving droplets with the correct focus while maintaining the image brightness for the visualization. A shorter exposure time would lead to a reduction in image brightness, making it more difficult to observe the droplets. For the optical configuration used in this work, the pixel size was 12 μm.

(a) (b)

Figure 4.5: a) CR600x2 high-speed camera with a magnifying lens Zoom 6000®; b) Photron FASTCAM mini UX50 with 1.3 Megapixel.

Additionally, for the visualization and detection of disruptive burning phenomena, a Photron FASTCAM mini UX50 with 1.3 Megapixel image resolution at frame rates up to 2,000fps and frame rates up to 160,000fps at reduced image resolution was required, allowing the image acquisition in grayscale. To enhance the micro-explosion visualization, different frames per second (2000, 3200, 4000, and 5000 fps) and shutter (1/16000s and 1/20000s) were tested.

Regardless of the high-speed camera, these are connected to a computer that triggers the camera and stores the collected images for further analysis. The spatial resolution micron/pixel is a critical parameter for the image acquisition system, representing the relation between the physical length and image pixels. A high spatial resolution is essential to ensure precise analysis of small droplets. To attain this, a magnification lens, Zoom 6000® Lens System produced by Navitar, was coupled to the camera. After each experiment, calibration was required to convert the scale from pixels to microns by placing a reference object with 76 μm diameter in the focal plane. Subsequently, it was possible to extract data regarding droplet size and velocity.

To visualize the droplet with maximum detail and contrast, an imaging backlight imaging was the selected method to study the phenomena occurring inside the DTF. This is a well-established technique extensively used in studies focused on droplet characterization, enabling the tracking of droplet size, position, and other properties. Figure 4.6 shows how the equipment is arranged to capture the droplet burning behavior. The high-speed camera is placed in a DTF opposite window compared to the illumination. As mentioned previously, the illumination set, which comprises an LED light and a diffusion glass, was placed in front

of one of the rectangular windows.

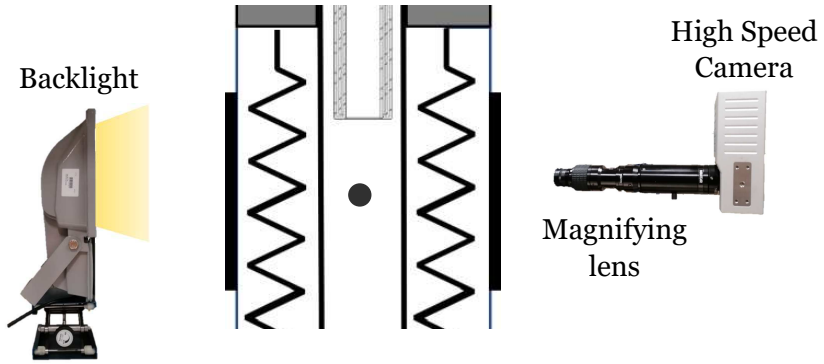

Figure 4.6: Schematic of the arrangement employed for the image acquisition.

Essentially, it involves aligning a light source with a high-speed camera and positioning a droplet between these two systems. To ensure the complete acquisition of the temporal evolution of droplet size reduction, the system was placed in different vertical positions along the DTF in each experiment performed.

4.2.2 Operating Conditions

Following the introduction of the experimental methodology, a brief explanation regarding the operating conditions employed in the single droplet combustion experiments will be provided. In this particular context, the furnace temperatures test in each fuel, along with the corresponding operating conditions, are presented.

As described in the experimental setup, falling droplets are released into the drop tube furnace at elevated temperatures. The purpose of using a falling droplet method is to evaluate and visualize the droplet movement and combustion without using a supporting fiber. Several studies in the literature focus on nanofuel combustion employing a filament for droplet support. These studies typically involve larger initial droplet diameters (≈ 1 mm), and the presence of filament can affect disruptive burning events. The current investigation provides a satisfactory compromise between experimental work and practical conditions by employing relatively high furnace temperature, smaller and spherical droplet diameter, and eliminating the need for a supporting fiber. This approach introduces a novel perspective to the field. A droplet generator system releases a stream of droplets and enters the drop tube furnace through its injector. As previously discussed, the drop tube furnace injector facilitates the entrance of air and droplets through distinct inlets. Figure 4.7 provides a detailed view of the drop tube furnace injector, highlighting the different inlets. Before conducting the experiments, an analysis of the operating conditions regarding the airflow inside the quartz tube is required.

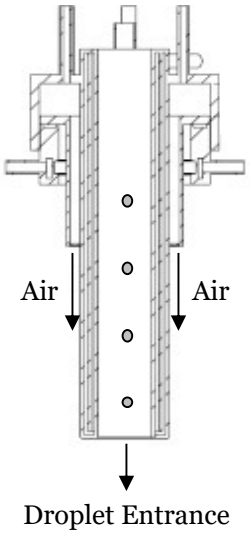

Figure 4.7: Drop tube furnace injector.

For the airflow characterization, the Reynolds number can be expressed by:

$$Re_{af} = \frac{U_\infty L}{\nu_{air}}, \quad (4.1)$$

where the mean airflow velocity, U_∞ and the characteristic length, L, employed was the quartz tube inner diameter, $D_{tube} = 0.066$ m. The kinematic viscosity of air is portrayed as ν_{air}. The mean airflow velocity is determined by Equation (4.2):

$$U_\infty = \frac{Q_{inj}}{A_{tube}} \frac{\rho_\infty (T_{inj})}{\rho_\infty (T_\infty)}, \quad (4.2)$$

where Q_{inj} is the air flow rate injected, A_{tube} is the cross-sectional area of the quartz tube, ρ_∞ is the air density, and T_{inj} is the air injection temperature, estimated to be around 20 °C. Table 4.1 shows the mean airflow velocity, air Reynolds number, and the corresponding parameters used to determine its value at the tested furnace temperatures.

Table 4.1: Airflow conditions for each furnace temperature.

	Furnace temperatures			
	600 °C	800 °C	1000 °C	1100 °C
T_∞ (K)	873.15	1073.15	1273.15	1373.15
ρ_∞ (kg m^{-3})	0.39	0.32	0.27	0.25
ν_∞ (m^2 s^{-1})	$9.98E-05$	$1.39E-04$	$1.84E-04$	$2.08E-04$
Q_{inj} (m^3 s^{-1})	0.000095			
A_{tube} (m^2)	0.0034			
T_{inj} (K)	293.15			
ρ_{inj} (kg m^{-3})	1.20			
U_∞ (m s^{-1})	0.08	0.10	0.12	0.13
Airflow Reynolds Number	55.89	49.49	44.53	42.44

The air properties for each furnace temperature are depicted in Appendix C.1 and C.2. Results show that the Reynolds number inside the quartz tube is relatively low, indicating a laminar airflow regime with reduced turbulence intensity. These conditions establish a stable and favorable environment for conducting single droplet experiments. Additionally, it is evident that the Reynolds number decreases as the air temperature increases, primarily due to a more pronounced rise in viscous forces compared to inertial forces.

Several working conditions are considered for the liquid fuels and alternative fuels with aluminum particles to understand the influence of the furnace temperature in single droplet combustion. Regarding the liquid fuels, a conventional fuel (jet fuel), an alternative fuel (HVO), and a mixture of HVO and oleic acid were tested, as shown in Table 4.2.

Table 4.2: Furnace temperatures considered on single droplet combustion for liquid fuels.

Fuels		**Furnace temperatures**			
		1100 °C	1000 °C	800 °C	600 °C
Liquid Fuels	HVO	✔	✔	✔	✔
	HVO + 4% OA		✔	✔	
	Jet A-1		✔	✔	✔

HVO and jet fuel were evaluated for furnace temperatures ranging from 600 °C to 1100 °C. Whereas, for HVO + 4% OA, the only furnace temperatures of 800 °C and 1000 °C were tested for comparison purposes, as will be further discussed.

Table 4.3 shows the furnace temperatures employed in the study dedicated to HVO with aluminum particles. Different particle sizes and concentrations were evaluated. At the furnace temperature of 1100 °C, only nanofuels were studied.

Table 4.3: Furnace temperatures considered on single droplet combustion for HVO with aluminum particles. Study cases are considered with a check mark.

Fuels	**Particle size**	**Particle concentration**	**Furnace temperatures**			
			1100 °C	1000 °C	800 °C	600 °C
HVO + Aluminum Particles	40 nm	0.2% Al		✔	✔	✔
		0.5% Al	✔	✔	✔	
		1% Al	✔	✔	✔	
		1% OA + 1% Al		✔	✔	
		2% OA + 2% Al		✔	✔	
		4% OA + 4% Al		✔	✔	
	70 nm	0.5% Al	✔			
		1% Al	✔			
	5 µm	0.5% Al		✔	✔	
		1% Al		✔		

The influence of the addition of surfactant in nanofuels was investigated and compared for

furnace temperature at 800 °C and 1000 °C. Identifying the furnace temperature tested for each fuel is relevant to clarifying and comparing the influence of adding metal particles and surfactants to liquid fuel.

The initial droplet diameter is analyzed after introducing the environmental conditions for each fuel. As previously stated, a monosize droplet generator injects a single droplet into the drop furnace. This droplet generation system requires a syringe pump, a syringe, a function generator, and a droplet generator head. A schematic view of the droplet generator head is present in Figure 4.8.

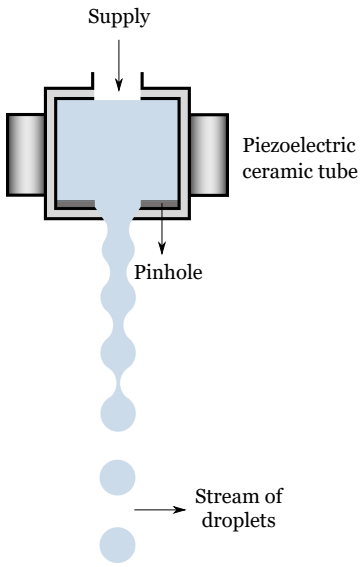

Figure 4.8: Schematic view of the MDG-100.

The droplet generator head is developed with a liquid reservoir containing a piezoelectric component that causes vibrations. These vibrations propagate from the reservoir through precision pinholes, leading to the liquid jet breakup. When a suitable frequency is applied to the disintegrating liquid jet, it produces uniformly sized droplets with a certain diameter and uniform spacing between neighboring ones. The following Equation gives a relation between the obtained diameter of MDG, where Q is the liquid flow rate, and f is the excitation frequency [398]:

$$D^3 = \frac{6Q}{\pi f} \quad (4.3)$$

As noted, the experiments were conducted considering a liquid flow rate of 1.3 mL/min and 2.1 kHz, resulting in a stream of droplets measuring approximately 270 μm. Since the experimental setup configuration used for single droplet combustion requires that a droplet moves from the MDG to the rotating disk and ultimately into a quartz tube. As a result, an initial droplet diameter of 250 μm was considered in the present work.

4.2.3 Image Data Processing

The experiments of single droplet combustion were recorded and stored as multiple images, enabling the extraction of pertinent details concerning this phenomenon. The collection of information through images is defined as image data processing. This method permits procedures on an image to get an improved image or obtain valuable information. Figure 4.9 shows the image data processing methodology. Firstly, the images are captured using a camera and subsequently stored in a computer, allowing later image processing.

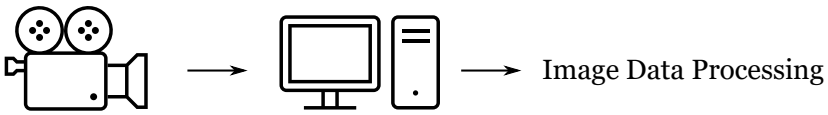

Figure 4.9: Data acquisition method.

After each series of experiments, the recorded videos were reviewed, and frames containing visible droplets were extracted for subsequent analysis. To maintain the accuracy of the results, only droplets in the focal plane while passing through the area recorded by the camera were subject to analysis. Images can be stored and retrieved easily to interpret the droplet history in terms of visualization, diameter, and velocity. In the context of droplet visualization, a crucial aspect is the identification of the droplet flame. The identification and visualization of the droplet flame were challenging due to the absence of aromatics in the biofuel employed in this study, as discussed in the results section. Consequently, an in-house algorithm was developed in MATLAB to ensure the phenomenon of single droplet combustion and droplet inter-spacing (space between droplets). Figure 4.10 shows an illustration and original images to obtain the visualization droplet flame. As depicted in Figure 4.10, the visualization of the flame is quite difficult. Due to this, a representation of the MATLAB algorithm is provided, being merely illustrative to highlight the flame to aid in identifying droplet combustion.

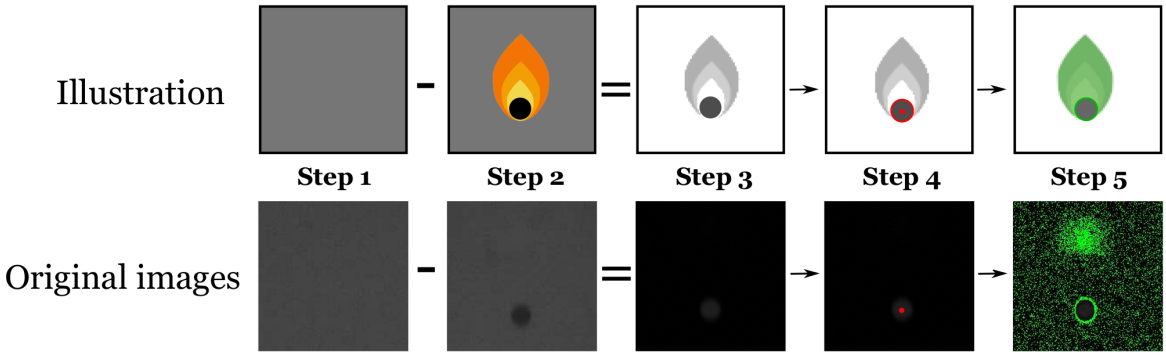

Figure 4.10: Illustration of the droplet flame image analysis using data processing.

Firstly, an image evidencing a droplet inside the DTF is selected. Thereafter, a background image and droplet image are read in the MATLAB algorithm, as shown in step 1 and step 2 in Figure 4.10. These images are subtracted to highlight the droplet and its flame (step 3). Since the CMOS camera provides images in RGB format, the function ”rgb2gray” is applied to convert the image into a grayscale. To ease the identification of the flame, the droplet

centroid is detected, as displayed in step 4. Finally, a green colormap is used to enhance the image clarity. Applying a colormap to the image accentuates the data range in the visualization, enabling it to be distinguished from the remaining data collection. A colormap is a matrix of values representing the colors for surface, image, and patch objects. In this context, the flame is highlighted, evidencing its presence in the image. A droplet flame identification process was carried out for each fuel to verify the ignition of the droplet inside the quartz tube. To guarantee the single droplet phenomenon, minimal space between the droplets is required. As previously mentioned, the algorithm for flame detection permits droplet centroid identification, enabling the confirmation of the inter-space between droplets. Figure 4.11 displays the distance between two droplets to ensure no interferences from the droplet–droplet interaction in this study.

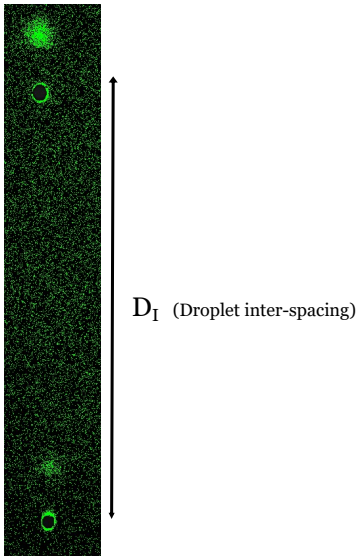

Figure 4.11: Single droplet combustion: droplet inter-spacing.

According to the literature, droplets should be spaced at least 30 diameters apart to provide independent burning [399, 400]. Subsequently, each analysis was performed with approximately 50–60 droplet diameter distance.

An image detection algorithm was also developed to determine droplet properties (e.g., droplet size evolution, burning rate, and droplet velocity). The ImageJ open-source software treated the data to analyze and process scientific images. Figure 4.12 shows the various steps performed in ImageJ to obtain the droplet characteristics. Initially, the image is introduced in the software; subsequently, the Huang threshold method was employed to obtain edge detection and pixel values. A region of interest (ROI) surrounding the droplet was established, and the thresholds were calibrated to ensure precise measurements. To apply the threshold, every frame had to be converted to a 16-bit image. Once the region of interest (ROI) is established, the droplet outline is marked through the brightness gradient derived from the light transition to darker gray. This approach facilitates the characterization of the droplet for further analysis. A brightness gradient was determined for each pixel for each droplet image. This gradient revealed a distinct change from lighter gray to darker gray pixels in the

vicinity of the droplet surface.

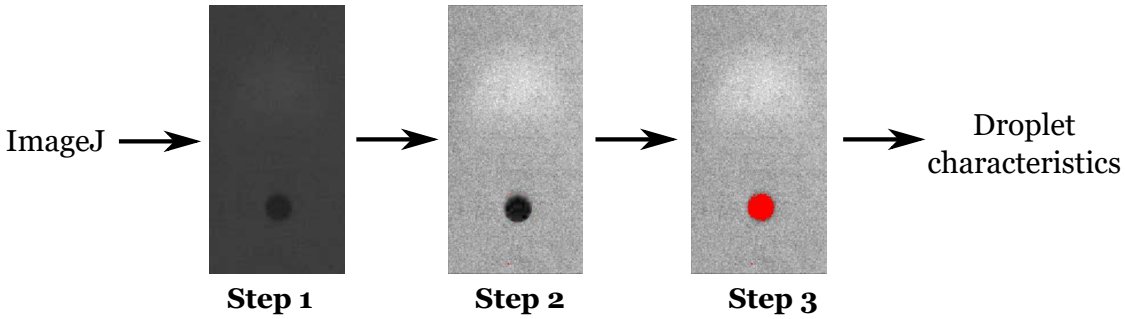

Figure 4.12: Illustration of the image analysis procedure utilizing ImageJ for data processing.

Subsequently, the droplet diameter was determined through the instantaneous droplet area given by image analysis related to a circle, where r is the droplet radius, as depicted in Equation (4.4):

$$A_d = \pi r^2 \,. \quad (4.4)$$

Determining the droplet diameter using the captured images provides insights into the droplet history regarding droplet size evolution and burning rate. To ensure that the droplet size evolution curve and burning rate are independent of the sample size, a statistical analysis was conducted. The purpose is to determine the minimum number of droplets for the analysis. Therefore, the droplet size evolution and burning rate were evaluated as a function of the number of droplets, using 10 to 45 droplets for each nanofuel. In the present work, nanofuels were selected due to their disruptive burning behavior, which could affect the droplet size history. Figure 4.13 shows the variation of the burning rate as a function of the number of droplets analyzed. This examination was conducted using HVO with aluminum nanoparticles in a size of 40 nm with two different particle concentrations.

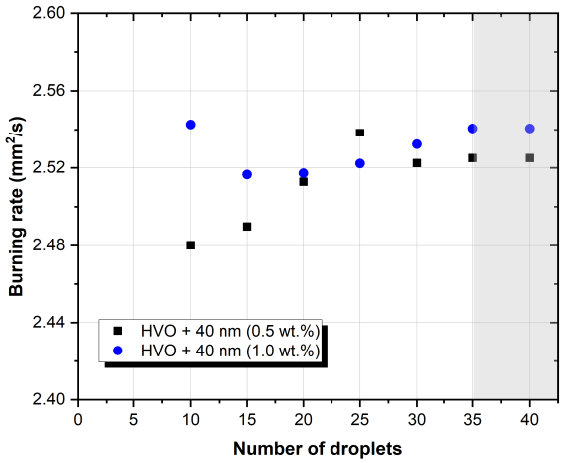

Figure 4.13: Analysis of burning rate as a function of the sample size.

The droplet size evolution was divided into five sections, and droplets were progressively incorporated into the curve to assess the impact of the number of droplets on the analysis. Consequently, the burning rate was extracted from the droplet size evolution curve. In the present work, a minimum of 35 droplets is needed for a statistical convergence, where no significant variation in the droplet size evolution curves and burning rate was noticed. Subsequently, the D^2/D_0^2 curves will be presented in the results section, considering 40 droplets with a standard deviation of 0.05, as will be described later.

In terms of droplet velocity, the coordinates of the droplet centroid were determined for sequential frames, and the distance between these points was calculated. Then, this distance was divided by the time difference between frames to determine the droplet velocity, as shown in Equation (4.5):

$$U_d = \frac{\sqrt{|x_b - x_a|^2 + |y_b - y_a|^2}}{\Delta t}. \quad (4.5)$$

The image data processing employed in the present work for the droplet characteristics regarding flame, diameter, and velocity was already presented. This procedure remains consistent regardless of the type of fuel used, whether it be pure liquids or nanofuels. However, introducing particles into liquid fuels results in disruptive combustion behavior. As a result, it is crucial to investigate these phenomena to achieve a deeper understanding of nanofuel droplet combustion. In this context, Figure 4.14 shows the procedure used to study the disruptive burning phenomena spotted in nanofuel. Initially, micro-explosions were selected and identified to find the region of interest for subsequent analysis. For each furnace temperature, ten micro-explosions were analyzed, and more than thirty images were considered for the individual disruptive event.

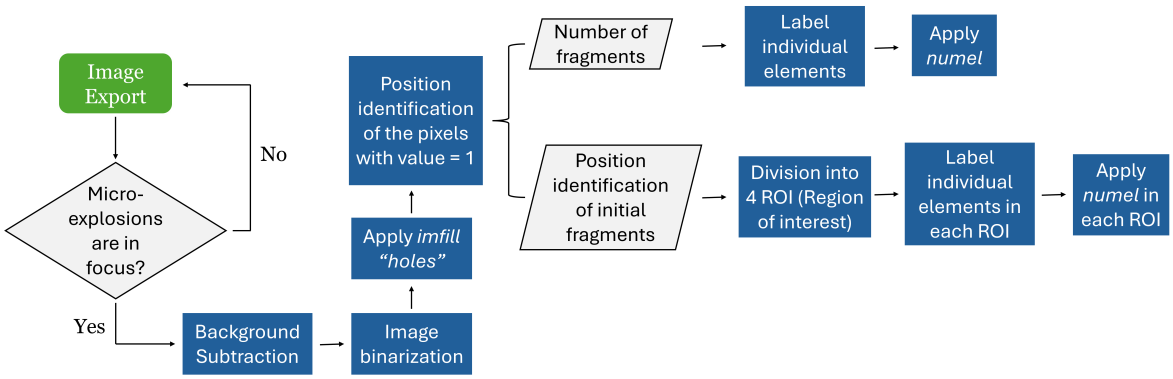

Figure 4.14: Illustration of the image data processing for micro-explosions.

Subsequently, a MATLAB algorithm was developed, involving image subtraction, binarization, and identifying elements in the recorded images. Prior to the image data processing, a detailed procedure dedicated to the acquisition, selection, and acquisition of an image of the micro-explosion in focus is performed. After this, the identification of the region of interest is highlighted.

The image data processing starts with subtracting the background from the micro-explosion images to accentuate the disruptive outcomes. In the following step, the images were subjected to binarization using a threshold value of 0.09. For the micro-explosions investigation, a high-speed camera, specifically the Photron FastCam mini coupled with a high magnification lens, was employed to enhance visualization quality. After this, a MATLAB function named "$imfill$" was employed to identify the position of pixels with the highest value (white pixels). Ultimately, the algorithm provides the maximum count of fragments present in the images. In this scenario, elements are labeled using a "$vislabels$" function, and the number of fragments is determined using the "$numel$" function, as displayed in Figure 4.15 a). The purpose of examining the number of fragments relies on the influence of particle concentration of nanofuels to understand its impact on disruptive burning events.

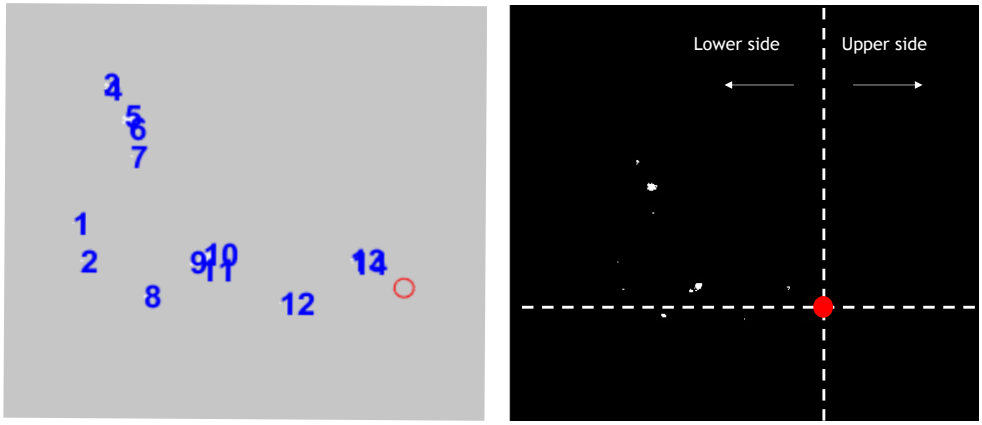

(a) (b)

Figure 4.15: Images obtained in image data processing for micro-explosions: a) Number of fragments, b) Position identification of initial fragments.

The micro-explosions were divided into 4 regions of interest (ROI) to enhance the phenomena understanding. These ROIs aim to identify and count the fragments on the upper and lower sides and consider the position of the primary droplet disruption. The objective of this analysis is to acquire a deeper understanding of the factors leading to the disruption of nanofuel droplets. Due to this, different regions of interest are explored, considering the lower side, which corresponds to the front of the droplet, and the upper side, representing the rear of the droplet.

4.3 Single Droplet Combustion: Experimental Results

The present section is dedicated to the results and discussion of the experimental study concerning single droplet combustion. Falling droplet at T_∞ = 1100 °C, 1000 °C, 800 °C and 600 °C are explored. HVO and Jet A-1 are primarily investigated to understand how adding metal particles affects droplet combustion. Concerning the addition of particles, nano-size particles of 40 and 70 nm are considered, and 5 μm to evaluate the potential benefits of utilizing nanoparticles in contrast to micron-sized particles. As outlined earlier in the literature review, numerous investigations suggest an optimal particle concentration enhances the

single droplet combustion performance. Thus, this section addresses the impact of low and high particle concentrations in the evolution of droplet size and the burning rate of nanofuel. Finally, an analysis of disruptive burning phenomena is provided. A visualization and an examination of the micro-explosion intensity concerning different particle concentrations and furnace temperature are discussed. The overall findings were already published and are available in [16, 19, 216, 401].

4.3.1 Visualization and Description of Pure Fuels Combustion

For a proper investigation of the effects of aluminum particles on HVO, a preliminary analysis is focused on the single droplet combustion of HVO to serve as a baseline for further comparison. In addition, a conventional jet fuel, Jet A-1, is evaluated for a comparative analysis with the alternative fuels. It is important to highlight that pure fuels correspond to fuels that do not involve the addition of aluminum particles.

Droplet size evolution, burning rate, and flame intensity are compared for Jet A-1 and pure HVO at three furnace temperatures T_∞ = 1000 °C, 800 °C and 600 °C. Concerning the lowest furnace temperature, regardless of the fuel, the visualization and identification of auto-ignition were not possible in the majority of the droplets. In this context, the droplet size evolution and the burning rate at this particular temperature will not accurately compare all operating conditions. Droplets are injected in the quartz tube after stabilization of the furnace temperature, as shown in Figure 4.3. The air is introduced in the quartz tube and heats due to the electric coils presented in DTF. The droplet begins to vaporize from its surface when entering the hot environment. Consequently, auto-ignition occurs immediately upon fuel vapor, and air mixing is in an adequate proportion, leading to a diffusion flame formation. In addition, ignition delay was not evaluated in the present work due to the constraints in the experimental setup.

Visualization and droplet size evolution of single droplet combustion of HVO and Jet A-1 at T_∞ = 800 °C and T_∞ = 1000 °C is presented in Figure 4.16 and Figure 4.17, respectively. Figure 4.16 and Figure 4.17 a) shows the square of the normalized droplet diameter as a function of the normalized time for HVO and Jet A-1, where D_0 is the initial droplet diameter. Each curve was developed using 40 droplets, as previously mentioned, and a five-point moving average was employed for the smoothening purpose. In addition, for diameters below D^2/D_0^2 = 0.1, it was not feasible to accurately measure the droplet diameter. Due to this, subsequent values were derived using the best-fit trend line for each droplet size evolution curve discussed in this study. The results show that conventional jet fuel and biofuel obeyed the D^2 - law. Therefore, the normalized square diameter decreases linearly with a nearly constant rate defined as the burning rate (K). By comparing the droplet size evolution curves presented in Figure 4.16 a), the results suggest that droplets of pure HVO display a longer lifetime however normalized droplet diameter evolution is quite similar for most of the lifetime compared with Jet A-1. The primary distinction between the fuels is observed at the end of the droplet lifetime. Moreover, no disruptive burning phenomena are spotted.

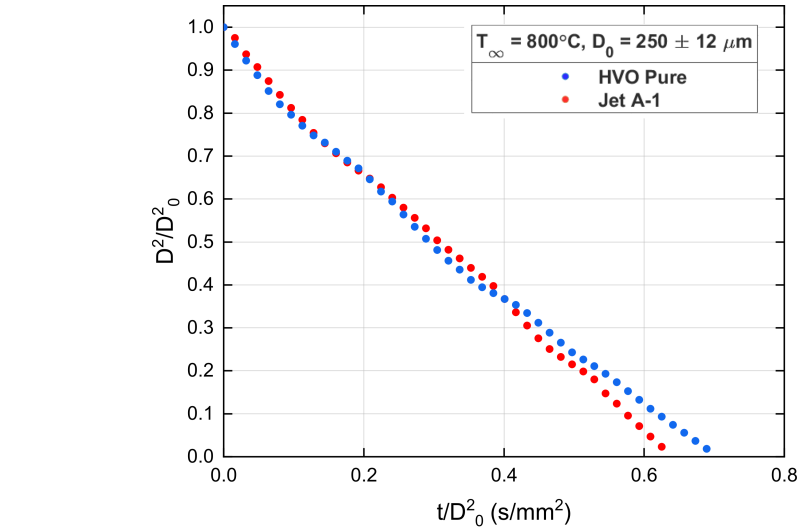

(a)

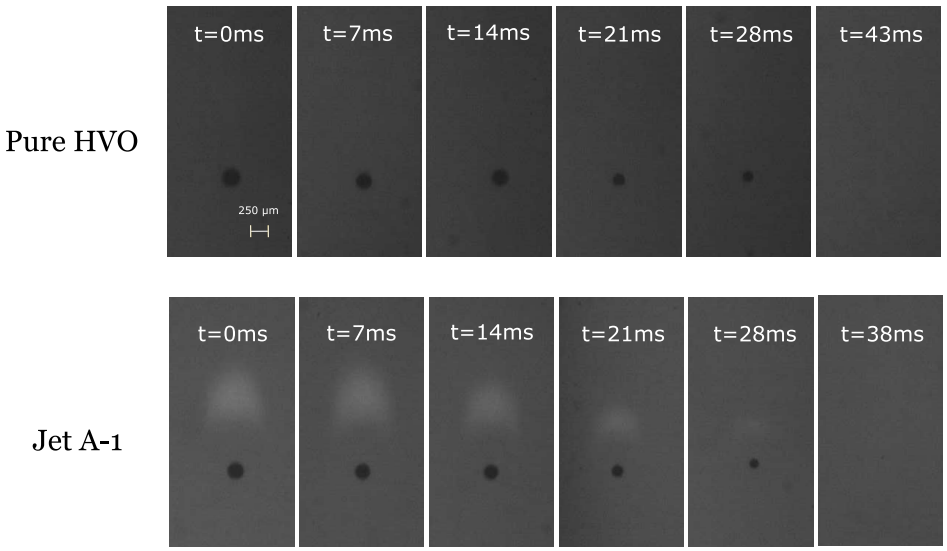

(b)

Figure 4.16: Jet A-1 and HVO combustion at T_∞ = 800 °C: a) Droplet size evolution; b) Visualization of single droplet combustion.

It is essential to mention that the ignition of Jet A-1 occurs at a smaller distance from the tip of the DTF injector related to the HVO. This observation can be attributed to compounds with lower boiling points (lighter compounds) present in Jet A-1 composition [402]. Considering the temperature profile inside the quartz tube, presented in Figure 4.3, for a furnace temperature of T_∞ = 800 °C, droplets ignite in a region between in 3 to 4 cm from the tip of the injector. The maximum standard deviation in droplet size evolution curve at T_∞ = 800 °C for Jet A-1 was ±0.05, and for HVO, it was ±0.08. Increasing the furnace temperature, similiar findings with T_∞ = 800 °C are noticed. In this context, Figure 4.17 a) shows the droplet size evolution of HVO and Jet A-1 at T_∞ = 1000 °C where the normalized square diameter decreases linearly with time without any disruptive burning phenomena. The results indicate that by increasing the furnace temperature, the combustion characteristics of conventional and alternative jet fuel are practically similar, where curves of the droplet size

evolution nearly overlap. Similar findings were previously reported by [379, 403, 404]. The maximum standard deviation in droplet size evolution curve at T_∞ = 1000 °C for Jet A-1 and HVO are ±0.06 and ±0.08, respectively.

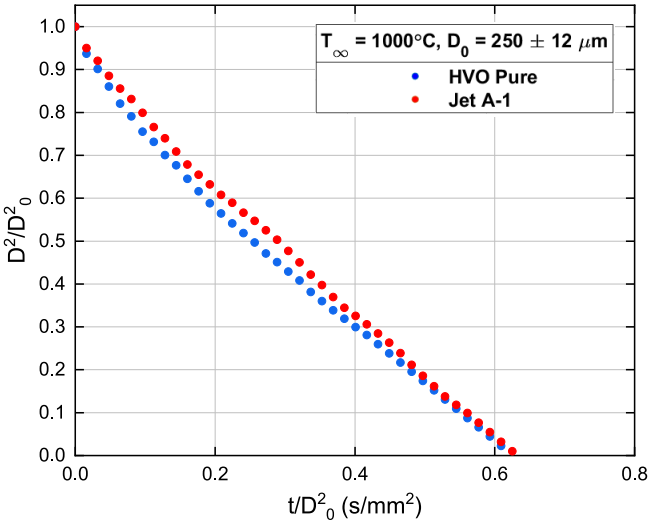

(a)

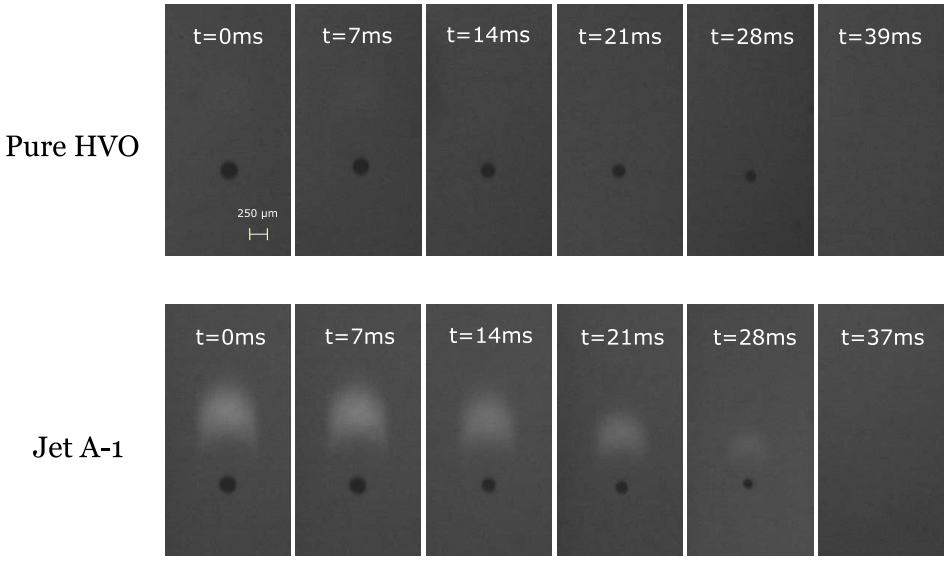

(b)

Figure 4.17: Jet A-1 and HVO combustion at T_∞ = 1000 °C: a) Droplet size evolution; b) Visualization of single droplet combustion.

In terms of visualization provided in Figure 4.16 and Figure 4.17 b) as time evolves, the droplet diameter reduces as described in the droplet size evolution, and no disruptive burning phenomena are noticeable regardless of the fuel and furnace temperature considered. The frame when the ignition is detected, characterized by the appearance of a diffusion flame, is defined as t = 0 ms, as indicated in the sequences of images. One of the significant contrasts displayed in the fuels single droplet combustion visualization is flame intensity. Moreover, the visualization suggests that a symmetric spherical flame is not evident. A brighter flame is noticed for Jet A-1 due to the presence of high aromatic content, as previously noted by [403]. This result is pertinent to research focused on pollutant emissions. In this con-

text, a reduction in pollutant emissions is reported when HVO is used due to the absence of aromatics [379,403,404]. On the other hand, identifying an HVO flame is considerably challenging since the biofuel does not possess aromatics in its composition, displaying a flame with a lower intensity. In addition, it is also observed that the flame intensity decreases as the droplet shrinks along its lifetime, as depicted in Figures 4.16 and Figure 4.17 b). Due to the challenges in clearly identifying if there is an envelope or wake flame in the present work, particularly with HVO, a comparative analysis with the flame regime maps developed by Pandey et al. [405] is presented. According to the flame regime map provided by Pandey et al. [405], if the droplet Reynolds number relies on the range of 0 < Re_d < 5 for the entire droplet size, is predicted that the burning process would be characterized by an envelope flame surrounding the droplet. The droplet Reynolds number can be written as follows [406]:

$$Re_d = \frac{U_{rel} D}{\nu_g}\,, \quad (4.6)$$

where D is the droplet diameter and U_{rel} is the relative velocity between the droplet and the free stream that can be determined by the following expression:

$$U_{rel} = U_d - U_\infty\,. \quad (4.7)$$

The airflow Reynolds number was already presented in Equation (4.1). Consequently, the primary analysis is dedicated to the droplet velocity. Figure 4.18 shows the droplet velocity as a function of the normalized droplet diameter at T_∞ = 800 °C and T_∞ = 1000 °C. As earlier described in the experimental methodology, the droplet velocity was determined by the centroid position for two sequential frames divided by the time between the two frames. Afterward, a polynomial function is applied to the experimental data points to obtain velocity curves for pure fuels in the two furnace temperatures.

At the early stages, where D^2/D_0^2 is between 1.0 and 0.7, HVO droplet velocity is slightly higher than Jet A-1, however, as the droplet diameter is reducing the velocity tendency is quite similar, regardless of furnace temperature. The maximum standard deviation in droplet velocity at T_∞ = 800 °C was ±0.2 m/s and at T_∞ = 1000 °C was ±0.1 m/s. Thus, a detailed examination regarding the droplet Reynolds Number for HVO and Jet A-1 at T_∞ = 800 °C and T_∞ = 1000 °C is displayed in Figure 4.19. The gas kinematic viscosity ν_g was estimated at the mean temperature $\overline{T}_2 = (T_f + T_\infty)/2$, for the gaseous region outside the flame front [406].

This finding indicates a decrease in the droplet Reynolds number as the droplet diameter decreases. Additionally, air viscosity increases with temperature related to higher values of T_∞, leading to a reduction in the droplet Reynolds number. Notably, the estimated droplet Reynolds number values remain relatively low due to the experimental conditions involving small initial droplet diameters and high-temperature environments. As reported by Incor-

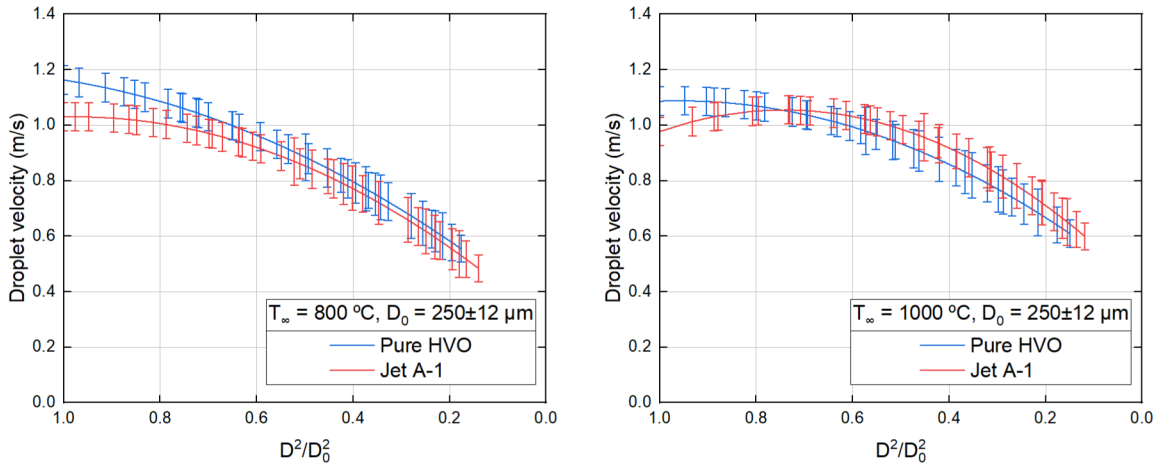

Figure 4.18: Droplet velocity as a function of the normalized droplet diameter at a) T_∞ = 800 °C; b) T_∞ = 1000 °C.

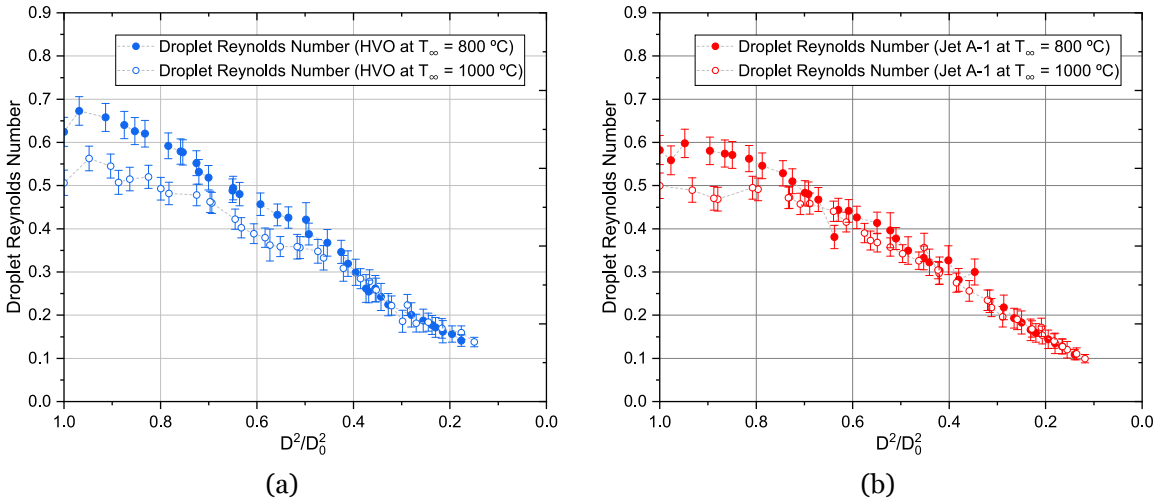

Figure 4.19: Droplet Reynolds Number as a function of the droplet squared ratio at furnace temperatures of T_∞ = 800 °C and T_∞ = 1000 °C.

pera [407], for $Re_d \leq 2$, no separation effects are noticed. Consequently, in the present study, this phenomenon is negligible. Regarding the flame characteristics, Pandey et al. [405] proposed a flame regime map that enables the classification of the flame behavior, ranging from an envelope flame to a wake structure, by considering the droplet Reynolds number. Considering that the Reynolds number relies on the range of $0 < \mathrm{Re}_d < 5$, it was confirmed that the burning process would be characterized by an envelope flame surrounding the droplet.

After describing the fuel combustion behavior involving visualization, droplet size evolution, and flame characterization, the burning rate between HVO and Jet A-1 is presented. Evaluating droplet size evolution allows investigating how fast the liquid evaporates, which can be quantified as the burning rate. This parameter is critical for understanding fuel performance under engine operating conditions. Figure 4.20 displays the temporal evolution of burning rate and final burning rate for the Jet A-1 and pure HVO at T_∞ = 800 °C and T_∞

= 1000 °C. The horizontal lines correspond to the final burning rate, considering the entire droplet lifetime, where the red and blue lines are related to the Jet A-1 and HVO, respectively. The burning rate can be determined by $K_c = d(D^2)/dt$. The results indicate that at the lowest furnace temperature, T_∞ = 800 °C, Jet A-1 presents a slightly higher burning rate (1.51 mm^2/s) compared to pure HVO (1.41 mm^2/s). Furthermore, an increase in furnace temperature results in a higher final burning rate, with the pure fuels exhibiting comparable values, as shown in Figure 4.20 b). Regarding the temporal evolution of the burning rate, the analysis reveals that liquid fuel evaporates without any significant disturbance. This leads to an approximate constant burning rate value, regardless of furnace temperature.

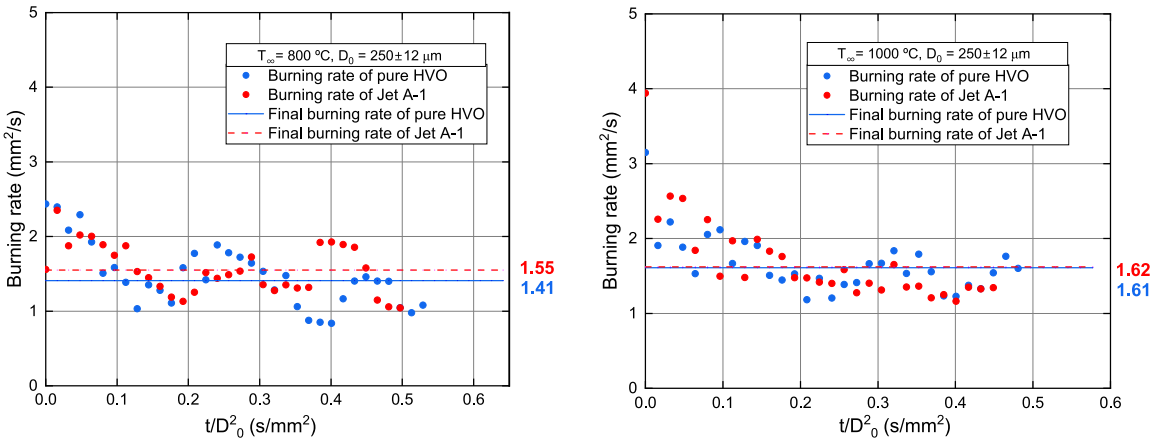

Figure 4.20: Temporal evolution of burning rate and final burning rate for the Jet A-1 and pure HVO: a) T_∞ = 800 °C; b) T_∞ = 1000 °C.

As mentioned in the introduction of this section, four furnace temperatures were considered, ranging from T_∞ = 600 °C to 1100 °C. However, a more detailed analysis was provided only for 800 °C, 1000 °C, where the lowest furnace temperature was unable to offer an accurate comparative analysis since the majority of the droplets were only in the evaporation process. An experimental study was conducted with a different exhaust system concerning the highest temperature, T_∞ = 1100 °C. Consequently, to guarantee the accuracy of the results, the analysis was carried out independently. Figure 4.21 shows the average burning rate of pure HVO and Jet A-1 for $D^2/D_0^2 > 0.2$ at three furnace temperatures.

The result for the highest temperature, T_∞ = 1100 °C, is included to clarify the impact of furnace temperature on the burning rate, given that a comprehensive comparison with the remaining furnace temperatures was not conducted. It is evident that increasing the furnace temperature leads to a higher burning rate, regardless of the furnace temperature. A more pronounced difference between the fuels is noticed at the lowest furnace temperature.

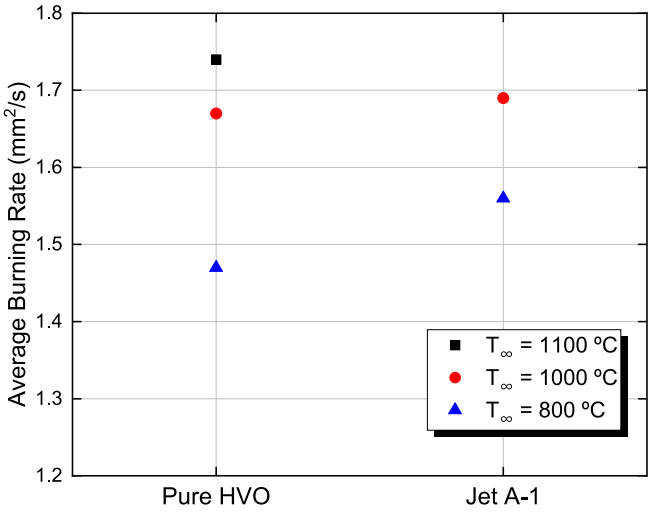

Figure 4.21: Average burning rate of pure HVO and Jet A-1 for $D^2/D_0^2 > 0.2$.

4.3.2 The Addition of Particles to an Alternative Jet Fuel

The previous section described the combustion of pure HVO and Jet A-1. It was noticed that HVO provides satisfactory results; however, the addition of energetic particles to enhance the combustion performance of biofuels is being explored. Thus, aluminum particles were added to the biofuel to enhance its performance, potentially decreasing fuel volume usage and increasing fleet-wide energy efficiency. In this context, nanoparticles are being considered as possible solutions to increase volumetric energy density, enhancement of the catalytic activity, lower ignition delay, higher ignition probability, higher volumetric heat release rates, and faster burning rates [29]. Therefore, the primary approach will be dedicated to the influence of the particle size. As indicated earlier, all the droplet size evolution curves related to the investigation of adding aluminum particles to liquid fuels are developed considering 40 droplets, and to smoothen the curves, a five-point was employed. The initial droplet diameter (D_0) corresponds to the droplet diameter as it enters the quartz tube and ignites.

In light of the limitations and alterations in the experimental configuration, the following results are primarily devoted to the highest temperature, T_∞ = 1100 °C. Thus, pure HVO and HVO with nanoparticles in size 40 and 70 nm and two particle concentrations (0.5 and 1.0 wt.%) are evaluated qualitatively and quantitatively. Figure 4.22 shows a sequence of instantaneous images of the tested fuels at a furnace temperature at T_∞ = 1100 °C. It is essential to mention that the different instants correspond to a droplet burning in different vertical positions at the drop tube furnace, followed by the CMOS high-speed camera coupled with a high magnification lens to capture the single droplet behavior. For these experiments, five different camera positions were used to guarantee the visualization and analysis detail of the droplet lifetime. Prior to the droplet injection, the air inside is heated by the electric coils at the DTF. It creates an appropriate environment to evaluate the pure HVO and nanofuels as displayed in Figure 4.3. When the droplet enters the quartz tube, it heats and ignites, which consequently leads to the formation of a diffusion flame. When the ignition is detected, characterized by the appearance of a diffusion flame, the frame is defined as t = 0 ms, and the

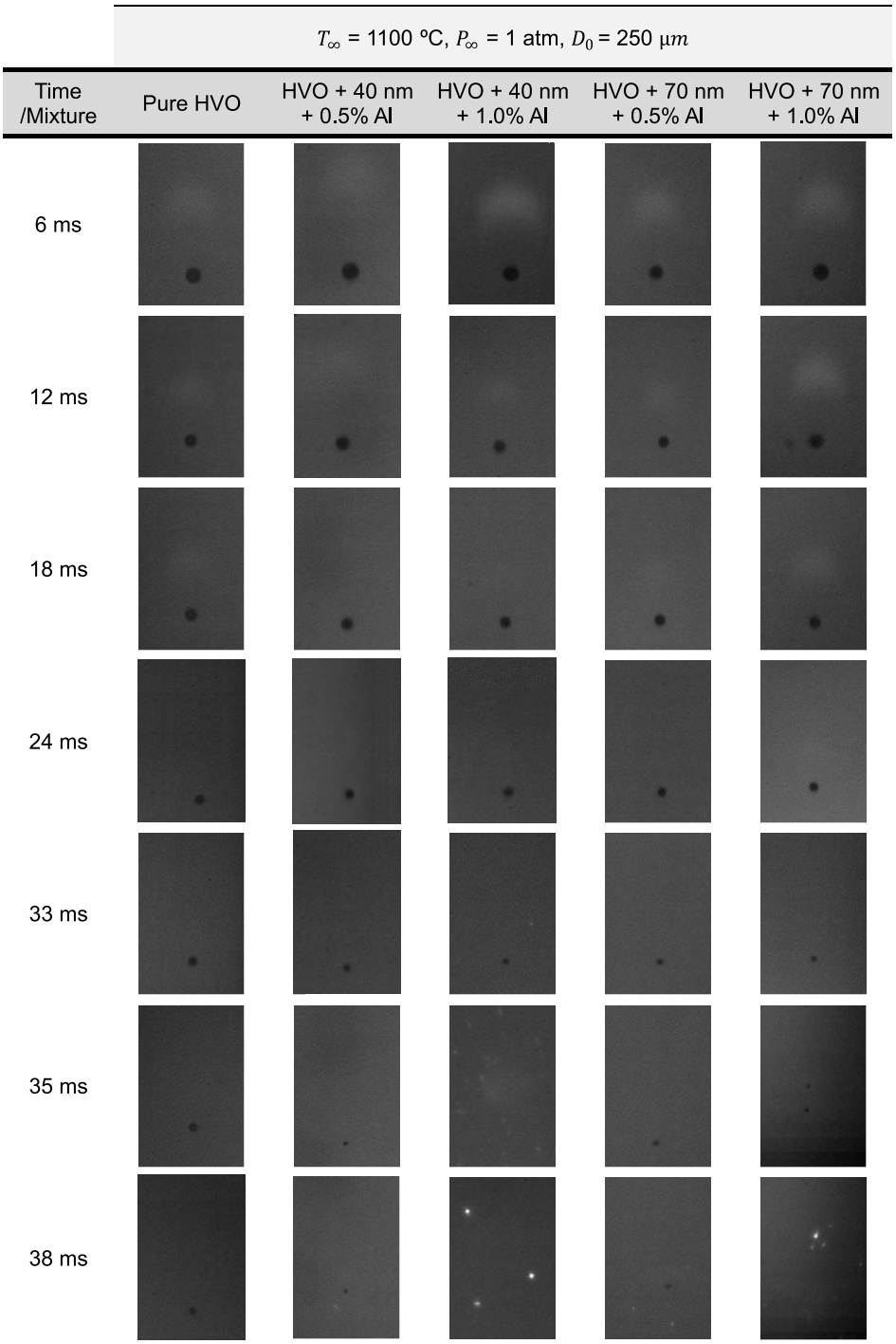

Figure 4.22: Sequence of instantaneous images of pure HVO and nanofuels at a furnace temperature at T_∞ = 1100 °C.

droplet diameter measurements begin approximately 1 cm from the injector tip. When the droplet is exposed to a high ambient temperature, vaporization arises from the surface, generating a proper proportion of fuel/air mixing and leading to droplet autoignition. As noted in the visualization description concerning pure fuels, the flame intensity is notably challenging, and a brief analysis has previously been offered. An observation in Figure 4.22 indicates that the droplet diameter reduces as time evolves and that HVO presents a longer lifetime. However, a disruptive burning phenomenon is spotted when nanoparticles are added to the

biofuel, regardless of the particle size and concentration. The nanofuels possess a shorter lifetime, and a micro-explosion indicates the end of the droplet lifetime. The detection of this event occurs when agglomerates of nanoparticles leave the primary droplet and ignite, producing intense bright spots. For a lower concentration of HVO + 40 nm + 0.5 wt.%, micro-explosions occurred at later instants compared to HVO + 40 nm + 1.0 wt.%. As shown in Figure 4.22, the micro-explosion of HVO + 40 nm + 1.0 wt.% occurs at t = 33 ms, and the micro-explosion of HVO + 40 nm + 0.5 wt.% at t = 38 ms, approximately 5 ms later. The onset of micro-explosions shows that an increase in the particle concentration and reduction in the particle size promotes the occurrence of micro-explosions earlier in the droplet lifetime, even though these phenomena only occur with a slight instant difference.

Regarding the quantitative analysis of adding aluminum nanoparticles to HVO, Figure 4.23 presents the normalized temporal history of the diameter squared of pure HVO and nanofuels at T_∞ = 1100 °C. The classical liquid droplet combustion theory states that the normalized square diameter decreases linearly with time, with a nearly constant slope defined as the burning rate (K_c). The results show that the falling droplet of pure HVO burns as a fully liquid droplet without disruptive burning phenomena. However, for nanofuels, the curves present a different behavior, indicating that the presence of nanoparticles influences the droplet size evolution. The quantitative results suggested that adding aluminum nanoparticles to HVO results in a departure from the D^2-law, agreeing with the qualitative description of nanofuel droplet evaporation and combustion, as discussed in the previous paragraphs. At the later stages of the droplet lifetime, the formation of the nanoparticle aggregates evidence a reduction in evaporation, showing a different evolution of the curve. During the steady-state phase, the droplet diameter is reduced considerably, and no micro-explosions are detected at this stage.

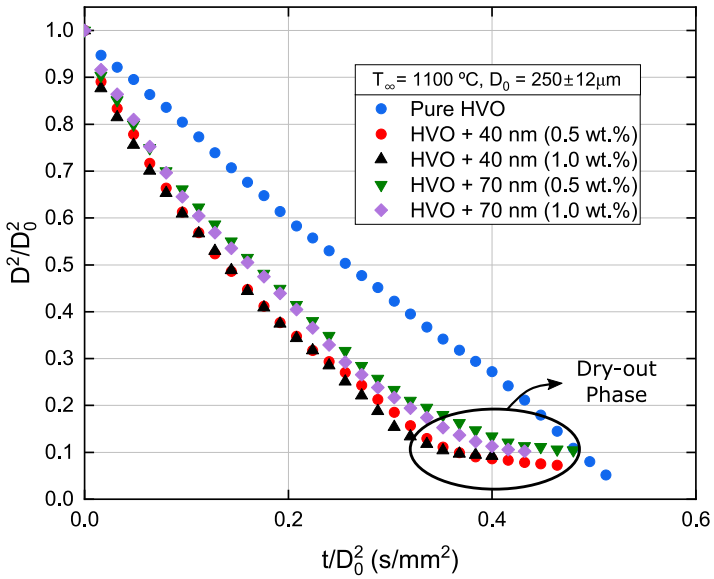

Figure 4.23: Droplet size evolution of pure HVO and nanofuel at T_∞ = 1100 °C.

The nanofuel droplet combustion displayed four different combustion phases: (i) a classical steady-state phase, (ii) a dry-out phase, (iii) a disruptive behavior phase, followed by (iv) a

particle combustion phase, characterized by the appearance of bright spots, indicating the combustion. The identification of the dry-out phase is identified when a based on a decrease in the reduction rate of the droplet diameter is evident, as depicted in Figure 4.23 marked by a black circle. Aluminum nanoparticles aggregation at the droplet surface difficult the vaporization of liquid fuel that remains at the end of the droplet lifetime. Consequently, the normalized squared diameter of the nanofuel is approximately constant for a few instants until disruptive burning phenomena are denominated as micro-explosion occurs. Micro-explosions were intensively studied for emulsions. Emulsions are composed of liquid fuels with different boiling points in certain conditions, leading to micro-explosions [29,408]. On the other hand, nanofuel is composed of a solid and liquid phase, and the phenomenon of micro-explosions is explained by a different mechanism, as will elaborated in detail later. In this respect, micro-explosions lead to secondary atomization, dispersing particle agglomerate and remaining liquid fuel, which promotes a reduction in the droplet lifetime. The nanoparticle dynamics inside the droplet affect the droplet evaporation and combustion. Comparing the nanofuels, the temporal droplet reduction curves practically overlap, where a slight difference can be detected from each particle size. However, the present results agree with the findings presented in the literature, i.e., a reduction in the particle size leads to an increase in the wet surface area when a constant particle concentration is considered. This fact promotes an increase in the evaporation rate. In this scenario, the particle concentrations seem to impact the dry-out phase.

To assess the effects of incorporating nanoparticles into biofuels and to align with the previous findings, Figure 4.24 displays the droplet lifetime of pure HVO and nanofuels at T_∞ = 1100 °C. At t = 0 s, the initial droplet diameter for all the fuels is 250 μm, and the droplet lifetime corresponds to the time of the total consumption of the primary droplet. As already mentioned, the droplet of pure HVO depicts a longer lifetime when compared with the nanofuel droplets. For the nanofuels, regardless of the size and concentration of aluminum particles, a disruptive burning phenomenon occurs, pronouncing the end of the droplet lifetime. An increase in the particle concentration leads to an earlier occurrence of a micro-explosion. Its effect on droplet lifetime is negligible for the investigated particle size range. Droplets of HVO + 40 nm + 1.0 wt.% with the highest nanoparticle concentration have the shortest burning time for the experimental conditions studied in this work.

In short, the findings suggest that regardless of the particle size and concentration, a notable improvement in biofuel burning was observed. The observed effects are predominantly attributable to the particle concentration, while particle size variation presents similar outcomes. To understand how different particle sizes affect the combustion of HVO, an investigation is carried out in terms of droplet size evolution and the burning rate of alternative jet fuel with particles in a nano and micron scale. Firstly, it should be pointed out that two furnace temperatures T_∞ = 800 °C and T_∞ = 1000 °C are considered. Consequently, the description of the pure HVO for both furnace temperatures was previously provided for the comparative analysis. For this evaluation, a low particle concentration of 0.5 wt.% and two particle sizes (40 nm and 5 μm) were considered to evaluate the influence of adding alu-

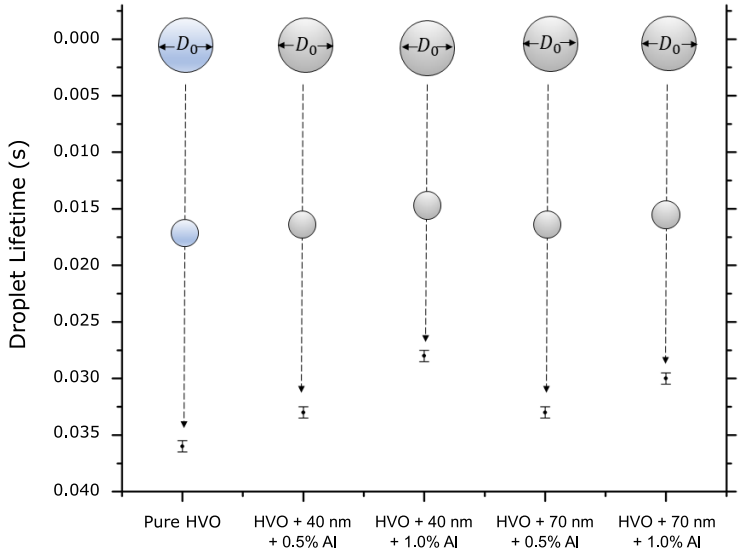

Figure 4.24: Droplet lifetime of pure HVO and nanofuels at T_∞ = 1100 °C ($D_0 = 250\mu m$).

minum particles to the biofuel.

For simplification the sequences of images presented in Figure 4.25 are exclusively concerned with the visualization of HVO + 40 nm + 0.5% Al and HVO + 5 μm + 0.5% Al at T_∞ = 800 °C and T_∞ = 1000 °C. The visualization of pure HVO for both furnace temperatures is displayed in Figure 4.16 and Figure 4.17. The sequence of images shows that the droplet diameter is reducing as time evolves, and the droplet flame presents a lower intensity due to the lack of aromatics content in HVO. The droplet enters the quartz tube, and the liquid fuel begins to be consumed no obvious particle expulsion was observed for the majority of the droplet lifetime. This leads to a preferential increase in particle concentration at the droplet surface, attributed to the interaction between heat and mass transfer. As time evolves, the solid phase becomes predominant within the droplet, and agglomeration hinders vaporization, potentially leading to local hot spots. These hot spots induce biofuel vapor nucleation, resulting in a micro-explosion and ejection of intense bright spots in several directions [237].

Disruptive burning phenomena are an interesting outcome to induce secondary atomization since the liquid and solid phases are dispersed, enhancing fuel/air mixture, reducing the droplet lifetime, and improving combustion efficiency [159, 165]. For the two furnace temperatures and particle sizes, micro-explosion appears due to the presence of particles in the biofuel. In this examination, the probability of a micro-explosion occurrence is 100% concerning HVO + 40 nm + 0.5% Al and HVO + 5 μm + 0.5% Al at T_∞ = 800 °C and T_∞ = 1000 °C. As noted in several studies presented in the literature, the appearance of micro-explosions as a consequence of adding particles to liquid fuel is evident [206, 219], as well in the previous analysis employing a higher furnace temperature T_∞ = 1100 °C. Besides the fact that both particle sizes display micro-explosions, HVO + nano-sized particles seem to disperse better than micron-sized particles, however the latter possesses micro-explosions with a higher intensity which can be related to the particle agglomeration, as shown in Figure 4.25. An

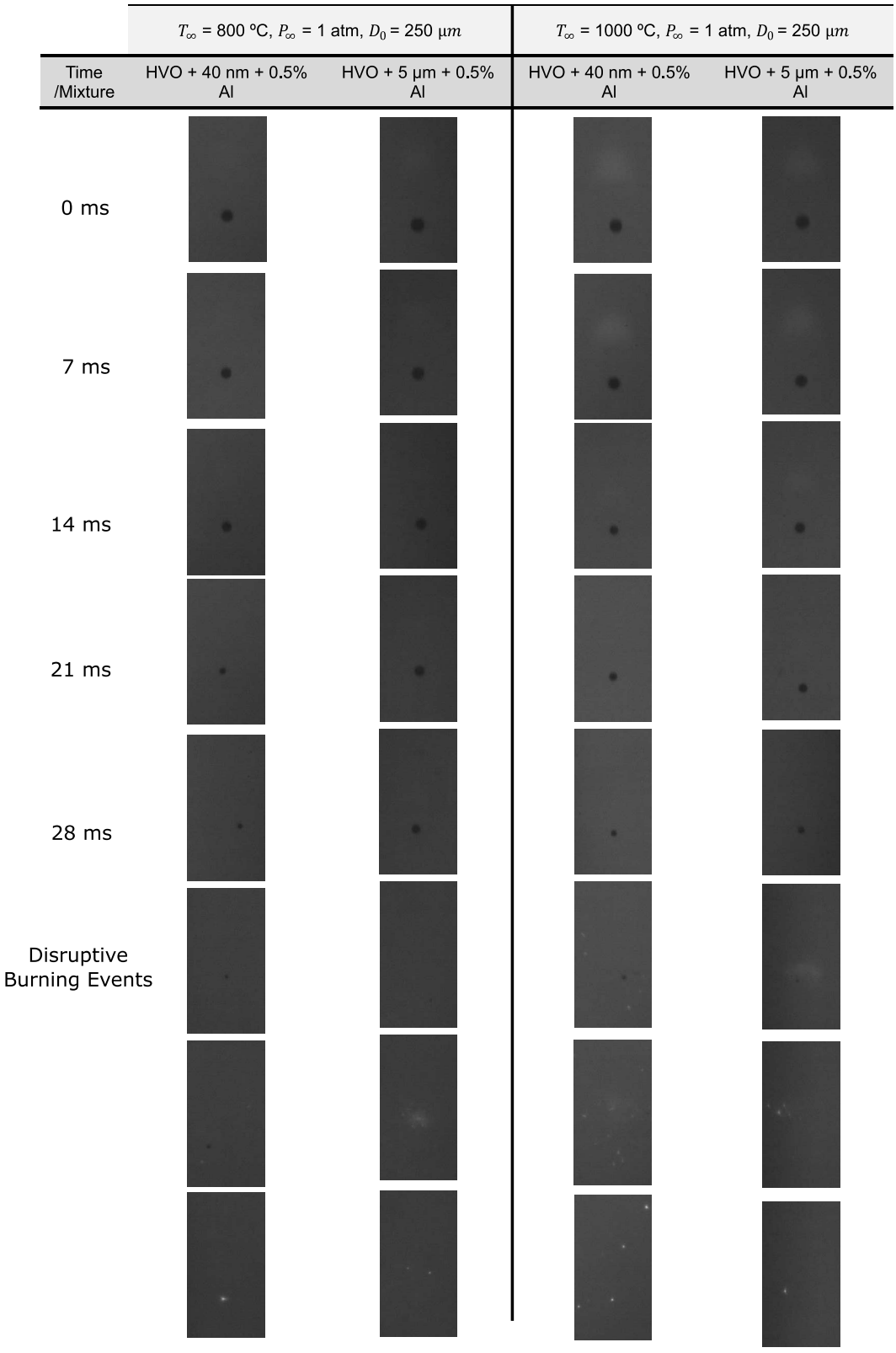

Figure 4.25: Sequence of instantaneous images of HVO + 40 nm + 0.5% Al and HVO + 5 μm + 0.5% Al at T_∞ = 800 °C and T_∞ = 1000 °C.

analysis of the micro-explosions for fuels with nano and micron particles was performed by Gan and Qiao [206]. The authors reported that micron suspension forms a densely packed, impermeable shell and nanosuspension a porous, more uniformly distributed spherical ag-

gregate that affects droplet evaporation and combustion. After the occurrence of micro-explosions, particle agglomerates are dispersed in the quartz tube environment and are projected from the explosion region and burned. The aluminum combustion characterizes this final event. The residue derived from this final event is violently projected away, ascending as the smoke tail. However, the combustion residue was not collected due to limitations on the experimental setup.

The quantitative analysis concerning the addition of particles to liquid fuel is displayed in Figure 4.26. The normalized droplet diameter as a function of the normalized time is provided for T_∞ = 800 °C and T_∞ = 1000 °C. The droplet size evolution of HVO with aluminum particles differs from pure HVO.

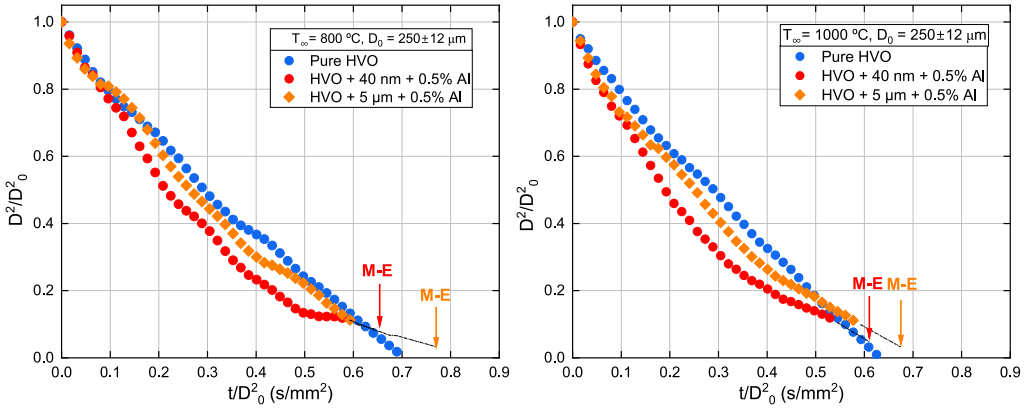

Figure 4.26: Droplet size evolution of pure HVO and HVO with nano and micron particles: a) T_∞ = 800 °C; b) T_∞ = 1000 °C.

The later presents a steady burning, however aluminum particles dispersed in HVO present a dry-out phase, where the droplet diameter does not reduce linearly with time and where a reduction of the burning rate is identified in this phase, regardless of the particle size. Figure 4.26 a) shows that the addition of nanoparticles can produce a steeper droplet size regression curve compared with pure HVO. In contrast, this effect is not observed with micron-sized particles presenting a curve closer to the HVO, indicating a lower burning rate. This observation is consistent with the highest temperature, displayed in Figure 4.26 b). It is important to highlight that at the end of the droplet size evolution curves was not possible to determine experimentally due to the considerable small size of the droplet, thus it provided an estimation where micro-explosions appear by the number of frames until this phenomenon occurs. The dry-out phase is initiated earlier under higher temperatures, indicating a more pronounced curvature in the normalized droplet diameter, e.g., in nanofuel, as shown in Figure 4.26 b). The results also show that micro-explosions, which are marked in Figure 4.26 occur later for micron-sized particles suspended in HVO, which can be related to findings reported in [409]. The authors stated that increasing the particle size increases the time to disruption since the inter-particle distance increases and decreases the surface area, which can delay the micro-explosion and be responsible for the droplet size evolution difference

compared with nanoparticles. Consequently, it is noticed that micron-sized particles in a liquid fuel present a longer lifetime even in comparison with HVO. Higher furnace temperature leads to a higher burning rate for all fuels.

To proceed with the investigation devoted to the influence of the particle size of energetic material in a liquid biofuel, the temporal evolution of the burning rate is evaluated. Figure 4.27 shows the temporal evolution of the burning rate of HVO with nano and micron particles at a) T_∞ = 800 °C and b) T_∞ = 1000 °C. Regardless of the particle size added to HVO, fluctuations in the temporal evolution of the burning rate are presented. This observation is achieved compared to pure HVO, which displays a more constant temporal evolution of the burning rate. Nevertheless, the burning rate values are significantly higher in the initial stages. However, as time evolves, a significant reduction is noticed due to the accumulation of particles within the droplet as evaporation occurs, leading to the formation of the dry-out phase.

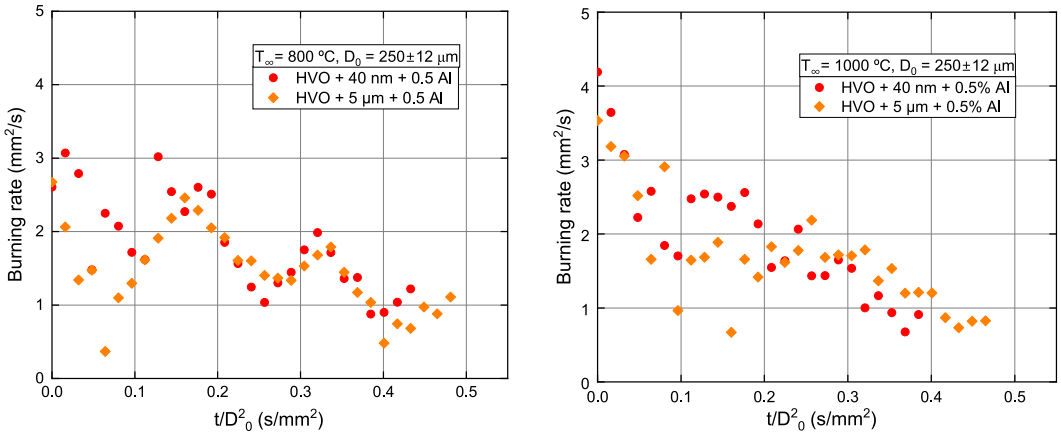

Figure 4.27: Temporal evolution of the burning rate of HVO with nano and micron particles: a) T_∞ = 800 °C; b) T_∞ = 1000 °C.

Increasing the furnace temperature increases the burning rate, as shown in Figure 4.27 b). Finally, considering the particle size range used in this work, the most encouraging results were obtained for HVO + 40 nm (0.5 wt.%), presenting a higher burning rate and lower lifetime. Based on the previous findings, the most promising results were achieved for fuels composed of HVO and nanoparticles in a size of 40 nm. Due to this, to address the influence of the particle concentration in single droplet combustion, nanofuels should be used exclusively, considering nanoparticles of 40 nm. As described in the operating conditions, low and high particle concentrations were explored, ranging from 0.2 to 4.0 wt.%. A low particle concentration is considered for values below 1.0%. On the contrary, high particle concentrations rely on values > 1.0 %. For the high particle concentration, the use of a surfactant, oleic acid (OA), was required to enhance nanoparticle dispersion in the liquid biofuel to ensure that the nanofuel remains stable during the experiments. Thus, three nanofuels with aluminum nanoparticle concentrations of 1.0 wt.%, 2.0 wt.% and 4.0 wt.% were prepared and tested. In a theoretical approach, the increment of aluminum particle concentration increases the

energy content of the fuel, a desired outcome for the mobility industry. Concerning the lower particle concentration no surfactant was added, as noticed in the description of the droplet size evolution of HVO + 40 nm + 0.5% Al provided in Figure 4.26 and Figure 4.27. Consequently, a brief description of a nanofuel droplet combustion with a lower particle concentration without using surfactant was already provided. Due to this, the following analysis is dedicated to the addition of nanoparticles in a high particle concentration to evaluate the influence of the particle, as well as the addition of the surfactant. In the conclusive analysis of these results, a comparison between low and high particle concentrations is outlined regarding the average burning rate.

For the experimental study focus on the variation of particle concentration equal to or higher than 1.0 wt.%, a surfactant-to-nanoparticle mass ratio of 1:1 was used, and two furnace temperatures were considered, T_∞ = 800 °C and T_∞ = 1000 °C. Before evaluating the combustion of the nanofuel droplets, it is essential to evaluate the combustion characteristics of pure HVO and HVO + OA droplets as a baseline for comparison. Furthermore, the highest concentration of surfactant (4.0 wt.%) used to enhance the stability of nanofuel was also employed for a clearer understanding of nanoparticle effects. As previously mentioned, the droplet size evolution of each fuel was not acquired for the heating phase due to the optical limitations of the experimental setup. The droplet autoignition occurs when the droplet leaves the injector tip and is susceptible to high temperatures. The visualization of droplet combustion of HVO + 4% OA and three nanofuels are display in Figure 4.28 and Figure 4.29 at $T_\infty = 800$ °C and $T_\infty = 1000$ °C, respectively. The visualization of the pure HVO combustion is also presented in Figure 4.16 and Figure 4.17. As stated, a high-speed camera with a high-magnification lens was used to rigorously capture the combustion process and identify potential disruptive burning phenomena. The ignition frame is defined as t = 0 ms, with a droplet diameter of approximately 250 μm. The visualization reveals that as time progresses, the droplet diameter decreases, and regardless of the furnace temperature, only including nanoparticles as an additive leads to disruptive burning phenomena. Pure HVO and HVO + 4.0 wt.% OA does not display any puffing or micro-explosion during the droplet lifetime. However, all the nanofuels studied exhibited micro-explosions with an occurrence rate of 100% at the end of their lifetime, regardless of the experimental conditions and particle concentration, as already discussed in the previous results. Since these phenomena are exclusively observed when nanoparticles are introduced, strongly suggesting their active involvement in driving its occurrence. A brief elucidation regarding these events has already been provided, and a more in-depth explanation will be presented. As discussed earlier, as the liquid fuel evaporates, the nanoparticles remain inside the droplet since no ejections are identified during the main course of the combustion. The droplet surface is receding rapidly, sweeping in the nanoparticles that remain inside the droplet. Subsequently, the concentration of the solid phase increases and begins preferentially at the droplet surface, where mass and heat exchange occur. Due to this, it is essential to confirm the relative motion of the regressing surface and particles. According to [226, 227], the Péclet Number (Pe) can evaluate this relative motion. This dimensionless number can be given by the following expression:

$$Pe = \frac{K_c}{8\mathcal{D}_{pl}}\,, \quad (4.8)$$

where K_c is the evaporation rate, and D is the particle diffusion coefficient in the liquid droplet, estimated by the Einstein-Stokes relation.

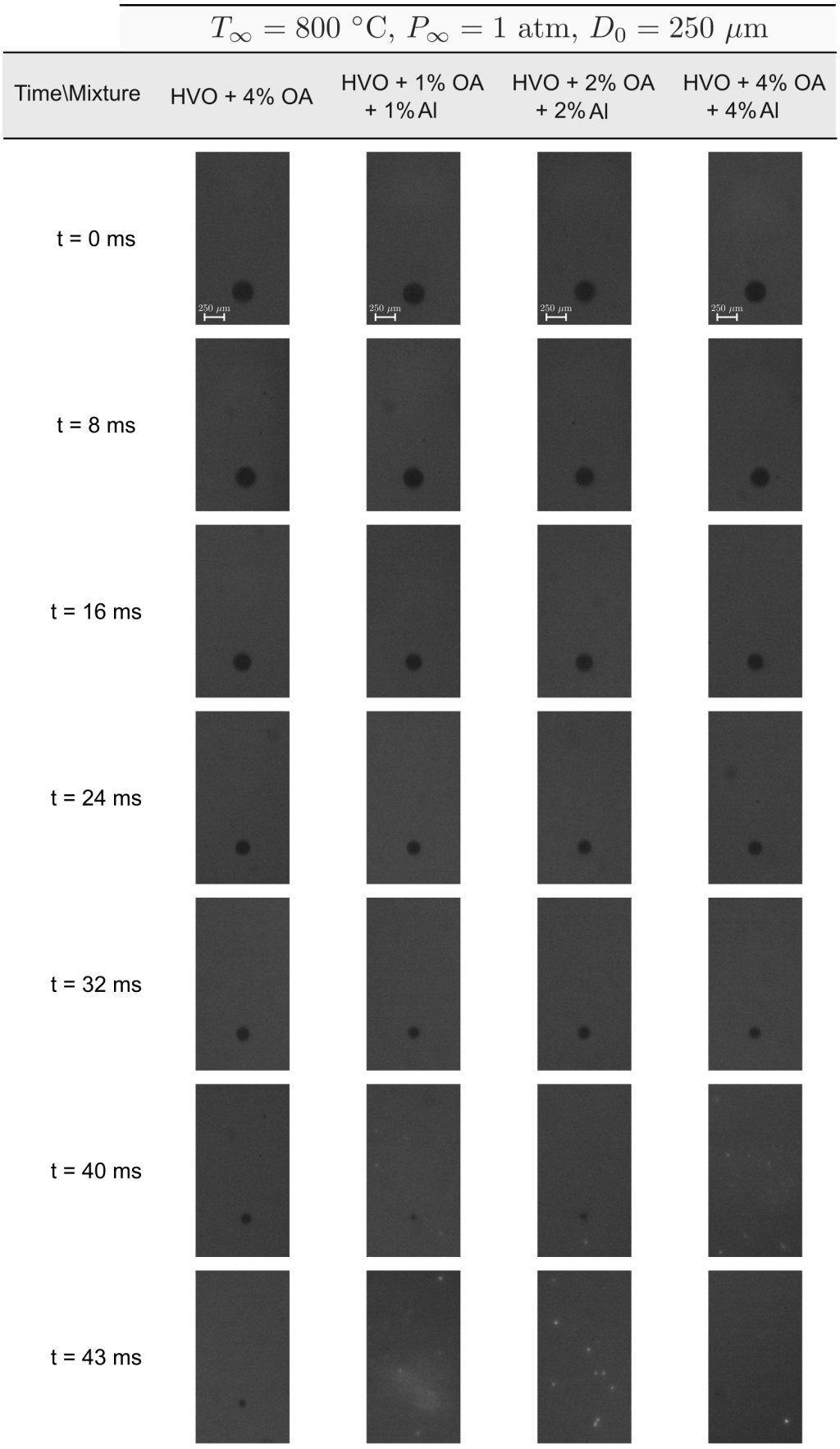

Figure 4.28: Sequence of instantaneous images of HVO + 4% OA and nanofuels at a furnace temperature of $T_\infty = 800\ ^\circ\text{C}$.

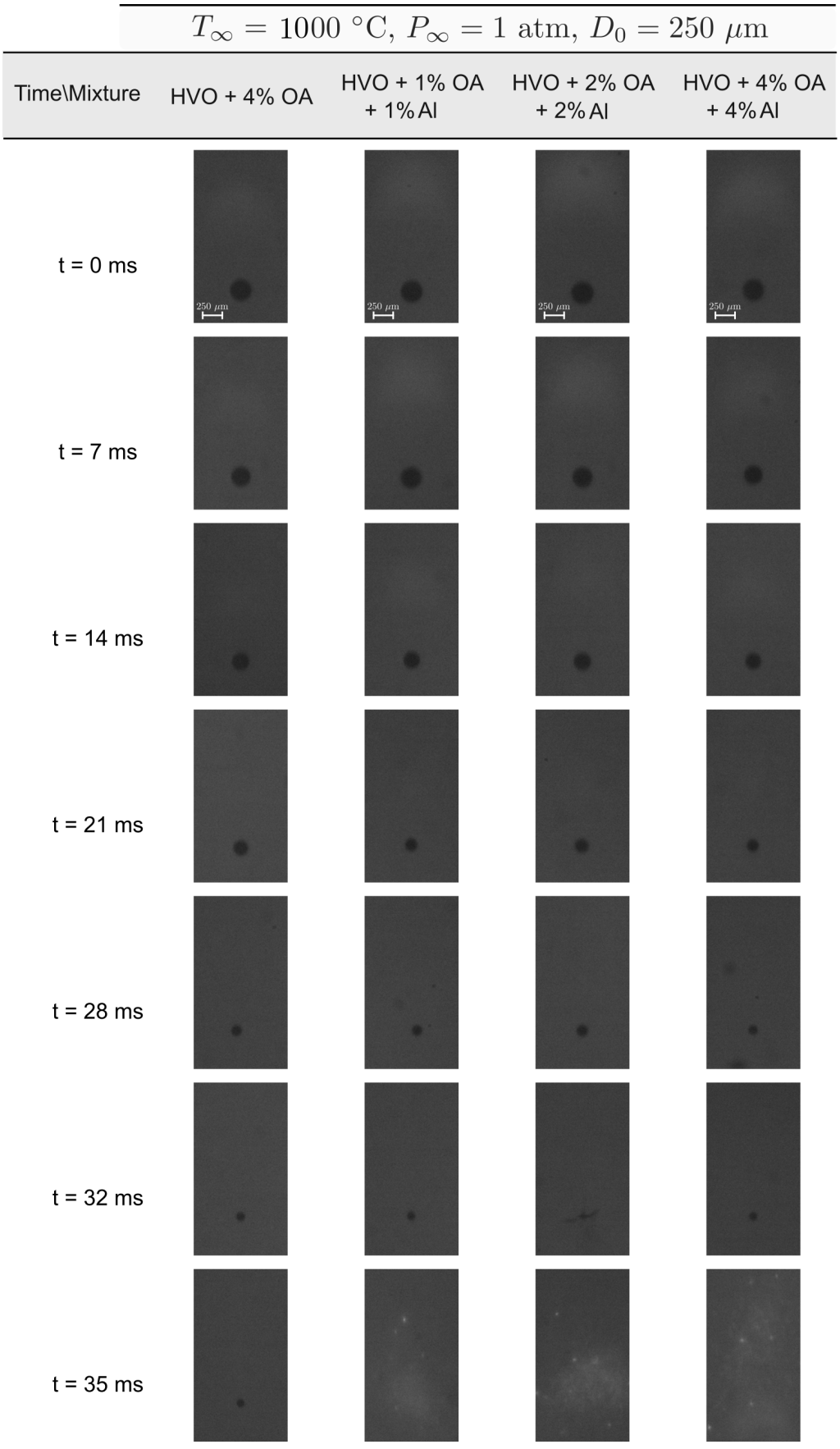

Figure 4.29: Sequence of instantaneous images of HVO + 4% OA and nanofuels at a furnace temperature of $T_\infty = 1000\ ^\circ\text{C}$.

The Einstein-Stokes relation is expressed by [226]:

$$\mathcal{D}_{pl} = \frac{k_B T_l}{6\pi\mu_l r_p}, \quad (4.9)$$

where k_B is the Boltzmann constant, T_l and μ_l are, respectively, the liquid temperature and dynamic viscosity and r_p is the particle radius. When $Pe \ll 1$, the particles have enough time to diffuse through the droplet, which leads to a packed spherical particle aggregate. On the other hand, when $Pe \gg 1$, the time to diffuse the particles through the droplet is insufficient, resulting in an accumulation on the droplet surface. Considering Equation (4.8), the values of r_p are in nanoscale, and temperature is approximately $280\ ^\circ$C acquired from the distillation curve displayed in Figure 3.4. The viscosity values were obtained from [410,411]. Due to this, an approximate value of Pe was estimated to be of the order of 1000, i.e., $Pe \gg 1$. This Pe value asserts that the particles are agglomerating at the droplet surface before notable particle redistribution occurs by diffusion. The liquid biofuel evaporates more quickly than the diffusion of aluminum particles, evidencing that convective transport dominates over diffusive transport. Consequently, as droplet evaporation proceeds, this particle agglomeration near the surface originates a thicker shell. The strength of the shell increases as its thickness becomes greater. Due to this, the shell becomes more resistant to the compressive capillary forces induced by the regression of the droplet surface. Eventually, the strength of the shell becomes greater than the compressive stress, which leads to a stop in shell shrinkage. After that, the evaporation front from the outer surface of the droplet moves inward, causing the shell to dry out and form a dry crust [236]. The shell heated up, the droplet temperature exceeds the boiling point of the liquid fuel promoting nucleation of the liquid fuel that remains inside the shell of particles [237]. Consequently, a shell is forming, becoming more resistant to the compressive capillary forces induced by the regression of the droplet surface. At some point, the shell strength overcomes the compressive stress, which ceases shell shrinkage. During this procedure, the shell is heated up hence the droplet temperature exceeds the boiling point of the liquid fuel. This promotes nucleation of the liquid fuel that remains inside the shell of particles [237]. As a result, the pressure inside the structure increases, ultimately prompting the shell to disintegrate, promoting the appearance of disruptive burning phenomena. Later, the final residue is aggressively projected away, eventually ascending as the smoke tail occurring from the aluminum combustion [237]. The occurrence of microexplosions has a notable impact not only on the duration of the droplet lifetime but also on atomization, as it enhances the dispersion of the solid phase. Unfortunately, the available experimental setup does not facilitate collecting combustion residues or measuring heat released by nanoparticles. These aspects are crucial for evaluating their impact on emissions and potential damage to the combustion chamber.

Figure 4.30 shows the droplet size evolution of pure HVO, HVO with the addition of 4.0 wt.% of OA at a) $T_\infty = 800\ ^\circ$C and b) $T_\infty = 1000\ ^\circ$C. droplet combustion of pure HVO and HVO + 4.0 wt.% OA for both furnace temperatures is in good agreement with the D^2-law, without the

existence of disruptive behavior phenomena, as noted previously. The maximum standard deviation for the curves of HVO + 4.0 wt.% OA is 0.0019 mm^2/mm^2. Concerning the droplet size evolution of HVO + 4.0 wt.% OA, a near overlap with the temporal history of the diameter squared of pure HVO for both furnace temperatures is noticed. The most pronounced difference in the curves is displayed at the later stages of the droplet lifetime for $T_\infty = 800$ °C for diameters below D^2/D_0^2 = 0.25. This results in a slight departure between pure HVO and HVO + 4.0 wt.% OA resulting in a small extension of the lifetime of the HVO with surfactant. The small difference in the volatilities of OA can be attributed to this phenomenon since the boiling point of oleic acid is 360 °C, whereas HVO ranges from 180 to 308 °C, resulting to the preferential gasification of the more volatile component, i.e., HVO [142]. As evaporation occurs, the relative concentration of OA in the droplet increases, eventually influencing the combustion behavior after reaching a critical level. On the other hand, a distinct behavior is noticed for a higher furnace temperature. This leads to the hypothesis that preferential gasification is suppressed at high furnace temperatures. This outcome is highly promising since adding small concentrations of OA significantly increases the stability of nanofuels without jeopardizing the burning characteristics of HVO. Similar findings were already reported by Javed et al. [221, 412]. The authors investigated the impact of adding small concentrations of oleic acid to n-heptane and kerosene droplets at high temperatures. The authors reported that its influence is negligible in the combustion behavior compared to pure fuels.

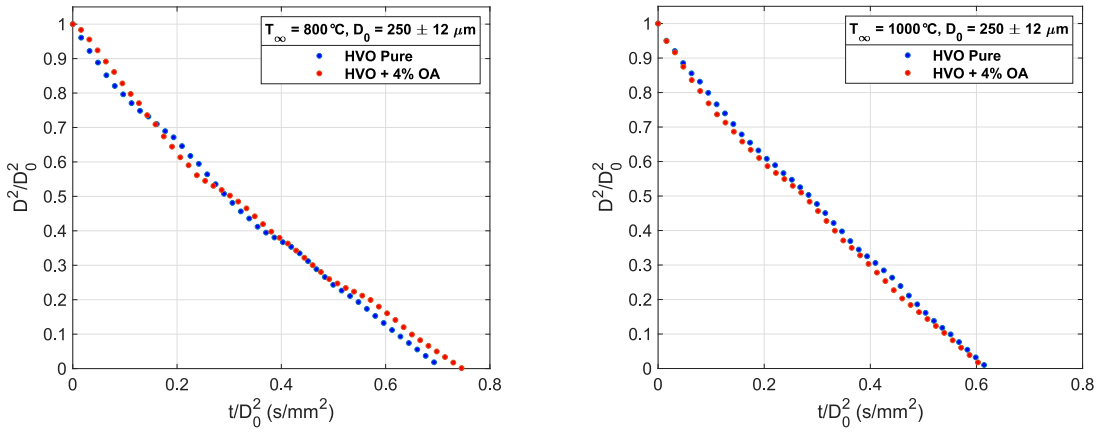

(a) (b)

Figure 4.30: Droplet size evolution of pure HVO, HVO with the addition of 4.0 wt.% of OA: a) $T_\infty = 800$ °C; b) $T_\infty = 1000$ °C.

Since the combustion characteristics of HVO droplets with 4.0 wt.% OA did not show significant differences compared to pure HVO droplets, no further concentrations were explored, and the independent role of nanoparticles can be analyzed. Figure 4.31 shows droplet size evolution of pure HVO, HVO with the addition of 4.0 wt.% of OA and the different nanofuels studied for a) $T_\infty = 800$ °C and b) $T_\infty = 1000$ °C. The maximum standard deviation for all curves featured in Figure 4.31 a) is 0.0038 mm^2/mm^2, and for all curves depicted in Figure 4.31 b) it is 0.0063 mm^2/mm^2. Similar to the previous findings, adding nanoparticles to the HVO leads to a departure from the D^2-law. In addition, during steady-state combustion, the droplet burning rate increases, regardless of particle concentration and fur-

nace temperature conditions. A classical steady-state, dry-out, disruptive behavior is evident. The steady-state and dry-out phase identification for both temperatures is displayed in Figure 4.31. Regardless of the nanoparticle concentration, all the nanofuels studied presented a similar droplet size evolution. This effect can be attributed to radiation absorption by the aluminum nanoparticles, as highlighted in the literature as one of the mechanisms presented in nanofuel combustion.

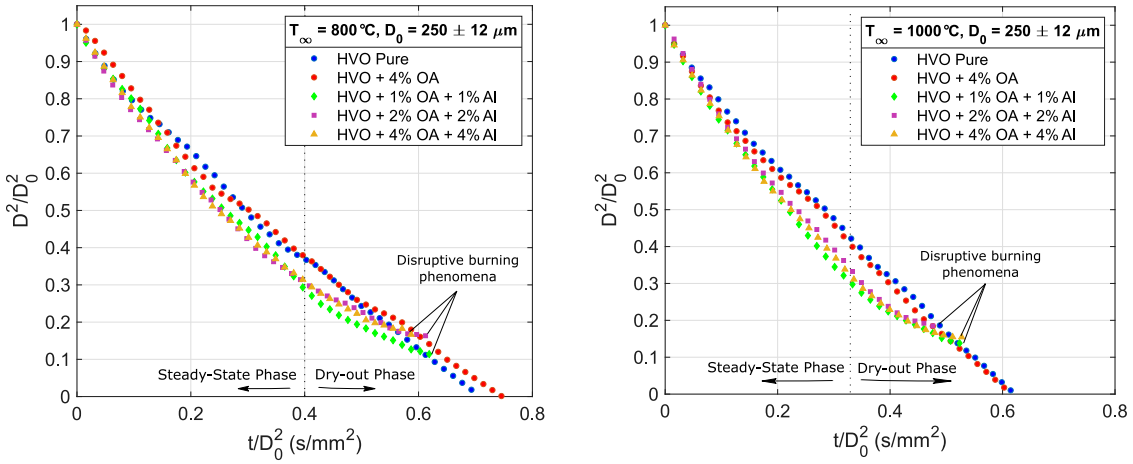

Figure 4.31: Droplet size evolution of pure HVO, HVO with the addition of 4.0 wt.% of OA and the different nanofuels studied for: a) $T_\infty = 800$ °C; b) $T_\infty = 1000$ °C.

Radiation absorption can increase the energy budget available for liquid fuel evaporation. Thus, increasing the particle concentration increases the quantity of nanoparticles, which will not produce any noticeable improvement if the droplet already absorbs all the incoming radiation energy. These results indicate the potential use of nanofuel at low particle concentrations. As noticed a particle concentration of 1.0 wt.% of aluminum nanoparticles provides a substancial enhancement in the burning rate, particularly during the steady-state, offering a reduction of the droplet lifetime, while ensuring a better suspension and long lasting stability of the nanoparticles on the base fuel. In addition, using nanofuel with low particle concentration is more cost-effective and reduces equipment wear, which is crucial to address their viability for real-world application. Concerning the dry-out phase, its onset is approximately at t/D_0^2 = 0.4 s/mm^2 and t/D_0^2 = 0.35 s/mm^2 for T_∞ = 800 °C and T_∞ = 1000 °C, respectively. This conclusion is obtained qualitatively based on the curvature, and there is no precise evaluation method. The dry-out phase appears due to the solid phase of a nanofuel that remains inside the droplet as the liquid phase is evaporation. With time, resistance to the liquid fuel is developed, resulting in a reduction rate of the droplet diameter. Besides that, the dry-out phase appears more influenced by furnace temperature, where the particle concentration causes a negligible effect. The onset of the disruptive burning phenomena seems to have a minimal influence in the analysis concerning high particle concentration, as shown in Figure 4.31. Moreover, a specific behavior is identified in comparison with the micro-explosion provided by the fuels using nano and micron-size particles without the use of the surfactant. This observation suggests that the addition of surfactant in the occurrence

of disruptive burning phenomena can promote the efficiency of the process, as will be discussed in the subsequent section.

For comparison purposes between the nanofuels at two furnace temperatures, Figure 4.32 shows the average burning rate. Instead of displaying the droplet burning rate as a function of time, it was defined to present the average burning rate, as given the circumstances, the latter introduces much more useful information regarding the burning behavior of isolated droplets. To correctly investigate the enhancement in the droplet burning rate, this was calculated using its average value and disregarding the dry-out phase, i.e., for D^2/D_0^2 < 0.3. For pure HVO and HVO + 4.0 wt.% OA, regardless of the furnace temperature, the maximum standard deviation is 0.334 mm^2/s and 0.369 mm^2/s, respectively. For the nanofuels, the maximum standard deviation for the burning rate is 0.55 mm^2/s. This analysis involves nanofuel with a particle size of 40 nm and low and high particle concentrations. The latter also includes the surfactant addition. It can be noticed that the improvement in the burning rate is more notorious for higher furnace temperatures related to more radiation energy being transmitted from the DTF walls. This observation is following the droplet size evolution previously presented. Additionally, the results show that the lowest particle concentration produces a minor enhancement in the burning compared with HVO. Moreover, the burning rate of HVO + 4% OA is quite similar to the HVO. The influence of surfactant appears to contribute to the burning rate, where there is a slight difference in the burning rate as the furnace temperature varies for HVO + 0.5% and HVO + 1.0%. This effect was noticed when surfactant was added to the particle concentration of 1.0%.

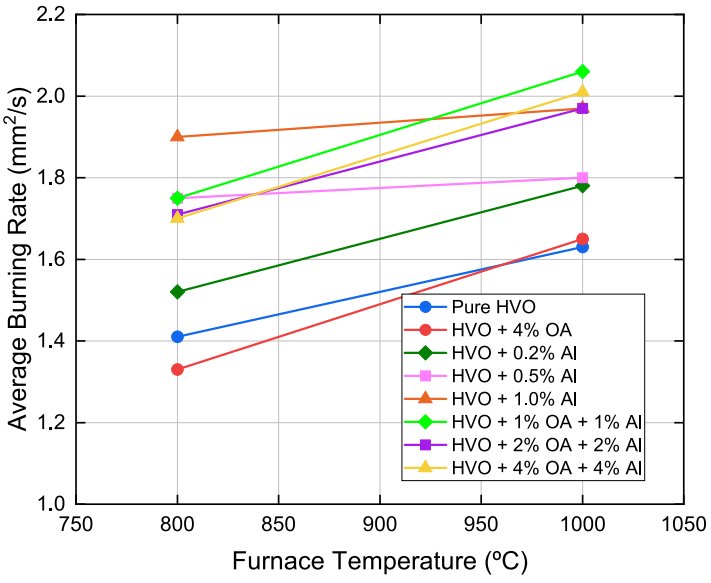

Figure 4.32: Average droplet burning rate for the steady-state combustion phase ($D^2/D_0^2 > 0.3$) of pure HVO, HVO with the addition of 4.0 wt.% of OA and the different nanofuels with a particle size of 40 nm studied as a function of the furnace temperatures T_∞ = 800 °C and T_∞ = 1000 °C.

As previously discussed in the analysis of high particle concentration, an increase in the amount of nanoparticles inside the droplet does not result in an enhancement of the burning rate.

4.3.3 Disruptive Burning Phenomena

The previous findings reported disruptive burning phenomena when aluminum particles were added to the liquid biofuel regardless of the furnace temperature, particle size, and concentration. Concerning the studies present in the literature, the majority involving nanofuels or micron-sized particles stably suspended in a liquid fuel are developed in a fiber suspension technique [29,195,393]. This experimental method can act as a nucleating surface, promoting heterogeneous boiling related to a certain low degree of superheat. Consequently, a continuous bubble formation potentially leads to a disruptive burning phenomenon [29]. Thus, the present work confirms that disruptive burning phenomena can be detected without using the suspended droplet method due to the addition of particles. Guerieri et al. [413] developed a study using a falling droplet method, using an aluminum additive, and also spotted disruptive burning events. Disruptive burning phenomena are characterized by two outcomes: puffing and micro-explosion. According to Javed et al. [219], a micro-explosion s is a complex process involving multicomponent, multiphase, and multiscale interactions. Prior to the occurrence of micro-explosion, puffing was commonly noticed. The micro-explosions correspond to the total disintegration of the primary droplet, while on the other hand, puffing in most studies involving emulsions is defined as the release of volatile components, resulting in a partial disintegration [159,165].

Since the nanoparticles offer the most promising outcomes, attention is directed toward their effect on the single droplet combustion process, particularly at the end of the dry-out phase, where disruptive burning phenomena are observed. These events promote secondary atomization, dispersing particle agglomerate and remaining liquid fuel, promoting a reduction in the droplet lifetime. Despite the fact that the behavior of micro-explosions is stochastic, a quantification of these events is required. The analysis of the disruptive burning phenomena in the present study focuses on a nanofuel droplet predominantly composed of fuel, a liquid phase, HVO, and solid aluminum nanoparticles in different concentrations. In addition, falling droplets are inserted into a high temperature provided by the drop tube furnace. Due to this, the liquid fuel evaporates, and as time proceeds, the nanoparticles persist inside the droplet and accumulate at the droplet surface. Due to this, the nanoparticle concentration increases and affects the biofuel evaporation, leading to a slower reduction of the droplet diameter at the end of its lifetime. This hinders biofuel vaporization, and as a result, the droplet surface behaves as a ”shell”, increasing the droplet temperature and leading to the nucleation of the liquid fuel. As a result, the pressure inside the droplet rises, ultimately prompting the shell to explode, resulting in a puffing or micro-explosion.

An investigation dedicated to the disruptive burning phenomena of a nanofuel using a particle size of 40 nm and different particle concentrations, and two furnace temperatures is considered to better understand their nature and phenomenology. Puffing and micro-explosions were studied using a falling droplet method to avoid interfering with intrusive elements. A preliminary study is presented focus on HVO + 40 nm + 1.0% Al at T_∞ = 800 °C and T_∞ = 1000 °C in terms of visualization, micro-explosions fragments and duration. A visualization

of the end of droplet lifetime of HVO + 40 nm (1.0 wt.%) at T_∞ = 800 °C is displayed in Figure 4.33. The instant t = 0 ms is defined as the micro-explosion moment. As can be seen, the primary droplet disintegrates, and its original shape is no longer spherical. However, prior to this event, the droplet deforms, and puffing is detected at t = -0.9375 ms. At this point, the droplet did not release any noticeable fragments. On the other hand, when the micro-explosion occurs, several fragments were released with smaller dimensions than the primary droplet, as shown at t = 0.3125 ms. As time proceeds, the number of fragments increases, and bright spots are identified as the aluminum combustion. From t = 0.625 ms to t = 0.9375 ms, the ignited fragments are dispersed in the quartz tube and appear to rotate in turn of the explosion position. During this process, the ignited fragments ascend, causing their detection to be progressively more challenging (t = 1.5625 ms). Moreover, a substantial portion of the deformed droplet remains visible, with minimal change in its position. The ignition of this part, initiated at t = 5.625 ms, is noticeable at its surface brightness. As time progresses, an intense bright spot appears, which gradually extinguishes. Finally, a combustion residue is violently projected away, ascending as the smoke tail.

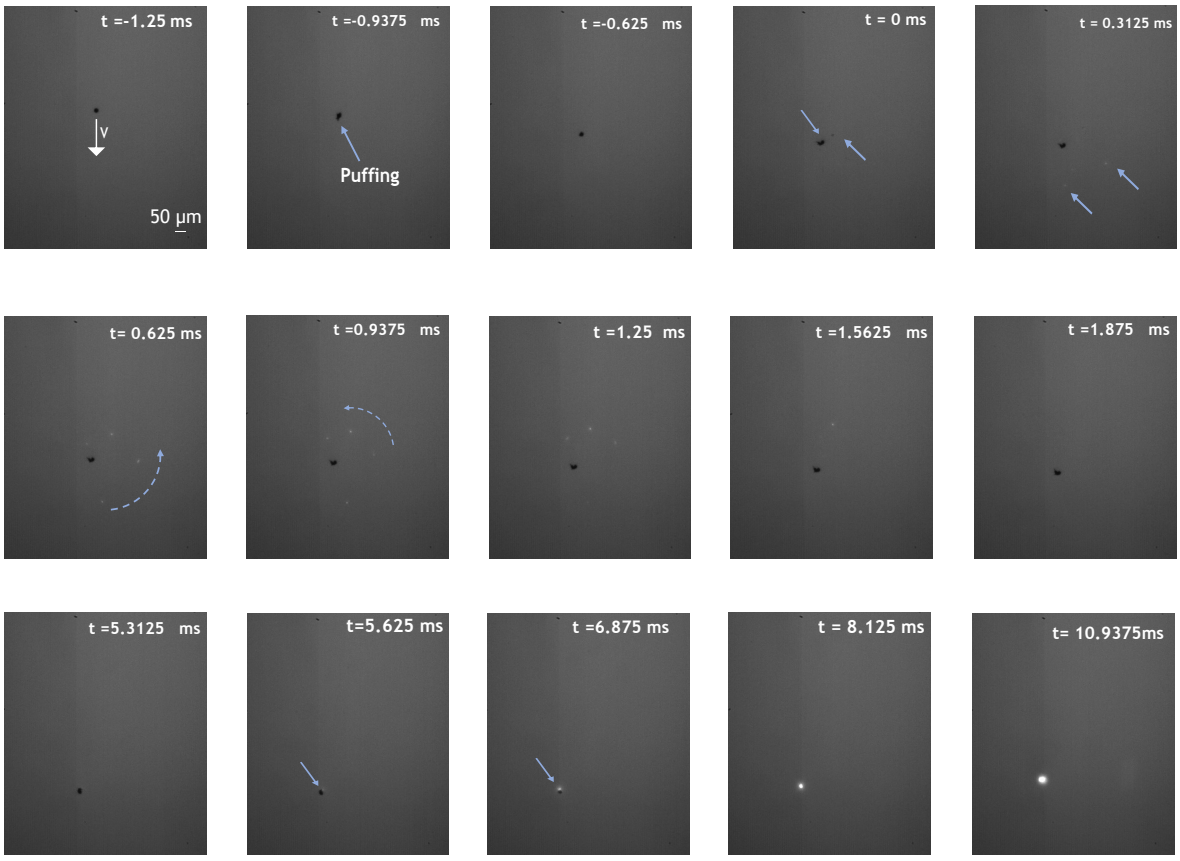

Figure 4.33: Disruptive burning phenomena for HVO + 40 nm (1.0 wt.%) at T_∞ = 800 °C, where t = 0 ms corresponds to the beginning of the micro-explosion.

Figure 4.34 shows the development of the disruptive events occurred at T_∞ = 1000 °C. As noted before, prior to the micro-explosion (t = 0 ms), puffing is evident where at least two fragments are ejected. When the micro-explosion begins, a large number of ignited fragments are released in various directions, promoting intense bright spots inside the quartz tube. The ignited fragments rotate and ascend, possessing different dimensions. The largest

fragment from the micro-explosion is divided into two elements, as displayed in t = 1.5 ms. As a result, another intense explosion occurs from t = 1.5 ms until t = 3.0 ms, leading to the appearance of more small fragments projected from the initial position. Subsequently, these fragments ignite, and finally, the droplet totally disintegrates.

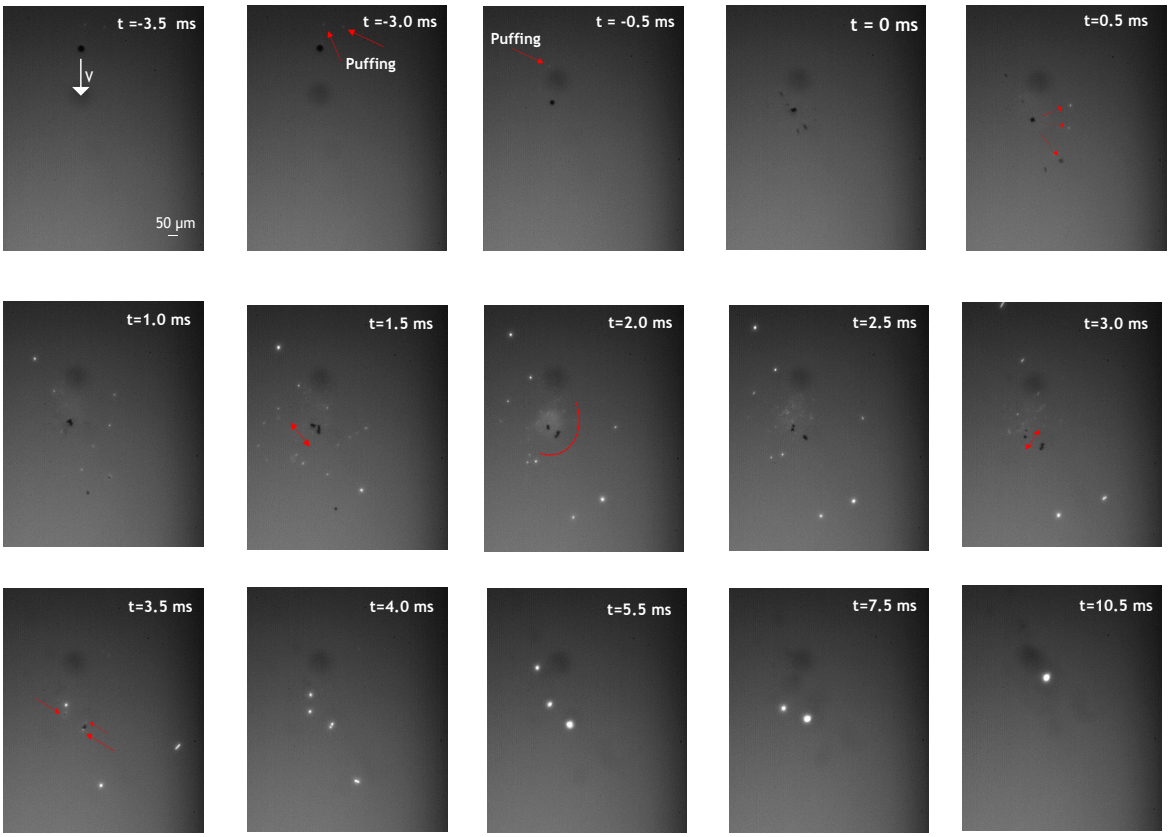

Figure 4.34: Disruptive burning phenomena for HVO + 40 nm (1.0 wt.%) at T_∞ = 1000 °C, where t = 0 ms corresponds to the beginning of the micro-explosion.

When comparing the phenomena of puffing and micro-explosions as a function of furnace temperature, it was noticed that both events occur for the operating conditions used in the present study. Nevertheless, the phenomena are more intense at T_∞ = 1000 °C, where the primary droplet disintegrates into large fragments that eventually disrupt into multiple smaller particles that eventually lead to its ignition. At the lowest furnace temperature, a considerable portion of the droplet deforms and, as time evolves, ignites as a single fragment. In this context, evaluating the maximum number of fragments released from the micro-explosions is essential. This investigation was performed and is provided in Figure 4.35. In this case, a nanofuel of HVO + 40 nm + 1.0% Al explores the maximum number of fragments after the micro-explosion occurrence at the two furnace temperatures. This quantification method for micro-explosion intensity is an empirical approach based on the image data processing previously mentioned. It plays a relevant role in the nanofuel field in understanding the effectiveness of fuel atomization and droplet lifetime. The analysis included fragments only when their size was larger than the pixel size. To evaluate the influence of the furnace temperature on the micro-explosion intensity, a sample of 10 micro-explosions was examined

and randomly sorted. In virtue of these observations, micro-explosion intensity is related to the number and distribution of fragments ejected from the primary droplet in the present work. The blue dashed line corresponds to the average value of fragments number at T_∞ = 800 °C, and the red dashed line at T_∞ = 1000 °C, respectively.

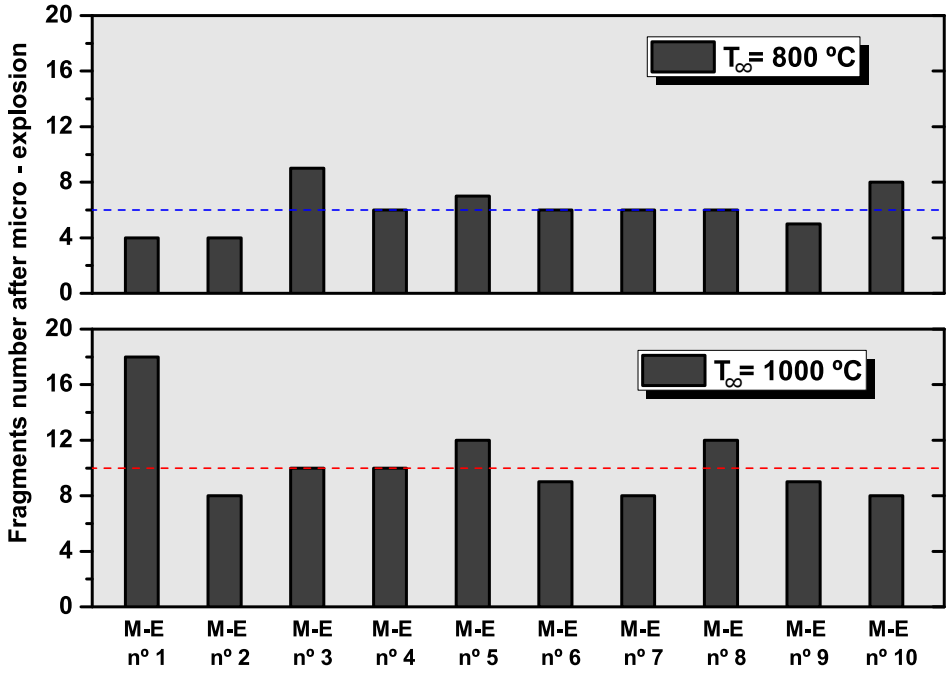

Figure 4.35: Number of fragments as a quantification method for micro-explosion intensity at different furnace temperatures for HVO + 40 nm (1.0 wt.%).

The presentation of these lines is merely to ease the comprehension of data. The results indicate that the number of fragments is higher for the highest furnace temperature. As discussed in the visualization, at T_∞ = 1000 °C, observations indicated that the largest fragments could disintegrate into smaller components, leading to an effective dispersion. The dispersion of the particles greatly enhances the surface area of the final agglomerates and consequently increases the air/fuel mixture of the solid phase fuel. Furthermore, at T_∞ = 800 °C, several micro-explosions release a large fragment that burns individually without disrupting several elements after the explosion. This observation could be related to the increase in the furnace temperature, which allows a quick accumulation of aluminum nanoparticles at the droplet surface, consequently increasing its temperature and promoting an intense explosion. To gain a better understanding of this subject, an analysis of the micro-explosion lifetime is performed. Figure 4.36 shows a relation between the maximum number of fragments and the micro-explosion duration. Each color point corresponds to a micro-explosion, where the red points correspond to T_∞ = 1000 °C and blue points correspond to T_∞ = 800 °C. It is essential to mention that 20 micro-explosions were considered due to the limitation in the field of view and the micro-explosion tracking. A clear trend was challenging to notice due to unpredictability related to the phenomenon and the influence of temperature on the extinction of the fragments.

The majority of micro-explosions occurred from approximately 0.010 s to 0.020 s. It appears

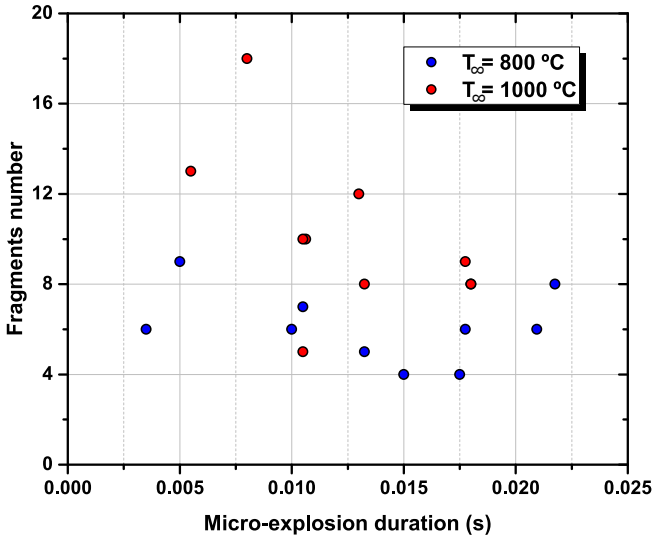

Figure 4.36: A relation between the number of fragments with the micro-explosion duration different furnace temperature for HVO + 40 nm (1.0 wt.%).

that the highest number of fragments generated by the micro-explosions is associated with a shorter duration. However, further studies should be conducted using a larger sample and additional furnace temperatures. In a falling droplet method, the convective environment and the flame position could be pertinent factors that potentially influence the micro-explosion events. In light of this, Figure 4.37 shows the number of fragments at each region of interest for the two furnace temperatures. The purpose is to understand if the flame position affects the onset of the micro-explosions. The red circle displayed in the center of the image represents the explosion position, and based on this, four regions (upper side - right and left; lower side - right and left) were delimited with a maximum length of 500 pixels. Thus, the upper side has an opposite direction to the downward movement of the droplet, whereas the lower side follows the droplet motion. First, it is important to highlight that the number of fragments presented in Figure 4.37 is only referent to the instant after the micro-explosions when the fragments were spotted. Therefore, contrary to the explanations provided earlier, the number of fragments for T_∞ = 800 °C seems higher. This observation is due to the identification of fragments immediately following the micro-explosions, and as noticed in Figure 4.34, as the time proceeds for a higher furnace temperature, the largest fragments tend to disrupt, producing more fragments with reduced time. A total of 60 fragments were considered, and different colors represent the results for the furnace temperature. The results suggest that neither side has a considerable number of fragments to distinguish. However, the lower side possesses a higher number of fragments. Therefore, it was noticed that the droplet flame position does not affect the disruptive event. At the moment of a micro-explosion, the droplet flames are already extinguished, being easily identified on the upper side.

The impact of the furnace temperature was already described in detail. However, as noted in the sequences of images provided regarding the combustion of nanofuel, particle concentration seems to play a relevant role in these phenomena.

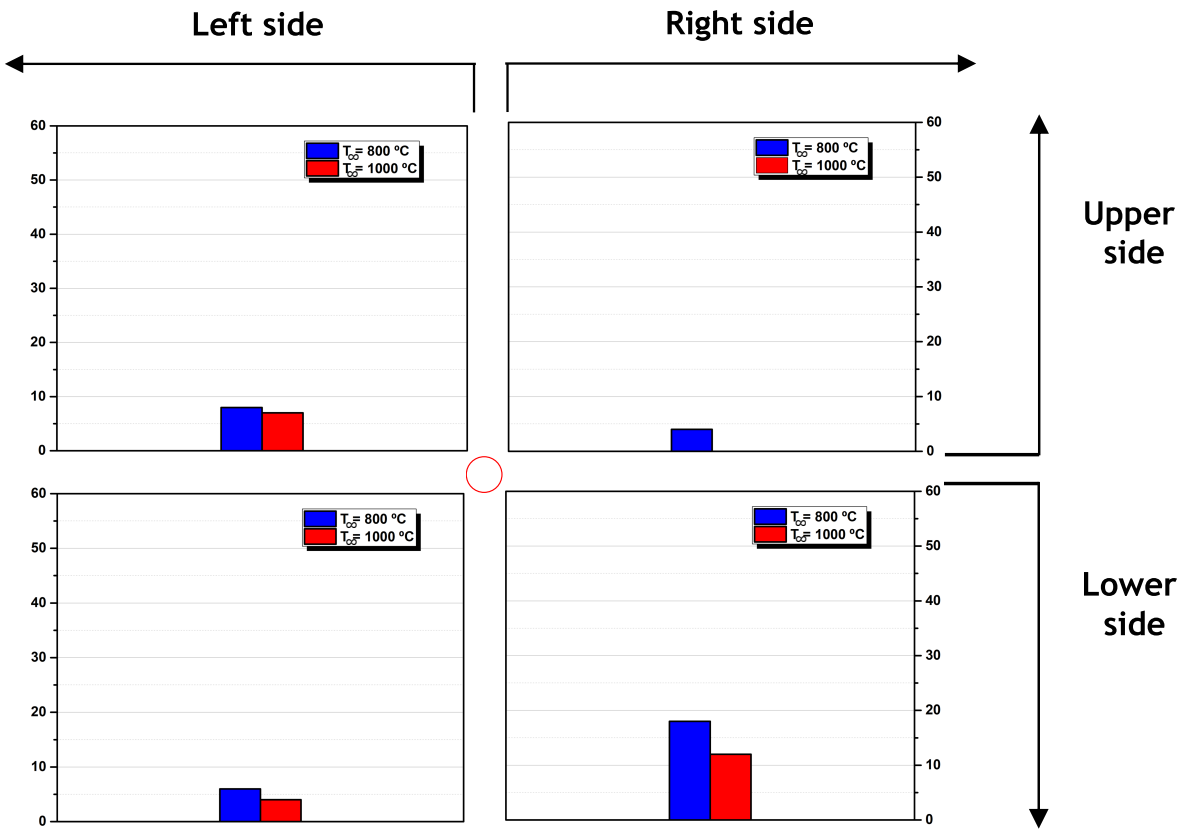

Figure 4.37: Number of fragments at each region of interest after the micro-explosion for HVO + 40 nm (1.0 wt.%).

Thus, the micro-explosion intensity is evaluated for three particle concentrations: 0.2, 0.5, and 1.0 wt.%. Figure 4.38 shows the micro-explosions intensity as a function of the particle concentration for T_∞ = 800 °C and T_∞ = 1000 °C.

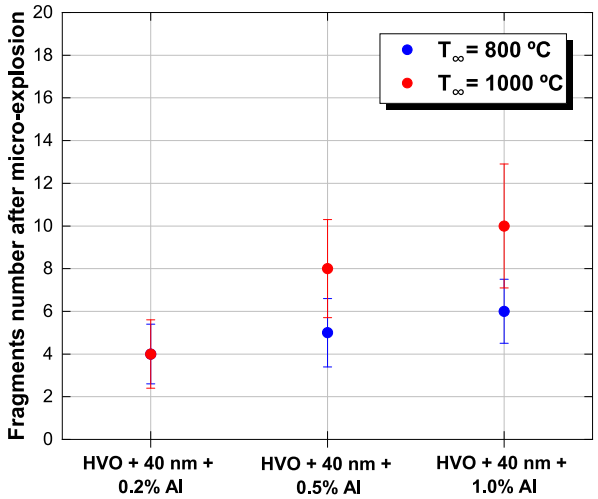

Figure 4.38: Number of fragments as a quantification method for micro-explosion intensity as a function of the particle concentration at different furnace temperatures.

For this analysis, 10 micro-explosions were considered for each particle concentration. The results show that increasing the nanoparticle concentration leads to an increase in the number of fragments and the projection distance. However, a weaker fragmentation occurs for

lower concentrations (0.2 wt.%), indicating a decrease in the micro-explosion intensity. For a concentration of 0.2 wt.%, no significant difference between the furnace temperature is noted concerning the micro-explosion. Nevertheless, increasing the particle concentration, it is observed that the micro-explosion intensity increases as the furnace temperature increases. This can be attributed to the higher amount of particles in the droplet, which allows for a higher dispersion and an increase of the nucleation sites for the onset of this event. In addition, a higher furnace temperature allows for ease of particle combustion. Similar findings concerning the increase of micro-explosion intensity with the increase of particle concentration were provided by [238, 414, 415].

The quantification of micro-explosions for high particle concentration was not carried out due to the limitations in the samples for this condition. Consequently, only the visualization is provided for particle concentrations of 1.0, 2.0, and 4.0 wt.%. This visualization also reveals the influence of adding surfactant to a nanofuel. Figure 4.39 and Figure 4.40 shows the sequence of images regarding the influence of high particle concentration at T_∞ = 800 °C and T_∞ = 1000 °C, respectively. A time interval of 1 ms separates the frames in each sequence.

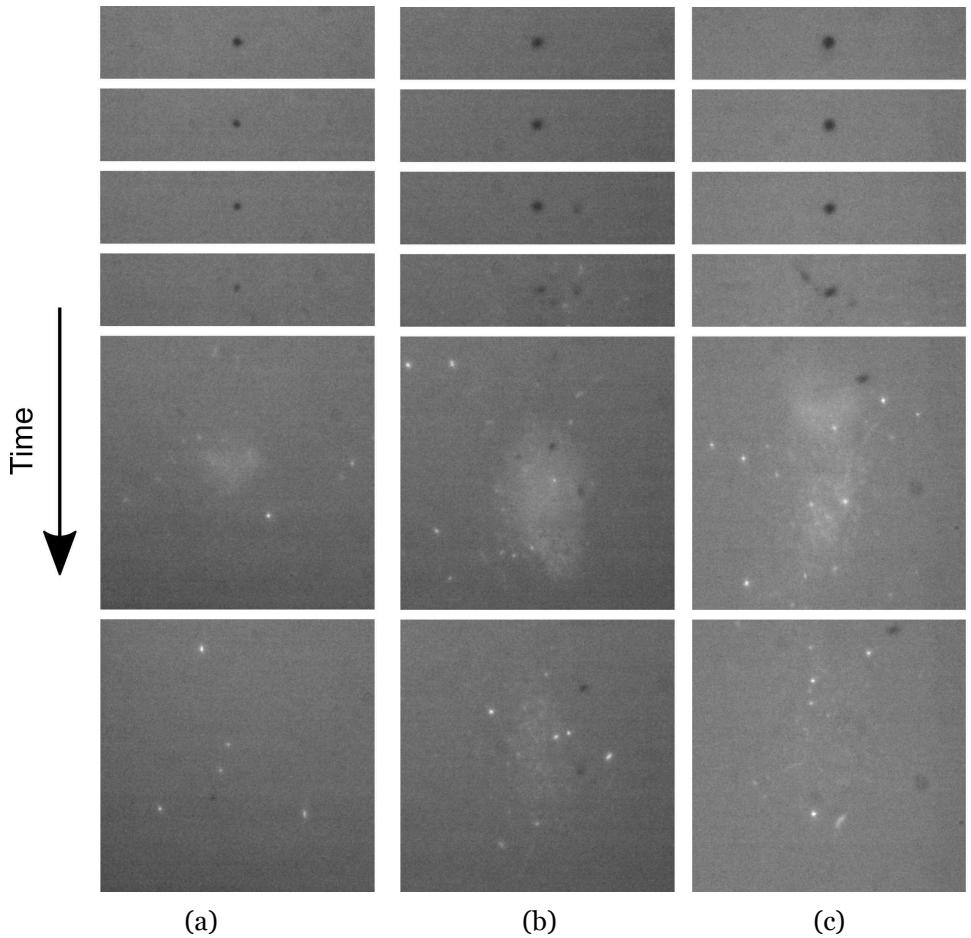

Figure 4.39: Micro-explosions at $T_\infty = 800$ °C for different nanofuels: a) HVO + 1% OA + 1% Al; b) HVO + 2% OA + 2% Al; c) HVO + 4% OA + 4% Al.

Particle ejection and droplet expansion are spotted regardless of particle concentration and furnace temperature. Particle ejection is the most commonly observed, where a small amount

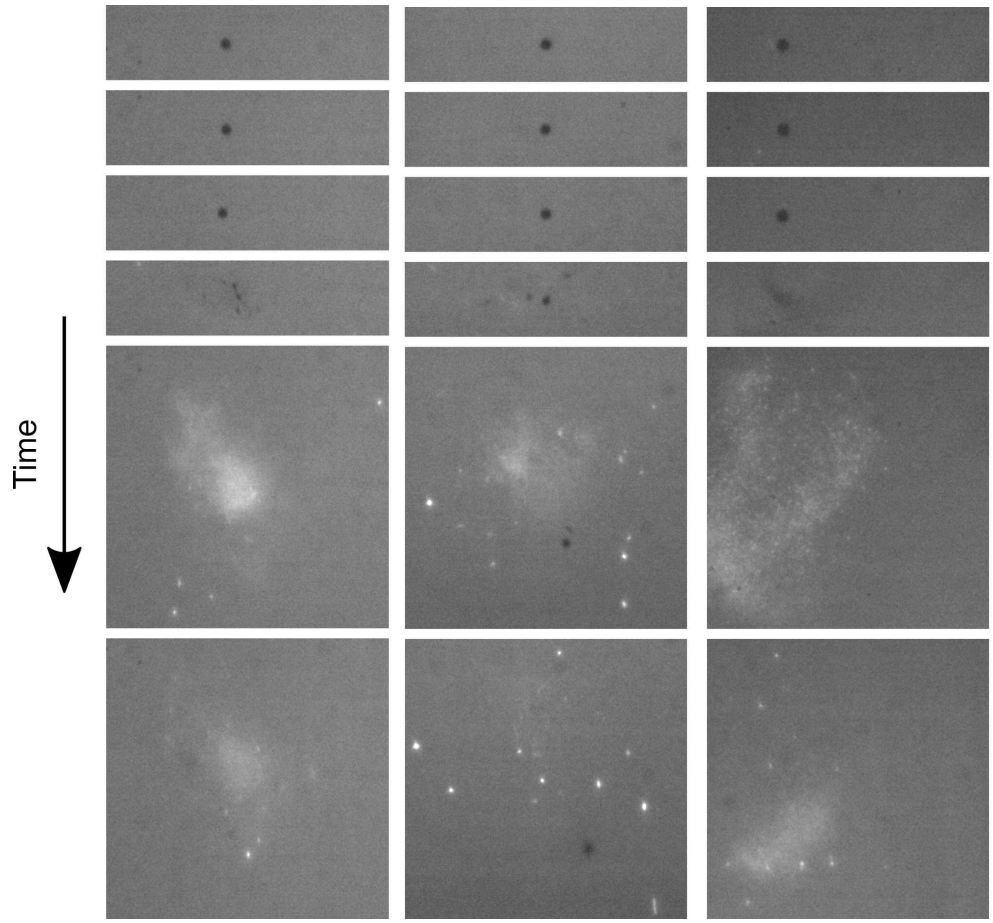

Figure 4.40: Micro-explosions at $T_\infty = 1000\ ^\circ$C for different nanofuels: a) HVO + 1% OA + 1% Al; b) HVO + 2% OA + 2% Al; c) HVO + 4% OA + 4% Al.

of nanoparticles are expelled from the primary droplet, igniting instantaneously and forming a bright spot characteristic of aluminum combustion, as previously described as puffing. Droplet expansion before micro-explosion occurred repeatedly, with a notable but temporary increase in droplet size. Besides that there is no quantification analysis on these particle concentration, the visualization of Figure 4.39 and Figure 4.40 shows that higher particle concentration and furnace temperature promotes a higher micro-explosion intensity.

4.4 Numerical Methodology

The present section presents the theoretical formulation and solution approach of the mathematical model in depth. In this context, a simplified macroscopic model is developed using the Python programming language to better understand the combustion phenomena associated with single droplet combustion. The mathematical model results are compared with the experimental findings on pure fuels and nanofuel droplets. Concerning the nanofuel droplets, an investigation dedicated to the furnace temperature, as well as the particle concentration, is performed. The purpose is to understand the mechanisms that affect nanofuel droplet combustion, e.g., particle aggregation and radiation absorption. It is essential to

highlight that, in numerical terms, the aluminum combustion and disruptive burning phenomena are out of the scope of the present work. As described in chapter 2, there are several approaches in modeling terms to predict the droplet size evolution for pure fuels.

In the present work, the basis of the mathematical model remains in the D^2 law. However, several assumptions are incorporated. Firstly, a surrogate fuel for the HVO is evaluated, considering its composition. The numerical results are compared with the droplet size evolution and burning rate obtained in the experimental results for pure HVO. Additionally, the model incorporates the convective effects since the present work focuses on falling droplets where heat and mass transfer processes are influenced by external convection, affecting the droplet burning rate. Subsequently, the addition of nanoparticles to a liquid fuel is explored. To accomplish this, an analysis of the radiation absorption as well as the influence of particle agglomeration is performed concerning the particle concentration. The mathematical model is described in detail in the following subsections.

4.4.1 Hexadecane as a Surrogate Fuel

Firstly, to understand the effect of adding nanoparticles to a liquid fuel, it is essential to investigate the combustion of the pure fuel droplet in numerical terms. As previously mentioned, the pure fuel used in this study is HVO biofuel produced from NESTE, a multi-component fuel. Consequently, its thermophysical properties were simplified and introduced in the mathematical model. Since the volatility and the thermophysical properties of HVO components do not differ significantly, the burning behavior of HVO may be represented approximately to a single-component fuel. The HVO comprises alkanes with typical carbon numbers from C_{15} to C_{18} [371]. Consequently, hexadecane ($C_{16}H_{34}$) was tested as a surrogate fuel of HVO as well as HVO with OA, being one of the main constituents of biofuel. This specific approach was employed to simplify the modeling complexities. Consequently, hexadecane was selected, being one of the heaviest components in HVO [372].

Considering the simplified interpretation of the D^2-law for droplet combustion, as indicated by the Equation (2.40), the thermophysical properties were evaluated following the approach of Law and Williams [406]. This approach allows accurate theoretical predictions against a large amount of experimental data over various conditions. Moreover, it is also assumed that the environment temperature is equal to the furnace temperature, T_∞. This assumption is reasonable, as seen in Figure 4.3. The authors Law and Williams [406] suggested calculating the liquid fuel density at the droplet surface temperature

$$\rho_l = \rho_l \left(T_s \right) , \quad (4.10)$$

and proposed the following approximations for the gas thermal conductivity and the gas specific heat, respectively,

$$k_g = \overline{\chi} k_F \left(\overline{T}_1\right) + \left(1 - \overline{\chi}\right) k_{Ox} \left(\overline{T}_1\right) , \quad (4.11)$$

$$c_{pg} = c_{pF} \left(\overline{T}_1\right) , \quad (4.12)$$

where k_F and k_{Ox} are the thermal conductivities of fuel vapor and oxidizer, the air in the present case, $\overline{\chi}$ is related to an average fuel mole fraction in the gaseous region inside the flame front. The gas thermal conductivity and heat capacity curves of hexadecane as a function of temperature were only available for 1000 K and 1500 K, respectively. Consequently, they were extrapolated up to 2000 K using the Excel forecast sheet. These extrapolations are graphically represented in the Figure 4.41.

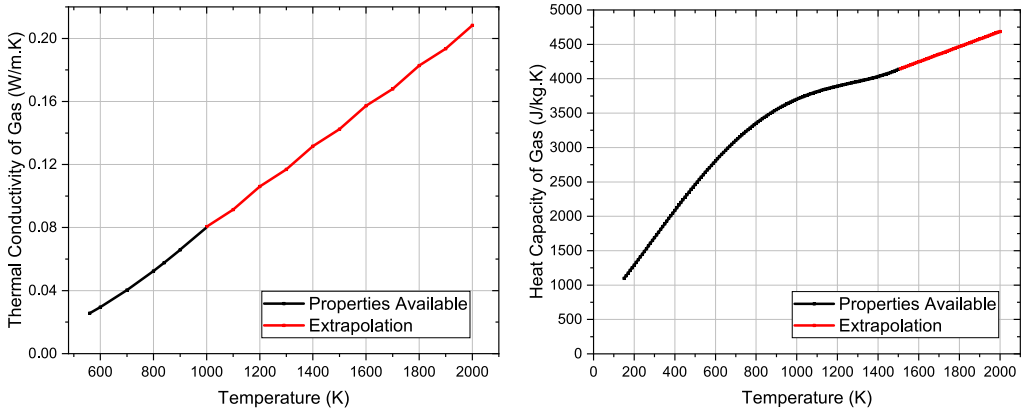

(a) (b)

Figure 4.41: Extrapolation of hexadecane a) Gas thermal conductivity; b) Gas heat capacity, adapted from [416].

A value of $\overline{\chi}$ = 0.4 was considered since it provides a good agreement with experiments [406]; and c_{pF} is the specific heat of fuel vapor. The authors also proposed to evaluate the properties presented in Equations (4.11) and (4.12) at an average temperature of $\overline{T}_1 = (T_s + T_f)/2$, as previously mentioned the region 1 inside the front flame. To estimate the flame temperature, denoted as T_f, based on the thermophysical properties, an assumption was considered that exhibits negligible deviation from the adiabatic flame temperature observed in a stoichiometric system under constant pressure. In this system, the initial fuel temperature corresponds to its boiling point, T_{boil}, while T_∞ represents the initial air temperature. Despite the potential for dissociation to decrease the flame temperature, particularly under stoichiometric conditions and high environment temperatures, incorporating its effect into the flame temperature estimation would introduce further complexity. Hence, disregarding the influence of the dissociation on the flame temperature was deemed appropriate to maintain simplicity.

4.4.2 Incorporation of the Convective Effects

In the present work, a falling single droplet combustion experiment is employed where the heat and mass transfer processes are influenced by external convection, which usually affects the droplet burning rate [137]. The Richardson Number was estimated to determine the importance of natural convection relative to forced convection for the conditions under which

the experiments were conducted:

$$Ri_d = \frac{Gr_d}{Re_d^2}\,. \quad (4.13)$$

Generally, if $Ri_d \ll 1$, natural convection effects may be ignored. Conversely, if $Ri_d \gg 1$, forced convection effects may be neglected. Otherwise, for $Ri_d \approx 1$, the combined effects of free and forced convection must be considered [417]. According to Law and Williams [406], the droplet Grashof Number is defined as

$$Gr_d = \frac{g\beta_g \left(T_f - T_\infty\right) D^3}{\nu_g^2}\,, \quad (4.14)$$

where g is the acceleration due to gravity, β_g is the gas coefficient of thermal expansion, $\beta_g \simeq 1/T_g$ for ideal gases and ν_g is the gas kinematic viscosity. The expressions for the droplet Reynolds number and relative velocity between the droplet and the free stream are provided in Equation 4.6 and Equation 4.7, respectively. The airflow Reynolds number was previously described in Equation. (4.1). Table 4.4 shows the estimated magnitude order from experimental results. Therefore, only forced convection is expected to influence the droplet burning rate, whereas natural convection can be neglected, as displayed in Table 4.4.

Table 4.4: Estimated magnitude order from experimental results.

Parameters	**Order of magnitude** ($\mathcal{O}$)
g	$10\,m\,s^{-2}$
β_g	$10^{-3}\,K^{-1}$
$(T_f - T_\infty)$	$10^{3}\,K$
D^3	$10^{-11}\,m^3$
ν_g^2	$10^{-7}\,m^4\,s^{-2}$
Gr_d	10^{-3}
U_{rel}	$1\,m\,s^{-1}$
D	$10^{-4}\,m$
ν_g	$10^{-4}\,m^2\,s^{-1}$
Re_d	1
Ri_d	$10^{-3} \ll 1$

Since the present work incorporates the convective effects, the burning rate can be defined in Equation (2.39). A detailed description of the convective effects is presented below. To incorporate the effects of forced convection into the droplet combustion model, the formulation presented in Turns [128] was adopted. The approach is straightforward and based on film theory, maintaining the desired simplicity. It replaces the heat and mass transfer boundary conditions at infinity with the same conditions moved inward to the so-called film radius, δ_T for energy and δ_M for species. Figure 4.42 illustrates how the film radii intensify temperature and species concentration gradients, which increases the heat and mass transfer rates at the

droplet surface.

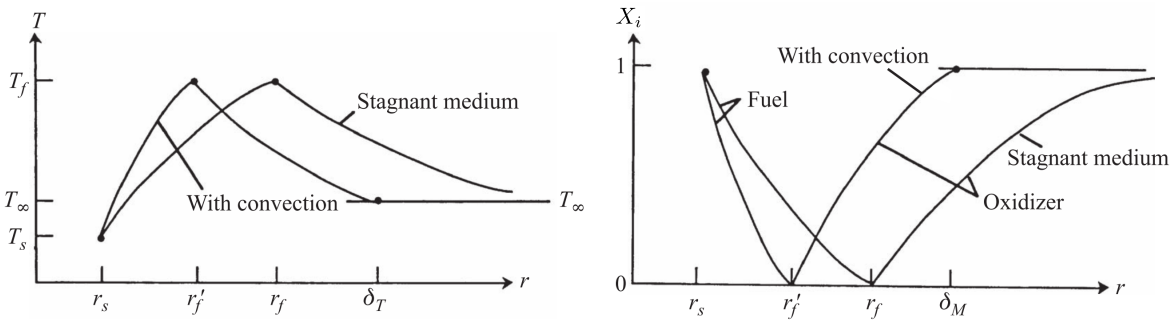

Figure 4.42: Comparison of temperature and species profiles with and without forced convection. Theoretical film thicknesses are indicated by δ_T (temperature) and δ_M (species) [128].

The film radii are defined, in terms of the droplet Nusselt Number, Nu_d, for heat transfer, and the droplet Sherwood Number, Sh_d, for mass transfer, as follows [128]:

$$\frac{\delta_T}{r_s} = \frac{Nu_d}{Nu_d - 2} \quad \text{(4.15a)}$$

$$\frac{\delta_M}{r_s} = \frac{Sh_d}{Sh_d - 2}\,. \quad \text{(4.15b)}$$

Note that $Nu_d = 2$ for a quiescent medium, and then one would recover $\delta_T \to \infty$. Since unity Lewis number is assumed, $Nu_d = Sh_d$. To evaluate Nu_d, Faeth [418] proposed the following correlation

$$Nu_d = 2 + \frac{0.555 Re_d^{1/2} Pr_g^{1/3}}{\left[1 + \frac{1.232}{Re_d Pr_g^{4/3}}\right]^{1/2}}\,, \quad \text{(4.16)}$$

where Pr_g is the gas Prandtl number. Equation (4.16) applies to both droplet evaporation and combustion and is valid for low and high Re_d values up to $Re_d = 1800$ [142]. Re_d in Equation (4.16) was evaluated according to Equation (4.6). U_{rel} was calculated using Equation (4.7), where U_d was determined from the results of the experiments conducted and U_∞ can be determined using Equation (4.2), where its relevant parameters are displayed in Table 4.1 for each furnace temperature. ν_g in Equation (4.6) and Pr_g in Equation (4.16) were approximated to those of air and evaluated at a mean temperature $\overline{T}_2 = (T_f + T_\infty)/2$ [406]. Consequently, as previously stated by Turns [128], the burning rate constant considering the convection effects is presented in Equation (2.39). Figure 4.43 shows the droplet Nusselt Number as a function of the droplet squared ratio at furnace temperatures of T_∞ = 800 °C and T_∞ = 1000 °C, where the red dashed line corresponds to Nu_d = 2, a case where there is no convection. The results suggest that the droplet Nusselt number decreases with increasing air temperature and the decrease of the droplet diameter. Moreover, it can be concluded that

the experimental study was performed under weak, forced convection in a laminar regime.

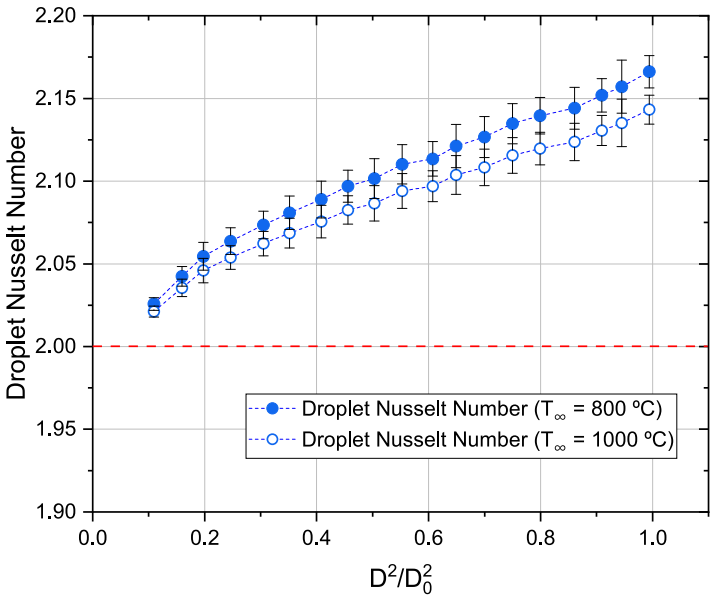

Figure 4.43: Droplet Nusselt Number as a function of the droplet squared ratio at furnace temperatures of T_∞ = 800 °C and T_∞ = 1000 °C.

4.4.3 Incorporation of Nanoparticles in a Liquid Droplet

As highlighted above in the section introduction, the addition of nanoparticles to a liquid fuel is evaluated using a modeling approach. This investigation mainly explored two mechanisms that affect the nanofuel droplet combustion radiation absorption and particle agglomeration.

The effect of radiation is typically disregarded, as reported in Table 2.4. Radiation absorbed by the droplet is frequently neglected since most liquid fuels are considered transparent to radiation [225]. In this respect, thermal conduction only accomplishes heat transfer to the droplet surface. According to the literature, the radiative heat transfer can become significant as the nanoparticles suspended in the droplet absorb the radiation energy emitted by the droplet flame and, in some cases, by an external heating source [215, 221]. Consequently, the radiation absorption increases the energy per unit of time available to vaporize the droplet, affecting the burning rate of nanofuel droplets, as will be discussed later. To include the effects of radiative heat transfer in the simplified macroscopic model resulting from the addition of nanoparticles, blackbody radiation was assumed to be emitted from infinity, i.e., from the DTF walls in a spherically symmetric field. The blackbody radiation assumption is due to the surface of the DTF walls being much larger than the droplet surface [407]. It was also considered that the gaseous phase surrounding the droplet is passive to radiation. This means that the interaction between the gas phase and the radiation is neglected. For the present study, it is assumed that all radiation is absorbed at the droplet surface, which is entirely filled with nanoparticles. Based on this, the effect of the radiation absorption should be included in the surface energy balance at the droplet liquid-vapor interface. Consequently, the heat transferred into the droplet surface is now given by

$$-\left[-k_g 4\pi r^2 \frac{dT}{dr}\right]_{r_s} + \dot{Q}_{rad} = \dot{m}_F h_{fg}\,, \quad (4.17)$$

where $\dot{Q}_{rad}$ is the net radiation heat transfer rate at the droplet surface, determined as follows

$$\dot{Q}_{rad} = A_d\left(G_w - J_d\right) = A_d \sigma_B \left(\alpha_d T_w^4 - \varepsilon_d T_s^4\right)\,, \quad (4.18)$$

where A_d is the droplet surface area, G_w is the DTF walls irradiation, J_d is the droplet radiosity, σ_B is the Stefan-Boltzmann constant and α_d and ε_d are, respectively, the droplet absorptivity and emissivity. Note that, for the calculation of $\dot{Q}_{rad}$, it was assumed that the nanofuels droplets are opaque, i.e., their transmissivity is zero, τ = 0. The assumption is supported by the experimental findings of Gan and Qiao [230], who investigated the UV-Vis transmittance (190–900 nm) of ethanol-based fuel containing aluminum nanoparticles. Their results showed that even at a low concentration of 0.1 wt.% aluminum, the nanofuel exhibited a nearly constant radiation transmittance of approximately 2%. As previously noted, it is assumed that all radiation is absorbed at the droplet surface, which is entirely filled with nanoparticles. It is essential to note that future studies should conduct a detailed analysis of the particle concentration influence. Defining, for convenience, $q_{rad} = \dot{Q}_{rad}/\dot{m}_F$ and substituting into Equation (4.17), yields

$$-\left[-k_g 4\pi r^2 \frac{dT}{dr}\right]_{r_s} = \dot{m}_F\left(h_{fg} - q_{rad}\right)\,, \quad (4.19)$$

which provides a revised definition of the effective latent heat of vaporization

$$h_{fg,eff} = h_{fg} - q_{rad}\,. \quad (4.20)$$

Thus, the droplet size evolution continues to be determined by Equation (2.40), and K_c is still evaluated by Equation (2.39). Thus, $B_{o,q}$ is calculated by Equation (4.21) for nanofuel droplets, emphasizing the primary outcome of the original model modification:

$$B_{o,q} = \frac{\Delta h_c/\nu_{of} + c_{pg}\left(T_\infty - T_s\right)}{h_{fg,eff}}\,. \quad (4.21)$$

As discussed earlier, the accumulation of particles during the evaporation and combustion of nanofuel droplets may significantly affect the behavior of these processes. According to the literature reviewed, agglomeration or aggregation of nanoparticles near the droplet surface creates a resistance for the liquid to evaporate, thus decreasing the burning rate. This effect is mainly felt in the last phase of the droplet lifetime, the so-called dry-out phase, where

a shell of particles is formed, and evaporation occurs only when the liquid inside the shell reaches the outer surface through capillary action [195, 222, 226]. Although occurring on distinct time scales, this phenomenon resembles droplet drying, which is employed in diverse industries for solid particle formation and is well-established. Examples of such industries include pharmaceuticals [419, 420].

A single droplet drying model was combined into the simplified single droplet combustion model previously described to obtain insights into the physical phenomena associated with particle agglomeration during combustion. It was based on the hypothesis developed by Mezhericher et al. [236] and later improved by Maurice et al. [235]. Due to slow particle diffusion, as the surface regresses, nanoparticles accumulate near the droplet surface [234], which eventually leads to a shell of particles [226]. This refers to the first drying phase ending and initiating the transition into the subsequent phase, known as the second drying phase [235]. During this phase, a shell of accumulated nanoparticles introduces a mass resistance that hinders the evaporation of the liquid fuel. As the evaporation progresses, the shell gradually thickens, causing a decrease in the evaporation rate. Ultimately, a critical point is reached. This occurs when the resistance of the shell becomes more significant than the compressive capillary forces applied to its surface, leading to a nearly constant diameter of the shell [236]. At this moment, the droplet enters the second drying phase. Subsequently, the shell of particles undergoes drying, promoting the nucleation of the residual liquid fuel presented within the droplet [237]. Consequently, the internal pressure of the droplet rises, ultimately leading to the disruptive burning phenomena [393]. The modeling and prediction of micro-explosions, more concretely aluminum particle combustion that occurs at the end of the droplet lifetime, are beyond the scope of this study and will be investigated in future research. This theoretical model primarily focuses on the first drying phase since the outer diameter of the droplet remains relatively constant during the second drying phase. However, the transitional period between the first and second drying phases is incorporated into the model as part of the first drying phase. This decision is based on the ratio between the characteristic times of droplet evaporation and shell shrinkage and thickening, which includes the phenomenon of particle rearrangement of the shell formed on the droplet surface as it recedes, holds a theoretical value of approximately $\mathcal{O}(10)$ [236]. In the present mathematical model, the assumptions associated with the accumulation of particles in the droplet surface are related to the previous studies [235, 236]. Initially, the analysis considers the radial symmetry of transport phenomena, aligning with the principles outlined in the D^2-law for droplet combustion. Additionally, intra-droplet circulation is disregarded, and it is assumed that spontaneous agglomeration of nanoparticles within the droplet does not occur. Moreover, all nanoparticles are assumed to be uniform in size and spherical. Based on these assumptions, the transport of nanoparticles within the droplet can be described using Fick's second law [235]:

$$\frac{\partial Y_{np}(r,t)}{\partial t} = \frac{1}{r^2}\frac{\partial}{\partial r}\left(r^2 \mathcal{D}_{pl}\frac{\partial Y_{np}}{\partial r}\right), \quad (4.22)$$

for $0 \leq r \leq r_s(t)$, where Y_{np} is the volume fraction of nanoparticles and $\mathcal{D}_{pl}$ is the diffusivity coefficient of particles in liquids, which can be calculated from Einstein-Stokes relation [226], displayed in Equation (4.9). For the initial condition of Equation (4.22), it is assumed that initially, the nanoparticles inside the droplet are spherical and uniformly distributed so

$$Y_{np}(r, t = 0) = Y_{np,o}(r)\,, \quad (4.23)$$

where $Y_{np,o}$ is the initial volume fraction of nanoparticles in the nanofuel mixture. The corresponding boundary conditions are [235]

$$\frac{\partial Y_{np}(r,t)}{\partial r} = 0 \;\; r = 0 \qquad (4.24a)$$

$$\frac{\partial}{\partial t}\left[\int_0^{r_s(t)} Y_{np}(r,t)\rho_{np}4\pi r^2 dr\right] = 0 \;\; r = r_s(t)\,, \quad (4.24b)$$

where ρ_{np} is the density of the nanoparticles material. The first boundary condition is due to the spherical symmetry of the problem, and the second one describes the conservation of overall solid mass within the droplet, as the nanoparticles are considered to remain in the droplet interior during the evaporation process [236]. Based on the species volume fraction within the droplet, it becomes apparent that a specific instant exists when the solid content attains a saturation value on the droplet surface [235]. In this study, the saturation value was assumed to be $Y_{np,max} = Y_{np,sat} = 0.6$, indicating the maximum theoretical value for orthorhombic packing of mono-sized spheres [421]. This particular point, commonly referred to as the "locking point" [235, 236], means the onset of agglomeration among the nanoparticles that were previously independent. As a result, a thin shell composed of connected solid particles is formed through intermolecular attractive forces [235]. This moment marks the initiation of the transition period.

When the transition starts, a thin layer of nanoparticles is submerged while the liquid evaporates from the surface until the agglomerated particles are exposed to the surrounding gas [235]. At this stage, both internal and external pressures act on the droplet. The internal pressure of the droplet counteracts the external pressure, reducing the capillary compression effect to some extent [235]. The development of the mathematical expressions for those pressures is elaborately described in Mezhericher et al. [236]. In the present work, only the final expressions will be presented for simplification purposes. Consequently, the external pressure exerted on the shell is caused by both capillary effects and interfacial tension of the liquid, which is given by [235, 236]

$$P_{ext}(t) = 2\sigma\cos(\theta)\left[\frac{3}{2r_p}\left(\frac{1-\varepsilon}{\varepsilon}\right) + \frac{1}{r_s(t)}\right], \quad (4.25)$$

where σ is the liquid fuel surface tension at T_s; θ is the contact angle, i.e., the angle where the liquid-vapor interface meets the solid surface; and ε is the shell porosity, $\varepsilon = 1 - Y_{np,sat} = 0.4$ [421]. The liquid fraction primarily influences the internal pressure exerted on the shell. Once the shell is formed, the pressure within the droplet does not undergo instantaneous changes but rather maintains the same value as the internal pressure before shell formation [236]. The evaluation of the internal pressure within the droplet follows the Laplace–Young Equation and is expressed by [235, 236]

$$P_{int}(t) = \frac{2\sigma}{r_s(t)}. \quad (4.26)$$

Considering the shell of agglomerated nanoparticles as a pseudo-continuous solid body, the radial and tangential mechanical stresses within this spherical shell caused by internal and external pressures can be approximated by [235, 236]:

$$\sigma_{mr}(r) = \frac{P_{ext}b^3\left(r^3 - a^3\right)}{r^3\left(a^3 - b^3\right)} + \frac{P_{int}a^3\left(b^3 - r^3\right)}{r^3\left(a^3 - b^3\right)} \quad (4.27)$$

$$\sigma_{m\psi}(r) = \frac{P_{ext}b^3\left(2r^3 + a^3\right)}{2r^3\left(a^3 - b^3\right)} - \frac{P_{int}a^3\left(2r^3 + b^3\right)}{2r^3\left(a^3 - b^3\right)} \quad (4.28)$$

for $a \leq r \leq b$, where a and b are, respectively, the inner and outer radii of the shell. The presence of capillary effects on the outer surface of the shell causes additional compressive capillary forces performing tangentially on the nanoparticles [236]. In the case of a liquid bridge formed between two spherical particles, as depicted in Figure 4.44, these additional compressive capillary forces contribute towards the tangential stress experienced at the droplet surface [235, 236].

Where α_h is the half-filling angle and L_L and ρ are the principal radii of the liquid meniscus. In this work it was assumed that $\theta = 30°$, $\alpha = 45°$ and $\rho = \infty$, so that $L = r_p\sin(\alpha)$.The condensed shell containing agglomerated nanoparticles undergoes collapse or rearrangement due to droplet evaporation, provided that the following buckling criterion is fulfilled [235, 236].

$$\max\left(|\sigma_{mr}|, |\sigma_{m\psi}|\right) > \sigma_{my}. \quad (4.29)$$

Here, σ_{my} represents the yield stress of the shell. Since the literature does not provide an

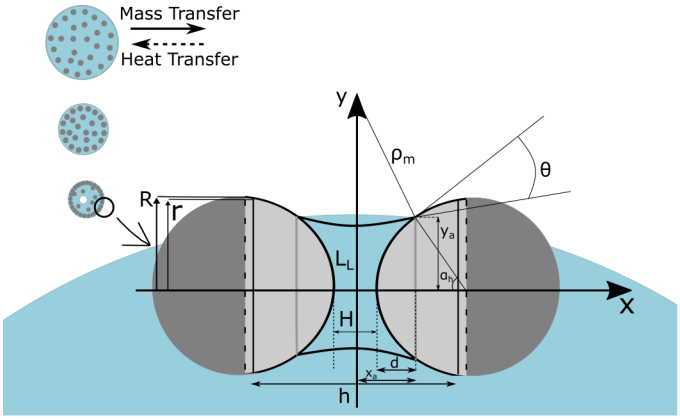

Figure 4.44: Schematic of a liquid bridge between two particles, adapted from [422].

available value for σ_{my} of the agglomerated nanoparticle shell, and its direct measurement would be highly challenging, this parameter must be determined by fitting with experimental findings.

Following the collapse of the shell, this iterative process continues until the shell attains a sufficient thickness to suffer the capillary pressure, resulting in no agreement of the buckling criterion defined by Equation (4.29) [235]. The repeating process of evaporation and shell collapse, which characterizes the transition period, is well explained in [236]. The point at which the buckling criterion is not achieved determines the end of the transition period and the onset of the second drying phase, where the outer diameter of the droplet remains constant until a micro-explosion occurs. Consequently, following the initial droplet shrinkage primarily governed by the D^2-law, considering the radiation effects, the further reduction in droplet size ceases due to constraints imposed by particle packing

$$\frac{dD^2}{dt} = 0\,. \quad (4.30)$$

The relative motion of the regressing droplet surface and the nanoparticles can be assessed by comparing the time scales, which can be quantified using the Péclet number [226] is displayed in Equation (4.8) as previously discussed. Consequently, during the evaporation process, nanoparticles have insufficient time to diffuse and are quickly included on the regressing droplet surface [226], as shown in Table 4.5. Hence, it can be assumed that the diffusion of nanoparticles in the liquid is negligible.

This significantly simplifies the way of determining the species concentration profile within the droplet, as now one merely has to determine the amount of nanoparticles dragged inward by the recessing droplet surface. Therefore, instead of solving Equation (4.22), the volume fraction of nanoparticles inside the droplet was obtained in a simplified manner, both in time and in the radial direction. To better understand this approach, Figure 4.45 shows the volume fraction profile of nanoparticles within the droplet. It divided the initial droplet radius into radial shells of the same thickness Δr. As the evaporation progresses, the nanoparticles

Table 4.5: Continued estimated magnitude order from experimental results.

Parameters	**Order of magnitude** ($\mathcal{O}$)
K_c	$10^{-6}\, m^2\, s^{-1}$
k_B	$10^{-23}\, J\, K^{-1}$
T_l	$10^{3}\, K$
μ_l	$10^{-2}\, Pa.s$
r_p	$10^{-8}\, m$
$\mathcal{D}_{pl}$	$10^{-10}\, m^2\, s^{-1}$
Pe	$10^{3} \gg 1$

near the droplet surface are integrated into the closest radial shell to the regressing droplet surface until the saturation point is achieved and the transition period begins. Afterward, the nanoparticles are included in the two closest radial shells to the surface, and so on, increasing the number of radial shells that include dragged nanoparticles and, therefore, increasing the thickness of the shell of agglomerated nanoparticles.

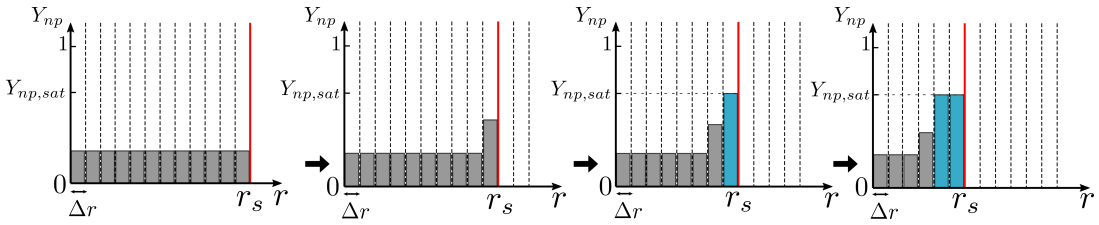

Figure 4.45: Schematic of the numerical approach to obtain volume fraction profile of nanoparticles inside the droplet.

Based on the proposed theoretical framework for the combustion of isolated nanofuel droplets, a computational solution algorithm was developed. This algorithm is illustrated in Figure 4.46.

To obtain the diameter squared, D^2, as a function of time, the explicit Euler method was used. Time step and grid studies were performed. Subsequently, a time step $\Delta t = 1 \cdot 10^{-5}$ s was considered, and grid analysis showed that by discretizing the droplet radius into 1000 radial shells, i.e., for a radial shell thickness of $\Delta r = 1.25 \cdot 10^{-7}$ m, grid independence was achieved.

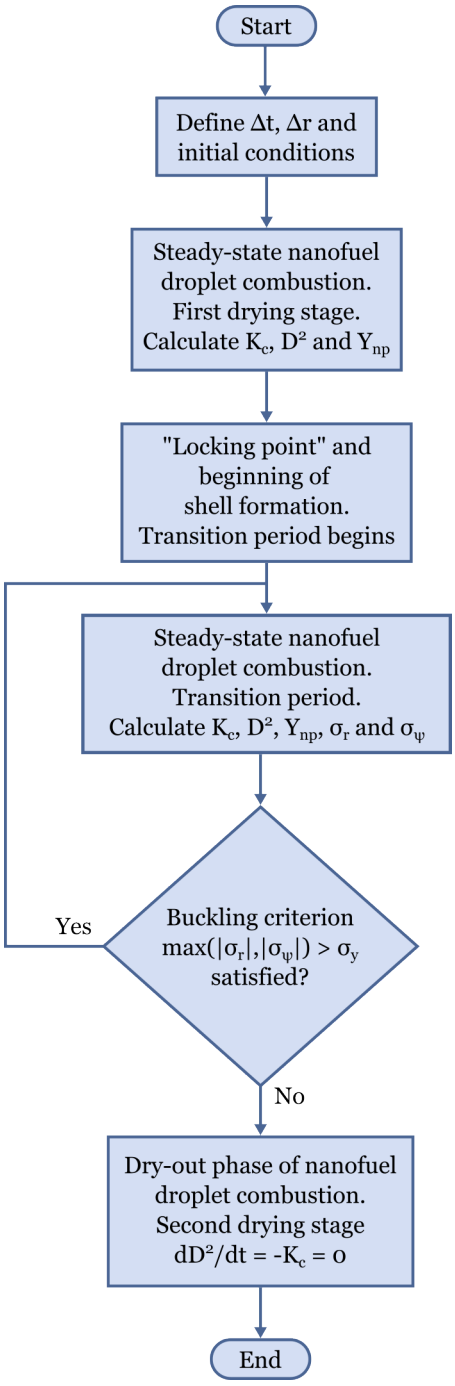

Figure 4.46: Flowchart of the model solution algorithm.

4.4.4 Sensitivity Analysis

A sensitivity analysis is performed to test the model robustness by understanding whether variations in certain parameters affect the findings. Thus, the sensitivity analysis for the fuel gas thermal conductivity, heat capacity, and absorptivity are performed with respect to the average burning rate for both furnace temperatures. Figure 4.47 shows the influence of the fuel gas thermal conductivity in the average droplet burning rate. The analysis shows that with an extrapolation uncertainty of approximately 20%, the droplet burning rate would change by a maximum of approximately 10%. It can be affirmed that the model is relatively

insensitive to variations in the value of k_F, indicating that errors in the extrapolation of this parameter do not promote substantial deviations in the final model results.

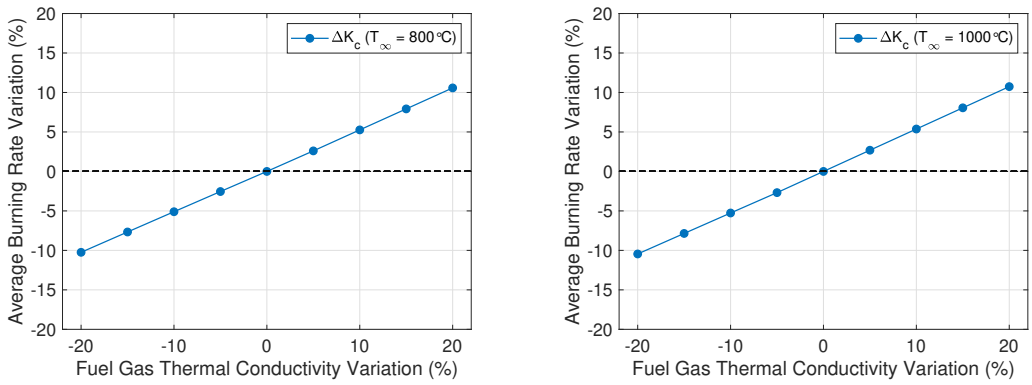

(a) (b)

Figure 4.47: Influence of the fuel gas thermal conductivity in the average droplet burning rate for: a) $T_\infty = 800$ °C; b) $T_\infty = 1000$ °C.

Concerning the fuel gas heat capacity, Figure 4.48 shows the variation of this parameter concerning the average burning rate. The results indicate that an extrapolation up to 10% leads to a variation of the average burning less than 10%. Similarly to the k_F, the model is also not very sensitive to variations in the value of c_{pF} and, thus, deviations arising from the extrapolation do not affect the results obtained from the theoretical model.

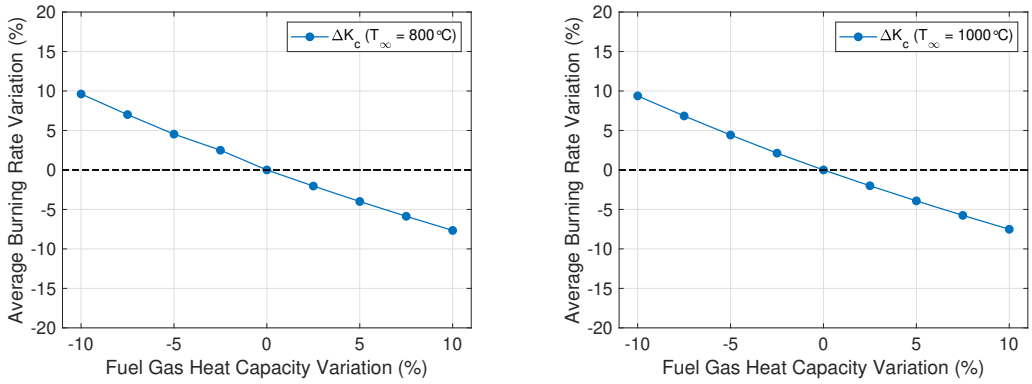

(a) (b)

Figure 4.48: Influence of the fuel gas heat capacity in the average droplet burning rate for: a) $T_\infty = 800$ °C; b) $T_\infty = 1000$ °C.

4.5 Single Droplet Combustion: Mathematical Model Results

The present section is dedicated to the results regarding the simplified macroscopic model. The model was previously described, and the experimental findings presented in this study provide valuable support for developing a mathematical model to evaluate the droplet size evolution and burning rate. Prior to the analysis of the performance of the model on its ability to predict the combustion behavior of isolated nanofuel droplets, the model is validated for pure fuels. In terms of nanofuel droplet combustion, radiation absorption, and particle

agglomeration results are presented. Finally, a comparison between the experimental and numerical findings is discussed.

4.5.1 Pure Fuels

The initial analysis was conducted on the pure HVO. The experimental analysis showed no substantial differences in the combustion process in pure HVO and HVO with 4.0 wt.% OA. Thus, the influence of OA addition was neglected in the mathematical model. As pointed out in the description of the mathematical model, the properties of the liquid fuel were approximated to those of hexadecane. Figure 4.49 shows the Comparison between experimental and numerical results for the droplet size evolution of pure HVO and HVO with the addition of 4.0 wt.% of OA at a) $T_\infty = 800$ °C, b) $T_\infty = 1000$ °C. The prediction of the combustion of pure HVO and HVO + 4.0 wt.% OA was performed assuming n-hexadecane as a surrogate fuel to estimate the combustion dynamics and the incorporation of the convective effects.

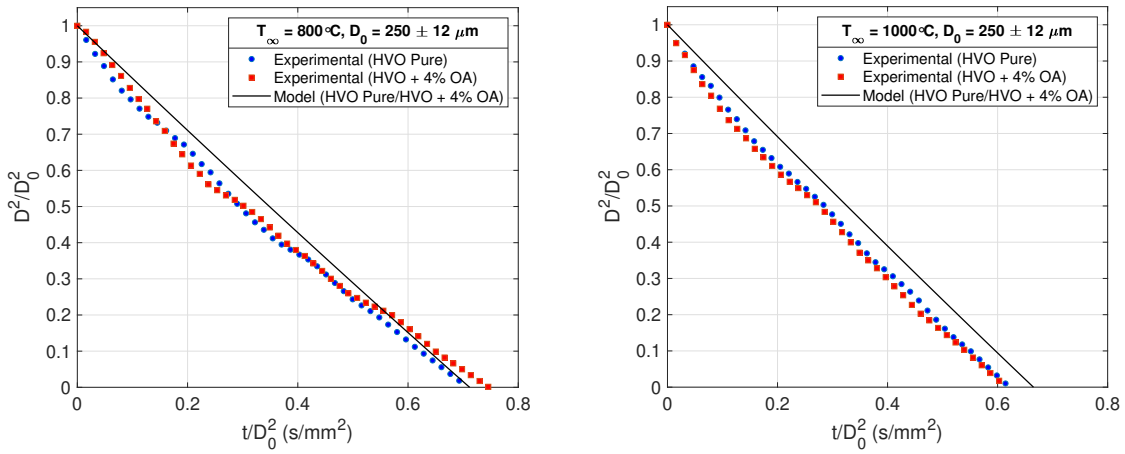

(a) (b)

Figure 4.49: Comparison between experimental and numerical results for the droplet size evolution of pure HVO and HVO with the addition of 4.0 wt.% of OA: a) $T_\infty = 800$ °C; b) $T_\infty = 1000$ °C.

The mathematical model predicts droplet size evolution regardless of the furnace temperature, evidencing a linear droplet diameter reduction as time evolves. The model accurately predicts the behavior at $T_\infty = 800$ °C. However, the model overpredicts the droplet diameter variation for higher temperatures compared to the experimental results. For comparison purposes, the average burning rate for experimental and numerical results is provided in Figure 4.50.

The findings indicate that the simplified theoretical model could accurately predict the physical phenomena observed during the combustion of isolated droplets of pure HVO and HVO with the addition of 4.0 wt.% OA. The assumptions of using hexadecane as a surrogate fuel of HVO suggest a feasible alternative for biofuel to be approximated as a single-component fuel. A sensibility analysis was performed, focusing on potential uncertainties regarding the estimation of model parameters, and is presented in the numerical methodology. This analysis aimed to assess the robustness of the model by examining the substantial variations of

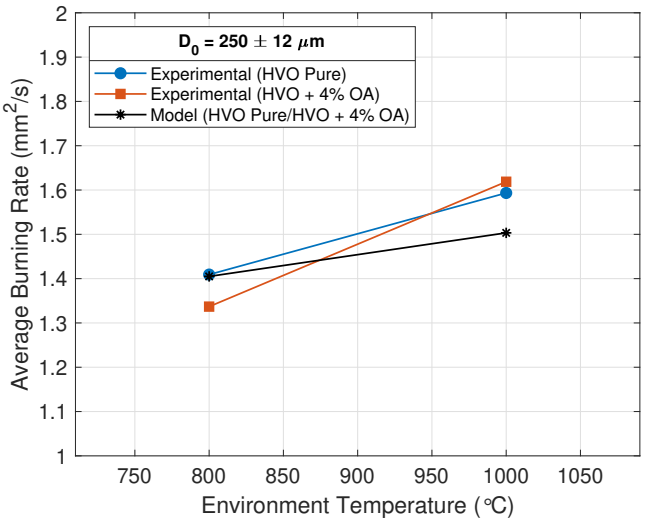

Figure 4.50: Comparison of average burning rate for experimental and numerical approaches at both furnace temperature: $T_\infty = 800$ °C; $T_\infty = 1000$ °C.

these parameters in average droplet burning rates under the two furnace temperatures. In light of this, it can be affirmed that the model exhibits robustness within the scope of this study, hence can accurately replicate the underlying physical phenomena that occur during the combustion of isolated liquid fuel droplets, thereby validating its reliability. Following the validation of the model and the discussion of the results for pure liquid fuels, numerical simulations were carried out considering the addition of nanoparticles.

4.5.2 Nanofuels

As highlighted in the numerical methodology, the impact of nanoparticles on droplet combustion behavior is addressed. The experimental and numerical findings will be compared in terms of droplet size evolution and burning rate. The analysis concerning the nanofuel evaluation is conducted from higher particle concentrations. For nanofuels predictions, the gas domain analysis remains unchanged compared to pure liquid, including the effects of nanoparticle addition in terms of radiation absorption and particle agglomeration. The nanoparticles are considered insoluble with uniform size and distribution. Regarding the particle aggregation, the yield stress of the shell, σ_y = 10 MPa, was determined by fitting with the experimental results. In light of this, Figure 4.51 shows the numerical results obtained for the droplet size evolution for each nanofuel at the two furnace temperatures. Experimental results are also displayed in Figure 4.51 for a better understanding. The droplet size evolution for each condition is exhibited by a black line showing the steady-state and dry-out phases. The latter is evidenced by a constant diameter at the end of the droplet lifetime. In this context, the nanofuel predictions exhibit a steeper and more abrupt transition between the steady-state and dry-out phase in contrast to the experimental observations, where this transition appears smoother. This finding is a consequence of the assumption integrated into the employed model, pointing out that the transition between phases occurs without any mass resistance arising from the formation of the shell of nanoparticles at the droplet

surface.

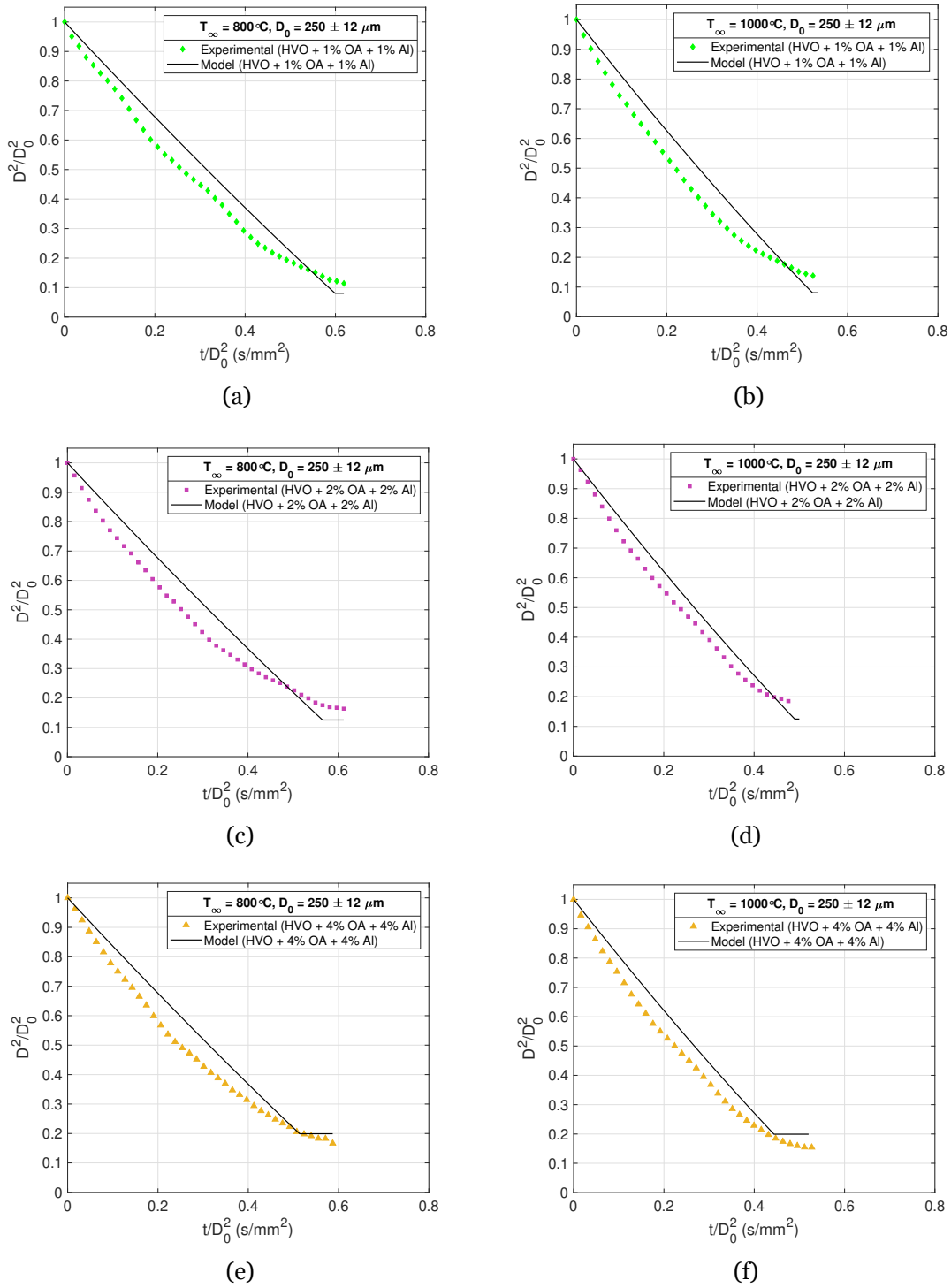

Figure 4.51: Comparison between experimental and numerical data for the droplet size evolution of: a) HVO + 1% OA + 1% Al ($T_\infty = 800$ °C); b) HVO + 1% OA + 1% Al ($T_\infty = 1000$ °C); c) HVO + 2% OA + 2% Al ($T_\infty = 800$ °C); d) HVO + 2% OA + 2% Al ($T_\infty = 1000$ °C); e) HVO + 4% OA + 4% Al ($T_\infty = 800$ °C); f) HVO + 4% OA + 4% Al ($T_\infty = 1000$ °C).

Further research into this transition would be relevant to achieve better accuracy in the model results. The effect of the particle concentration is noticeable in the dry-out phase, where an increase in the particle concentration leads to an increase in the dry-out phase, which may be

attributed to the fact that a higher amount of nanoparticles remain within the droplet during the combustion process. Thus, an increased particle concentration corresponds to a higher solid phase during the final phase of the droplet lifetime. In this context, the evolution of the solid volume fraction inside the droplet during the combustion process was performed. Figure 4.52 shows the model predictions on the evolution of the solid volume fraction inside the droplet for the nanofuels studied a) at $T_\infty = 800$ °C and b) $T_\infty = 1000$ °C. Moreover, the combustion process reveals a correlation between shell thickness and droplet size, characterized by an exponential fitting, as shown in Figure 4.51. The results reveal that the maximum solid volume fraction is obtained at an earlier stage when the particle concentration is higher, regardless of the furnace temperature. Besides that, the shell at the beginning of the second drying stage is predicted to be thicker for a higher initial particle concentration. The model estimated that for the beginning of the second drying stage, the shell thickness was approximately 2.6 μm for the nanofuel with 1 wt.% of aluminum nanoparticles, 3.4 μm for the nanofuel with 2 wt.% of aluminum nanoparticles and 4.1 μm for the nanofuel with 4 wt.% of aluminum nanoparticles.

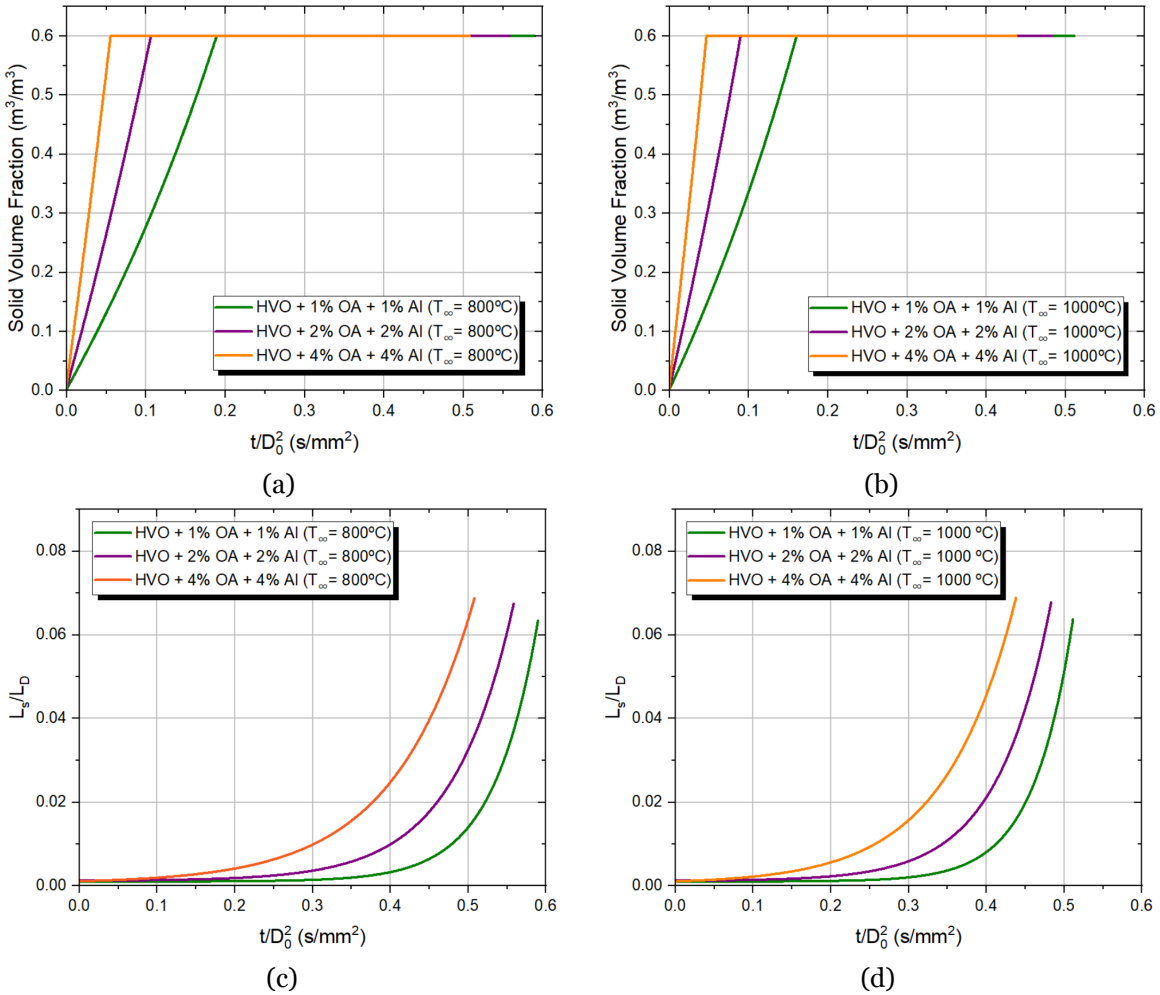

Figure 4.52: Solid volume fraction at: a) $T_\infty = 800$ °C; b) $T_\infty = 1000$ °C. Shell thickness and droplet radius ratio at: c) $T_\infty = 800$ °C; d) $T_\infty = 1000$ °C.

The simplified model predictions reasonably capture the single droplet combustion behavior

of nanofuels when radiation absorption and particle aggregation are included. However, it should be stated that the model slightly underpredicted the droplet burning rate during the steady-state phase for all nanofuels investigated. Overall, the simplified model could accurately reproduce the combustion characteristics of nanofuel droplets. As a result, it provided valuable insights into the underlying physical processes, enhancing the understanding that contributes to the broader knowledge of nanofuel combustion phenomena. Further research on predicting the disruptive burning phenomena and multi-component physics should be explored to understand the nanofuel combustion phenomena better.

4.6 Summary

The present chapter focuses on single droplet combustion, addressing experimental and numerical investigations. From the point of view of the experimental study, falling droplets of conventional and alternative jet fuel are studied in a drop tube furnace at high temperatures, avoiding the use of a supporting fiber. The findings reveal that HVO and Jet A-1 present a similar combustion behavior, following the D^2-law without the occurrence of disruptive burning phenomena. On the other hand, when aluminum nanoparticles are added to the HVO, a deviation from the D^2-law is noticeable, as well as disruptive burning phenomena, regardless of the furnace temperature, particle size, and concentration. Consequently, the droplet size evolution is affected, and the burning rate is enhanced, depending on the particle concentration. Particle agglomeration and radiation were identified as relevant mechanisms responsible for the differences between a nanofuel and a pure liquid fuel. Regarding the experimental study dedicated to the disruptive burning phenomena in nanofuel, a higher particle concentration and furnace temperature promote a higher micro-explosion intensity. This phenomenon requires additional oversight since hot spots can cause cracking, potentially resulting in premature engine failure. However, the current experimental configuration does not permit assessing the heat produced by micro-explosions, limiting the investigation into their impacts on emissions and potential damage in a real combustion chamber. These concerns can be further examined in the spray combustion chamber. Nevertheless, the studies of nanofuel spray combustion are relatively limited, highlighting the necessity of such studies to better understand the potential benefits of nanofuels.

Chapter 5

Spray: Non Reacting Conditions

5.1 Introduction

An understanding of the principles of atomization is required for diverse applications. Sprays have been employed in gas turbines, rockets, and diesel engines. Besides its wide use in engineering and industrial manufacturing processes, atomization also plays a relevant role in several fields, such as agriculture, medicine, and food technology [257]. Typically, a spray is classified as a two-phase flow. The liquid refers to dispersed or discrete phases manifest in the form of droplets or ligaments, and the gas phase is the continuous phase. Focusing on combustion systems, atomization aims to provide fuel injection, allowing the conversion of fuel liquid bulk into small droplets. In this respect, liquid fuels are atomized prior to the combustion to maximize the surface area between the liquid and its surrounding environment, enhancing the mechanisms of heat and mass transfer. As previously stated by Lefebvre [55], fuels do not possess satisfactory volatility to generate enough vapor amounts essentially to disrupt ignition and combustion. Thus, the atomization process permits the release of a considerably high number of droplets, resulting in a substantially increase surface area, enhancing the combustion process and leading to faster and cleaner combustion. Large droplet sizes influence the ignition process, as well as its evaporation rate. Additionally, the atomization process plays a vital role in the fuel-air mixing that is intricately associated with combustion efficiency, stability limits, and emissions.

A deep understanding of cleaner fuels and improved propulsion devices requires an evaluation of spray dynamics. Liquid jet atomization typically occurs in two distinct phases: primary breakup of the liquid jet near the atomizer exit and secondary atomization. The former corresponds to larger droplets and liquid ligaments formed in the primary disintegration that may exhibit instability, leading to fragmentation into smaller ones and promoting secondary atomization. Introducing alternative fuels in combustion systems has the potential to influence their performance as the properties of these fuels may differ from those of conventional ones. Consequently, the present section focuses on a detailed study dedicated to the spray investigation under non reacting conditions. Experiments dedicated to primary and secondary atomization will be discussed for conventional and alternative jet fuels. An experimental rig was developed to accomplish this objective, employing a commercial air-assisted atomizer with external mixing. The spray is visualized using a high-speed camera under several air-fuel ratios to comprehend their influence on spray behavior. Subsequently, image data processing is performed to evaluate the spray cone angle and breakup length. Additionally, detailed measurements of droplet sizes and velocities were acquired by Phase-Doppler

Interferometry. Considerable attention is provided to the droplet size distribution and air-liquid interactions to understand the influence of the fuel physical properties on the spray dynamics and address the impact of adding nanoparticles to a liquid fuel. Conducting this investigation for non reacting conditions is a requirement for future design and development of laboratory combustion chambers to compare the performance of alternative and conventional liquid fuels, as will discussed in chapter 6.

5.2 Experimental Methodology

Spray characterization in non-reactive environments is performed using two diagnostic techniques: the imaging technique and the Phase-Doppler Interferometry. Moreover, an experimental setup dedicated to each technique was developed to ease the data acquisition. The imaging technique permits spray visualization using a high-speed camera and measurements related to the breakup structures, length, and spray cone angle. These measurements are based on post-processing of the recorded images. A detailed description of the algorithms developed to accomplish this purpose will also be provided. Additionally, this imaging technique allowed the identification of primary and secondary atomization. For the secondary atomization analysis, a Phase-Doppler Interferometer (PDI) is used to obtain the droplet diameter and velocity distributions. A brief description of this approach and the methodology adopted is presented, including the operating conditions for each fuel tested.

5.2.1 Experimental Setup - Imaging Technique

Spray visualization is typically performed through an imaging technique, such as backlight imaging. This non-intrusive optical imaging method allows the acquisition of qualitative and quantitative details on spray morphology. The backlight technique is executed using a light source and imaging detectors, commonly defined as high-speed cameras coupled with a specific lens for the purpose. The methodology of this technique involves positioning a test object between the light source and the camera. In the absence of a test object for analysis, a white image with a uniform background intensity is provided since the light source is directly projected to the camera. Subsequently, when the test object, such as a spray, is positioned for evaluation, a shadow area is generated in the recorded image due to the obstruction on the light path. This technique aims to acquire high-contrast images of the spray to evaluate its properties in terms of breakup length (BL) and spray cone angle (SCA) through image data processing. Figure 5.1 shows the experimental setup used for the imaging technique, which comprises an illumination set, image acquisition, and injection system. As depicted in Figure 5.2, an air-assisted atomizer, specifically the SCHLICK Two-Substance Nozzle Model (0/2) with external mixing, is employed in the injection system. In this context, the air and fuel flowrate are controlled independently, where the liquid orifice has a diameter of 0.8 mm. Regarding the air, an annular section, with inner and outer diameters of 3 and 5 mm, is presented in the nozzle. The air-assisted atomizer releases the liquid through a central orifice, while the atomizing air is released concentrically from the periphery of the nozzle.

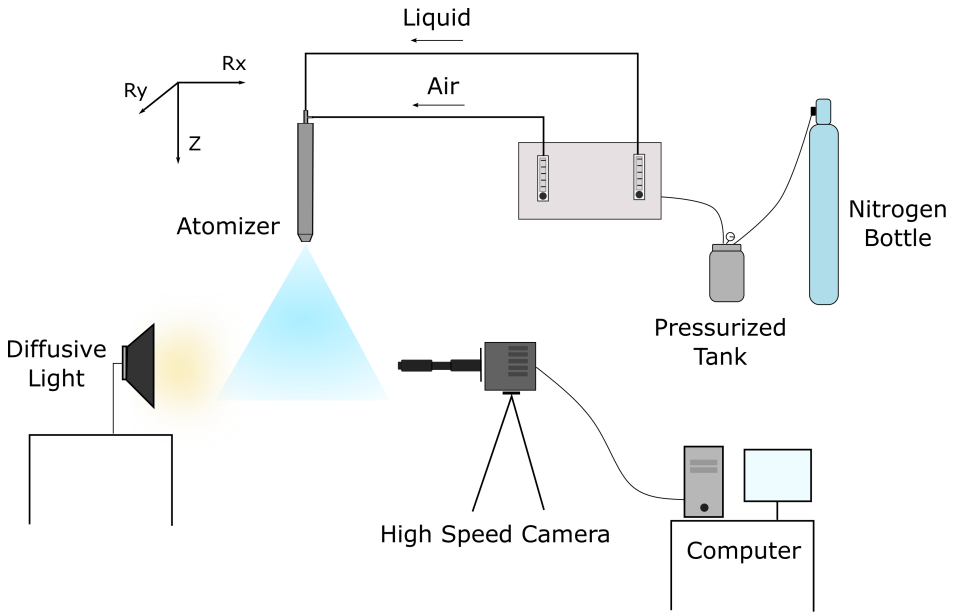

Figure 5.1: Illustration of the experimental setup for spray visualization.

Figure 5.2 c) shows the air swirl grooves in the atomizer nozzle with an angle of approximately 45°. In practical applications, swirl enhances mixing, increases residence time, and improves flame stability in the case of combustion [354]. Therefore, this atomizer was selected based on considering the development of a combustion chamber for liquid fuels.

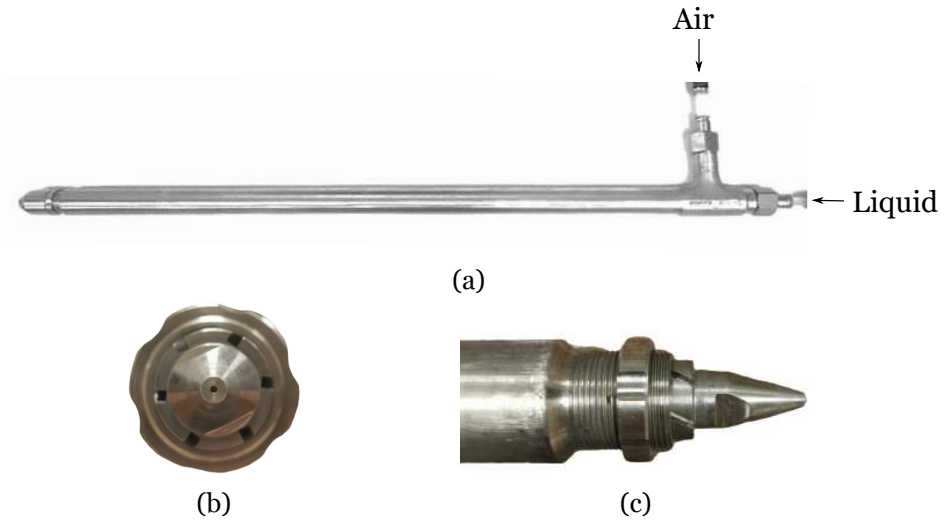

Figure 5.2: SCHLICK Two-Substance Nozzle Model, 0/2 atomizer a) side view, b) liquid nozzle front view, c) liquid nozzle side view.

The atomizer is placed in a rigid structure that allows it to move in three axes, as shown in Figure 5.1. Additionally, it was positioned vertically downwards to prevent droplet overlap during recirculation. A rotameter ABB PurgeMaster with a maximum capacity of 1.15 L/h was used for fuel injection on the atomizer. This fuel rotameter is employed for conventional and alternative jet fuel. Due to this, calibration is required to understand the effective flowrate released by the atomizer, as will be further explored. The fuel rotameter is connected to a pressurized tank at 1 bar with a maximum volume of 2 L. The pressurization is

performed using a nitrogen bottle connected to the fuel tank. A rotameter BB PurgeMaster with a maximum capacity of 54 L/min was used for the air atomization, provided by the laboratory compressor at 2 bar controlled through a manual valve. Fuel and air rotameters are depicted in Figure 5.3. Since the present work focuses on non reacting conditions, the air and fuel were investigated in ambient and atmospheric conditions.

Figure 5.3: Illustration of the experimental setup for spray visualization .

Regarding the image acquisition system, a high-speed camera, the FASTCAM Mini AX100, coupled with a high magnification lens, was placed perpendicularly on the spray for the image acquisition system. The magnification lens comprises a 6.5×Zoom, 12 mm FF, a 0.25×lens attachment, and a 2.0×short adapter with a magnifying range of 0.35-2.25, leading to an increase in the spatial resolution up to 8.2 µm/pixel. An LED illumination of 80 W with diffusing glass was positioned ahead of the spray to enhance the visualization. The use of high speed is required for the spray visualization, as well as measurements of the breakup length and spray cone angle. Thus, the high-speed parameters employed in these analyses are displayed in Table 5.1.

Table 5.1: High-speed camera conditions for breakup length and spray cone angle measurements.

	Frame Rate (fps)	**Shutter Speed (1/s)**	**Resolution**
Breakup Length	4000	16000 and 40000	1024×1024
Spray Cone Angle	10000	90000	768×528

5.2.2 Experimental Setup - Phase-Doppler Interferometer

The present work employs a Phase-Doppler Interferometer technique to explore the droplet diameters and velocities distributions of conventional and alternative jet fuels. This single-point laser diagnostic technique allows measurements of individual droplet diameters and velocity components in a polydisperse environment. A PDI system provides quantitative spray measurements through the analysis of the spherical droplets when they traverse the control volume of the equipment. This technique is valuable when at a considerable distance from the nozzle, as obtaining sharp images of individual droplets becomes challenging.

Figure 5.4 illustrates the experimental setup of the Phase-Doppler Interferometry. The experiments are performed using a FlowExplorer 1D transmitting and receiving optics connected to a BSA F100 processor from Dantec Dynamics. The processor is connected to a computer for further analysis of the measurements.

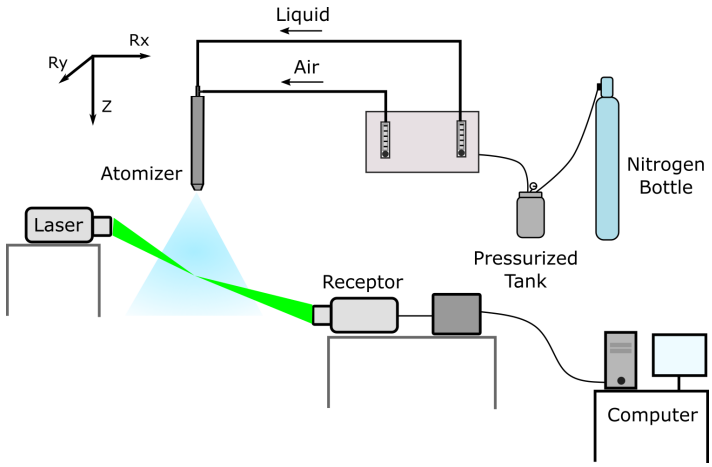

Figure 5.4: Illustration of the experimental setup for PDI measurements.

Concerning fuel injection, a comparable method to the imaging technique is employed, using a fuel rotameter and a pressure tank, as shown in Figure 5.1. Concerning the operating conditions, the fuel and air interaction occurred under ambient and atmospheric conditions. Along with this, various air-fuel ratios (AFR) are considered, as will be further described. The atomizer operates along three axes (Rx, Ry, and Z), enabling it to vary its position in order to obtain a more detailed understanding of the spray, as shown in Figure 5.5. The negative values of the axial velocity (U) are considered to be in the downward direction, consistent with the behavior of the secondary droplets. For each position, a sample size of 5000 droplets is considered, consistent with the literature, which ensures that this quantity is sufficient to stabilize the results [331, 423].

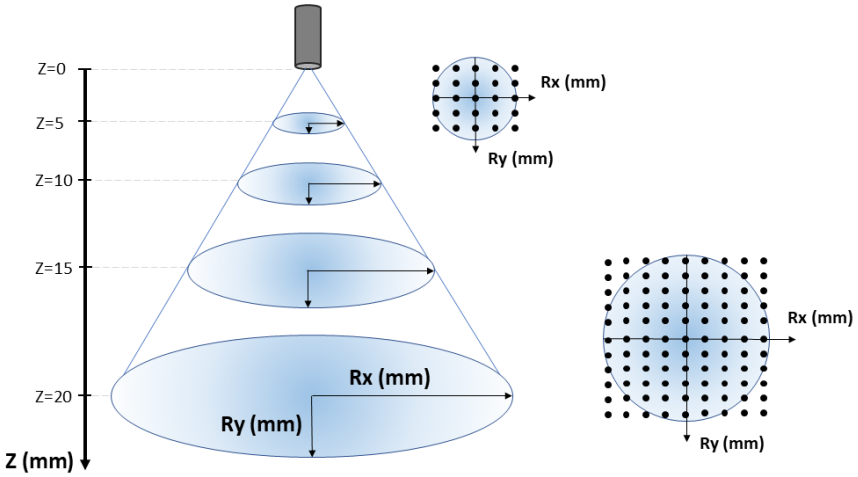

Figure 5.5: Illustration of radial and axial positions considered for the PDI measurements.

To evaluate the spray dynamics, it is imperative to accurately measure the droplets size and velocity. The nozzle is defined as the Z = 0 mm and the control volume created by the in-

tersection of two laser beams. Measurements were conducted on individual droplets as they traversed the control volume. The receiving optics projects a segment of the scattered light onto multiple detectors. Each detector converts the optical signal into a Doppler burst with a frequency linearly proportional to the droplet velocity. The phase shift between the Doppler signals from different detectors directly measures the droplet diameter [424]. If the droplet size values and velocities are identical for each negative and positive position of the atomizer, the spray is symmetrical. The system is used for transmitting optics laser power of 90 mW for the axial velocity (U) component measurements, with a wavelength of 660 nm. The focal length is 500 mm, the beam spacing is 37 mm. The receiving optics was a fiber PDA, with a receiver focal length of 400 mm. The detailed characteristics of PDI, such as optical configuration and software parameters, are displayed in Table 5.2. The refractive index for the Jet A-1, HVO, and nanofuels are provided in chapter 3.

Table 5.2: PDI Measurement Configuration.

Transmitting Optics	
Beam System	U1
Laser power	90 mW
Wavelength	660 nm
Focal length	500 mm
Beam spacing	37 mm
Receiving Optics	
Receiver Type	Fiber PDI
Scattering angle	31°
Receiver focal length	400 mm
Software Parameters	
Photomultiplier Sensitivity	900 V
Signal Gain	16 dB
Center Velocity	-16.34 m/s
Velocity Span	43.03 m/s

5.2.3 Operating Conditions

As highlighted in the description of the experimental setup, a fuel rotameter controlled the flowrate of conventional and alternative fuels. Due to this, prior to the data collection, a calibration procedure was conducted to assess the effective flowrate dispensed by the atomizer. The purpose is to establish the fuel conditions considered in the present work and assess the effective fuel flowrate for a rigorous comparison between the various fuels. The fuel calibration relied on the theoretical flowrate and the effective flowrate. The theoretical flowrate is related to the volumetric flowrate that should be released by the rotameter described by the manufacturer. However, when a specific theoretical flowrate is imposed, fuel flowrate release departs from the expected value since alternative and conventional fuels possess different physical properties, especially viscosity. Consequently, the effective flowrate was measured through the calibration procedure, which corresponds to the fuel volumetric flowrate released by the rotameter. This approach involves the measurements of the dispensed fuel in a volumetric tube over a specified time interval for each fuel flowrate case. The sampling

duration is approximately two to three minutes, and the collected liquid mass is measured using a digital scale after subtracting the weight of the volumetric tube, leading to the mass and volumetric flowrate calculation. This analysis was carried out for each fuel and flowrate condition three times. Figure 5.6 shows the rotameter calibration for each fuel employed in the present work.

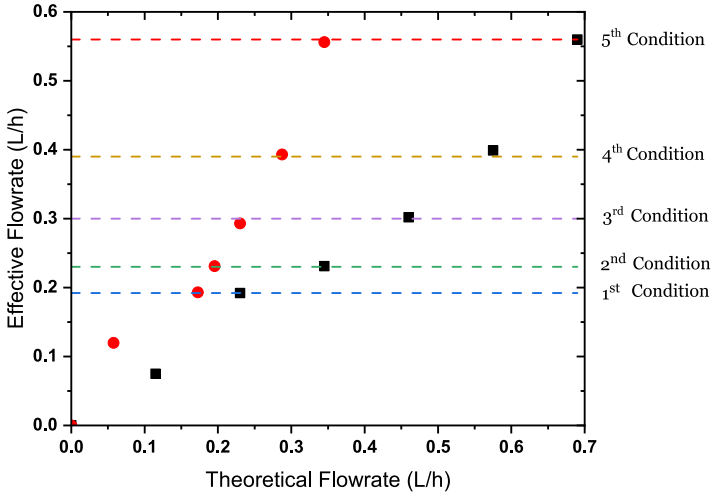

Figure 5.6: Rotameter calibration for alternative and conventional jet fuel: ■ - HVO, HVO + 0.5% Al, HVO + 1% Al; ● - Jet A-1

Five different fuel flowrates conditions were examined for each type of fuel considered in this study. The analysis reveals that regardless of the flowrate imposed, HVO and nanofuels possess similar effective flowrate. The nanofuels considered in this particular study are HVO with aluminum nanoparticles in a size of 40 nm and a particle concentration of 0.5 wt.% and 1 wt.%. For the spray analysis under non reacting, no additional particle size and concentration are explored following the results obtained in the single droplet combustion. The most significant difference is associated with Jet A-1 concerning alternative fuels. The values for the fuel flowrates displayed in Figure 5.6 were considered based on the minimum and maximum power output intended for the combustion chamber design. The combustion chamber was designed based on the literature for burning alternative fuels, such as biofuel and nanofuels, with a power output between 2 and 6 kW, as described in chapter 6.

After the fuel calibration, the operating conditions regarding the imaging technique and Phase-Doppler Interferometry are established. In this context, different air and fuel ratios are defined for deeper insight into the dynamics of the spray, using Jet A-1, HVO, and HVO with aluminum nanoparticles. The first phase of experiments is devoted to the imaging technique in order to visualize the spray and determine the primary and secondary atomization. Focusing on the experiments dedicated to the spray dynamics under non reacting conditions using the imaging technique, the breakup length, and the spray cone angle is evaluated. To accomplish this purpose, various fuel and air flowrates were considered to better understand the fuel and liquid interactions. For a detailed analysis, the operating conditions applied in the imaging technique are presented in Table 5.3.

Table 5.3: Operating conditions employed in the experiments related to the imaging technique. Based on that, experiments are dedicated to the breakup length (BL), and spray cone angle (SCA).

		Jet A-1		**HVO**		**HVO+0.5% Al**	**HVO+1% Al**
	$\dot{m}_a$	BL	SCA	BL	SCA	BL	BL
1st Condition	0.11 g/s	✔		✔		✔	
	0.22 g/s	✔		✔		✔	
	0.33 g/s		✔		✔		
	0.66 g/s		✔		✔		
2nd Condition	0.11 g/s	✔		✔		✔	
	0.22 g/s	✔	✔	✔	✔	✔	
3rd Condition	0.11 g/s	✔		✔		✔	
	0.22 g/s	✔		✔		✔	
4th Condition	0.11 g/s	✔		✔		✔	✔
	0.22 g/s	✔	✔	✔	✔	✔	
	0.33 g/s	✔	✔	✔	✔	✔	
	0.55 g/s		✔		✔		
5th Condition	0.11 g/s	✔		✔		✔	✔
	0.22 g/s	✔		✔		✔	✔

Different sets of experiments are carried out that rely on the breakup length (BL), and spray cone angle (SCA). The checkmark (✔) highlights the operating condition for each fuel and set of experiments.

Regarding the measurements of the droplet size and velocity distributions, Phase-Doppler Interferometry is employed. The PDI measurements are performed in several axial and radial positions with respect to the atomizer exit (Z = 0 mm). For the axial locations, four positions are considered: Z = 5, 10, 15, and 20 mm. The selection of these distances was correlated to the breakup structure of the spray. Since PDI relies on breaking the spray into droplets, its use is not applicable to study the primary atomization, where the instabilities begin to develop. Therefore, an initial axial position was chosen after the primary atomization. For each Z, a set of measurements was performed along the radial-X and radial-Y axes in 2 mm steps for the two perpendicular axes, as displayed in Figure 5.5. A summary of the positions used in PDI measurements is presented in Table 5.4. Similar to the imaging technique, different air and fuel flowrates are considered for each PDI measurement. Table 5.5 shows the operating conditions used in the PDI technique. The fuel dimensionless numbers for each operating condition are displayed in Appendix E.1.

Table 5.4: Axial (Z) and radial distances (Rx and Ry) employed in the experiments related to the Phase-Doppler Interferometry measurements.

Axial Distance	**Radial Distance**	
Z	Rx	Ry
5 mm	-6 mm to 6 mm	-6 mm to 6 mm
10 mm	-10 mm to 10 mm	-10 mm to 10 mm
15 mm	-10 mm to 10 mm	-10 mm to 10 mm
20 mm	-10 mm to 10 mm	-10 mm to 10 mm

Table 5.5: Operating conditions employed in the experiments related to the Phase-Doppler Interferometry measurements.

		Jet A-1	**HVO**	**HVO+0.5% Al**	**HVO+1% Al**
1st Condition	$\dot{m}_a$ = 0.33 g/s	✔	✔	✔	✔
	$\dot{m}_a$ = 0.66 g/s	✔	✔	✔	✔
4th Condition	$\dot{m}_a$ = 0.22 g/s	✔	✔		
	$\dot{m}_a$ = 0.33 g/s	✔	✔	✔	
	$\dot{m}_a$ = 0.55 g/s	✔	✔	✔	

5.2.4 Image Data Processing

The imaging technique allows qualitative and quantitative measurements of the spray dynamics. Spray visualization is a method to investigate spray morphology and provide deeper insights into both primary and secondary atomization processes. After primary atomization, ligaments and large droplets are spotted, which subsequently fragment into smaller droplets, indicating secondary atomization. The region closer to the nozzle, where the primary atomization occurs, is characterized by an optically dense region of ligaments and droplets obstructing accurate examination. Consequently, this study explores the application of visual inspection and image data processing techniques dedicated to analyzing primary atomization. PDI measurements of secondary atomization complement these methods to investigate the spray dynamics under non-reactive conditions in depth.

Obtaining quantitative measurements from image acquisition requires image data processing, which is essential to ensure that the imaging technique can provide reliable and consistent measurements. An imaging technique was applied to different fuels and air-fuel ratios to provide a set of data images. To perform detailed measurements of the spray characteristics, the set of images should be carefully treated. Additionally, the spray properties are space-dimensional properties, which require the conversion of pixels to physical dimensions, as will be further discussed. In this context, a detailed explanation of the algorithms dedicated to the measurements of breakup length and spray cone angle developed in the MATLAB software is provided.

5.2.4.1 Breakup Length

The breakup length for the Jet A-1, HVO, and nanofuels are explored, which can provide valuable insight into the atomization quality. The measurements of the breakup length are challenging, and due to this, several images were recorded in focus structures to be further analyzed. To accomplish this purpose, an algorithm in MATLAB software was developed. An illustration of the algorithm dedicated to breakup length measurements is shown in Figure 5.7.

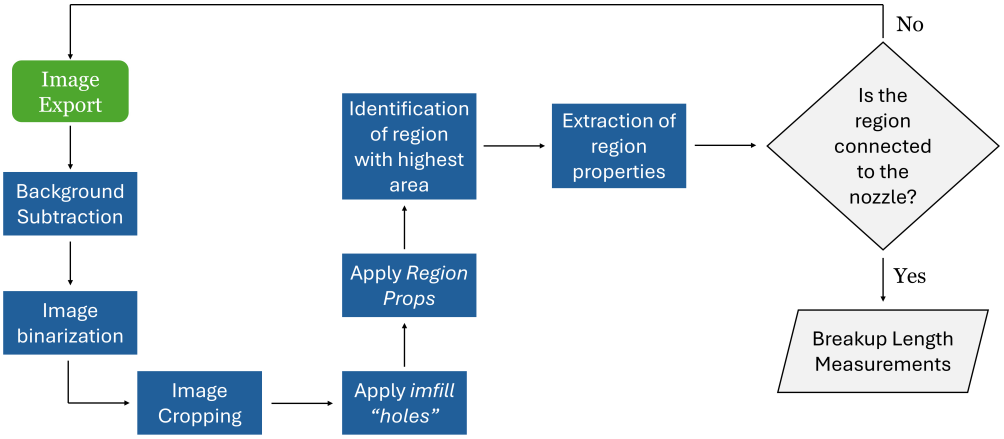

Figure 5.7: Illustration of the image data processing for breakup length.

A series of actions are performed to acquire the breakup length of each fuel, requiring instantaneous breakup length images and background images, as shown in Figure 5.8. The first step is dedicated to subtracting the background and instantaneous breakup length images. Then, the subtracted image is applied and binarized through a threshold value selected based on a meticulous analysis, as shown in Figure 5.8 b).

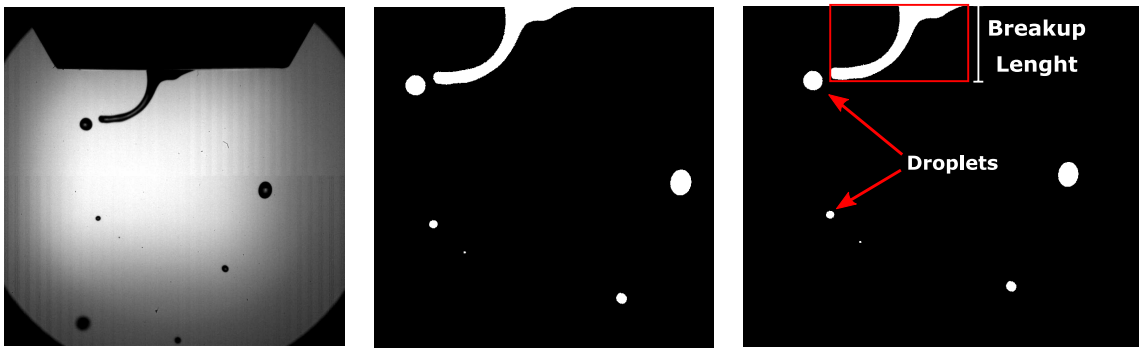

(a) (b) (c)

Figure 5.8: Image data processing for breakup length: a) Original image; b) Cropped image; c) Identification of the breakup length.

The image was cropped to highlight the spray structure. The breakup length corresponding to the continuous fluid structure was identified, and its dimensions were determined by a function noted as "region props". In this context, the breakup length represents the maximal extent along the axial direction, identified as the structure with the highest area. Moreover, the position of the region box is analyzed to ensure that the measurements are only focused

on the continuous portion of the jet, measured from the nozzle to the breakup point. If the analyzed region is not connected to the nozzle, the image is discarded, and a novel image is investigated. All data related to the height, width, and position of the breakup structure were exported in a matrix for further evaluation. In this particular analysis, the evaluated data corresponds to a continuous liquid portion attached to the atomizer nozzle, and any secondary droplets are discarded, as shown in Figure 5.8 c). The standard deviation of each operating condition is provided in the results section. As previously mentioned, the spray characteristics are analyzed by image data processing, which requires a conversion of pixels presented in images to physical dimensions. Consequently, the atomizer nozzle is used as a reference, and a pixel conversion to mm is performed. Table 5.6 shows the pixel size of all the fuels tested in the breakup length experiments.

Table 5.6: Pixel size concerning the breakup length experiments for all the fuels.

Fuels	**Pixel Size**
Jet A-1	0.035 mm/pixel
HVO	0.031 mm/pixel
HVO + 0.5% Al	0.032 mm/pixel
HVO + 1% Al	0.021 mm/pixel

The analysis of the breakup length can be difficult and requires examining the threshold value and the number of frames required for the analysis. Figure 5.9 and 5.10 show the influence of the number of frames and the threshold value, respectively. Different air flowrate were considered using the 4^{th} fuel operating condition displayed in Figure 5.6.

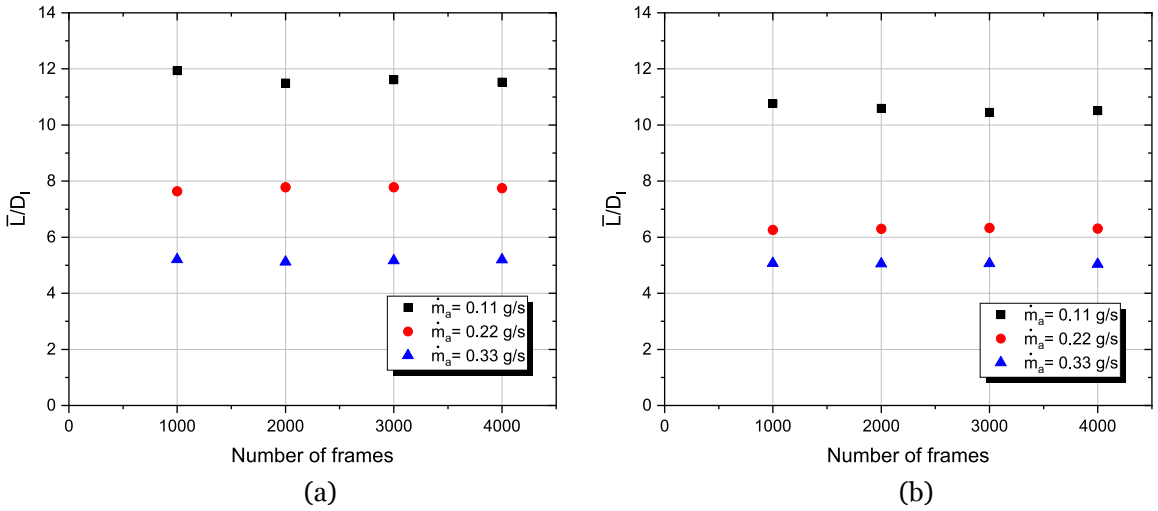

Figure 5.9: Influence of the number of frames in the breakup length analysis: a) HVO; b) Jet A-1. Three different air flowrate are considered using 4^{th} fuel operating conditions.

The results show no significant variations in the breakup length in the amount of data explored. Due to this, 4000 frames were considered, guaranteeing that it is possible to understand the influence of the AFR on the breakup length using a threshold value of 0.2, as displayed in Figure 5.10. This value was selected to guarantee the repeatability and independence of the sample size. The mean breakup length ($\overline{L}$) is evaluated as the arithmetic mean

of instantaneous breakup length values obtained in the 4000 frames and subsequently normalized by the nozzle diameter (D_l), as will be discussed in the results section.

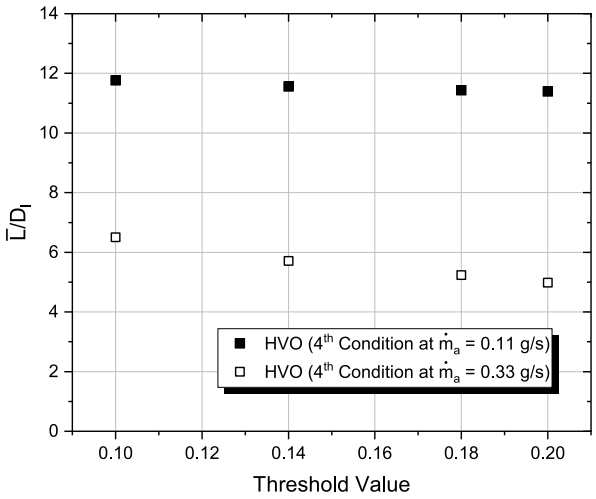

Figure 5.10: Influence of the threshold value in the breakup length analysis for HVO in the 4^{th} conditions under two air flowrates.

5.2.4.2 Spray Cone Angle

To determine the spray cone angle (SCA), an in-house algorithm was developed to process the image data in MATLAB software. A brief illustration of the spray cone angle algorithm is displayed in Figure 5.11.

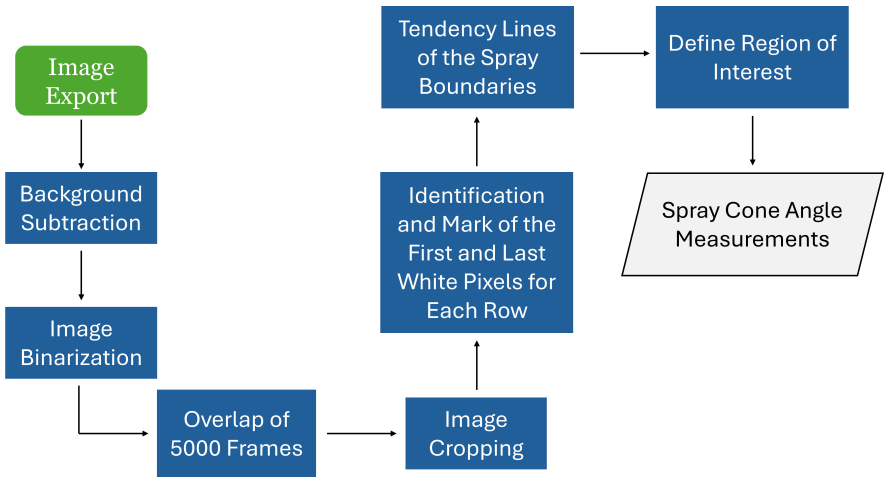

Figure 5.11: Illustration of the image data processing for spray cone angle.

The analysis starts with the background subtraction followed by an image binarization using a threshold value. In the image matrix, the spray is identified with a value equal to 1, and the rest of the image is equal to 0. Since the spray is considered a group of droplets, an overlap of several frames is performed to capture the spray morphology as displayed in Figure 5.12.

In this analysis, 5000 frames are considered to determine the spray cone angle. This value was selected based on a statistical study, as will be further discussed in this subsection. Subsequently, the spray edges were identified and marked as the first and last white pixels with

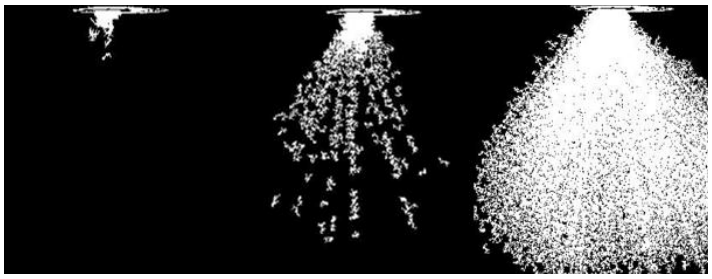

Figure 5.12: Visualization of the binarization of the spray using several frames.

red and green cross marks for each row of the image. Then, two lines with the best fitting describe the spray periphery. Finally, a region of interest (ROI) is defined and highlighted by blue, red, and green lines, as shown in Figure 5.13. Based on this, the spray cone angle is achieved by trigonometric relationships.

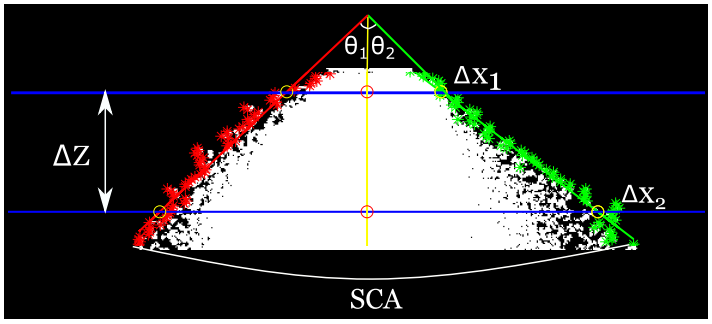

Figure 5.13: Illustration of the parameters relevant for the SCA analysis.

The equation related to the spray cone angle measurements is given by:

$$SCA(^{\circ}) = 2tan^{-1}\left(\frac{\Delta x_1 - \Delta x_2}{2\Delta Z}\right) \quad (5.1)$$

where x_1, x_2 and Z are the parameters displayed in Figure 5.13. The uncertainties in this study were exclusively attributed to the spray boundaries. Thus, a maximum uncertainty associated with their location was defined to be ± 2 pixel. Therefore, the associated absolute error can be calculated with the following equation:

$$|\Delta SCA| = \left|\frac{\partial f}{\partial x_1}\right| \cdot |\Delta x_1| + \left|\frac{\partial f}{\partial x_2}\right| \cdot |\Delta x_2| + \left|\frac{\partial f}{\partial Z}\right| \cdot |\Delta Z| \quad (5.2)$$

The absolute error was analyzed for all the operating conditions, with the maximum value of 1.7°. To explore the swirl effect, two angle angles (θ_1, θ_2) were analyzed with respect to vertical central lines coincident with the atomizer nozzle exit as displayed in Figure 5.13. The asymmetry of the spray will be discussed in the results section. The pixel size related to the spray cone angle is presented in Table 5.7.

Table 5.7: Pixel size concerning the spray cone angle measurements for all the fuels.

Fuels	Pixel Size
Jet A-1	0.053 mm/pixel
HVO	0.062 mm/pixel

A statistical study determined the specific number of frames and threshold values. Figure 5.14 shows the influence of the threshold value and number of frames in the spray cone angle. HVO and Jet A-1 are considered in the 4^{th} conditions at two air flowrates for this examination. The results show that the spray cone angle is more sensitive to threshold variations than the number of frames. Based on that, the experiments obtained 5000 frames and a threshold value of 0.18. A more detailed analysis regarding the number of frames and threshold on the spray cone angle is displayed in Appendix D.1 and Appendix D.2.

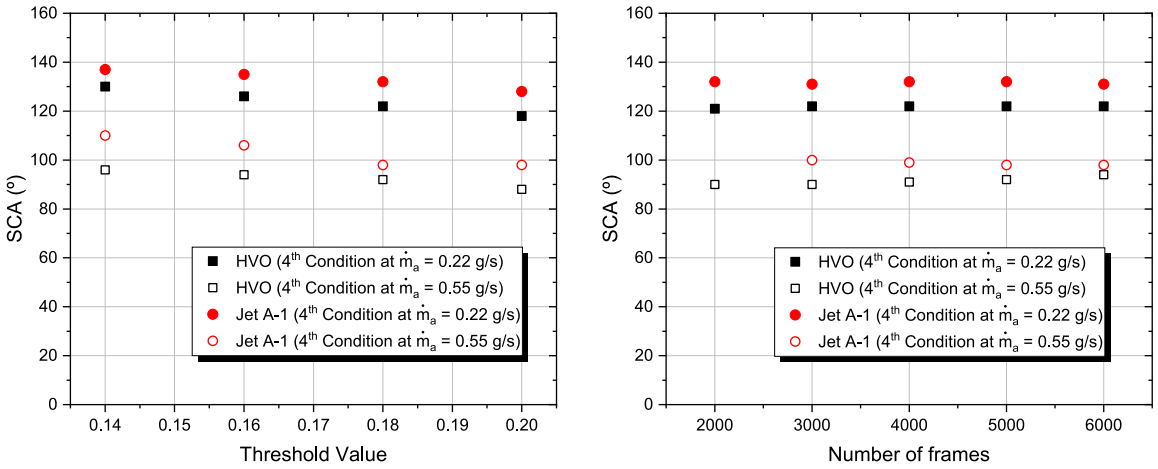

Figure 5.14: Influence of the a) threshold value and b) number of frames in the SCA analysis.

5.3 Experimental Results

The present section is dedicated to experimental results concerning the near and far fields of spray. Qualitative and quantitative results regarding the atomization of conventional and alternative jet fuel are acquired by imaging technique and Phase-Doppler Interferometer. Firstly, the visualization is presented, followed by a brief discussion of the breakup structures at several air-fuel ratios. Subsequently, a detailed examination is provided, and a comparative analysis with breakup length correlations presented in the literature is performed. Following this, a brief investigation of the spray cone angle is conducted. Finally, PDI analysis is provided, elucidating the overall spray behavior for different AFRs under several axial and radial distances. Additionally, the addition of nanoparticles is explored in the atomization process.

5.3.1 Visualization

Visualization for a wide range of operating conditions was performed using a high-speed camera to capture the breakup structures in detail. This visualization provides insights regarding the breakup of conventional and alternative fuels, which will be scrutinized further in terms of mean breakup length. The results offer a qualitative analysis near the nozzle orifice to enhance understanding of the air-fuel interaction and the primary atomization. The first process, denominated primary atomization, occurs near the jet nozzle, where shear forces at the air and fuel interface destabilize the liquid jet, leading to its fragmentation into droplets and ligaments. To understand this, the visualization regarding the fuel flowrate variation is presented in Figure 5.15 and Figure 5.16. For this analysis, the fuel flowrate is increased while the air flowrate is kept similar in both figures. Regardless of the fuel flowrate imposed, a continuous cylindrical body is detected released by the atomizer nozzle. This liquid jet is subjected to the airflow, creating instabilities. Figure 5.15 shows the development of the liquid jet for the lowest fuel flowrate where the liquid jet remains attached to the nozzle and elongates. As the time evolves, its thickness gradually reduces and from Figure 5.15 a) to c), the expansion of the liquid jet is noticeable with a large head droplet attached to its extremity. As the liquid jet continues to extend and its thickness decreases, it becomes increasingly susceptible to disruption, which is clearly spotted in Figure 5.15 c) to f).

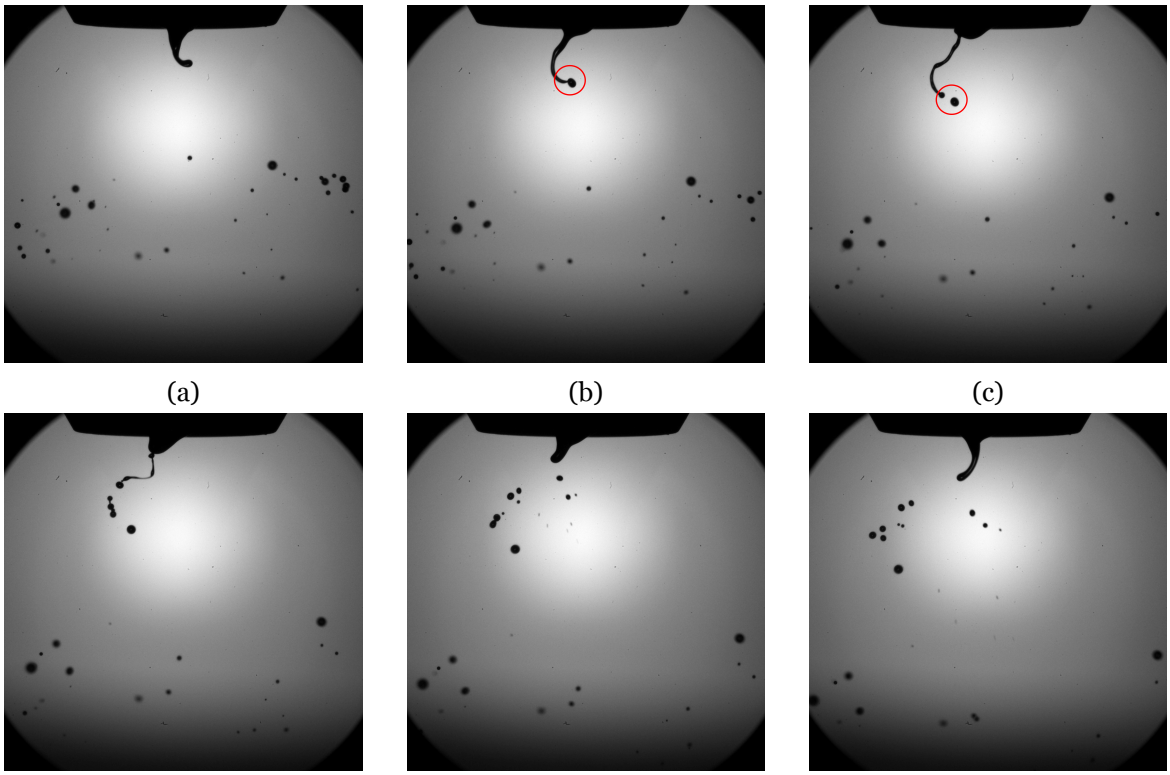

Figure 5.15: Sequence of images of HVO equally spaced 1.5 ms under the following conditions: 1^{st} fuel condition, $\dot{m}_a$ = 0.11 g/s.

Under higher fuel flowrate conditions, in Figure 5.16, it is observed that the liquid jet attached to the nozzle extends farther than the one depicted in Figure 5.15. Besides that, several in-

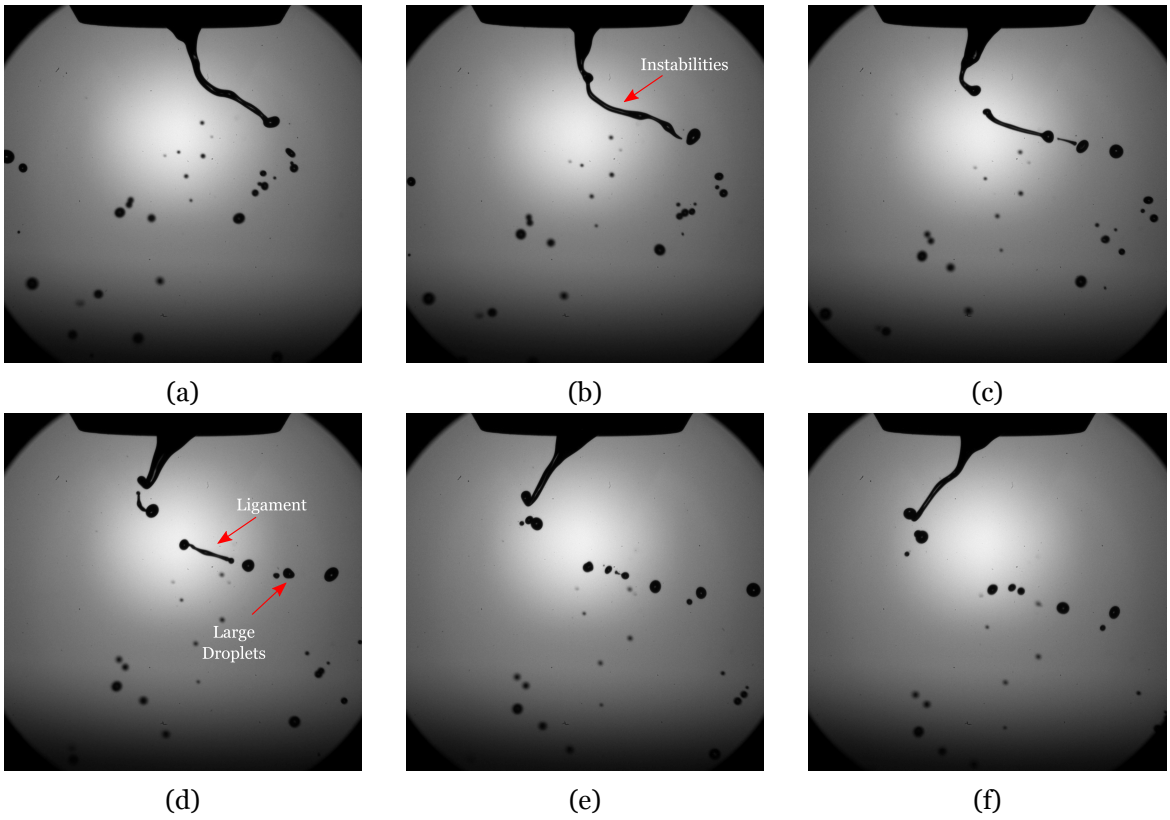

Figure 5.16: Sequence of images of HVO equally spaced 1.5 ms under the following conditions: 5^{th} fuel condition, $\dot{m}_a$ = 0.11 g/s.

stabilities are spotted as the liquid jet is extended. These primary instabilities grow as they move downstream and finally cause the breakup of the jet [292]. Eventually, the ligament detaches Figure 5.16 (e) from the nozzle and breaks up into ligaments and large droplets. The breakup occurs due to aerodynamic forces caused by the airflow in the liquid jet with a relatively low velocity, which increases the kinetic energy of the liquid phase and induces liquid stretching. As a result, the liquid breaks when the aerodynamic forces overcome the surface tension [425]. After the ligament fragmentation into droplets, a new continuous liquid portion is released from the nozzle that flaps in an opposite direction with respect to the vertical axis. This phenomenon is denominated as jet flapping. Jet flapping is characterized by a lateral oscillation of the jet core around the axis of the atomizer, which can be enhanced due to air swirl, especially when in a lower airflow, being responsible for the lateral growth of the spray [260, 282]. As previously stated, in this experimental study, fuel atomization is achieved using an air-assisted atomizer possessing a swirl. The analysis demonstrates that an increase in the fuel flowrates displays a longer liquid portion that releases a variety of filaments with different sizes and shapes, as well as large droplets. For lower fuel flowrates, the liquid jet fragmentation seems to produce smaller droplets, as will be further discussed.

To visualize the influence of the airflow on the HVO liquid jet, the air flowrate was increased, as depicted in Figure 5.17. This analysis considered three air flowrates ($\dot{m}_a$ = 0.11 g/s, 0.22 g/s, and 0.33 g/s), while the fuel flowrate was kept constant to comprehend its influence in the atomization process. For the lowest air flowrate, the development of a liquid jet is similar

to the previous description provided for Figures 5.15 and 5.16. However, the jet breakup behavior is significantly affected when the air velocity increases, with a noticeable reduction in length and in the size of the droplets released by the fragmentation. Furthermore, the detachment of liquid from the surface of the jet occurs with greater intensity. The influence of the airflow also promotes a helical deformation in the liquid jet, resulting in the fragmentation of liquid blobs. It is noted that the development of liquid sheets is accompanied by substantial rims and ligaments [338]. Additionally, increasing the air flowrate means no elongation of the liquid portion, and its thickness is significantly reduced, leading to a more intense atomization. This observation is caused by the increase of the air velocity that promoted an increase in shear between the liquid and air stream [306]. The air velocity increase proves the atomization effectiveness, which leads to an increase in the aerodynamic Weber number, as shown in Appendix E.1. The interpretation and comparison of the different dimensionless numbers are relevant to understanding the topology of the breakup structures.

Following the brief description of the influence of the air and fuel flowrate variation, the visualization for the different fuels tested is provided. Figure 5.18 shows the liquid and air interaction 5^{th} fuel condition and $\dot{m}_a$ = 0.22 g/s for a-c) HVO, d-f) Jet A-1, g-i) HVO + 1% Al. As highlighted in the previous HVO image sequence, bag breakup is detected under these specific conditions. This phenomenon is perceived when a thin balloon or bag-like structure is near the nozzle. In this case, the breakup of the liquid portion is initiated as a consequence of the bag formation. As time evolves, the bag expands until it eventually ruptures. The disruption of the bag promotes the formation of droplets and ligaments, which can be amplified by the swirl presence. The swirl provides an addition of angular momentum and tends to propel larger droplets or liquid fragments toward the periphery due to centrifugal forces, and this effect persists along their trajectory due to the greater momentum of the larger droplets [271, 290]. The breakup occurs when the surface tension is overcome by the effect of atomizing air, resulting in the formation of smaller droplets, while its rim fragments release liquid lumps or large droplets, as illustrated in Figure 5.18.

A similar dynamic is detected for Jet A-1, where a bag breakup is spotted. The physical properties of each fuel were reported, and the main difference was related to viscosity, which can play a significant role in atomization. However, to comprehensively assess if there is a notable distinction between HVO and Jet A-1, a quantitative evaluation of the breakup length and secondary breakup is essential, as will be discussed in the following results. In respect to the characterization of the bag breakup, this phenomenon was spotted for low aerodynamic Weber number as respected in Appendix E.1, which does not follow the morphology classification defined by [244]. However, it should be pointed out that the physical properties of the fuels are not similar to the works presented in the literature, as well as the nozzle geometry. A relevant characteristic of this atomizer is the presence of a swirl, which significantly affects the spray dynamics. A deviation to the transition regimes with respect to the Lasheras and Hopfinger [244] was also reported by [290].

The addition of nanoparticles to the liquid fuel is presented in Figure 5.18 g) to i). For this

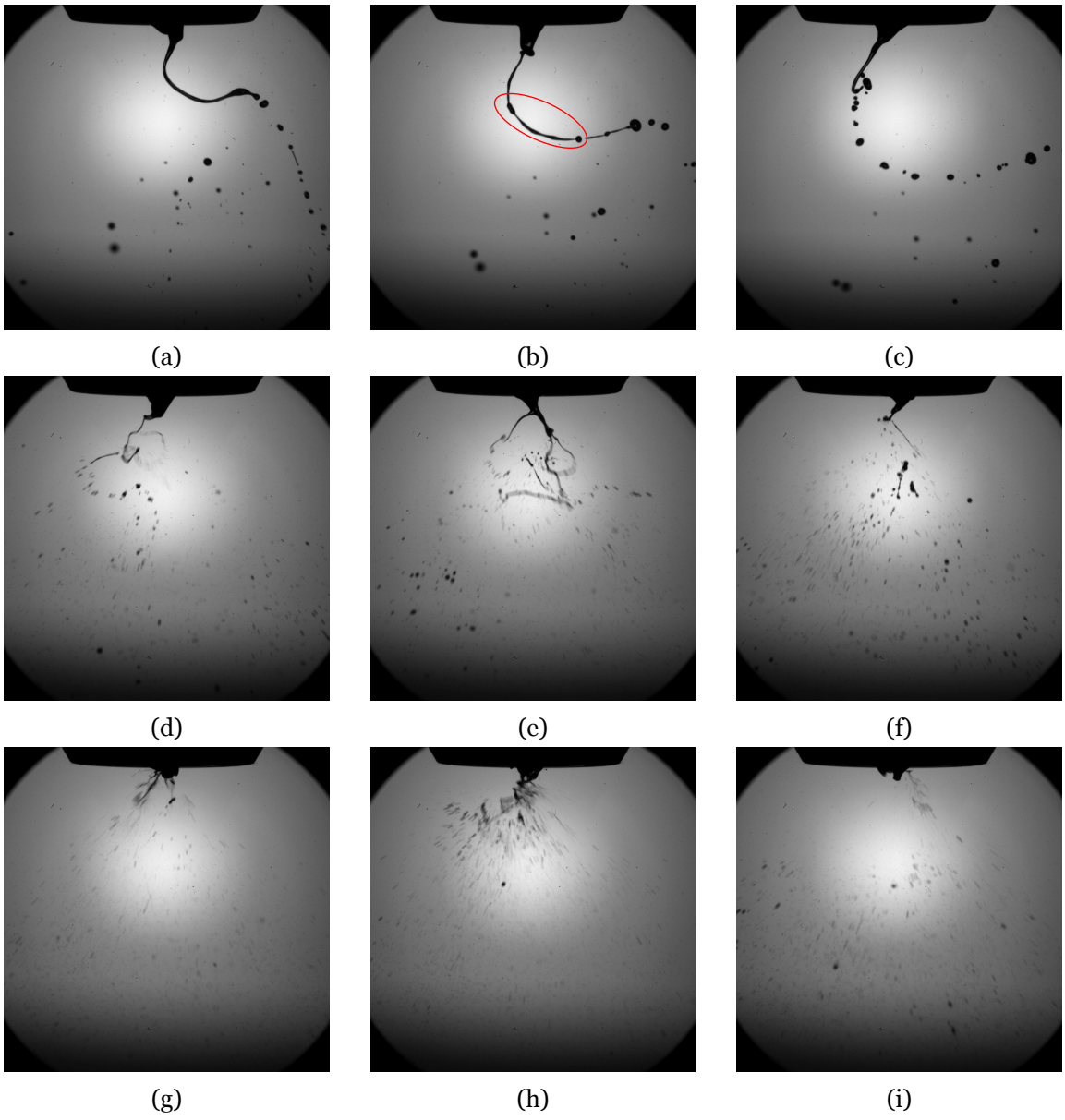

Figure 5.17: Sequence of images of HVO equally spaced 2.25 ms under the following conditions for 4^{th} fuel condition: a-c) $\dot{m}_a$ = 0.11 g/s; d-f) $\dot{m}_a$ = 0.22 g/s; g-i) $\dot{m}_a$ = 0.33 g/s.

analysis, aluminum particles in a size of 40 nm and a particle concentration of 1.0 wt.% are considered. The results reveal that liquid leaves the nozzle and disintegrates quickly. The sequence of images shows that the liquid jet distorts into arcs, stretches, and forms long and thin ligaments with instabilities. Analogous to the other fuels, thin filaments are spotted, and disruption of membranes results in small droplets. Moreover, a phenomenon denominated as flapping bag breakup was detected. This outcome is noticeable due to flapping instability when the bag-like structure exhibits oscillations around the central axis, leading to improved atomization due to the effective disruption of this structure, as previously reported by [426]. The authors attribute this event to the enhanced interaction between the bag structure and swirling atomizing air under reduced surface tension conditions amplified by the local recirculation zones [426].

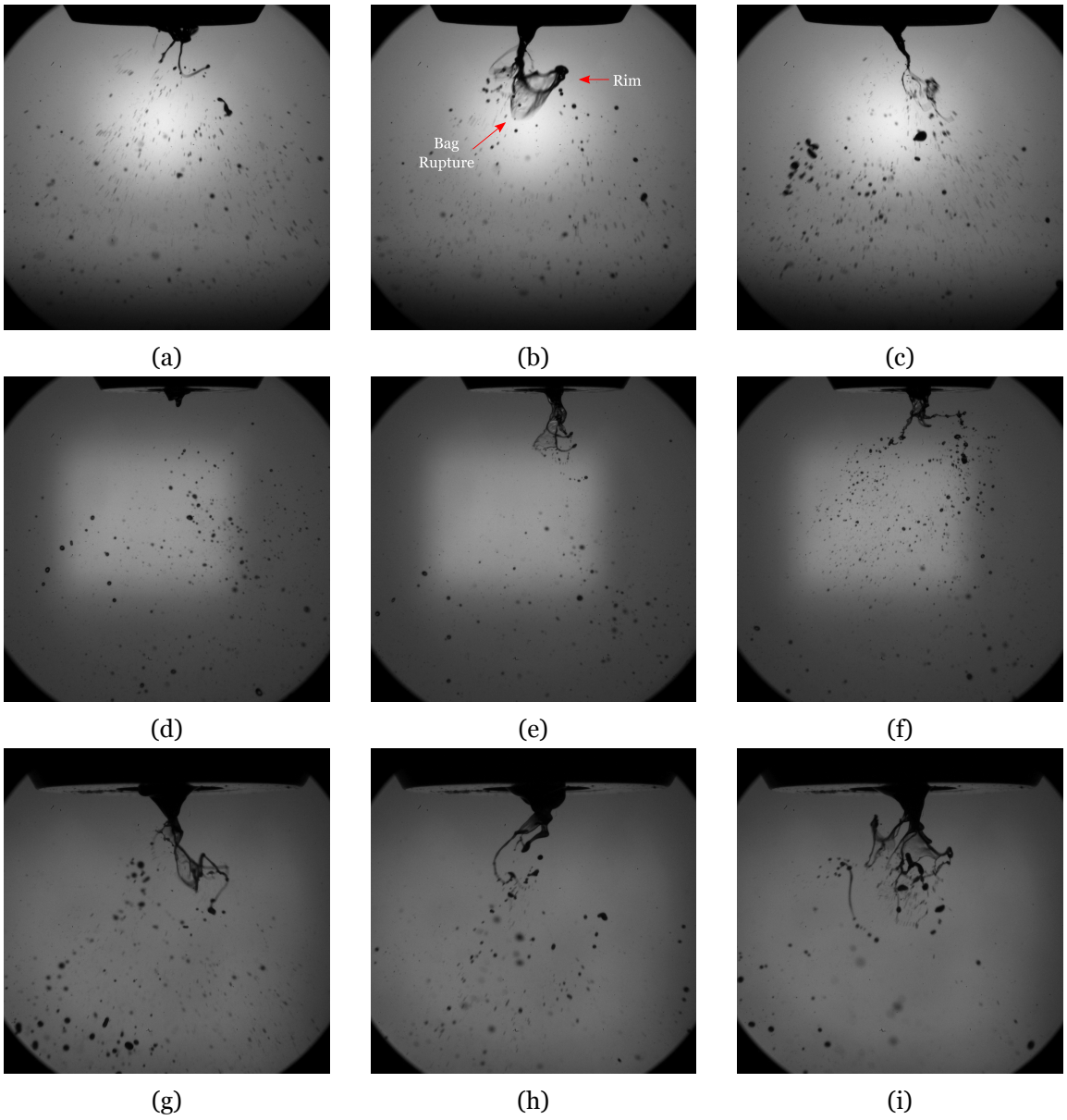

Figure 5.18: Sequence of images equally spaced 2.25 ms under the following conditions for 5^{th} fuel condition and $\dot{m}_a$ = 0.22 g/s for: a-c) HVO; d-f) Jet A-1; g-i) HVO + 1% Al.

5.3.2 Breakup Length

For a deeper understanding and comparison between the primary atomization of an alternative and conventional jet fuel, detailed measurements dedicated to the breakup are performed. The breakup length is defined as the continuous longitudinal extension of the liquid jet from the nozzle until the rupture point. This rupture is triggered by the aerodynamic forces from the high-speed gas flow act on the low-speed liquid jet, increasing the liquid kinetic energy and causing the fuel surface to stretch [425]. In this respect, the visualization provides information regarding the breakup characteristics, allowing measurements of its length through image data processing. The analysis of the primary atomization region is usually characterized by the jet breakup length being a signature of the atomization quality, as previously stated by [296]. This region is mainly characterized by large, irregular, ligament-

like elements [418]. An investigation focused on the primary breakup length is essential for the performance of fuel injectors and for the development of computational models of the atomization process, since it highlights where the fully developed multiphase flow region begins. Figure 5.19 shows the mean of instantaneous breakup length ($\overline{L}$) in the axial direction normalized by the liquid bore diameter of the atomizer (D_l). This analysis focuses on the influence of increasing the fuel velocity on the breakup length while remaining constant in the air velocity. The evaluation of the increase in fuel velocity is expressed in the horizontal axis by the liquid Reynolds number for all the fuels tested in the present study. The liquid Reynolds Number is defined by the following expression:

$$Re_l = \frac{U_l D_l}{\nu_l}, \quad (5.3)$$

where U_l is the fuel velocity, D_l liquid bore diameter and ν_l fuel kinematic viscosity. Regardless of the fuel employed, the results reveal that increasing the Re_L results in an increase in the breakup length. This means that longer breakup corresponds to higher fuel flowrates. Similar findings were already reported by Roudini and G. Wozniak [427]. The error bars presented in Figure 5.19 correspond to the standard deviation of the mean breakup length normalized by the liquid diameter orifice. The results also reveal no significant difference between pure HVO and HVO with aluminum nanoparticles in terms of mean breakup length normalized by the liquid bore diameter. Due to the viscosity value, the Reynolds number differs mainly between the Jet A-1 and alternative fuels.

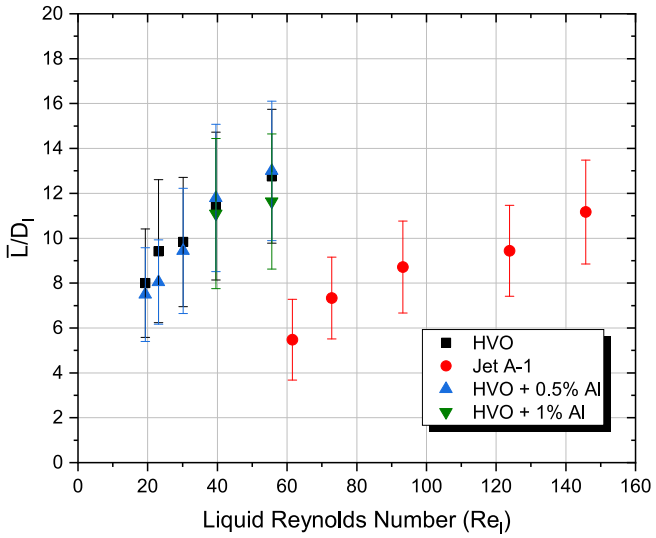

Figure 5.19: Influence of liquid Reynolds Number on the normalized mean breakup length, considering $\dot{m}_a$ = 0.11 g/s.

Subsequent to analyzing the influence of fuel flowrate, the variation of the air velocity was investigated. For this evaluation, the mean breakup length was normalized by liquid bore diameter, and the number of breakups was also explored. Since the present work employs an air-assisted atomizer, the air provides the energy required to disintegrate the liquid jet. Consequently, the aerodynamic Weber number is an essential dimensionless number to charac-

terize the primary atomization, incorporating the relative velocity between fluids and their physical properties. Figure 5.20 shows the influence of We_a in the normalized mean breakup length. The expression related to the aerodynamic Weber number (We_a) is displayed in Equation 2.49. Additionally, the breakup numbers events are displayed in Figure 5.20 for a) HVO and b) Jet A-1. The results reveal that an increase in the air velocity leads to lower breakup lengths, indicating that the influence of aerodynamic force on liquid disintegration is pronounced. As the aerodynamic Weber number increases, indicating that the aerodynamic forces acting on the gas exceed the fuel surface tension, the fuel and air interface experiences instabilities governed by capillarity, shear, acceleration, or a combination of these factors. Consequently, considerably low aerodynamic Weber number values may be undesirable in applications such as propulsion or additive manufacturing [281]. Identifying the primary atomization is also essential to analyze the droplet diameter and velocity distribution in the secondary atomization. In this context, detailed measurements of spherical droplets presented in the secondary atomization are required to fully compare spray characteristics of conventional and alternative fuels. Thus, the length of the primary atomization is explored to ease the PDI measurements. The results reveal that Jet A-1 presents a breakup length of 7.6, 4.56, and 3.6 mm from the lowest air velocity to the higher values, while HVO possesses 9.1, 5,8, and 4 mm. Consequently, the conditions with the lowest We_a were discarded from the PDI measurements since the measurements begin at Z = 5 mm, as presented in Table 5.4 and Table 5.5. A more detailed description of the results focused on the PDI measurements will be further elaborated. Furthermore, the frequency of liquid jet breakups was quantified. In this respect, it was observed that an increase in the aerodynamic effect produces a higher number of breakup events, regardless of the fuel. The analysis was performed on a sample of 4000 images for each fuel, and no notable distinctions were detected between the fuels.

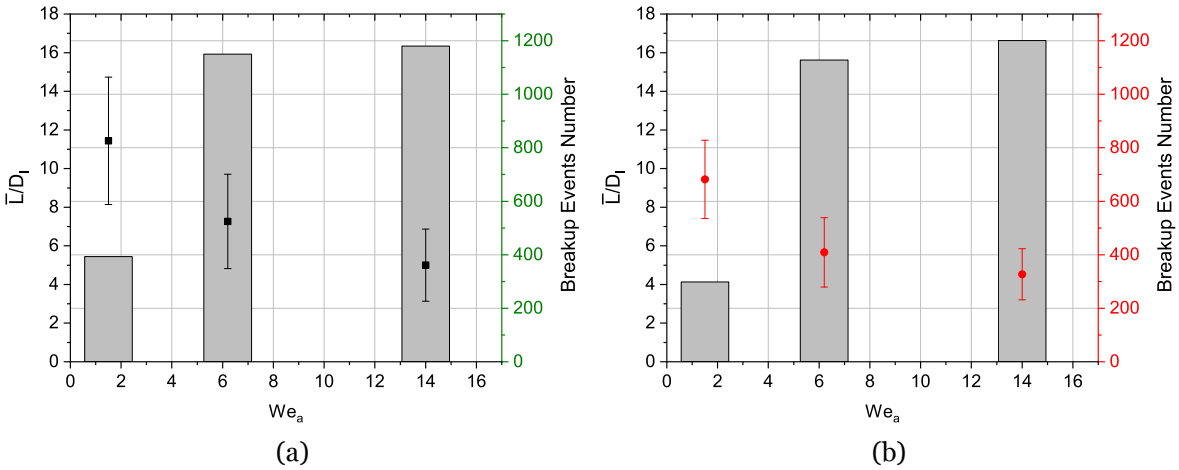

Figure 5.20: Influence of We_a in the normalized mean breakup length and breakup events for: a) HVO; b) Jet A-1.

As already mentioned, the breakup length can indicate atomization quality and be related to the droplet diameter on the secondary breakup. Due to this, in practical applications, such as aviation gas turbines, the combustion performance and emissions are significantly related to the atomization process. Figure 5.21 compares the breakup length of all the fuels employed in the present study. According to Lasheras and Hopfinger [244], the momentum flux ratio

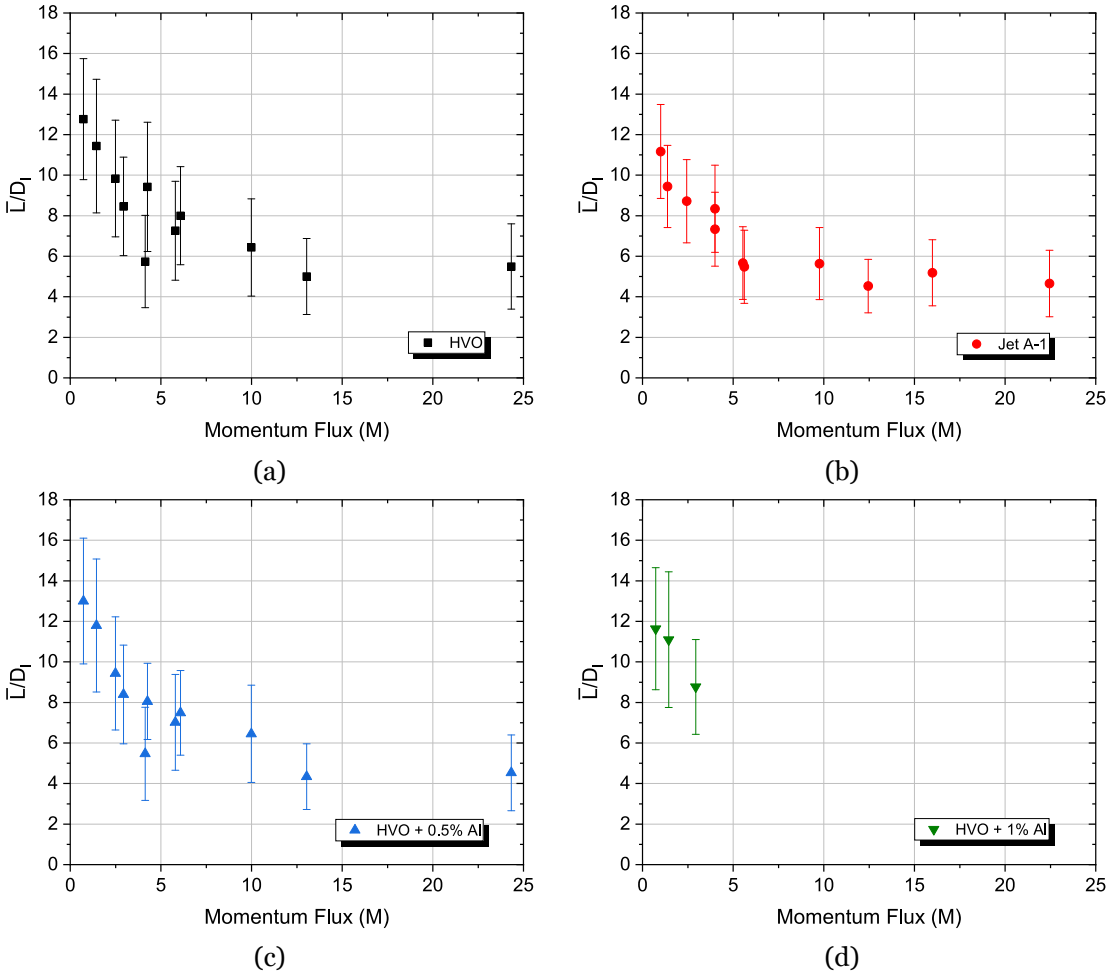

Figure 5.21: Normalized mean breakup length as a function of momentum flux (M) for: a) HVO; b) Jet A-1; c) HVO + 0.5 wt.% Al; d) HVO + 1.0 wt.%. Al.

(M) is the most relevant parameter for evaluating the breakup of an unbroken liquid core. The expression related to the momentum flux ratio is presented in Equation (2.50). In accordance with [244,283], if $M \ll 1$, the breakup is governed by the liquid jet. On the other hand, if $M \geq 1$, the breakup length is determined by the gas jet, whereas for considerably high M values, the length is very short. The breakup length corresponds to the maximum length from the nozzle liquid jet rupture point in the axial direction. The results show that increasing the momentum flux reduces the normalized mean breakup length regardless of the fuels used. For considerably lower M values, the normalized mean breakup length decreases sharply. As the momentum flux increases, it tends to converge at a constant rate. In practical applications, a shorter breakup length indicates a faster disintegration of the jet into smaller droplets, promoting a faster combustion process and enhancing the overall efficiency of the combustion systems. Additionally, the breakup length of the HVO and HVO with aluminum nanoparticles is slightly higher than the Jet A-1, which may be attributed to the higher viscosity of the alternative fuels. Moreover, an increase in the air flowrate leads to a shorter breakup length, and an opposite tendency is noticed for the increase in the fuel flow rate. This effect is pronounced by the aerodynamic force on liquid disintegration. Higher airflow is related to higher We_a, which can be explained by the increase in shear stress acting on the

fuel-air interface. Similar findings were reported by [252, 296].

Several authors provided correlations in literature to predict the mean breakup length through image analysis, as displayed in Table 2.9. Consequently, from the experimental results obtained in the present work, an empirical equation was formulated to predict the mean breakup length produced by an air-assisted atomizer with a swirl. Figure 5.22 shows the correlations provided in the literature, as well as the empirical correlation obtained in this work, highlighted by the blue, dashed line using the normalized mean breakup length results for conventional and alternative fuels.

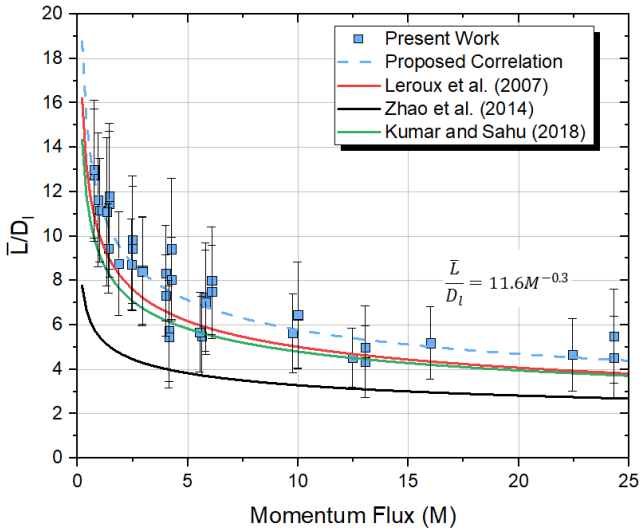

Figure 5.22: Normalized mean breakup length correlations.

The correlation obtained through the present study is expressed by:

$$\frac{\overline{L}}{D_l} = 11.6M^{-0.3} \quad (5.4)$$

This correlation indicates that the normalized mean breakup length exhibits a power law relation with the momentum flux ratio. This observation is in good agreement with the previous correlations [294–296]. In particular, the correlation proposed by [294] using shadowgraph analysis is quite similar to the one proposed in this present study, where the constant power law of the exponent is around –0.3 with respect to the momentum flux ratio. On the contrary, the correlation provided by Kumar and Sahu underpredicts the experimental data. According to the authors, the method employed in the analysis can be related to this difference [296]. To summarize, the breakup length is a relevant parameter to address the primary atomization of air-assisted atomization, depending on the fuel and relative velocity, the nozzle geometry, and the physical properties of the air and liquid fuel.

5.3.3 Spray Cone Angle

The results related to the spray cone angle are provided below. Firstly, the influence of the AFR on the spray cone angle for HVO and Jet A-1 was analyzed individually. This evaluation was conducted using 5000 frames and a threshold value of 0.18. Subsequently, half of the spray cone angle was investigated concerning the central line. The purpose is to address the spray symmetry and the potential impact of the swirl. As previously mentioned, an imaging technique was used to determine the spray cone angle. Spray cone angle can be defined as the angle formed between two lines drawn from the nozzle tip to the outer margins of the spray on either side, measured at a specified distance downstream of the flow [428]. To capture the complete cone angle of the spray, the image acquisition was carried out from a considerable distance, and the image data processing was performed in MATLAB software. Figure 5.23 shows the influence of the AFR in the spray cone angle (SCA) for a) HVO and b) Jet A-1. The results reveal that increasing the AFR while maintaining a constant fuel flowrate implies an increase in the air flowrate, suggesting a reduction in the spray cone angle. Additional higher AFR values were also evaluated. However, the results are not presented due to insufficient image contrast resulting from the finer atomization, which inhibited the possibility of determining the spray boundaries accurately. Due to this, this observation must comply with the results acquired in the Phase-Doppler Interferometer, as will be further discussed. The SCA measurements indicate that Jet A-1 displays a wider spray for approximately equal AFR compared to HVO.

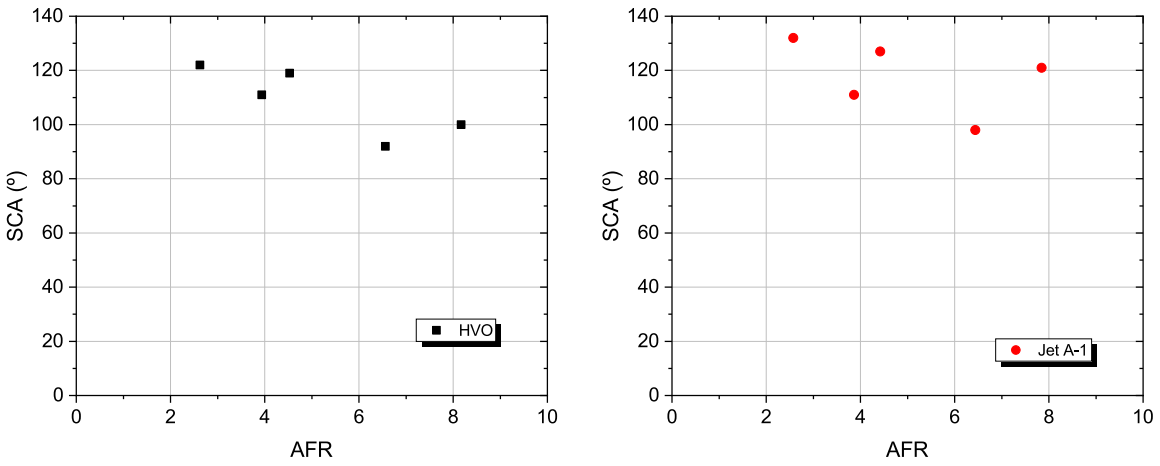

Figure 5.23: Influence of the AFR in the spray cone angle (SCA) for: a) HVO; b) Jet A-1.

This effect is due to HVO higher viscosity value compared to Jet A-1, which can reduce the SCA due to a dampening process reducing the tangential velocity. Wang and Lefebvre [429] reported that increasing fuel viscosity reduces the spray cone angle. The influence of viscosity in the decrease of the spray is a result of the effects of viscous forces that diminish the swirling motion of the liquid sheet and, hence, its initial emerging angle into the airflow [430]. An empirical equation to determine the half of the spray cone angle (θ) was developed by Giffen and Massey [255, 431].

$$tan(\theta) = 0.169\nu_L^{-0.131} \quad (5.5)$$

where ν_L is the fuel kinematic viscosity. The authors established this correlation for the cone half-angle and considered the influence of viscosity using a swirl-plate atomizer. Employing the correlation established by Giffen and Massey indicates that Jet A-1 possesses a spray cone angle of 113º whereas HVO presents an angle of 98º. This result follows the findings presented in Figure 5.23, highlighting that HVO possesses a lower spray cone angle as a consequence of its higher viscosity in comparison with Jet A-1. Measurements were taken from half of the spray on each side to evaluate the symmetry relative to a vertical line concentric to the atomizer nozzle. Figure 5.24 depicted the spray angle concerning the central line, identified as θ for a constant fuel flowrate, where θ_1 and θ_2 corresponds to the left and right side, respectively. This analysis considered the 4^{th} condition for HVO and Jet A-1. The findings suggest a slight deviation of θ_1 and θ_2. In more detail, the spray symmetric will be addressed in the following subsection, which is dedicated to the Phase Doppler Interferometer measurements.

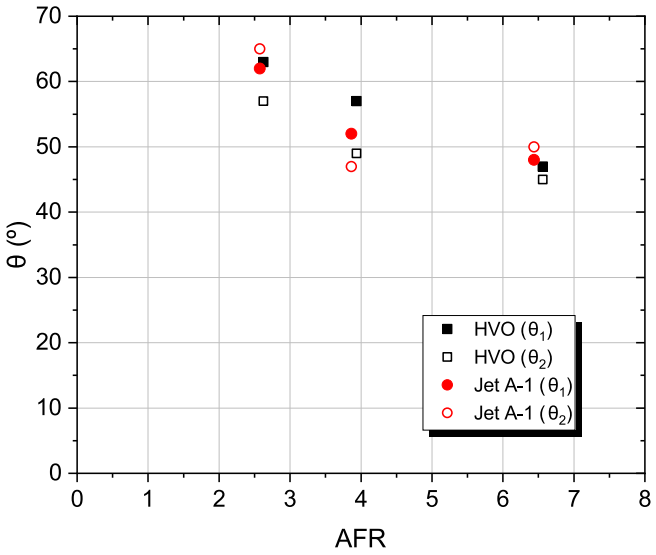

Figure 5.24: Half spray angle concerning the central line at the 4^{th} condition for HVO and Jet A-1.

The spray cone angle measurements are also valuable for the detailed analysis of droplet diameter and velocity distributions through the PDI technique. In this respect, primary atomization was visualized and identified, as previously stated. The spray cone angle measurements were performed approximately 7 mm below the nozzle atomizer, indicating that the spray possesses a width of 3.6 to 7 mm, depending on the air-fuel ratio. Due to this, the axial and radial positions employed in the experiments using a Phase Doppler Interferometer and displayed in Table 5.4 are capable of suitable the spray dynamics of conventional and alternative fuels.

5.3.4 PDI Results

The present subsection is dedicated to the experimental results of Phase-Doppler Interferometry (PDI) for conventional and alternative jet fuel. The PDI technique is employed to acquire the droplet size and velocity quantitative measurements in the radial and axial direction to better understand the spray dynamics. Moreover, different air-fuel ratios are considered for conventional and alternative fuels. Concerning the latter, nanofuels with a particle size of 40 nm and two particle concentrations (0.5 and 1.0 wt%.) are also explored. Consequently, the impact of adding nanoparticles to a liquid fuel is investigated in terms of spray behavior. The results presented in the previous subsection were mainly concerned with the different morphological changes of the spray, such as bag and ligament breakup acquired by an imaging technique. However, in the near region nozzle, measurements using the PDI system of the high droplet number density are challenging. They are unsuitable because of the intense scattering of light that obscures the internal details. Concerning the far field, the droplets are considerably small and cannot be acquired with precision with an image speed camera; due to this, the PDI technique is commonly employed to evaluate the secondary atomization through simultaneous local measurements. The results in this current subsection are only dedicated to the droplet diameter and velocity distribution of liquid fuels in the spray dynamics, which will be further used in the laboratory combustion chamber. From a combustion perspective, evaluating droplet diameter and velocity distributions is relevant to understanding fuel distribution within the combustor, which is essential to fuel performance. A summary of the operating conditions and the axial and radial positions are presented in Table 5.5 and Table 5.4, respectively. For each position, a sample of 5000 is considered, consistent with the literature, which ensures that this quantity is sufficient to stabilize the results [331, 423].

To gain an overall insight into the distribution of droplets in both axial and radial directions and the reliability of the measurements, Figure 5.25 shows data rate and spherical validation for Jet A-1. This analysis is performed considering four axial distances. The black, red, blue, and green lines correspond to Z = 5 mm, Z = 10 mm, Z = 15 mm, and Z = 20 mm from the atomizer nozzle. The Y-Axis was kept constant equal to zero, whereas the X-Axis varies from -10 to 10 mm, equally spaced 2 mm. Moreover, two AFR are considered, the results for an AFR of 7.9 are displayed in Figure 5.25 a) and b) while the data for an AFR of 15.7 is displayed in Figure 5.25 c) and d). Regardless of the AFR, increasing the axial distance (Z), it is observed that the data rate decreases and the spherical validation increases. As noted previously, a high droplet number density is commonly presented in the near nozzle, as shown in Figure 5.25. Concerning the spherical validation, the lowest values are presented in Z = 5 mm. As previously mentioned, the breakup length is higher in a considerably low air-fuel ratio. Due to this, to ensure that during the experiments, the measurements are concerned, the secondary droplet axial distance < 5 mm, as discarded in the PDI analysis since the spray is not completely developed. For axial locations of 10 mm $\leq$ Z $\leq$ 20 mm, the spherical validation is approximately between 80 % to 100 %, as displayed in Figure 5.25 b) and d). It is important to mention that a high validation rate in the spray indicates that the

droplets are predominantly spherical. Regarding the radial distance, Figure 5.25 shows that the droplets are highly concentrated in an annular region. The concentration reaches a peak before gradually becoming more uniform and spreading at higher location axial locations. In other words, the central region provides a low data rate, subsequently increasing and reducing significantly in the spray external boundaries. This behavior indicates that the spray is a hollow cone also influenced by the presence of the swirl where the tangential momentum transports the droplets to an outer zone [249].

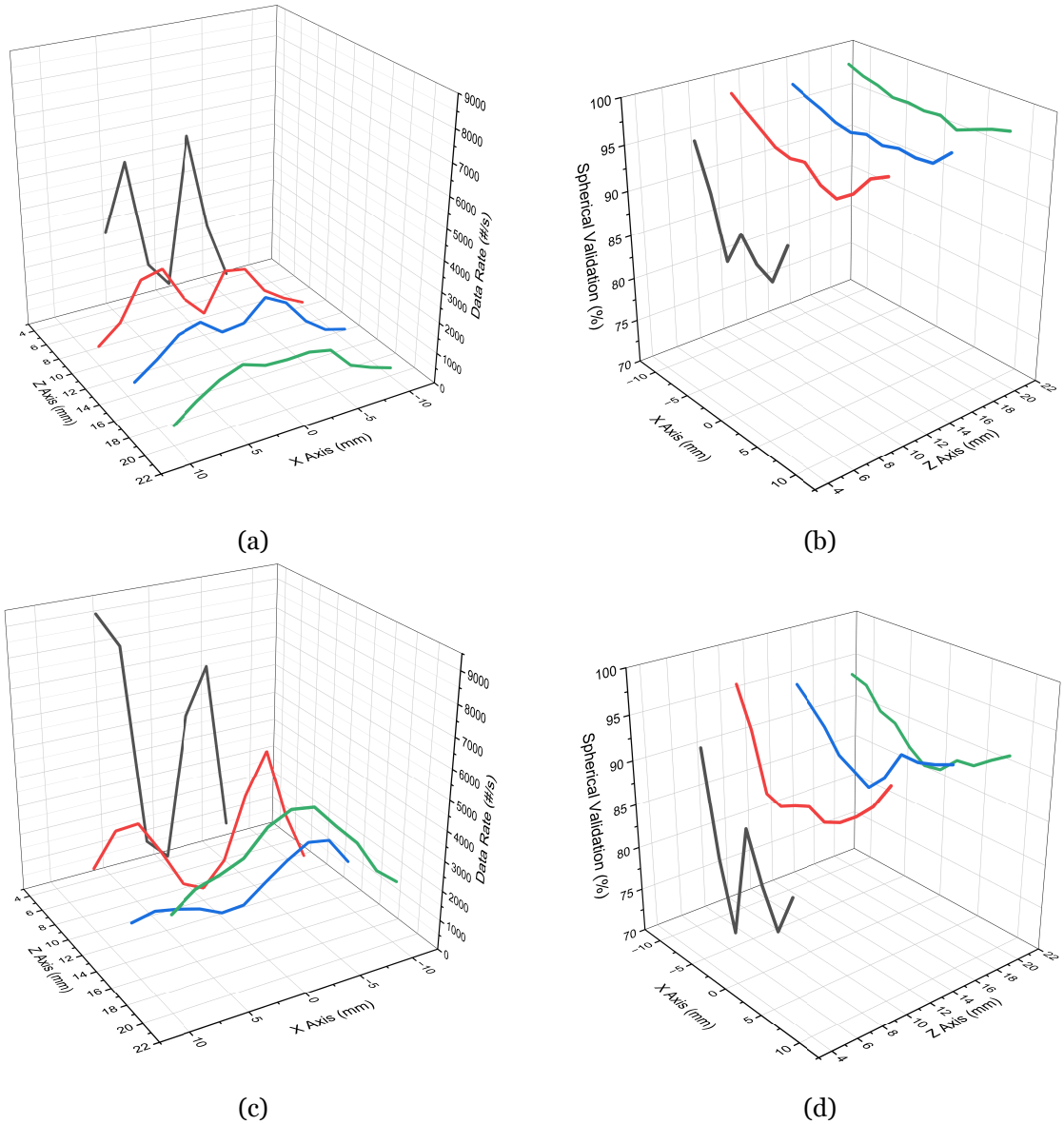

Figure 5.25: Jet A-1 calibration parameters at AFR = 7.9 for a) data rate; b) spherical validation. For an AFR = 15.7: c) data rate; d) spherical validation.

After a brief elucidation of the spray data rate and spherical validation, the influence on the axial velocity and Sauter mean diameter in the axial distance is provided. Sauter mean diameter, SMD or D_{32} is used as an indicator of spray atomization commonly evaluated in applications where the surface area plays a significant role, such as combustion. Further-

more, it is strongly influenced by the atomizer type and the flow characteristics, mainly the AFR. The Sauter mean diameter is the ratio of the total droplet volume to their surface areas as presented in the following expression:

$$D_{32} = \frac{\sum_{i=1}^{n} n_i d_i^3}{\sum_{i=1}^{n} n_i d_i^2} \quad (5.6)$$

The Sauter mean diameter will be employed in this analysis to avoid potential misinterpretations associated with the use of the arithmetic mean. Figure 5.26 and Figure 5.27 show the influence of the axial and Y-axis distance on the axial velocity and Sauter mean diameter for HVO and Jet A-1 at an AFR ≈ 8, respectively. Four axial distances are considered: Z = 5, 10, 15, and 20 mm. The results show that increasing the distance from the nozzle reduces the axial velocity, and the SMD reduces, regardless of the fuel employed. Moreover, the highest values for the axial velocity are present in the central region of the spray. In alignment, the lowest values of SMD are also found in the core area. Conversely, at the spray boundary, the droplets possess a higher diameter and lower axial velocity. As the radial distance increases, the axial velocity decays, and the highest value for the axial velocity is closer to the centerline of the atomizer. The lower velocity in the edges of the spray can be related to the momentum transfer with the surrounding air as similar noticed for the increase in the axial distance [299]. Concerning the axial velocity, as the axial distance increases, the axial velocity of the droplets commonly decreases, indicating a continuous deceleration as they move farther from the atomizer nozzle. Additionally, the velocity profiles tend to flatten with increasing axial distance, leading to a more uniform velocity distribution downstream due to air resistance and drag effects [265, 318]. The spray is not perfectly symmetrical since different distributions are presented on both sides of the radial distance concerning the central line (Y = 0 mm), as will be further discussed.

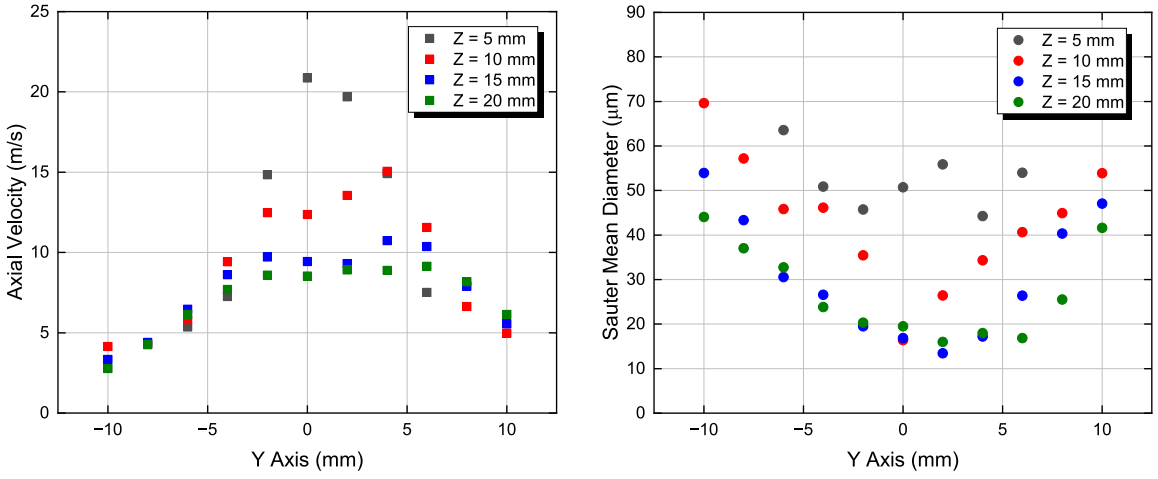

(a) (b)

Figure 5.26: Influence of the axial distance for HVO: a) axial velocity; b) Sauter mean diameter.

To evaluate the axial velocity distributions, Figure 5.28 shows the histograms at the central and boundary regions for HVO at AFR of ≈ 8. In this respect, two axial distances are ex-

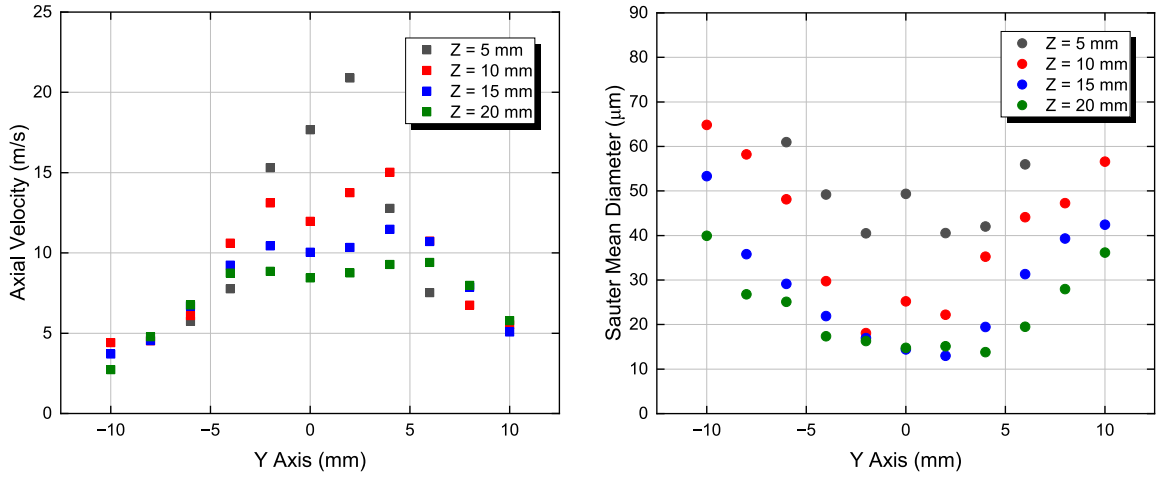

(a) (b)

Figure 5.27: Influence of the axial distance (Z) for Jet A-1: a) axial velocity; b) Sauter mean diameter.

plored: Z = 5 mm and Z = 15 mm. The central region is defined for X = 0 mm and Y = 0 mm, whereas the boundary corresponds to X = 6 mm, Y = 6 mm for Z = 5 mm and X = 10 mm, Y = 10 mm for Z = 15 mm. As outlined earlier, in the inner region, the droplet possesses a higher velocity even at higher axial distances than the boundary region. In addition, negative values are also spotted in the histograms. This indicates an accelerating field in the direction opposite to the main flow, induced by the swirl effect of the atomizer. The bimodal distribution highlights the recirculation phenomenon, as displayed in Figure 5.28 b). Regarding SMD, the largest diameter for both fuels is presented in Z = 5 mm, indicating that the liquid fuel is being atomized as the axial distance increases. As the axial distance increases from Z = 5 mm to Z = 15 mm, the SMD diminishes; from that point, no significant differences are noticeable at Z = 15 and Z = 20 mm, and a more stable droplet size distribution at larger distances is identified. Due to this, the following results are only related to Z = 15 mm. The SMD increased to the spray outer edges as the radial distance increased from the centreline. This behavior is characteristic of swirling injectors, where larger droplets formed by shear forces are centrifuged outward relative to the smaller droplets [249]. This means that the droplets with a higher diameter possess higher inertia remaining in the spray boundaries, whereas the small droplets are easily transported to the central region [432]. Figure 5.29 shows the histograms regarding the droplet diameter in the a) central (Y = 0 mm) and b) boundary (Y = 6 mm and Y = 10 mm) regions as the axial distances increase from Z = 5 mm to Z = 20 mm. The bin width was determined based on Scott's rule as discussed in Panão et al. [327]. Moreover, the X-axis (X = 0 mm) was kept constant, and only HVO at AFR of ≈ 8 in this analysis for simplification purposes. This visualization is provided to ease understanding of the spray droplet diameter as a function of the axial and radial distance. The results show that the smaller droplets are located in the central region, as previously discussed. For the positions X = 0 mm, Y = 0 mm, Z = 10 mm and X = 0 mm, Y = 0 mm, Z = 15 mm, the observations highlight a considerable number of droplets at a reduced size ranging from approximately 0 to 40 μm. However, taking into consideration the same axial positions at the boundary regions, the results indicate that there are droplets with a wide range of diameter

until approximately 100 μm.

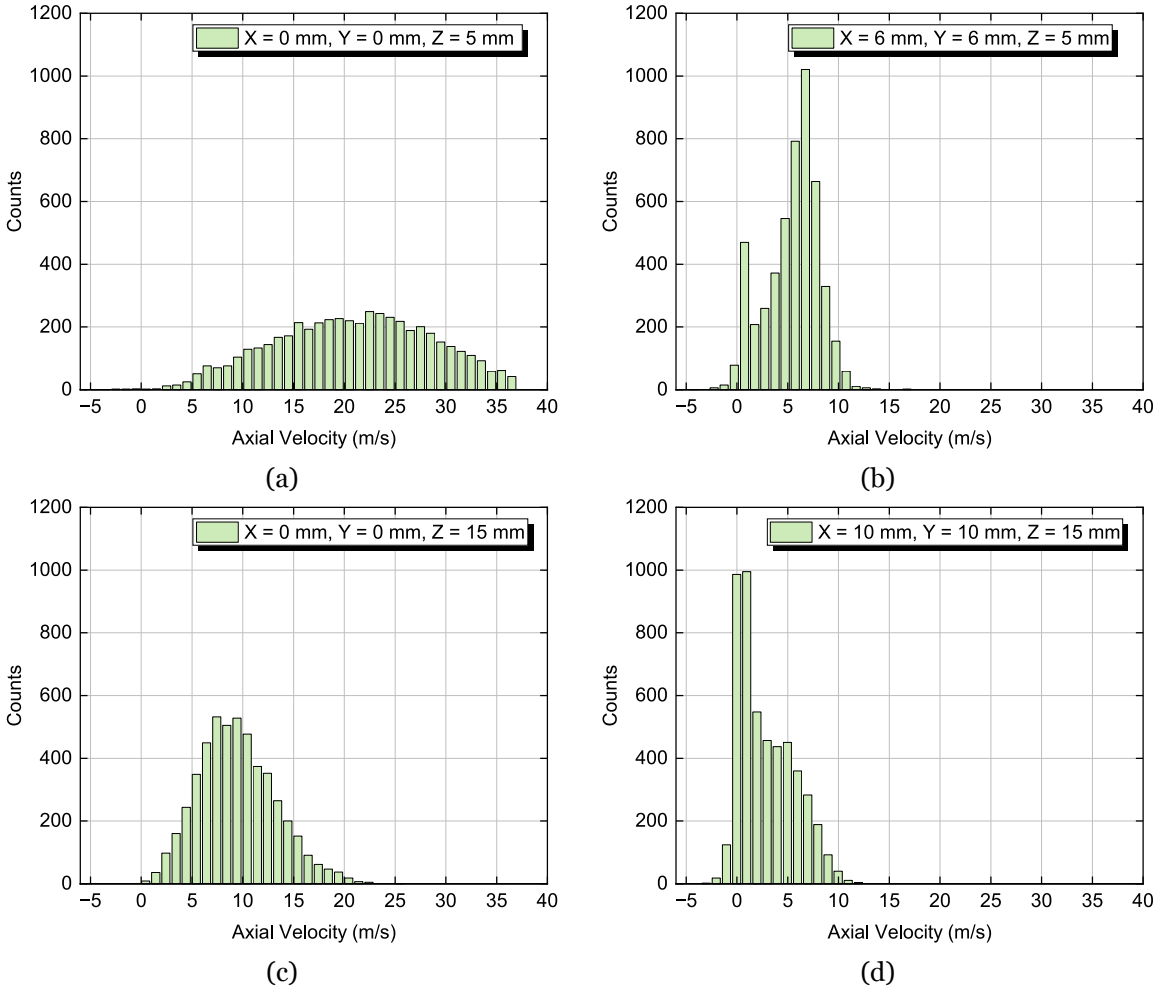

Figure 5.28: Histogram of droplet axial velocity for HVO at AFR ≈ 8 in the following positions: a) X = 0 mm, Y = 0 mm, Z = 5 mm; b) X = 6 mm, Y = 6 mm, Z = 5 mm; c) X = 0 mm, Y = 0 mm, Z = 15 mm; d) X = 10 mm, Y = 10 mm, Z = 15 mm.

Following the analysis regarding the influence of the axial and radial distance on the axial velocity and SMD, a subsequent discussion concerns the impact of air-fuel ratio variations. The purpose is to understand how the AFR affects the spray dynamics. Figure 5.30 and Figure 5.31 show the influence of the fuel and air mass flow on the axial velocity and Sauter mean diameter for HVO and Jet A-1, respectively. Firstly, the air mass flowrate is maintained constant, and an increase in the fuel mass flowrate is explored. Subsequently, the increase of the air mass flowrate is evaluated for a constant fuel mass flowrate. Based on that, three AFRs are explored for each fuel. Regardless of the fuel, an increase in fuel mass flow rate while remaining constant in the air mass flowrate indicated that the Sauter mean diameter increased. This finding is observed for all the Y-Axis being more perceptible for HVO, as shown in Figure 5.30. Concerning the axial velocity, no significant variations are noticeable when the fuel mass flowrate increases. This observation can be attributed to the constant air mass flowrate. However, when the air flowrate increases, an increase in the axial velocity is notorious, which leads to a reduction in the Sauter mean diameter as a consequence

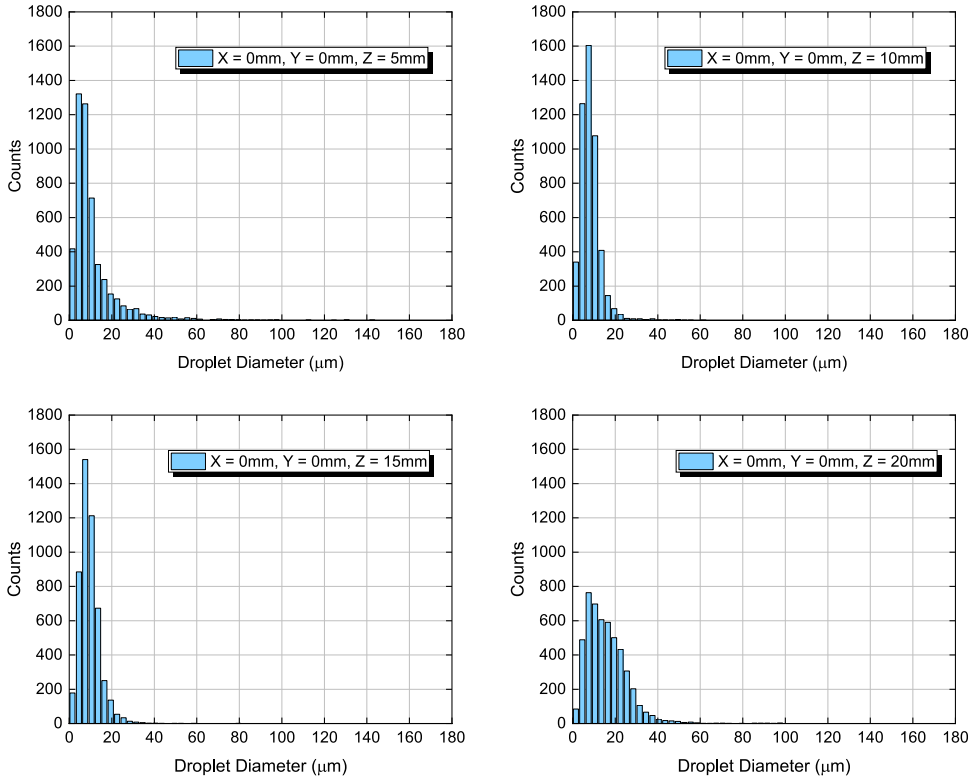

(a)

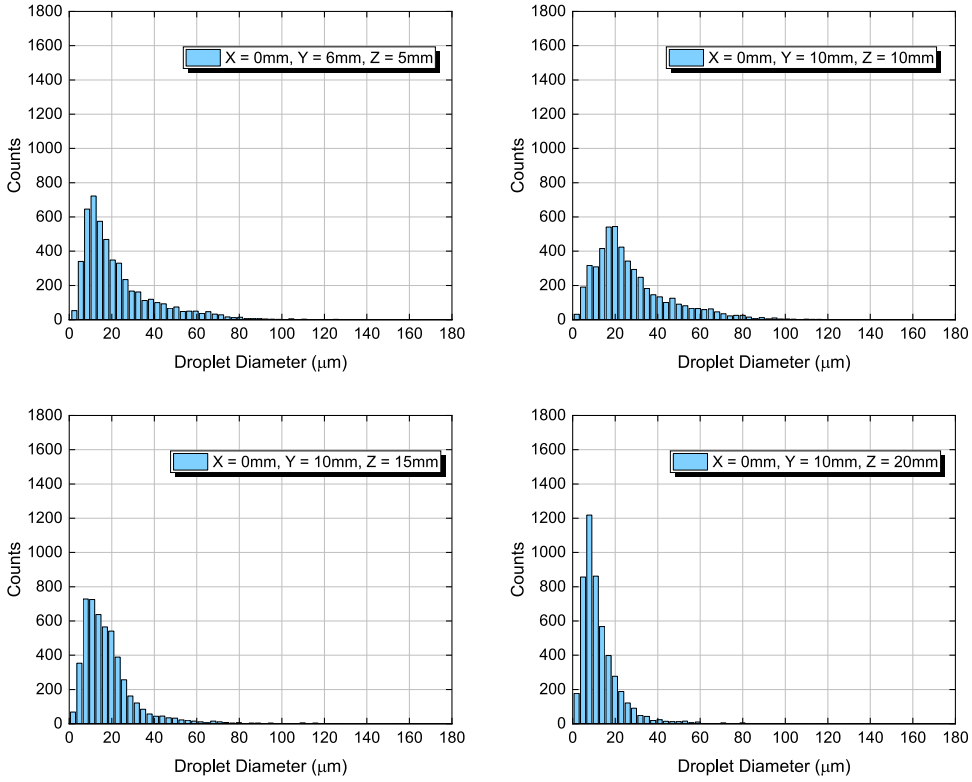

(b)

Figure 5.29: Droplet diameter histograms for HVO considering several axial distances at an AFR ≈ 8: a) central region; b) boundary region.

of the increase in the relative velocity, which promotes a more significant instability in the liquid [299].

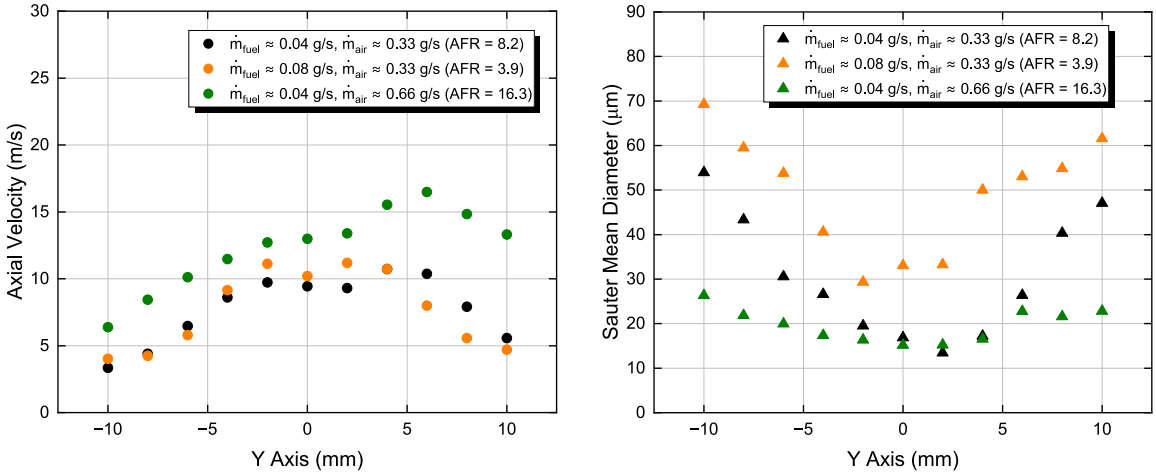

Figure 5.30: Influence of the fuel and air mass flowrate for HVO: a) axial velocity; b) Sauter mean diameter.

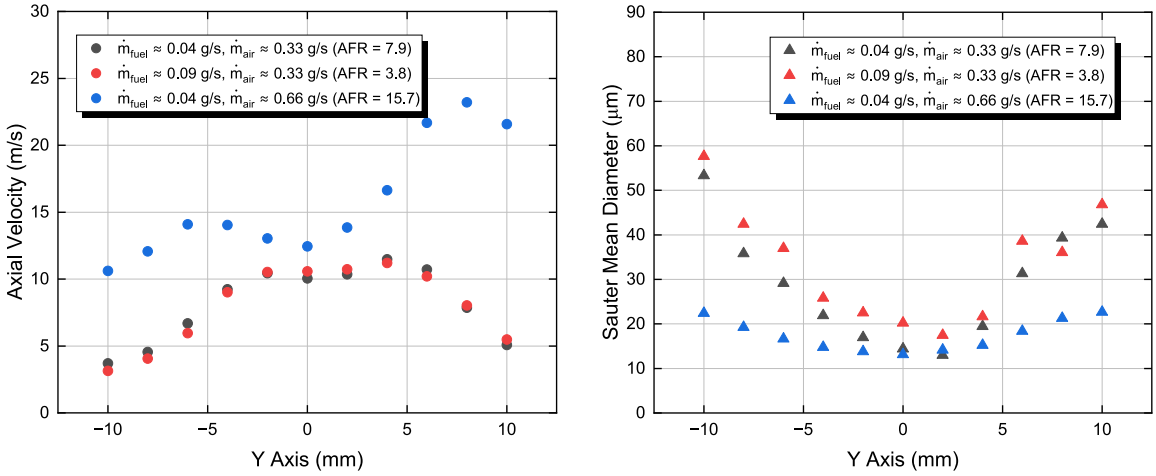

Figure 5.31: Influence of the fuel and air mass flowrate for Jet A-1: a) axial velocity; b) Sauter mean diameter.

Moreover, the spray pattern exhibits a more uniform Sauter mean diameter for a constant fuel flowrate and a higher air velocity, leading to a high AFR. For a lower AFR, the kinetic energy of the atomizing air is insufficient to overcome the viscous and surface tension forces hindering the liquid atomization. Thus, as the AFR increases, the energy available to break down the fuel jet into smaller droplets increases, resulting in a more effective disintegration of the fuel jet into smaller droplets. In addition, a different behavior in the axial velocity is perceptible for the highest AFR. For an air mass flowrate of 0.33 g/s, the results show that the axial velocity evolution from the centreline to the spray edges (Y = 0 mm to Y = 10 mm and Y = - 10 mm) is practically symmetrical. Nevertheless, when the AFR is increased to a value of approximately 16 for both fuels, the positive values in the Y-axis show a high and pronounced peak in the axial velocity. Due to this, further analysis comparing the spray patterns in the X and Y axes will be performed to better understand this observation.

Before evaluating the spray pattern considering the X and Y axes, a comparative analysis focused on the Sauter mean diameter of the conventional and alternative jet fuel is provided in Figure 5.32. The purpose is to understand better the impact of the AFR on the diameter size distribution at Z = 15 mm. Due to this, a fuel mass flowrate is kept constant while the air flowrate is increased. To ease the interpretation, the data points are connected by color lines. The red color corresponds to Jet A-1, while the blue is referent to HVO. Figure 5.32 a) and b) shows that the Jet A-1 possesses a slightly lower Sauter mean diameter, which can be related to the high viscosity of HVO in comparison with Jet A-1. However, as the air flowrate increases to approximately 0.55 g/s, the Sauter mean diameter for HVO and Jet A-1 shows nearly identical values. The observation highlights the significant influence of aerodynamic forces on the overall dynamics of spray formation. Overall, the findings suggest that Jet A-1 and HVO behave quite similarly in the atomization process. This observation is achieved for different air-fuel ratios. These results are significant in researching alternative energy sources for aviation, reinforcing the idea that sustainable and green fuels can be further used to address environmental concerns. Therefore, in terms of atomization analysis, HVO is a suitable biofuel fuel to replace conventional aviation fuel.

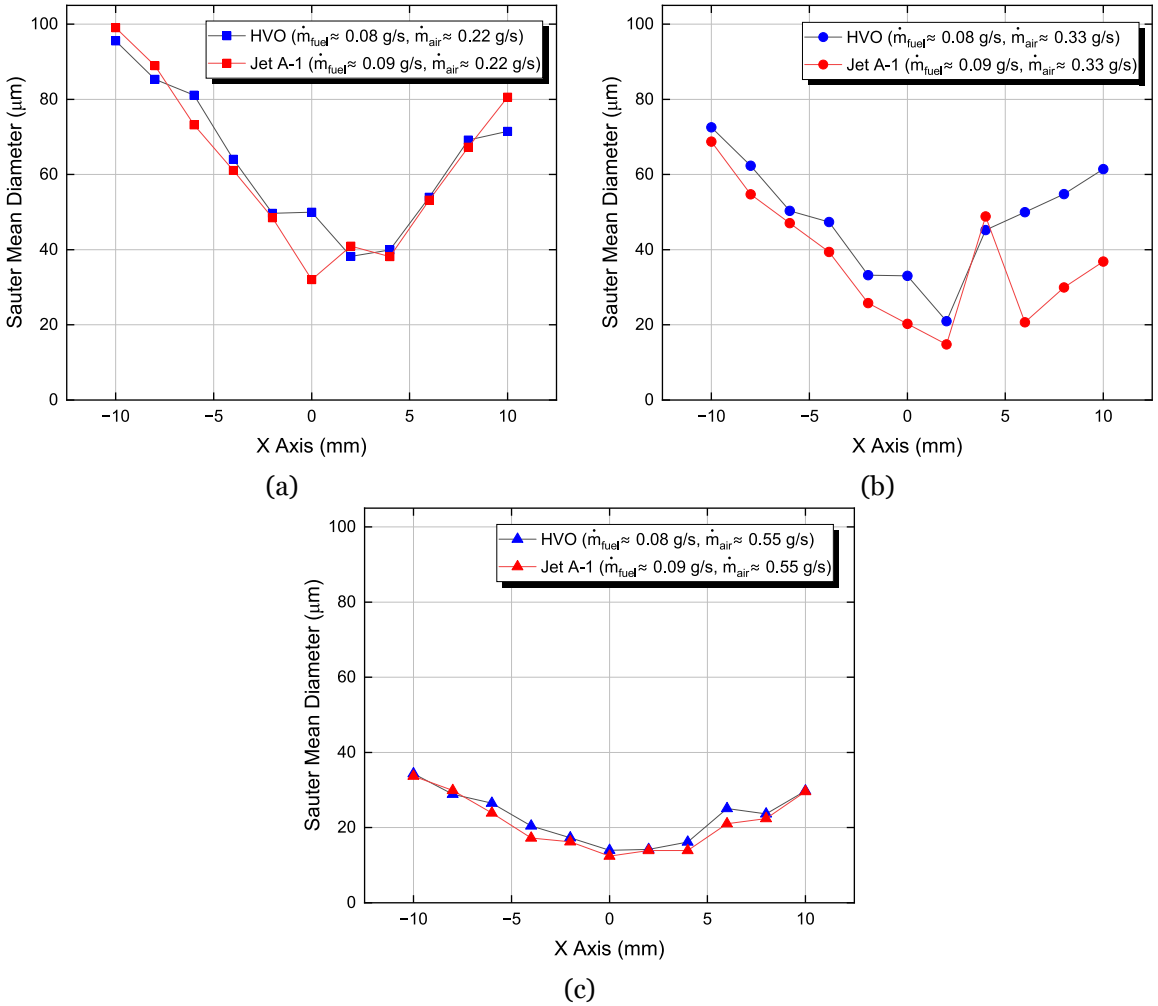

Figure 5.32: HVO and Jet A-1 comparison in terms of SMD for a constant fuel flowrate and different air flows: a) $\dot{m}_{air} \approx 0.22$ g/s; b) $\dot{m}_{air} \approx 0.33$ g/s; c) $\dot{m}_{air} \approx 0.55$ g/s.

The proceeding analysis is dedicated to investigating axial velocity and Sauter mean diameter distribution considering the two radial axes (X and Y). To attain this purpose, the atomization of HVO and Jet A-1, a planar distribution at Z = 15 mm for SMD and axial velocity of the droplets is depicted in Figure 5.33 and Figure 5.34, respectively. The purpose is to obtain insights into the droplet distribution in both radial axes concerning different AFRs.

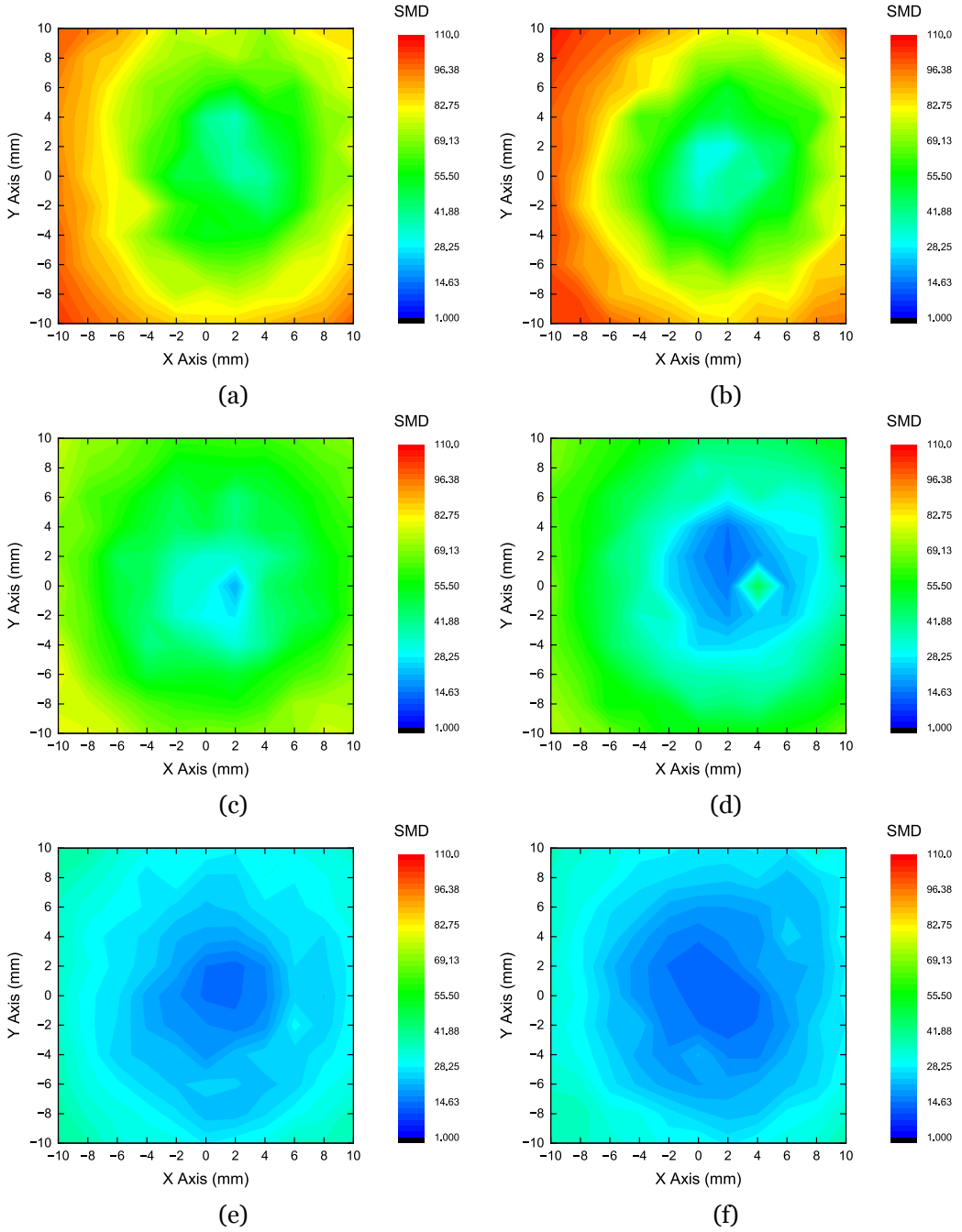

Figure 5.33: Contour of the Sauter mean diameter for X and Y radial distances for HVO: a) AFR = 2.6; c) AFR = 3.9; e) AFR = 6.5. For Jet A-1: b) AFR = 2.6; d) AFR = 3.9; f) AFR = 6.4.

Similar AFRs considered in Figure 5.32 are employed in the contour analysis. As previously noted, regardless of the fuel employed, an increase in the AFR promotes a reduction in the SMD in both the X and Y axes, with the decrease being approximately equal in both directions. Despite the AFR, the larger droplet diameters are presented mainly on the periphery

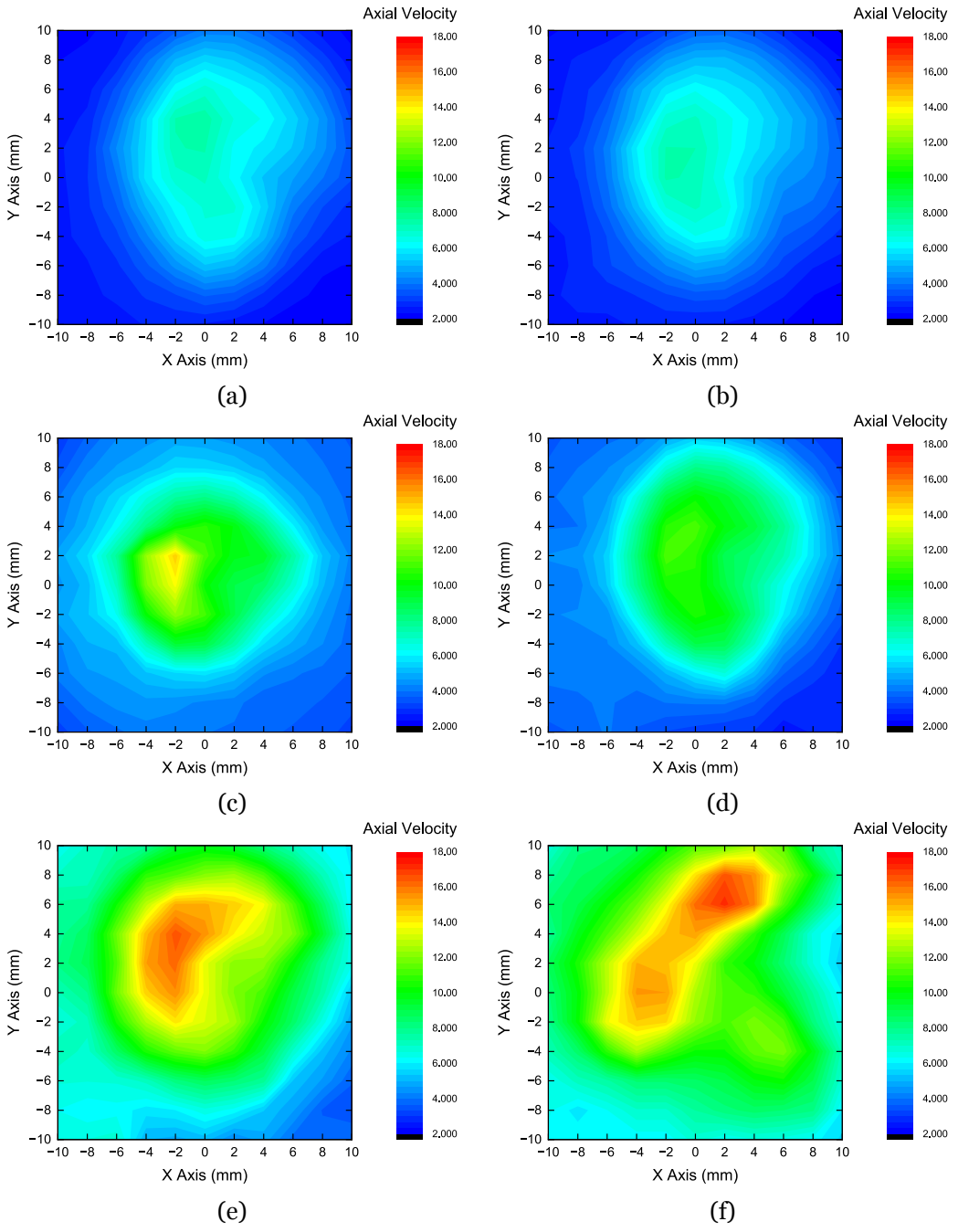

Figure 5.34: Contour of the axial velocity for X and Y radial distances for HVO: a) AFR = 2.6; c) AFR = 3.9; e) AFR = 6.5. For Jet A-1: b) AFR = 2.6; d) AFR = 3.9; f) AFR = 6.4.

of the spray. Therefore, the lowest values of SMD are located in the central region of the spray, displaying a ”bowl” shape. At AFR of approximately 3.9 and 6.4, the reduction in the SMD for Jet A-1 in the central region is more perceptible. In addition, the increase of the AFR also results in a spray with a higher uniformity in the droplet size for conventional and alternative jet fuel, as displayed in Figure 5.33 e) and f), as well in Figure 5.32. In terms of axial velocity, the spray pattern along the X and Y axes is not entirely symmetrical. This observation is more pronounced at the highest AFR which contrasts with the previously discussed Sauter Mean Diameter (SMD) distribution. A possible explanation is that an increase in air flow rate enhances the swirl effect, which becomes more perceptible, as shown in the

contour in Figure 5.34 e) and f). Kirar et al. [433] employed a PIV technique to evaluate the flow field for different swirl strengths. The authors stated that for a fixed value of the swirl number, the increase in the Weber number increases the magnitude of velocity, leading to stronger annular flow with a recirculating zone in the centerline region. As a result, with an increase in the Weber number, the aerodynamic force acting on the droplet becomes more significant. Concerning the velocity distribution in the overall spray pattern, the results indicate that regardless of the AFR, the highest axial velocity values are presented in the central region. In contrast, the lowest values are spotted in the spray boundaries, being minimal for the lowest AFR. Additionally, the results indicate that increasing the AFR of the spray is wider than the results provided in the spray cone angle measurements. As previously mentioned, the imaging technique is unsuitable for acquiring detailed measurements concerning small droplets, which, for quantitative analysis, can be subject to interpretation and may not achieve a high level of accuracy. Consequently, as the AFR increases, the droplet size diminishes, becoming more challenging to capture using the high-speed camera, which can explain the difference between the SCA and PDI results. PDI is a more robust technique that provides detailed, high-resolution, and quantitative droplet sizes and velocities measurements. Based on that, for the present experiments, an increase in the AFR leads to a wider spray pattern, as shown in Figure 5.34. Employing an air-assisted atomizer with external mixing and swirl, the findings suggest an increase in the air velocity, enhancing the radial dispersion of the fuel droplets, improving fuel dispersion, and resulting in a wider spray pattern [318].

Following an introductory overview of the overall spray dynamics involving pure liquid fuels at different air-fuel ratios and radial and axial distances, the addition of nanoparticles in HVO is explored. Figure 5.35 shows the axial velocity and Sauter mean diameter for HVO and a nanofuel composed of HVO and aluminum nanoparticles in a size of 40 nm and a particle concentration of 0.5 wt.%. Different axial distances are investigated, ranging from Z = 5 mm to Z = 15 mm. Additionally, the fuel mass flowrate is kept constant ($\dot{m}_{fuel} \approx 0.08$ g/s), and two air mass flowrate are considered. The blue results correspond to the highest AFR, whereas red marks the lowest AFR. As discussed, high AFR leads to higher axial velocity and lower SMD for HVO and nanofuel. The results do not provide conclusive evidence that the nanofuel displays significantly distinct behavior relative to pure HVO. In particular, the Y-axis coordinates the Sauter mean diameter for nanofuel, which is slightly lower as displayed in Figure 5.35 e). In contrast, Figure 5.35 a), the HVO reveals a minor reduction in SMD. This observation can be correlated with the similar physical characteristics of the nanofuel and HVO. As previously discussed, adding nanoparticles in a size of 40 nm and a particle concentration of 0.5 wt.% does not significantly affect the surface tension and viscosity compared to HVO, which does not affect the droplet diameter.

To understand the impact of the particle concentration in the spray dynamics of nanofuels, two particle concentrations of 0.5 and 1.0 wt.% are considered, and a particle size of 40 nm. Figure 5.36 shows the axial velocity and the Sauter mean diameter for nanofuels at two axial distances a), b) Z = 10 mm and c), d) Z = 15 mm.

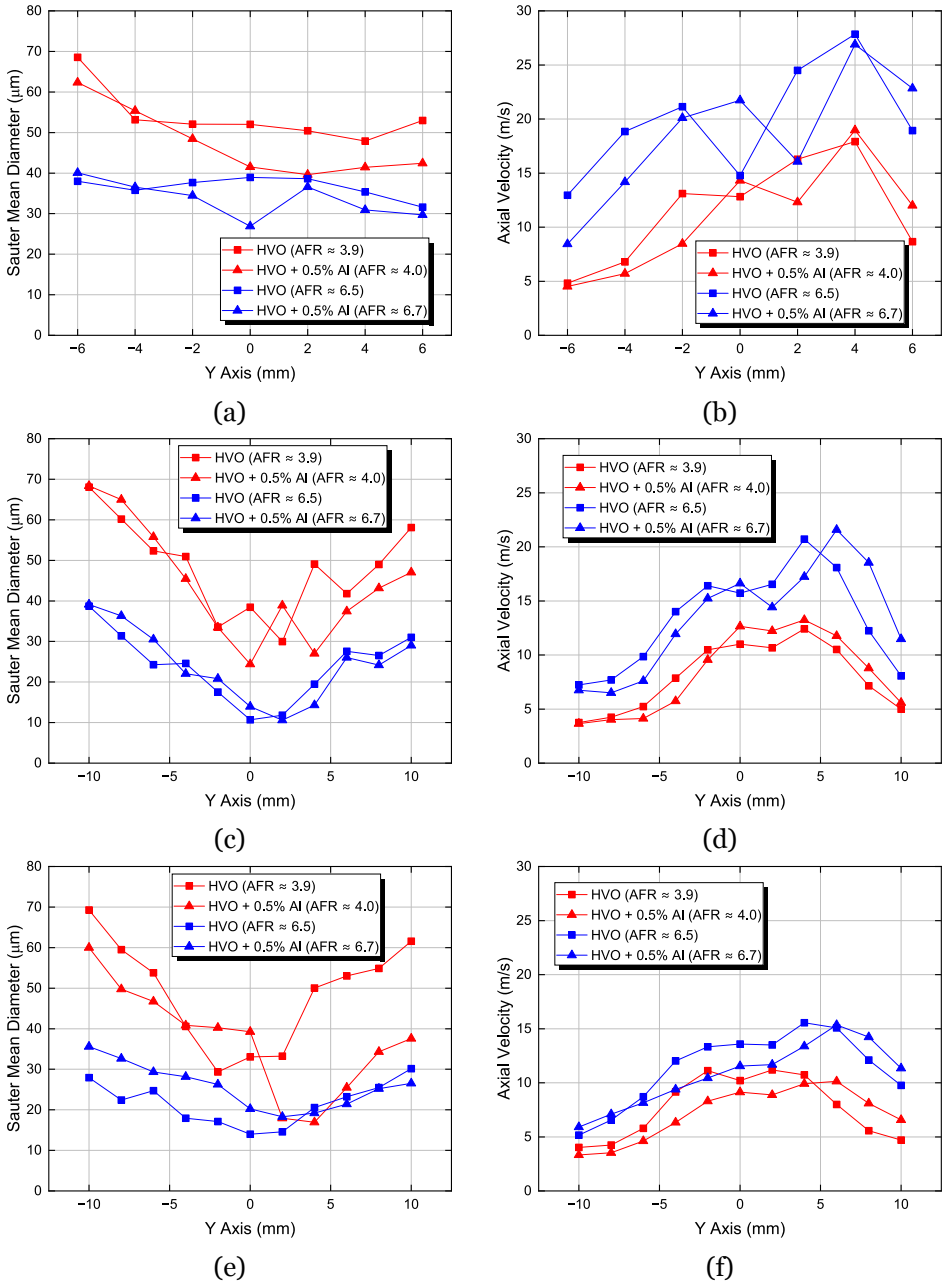

Figure 5.35: Pure HVO and HVO + 0.5% Al comparison in terms of a, c, e) Sauter mean diameter and b, d, f) axial velocity. In addition, a, b) corresponds to Z = 5 mm, c, d) corresponds to Z = 10 mm and e, f) corresponds to Z = 15mm.

For this investigation, the fuel mass flowrate is ≈ 0.04 g/s, and two air flowrate are analyzed. The investigation reveals that HVO + 1.0 wt.% presented a higher axial velocity, regardless of the AFR and axial distance. Moreover, the nanofuel with the higher particle concentration possesses larger droplets at Z = 10 mm and Z = 15 mm. As the changes in physical properties are not clearly evident, a potential explanation could be the role of the nanoparticles in the fragmentation of the liquid that takes place during atomization. To better understand this effect, an evaluation concerning higher particle concentration is required for future studies. The influence in the atomization process of adding nanoparticles to a liquid fuel was already investigated by Kannaiyan and Sadr [341]. The authors added alumina nanoparticles in a

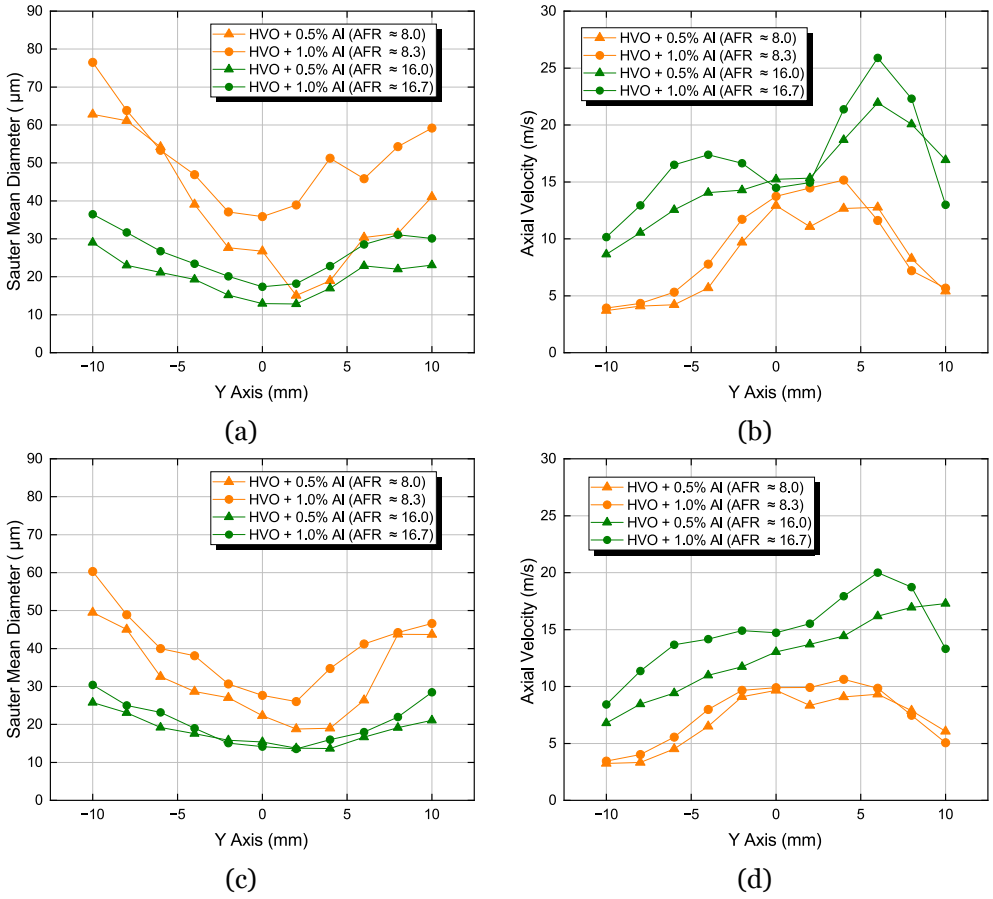

Figure 5.36: HVO + 0.5% Al and HVO + 1.0% Al comparison regarding a, c) Sauter mean diameter and b, d) axial velocity. In addition, a, b) corresponds to Z = 10 mm and c, d) corresponds to Z = 15 mm.

size range of 27-43 nm and particle weight concentrations of 0.5%, 1%, and 2%. The results show that the mean droplet diameters of the nanofuel spray were found to be lower than those of the base fuel and at a higher velocity. However, the results provided in the present study involving a spray of a nanofuel composed of HVO and aluminum nanoparticles using an air-assisted atomizer show that using nanoparticles does not enhance the atomization process.

For a detailed analysis of the influence of nanoparticles in liquid fuel, the probability density function (PDF) is explored since it offers a more precise and comprehensive representation of droplet size distributions compared to single-value metrics. Figure 5.37 and Figure 5.38 show the probability density function for an AFR ≈ 8 and AFR ≈ 16, respectively. The purpose is to compare HVO and nanofuels at two particle concentrations. For each set of images, two axial distances and 3 radial distances are considered. For an AFR ≈ 8, the analysis is performed at Z = 10 mm (Y = -6, 0 and 6 mm) and Z = 15 mm (Y = -6, 0 and 6 mm). In this context, the results provided in Figure 5.37 indicate that, in a general perspective, HVO presents the smallest droplet sizes. On the contrary, HVO + 1.0% Al has a larger droplet diameter. The analysis reveals that adding nanoparticles does not enhance the atomization process. In alignment with this, increasing particle concentration leads to larger droplets. To evaluate the aerodynamic influence on the HVO and nanofuels, Figure 5.38 shows the

probability density function for the fuels previously mentioned for an AFR ≈ 16.

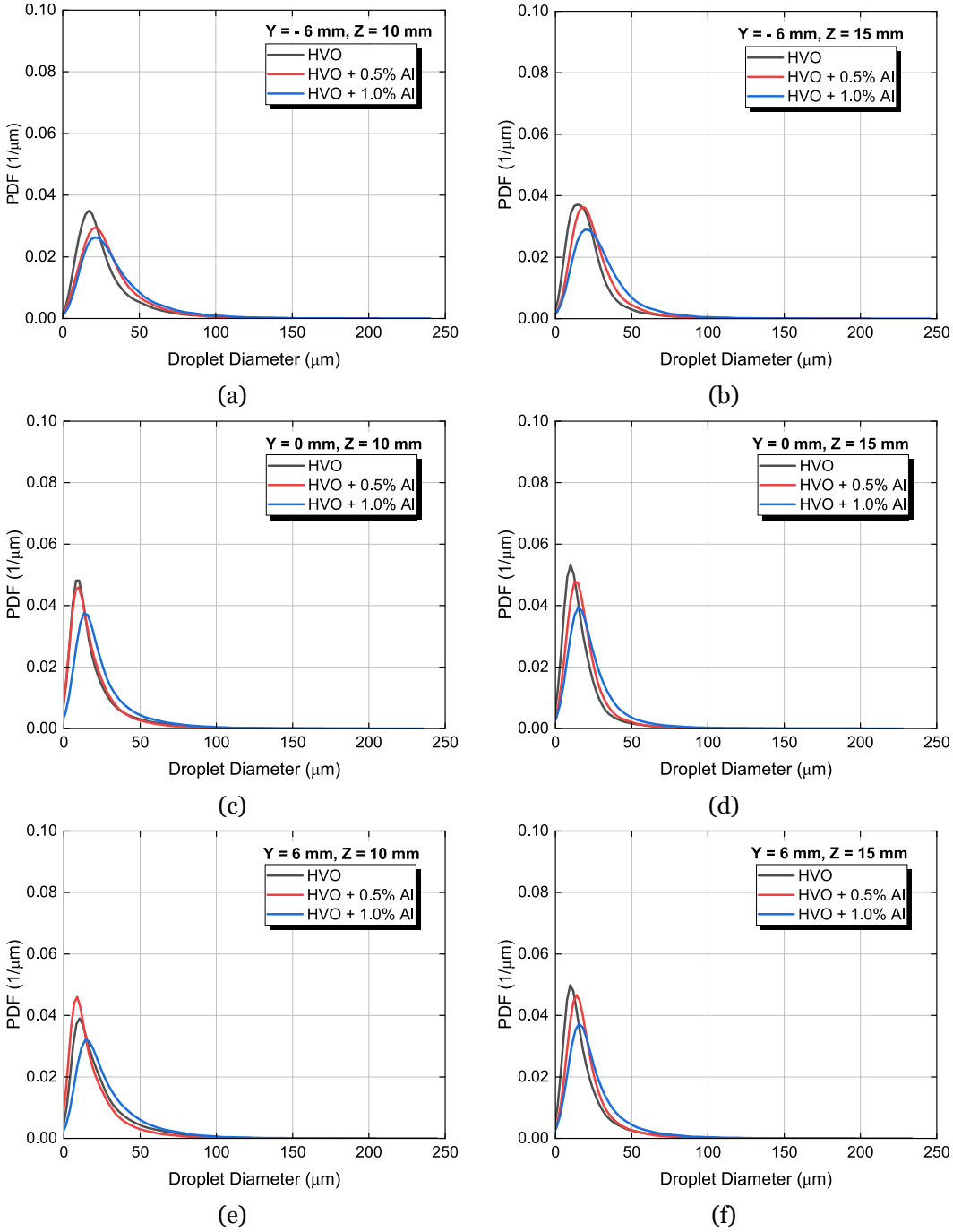

Figure 5.37: Probability density function of HVO, HVO + 0.5 wt.% and HVO + 1.0 wt.% at different radial and axial distances for an AFR ≈ 8.

For this analysis, two axial distances and three radial distances are explored. As observed in Figure 5.37, the behavior for Z = 10 mm and Z = 15 mm exhibit notable similarities. Due to this, in Figure 5.38 considered a closer distance to the nozzle exit, Z = 5 mm (Y = -4, 0 and 4 mm) and Z = 10 mm (Y = -6, 0 and 6 mm). The results show that for the lowest axial distance, contrary to the earlier discussion, HVO presents the larger droplet diameter, regardless of the radial distance. However, when the axial distance increases to Z = 10 mm, similar observations are obtained compared to Figure 5.37. For Z = 10 mm, at an AFR ≈ 16,

regardless of the radial distance, HVO possesses the smaller droplet, whereas HVO + 1.0 % Al presents the larger droplet diameter.

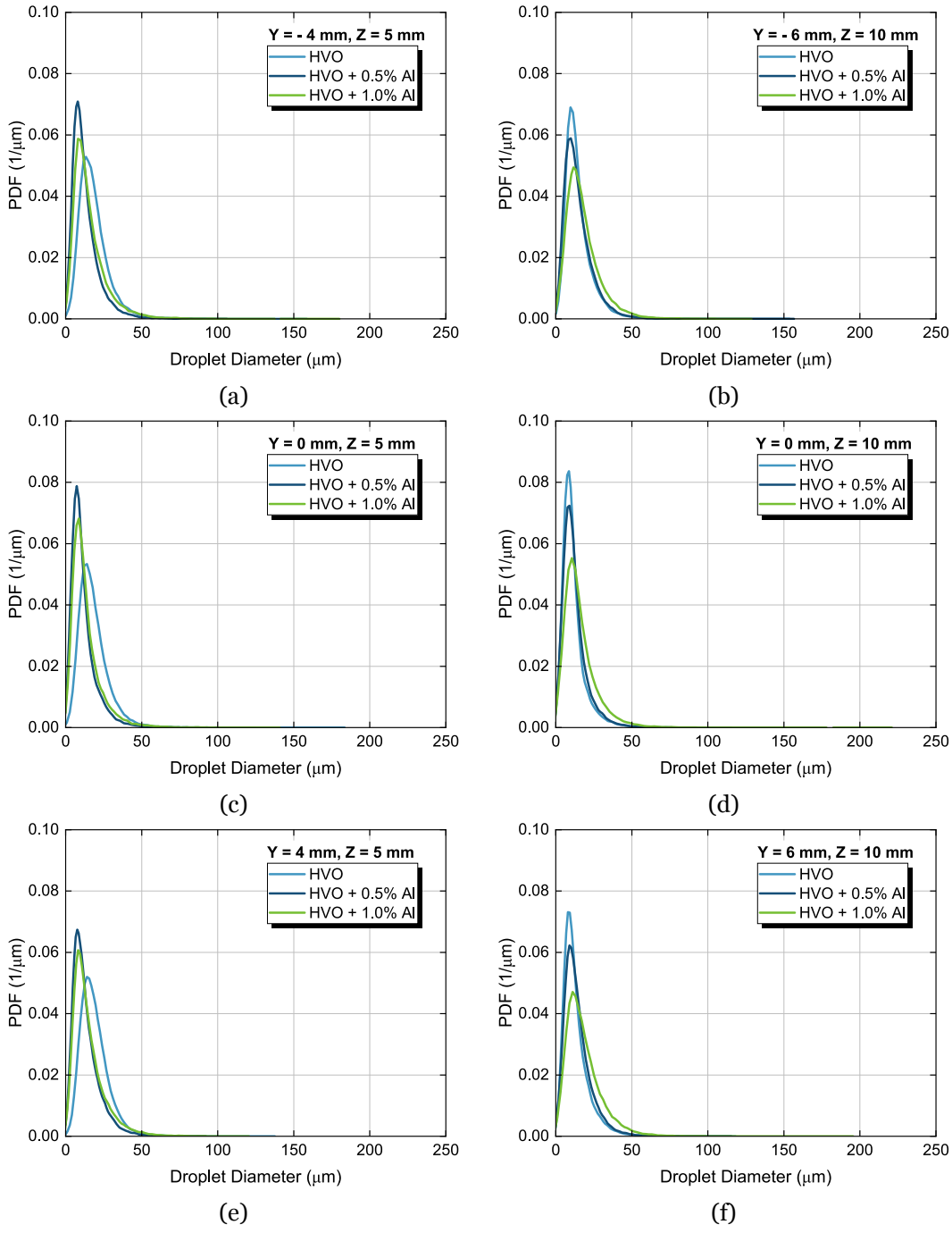

Figure 5.38: Probability density function of HVO, HVO + 0.5 wt.% and HVO + 1.0 wt.% at different radial and axial distances for an AFR ≈ 16.

A hypothesis for this observation is that an axial distance of Z = 5 mm is not fully developed, and the nanoparticles can potentially possess a role in liquid fragmentation. Nonetheless, at greater axial distances and regardless of AFR, the findings indicate that HVO yields a smaller droplet diameter, and HVO with a higher particle concentration adversely affects the atomization efficiency. The influence of the physical properties can be discussed to understand this observation. As noted in chapter 3, for nanofuels composed of HVO and aluminum

nanoparticles of 40 nm and a particle concentration of 0.5 wt.% and 1.0 wt.%, viscosity, surface tension, and density remain largely unchanged compared to the base fuel. Consequently, physical properties do not appear to contribute to an increase in droplet diameter in nanofuels. An analysis of the influence of the physical properties was also carried out for the pure fuels involving HVO and Jet A-1, where a significant variation in the viscosity is reported. However, the findings suggest that in the atomization strategy employed in this study, the aerodynamics possess a more notable impact, leading to remarkably close droplet diameter for HVO and Jet A-1. Based on that, it is concluded that the addition of nanoparticles affects the atomization process, and a more detailed and microscopic analysis should be carried out. The objective is to gain a deeper understanding of how nanoparticles influence atomization, as physical properties do not explain the current findings. Additionally, exploring higher particle concentrations (> 1.0 wt.%) is necessary to determine whether increasing particle concentration consistently leads to larger droplets.

The displayed PDFs establish a baseline for using probability mathematical functions to elucidate the underlying mechanisms of liquid atomization processes. In addition, using probability mathematical functions to describe the droplet size distribution is valuable for numerical investigations. Consequently, an analysis comparing Jet A-1, HVO, and HVO + 1.0 wt.% employing a Log-normal and Gamma distributions fitting is shown in Figure 5.39. The equation regarding each mathematical function can be found in Panão et al. [327]. The results regarding the mathematical function fitting correspond to an AFR $\approx$ 8 for a Y-axis = 0 and three axial distances, Z = 5, 10, and 15 mm. The findings indicate that the Log-normal distribution provides a better fit to the experimental data than the Gamma distribution. This observation is achieved for all the fuels and axial distance. In this respect, Gamma distribution overpredicts the results, indicating that the spray possesses larger droplets. According to Zhao and Liu [245], the Gamma distribution is commonly used to represent the ligament breakup. On the other hand, the Log-normal is capable of predicting the overall droplet size. The use of Log-normal distribution to fit experimental data acquired from an air-assisted provides satisfactory results, as already described by Wu et al. [326]. The findings of the current study indicate that the Log-normal distribution is in good agreement with the PDFs of HVO, Jet A-1, and nanofuel. Additionally, an analysis of the mathematical functions fitting shows a similar behavior of nanofuel, HVO, and Jet A-1. However, investigation for a nanofuel spray under non reacting should be conducted for higher particle concentration (>1.0 wt.%)

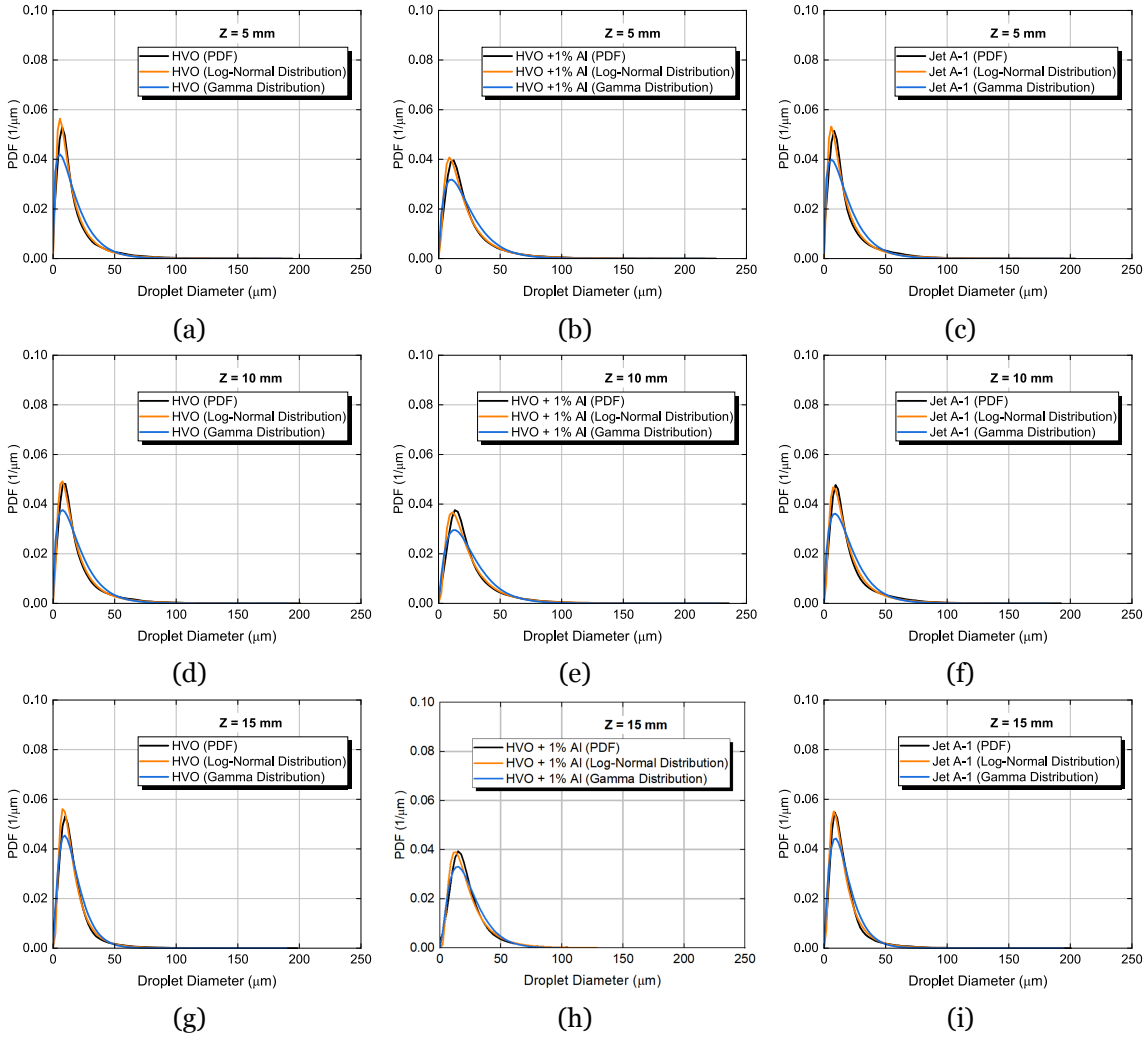

Figure 5.39: Log-normal and Gamma distributions fitting for HVO, HVO + 0.5% Al and Jet A-1 for an AFR ≈ 8.

5.3.5 Summary

The present chapter explored the spray under non reacting conditions. To accomplish this purpose, experiments concerning primary and secondary atomization are discussed. This analysis serves as the basis for the development of a combustion chamber for liquid fuels to gain insight into the droplet distribution and characteristics. Due to this, Jet A-1, HVO, and nanofuels composed of HVO with aluminum nanoparticles in a size of 40 nm and two particle concentrations (0.5 and 1.0 wt.%) are considered. Different air-fuel ratios are explored to better understand the impact of the aerodynamic effect. The visualization provided the identification of different morphological features in the spray, such as droplet formation, ligament structures, and bag shapes, during spray breakup and being notably affected by the AFR. In addition, the visualization provides findings regarding the breakup characteristics, allowing measurements of its length through image data processing. Increasing the liquid Reynolds number leads to an increase in the breakup length where there is no significant difference between pure HVO and HVO with aluminum nanoparticles. In contrast, increasing the air velocity leads to lower breakup lengths, indicating that the influence of aerodynamic force on liquid disintegration is pronounced. A correlation was developed based on the ex-

perimental data concerning the breakup. The findings suggest that the normalized mean breakup length exhibits a power law relation with the momentum flux ratio being in good agreement with the previous correlations. An investigation dedicated to the spray droplet size and velocity distribution indicates that the highest values of axial velocity and the lowest Sauter mean diameter (SMD) values are presented in the central region of the spray. This observation is noticeable for all the fuels and AFRs. In addition, as the axial distance increases, the axial velocity of the droplets commonly decreases, indicating a continuous deceleration as they move farther from the atomizer nozzle, leading to a more uniform velocity distribution downstream. Concerning the radial distance, larger droplets display reduced axial velocity and are predominantly found in the spray periphery. Increasing the AFR results in higher axial velocities and reduced droplet diameter with a higher uniformity. The PDI technique offers detailed and high-resolution measurements of droplet sizes and velocities, indicating that an increase in the air-fuel ratio correlates with a wider spray pattern due to the radial dispersion of the fuel droplets, improving its dispersion. In general, the spray dynamics of HVO and Jet A-1 show considerable similarities. However, when an aluminum nanoparticle in a size of 40 nm and a particle concentration of 1.0 wt.% to liquid HVO, the results show that the nanofuel possesses a larger droplet diameter. A further study concerning the influence of particle concentration should be carried out since the physical properties do not answer the difference concerning HVO and nanofuel spray behavior.

Chapter 6

Spray: Reacting Conditions

6.1 Introduction

Environmental concerns and the depletion of fossil fuels have prompted the scientific community to explore the atomization and combustion of alternative fuels in engines, rockets, and aircraft gas turbines to reduce fuel consumption and emissions [264]. Laboratory burners are developed to serve as a basis for investigating potential alternatives. In real applications, burners are selected based on their ability to meet emission targets by promoting uniform and complete combustion to provide a high combustion efficiency. Gas turbines depend on a burner where the fuel combined with high-pressure air leads to the combustion. Consequently, the resulting high-temperature exhaust gas turns the power turbine and produces thrust when passed through a nozzle. Laboratory burners are designed to replicate real engine operations to investigate potential alternative fuels. Aeronautical gas turbine burners are commonly confined with a high swirl level and composed of materials that can withstand high combustion temperatures. The liquid fuel injection requires a high level of fuel atomization, which can be obtained using an air-blast or air-assisted injector. Furthermore, it also requires a coflow air admission with enough swirling motion to promote a central recirculation zone that aids fuel and air mixing and flame stabilization. A compact and stable reaction area is generated where the combustion rate increases since hot recirculation air keeps feeding the flame root, reducing the required combustion chamber volume and improving the aircraft power-to-weight ratio [264].

Considering the points discussed above, the present section focuses on developing a laboratory combustion chamber for liquid fuels. The purpose is to compare conventional and alternative jet fuel spray combustion. The latter involves pure biofuel and nanofuels. Thus, a modular combustion testing facility was designed and built to be capable of temperature distribution, flow field, and emissions measurements. The burner is placed vertically, where the primary and secondary air and fuel flow upward, to avoid problems during the combustion chamber operation. The overall structure of the project is first introduced, and the most relevant components are elucidated. The operating conditions are also discussed for the burner accuracy, safety, and flexibility. Relevant features concerning the dimensions of the constituents, annular axial swirler design, and flammability limits are also addressed. At last, the final laboratory combustion chamber is displayed, and preliminary experiments are discussed to validate the development of this combustion system.

6.2 Initial Design Considerations

After a careful review dedicated to developing a laboratory combustion chamber for liquid fuels, an initial design of the concept is presented in Figure 6.1. The design of the combustion chamber presented in this study was focused on an experimental setup previously developed by Chong and Hochgreb [247] involving the spray combustion of jet fuel and biodiesel. A description of the current design of the laboratory combustion chamber is also provided in [351]. The overall facility considered in this work comprises the exhaust system, combustion chamber, swirl burner, and flow delivery system. The exhaust system is responsible for extracting the combustion products for safety reasons. This system will play a crucial role in evaluating nanofuels in spray combustion. Nanofuel combustion promotes emissions regarding particle combustion, which should be considered since their consequences on the environment and human health are not fully understood. The exhaust system used is available at the laboratory and used in previous studies of gas combustion.

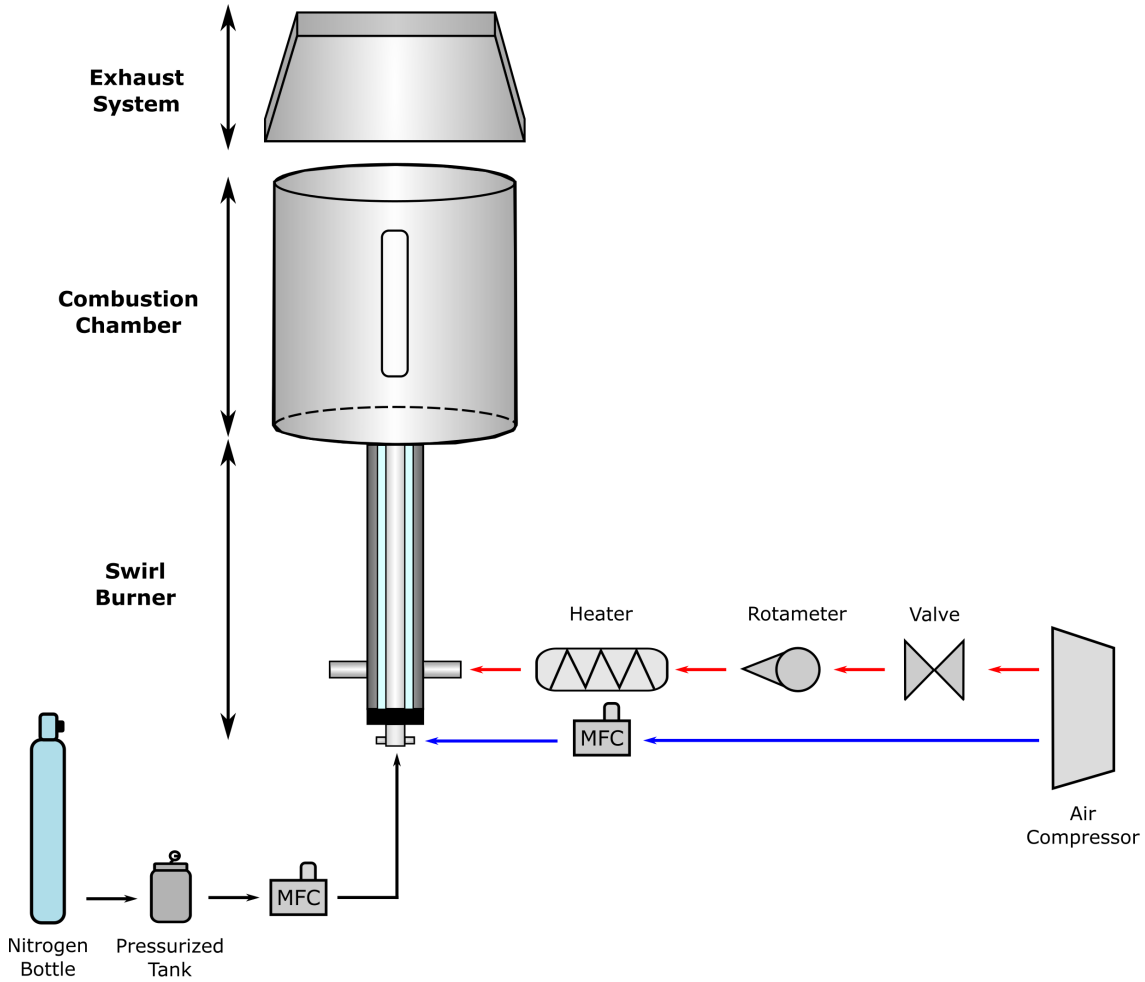

Figure 6.1: Spray combustion chamber and fuel and air delivery system.

Figure 6.2 shows the design of the combustion chamber component, where the spray combustion is carried out. This component possesses two lateral windows placed on opposite sides of the chamber wall for optical access and to provide access to induce ignition. The windows are composed of quartz glass to support high temperatures. In addition, a steel

structure to cover the glass windows is also added to address potential temperature losses and allow the introduction of thermocouples in the reaction zone. It should be mentioned that Solidworks software was used to develop all design components.

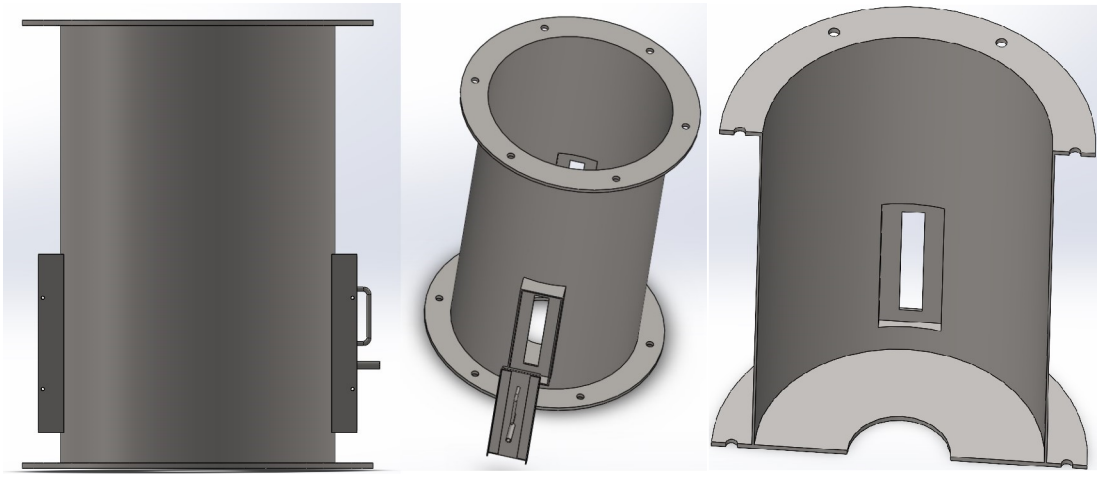

Figure 6.2: Combustion chamber design.

At the top and bottom extremities of the combustion chamber, two flanges are presented to attach this element to the swirl burner and couple an exhaust system. At preliminary evaluations, an exhaust attached to the combustion chamber was used. However, due to the excessive suction, the flame was extinguished. Consequently, a larger exhaust system above the combustion chamber already presented in the combustion laboratory was used, as previously mentioned. For future studies involving different operating conditions, the connection of an exhausted system is possible due to this modular configuration of the combustion chamber. The exterior of the combustion chamber is enveloped in fiberglass insulation and aluminum tape to aid in maintaining high temperatures inside the combustion chamber. The specific dimensions of the combustion chamber are discussed later. The materials required for the combustion chamber should be carefully selected in light of the high temperature concerns. The purpose is to select a material that provides resistance to heat and corrosion and can operate at high temperatures. In this respect, are proper candidates AISI304 and AISI316, where the former presents a melting point around 1450 °C and the latter around 1400°C. Based on that and considering the economic costs, AISI304 was selected to construct the laboratory combustion chamber.

Regarding the swirl burner, an illustration of the interior section view is presented in Figure 6.3. As previously described in the chapter 5, an air-assisted atomizer with external mixing is employed, providing a full description of this equipment. The atomizer is placed in the central zone of the swirl burner, and all the tubes that compose this system are concentric. The secondary air in the swirl burner is introduced by two inlets that allow its flow into the external section. The secondary air was heated before its introduction to the swirl burner. The purpose is to aid the vaporization of the fuel droplets. Consequently, inner insulation is required to prevent high fuel temperatures above the final boiling point and auto-ignition temperatures, which results in the nucleation of the fuel inside the atomizer. This phenomenon

will produce an irregular fuel delivery in the combustion chamber, consequently impacting the dynamics and efficacy of the spray combustion process. Due to this, the inner insulation is placed between two stainless steel tubes, avoiding direct contact with the atomizer and secondary air. It is important to highlight that in this chapter, the primary air corresponds to atomizing air, and the secondary air is the remaining air required for the overall combustion process. Similar to the combustion chamber, the exterior of the swirl burner is covered by fiberglass insulation and aluminum tape to reduce the heat losses of the secondary air to the surrounding environment, ensuring a high temperature of the secondary air previously heated before entering the swirl burner.

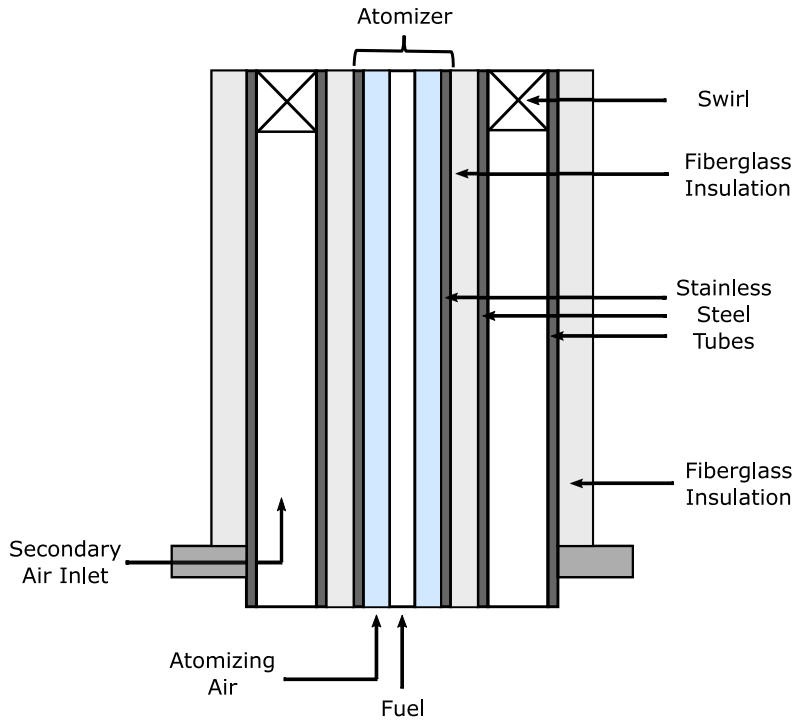

Figure 6.3: Swirl burner design.

As illustrated in Figure 6.1, the laboratory combustion chamber comprises a fuel and air delivery system. In this respect, the delivery systems for the fuel and primary and secondary air are independently controlled. The fuel supply system is composed of the atomizer, where the fuel flow rate is controlled by a mass flow controller (MFC), model CODA KCO-Series Mass Flow Controllers. In addition, a nitrogen bottle was used to pressurize the fuel tank at 1-2 bar. The black line represents the fuel delivery system presented in Figure 6.1. Regarding the primary and secondary, the supply is provided by an Atlas Copco compressor, model GF7FF, with a capacity of 15.7 L/s at 10 bar. To ease the interpretation of the primary and secondary air delivery lines, the blue line represents the former, whereas the red represents the latter. An MFC model MCR-100 SLPM controls the primary air. The secondary air is controlled by a KDG rotameter, model 2000, with a capacity of 500 L/min. A summary regarding the specific of each control device for the delivery system is presented in Table 6.1. As noted, the secondary air is preheated before entering the swirl burner. To accomplish this purpose, an Osram Sylvania heating system, model SureHeat, was used to supply the required energy for droplet vaporization and ignition. For the heated air, a temperature of

400 °C was initially selected to ensure that it is higher than the final boiling point of HVO to mitigate the substantial thermal losses that preheated air will encounter until it reaches the combustion chamber. The HVO was considered for this analysis since it is the less volatile fuel, which will be discussed later.

Table 6.1: Delivery components specifications.

	Liquid Fuel	**Primary Air**	**Secondary Air**
Equipment	Mass flow controller	Mass flow controller	Rotameter
Model/Brand	SLPM CODA KCO-Series Mass Flow Controllers	MCR-100	KDG rotameter model 2000
Standard Accuracy	±0.6% of reading or ±0.2% of full scale	±0.8% of reading or ±0.2% of full scale	±2.5% of full scale

6.2.1 Operating Conditions

After a short overview of the most relevant equipment and systems in the laboratory combustion chamber, the following analysis is dedicated to the operating conditions. For simplification, the operating conditions will be established for the pure fuels, concretely, HVO, and Jet A-1. Concerning the operating conditions for nanofuels, the most promising results are related to the nanofuel with lower particle concentration, where no significant difference in the physical properties compared to the pure biofuel is reported. In this context, the required fuel and air flowrates for primary and secondary air for Jet A-1 and HVO are discussed. Additionally, the heating power required by the air heater is also examined. As presented in chapter 3 the chemical composition of HVO relies on $C_{15}H_{32}$-$C_{18}H_{38}$. Consequently, for simplification purposes, hexadecane $C_{16}H_{34}$ was considered a surrogate fuel for HVO since a reasonable approximation was presented in chapter 4. Regarding Jet A-1, average chemical composition is $C_{11}H_{21}$. The stoichiometric combustion reaction of HVO and Jet A-1 are presented in Equation (6.1) and Equation (6.2), respectively.

$$C_{16}H_{34} + 24.5\left(O_2 + \frac{79}{21}N_2\right) \rightarrow 16CO_2 + 17H_2O + \frac{553}{6}N_2 \quad (6.1)$$

$$C_{11}H_{21} + 16.25\left(O_2 + \frac{79}{21}N_2\right) \rightarrow 11CO_2 + 10.5H_2O + 61.13N_2 \quad (6.2)$$

Firstly, the laboratory combustion chamber power output should be established. Similar to Chong and Hochgreb [247], a power output of 2 to 6 kW is defined for safety and consumption reasons. Based on that, the fuel flowrate for each power output can be determined by the following expression:

$$\dot{m}_{fuel} = \frac{PowerOutput}{LHV} \quad (6.3)$$

where $\dot{m}_{fuel}$ is the fuel flowrate and LHV is the lower heating value. The lower heating values for HVO and Jet A-1 are LHV_{HVO}= 43.9 $MJkg^{-1}$, LHV_{JetA-1}= 43 $MJkg^{-1}$, respectively.

Following the estimation of the fuel flowrate for each power output defined for this investigation, the flowrate of the primary air is examined. An air-fuel ratio (AFR) of 2 is considered since it provides a reasonable approach for conducting the experiments. This AFR corresponds to the fuel and primary air mass flowrates. Table 6.2 shows the fuel and primary air flowrates for several power outputs considered for the design of the laboratory combustion chamber.

Table 6.2: Fuel and primary air flowrate for several power outputs.

		Power Output (kW)		
		2	**4**	**6**
HVO	$\dot{m}_{fuel}$ (g/s)	0.046	0.091	0.137
	$\dot{m}_{primary}$ (g/s)	0.091	0.182	0.273
Jet A-1	$\dot{m}_{fuel}$ (g/s)	0.047	0.093	0.14
	$\dot{m}_{primary}$ (g/s)	0.093	0.186	0.279

After acquiring the values for the fuel and primary air flowrates, the following analysis concerns the total air required for the combustion process. Subsequently, the equivalence ratio (ϕ) should be explored using the following expression:

$$\phi = \frac{\frac{\dot{m}_{fuel}}{\dot{m}_{totalair}}}{\left(\frac{\dot{m}_{fuel}}{\dot{m}_{totalair}}\right)_{stio}} \quad (6.4)$$

where $\dot{m}_{totalair}$ is the mass flow rate of the total air for combustion (primary air and secondary air), and the subscript $stio$ corresponds to stoichiometric. The values for each fuel can be determined with the aid of the relations presented in Equation (6.1) and Equation (6.2). Consequently, the total air for combustion for the different fuels derived from Equation (6.4). Figure 6.4 shows the mass flow rate of the total air for combustion for Jet A-1 and HVO at different power outputs. In addition, the total air required for the combustion is displayed as a function of several equivalence ratios where no significant difference between Jet A-1 and HVO is presented.

After defining the primary air flowrate and total air required for the design of the combustion chamber, the secondary air corresponds to the subtraction of these two parameters. As previously noted, the secondary air is preheated initially at a temperature of 400 °C. Subsequently, Figure 6.5 shows the volumetric flow rates of the secondary air for a) HVO and b) Jet A-1 at $T = 20$ °C and $T = 400$ °C. The ambient temperature is assumed as $T = 20$ °C. Furthermore, the influence of secondary air is represented by the equivalence ratio at different power outputs. It is important to highlight that the volumetric flowrate can be obtained by a relation between the mass flowrate and the air density at the specific temperature. Due

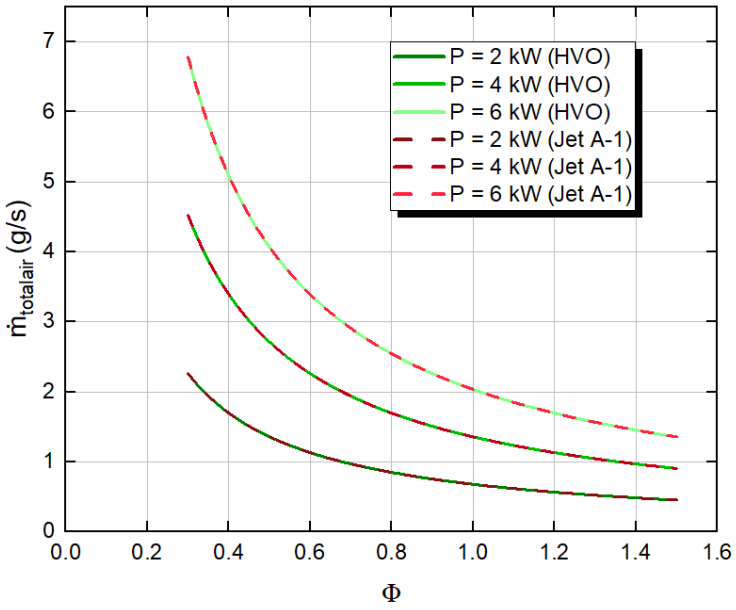

Figure 6.4: Total air mass flow rate for HVO and Jet A-1, considering an AFR = 2.

to this, high temperatures lead to higher values for the secondary air. Increasing the equivalence ratio results in lower secondary airflow rates regardless of the fuels employed.

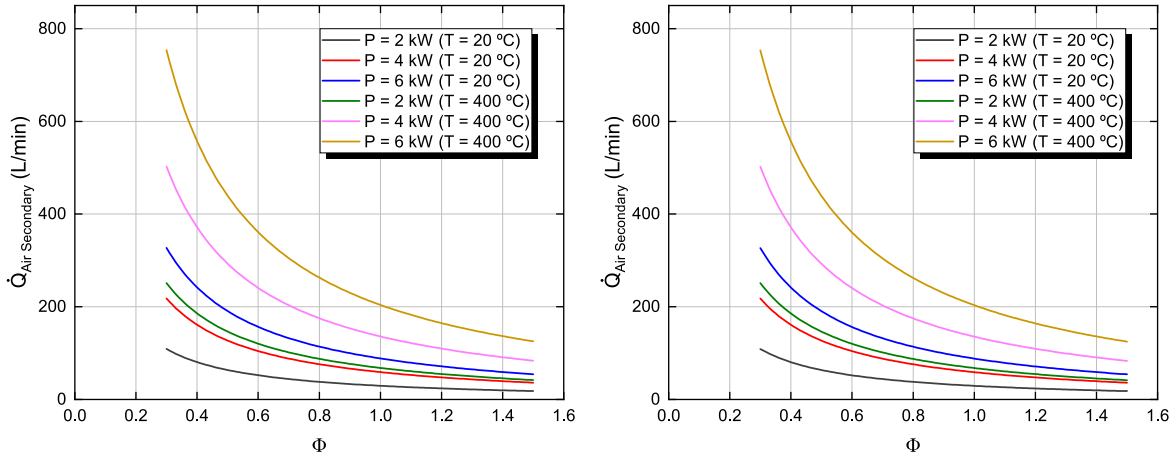

Figure 6.5: Volumetric flow rates of the secondary air: a) HVO; b) Jet A-1.

Considering the required secondary air flowrate, an analysis of the required heating power to increase the secondary air temperature from room temperature to 400 °C provided by the heater is essential. The purpose is to ensure that the heater is capable of achieving the requirements of the design. The Osram Sylvania heating system, model SureHeat, has a maximum power of 30 kW and is connected to a control panel. The temperatures are monitored by two type K thermocouples located at the inlet and outlet of the system. This examination is conducted by an energy balance where heating power can be given by:

$$Heating\ Power = \dot{m}_{secondary} \times (c_{p,air}(T_h)T_h - c_{p,air}(T_0)T_0) \quad (6.5)$$

which T_h = 400 °C, T_0 = 20 °C and $c_{p,air}$ is the specific heat of air at a given temperature. In this respect, $c_{p,air}(20°C)$ = 1.007 $kJkg^{-1}K^{-1}$ and $c_{p,air}(400°C)$ = 1.055 $kJkg^{-1}K^{-1}$ [407]. Figure 6.6 shows the operating condition regarding the heating power of the secondary air for HVO and Jet A-1. The highest value corresponds to HVO for a power output of 6 kW and ϕ = 0.3. Consequently, it is confirmed that the heater is suitable to achieve the desired temperature for the secondary air.

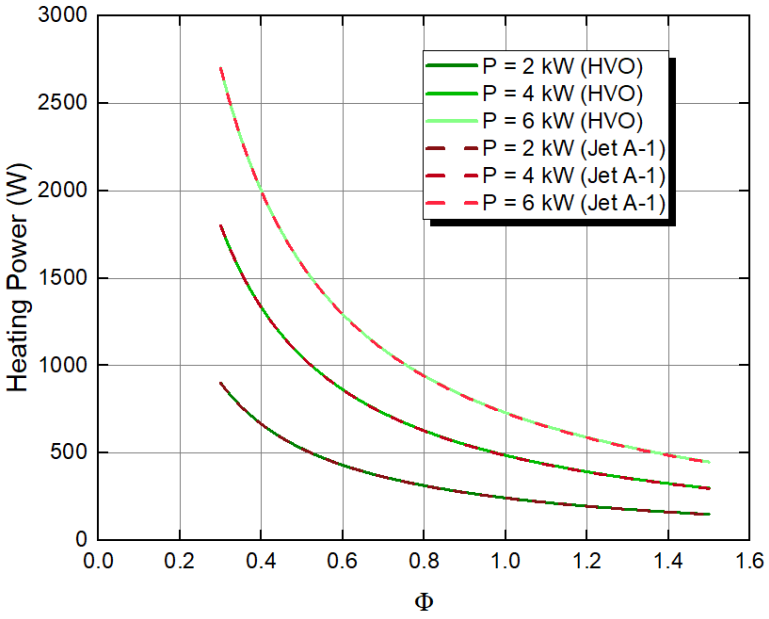

Figure 6.6: Heating power requirements for secondary air for HVO and Jet A-1, considering an AFR = 2.

The current section describes the initial design considerations involving the most relevant components and the operating conditions. To ease the further understanding of the development of the laboratory combustion chamber, Table 6.3 shows an overview of the specifications.

Table 6.3: Summary of the design specifications.

	Specifications
Power output (kW)	6
$\dot{m}_{fuel}$ (g/s)	≈ 0.14
$\dot{m}_{primary}$ (g/s)	≈ 0.27
$\dot{m}_{secondary}$(g/s)	≈ 4.06
Equivalence Ratio (ϕ)	0.47
T_0 of room ($°C$)	20
T_h of secondary air ($°C$)	400

6.3 Preliminary Setup Challenges

A brief description of the combustion chamber component and swirl burner was previously presented. However, the specific dimensions of each constituent system should be carefully

evaluated to meet the requisites of this laboratory combustion chamber. Challenges concerning insulation, fuel delivery, and flammability limits are also addressed.

6.3.1 Target Temperature for Liquid Fuel Operation

In spray combustion, liquid fuel injection is a relevant subject. As previously mentioned, an air-assisted atomizer is employed and placed in the central region of the swirl burner component. Therefore, rigorous analysis of the fuel heating during the combustion chamber operation is essential. This evaluation is driven by the potential overheating of the fuel line caused by the preheated secondary air, resulting in preferential fuel evaporation affecting the spray combustion performance. Fuel volatility is fundamental to providing proper fuel and air mixing to promote combustion. However, inside the atomizer, the fuel volatility must be minimized. Based on this, the volatility limits of the fuels should be investigated. Figure 6.7 shows the most relevant properties of Jet A-1 and HVO for the design. Conventional and alternative jet fuels are multi-component fuels. As mentioned in chapter 3, the distillation curve gives essential information on how each fuel vaporizes. Figure 6.7 shows that Jet A-1 has a reduced 10 vol% distillation temperature compared to HVO due to its chemical composition as noted in chapter 3. Furthermore, a similar observation is achieved for the final boiling point, indicating that HVO presents a higher final boiling point than HVO. It is confirmed that Jet A-1 is a more volatile fuel than HVO. In addition, the auto-ignition temperature was also considered for safety reasons. This temperature corresponds to the lowest temperature when a fuel spontaneously ignites in the air without an external ignition source. For Jet A-1, the auto-ignition temperature is well defined (210 $^{\circ}C$). However, for HVO, this information is scarce, and an approximate value of 204 $^{\circ}C$ was considered [434].

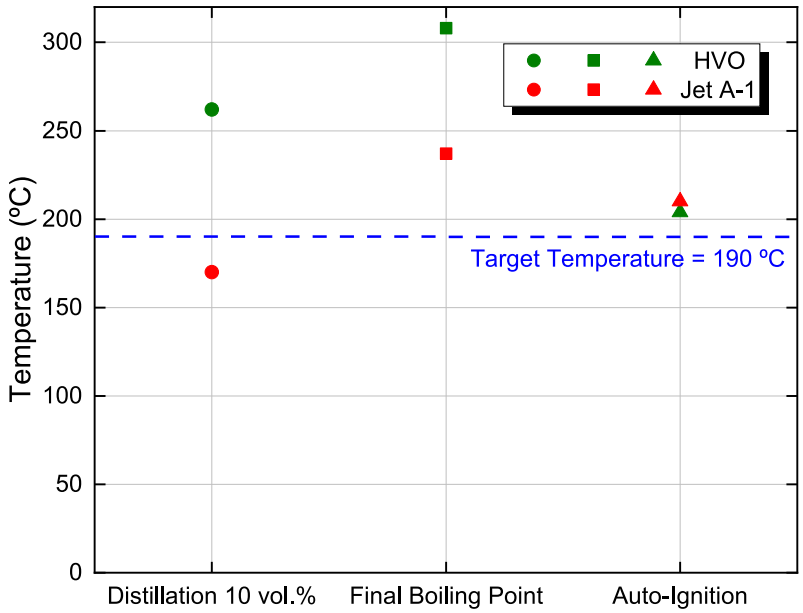

Figure 6.7: Auto-ignition, final boiling point, and 10 vol% distillation temperatures for Jet A-1 and HVO.

Concerning the influence of temperature on the properties that affect the fuel droplet diameter, it has been widely argued that an increase in the fuel temperature leads to a reduction in viscosity and surface tension, resulting in a decrease in the droplet diameter, as discussed

in the chapter 2. Nevertheless, the beneficial effect on the droplet diameter caused by the temperature increase must be considered to avoid preferential fuel volatility, an intermittent fuel delivered inside the combustion chamber. The design aims to balance the insights mentioned above, and to accomplish this purpose, a target temperature of 190 $^{\circ}C$ is defined. This temperature was selected, considering the fuel with the most volatility. It is also important to highlight that the target temperature is attributed to the primary air instead of the fuel line for precautionary reasons.

6.3.2 Swirl Burner Design

Careful attention to the swirl burner design must be considered to address the concern regarding fuel overheating. In this respect, the dimensions of the swirl burner, insulation thickness, and annular axial swirler dimensions should be defined. Concerning the annular axial swirler, as noted in Figure 6.3, this component is presented at the top of the swirl burner, being responsible for the induction of the swirling flow of the secondary air. According to Beer and Chigier [356], swirl number (S_N) is a dimensionless parameter usually employed to describe the amount of rotation imparted to the axial flow and can be defined by:

$$S_N = \frac{2G_\theta}{D_s G_x} \quad (6.6)$$

where G_θ is the axial flux of angular momentum, D_s is the swirler outer diameter, and G_x is the axial flux of axial momentum. Additionally, the authors provide formulations for the calculation of swirl numbers for a range of swirl generator types where the swirl number for an annular axial swirler with constant vane angle (θ) is given

$$S_N = \frac{2}{3}\left(\frac{1-(D_h/D_s)^3}{1-(D_h/D_s)^2}\right) tan\theta \quad (6.7)$$

where D_h and D_s represent the swirler hub diameter and the swirler outer diameter, respectively, and θ, is the angle of the blade from the centreline. Figure 6.8 highlights each characteristic to ease understanding of these parameters.

Considering the values for the swirl number (S_N), numerous studies have been presented in the literature. A preliminary investigation on this subject was conducted by Tangirala et al. [435]. The authors stated that the swirl number (S_N) ranges from 0 to 0.6, and no recirculation zone will be generated. However, a toroidal recirculation zone is formed for a swirl number higher than 0.6, allowing the hot gases from combustion to return to the flame reaction zone and increasing the flame stability. Nevertheless, there is a limit for the swirl number (S_N) values. In this respect, swirl numbers ranging from 1 to 4 show a notable reduction in flame stability and turbulence levels. Due to this, excessive swirl can result in the flame approaching the enclosure walls, creating regions of localized hot spots [247, 435].

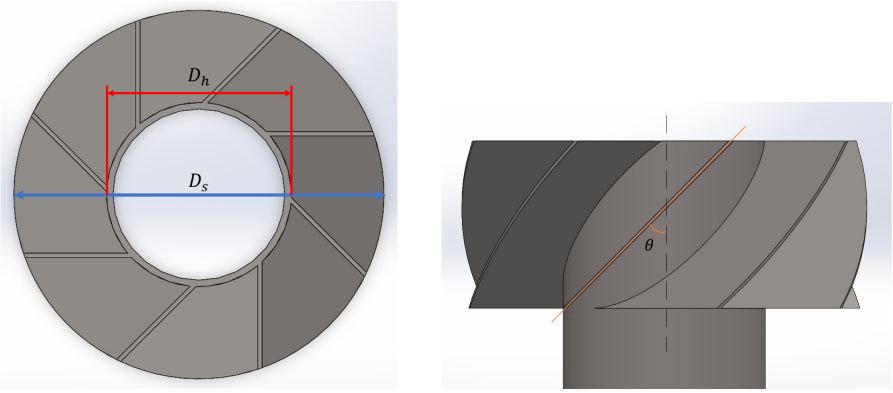

Figure 6.8: Swirl parameters: a) Hub and outer diameter; b) Angle (θ).

The definition of the swirl number is an initial step to determine the characteristics of the annular axial swirler. Considering Equation (6.7), the values of D_h/D_s and θ should be evaluated. Figure 6.9 shows the D_h/D_s as a function of the vane angle (θ), considering several swirl numbers from 0.6 to 0.78, broadening the perspective for the design. For D_h/D_s, only values higher than 1 are considered since D_s cannot be less than D_h. This scenario is highlighted by the red line ($D_h = D_s$), representing the lower limit of the (D_h/D_s) value. Regarding the vane angle, results from 30° to 60° are provided.

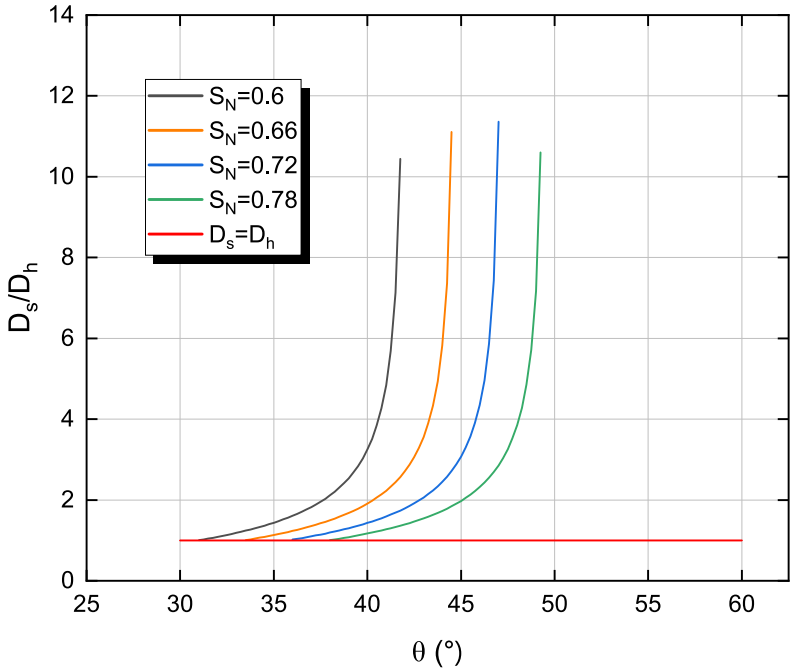

Figure 6.9: Swirl vane angle (θ) for 0.6 < S_N < 0.78.

The results show that for a swirl number between 0.6 and 0.78, θ varies between 31° and 49°. Consequently, based on the literature findings, a fixed value of 0.78 was defined for the swirl number, where θ is 45° and $D_h/D_s \approx 2$ are selected.

To guarantee optimal Jet A-1 and HVO performance, a thermal insulation coating is uti-

lized between the atomizer and the secondary air channel to minimize heat transfer from the preheated air (secondary air) to the fuel. Concerning the thermal insulation coating, it is essential to consider two important factors: the material and its thickness. The material selected for the thermal insulation coating must exhibit excellent thermal insulating properties, specifically low thermal conductivity, to ensure the maintenance of optimal fuel temperature. For the present work, fiberglass was chosen as a thermal insulator, capable of operating until temperatures of 750 $^{\circ}C$. Moreover, it has excellent thermal insulation capabilities and is an economically advantageous selection.

A heat exchanger problem will be considered to determine the thermal insulation coating thickness and length of the swirl burner. This analysis will be complemented by a prior description provided in [351, 407]. To better understand, the real heat transfer problem is displayed in Figure 6.10 highlighting the most relevant inlet and outlet flows and the insulation localization with respect to the atomizer.

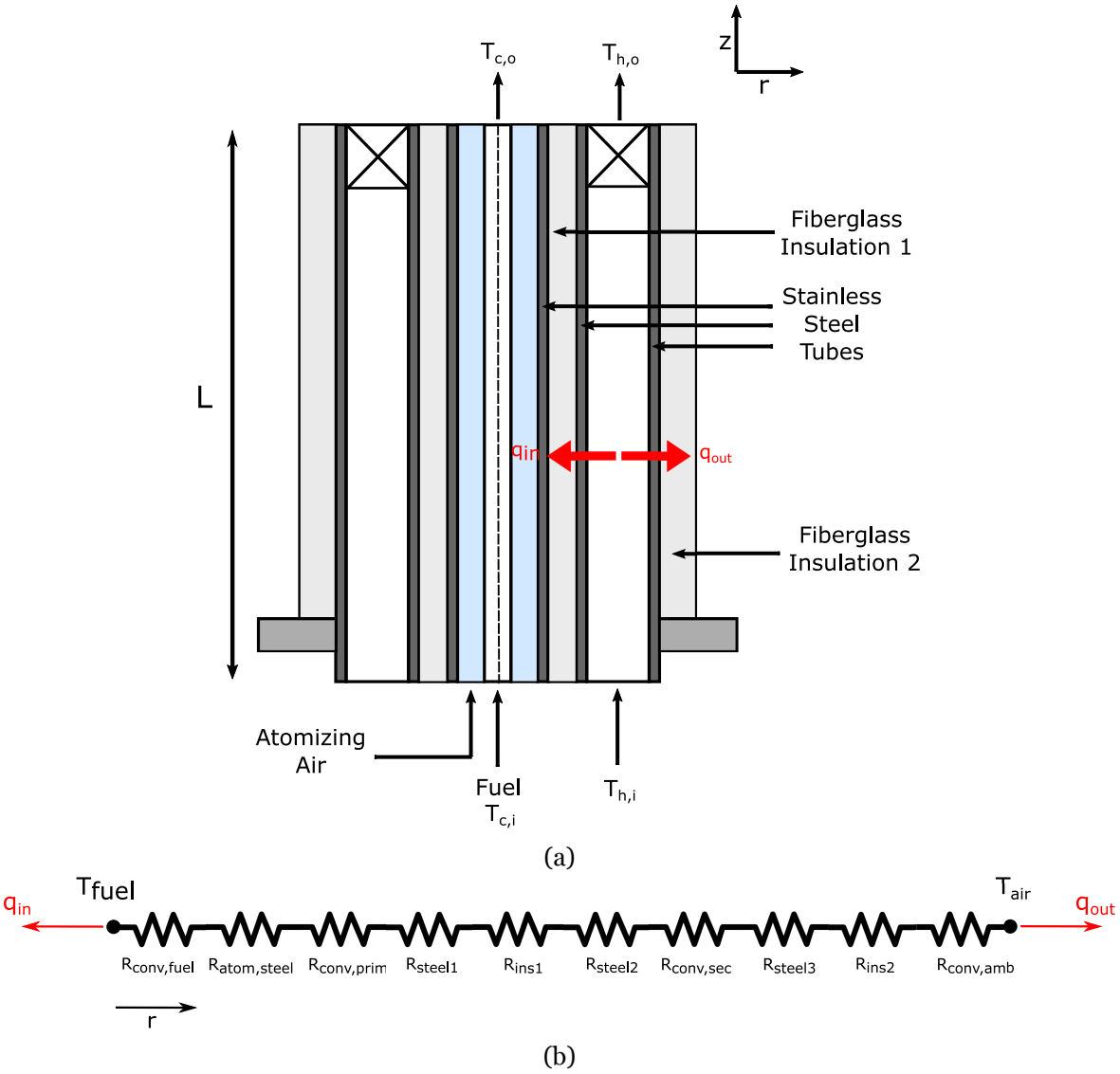

Figure 6.10: General heat transfer problem of the swirl burner: a) Illustration; b) Thermal circuit.

As previously mentioned, secondary air is the heat source for the problem. It is responsible for the inner heat rate expressed as q_{in} in the atomizer direction, and the outer heat rate expressed as q_{out} is responsible for the heat release to the ambient air. The inner and outer heat rates are represented by two red arrows in Figure 6.10 a). The direction of the fuel and air flows aligns with the z-axis, traveling from the lower section to the upper section of the swirl burner. The subscription "h" and "c" correspond to the hot and cold fluids, whereas "i" and "o" correspond to the inlet and outlet, respectively. Following this, $T_{h,i}$ and $T_{h,o}$ represent the hot fluid inlet and outlet temperature of the secondary air, and $T_{c,i}$ and $T_{c,o}$ represents the cold fluid inlet and outlet temperature of the liquid fuel. To avoid fuel overheating, insulation 1 is placed adjacent to the atomizer, while insulation 2 prevents temperature losses for the ambient. The swirl burner length is represented by L. Figure 6.10 b) displays the thermal circuit of the real heat transfer problem where thermal contact resistance between different materials, potential free convection existing in an air gap between a steel tube and an insulation coating as well as potential free convection in an air gap between the atomizer and the steel tube are discarded. Thus, $R_{conv,fuel}$, $R_{conv,prim}$, $R_{conv,sec}$ and $R_{conv,amb}$ corresponds to the thermal resistance associated with internal forced convection created by the fuel flow, primary air, secondary air and the thermal resistance associated with free convection heat transfer from the ambient air, respectively. The remaining resistances are conduction resistances. In this respect, $R_{atom,steel}$ corresponds to the conduction resistance of stainless steel of the atomizer presented between the fuel and the primary air. The three R_{steel} stainless steel tubes divide the different components. Taking into consideration the target temperature of 190 $^{\circ}C$, the temperature of the fuel (T_{fuel}) must not exceed this value, indicating that $T_{c,o}$ should be less or equal to 190 $^{\circ}C$.

To solve the actual heat transfer problem, an analysis is performed within the context of a heat exchange model. This is a suitable approach previously presented in Incropera [407], where hot and cold fluids flow concentrically, separated by a solid wall. Moreover, heat transfer between the heat exchanger and its surroundings, as well as the potential and kinetic energy changes, are negligible [407]. For simplification and safety reasons, the cold fluid in the heat exchanger approach is the primary air. Therefore, if the higher limit for the primary air temperature is 190 $^{\circ}C$, the fuel temperature will not exceed this value, preventing partial volatility of the fuel. In summary, the cold and hot fluids are the primary and secondary air for the heat exchanger approach, respectively. As indicated in 6.10 a) primary and secondary airflow in a similar direction (z-axis) from the bottom to the top of the swirl burner. Therefore, the real heat transfer problem is considered a parallel flow heat exchanger, where axial conduction along the tubes is neglected, meaning heat transfer is dominated by the radial direction (r-axis) [407]. An illustration of a parallel flow heat exchanger is displayed in Figure 6.11. The variables presented in Figure 6.11 possess a similar meaning to those described in the real heat transfer problem. This illustration shows the temperature distributions for a parallel-flow heat exchanger as a function of the axial distance (x), where the subscripts 1 and 2 correspond to the start and end of the heat exchanger, respectively. The temperature difference, ΔT, is initially significant and reduces progressively with axial distance, x. As axial distance increases, the temperature of the hot fluid gradually reduces. In contrast, the tem-

perature of the cold fluid increases, and the $T_{c,o}$ never surpasses $T_{h,o}$ [407]. In this approach, the q_{out} is equal to zero, and only q_{in} will be considered, which results in an overestimation of cold and hot fluid temperature compared to the real heat transfer problem.

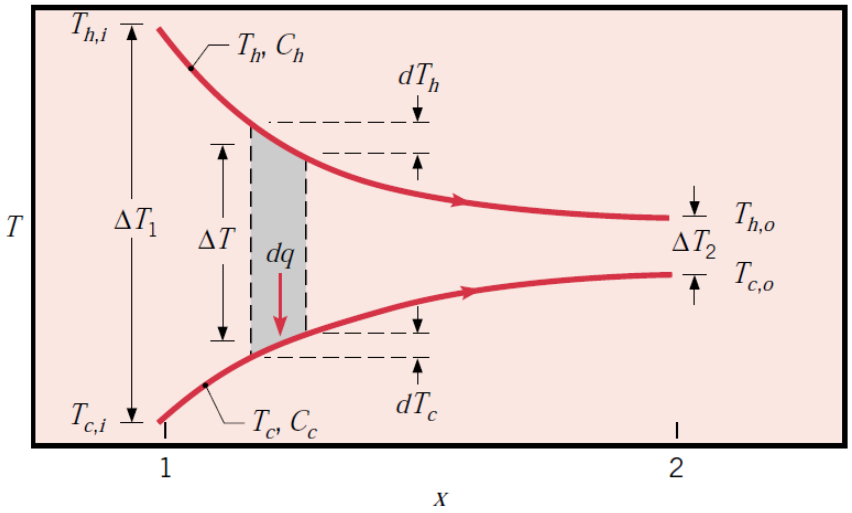

Figure 6.11: Temperature distributions for a parallel-flow heat exchanger, adapted from [407].

Based on that, an initial step is to evaluate the total thermal resistance (R_{tot}) between the hot and cold fluids. The total thermal resistance (R_{tot}) can be given by

$$R_{tot} = \frac{1}{UA} \quad (6.8)$$

where A is the area of the wall normal to the direction of heat transfer, and U is the overall heat transfer coefficient, a relevant parameter of a heat exchanger study.

To improve comprehension, Figure 6.12 shows an illustration and the thermal circuit of the approach of the heat transfer problem for the swirl burner. This image is provided for illustrative purposes only, and the radius of the individual components is not accurately depicted. The inner and the outer radius of the primary air flow are defined by $r_{pri,i}$ and $r_{pri,o}$, respectively, whereas r_{atom} represents the atomizer radius. As previously mentioned, three steel tubes composed the swirl burner. Due to this, $r_{tube1,o}$ is the outer radius of the steel tube 1, $r_{rtube2,i}$ and $r_{rtube2,i}$ corresponds designate the inner and outer radius of the steel tube 2. Tube 1 has a thickness of 1 mm, and tube 2 has a thickness of 2 mm. The remaining steel tube corresponds to the external part of the swirl burner. Regarding the insulation coating, r_{ins} reflects the radius of the fiberglass coating inside the swirl burner. The variables h_c and h_h are the cold and hot fluids convection coefficients, respectively. In contrast, the k_{atom} is the thermal conductivity of the steel that constitutes the atomizer, as shown in Figure 6.12 b). The central black zone corresponds to the inner area of the atomizer where the liquid fuel flows. The external black regions of the swirl burner represent the boundaries of the heat exchanger analysis indicated in Figure 6.10 as the insulation 2.

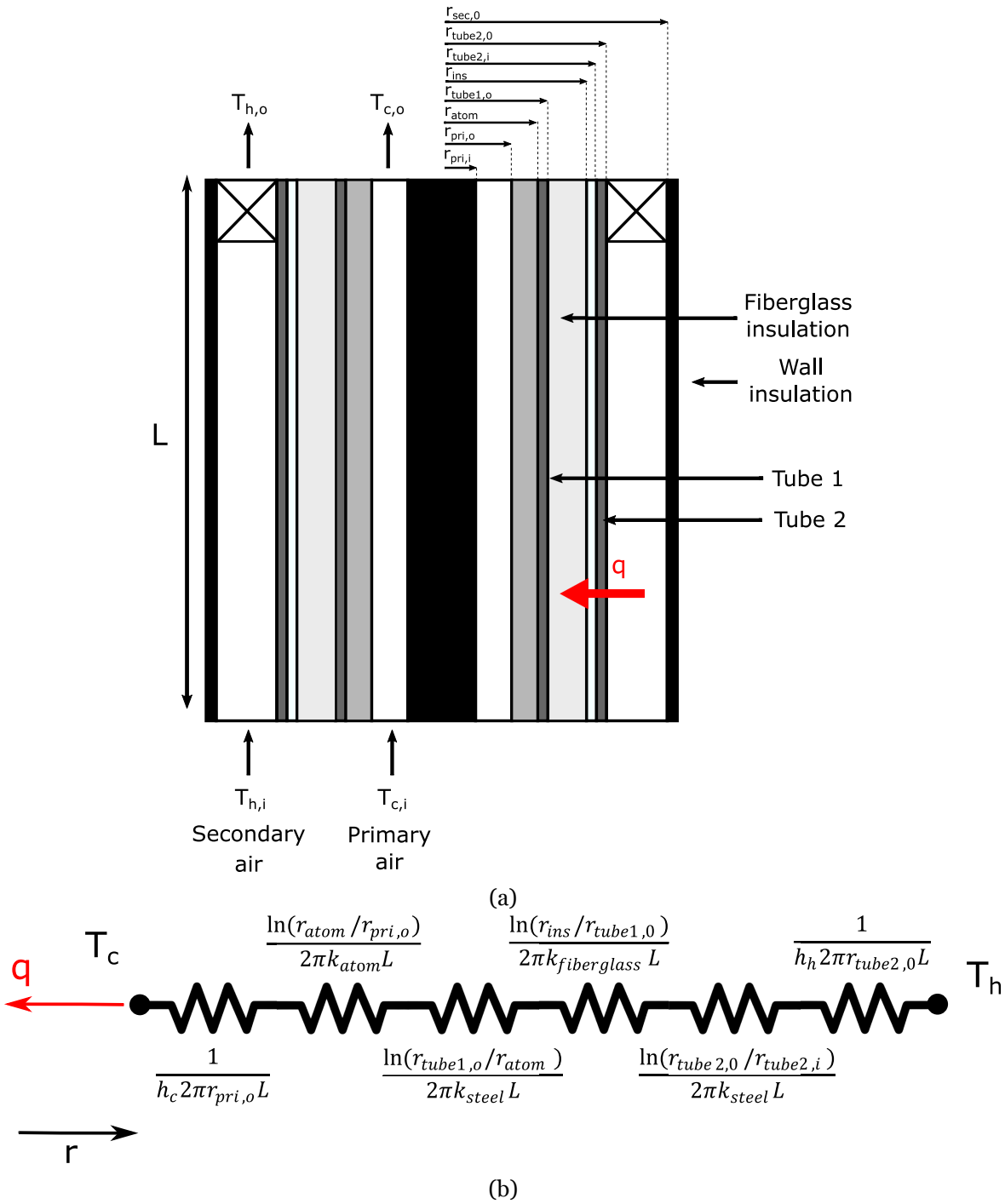

Figure 6.12: An approach of the heat transfer problem for the swirl burner: a) Illustration; b) thermal circuit.

To determine the conduction (R_{cond}) and convection (R_{conv}) resistances, the following Equation should be considered [407]:

$$R_{conv} = \frac{1}{hA} \quad (6.9)$$

$$R_{cond} = \frac{ln(r_2/r_1)}{2\pi Lk} \quad (6.10)$$

where h is the convection coefficient, r_1 and r_2 is the inner and outer radius of the cylindrical wall, respectively. L is the length of the system, while k corresponds to the thermal conductivity. Consequently, R_{tot} is given by the following equation:

$$R_{tot} = \frac{1}{h_c 2\pi r_{pri,o} L} + \frac{ln(r_{atom}/r_{pri,o})}{2\pi k_{atom} L} + \frac{ln(r_{tube1,o}/r_{atom})}{2\pi k_{steel} L} + \frac{ln(r_{ins}/r_{tube1,o})}{2\pi k_{fiberglass} L} + \frac{ln(r_{tube2,o}/r_{tube2,i})}{2\pi k_{steel} L} + \frac{1}{h_h 2\pi r_{tube2,o} L} \quad (6.11)$$

It is important to highlight that the resolution of this problem is developed by the operating conditions established in Table 6.3. Following Incropera [407], for the heat exchanger analysis effectiveness-NTU (or NTU) method is employed since $T_{c,o}$ and $T_{h,o}$ are known as will be discussed in the experiments concerning the temperature measurements inside the swirl burner. However, a prerequisite in this design is that the value $T_{c,o}$ should not exceed 190 $^{\circ}C$. After the heat exchanger analysis through the NTU method, a value of $T_{c,o} \leq 190\ ^{\circ}C$ is expected. As indicated by Incropera [407] in the NTU method requires the initial calculation of the maximum possible heat transfer rate (q_{max}) given by the following equation:

$$q_{max} = C_{min}(T_{h,i} - T_{c,i}) \quad (6.12)$$

where C_{min} is equal to C_c or C_h, whichever is smaller. C_c and C_h is cold and hot capacity rates, respectively, that can be achieved by the following Equation:

$$C_c = \dot{m}_c c_{p,c} \quad (6.13)$$

$$C_h = \dot{m}_h c_{p,h} \quad (6.14)$$

where $c_{p,c}$ and $c_{p,h}$ are the specific heat of cold and hot fluid and, $\dot{m}_c$ and $\dot{m}_h$ the mass flow rates of cold and hot fluid respectively. An additional critical variable of the NTU method is the effectiveness ε, a dimensionless parameter defined as the ratio between the actual heat transfer rate (q) and the maximum possible heat transfer rate (q_{max}) and its value range of $0 \leq \varepsilon \leq 1$. The following Equation represents the effectiveness (ε):

$$\varepsilon = \frac{q}{q_{max}} \quad (6.15)$$

In this respect, q is the total heat transfer rate between the hot and cold fluids, and there is negligible heat transfer between the heat exchanger and the ambient. Under the assumption of steady-state conditions and with awareness of q, $T_{c,i}$ and $T_{h,i}$, the temperature for the outlet conditions for the hot and cold fluids can be obtained by [407]:

$$q = \dot{m}_c c_{p,c}(T_{c,o} - T_{c,i}) = C_c(T_{c,o} - T_{c,i}) \quad (6.16)$$

$$q = \dot{m}_h c_{p,h}(T_{h,i} - T_{h,o}) = C_h(T_{h,i} - T_{h,o}) \quad (6.17)$$

Moreover, the effectiveness ε shows dependence on C_r and NTU: $\varepsilon = f(NTU, C_r)$ [407]. The C_r is the heat capacity ratio and can be defined as $Cr = C_{min}/C_{max}$. The *number of transfer numbers* (NTU) is a dimensionless parameter that is widely used for heat exchanger analysis and is defined as

$$NTU = \frac{UA}{C_{min}} \quad (6.18)$$

For a parallel flow heat exchanger, the effectiveness - NTU relation is presented by:

$$\varepsilon = \frac{1 - exp[-NTU(1 + C_r)]}{1 + C_r} \quad (6.19)$$

Several unknown variables related to the swirl burner/heat exchanger dimensions must be addressed to solve the heat exchanger problem. However, a few variables have already been defined. The thickness of tube 1 and tube 2 are 1 and 2 mm. In addition, the atomizer dimensions are provided in chapter 5. Due to this, the dimension from 0 to $r_{tube1,o}$ is known. As previously mentioned, the main objective of this approach is to determine the thickness of the fiberglass insulation (ranging from r_{ins} to $r_{sec,0}$) and the length of the swirl burner (L). Consequently, employing the NTU method is it possible to determine r_{ins}, $r_{sec,0}$ and L, ensuring a temperature $T_{c,o}$ close to 190 $^{\circ}C$ through an iterative process. In this respect, fixing a value for L, the remaining unknown variables r_{ins}, $r_{tube2,i}$, $r_{tube2,o}$, $r_{sec,o}$ depend on the coating thickness. In other words, for a constant L, the coating thickness is incremented until $T_{c,o}$ achieves convergence at 190 $^{\circ}C$. This iterative process to solve the heat exchanger model was conducted using Matlab Software. To address the problem, a more conservative assumption is adopted where the secondary air reaches the swirl burner inlet at $T_{h,i}$ = 400 $^{\circ}C$, discarding any losses for the ambient. The primary air is assumed to enter at room temperature ($T_{c,i}$ = 20 $^{\circ}C$). For the iterative process, the previous value selected for the axial swirl component was considered ($D_h/D_s \approx 2$) to ease the calculation of the remaining unknown variables. An initial L value is chosen and set, following an arbitrary insulation thickness selection that allows the calculation of R_{tot}. From there, UA, NTU, and ε are determined, ultimately de-

termining q and leading to the final calculation of $T_{c,o}$. Based on that, 3 values for L were considered L_1 = 0.2 m, L_2 = 0.35 m and L_3 = 0.6 m, providing the results displayed in Table 6.4. As previously mentioned, t_{ins} is initially considered with 0 mm and increases until the problem converges for $T_{c,o} \leq 190\ ^{\circ}C$.

Table 6.4: Heat exchanger results for L_1 = 0.2 m, L_2 = 0.35 m and L_3 = 0.6 m.

	L_1=0.2m	**L_2=0.35m**	**L_3=0.6m**
t_{ins} (mm)	0	5	24
$T_{c,o}$ ($^{\circ}C$)	159.3	185.8	189.7
$D_{pri,i}$ (mm)	11.3	11.3	11.3
$D_{pri,o}$ (mm)	15.8	15.8	15.8
D_{atom} (mm)	25.1	25.1	25.1
$D_{tube1,o}$ (mm)	N/A	27.1	27.1
D_{ins} (mm)	N/A	37.1	75.1
$D_{tube2,i}$ (mm)	25.1	39.1	77.1
$D_{tube2,o}$ (mm)	29.1	43.1	81.1
$D_{sec,o}$ (mm)	57.1	85.2	160.3

Due to this, the condition for L_1 = 0.2 m is not applicable and possesses a shorter length. Thus, only L_2 and L_3 will be considered for further analysis. However, a variation of the length of the swirl burner will have an impact on the axial swirl dimensions, as noted in Table 6.4 for the values of $D_{tube2,o}$ and $D_{sec,o}$ being affected by insulation thickness t_{ins}. In this context, as the insulation thickness increases, the dimensions of the swirler become larger, having a direct impact on the Reynolds number of the secondary air flow exiting the swirler and entering the chamber. Consequently, increasing the Reynolds number enhances the recirculation zone, leading to more turbulence on the swirl burner, inducing more air and fuel mixing [436]. Based on that, the influence of swirl burner length on the Reynolds Number of the secondary air is explored. The Reynolds Number is evaluated for two swirlers having a t_{ins} ranging from 5 mm to 30 mm, to be further compared with the length provided in Table 6.4. The Reynolds Number in this analysis is focused on the flow dynamics at the combustion chamber inlet, where the length of the swirl burner corresponding to the highest Reynolds number is utilized as the basis for design selection. Figure 6.13 shows the most relevant characteristics of the swirler exit for the analysis of the Reynolds Number.

To guarantee uniform size characteristics among the swirlers, the angle (α) between the blades and the swirler hub is considered 50.5° for all the swirlers evaluated. Regarding the length of the blades, the design ensures that the blade lengths are sufficient to ensure all the flow experiences deflection by the blades. The Equation 2.43 determines the Reynolds Number displayed in chapter 2, where the characteristic dimension corresponds to the D_H, the hydraulic diameter of the exit channel. Thus, the hydraulic diameter of the exit channel can be obtained by the following expression:

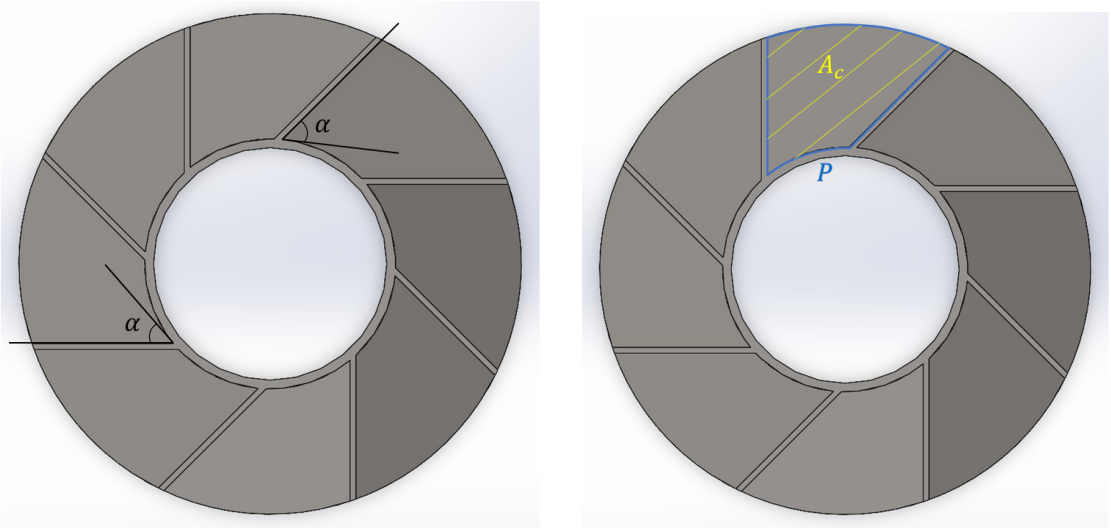

(a) (b)

Figure 6.13: Swirl blade: a) Angle (α); b) Dimensions.

$$D_H = \frac{4A_c}{P} \quad (6.20)$$

where A_c and P are the cross-sectional area and the wetted perimeter, respectively presented in Figure 6.13. For an initial approach, the number of vanes is 8, leading to a total cross-sectional area of $8A_c$ and a total wetted perimeter of $8P$. The values of A_c and P are extracted from Solidworks software. For a better understanding of the velocity dynamics in the swirler, Figure 6.14 illustrates the axial swirler velocity where V_1 represents the inlet flow velocity, V_2 the exit flow velocity, and V_{2a} the axial component of the exit velocity.

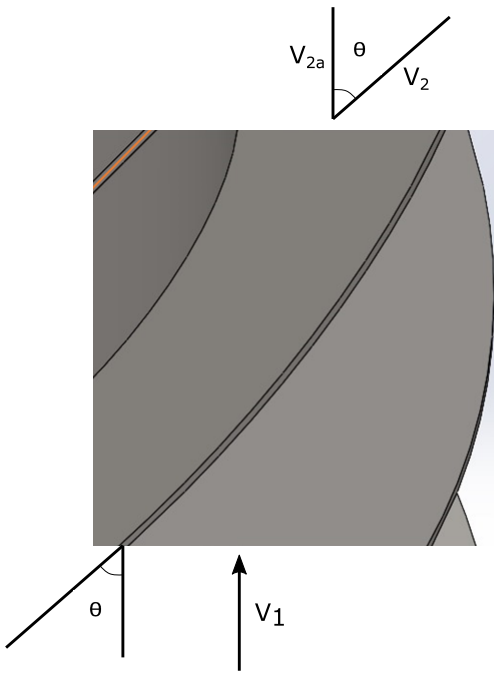

Figure 6.14: Axial swirler velocity representation.

In addition, absolute velocity V_2 follows the blade angle θ = 45° as previously discussed in the initial swirl design specifications. Considering the conservation of mass, V_{2a} can be expressed as:

$$\dot{m} = \dot{m}_1 = \dot{m}_2 \ (=) \ \dot{m} = \rho_2 . 8 A_c . V_{2a} \ (=) \ V_{2a} = \frac{\dot{m}}{\rho_2 . 8 A_c} \quad (6.21)$$

where $\dot{m}_1$ and $\dot{m}_2$ is the mass flow rate at the inlet and exit of the swirler, respectively. ρ_2 is the mass density of the air at the exit, and assuming that the mass density of the air remains constant at the swirler: $\rho = \rho_1 = \rho_2$. Simplifying the Reynold number for the swirl is expressed by:

$$Re_2 = \frac{\rho_2 V_{2a} D_H}{\mu_2} = \frac{\rho_2 \frac{\dot{m}}{\rho_2 . 8 A_c} \frac{4 A_c}{P}}{\mu_2} = \frac{4\dot{m}}{8 P . \mu_2} \quad (6.22)$$

For evaluating the Reynolds Number, the operating conditions provided in Table 6.3 are considered, and for conservative approaches, two temperatures are established. The purpose is to take into account that temperature losses can occur. In this context, Re_2 is also evaluated for a minimum temperature of 210 $°C$ and a maximum temperature of 400 $°C$. The results for this analysis are provided in Figure 6.15, showing the influence of the insulation thickness variation for the two temperatures and its relation in percentage.

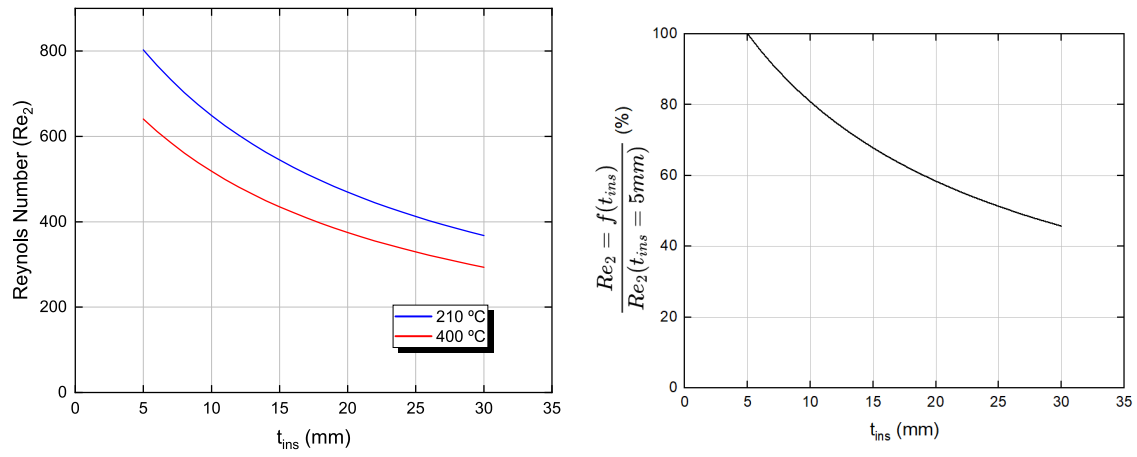

Figure 6.15: Reynolds number at the swirler exit: a) Function of insulation thickness for two temperatures; b) Insulation thickness influence in percentage.

As a result, a significant variation in the Reynolds number is observed between a burner of length L_2 (t_{ins} = 5 mm) and L_3 (t_{ins} = 24 mm). Considering the results of Figure 6.15 b), the Reynolds number at the swirler exit for length L_3 is 52.66% of the value for length L_2. Due to this, the length swirl burner selected for the design is L_2 = 0.35 m. For clearer interpretation, Table 6.5 shows the final specifications for the swirl burner dimensions.

Table 6.5: Summary of the swirl burner dimensions.

	Specifications
L (m)	0.35
t_{ins} (mm)	5
D_{atom} (mm)	25.1
$D_{tube1,o}$ (mm)	27.1
D_{ins} (mm)	37.1
$D_{tube2,i}$ (mm)	39.1
D_h=$D_{tube2,o}$ (mm)	43.1
D_s=$D_{sec,o}$,o (mm)	85.2

The previous analysis was carried out considering an annular swirled with 8 blades. To extend the design of the laboratory combustion chamber, an evaluation of a swirler with 8, 10, 12, 14, and 16 blades is considered. Firstly, it is important to highlight that similar operating conditions are addressed: S_N = 0.78, AFR = 2, θ = 45°, α = 50.5°, D_h = 43.1 mm and D_s = 85.2 mm. Consequently, Equation (6.22) is adapted from a general form:

$$Re_2(N) = \frac{4\dot{m}}{NP.\mu_2} \quad (6.23)$$

where N is the number of blades and μ_2 corresponds to the fluid at $T = 400$ °C. The correspondent wetted perimeter (P) for each swirler was extracted from the Solidworks software. Figure 6.16 shows the Reynolds Number for HVO and Jet A-1 considering several number of blades as a function of the equivalence ratio (ϕ).

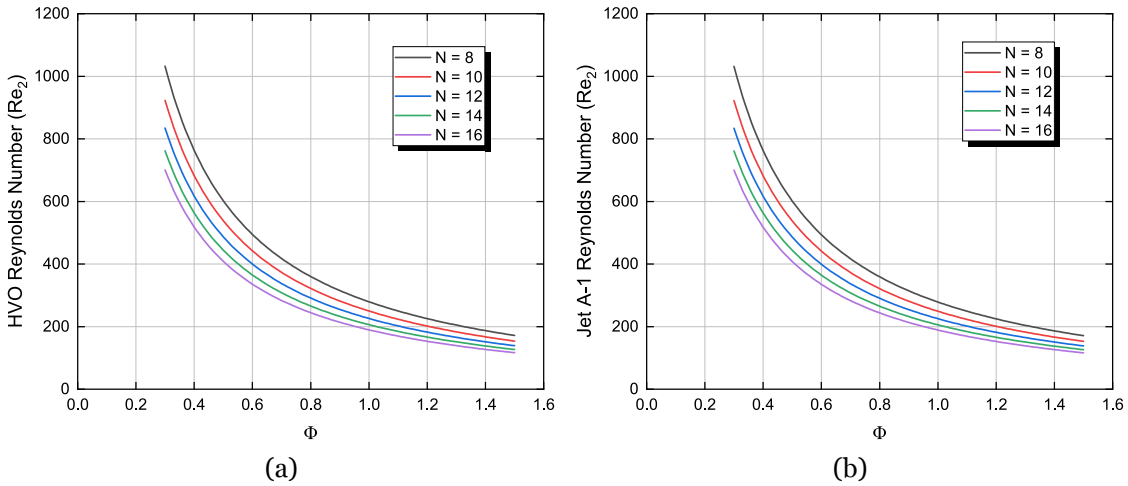

Figure 6.16: Reynolds Number considering several blades number: a) HVO; b) Jet A-1.

The analysis indicates that the number of blades significantly affects the Reynolds number, where a lower number of blades leads to an increase in the Reynolds number. Consequently, the axial swirler utilized in this project is designed with 8 blades, and an alternative configuration using 12 blades was also fabricated to understand its impact on the spray combustion

process. Consequently, the most relevant features concerning the swirl burner design were presented in this subsection. Following that, the design of the combustion chamber is addressed.

6.3.3 Combustion Chamber Design

The dimensions of the combustion chamber play a key role in ensuring the availability of enough air volume to provide adequate fuel combustion. As noted above, the specifications provided in Table 6.3 act as a starting point to facilitate the design process. Besides that, particular attention is given to the combustion chamber volume to guarantee that it is capable of operating under different operating conditions (richer and lean conditions). Thus, evaluating the reaction volume is fundamental to establishing the appropriate dimensions for the combustion chamber. The following expression provides a simplified representation of the reaction volume:

$$Reaction\,Volume = \dot{Q} \times residence\,time \quad (6.24)$$

Equation (6.24) states the relation between the fuel and air volumetric flowrate and the residence time. An understanding of the residence time can be derived from the droplet lifetime. An analysis of the droplet lifetime was deeply explored in chapter 4. The droplet lifetime and burning rate were analyzed, and an initial droplet diameter of 250 μm was considered. The droplet lifetime is highly related to the burning rate, as noted in Equation (2.40). The burning rate for Jet A-1 and HVO at $T_\infty = 800$ °C and $T_\infty = 1000$ °C are provided in chapter 4, where the conventional jet fuel possesses a slight higher burning rate for the lowest furnace temperature. A spray contains various droplets with diameters on the order of micrometers that exhibit a wide range of velocities. To evaluate its droplet diameter distribution and velocity under non reacting, a Phase-Doppler Interferometry is commonly employed, as shown in chapter 5. The results regarding this subject indicate no significant difference in terms of the droplet diameter for Jet A-1 and HVO to affect the reaction volumes notably. Thus, the results provided in the single droplet combustion and spray under non reacting conditions serve as a plausible basis for designing the laboratory combustion chamber. Finally, the evaluation of the volumetric flowrates is addressed. The values fuel and air volumetric flowrates corresponds to the $\dot{Q}_{fuel}$, $\dot{Q}_{primary}$, $\dot{Q}_{secondary}$ were previously discussed. Table 6.3 displays the mass flowrate for each parameter. The mass flow rate is divided by the fluid density at the specified operating temperature to determine the volumetric flow rate. In this context, the fuel and primary air are delivered at room temperature (20 $^\circ C$), whereas the secondary air is at 400 $^\circ C$. Since the lower heating values of Jet A-1 and HVO are quite similar, for a specific power output, the $\dot{Q}_{fuel}$ for each fuel are essentially identical. Moreover, the $\dot{Q}_{primary}$, $\dot{Q}_{secondary}$ for both fuels are roughly similar. Due to this, the reaction volumes of conventional and alternative jet fuel are considered similar for simplification purposes.

The work developed by Chong and Hochgreb [247] plays a pivotal characteristic in obtain-

ing the dimensions of the combustion chamber since similar operating conditions with the present study were established. The combustion chamber designed by Chong and Hochgreb [247] is a circular quartz tube with a volume of approximately 1.414 dm^3. In contrast with the work of Chong and Hochgreb [247], the laboratory combustion chamber in this study comprises AISI304 instead of a quartz tube. The main reason is the effect of the radiation absorption of nanofuels that play a relevant role in the combustion process of these fuels, as previously discussed in chapter 4. Focus on determining the volume of the combustion chamber, a relation of the maximum Sauter mean diameter between the present and Chong and Hochgreb [247] works are essential to acquire a proper combustion chamber volume. Simplifying and based on the finding provided by the spray under non reacting conditions, a maximum Sauter mean diameter of 150 and 45 μm for the present and Chong and Hochgreb [247] works was established to have a tolerance range. In light of this, a minimum volume of approximately 16 dm^3 is required. For a safer design approach, the final volume of the combustion chamber is oversized to 20 dm^3 to satisfy the prior conditions defined.

After defining the volume of the combustion chamber, the corresponding specific dimensions are determined. According to the literature [437, 438], a relation can be established in confined systems exhibiting swirl. Thus, the confinement ratio (CR) can be defined as the ratio of the inner diameter of the combustion chamber ($D_{chamber}$) and to the swirl burner exit diameter (D_s) using the following equation:

$$CR = \frac{D_{chamber}}{D_s} \quad (6.25)$$

The confinement ratio (CR) influence was analyzed in detail by [437, 439]. According to Syred et al. [439], a CR > 2.82 is recommended for small combustion systems to obtain less interaction between the swirling flow and the chamber confinement and a more stable inner recirculation zone (IRZ), enhancing flame stabilization. Concerning the findings of Ji et al. [437], three confinement ratios were considered: CR = 2, 2.5, and 3. The results show that the size of the inner and outer recirculation zone (IRZ and ORZ) increased with an increase in CR, which means that the surface area to recirculate the hot burned products to ignite the reactants became larger. Moreover, increased CR postponed the transition from stable to unstable. Therefore, for the design of the combustion chamber, a confinement ratio (CR) of 3 was selected, leading to $D_{chamber}$ of 255.6 mm following Equation (6.25) where the swirling outer diameter value (D_s) is defined as 85.2 mm. Given that the $D_{chamber}$ and $V_{chamber}$ are already defined, the $H_{chamber}$ is 389.8 mm, taking into account the established formula for the volume of a cylinder. Table 6.6 summarizes the combustion chamber design specifications.

After providing the most relevant dimensions and operating conditions for the design of the laboratory combustion chamber, the flammability limits are analyzed for safety reasons. The boundaries of the equivalence ratio range under which flame propagation can occur are referred to as the flammability limits. In other words, it specifies the range of concentrations

Table 6.6: Summary of the combustion chamber design specifications.

Combustion Chamber Design	Specifications
Volume (dm^3)	20
Diameter (mm)	255.6
Height (mm)	389.8

at which gases or vapors can ignite. The lower flammability limit (LFL) corresponds to a lean mixture, whereas the upper flammability limit (UFL) corresponds to a rich mixture. Moreover, the temperature significantly affects the flammability limits in contrast to pressure. The flammability limits are commonly expressed for a temperature of $25°C$ and pressure of 1 atm. For Jet A-1, the flammability is widely discussed and related to the kerosene indicating that $LFL_{25} = 0.7\ vol\%$; $UFL_{25} = 5\ vol\%$ [440–442]. For HVO, this information is relatively limited. According to Xing et al. [443] the flammability limits for HVO are $LFL_{25} = 0.6\ vol\%$; $UFL_{25} = 7.5\ vol\%$. It is important to mention that the flammability limits are commonly expressed as vol% fuel in air.

To estimate the upper and lower flammability limit, two methods are considered previously provided in [444,445]. The adapted Burgess-Wheeler Law proposed by Zabetakis et al. [444] is given by:

$$LFL_T = LFL_{25} - \frac{0.75}{\Delta H_c}(T - 25) \quad (6.26)$$

$$UFL_T = UFL_{25} + \frac{0.75}{\Delta H_c}(T - 25) \quad (6.27)$$

For Zabetakis [445], the limits were estimated for paraffin hydrocarbons and are expressed as:

$$LFL_T = LFL_{25} - \frac{LFL_{25}}{(1300 - 25)}(T - 25) \quad (6.28)$$

$$UFL_T = UFL_{25} + 0.0000721(T - 25) \quad (6.29)$$

where ΔH_c is the net heat of combustion, the subscript T is the temperature of the measured flammability limit, and the subscript 25 is the flammability limit given for $25°C$.

Since the present design is focused on an equivalence ratio of ϕ = 0.47, the LFL is evaluated, providing the safest design scenario for both methods. Moreover, flammability limits are evaluated ranging temperature from the temperature axis ranges from 25 $°C$ to 450 $°C$, since

400 $°C$ is the inlet temperature for the secondary air. To apply the method of Zabetakis et al. [444], it is necessary to determine the net energy release from fuel combustion, ΔH_c, which can be provided by the following equation:

$$\Delta H_c = LHV.M_{fuel} \quad (6.30)$$

where M_{fuel} is the molar mass of the fuel. The results for ΔH_c regarding HVO and Jet A-1 are provided in Table 6.7.

Table 6.7: Values of LHV, M_{fuel} and ΔH_c for HVO and Jet A-1.

	LHV (MJ/kg)	M_{fuel} **(kg/kmol)**	ΔH_c **(kcal/mol)**
HVO	43.9	226	2371
Jet A-1	43.0	153	1572

Based on that, the LFL for each method is evaluated for HVO and Jet A-1, and the results are displayed in Figure 6.17 as a function of the temperature. The analysis indicates that Zabetakis et al. [444] provide the most conservative prediction of the LFL, as its higher LFL values create a safer design scenario.

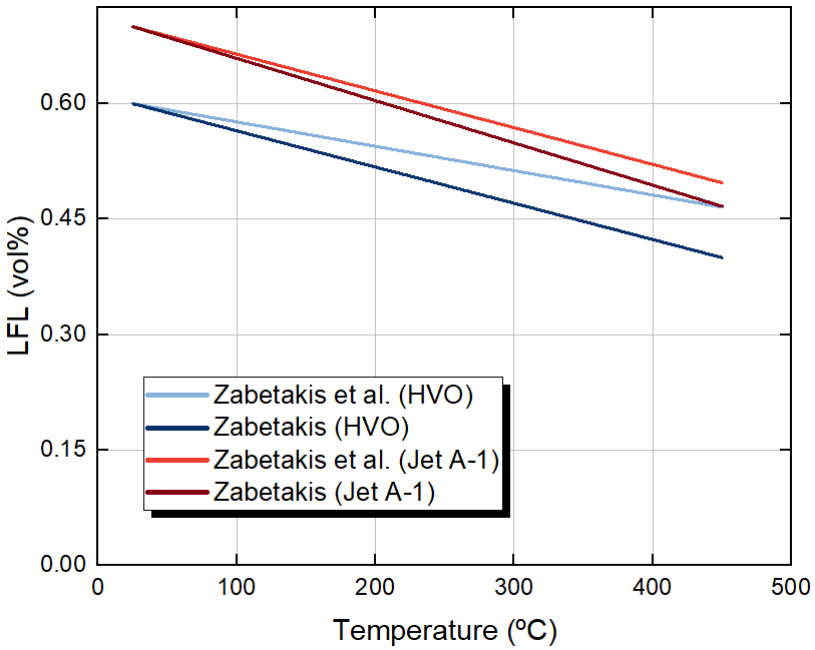

Figure 6.17: Evaluation of LFL for Zabetakis et al. and Zabetakis [444] [445].

Considering this analysis, the graphical representation of the flammability limits of Jet A-1 and HVO will be provided concerning the method developed by Zabetakis et al. [444]. The results for the LFL were already presented, and the UFL can be determined using the Equation (6.27). Contrasting with the previous analysis, the influence of the equivalence ratio (ϕ) is addressed. To accomplish this purpose, combustion reactions of the fuels are expressed in terms of ϕ. According to the stoichiometric reaction of HVO and Jet A-1 outlined in Equation

(6.1) and Equation (6.2), the equivalence ratio can be simplified for each fuel in the following expressions:

$$\phi = \frac{24.5\left(1+\frac{79}{21}\right)}{\frac{100}{vol\%\ HVO}-1} \quad (6.31)$$

$$\phi = \frac{16.25\left(1+\frac{79}{21}\right)}{\frac{100}{vol\%\ A{-}1}-1} \quad (6.32)$$

Figure 6.18 shows the flammability limits for a) HVO and b) Jet A-1 in logarithmic scale. In addition, the auto-ignition temperature for each fuel is presented.

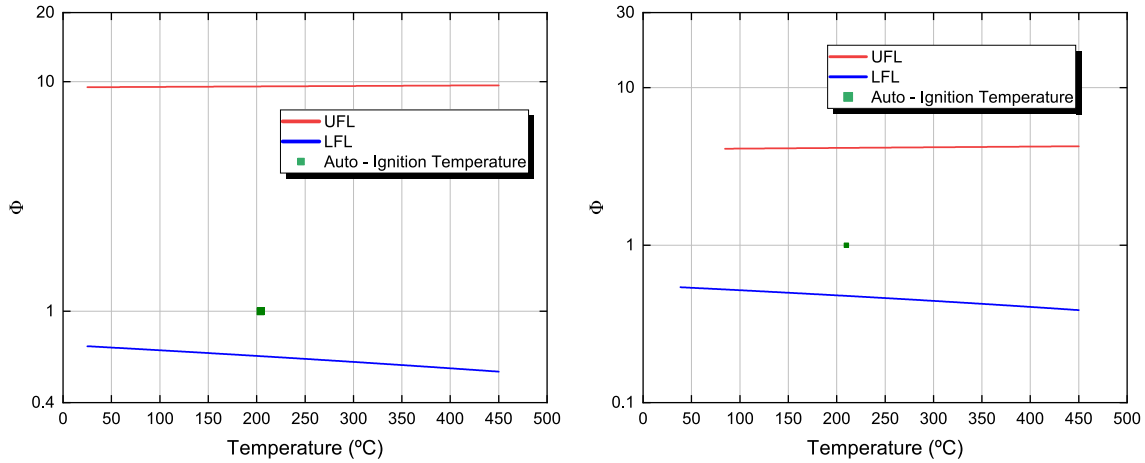

Figure 6.18: Flammability limits for: a) HVO; b) Jet A-1.

This graphical representation supports the design of the laboratory combustion chamber for further operating conditions. Also, it elucidates the flammability limits for HVO and Jet A-1 to aid in the execution of the experiments.

6.4 Final Design of Combustion Chamber

The current section is dedicated to the final design and assembly of the laboratory combustion chamber. In addition, experiments concerning the temperature profile inside the swirl burner are also addressed. The preliminary results involving the fuel spray combustion are presented in the summary section of the current chapter. Firstly, it is important to mention that the final design possesses slight dimensional discrepancies due to the commercial materials that present restrictive dimensions. However, the variation in dimensions is minimal and does not influence the overall outcome of the project. Figure 6.19 shows the most relevant components of the combustion system and its general dimensions. The combustion chamber and swirl burner are placed in a steel structure to support all the equipment and ease the operation. The bottom part of the system corresponds to the swirl burner with

a height of 370 mm, where the atomizer support length is also included. The combustion chamber is at the top of the combustion system, where the spray combustion occurs, possessing a diameter of 254 mm and a height of 412.5 mm, considering the two flanges. These two flanges are placed at the top and bottom of the combustion chamber to connect an exhaust system and the steel structure. All of these elements are attached with several screws. As shown in Figure 6.19, the combustion chamber possesses optical access to visualize the spray, perform measurements, and to have an entry to force the ignition. The combustion chamber and swirl burner are both covered with fiberglass insulation and aluminum tape to prevent heat losses for the ambient.

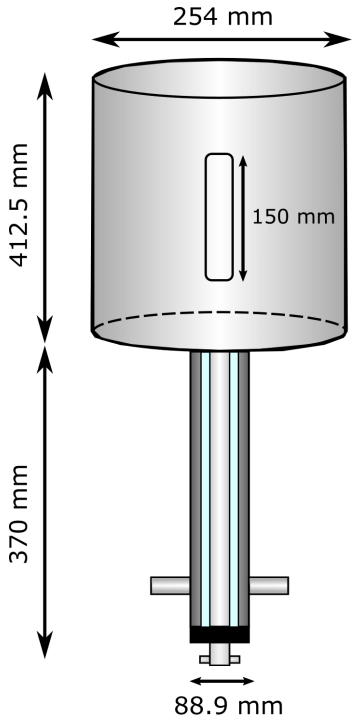

Figure 6.19: Overall dimensions of the combustion system.

For a better visualization of the combustion chamber, Figure 6.20 shows a technical drawing including the most relevant dimension and a top view of the manufactured chamber. In Figure 6.20 b) is it possible to identify the flange for the connection and axial swirler aligned with the chamber face. Regarding the axial swirler, Figure 6.21 shows the technical drawing of this component. An air swirler with 8 blades is employed for the preliminary experiments, similar to Figure 6.21. The dimensions of design for the axial swirler are presented with a minimal difference due to constraints in the manufacturing process that do not compromise the swirl number established as 0.78. This component is placed inside the swirl burner, as previously mentioned. A side and a front view of the swirler burner is displayed in Figure 6.22. In the front view, no insulation is presented to ease the visualization. In contrast, for the side view, is it possible to notice the swirl burner already covered by the fiberglass and aluminum tape. Figure 6.22 shows the atomizer and air-preheated inlet, as well as the connection with the steel structure. The air heater equipment is also displayed and perpendicularly placed concerning the swirl burner.

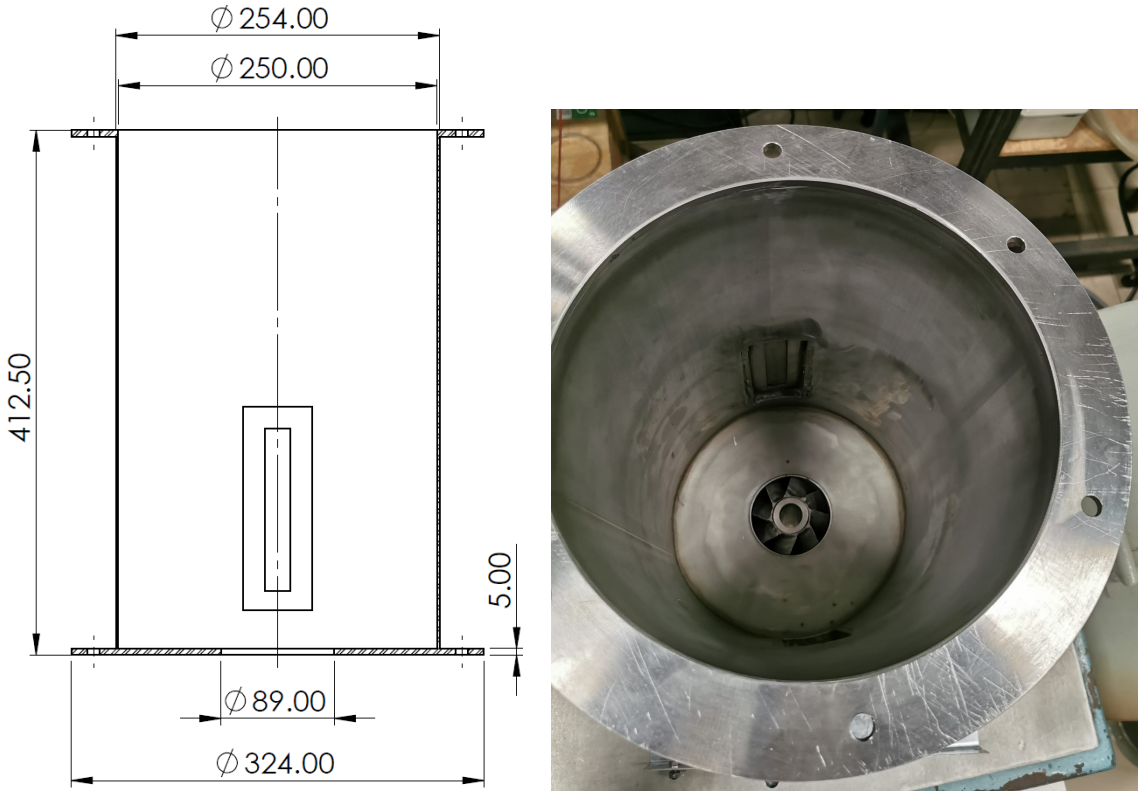

Figure 6.20: Combustion chamber: a) Technical drawing (units in mm); b) Top view.

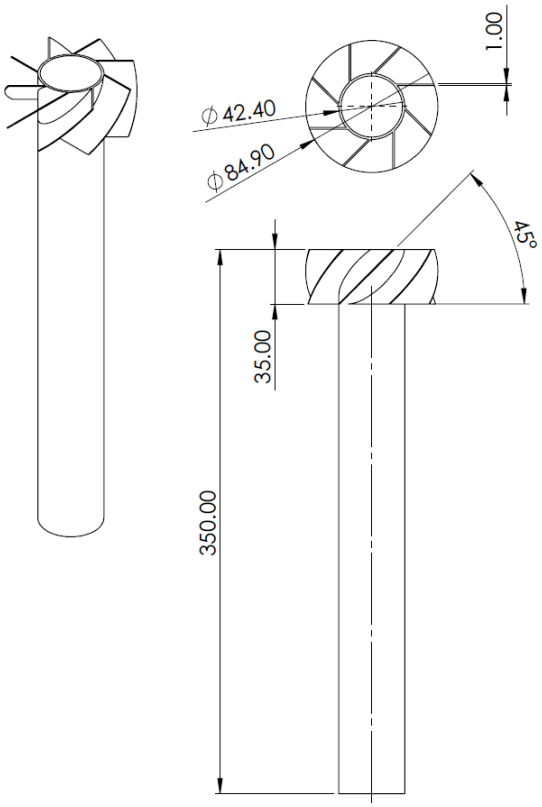

Figure 6.21: A technical schematic of the air swirler with 8 blades (units in mm).

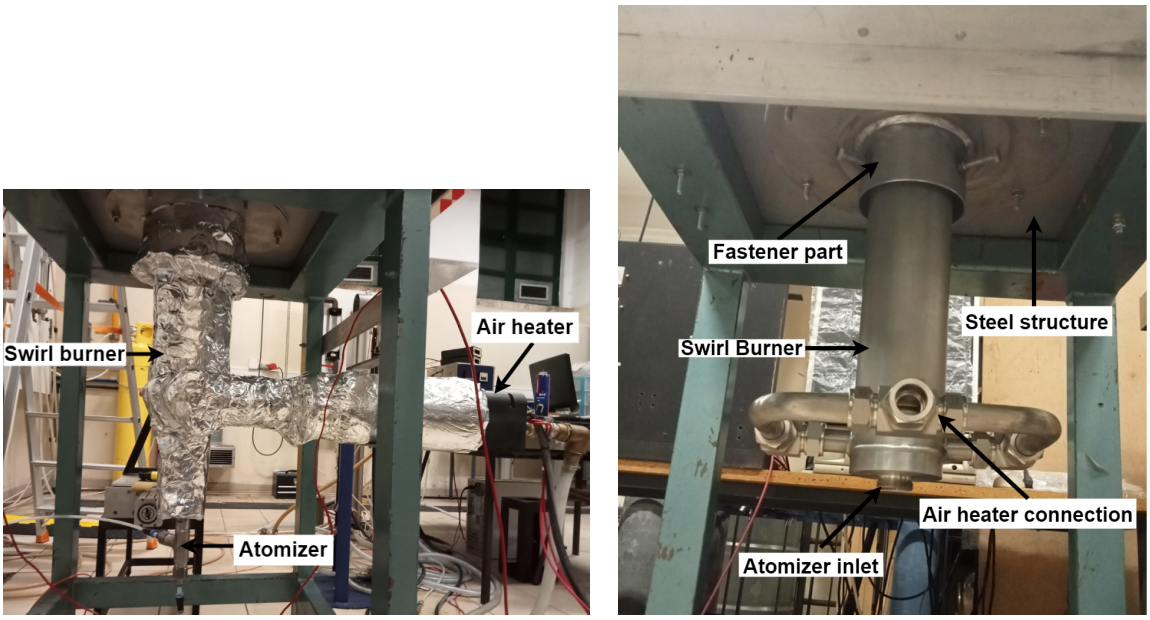

(a) (b)

Figure 6.22: Swirl burner: a) Side view; b) Front view.

Based on this, a brief overview of all the components placement, assembly, and dimensions was provided. To ensure that the design accomplished the prerequisites, an evaluation of the temperature inside the swirl burner is conducted. In addition, the purpose is to ensure proper spray combustion, avoid excessive vaporization, and evaluate the temperature of the secondary air entering the chamber to determine if the air and fuel mixture reaches a sufficient temperature for ignition. This analysis only involves the preheated secondary and primary air without liquid fuel in the atomizer. The temperature measurements were carried out using K thermocouples capable of evaluating temperatures from $-270°C$ to $1260°C$ and present a standard accuracy of $2.2°C$ or $\pm$0.75% of reading, whichever is greater. Figure 6.23 shows the thermocouple arrangement for the swirl burner temperature evaluation. Thermocouple 1 was placed above the swirler blades to measure the outlet temperature of the secondary air. This placement aims to confirm that the maximum possible temperature is achieved to enhance complete fuel vaporization, promote a more flammable mixture, and expand its range. Thermocouple 2 is placed at the outlet of the liquid fuel line, ensuring that the liquid fuel temperature does not exceed 190 $°C$. The thermocouple 3 is placed in the inlet of the secondary air.

Figure 6.24 shows the results of the temperature measurements inside the swirl burner for two input temperatures for the air heated. Initially, $T_h = 400$ °C is imposed to understand its influence in the outlet of the liquid line and secondary air. This temperature was selected based on the final boiling point of HVO. The measurements in thermocouple 1 indicated a temperature of 220 °C, whereas, in thermocouple 2, the temperatures reach 136 °C. This analysis reveals that a significant thermal loss between the air heater and the inlet is presented as already expected. Regarding thermocouple 2, a satisfactory result is noticed since the measurements are considerably lower than 190 °C, ensuring no liquid overheating is ob-

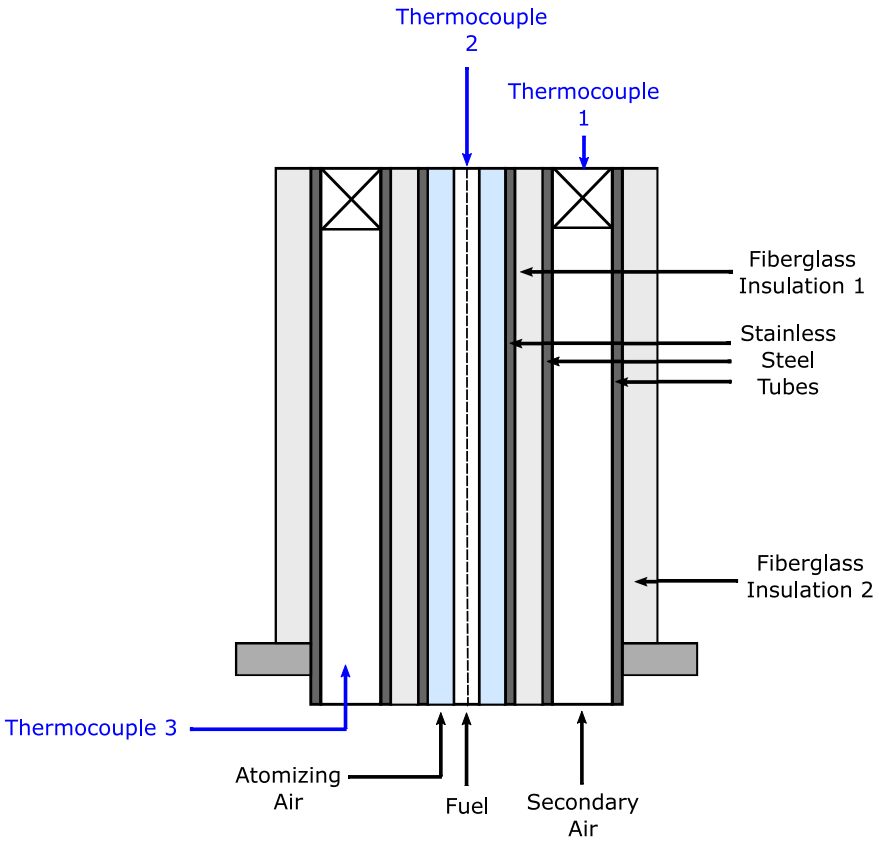

Figure 6.23: Thermocouple arrangement for temperature evaluation.

tained. As previously mentioned, Jet A-1 is the most volatile fuel, so a consideration regarding the distillation temperature of 10 vol.% is provided. This temperature is presented in Figure 6.24 marked by a dashed red line, highlighting 170 °C. As thermocouple 2 indicated satisfactory results for fuel operation, the temperature of the secondary air supplied by the air heater was increased to 500 $°C$. The purpose is to increase the temperature of the secondary air entering the chamber, leading to a higher temperature for the fuel and air mixture. The temperatures of thermocouples 1 and 2 increase with the increase of the input temperature of the air heater. As noted in the experiments with a $T_h = 400$ °C, significant thermal losses are evident in the air heater and the chamber inlet. As shown in Figure 6.24, the thermocouple 1 displays a temperature of 237 °C. Regarding thermocouple 2, the temperature obtained was 156 °C lower than the distillation temperature of Jet A-1 for 10 vol.%. Consequently, operating with a preheated air secondary air input of 500 °C, it remains within the safety limits for the fuel inside the atomizer.

Consequently, for further experiments, the input of the air heater is 500 °C. To gain deeper insights into the heat losses associated with the secondary air, an evaluation using thermocouple 3 is performed. This analysis allows an understanding of the heat losses experienced by the secondary air between the air heater and the swirl burner. Figure 6.25 shows the results for an input temperature of the air heater of 500 °C. The thermocouple 3 indicates a temperature of 289 °C, confirming that most heat losses for the secondary air occur between the air heater and the swirl burner inlet.

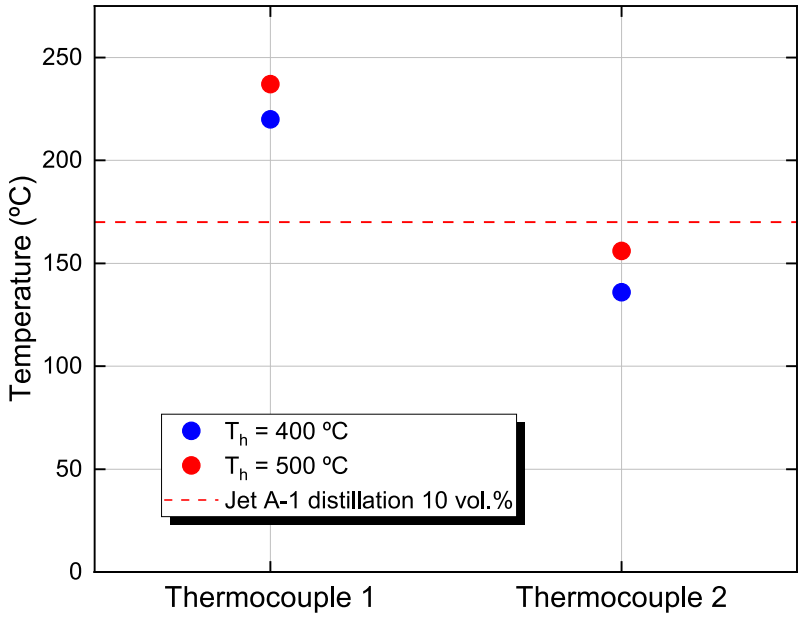

Figure 6.24: Temperature measurements of thermocouples 1 and 2 considering preheating of secondary air at 400 $^{\circ}C$ and 500 $^{\circ}C$.

Overall, the results indicate that the secondary air temperature entering the combustion chamber, measured by thermocouple 1, corresponds approximately to the final boiling point of Jet A-1 (237 °C). However, the final boiling point of HVO is higher than Jet A-1, as displayed in Figure 6.7. Consequently, the ignition of HVO is more challenging. To force the ignition, a blowtorch is used as the ignition source to aid the vaporization process. It is also important to mention that for further experiments, due to the reduced temperature of the secondary air at the chamber inlet, increasing the equivalence ratio could be required to produce flammable mixtures, considering that the temperature measurements were carried out using the operating condition indicated in Table 6.3.

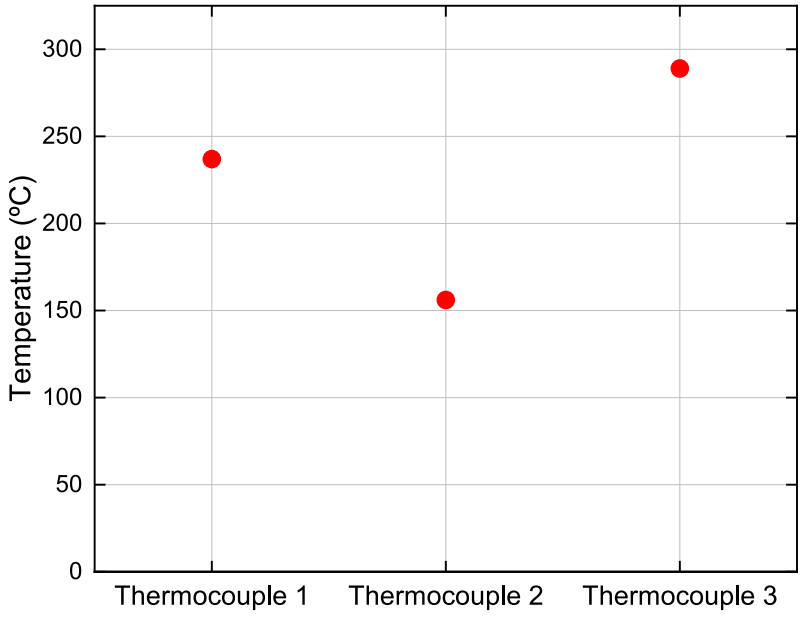

Figure 6.25: Temperature measurements of thermocouples 1, 2, and 3 considering preheating of secondary air at 500 $^{\circ}C$.

6.5 Summary

The present chapter was dedicated to the development of a laboratory combustion chamber. In this context, the most relevant components were built, considering a combustion chamber, an annular axial swirl, and a swirl burner. In addition, the experimental setup was developed while considering the fuel and air supply system. To accomplish this purpose, the most pertinent findings already discussed in this document involving single droplet combustion and spray dynamics played a relevant role. An air heater was employed to enhance the fuel droplet vaporization. Due to this, careful attention was initially given to the fuel volatility to guarantee that the operating conditions were adequate for this project. For the development of this design, a power output of 6 kW, AFR = 2, and an equivalence ratio of 0.47 was defined. The design was developed considering the liquid fuel temperature, a relevant aspect of the liquid fuel burner since excessive heating can promote partial fuel volatility, intermittent fuel delivery inside the combustion chamber, and safety concerns. Due to this, a conservative approach was considered, and the established dimensions were taken into account that the primary air and fuel temperature should not exceed 190 $^{\circ}C$. This goal was successfully achieved, ensuring a proper and safe operation of the laboratory combustion. An iterative process was carried out to find the optimal inner insulation thickness and swirl burner length. In addition, flow dynamics were considered, and an annular axial swirler was developed. The most relevant characteristics of an annular axial swirler were also analyzed and determined, considering the swirl burner dimensions. In the design specifications, the swirler possesses a swirl number (S_N) of 0.78, θ = 45°, α = 50.5°, D_h = 43.1 mm and D_s = 85.2 mm. The number of blades was also explored, and the most satisfactory results were provided for a swirler with 8 blades. Concerning the pre-heated secondary air, significant temperature losses were evident, mainly identified from the outlet of the air heater to the inlet of the swirl burner. A reduction of approximately 250 $^{\circ}C$ was noticed, requiring further experimental setup modifications to improve this aspect. The dimensions of the combustion chamber were defined, ensuring the availability of enough air volume to provide adequate fuel combustion for a wide range of operating conditions. To facilitate the experiments, two quartz windows are presented in the combustion chamber to assist the measurements and ignition. Regarding operability, the flammability limits of HVO and Jet A-1 were explored, and a graphical representation was provided for further studies. This experimental setup was constructed using AISI304, considering the economic aspects and for safety reasons due to the high temperatures during the combustion process. For the thermal insulation, fiberglass and aluminum tape covered the combustion chamber and swirl burner to prevent significant temperature losses.

Preliminary experiments involving spray combustion were performed with Jet A-1. Due to time constraints, HVO and nanofuel were not evaluated in the laboratory combustion chamber developed in the present studies. The Jet A-1 experiments were conducted following this specific methodology. First, primary and secondary air are inserted in the swirl burner, considering the temperatures established in the design. When the temperature reaches a stable temperature of approximately 240 ° C, the liquid fuel line is verified to ensure no bub-

bles are presented. To avoid issues concerning bubble formation before the fuel enters the swirl burner, the fuel line is straight and shortened between the mass flow controller and the atomizer. Before forcing the ignition, the fuel spray inside the combustion chamber is verified to be operating properly, and it is also verified if any considerable residues of liquid are placed inside the combustion chamber for precautionary purposes. Subsequently, ignition was achieved by using a blowtorch, which was directed at the fuel and air mixture through one of the lateral openings of the chamber. The operating conditions and the preliminary results are provided in Table 6.8 and Figure 6.26. The observation indicates that the spray combustion occurred in a continuous, uninterrupted spray, with the flames remaining stabilized for at least twenty minutes. Unfortunately, further assessments regarding flame temperature and emissions for the fuel were not performed due to the time limitation. However, the primary objective was successfully achieved by developing a modular laboratory combustion chamber for liquid fuels, ensuring safe and effective operation. In this respect, an experimental setup was developed from the conceptual design to the completed construction, capable of operating at a wide range of conditions, contributing to the investigation of sustainable and alternative fuels.

Table 6.8: Operating conditions of preliminary tests.

Secondary Air Condition	**AFR**	ϕ
204 L/min	2	0.47
	2.5	0.46
172 L/min	1.4	0.56
	2.3	0.55
159 L/min	2	0.59

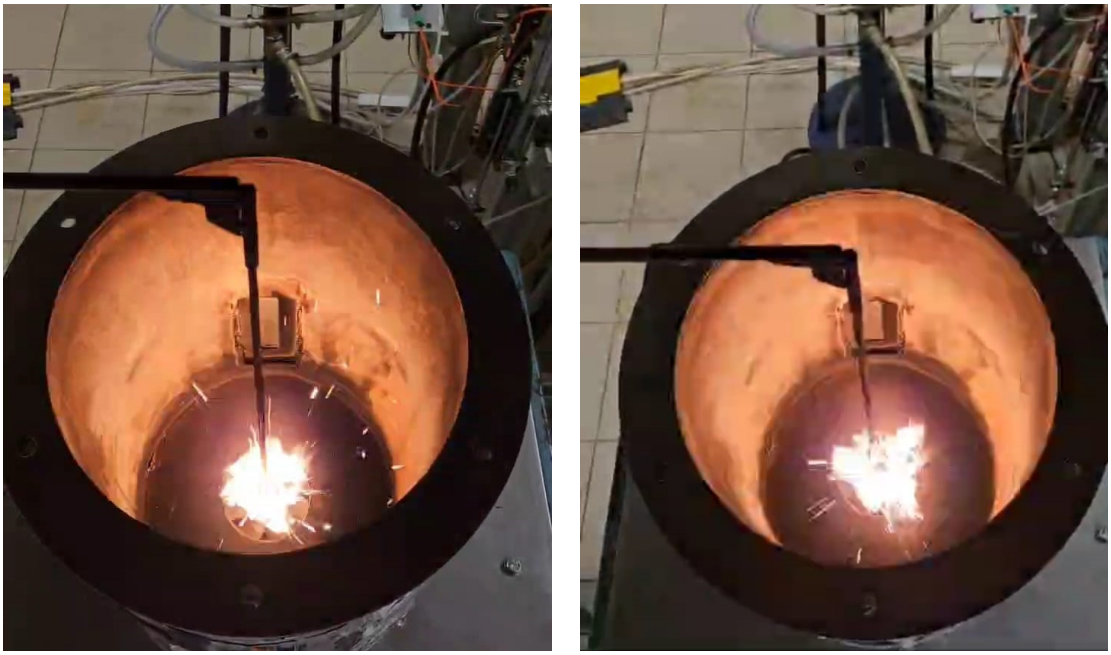

(a) (b)

Figure 6.26: Flame images for 6 kW power output: a) ϕ = 0.47 and AFR = 2; b) ϕ = 0.47 and AFR = 2.5.

Chapter 7

Closure

7.1 Work Summary and Main Conclusions

The addition of nanoparticles to enhance biofuel performance is a novel research subject in the atomization and combustion fields. This topic focuses on investigating alternative fuels to find additional solutions to reduce fossil fuel dependency while addressing environmental concerns. The addition of metallic nanoparticles in conventional fuel has been reported as an energy enhancement approach, providing increased energy, reducing liquid fuel consumption, and enhancing fuel efficiency. Nanofuels comprise nanoparticles ranging from 1 to 100 nm, stably suspended in a conventional liquid fuel. The evaporation and combustion of these fuels is a highly complex, multi-phase phenomenon in which several processes occur simultaneously. Thus, this subject requires further investigation to understand its impact on practical applications. Based on that, the present work fundamentally evaluates the addition of aluminum nanoparticles to a liquid biofuel using an experimental and numerical approach. Aluminum was selected due to its energy content, abundance, and relatively low production costs. In addition, pure HVO and Jet A-1 are also tested for comparison purposes. This investigation is conducted following several specific objectives.

Firstly, the preparation and stability of the nanofuel is addressed. Physical and chemical approaches to stabilize the nanoparticles in the liquid fuel are discussed, giving special focus to high particle concentrations. In this context, evaluations concerning low and high particle concentrations are addressed, guaranteeing experimental accuracy and proper evaluation of the physical properties. Afterwards, single droplet combustion investigations are performed in a drop tube furnace, which is a prerequisite for understanding spray combustion. Experiments in a drop tube furnace at different temperatures are carried out for HVO, Jet A-1, and several nanofuels. This experimental setup provides a satisfactory compromise between experimental work and practical conditions due to the use of relatively high furnace temperature, reduced droplet diameter, and no supportive fiber, which can offer a new perspective in this field. This analysis provided a basis for understanding the nanofuel droplet combustion in terms of droplet size evolution and disruptive burning phenomena. Following this, the results evidence a distinct combustion behavior of pure HVO and nanofuel. Due to this, a simplified macroscopic model is developed to address relevant factors that can contribute to this outcome. Subsequently, an experimental facility is developed using a commercial air-assisted atomizer to evaluate the spray behavior. The primary and secondary atomization evaluations address breakup length, spray cone angle, droplet size, and velocity, highlighting overall distributions in a combustion chamber. Conventional and alternative fuels are exam-

ined, considering the influence of their physical properties. The final objective is to develop a laboratory combustion chamber for liquid fuels from the design concept until its construction. The purpose is to investigate the spray combustion of nanofuels to perceive its potential impact, addressing its efficiency and emissions. Unfortunately, due to time constraints, the combustion chamber operability was only tested for Jet A-1, evidencing its possible use for alternative and sustainable liquid fuels research. The main conclusions of the present work focus on stability, single droplet combustion, and spray are provided.

Concerning the stability of the nanofuel, several particle sizes (40 nm, 70nm, and 5 μm) and concentrations (0.2, 0.5, 1.0, 2.0, and 4.0 wt.%) are explored. The results reveal that the fuel preparation significantly contributes to the nanofuel stability. Due to this, several preparation methods were evaluated to guarantee that the nanofuels would remain stable during single droplet combustion and spray experiments. A sonication process is highly essential to enhance the stability of nanofuel. The optimal parameters for power and time were defined, and an ice bath was added during this process. The findings reveal that substantially increasing the sonication power and time reduces the nanofuel stability, significantly increasing the nanofuel temperature during its process. Additionally, using an ice bath in the sonication is essential to maintain constant and low temperatures that enhance stability. Nevertheless, a nanofuel preparation process involving a magnetic stirrer and sonication does not guarantee a stable particle concentration up to 2.0 wt.%. An increment of aluminum particle concentration leads to an increase in the energy content of the fuel, a desired outcome for the mobility industry where a stable fuel is essential for its implementation in real applications. Therefore, a chemical process was added to enhance the stability of nanofuels, particularly for high particle concentration (>1.0 wt.%). Oleic acid, a surfactant, was added in the preparation process and displayed a significant enhancement in the stability of nanofuel with high particle concentration. A surfactant-to-nanoparticle mass ratio of 1:1 and the nanofuel with a particle concentration up to 4.0 wt.% provides stabilization for at least four hours. Overall, increasing the particle size and concentration reduces the stability. Adding aluminum nanoparticles and oleic acid leads to negligible variations in the density and surface tension of HVO. However, adding 4.0 wt.% aluminum nanoparticles and 4.0 wt.% oleic acid leads to an increase in viscosity of approximately 20%.

Single droplet combustion for conventional and alternative fuels was evaluated for 600, 800, 1000, and 1100 °C. For this analysis, Jet A-1, HVO, and HVO with aluminum particles in sizes of 40 nm, 70nm, and 5 μm, and particle concentration of 0.2, 0.5, 1.0, 2.0, and 4.0 wt.% are explored. For a furnace temperature of 600 °C, the analysis of the droplet combustion was discarded since the visualization and identification of auto-ignition were not possible in the majority of the droplets, not providing an accurate comparison for the remaining operating conditions. The results reveal that HVO and Jet A-1 present a similar combustion behavior, following the D^2-law without the occurrence of disruptive burning phenomena. Regardless of the particle size and concentration added to HVO, a deviation from the D^2-law is noticeable. In addition, a dry-out phase is spotted, followed by the occurrence of a disruptive burning phenomenon that determines the end of the droplet lifetime. For all the fuels involving

the addition of aluminum particles, a micro-explosion is detected. The results suggest that a higher particle concentration and furnace temperature promote a higher micro-explosion intensity. Regardless of the fuel employed, increasing the furnace temperature leads to an increase in the burning rate. A higher particle size leads to a longer lifetime in comparison with HVO. An enhancement of the burning rate is particularly noticed for nanofuels using a particle size of 40 nm. However, the overall droplet burning rate did not exhibit particular reliance on particle concentration where an optimal concentration is approximately 1.0 wt.%. Based on this, two mechanisms for these observations rely on radiation absorption and particle accumulation. The former provides an additional energy budget, accelerating the heating and enhancing the evaporation/burning rate of the droplet, thus allowing a greater heat release rate. On the other hand, particle aggregation at the droplet surface creates a resistance to the evaporation of liquid fuel, suppressing the evaporation/burning rate. Due to this, a clarification regarding the relation between particle concentration and particle agglomeration during the combustion process is provided by developing a simplified macroscopic model for nanofuels. Additionally, a simplified analysis of radiation absorption is provided. The model predicts the final droplet diameter before disruptive burning phenomena occur, indicating an increase in its diameter as the particle concentration increases.

Regarding the spray behavior under non reacting conditions, the visualization reveals different morphological features in the spray, such as droplet formation, where the air-fuel ratio notably affects ligament structures and bag shapes during spray breakup. The breakup length increases with the liquid Reynolds number and decreases with AFR, indicating that the influence of aerodynamic force on liquid disintegration is pronounced. The findings suggest that the normalized mean breakup length exhibits a power law relation with the momentum flux ratio, which agrees with the correlations presented in the literature. The addition of nanoparticles possesses a minimal influence on the breakup length compared with HVO. However, an analysis of the secondary atomization indicates that an increase in the particle concentration leads to an increase in the droplet diameter. In addition, the spray dynamics of HVO and Jet A-1 show considerable similarities, highlighting the potential use of biofuel to address the environmental concerns in the aviation sector. Regarding the overall spray dynamics, the results indicate that an increase in the AFR leads to a wider spray since using an air-assisted atomizer with external mixing and swirl enhances the radial dispersion of the fuel droplets, improving fuel dispersion. In addition, it results in a spray with reduced droplet diameter with a higher uniformity and higher axial velocities. At the spray edges, larger droplets with reduced axial velocity are detected, whereas the central region is characterized by considerable droplets with reduced size. The droplet size distribution was evaluated considering probability mathematical functions where the Log-normal produces the most satisfactory results.

A laboratory combustion chamber was designed and built to understand the influence of nanofuels on spray combustion. A design involving a combustion chamber, an annular axial swirl, and a swirl burner was developed, where special attention was given to the excessive fuel heating inside the atomizer, flammability limits, flow dynamics, and exhaust system.

The development of the spray combustion facility was successfully carried out, ensuring safe and effective operation. In this respect, no fuel overheating was reported during the preliminary experiments, and the Jet A-1 stable flame was observed, allowing further experiments using liquid fuels.

In summary, the stability of fuels with aluminum particles was enhanced, even at high particle concentrations. Adding nanoparticles presents a distinct droplet combustion behavior compared to the base fuel. In addition, it enhances the droplet burning rate ($\approx$ 15% for a furnace temperature of 800 °C) and promotes the occurrence of disruptive burning phenomena. Regarding this subject, attention to the nanoparticle combustion emissions and the impact of micro-explosion in real engines should be further addressed. Increasing the particle concentration leads to a spray with larger droplet diameters, negatively affecting the atomization of the fuels. It is concluded that the nanoparticles can be relevant in the combustion field. However, a more detailed study of the spray dynamics and the atomization strategy is required. These observations influence nanofuel spray combustion, an essential subject for further implementation in practical applications. Due to this, a combustion chamber was developed. The purpose is to analyze all of these findings from a broader point of view, addressing the viability of using such alternative fuels in aero-engines.

7.2 Suggestions for Future Work

The present work evaluated conventional and alternative fuels in experimental and numerical analyses, exploring pertinent topics. However, this thesis did not address several challenging issues that need further examination, particularly to understand the potential benefits of nanofuels. In light of this, suggestions for potential future research are provided. An investigation of the aluminum life cycle is recommended, and particular attention should be given to the emissions released from its combustion that can cause health and environmental issues. A qualitative analysis concerning nanofuel stability was conducted in the present study. For detailed precision and further implementation of nanofuel in practical applications, quantitative stability analysis of the nanofuel involving examining repulsive forces between the nanoparticles, e.g., zeta potential measurements, is recommended. An analysis dedicated to the thermal conductivity of nanofuels should be addressed since the findings presented in the literature on the enhancement of this property are contradictory. For the experimental setup dedicated to single droplet combustion, an exhaustion system capable of acquiring the residues released from the nanofuel should be implemented. In addition, a modification in the optical access of the drop tube furnace is suggested to capture the droplet heating phase. The disruptive burning phenomena in a real combustion chamber should be addressed since it can negatively impact engines. Concerning the spray behavior, a more detailed analysis of the addition of nanoparticles should be emphasized since the droplet size increment findings are not related to the physical properties, and an additional effect, e.g., particle aggregation, may be responsible for this observation. To address the applicability of nanofuels, experimental studies on the laboratory combustion chamber for HVO and nanofu-

els are recommended. Temperature and emissions profile measurements are suggested to compare conventional and alternative jet fuels.

Bibliography

[1] M. Z. A. Khan, H. A. Khan, S. S. Ravi, J. W. Turner, and M. Aziz, "Potential of clean liquid fuels in decarbonizing transportation–an overlooked net-zero pathway?" *Renewable and Sustainable Energy Reviews*, vol. 183, p. 113483, 2023.

[2] M. A. Ershov, V. D. Savelenko, N. O. Burov, U. A. Makhova, D. Y. Mukhina, D. R. Aleksanyan, V. M. Kapustin, M. M. Lobashova, A. V. Sereda, T. M. Abdellatief *et al.*, "An incorporating innovation and new interactive technology into obtaining sustainable aviation fuels," *Energy*, p. 128156, 2023.

[3] Y. Wang and J. J. Wu, "Thermochemical conversion of biomass: Potential future prospects," *Renewable and Sustainable Energy Reviews*, vol. 187, p. 113754, 2023.

[4] C. Lyu, X. Liu, Z. Wang, L. Yang, H. Liu, N. Yang, S. Xu, L. Cao, Z. Zhang, L. Pang *et al.*, "An emissions inventory using flight information reveals the long-term changes of aviation co2 emissions in china," *Energy*, vol. 262, p. 125513, 2023.

[5] D. S. Lee, D. W. Fahey, P. M. Forster, P. J. Newton, R. C. Wit, L. L. Lim, B. Owen, and R. Sausen, "Aviation and global climate change in the 21st century," *Atmospheric environment*, vol. 43, no. 22-23, pp. 3520–3537, 2009.

[6] I. Tiseo, "Distribution of carbon dioxide emissions produced by the transportation sector worldwide in 2020, by subsector," 2021.

[7] J. A. Okolie, D. Awotoye, M. E. Tabat, P. U. Okoye, E. I. Epelle, C. C. Ogbaga, F. Güleç, and B. Oboirien, "Multi criteria decision analysis for the evaluation and screening of sustainable aviation fuel production pathways," *Iscience*, 2023.

[8] G. Quante, N. Bullerdiek, S. Bube, U. Neuling, and M. Kaltschmitt, "Renewable fuel options for aviation–a system-wide comparison of drop-in and non drop-in fuel options," *Fuel*, vol. 333, p. 126269, 2023.

[9] L. Cui, S. Yue, X.-H. Nghiem, and M. Duan, "Exploring the risk and economic vulnerability of global energy supply chain interruption in the context of russo-ukrainian war," *Resources Policy*, vol. 81, p. 103373, 2023.

[10] G. Liu, B. Yan, and G. Chen, "Technical review on jet fuel production," *Renewable and Sustainable Energy Reviews*, vol. 25, pp. 59–70, 2013.

[11] S. Fawzy, A. I. Osman, J. Doran, and D. W. Rooney, "Strategies for mitigation of climate change: a review," *Environmental Chemistry Letters*, vol. 18, pp. 2069–2094,

2020.

[12] J. Locke, J. Dsilva, and S. Zarmukhambetova, "Decarbonization strategies in the uae built environment: An evidence-based analysis using cop26 and cop27 recommendations," *Sustainability*, vol. 15, no. 15, p. 11603, 2023.

[13] F. Afonso, M. Sohst, C. M. Diogo, S. S. Rodrigues, A. Ferreira, I. Ribeiro, R. Marques, F. F. Rego, A. Sohouli, J. Portugal-Pereira *et al.*, "Strategies towards a more sustainable aviation: A systematic review," *Progress in Aerospace Sciences*, vol. 137, p. 100878, 2023.

[14] P. Su-Ungkavatin, L. Tiruta-Barna, and L. Hamelin, "Biofuels, electrofuels, electric or hydrogen?: A review of current and emerging sustainable aviation systems," *Progress in Energy and Combustion Science*, vol. 96, p. 101073, 2023.

[15] D. Rochelle and H. Najafi, "A review of the effect of biodiesel on gas turbine emissions and performance," *Renewable and Sustainable Energy Reviews*, vol. 105, pp. 129–137, 2019.

[16] I. A. Ferrão, A. R. Silva, A. S. Moita, M. A. Mendes, and M. M. Costa, "Combustion characteristics of a single droplet of hydroprocessed vegetable oil blended with aluminum nanoparticles in a drop tube furnace," *Fuel*, vol. 302, p. 121160, 2021.

[17] S. Nam and H. Kim, "Combustion characteristics of a boron/ethanol nanofuel droplet: Optical and spectroscopic approach," *Ethanol Nanofuel Droplet: Optical and Spectroscopic Approach*.

[18] Z. Zhao, J. Chen, Z. Yang, C. Zhao, Y. Wei, W. Wang, H. Qiao, and W. Ao, "Ignition and combustion characteristics of magnesium-based nanofluid fuel," *Acta Astronautica*, vol. 223, pp. 234–241, 2024.

[19] I. A. Ferrão, T. S. Mendes, M. A. Mendes, A. S. Moita, and A. R. Silva, "Influence of aluminum nanoparticles in alternative fuel: Single droplet combustion experiments and modeling," *Fuel*, vol. 379, p. 132850, 2025.

[20] S. Aithal and P. Aithal, "Green and eco-friendly nanotechnology–concepts and industrial prospects," *International Journal of Management, Technology, and Social Sciences (IJMTS)*, vol. 6, no. 1, pp. 1–31, 2021.

[21] L. A. Kolahalam, I. K. Viswanath, B. S. Diwakar, B. Govindh, V. Reddy, and Y. Murthy, "Review on nanomaterials: Synthesis and applications," *Materials Today: Proceedings*, vol. 18, pp. 2182–2190, 2019.

[22] K. Kannaiyan, K. Anoop, and R. Sadr, "Effect of nanoparticles on the fuel properties and spray performance of aviation turbine fuel," *Journal of Energy Resources Technology*, vol. 139, no. 3, p. 032201, 2017.

[23] M. Jones, C. H. Li, A. Afjeh, and G. Peterson, "Experimental study of combustion characteristics of nanoscale metal and metal oxide additives in biofuel (ethanol)," *Nanoscale research letters*, vol. 6, pp. 1–12, 2011.

[24] K. Kannaiyan, R. Sadr, and V. Kumaravel, "Application of nanoparticles in clean fuels," *Nanostructured Materials for Energy Related Applications*, pp. 223–242, 2019.

[25] H. S. Sim, M. A. Plascencia, A. Vargas, J. W. Bennewitz, O. I. Smith, and A. R. Karagozian, "Effects of inert and energetic nanoparticles on burning liquid ethanol droplets," *Combustion Science and Technology*, 2018.

[26] G. Singh, M. Esmaeilpour, and A. Ratner, "The effect of acetylene black on droplet combustion and flame regime of petrodiesel and soy biodiesel," *Fuel*, vol. 246, pp. 108–116, 2019.

[27] M. Soltan, B. Al Abdulla, A. Al Dosari, K. Kannaiyan, and R. Sadr, "Spray performance of alternative jet fuel based nanofuels at high-ambient conditions," in *ASME International Mechanical Engineering Congress and Exposition*, vol. 52101. American Society of Mechanical Engineers, 2018, p. V007T09A062.

[28] K. Noh, H. Kim, S. Nam, and S. Song, "Study on the combustion characteristics of ethanol nanofuel," *Aerospace*, vol. 10, no. 10, p. 878, 2023.

[29] S. Basu and A. Miglani, "Combustion and heat transfer characteristics of nanofluid fuel droplets: A short review," *International Journal of Heat and Mass Transfer*, vol. 96, pp. 482–503, 2016.

[30] R. Suresh, S. Rajendran, K. Dutta, K. S. Khoo, and M. Soto-Moscoso, "An overview on light assisted techniques for waste-derived hydrogen fuel towards aviation industry," *Fuel*, vol. 334, p. 126645, 2023.

[31] D. R. Vardon, B. J. Sherbacow, K. Guan, J. S. Heyne, and Z. Abdullah, "Realizing "net-zero-carbon" sustainable aviation fuel," *Joule*, vol. 6, no. 1, pp. 16–21, 2022.

[32] ICAO, "Innovation for a green transition - 2022 environmental report," 2022.

[33] W.-C. Wang and L. Tao, "Bio-jet fuel conversion technologies," *Renewable and Sustainable Energy Reviews*, vol. 53, pp. 801–822, 2016.

[34] H. A. Edwards, D. Dixon-Hardy, and Z. Wadud, "Aircraft cost index and the future of carbon emissions from air travel," *Applied energy*, vol. 164, pp. 553–562, 2016.

[35] E. E. de Almeida and A. V. Oliveira, "An econometric analysis for the determinants of flight speed in the air transport of passengers," *Scientific Reports*, vol. 13, no. 1, p. 4573, 2023.

[36] P. J. Ansell, "Review of sustainable energy carriers for aviation: Benefits, challenges, and future viability," *Progress in Aerospace Sciences*, vol. 141, p. 100919, 2023.

[37] J. Heyne, B. Rauch, P. Le Clercq, and M. Colket, "Sustainable aviation fuel prescreening tools and procedures," *Fuel*, vol. 290, p. 120004, 2021.

[38] B. H. H. Goh, C. T. Chong, H. C. Ong, T. Seljak, T. Katrašnik, V. Józsa, J.-H. Ng, B. Tian, S. Karmarkar, and V. Ashokkumar, "Recent advancements in catalytic conversion pathways for synthetic jet fuel produced from bioresources," *Energy Conversion and Management*, vol. 251, p. 114974, 2022.

[39] K. S. Ng, D. Farooq, and A. Yang, "Global biorenewable development strategies for sustainable aviation fuel production," *Renewable and Sustainable Energy Reviews*, vol. 150, p. 111502, 2021.

[40] L. Liu, S. Cheng, J. Li, and Y. Huang, "Mitigating environmental pollution and impacts from fossil fuels: The role of alternative fuels," *Energy Sources, Part A*, vol. 29, no. 12, pp. 1069–1080, 2007.

[41] S. Kramer, G. Andac, J. Heyne, J. Ellsworth, P. Herzig, and K. C. Lewis, "Perspectives on fully synthesized sustainable aviation fuels: direction and opportunities," *Frontiers in Energy Research*, vol. 9, p. 782823, 2022.

[42] V. Ram and S. R. Salkuti, "An overview of major synthetic fuels," *Energies*, vol. 16, no. 6, p. 2834, 2023.

[43] U. Yildirim and S. Abanteriba, "Manufacture, qualification and approval of new aviation turbine fuels and additives," *Procedia Engineering*, vol. 49, pp. 310–315, 2012.

[44] L. Q. Maurice, H. Lander, T. Edwards, and W. Harrison Iii, "Advanced aviation fuels: a look ahead via a historical perspective," *Fuel*, vol. 80, no. 5, pp. 747–756, 2001.

[45] G. Hemighaus, T. Boval, J. Bacha, F. Barnes, M. Franklin, L. Gibbs, and J. Morris, "Aviation fuels: Techincal review. chevron products company," 2007.

[46] M. Romanczyk, "Chemical compositional analysis of jet fuels: Contributions of mass

spectrometry in the 21st century," *Mass Spectrometry Reviews*, p. e21825, 2022.

[47] J. T. Edwards, "Reference jet fuels for combustion testing," in *55th AIAA aerospace sciences meeting*, 2017, p. 0146.

[48] A. for Toxic Substances and D. R. (US), "Toxicological profile for jp-5, jp-8, and jet a fuels," 2017.

[49] S. Blakey, L. Rye, and C. W. Wilson, "Aviation gas turbine alternative fuels: A review," *Proceedings of the combustion institute*, vol. 33, no. 2, pp. 2863–2885, 2011.

[50] N. Gray, S. McDonagh, R. O'Shea, B. Smyth, and J. D. Murphy, "Decarbonising ships, planes and trucks: An analysis of suitable low-carbon fuels for the maritime, aviation and haulage sectors," *Advances in Applied Energy*, vol. 1, p. 100008, 2021.

[51] T. Edwards, "Advancements in gas turbine fuels from 1943 to 2005," 2007.

[52] G. R. Wilson III, T. Edwards, E. Corporan, and R. L. Freerks, "Certification of alternative aviation fuels and blend components," *Energy & Fuels*, vol. 27, no. 2, pp. 962–966, 2013.

[53] M. F. Shahriar and A. Khanal, "The current techno-economic, environmental, policy status and perspectives of sustainable aviation fuel (saf)," *Fuel*, vol. 325, p. 124905, 2022.

[54] B. MacIsaac and R. Langton, *Gas turbine propulsion systems*. John Wiley & Sons, 2011.

[55] A. H. Lefebvre and D. R. Ballal, *Gas turbine combustion: alternative fuels and emissions*. CRC press, 2010.

[56] M. Masiol and R. M. Harrison, "Aircraft engine exhaust emissions and other airport-related contributions to ambient air pollution: A review," *Atmospheric Environment*, vol. 95, pp. 409–455, 2014.

[57] L. Langston, "Turbines, gas," *Reference Module in Earth Systems and Environmental Sciences*, 2014.

[58] M. Braun-Unkhoff, T. Kathrotia, B. Rauch, and U. Riedel, "About the interaction between composition and performance of alternative jet fuels," *CEAS Aeronautical Journal*, vol. 7, pp. 83–94, 2016.

[59] B. E. Anderson, G. Chen, and D. R. Blake, "Hydrocarbon emissions from a modern commercial airliner," *Atmospheric Environment*, vol. 40, no. 19, pp. 3601–3612,

2006.

[60] I. Tesseraux, “Risk factors of jet fuel combustion products,” *Toxicology letters*, vol. 149, no. 1-3, pp. 295–300, 2004.

[61] M. Braun-Unkhoff, U. Riedel, and C. Wahl, “About the emissions of alternative jet fuels,” *CEAS Aeronautical Journal*, vol. 8, pp. 167–180, 2017.

[62] D. Wuebbles, M. Gupta, and M. Ko, “Evaluating the impacts of aviation on climate change,” *Eos, Transactions American Geophysical Union*, vol. 88, no. 14, pp. 157–160, 2007.

[63] Y. Liu, X. Sun, V. Sethi, D. Nalianda, Y.-G. Li, and L. Wang, “Review of modern low emissions combustion technologies for aero gas turbine engines,” *Progress in Aerospace Sciences*, vol. 94, pp. 12–45, 2017.

[64] H. Aygun and O. Turan, “Analysis of cruise conditions on energy, exergy and nox emission parameters of a turbofan engine for middle-range aircraft,” *Energy*, vol. 267, p. 126468, 2023.

[65] C. Grobler, P. J. Wolfe, K. Dasadhikari, I. C. Dedoussi, F. Allroggen, R. L. Speth, S. D. Eastham, A. Agarwal, M. D. Staples, J. Sabnis *et al.*, “Marginal climate and air quality costs of aviation emissions,” *Environmental Research Letters*, vol. 14, no. 11, p. 114031, 2019.

[66] V. Undavalli, O. B. G. Olatunde, R. Boylu, C. Wei, J. Haeker, J. Hamilton, and B. Khandelwal, “Recent advancements in sustainable aviation fuels,” *Progress in Aerospace Sciences*, vol. 136, p. 100876, 2023.

[67] “Saf - sustainability considerations [fact sheet],” International Civil Aviation Organization, 2018. [Online]. Available: https://www.iata.org/contentassets/d13875e9ed784f75bac90f000760e998/saf-and-sustainability.pdf

[68] Z. I. Rony, M. Mofijur, M. Hasan, S. Ahmed, F. Almomani, M. Rasul, M. Jahirul, P. L. Show, M. Kalam, and T. Mahlia, “Unanswered issues on decarbonizing the aviation industry through the development of sustainable aviation fuel from microalgae,” *Fuel*, vol. 334, p. 126553, 2023.

[69] ICAO, “Aviation and environment - 2019 environmental report,” 2022.

[70] “Corsia [fact sheet],” International Civil Aviation Organization, 2023. [Online]. Available: https://www.iata.org/en/iata-repository/pressroom/fact-sheets/fact-sheet---corsia/

[71] M. D. Staples, R. Malina, P. Suresh, J. I. Hileman, and S. R. Barrett, "Aviation co2 emissions reductions from the use of alternative jet fuels," *Energy Policy*, vol. 114, pp. 342–354, 2018.

[72] "Net zero 2050: sustainable aviation fuels [fact sheet]," International Civil Aviation Organization, 2023. [Online]. Available: https://www.iata.org/en/iata-repository/pressroom/fact-sheets/fact-sheet---alternative-fuels/

[73] A. Ficca, F. Marulo, and A. Sollo, "An open thinking for a vision on sustainable green aviation," *Progress in Aerospace Sciences*, vol. 141, p. 100928, 2023.

[74] M. Kaltschmitt and U. Neuling, *Biokerosene: Status and prospects*. Springer, 2017.

[75] R. Cracknell, S. Ciatti, S. Dorofeev, R. Eggels, K. McManus, and K. Nakata, "Decarbonization of mobility, including transportation and renewable fuels," *Proceedings of the Combustion Institute*, vol. 39, no. 1, pp. 1–9, 2023.

[76] C. Baldino, "Provisions for transport fuels in the european union's finalized "fit for 55" package," 2023.

[77] M. Colket and J. Heyne, *Fuel effects on operability of aircraft gas turbine combustors*. American Institute of Aeronautics and Astronautics, Inc., 2021.

[78] M. Colket, J. Heyne, M. Rumizen, M. Gupta, T. Edwards, W. M. Roquemore, G. Andac, R. Boehm, J. Lovett, R. Williams *et al.*, "Overview of the national jet fuels combustion program," *AiAA Journal*, vol. 55, no. 4, pp. 1087–1104, 2017.

[79] L. Colelli, V. Segneri, C. Bassano, and G. Vilardi, "E-fuels, technical and economic analysis of the production of synthetic kerosene precursor as sustainable aviation fuel," *Energy Conversion and Management*, vol. 288, p. 117165, 2023.

[80] V. Ballal, O. Cavalett, F. Cherubini, and M. D. B. Watanabe, "Climate change impacts of e-fuels for aviation in europe under present-day conditions and future policy scenarios," *Fuel*, vol. 338, p. 127316, 2023.

[81] C. Panzone, R. Philippe, A. Chappaz, P. Fongarland, and A. Bengaouer, "Power-to-liquid catalytic co2 valorization into fuels and chemicals: focus on the fischer-tropsch route," *Journal of CO2 Utilization*, vol. 38, pp. 314–347, 2020.

[82] S. Voß, S. Bube, and M. Kaltschmitt, "Aviation fuel production pathways from lignocellulosic biomass via alcohol intermediates–a technical analysis," *Fuel Communications*, vol. 17, p. 100093, 2023.

[83] N. Bullerdiek, U. Neuling, and M. Kaltschmitt, "A ghg reduction obligation for sustainable aviation fuels (saf) in the eu and in germany," *Journal of air transport management*, vol. 92, p. 102020, 2021.

[84] F. X. Johnson and M. Román, "Biofuels sustainability criteria relevant issues to the proposed directive on the promotion of the use of energy from renewable sources," 2009.

[85] W. Grimme, "The introduction of sustainable aviation fuels—a discussion of challenges, options and alternatives," *Aerospace*, vol. 10, no. 3, p. 218, 2023.

[86] E. Cabrera and J. M. M. de Sousa, "Use of sustainable fuels in aviation—a review," *Energies*, vol. 15, no. 7, p. 2440, 2022.

[87] S. Karatzos, J. D. McMillan, and J. N. Saddler, "The potential and challenges of drop-in biofuels," *Report for IEA Bioenergy Task*, vol. 39, 2014.

[88] X. He, N. Wang, Q. Zhou, J. Huang, S. Ramakrishna, and F. Li, "Smart aviation biofuel energy system coupling with machine learning technology," *Renewable and Sustainable Energy Reviews*, vol. 189, p. 113914, 2024.

[89] S. S. Doliente, A. Narayan, J. F. D. Tapia, N. J. Samsatli, Y. Zhao, and S. Samsatli, "Bio-aviation fuel: a comprehensive review and analysis of the supply chain components," *Frontiers in Energy Research*, vol. 8, p. 110, 2020.

[90] C. Bae and J. Kim, "Alternative fuels for internal combustion engines," *Proceedings of the Combustion Institute*, vol. 36, no. 3, pp. 3389–3413, 2017.

[91] P. Cavelius, S. Engelhart-Straub, N. Mehlmer, J. Lercher, D. Awad, and T. Brück, "The potential of biofuels from first to fourth generation," *PLoS Biology*, vol. 21, no. 3, p. e3002063, 2023.

[92] M. Shehab, K. Moshammer, M. Franke, and E. Zondervan, "Analysis of the potential of meeting the eu's sustainable aviation fuel targets in 2030 and 2050," *Sustainability*, vol. 15, no. 12, p. 9266, 2023.

[93] P. Moodley, "Sustainable biofuels: opportunities and challenges," *Sustainable Biofuels*, pp. 1–20, 2021.

[94] A. H. Hirani, N. Javed, M. Asif, S. K. Basu, and A. Kumar, "A review on first-and second-generation biofuel productions," *Biofuels: greenhouse gas mitigation and global warming: next generation biofuels and role of biotechnology*, pp. 141–154, 2018.

[95] M. A. Rumizen, "Qualification of alternative jet fuels," *Frontiers in Energy Research*, vol. 9, p. 760713, 2021.

[96] ICAO, "Annex 16 - carbon offsetting and reduction scheme for international aviation (corsia)," in *Environmental Protection*, vol. IV, 2023.

[97] A. Gunerhan, O. Altuntas, and H. Caliskan, "Utilization of renewable and sustainable aviation biofuels from waste tyres for sustainable aviation transport sector," *Energy*, vol. 276, p. 127566, 2023.

[98] E. Emmanouilidou, S. Mitkidou, A. Agapiou, and N. C. Kokkinos, "Solid waste biomass as a potential feedstock for producing sustainable aviation fuel: a systematic review," *Renewable Energy*, 2023.

[99] I. Abrantes, A. F. Ferreira, A. Silva, and M. Costa, "Sustainable aviation fuels and imminent technologies-co2 emissions evolution towards 2050," *Journal of Cleaner Production*, vol. 313, p. 127937, 2021.

[100] A. H. Bhatt, Y. Zhang, A. Milbrandt, E. Newes, K. Moriarty, B. Klein, and L. Tao, "Evaluation of performance variables to accelerate the deployment of sustainable aviation fuels at a regional scale," *Energy Conversion and Management*, vol. 275, p. 116441, 2023.

[101] N. Detsios, S. Theodoraki, L. Maragoudaki, K. Atsonios, P. Grammelis, and N. G. Orfanoudakis, "Recent advances on alternative aviation fuels/pathways: A critical review," *Energies*, vol. 16, no. 4, p. 1904, 2023.

[102] B.-Y. Yu and C.-C. Tsai, "Rigorous simulation and techno-economic analysis of a bio-jet-fuel intermediate production process with various integration strategies," *Chemical Engineering Research and Design*, vol. 159, pp. 47–65, 2020.

[103] C. Gutiérrez-Antonio, F. I. Gómez-Castro, J. G. Segovia-Hernández, and A. Briones-Ramírez, "Simulation and optimization of a biojet fuel production process," in *Computer Aided Chemical Engineering*. Elsevier, 2013, vol. 32, pp. 13–18.

[104] P. Misra, A. Alvarez-Majmutov, and J. Chen, "Isomerization catalysts and technologies for biorefining: Opportunities for producing sustainable aviation fuels," *Fuel*, vol. 351, p. 128994, 2023.

[105] A. L. Oldani, A. E. Solecki, and T. Lee, "Evaluation of physicochemical variability of sustainable aviation fuels," *Frontiers in Energy Research*, vol. 10, p. 1052267, 2022.

[106] M. A. Peters, C. T. Alves, and J. A. Onwudili, "A review of current and emerging

production technologies for biomass-derived sustainable aviation fuels," *Energies*, vol. 16, no. 16, p. 6100, 2023.

[107] M. F. Chagas, G. F. Ferreira, L. C. M. Gomes, L. M. Zanphorlin, L. Z. O. Martins, I. L. M. Sampaio, T. A. D. Hernandes, T. L. Junqueira, and E. R. Morais, "From enzyme to cell-factory: Economic and environmental assessment of biobased pathways to unlock the potential of long-haul transportation biofuels," *Chemical Engineering Journal*, vol. 469, p. 143878, 2023.

[108] A. Bauen, N. Bitossi, L. German, A. Harris, and K. Leow, "Sustainable aviation fuels: Status, challenges and prospects of drop-in liquid fuels, hydrogen and electrification in aviation," *Johnson Matthey Technology Review*, vol. 64, no. 3, pp. 263–278, 2020.

[109] S. Puschnigg, K. Fazeni-Fraisl, J. Lindorfer, and T. Kienberger, "Biorefinery development for the conversion of softwood residues into sustainable aviation fuel: Implications from life cycle assessment and energetic-exergetic analyses," *Journal of Cleaner Production*, vol. 386, p. 135815, 2023.

[110] A. Kopf, T. Bunsen, and M. Craglia, "The potential of e-fuels to decarbonise ships and aircraft," 2023.

[111] S. Gössling and A. Humpe, "Net-zero aviation: Time for a new business model?" *Journal of Air Transport Management*, vol. 107, p. 102353, 2023.

[112] M. Dossow, V. Dieterich, A. Hanel, H. Spliethoff, and S. Fendt, "Improving carbon efficiency for an advanced biomass-to-liquid process using hydrogen and oxygen from electrolysis," *Renewable and Sustainable Energy Reviews*, vol. 152, p. 111670, 2021.

[113] J. Peacock, R. Cooper, N. Waller, and G. Richardson, "Decarbonising aviation at scale through synthesis of sustainable e-fuel: A techno-economic assessment," *International Journal of Hydrogen Energy*, vol. 50, pp. 869–890, 2024.

[114] B. A. Adu-Gyamfi and C. Good, "Electric aviation: A review of concepts and enabling technologies," *Transportation Engineering*, p. 100134, 2022.

[115] M. Asli, P. König, D. Sharma, E. Pontika, J. Huete, K. R. Konda, A. Mathiazhagan, T. Xie, K. Höschler, and P. Laskaridis, "Thermal management challenges in hybrid-electric propulsion aircraft," *Progress in Aerospace Sciences*, vol. 144, p. 100967, 2024.

[116] K. Dahal, S. Brynolf, C. Xisto, J. Hansson, M. Grahn, T. Grönstedt, and M. Lehtveer, "Techno-economic review of alternative fuels and propulsion systems for the aviation sector," *Renewable and Sustainable Energy Reviews*, vol. 151, p. 111564, 2021.

[117] A. Barke, C. Thies, J.-L. Popien, S. P. Melo, F. Cerdas, C. Herrmann, and T. S. Spengler, "Life cycle sustainability assessment of potential battery systems for electric aircraft," *Procedia CIRP*, vol. 98, pp. 660–665, 2021.

[118] S. Sahoo, X. Zhao, and K. Kyprianidis, "A review of concepts, benefits, and challenges for future electrical propulsion-based aircraft," *Aerospace*, vol. 7, no. 4, p. 44, 2020.

[119] L. Rupcic, E. Pierrat, K. Saavedra-Rubio, N. Thonemann, C. Ogugua, and A. Laurent, "Environmental impacts in the civil aviation sector: Current state and guidance," *Transportation Research Part D: Transport and Environment*, vol. 119, p. 103717, 2023.

[120] M. Hornung, A. T. Isikveren, M. Cole, and A. Sizmann, "Ce-liner-case study for emobility in air transportation," in *2013 Aviation Technology, Integration, and Operations Conference*, 2013, p. 4302.

[121] L. Miniero, K. Pandey, G. De Falco, A. D'Anna, and N. Noiray, "Soot-free and low-no combustion of jet a-1 in a lean azimuthal flame (leaf) combustor with hydrogen injection," *Proceedings of the Combustion Institute*, vol. 39, no. 4, pp. 4309–4318, 2023.

[122] S. Saraji and S. Chen, *Sustainable Oil and Gas Using Blockchain*. Springer Nature, 2023, vol. 98.

[123] C. Wollf and D. Riefer, "Clean skies for tomorrow: Sustainable aviation fuels as a pathway to net-zero aviation," in *Proceedings of the World Economic Forum, Davos-Klosters, Switzerland*, 2020, pp. 21–24.

[124] J. Ling-Chin, A. Giampieri, M. Wilks, S. W. Lau, E. Bacon, I. Sheppard, A. J. Smallbone, and A. P. Roskilly, "Technology roadmap for hydrogen-fuelled transportation in the uk," *International Journal of Hydrogen Energy*, vol. 52, pp. 705–733, 2024.

[125] J. Scheelhaase, S. Maertens, and W. Grimme, "Synthetic fuels in aviation–current barriers and potential political measures," *Transportation Research Procedia*, vol. 43, pp. 21–30, 2019.

[126] P. S. Deora, Y. Verma, R. A. Muhal, C. Goswami, T. Singh *et al.*, "Biofuels: An alternative to conventional fuel and energy source," *Materials Today: Proceedings*, vol. 48, pp. 1178–1184, 2022.

[127] A. M. E.-D. Faik, "Quantitative investigation of the multicomponent fuel droplet combustion using high speed imaging and digital image processing," Ph.D. dissertation, University of Sheffield, 2017.

[128] S. R. Turns, *An Introduction to Combustion: Concepts and Applications*, 3rd ed. McGraw-Hill Education, 2012.

[129] N. Frössling, "Über die verdunstung fallender tropfen," *Gerlands Beiträge zur Geophysik*, vol. 52, no. 1, pp. 170–216, 1938.

[130] W. A. Sirignano, *Fluid dynamics and transport of droplets and sprays*. Cambridge university press, 2010.

[131] S. Sazhin, *Droplets and sprays*. Springer, 2014, vol. 345.

[132] F. Williams, "On the assumptions underlying droplet vaporization and combustion theories," *The Journal of Chemical Physics*, vol. 33, no. 1, pp. 133–144, 1960.

[133] W. E. Ranz, "Evaporation from drops-i and-ii," *Chem. Eng. Progr*, vol. 48, pp. 141–146, 1952.

[134] G. M. Faeth and D. R. Olson, "The ignition of hydrocarbon fuel droplets in air," *SAE Transactions*, pp. 1793–1802, 1968.

[135] A. Williams, "Combustion of droplets of liquid fuels: A review," *Combustion and flame*, vol. 21, no. 1, pp. 1–31, 1973.

[136] G. M. Faeth, "Current status of droplet and liquid combustion," in *Energy and combustion science*. Elsevier, 1979, pp. 149–182.

[137] C. Law, "Recent advances in droplet vaporization and combustion," *Progress in energy and combustion science*, vol. 8, no. 3, pp. 171–201, 1982.

[138] G. Faeth, "Evaporation and combustion of sprays," *Progress in Energy and Combustion Science*, vol. 9, no. 1-2, pp. 1–76, 1983.

[139] W. A. Sirignano, "Fuel droplet vaporization and spray combustion theory," *Progress in Energy and Combustion Science*, vol. 9, no. 4, pp. 291–322, 1983.

[140] G. Godsave, "Studies of the combustion of drops in a fuel spray—the burning of single drops of fuel," in *Symposium (international) on combustion*, vol. 4, no. 1. Elsevier, 1953, pp. 818–830.

[141] D. B. Spalding, "Combustion of liquid fuels," *Nature*, vol. 165, no. 4187, pp. 160–160, 1950.

[142] C. K. Law, *Combustion Physics*. Cambridge University Press, 2006.

[143] ——, "Recent advances in droplet vaporization and combustion," *Progress in Energy and Combustion Science*, vol. 8, no. 3, pp. 171–201, 1982.

[144] A. Buekens, "Combustion: physical and chemical fundamentals, modeling and simulation, experiments, pollutant formation," *International Journal of Environment & Pollution*, vol. 17, no. 3, pp. 291–291, 2002.

[145] M. Reimert, "Characterization of the autoignition of single droplets of fischer-tropsch fuels and development of surrogates," Ph.D. dissertation, Bremen, Universität Bremen, Diss., 2012, 2012.

[146] Z. Wang, B. Yuan, Y. Huang, J. Cao, Y. Wang, and X. Cheng, "Progress in experimental investigations on evaporation characteristics of a fuel droplet," *Fuel Processing Technology*, vol. 231, p. 107243, 2022.

[147] J. Wang, X. Huang, X. Qiao, D. Ju, and C. Sun, "Experimental study on effect of support fiber on fuel droplet vaporization at high temperatures," *Fuel*, vol. 268, p. 117407, 2020.

[148] S. S. Chung and O. Kawaguchi, "An experimental study on the evaporation of freely falling droplet under high temperature and high pressure gas stream," *KSME Journal*, vol. 4, pp. 172–177, 1990.

[149] G. Brenn, L. Deviprasath, F. Durst, and C. Fink, "Evaporation of acoustically levitated multi-component liquid droplets," *International journal of heat and mass transfer*, vol. 50, no. 25-26, pp. 5073–5086, 2007.

[150] S. Parag and V. Raghavan, "Experimental investigation of burning rates of pure ethanol and ethanol blended fuels," *Combustion and Flame*, vol. 156, no. 5, pp. 997–1005, 2009.

[151] A. Yadav, A. Chowdhury, and A. Srivastava, "Gas-phase thermography of droplet combustion and its application to characterize nanofuels," *International Communications in Heat and Mass Transfer*, vol. 120, p. 105054, 2021.

[152] K. Chung, "Law. combustion physics," *New York*, 2006.

[153] D. L. Dietrich, P. Struk, M. Ikegami, and G. Xu, "Single droplet combustion of decane in microgravity: experiments and numerical modelling," *Combustion Theory and Modelling*, vol. 9, no. 4, pp. 569–585, 2005.

[154] S. R. Gollahalli and T. Brzustowski, "Experimental studies on the flame structure in the wake of a burning droplet," in *Symposium (International) on Combustion*, vol. 14,

no. 1. Elsevier, 1973, pp. 1333–1344.

[155] L. Chen, G. Li, and B. Fang, "Droplet evaporation characteristics of aviation kerosene surrogate fuel and butanol blends under forced convection," *International Journal of Multiphase Flow*, vol. 114, pp. 229–239, 2019.

[156] A. H. Lefebvre, "Properties of sprays," *Particle & Particle Systems Characterization*, vol. 6, no. 1-4, pp. 176–186, 1989.

[157] C.-H. WANG, K.-H. SHY, and L.-C. LIEU, "An experimental investigation on the ignition delay of fuel droplets," *Combustion science and technology*, vol. 118, no. 1-3, pp. 63–78, 1996.

[158] S. Kotake and T. Okazaki, "Evaporation and combustion of a fuel droplet," *International Journal of Heat and Mass Transfer*, vol. 12, no. 5, pp. 595–609, 1969.

[159] G. Pacheco, A. Silva, and M. Costa, "Single-droplet combustion of jet a-1, hydroprocessed vegetable oil, and their blends in a drop-tube furnace," *Energy & Fuels*, vol. 35, no. 9, pp. 7232–7241, 2021.

[160] T. Saitoh, S. Ishiguro, and T. Niioka, "An experimental study of droplet ignition characteristics near the ignitable limit," *Combustion and Flame*, vol. 48, pp. 27–32, 1982.

[161] I. Awasthi, D. N. Pope, and G. Gogos, "Effects of the ambient temperature and initial diameter in droplet combustion," *Combustion and flame*, vol. 161, no. 7, pp. 1883–1899, 2014.

[162] W. Shang, S. Yang, T. Xuan, Z. He, and J. Cao, "Experimental studies on combustion and microexplosion characteristics of n-alkane droplets," *Energy & Fuels*, vol. 34, no. 12, pp. 16 613–16 623, 2020.

[163] Y. Xu, J. D. Brunson, C. T. Avedisian, Y. Shen, I. Keresztes, A. M. Condo Jr, and D. Phillips, "Burning of algae-derived biofuel droplets and their mixtures with jet fuel," *Energy & Fuels*, vol. 34, no. 1, pp. 929–935, 2019.

[164] D. C. K. Rao, S. Karmakar, and S. Som, "Puffing and micro-explosion behavior in combustion of butanol/jet a-1 and acetone-butanol-ethanol (abe)/jet a-1 fuel droplets," *Combustion Science and Technology*, vol. 189, no. 10, pp. 1796–1812, 2017.

[165] J. Shinjo, J. Xia, L. Ganippa, and A. Megaritis, "Physics of puffing and microexplosion of emulsion fuel droplets," *Physics of Fluids*, vol. 26, no. 10, 2014.

[166] B. Rauch, "Systematic accuracy assessment for alternative aviation fuel evaporation

models," Ph.D. dissertation, Universität Stuttgart, 2017.

[167] S. K. Gupta, P. Prabhudeva, M. Kumar, P. K. Ojha, and S. Karmakar, "Investigation on spray combustion characteristics of boron-loaded slurry fuel in a swirl-stabilized combustor," *Fuel*, vol. 323, p. 124316, 2022.

[168] P. R. Choudhury, "Slurry fuels," *Progress in Energy and Combustion Science*, vol. 18, no. 5, pp. 409–427, 1992.

[169] M. L. Pinns, W. T. Olson, H. C. Barnett, and R. Breitwieser, "Naca research on slurry fuels," Tech. Rep., 1958.

[170] A. R. Al-Dosari, "Influence of aluminum oxide nanofuel additives on the spray performance of alternative and conventional jet fuels at high ambient conditions," Ph.D. dissertation, 2019.

[171] S. U. Choi and J. A. Eastman, "Enhancing thermal conductivity of fluids with nanoparticles," Argonne National Lab.(ANL), Argonne, IL (United States), Tech. Rep., 1995.

[172] S. U. Choi, "Nanofluids: from vision to reality through research," 2009.

[173] W. Yu and H. Xie, "A review on nanofluids: preparation, stability mechanisms, and applications," *Journal of nanomaterials*, vol. 2012, no. 1, p. 435873, 2012.

[174] G. Singh, E. Lopes, N. Hentges, D. Becker, and A. Ratner, "Experimental investigation of the settling characteristics of carbon and metal oxide nanofuels," *Journal of Nanofluids*, vol. 8, no. 8, pp. 1654–1660, 2019.

[175] O. Mahian, E. Bellos, C. N. Markides, R. A. Taylor, A. Alagumalai, L. Yang, C. Qin, B. J. Lee, G. Ahmadi, M. R. Safaei *et al.*, "Recent advances in using nanofluids in renewable energy systems and the environmental implications of their uptake," *Nano Energy*, vol. 86, p. 106069, 2021.

[176] N. Sezer, M. A. Atieh, and M. Koç, "A comprehensive review on synthesis, stability, thermophysical properties, and characterization of nanofluids," *Powder technology*, vol. 344, pp. 404–431, 2019.

[177] M. Alktranee and P. Bencs, "Factors affecting nanofluids behaviour: A review," *International Review of Applied Sciences and Engineering*, vol. 14, no. 2, pp. 241–255, 2023.

[178] S. Chakraborty and P. K. Panigrahi, "Stability of nanofluid: A review," *Applied Thermal Engineering*, vol. 174, p. 115259, 2020.

[179] X. Zhang, L. Pan, L. Wang, and J.-J. Zou, "Review on synthesis and properties of high-energy-density liquid fuels: Hydrocarbons, nanofluids and energetic ionic liquids," *Chemical Engineering Science*, vol. 180, pp. 95–125, 2018.

[180] W. T. Urmi, M. Rahman, K. Kadirgama, D. Ramasamy, and M. Maleque, "An overview on synthesis, stability, opportunities and challenges of nanofluids," *Materials Today: Proceedings*, vol. 41, pp. 30–37, 2021.

[181] A. Asadi, F. Pourfattah, I. M. Szilágyi, M. Afrand, G. Żyła, H. S. Ahn, S. Wongwises, H. M. Nguyen, A. Arabkoohsar, and O. Mahian, "Effect of sonication characteristics on stability, thermophysical properties, and heat transfer of nanofluids: A comprehensive review," *Ultrasonics sonochemistry*, vol. 58, p. 104701, 2019.

[182] B. Buonomo, O. Manca, L. Marinelli, and S. Nardini, "Effect of temperature and sonication time on nanofluid thermal conductivity measurements by nano-flash method," *Applied Thermal Engineering*, vol. 91, pp. 181–190, 2015.

[183] K. Anoop, S. Kabelac, T. Sundararajan, and S. K. Das, "Rheological and flow characteristics of nanofluids: Influence of electroviscous effects and particle agglomeration," *Journal of applied physics*, vol. 106, no. 3, 2009.

[184] A. Amrollahi, A. Hamidi, and A. Rashidi, "The effects of temperature, volume fraction and vibration time on the thermo-physical properties of a carbon nanotube suspension (carbon nanofluid)," *Nanotechnology*, vol. 19, no. 31, p. 315701, 2008.

[185] J.-H. Lee, K. S. Hwang, S. P. Jang, B. H. Lee, J. H. Kim, S. U. Choi, and C. J. Choi, "Effective viscosities and thermal conductivities of aqueous nanofluids containing low volume concentrations of al203 nanoparticles," *International Journal of Heat and Mass Transfer*, vol. 51, no. 11-12, pp. 2651–2656, 2008.

[186] N. Ali, J. A. Teixeira, and A. Addali, "A review on nanofluids: fabrication, stability, and thermophysical properties," *Journal of Nanomaterials*, vol. 2018, no. 1, p. 6978130, 2018.

[187] A. S. Parveg and A. Ratner, "A comprehensive review of liquid fuel droplet evaporation and combustion behavior with carbon-based nanoparticles," *Progress in Energy and Combustion Science*, vol. 106, p. 101198, 2025.

[188] R. Taylor, S. Coulombe, T. Otanicar, P. Phelan, A. Gunawan, W. Lv, G. Rosengarten, R. Prasher, and H. Tyagi, "Small particles, big impacts: A review of the diverse applications of nanofluids," *Journal of applied physics*, vol. 113, no. 1, 2013.

[189] T. Kegl, A. K. Kralj, B. Kegl, and M. Kegl, "Nanomaterials as fuel additives in diesel

engines: A review of current state, opportunities, and challenges," *Progress in Energy and Combustion Science*, vol. 83, p. 100897, 2021.

[190] W. Ao, Z. Fan, Y. Gao, Y. Wang, P. Liu, and L. K. Li, "Ignition and combustion characteristics of boron-based nanofluid fuel," *Combustion and Flame*, vol. 254, p. 112831, 2023.

[191] D. S. Sundaram, V. Yang, and V. E. Zarko, "Combustion of nano aluminum particles," *Combustion, Explosion, and Shock Waves*, vol. 51, pp. 173–196, 2015.

[192] M. Jones, "Ignition and combustion characteristics of nanoscale metal and metal oxide additives in biofuel (ethanol) and hydrocarbons," Master's thesis, University of Toledo, 2011.

[193] D. Wen, "Nanofuel as a potential secondary energy carrier," *Energy & Environmental Science*, vol. 3, no. 5, pp. 591–600, 2010.

[194] K. Trowell, S. Goroshin, D. Frost, and J. Bergthorson, "Aluminum and its role as a recyclable, sustainable carrier of renewable energy," *Applied Energy*, vol. 275, p. 115112, 2020.

[195] J. W. Bennewitz, A. Badakhshan, and D. G. Talley, "Combustion characteristics of suspended hydrocarbon fuel droplets with various nanoenergetic additives," *Combustion Science and Technology*, vol. 193, no. 12, pp. 2111–2136, 2021.

[196] R. Thiruvengadathan, "Aluminum-based nano-energetic materials: state of the art and future perspectives," *Nano-energetic materials*, pp. 9–35, 2019.

[197] V. V. Smirnov, S. A. Kostritsa, V. D. Kobtsev, N. S. Titova, and A. M. Starik, "Experimental study of combustion of composite fuel comprising n-decane and aluminum nanoparticles," *Combustion and Flame*, vol. 162, no. 10, pp. 3554–3561, 2015.

[198] A. K. Yadav, K. Nandakumar, A. Srivastava, and A. Chowdhury, "Combustion of rocket-grade kerosene droplets loaded with graphene nanoplatelets—a search for reasons behind optimum mass loadings," *Combustion and Flame*, vol. 203, pp. 1–13, 2019.

[199] E. L. Dreizin, "Metal-based reactive nanomaterials," *Progress in energy and combustion science*, vol. 35, no. 2, pp. 141–167, 2009.

[200] R. Küçükosman, A. A. Yontar, and K. Ocakoglu, "Nanoparticle additive fuels: Atomization, combustion and fuel characteristics," *Journal of Analytical and Applied Pyrolysis*, vol. 165, p. 105575, 2022.

[201] A. M. Starik, A. M. Savel'ev, and N. S. Titova, "Specific features of ignition and combustion of composite fuels containing aluminum nanoparticles," *Combustion, Explosion, and Shock Waves*, vol. 51, pp. 197–222, 2015.

[202] M. Zha, X. Lv, Z. Ma, L. Zhang, F. Zhao, S. Xu, and H. Xu, "Effect of particle size on reactivity and combustion characteristics of aluminum nanoparticles," *Combustion Science and Technology*, vol. 187, no. 7, pp. 1036–1043, 2015.

[203] J. Lv, S. Wang, and B. Meng, "The effects of nano-additives added to diesel-biodiesel fuel blends on combustion and emission characteristics of diesel engine: a review," *Energies*, vol. 15, no. 3, p. 1032, 2022.

[204] I. Javed, S. W. Baek, and K. Waheed, "Effects of dense concentrations of aluminum nanoparticles on the evaporation behavior of kerosene droplet at elevated temperatures: The phenomenon of microexplosion," *Experimental thermal and fluid science*, vol. 56, pp. 33–44, 2014.

[205] F. S. Shariatmadar and S. G. Pakdehi, "Synthesis and characterization of aviation turbine kerosene nanofluid fuel containing boron nanoparticles," *Energy & Fuels*, vol. 30, no. 9, pp. 7755–7762, 2016.

[206] Y. Gan and L. Qiao, "Combustion characteristics of fuel droplets with addition of nano and micron-sized aluminum particles," *Combustion and Flame*, vol. 158, no. 2, pp. 354–368, 2011.

[207] W. K. Lewis, A. T. Rosenberger, J. R. Gord, C. A. Crouse, B. A. Harruff, K. S. Fernando, M. J. Smith, D. K. Phelps, J. E. Spowart, E. A. Guliants *et al.*, "Multispectroscopic (ftir, xps, and tofms- tpd) investigation of the core- shell bonding in sonochemically prepared aluminum nanoparticles capped with oleic acid," *The Journal of Physical Chemistry C*, vol. 114, no. 14, pp. 6377–6380, 2010.

[208] A. Arshad, M. Jabbal, Y. Yan, and D. Reay, "A review on graphene based nanofluids: Preparation, characterization and applications," *Journal of Molecular Liquids*, vol. 279, pp. 444–484, 2019.

[209] M. Malỳ, A. Moita, J. Jedelsky, A. Ribeiro, and A. Moreira, "Effect of nanoparticles concentration on the characteristics of nanofluid sprays for cooling applications," *Journal of Thermal Analysis and Calorimetry*, vol. 135, pp. 3375–3386, 2019.

[210] H. D. Koca, S. Doganay, A. Turgut, I. H. Tavman, R. Saidur, and I. M. Mahbubul, "Effect of particle size on the viscosity of nanofluids: A review," *Renewable and Sustainable Energy Reviews*, vol. 82, pp. 1664–1674, 2018.

[211] D. Mei, Y. Fang, Z. Zhang, D. Guo, Z. Chen, and C. Sun, "Analysis of surface tension for nano-fuels containing disparate types of suspended nanoparticles," *Powder Technology*, vol. 388, pp. 526–536, 2021.

[212] S. Tanvir and L. Qiao, "Surface tension of nanofluid-type fuels containing suspended nanomaterials," *Nanoscale research letters*, vol. 7, pp. 1–10, 2012.

[213] M. Shafique and X. Luo, "Nanotechnology in transportation vehicles: An overview of its applications, environmental, health and safety concerns," *Materials*, vol. 12, no. 15, p. 2493, 2019.

[214] R. Gupta and H. Xie, "Nanoparticles in daily life: applications, toxicity and regulations," *Journal of Environmental Pathology, Toxicology and Oncology*, vol. 37, no. 3, 2018.

[215] H. Tyagi, P. E. Phelan, R. Prasher, R. Peck, T. Lee, J. R. Pacheco, and P. Arentzen, "Increased hot-plate ignition probability for nanoparticle-laden diesel fuel," *Nano letters*, vol. 8, no. 5, pp. 1410–1416, 2008.

[216] I. A. Ferrão, M. A. Mendes, A. S. Moita, and A. R. Silva, "The addition of particles to an alternative jet fuel," *Fuels*, vol. 3, no. 2, pp. 184–206, 2022.

[217] T. Mendes, "Single droplet combustion of hydrotreated vegetable oil with the addition of aluminum nanoparticles: Experiments and modeling," Master Thesis, 2022.

[218] Y. Gan and L. Qiao, "Evaporation characteristics of fuel droplets with the addition of nanoparticles under natural and forced convections," *International Journal of Heat and Mass Transfer*, vol. 54, no. 23-24, pp. 4913–4922, 2011.

[219] I. Javed, S. W. Baek, and K. Waheed, "Effects of dense concentrations of aluminum nanoparticles on the evaporation behavior of kerosene droplet at elevated temperatures: The phenomenon of microexplosion," *Experimental Thermal and Fluid Science*, vol. 56, pp. 33–44, 2014, eighth Mediterranean Combustion Symposium.

[220] N. G. Emekwuru, "Nanofuel droplet evaporation processes," *Journal of the Indian Institute of Science*, vol. 99, no. 1, pp. 43–58, 2019.

[221] I. Javed, S. W. Baek, and K. Waheed, "Autoignition and combustion characteristics of heptane droplets with the addition of aluminium nanoparticles at elevated temperatures," *Combustion and Flame*, vol. 162, no. 1, pp. 191–206, 2015.

[222] J. Z. Liu, B. H. Chen, T. T. Wu, W. J. Yang, and J. H. Zhou, "Ignition and combustion characteristics and agglomerate evolution mechanism of aluminum in nal/jp-10

nanofluid fuel," *Journal of Thermal Analysis and Calorimetry*, vol. 137, pp. 1369–1379, 2019.

[223] S. Mosadegh, A. Ghaffarkhah, C. van der Kuur, M. Arjmand, and S. Kheirkhah, "Graphene oxide doped ethanol droplet combustion: Ignition delay and contribution of atomization to burning rate," *Combustion and Flame*, vol. 238, p. 111748, 2022.

[224] Y. Gan and L. Qiao, "Evaporation characteristics of fuel droplets with the addition of nanoparticles under natural and forced convections," *International Journal of Heat and Mass Transfer*, vol. 54, no. 23, pp. 4913–4922, 2011.

[225] S. Tanvir and L. Qiao, "Effect of addition of energetic nanoparticles on droplet-burning rate of liquid fuels," *Journal of Propulsion and Power*, vol. 31, no. 1, pp. 408–415, 2015.

[226] Y. Wei, W. Deng, and R.-H. Chen, "Effects of insoluble nano-particles on nanofluid droplet evaporation," *International Journal of Heat and Mass Transfer*, vol. 97, pp. 725–734, 2016.

[227] S. Tanvir, S. Biswas, and L. Qiao, "Evaporation characteristics of ethanol droplets containing graphite nanoparticles under infrared radiation," *International Journal of Heat and Mass Transfer*, vol. 114, pp. 541–549, 2017.

[228] R. Wang, G. Pan, S. Qian, L. Li, and Z. Zhu, "Influence of nanoparticles on the evaporation behavior of nanofluid droplets: A dh law and underlying mechanism," *Langmuir*, vol. 36, no. 4, pp. 919–930, 2019.

[229] S. Tanvir and L. Qiao, "Droplet burning rate enhancement of ethanol with the addition of graphite nanoparticles: Influence of radiation absorption," *Combustion and Flame*, vol. 166, pp. 34–44, 2016.

[230] Y. Gan and L. Qiao, "Radiation-enhanced evaporation of ethanol fuel containing suspended metal nanoparticles," *International Journal of Heat and Mass Transfer*, vol. 55, no. 21, pp. 5777–5782, 2012.

[231] K. Pandey and S. Basu, "How boiling happens in nanofuel droplets," *Physics of Fluids*, vol. 30, no. 10, p. 107103, 2018.

[232] Y. Gan and L. Qiao, "Optical properties and radiation-enhanced evaporation of nanofluid fuels containing carbon-based nanostructures," *Energy & Fuels*, vol. 26, no. 7, pp. 4224–4230, 2012.

[233] R. de Souza Lima, M.-I. Ré, and P. Arlabosse, "Drying droplet as a template for solid

formation: A review," *Powder Technology*, vol. 359, pp. 161–171, 2020.

[234] W. J. Gerken, A. V. Thomas, N. Koratkar, and M. A. Oehlschlaeger, "Nanofluid pendant droplet evaporation: Experiments and modeling," *International Journal of Heat and Mass Transfer*, vol. 74, pp. 263–268, 2014.

[235] U. Maurice, M. Mezhericher, A. Levy, and I. Borde, "Drying of droplet containing insoluble nanoscale particles: Numerical simulations and parametric study," *Drying Technology*, vol. 31, no. 15, pp. 1790–1807, 2013.

[236] M. Mezhericher, A. Levy, and I. Borde, "Modelling the morphological evolution of nanosuspension droplet in constant-rate drying stage," *Chemical Engineering Science*, vol. 66, no. 5, pp. 884–896, 2011.

[237] H. Li, C. D. Rosebrock, Y. Wu, T. Wriedt, and L. Mädler, "Single droplet combustion of precursor/solvent solutions for nanoparticle production: Optical diagnostics on single isolated burning droplets with micro-explosions," *Proceedings of the Combustion Institute*, vol. 37, no. 1, pp. 1203–1211, 2019.

[238] B. Ittoo, J. B. Ooi, M.-V. Tran, F. Jaliliantabar, G. H. Najafi, and V. Swamy, "Effects of dispersed multiwalled carbon nanotubes on the micro-explosion and combustion characteristics of 2-methylfuran–diesel mixture droplets," *Fuel*, vol. 316, p. 123308, 2022.

[239] M. Ghamari and A. Ratner, "Combustion characteristics of colloidal droplets of jet fuel and carbon based nanoparticles," *Fuel*, vol. 188, pp. 182–189, 2017.

[240] S. Li, Q. Yang, L. Ye, H. Du, Z. Zhang, X. Huang, and J. Xu, "Effect of nanoparticle concentration on physical and heat-transfer properties and evaporation characteristics of graphite/n-decane nanofluid fuels," *ACS omega*, vol. 7, no. 4, pp. 3284–3292, 2022.

[241] D. M. Kim, S. W. Baek, and J. Yoon, "Ignition characteristics of kerosene droplets with the addition of aluminum nanoparticles at elevated temperature and pressure," *Combustion and Flame*, vol. 173, pp. 106–113, 2016.

[242] K. Pandey, S. Basu, G. V, A. Potnis, and K. Chattopadhyay, "Self-tuning and topological transitions in a free-falling nanofuel droplet flame," *Combustion and Flame*, vol. 220, pp. 144–156, 2020.

[243] Q. Yang, S. Li, L. Ye, and X. Huang, "Understanding of contradiction on concentration effect on stability, physical properties, evaporation and microexplosion characteristics of al/jp-10/oleic acid nanofluid fuel," *Nanomaterials*, vol. 12, no. 19, p. 3446, 2022.

[244] J. C. Lasheras and E. Hopfinger, "Liquid jet instability and atomization in a coaxial gas stream," *Annual review of fluid mechanics*, vol. 32, no. 1, pp. 275–308, 2000.

[245] H. Zhao and H. Liu, "Breakup morphology and mechanisms of liquid atomization," *Environmental Impact of Aviation and Sustainable Solutions*, 2019.

[246] R. G. Pimentel, "Measurement and prediction of droplet size distribution in sprays," Ph.D. dissertation, Citeseer, 2006.

[247] C. T. Chong and S. Hochgreb, "Spray characteristics of an internal-mix airblast atomizer," *Applied Mechanics and Materials*, vol. 629, pp. 125–130, 2014.

[248] I. Ibrahim, T. Farag, M. Abdel-Baky, A. Abd El-samed, and H. Gad, "Experimental study of spray combustion characteristics of air-blast atomizer," *Energy Reports*, vol. 6, pp. 209–215, 2020.

[249] C. T. Chong and S. Hochgreb, "Effect of atomizing air flow on spray atomization of an internal-mix twin-fluid atomizer," *Atomization and Sprays*, vol. 25, no. 8, 2015.

[250] A. H. Lefebvre, "Atomization," in *Thermopedia*. Begel House Inc., 2011.

[251] C. Dumouchel, "On the experimental investigation on primary atomization of liquid streams," *Experiments in fluids*, vol. 45, pp. 371–422, 2008.

[252] M. Roudini and G. Wozniak, "Experimental investigation of spray characteristics of pre-filming air-blast atomizers," *Journal of Applied Fluid Mechanics*, vol. 11, no. 6, pp. 1455–1469, 2018.

[253] H. Gad, E. Baraya, T. Farag, and I. Ibrahim, "Effects of flow parameters on spray characteristics of a modified pressure swirl atomizer," *IOSR Journal of Mechanical and Civil Engineering*, 2020.

[254] Y. H. Nazeer, "Numerical modelling of in-nozzle flow transient effects and fuel atomization characteristics of an industrial atomizer," Ph.D. dissertation, City, University of London, 2020.

[255] A. H. Lefebvre and V. G. McDonell, *Atomization and sprays*. CRC press, 2017.

[256] M. D. Bohon, B. A. Metzger, W. P. Linak, C. J. King, and W. L. Roberts, "Glycerol combustion and emissions," *Proceedings of the combustion institute*, vol. 33, no. 2, pp. 2717–2724, 2011.

[257] K. Tingos, "Air-assist atomizer spray in cross-flow," B.S. thesis, 2022.

[258] N. Ashgriz, *Handbook of atomization and sprays: theory and applications*. Springer Science & Business Media, 2011.

[259] G. Hoffmann, B. Befrui, A. Berndorfer, W. F. Piock, and D. L. Varble, "Fuel system pressure increase for enhanced performance of gdi multi-hole injection systems," *SAE International Journal of Engines*, vol. 7, no. 1, pp. 519–527, 2014.

[260] S. K. Soni and P. S. Kolhe, "Liquid jet breakup and spray formation with annular swirl air," *International Journal of Multiphase Flow*, vol. 134, p. 103474, 2021.

[261] A. Garai, S. Pal, S. Mondal, S. Ghosh, S. Sen, and A. Mukhopadhyay, "Experimental investigation of spray characteristics of kerosene and ethanol-blended kerosene using a gas turbine hybrid atomizer," *Sādhanā*, vol. 42, pp. 543–555, 2017.

[262] C. M. Varga, J. C. Lasheras, and E. J. Hopfinger, "Initial breakup of a small-diameter liquid jet by a high-speed gas stream," *Journal of Fluid Mechanics*, vol. 497, pp. 405–434, 2003.

[263] P. Watanawanyoo, H. Mochida, H. Hirahara, and S. Chaitep, "Flow characteristics of fluid droplet obtained from air assisted atomizer," in *Fluids Engineering Division Summer Meeting*, vol. 44410, 2011, pp. 89–94.

[264] A. B. Lopes, N. Emekwuru, and K. Joshi, "Are the available data from laboratory spray burners suitable for cfd modelling validations? a review," *Energy Conversion and Management: X*, vol. 16, p. 100289, 2022.

[265] C.-P. Mao, V. Oechsle, and N. Chigier, "Drop size distribution and air velocity measurements in air assist swirl atomizer sprays," 1987.

[266] A. N. M. Yusoff, S. H. Amirnordin, and R. Y. S. Chin, "Spray characteristics of heavy fuel oil (hfo) in air assisted atomizer," *Fuel, Mixture Formation and Combustion Process*, vol. 2, no. 2, 2020.

[267] A. Rizkalla and A. H. Lefebvre, "Influence of liquid properties on airblast atomizer spray characteristics," 1975.

[268] G. Lorenzetto and A. H. Lefebvre, "Measurements of drop size on a plain-jet airblast atomizer," *AIAA journal*, vol. 15, no. 7, pp. 1006–1010, 1977.

[269] A. B. de la Rosa, A. Sobiesiak, and T. Brzustowski, "The influence of fuel properties on drop-size distribution and combustion in an oil spray," in *Symposium (International) on Combustion*, vol. 21, no. 1. Elsevier, 1988, pp. 557–566.

[270] S. Nukiyama, "Experiments on the atomization of liquids in an air stream, report 3, on the droplet-size distribution in a atomized jet," *Trans. Soc. Mech. Eng. Japan*, vol. 5, pp. 62–67, 1939.

[271] A. Dunand, J.-L. Carreau, and F. Roger, "Liquid jet breakup and atomization by annular swirling gas jet," *Atomization and sprays*, vol. 15, no. 2, 2005.

[272] K. O. Fong, X. Xue, R. Osuna-Orozco, and A. Aliseda, "Gas–liquid coaxial atomization with swirl in high-pressure environments," *International Journal of Multiphase Flow*, vol. 174, p. 104767, 2024.

[273] G. A. Vijay, N. S. V. Moorthi, and A. Manivannan, "Internal and external flow characteristics of swirl atomizers: a review," *Atomization and sprays*, vol. 25, no. 2, 2015.

[274] B.-J. Rho, S.-J. Kang, J.-H. Oh, and S.-G. Lee, "Swirl effect on the spray characteristics of a twin-fluid jet," *KSME International Journal*, vol. 12, pp. 899–906, 1998.

[275] C. Presser, A. Gupta, H. Semerjian, and C. Avedisian, "Droplet transport in a swirl-stabilized spray flame," *Journal of Propulsion and Power*, vol. 10, no. 5, pp. 631–638, 1994.

[276] P. Marmottant and E. Villermaux, "On spray formation," *Journal of fluid mechanics*, vol. 498, pp. 73–111, 2004.

[277] E. Hopfinger and J. Lasheras, "Explosive breakup of a liquid jet by a swirling coaxial gas jet," *Physics of Fluids*, vol. 8, no. 7, pp. 1696–1698, 1996.

[278] L. Rayleigh, "On the instability of jets," *Proceedings of the London mathematical society*, vol. 1, no. 1, pp. 4–13, 1878.

[279] T. Ahmed, "Atomization and combustion of hybrid electrohydrodynamic-air-assisted sprays," Ph.D. dissertation, 2022.

[280] V. Sivadas, M. Heitor, and R. Fernandes, "A functional correlation for the primary breakup processes of liquid sheets emerging from air-assist atomizers," 2007.

[281] N. Machicoane, R. Osuna-Orozco, and A. Aliseda, "Regimes of the length of a laminar liquid jet fragmented by a gas co-flow," *International Journal of Multiphase Flow*, vol. 165, p. 104475, 2023.

[282] A. Kumar and S. Sahu, "Large scale instabilities in coaxial air-water jets with annular air swirl," *Physics of Fluids*, vol. 31, no. 12, 2019.

[283] R. Reitz and F. Bracco, "Mechanism of atomization of a liquid jet," *The physics of*

Fluids, vol. 25, no. 10, pp. 1730–1742, 1982.

[284] R. Payri, F. J. Salvador, J. Gimeno, and J. De la Morena, "Analysis of diesel spray atomization by means of a near-nozzle field visualization technique," *Atomization and Sprays*, vol. 21, no. 9, 2011.

[285] A. M. Sterling and C. Sleicher, "The instability of capillary jets," *Journal of Fluid Mechanics*, vol. 68, no. 3, pp. 477–495, 1975.

[286] C. Miesse, "Correlation of experimental data on the disintegration of liquid jets," *Industrial & Engineering Chemistry*, vol. 47, no. 9, pp. 1690–1701, 1955.

[287] R. D. Reitz, *Atomization and other breakup regimes of a liquid jet*. Princeton University, 1978.

[288] M. Jadidi, S. Moghtadernejad, and A. Dolatabadi, "A comprehensive review on fluid dynamics and transport of suspension/liquid droplets and particles in high-velocity oxygen-fuel (hvof) thermal spray," *Coatings*, vol. 5, no. 4, pp. 576–645, 2015.

[289] N. Chigier and Z. Farago, "Morphological classification of disintegration of round liquid jets in a coaxial air stream," *Atomization and sprays*, vol. 2, no. 2, 1992.

[290] M. Kaczmarek, R. Osuna-Orozco, P. D. Huck, A. Aliseda, and N. Machicoane, "Spatial characterization of the flapping instability of a laminar liquid jet fragmented by a swirled gas co-flow," *International Journal of Multiphase Flow*, vol. 152, p. 104056, 2022.

[291] M. C. Esposito, "Analysis of primary atomization in sprays using direct numerical simulation," Ph.D. dissertation, Universitat Politècnica de València, 2019.

[292] G. Singh, A. Kourmatzis, A. Gutteridge, and A. Masri, "Instability growth and fragment formation in air assisted atomization," *Journal of Fluid Mechanics*, vol. 892, p. A29, 2020.

[293] H. Eroglu, N. Chigier, and Z. Farago, "Coaxial atomizer liquid intact lengths," *Physics of Fluids A: Fluid Dynamics*, vol. 3, no. 2, pp. 303–308, 1991.

[294] B. Leroux, O. Delabroy, and F. Lacas, "Experimental study of coaxial atomizers scaling. part i: dense core zone," *Atomization and Sprays*, vol. 17, no. 5, 2007.

[295] H. Zhao, H.-F. Liu, X.-S. Tian, J.-L. Xu, W.-F. Li, and K.-F. Lin, "Influence of atomizer exit area ratio on the breakup morphology of coaxial air and round water jets," *AIChE Journal*, vol. 60, no. 6, pp. 2335–2345, 2014.

[296] A. Kumar and S. Sahu, "Liquid jet breakup unsteadiness in a coaxial air-blast atomizer," *International journal of spray and combustion dynamics*, vol. 10, no. 3, pp. 211–230, 2018.

[297] C. Engelbert, Y. Hardalupas, and J. H. Whitelaw, "Breakup phenomena in coaxial air-blast atomizers," *Proceedings of the Royal Society of London. Series A: Mathematical and Physical Sciences*, vol. 451, no. 1941, pp. 189–229, 1995.

[298] R. Sikka, K. Vågsæther, D. Bjerketvedt, and J. Lundberg, "Experimental study of primary atomization characteristics of sonic air-assist atomizers," *Applied Sciences*, vol. 11, no. 21, p. 10444, 2021.

[299] M. Kumar, S. Karmakar, S. Kumar, and S. Basu, "Experimental investigation on spray characteristics of jet a-1 and alternative aviation fuels," *International Journal of Spray and Combustion Dynamics*, vol. 13, no. 1-2, pp. 54–71, 2021.

[300] J. Janicka, A. Sadiki, M. Schäfer, and C. Heeger, *Flow and combustion in advanced gas turbine combustors*. Springer Science & Business Media, 2012, vol. 102.

[301] D. Guildenbecher, C. López-Rivera, and P. Sojka, "Secondary atomization," *Experiments in Fluids*, vol. 46, no. 3, pp. 371–402, 2009.

[302] P. X. Pham, A. Kourmatzis, and A. R. Masri, "Simultaneous volume-velocity measurements in the near field of atomizing sprays," *Measurement Science and Technology*, vol. 28, no. 11, p. 115203, 2017.

[303] A. Giusti, "Development of numerical tools for the analysis of advanced airblast injection systems for lean burn aero-engine combustors," Ph.D. dissertation, Università degli Studi di Firenze, 2014.

[304] C. M. G. Rodrigues, "Modelling of spray-wall impingement," Ph.D. dissertation, Universidade da Beira Interior (Portugal), 2016.

[305] D. Sanadi, K. Rajamanickam, and S. Basu, "Analysis of hollow-cone spray injected in an unconfined, isothermal, coannular swirling jet environment," *Atomization and Sprays*, vol. 27, no. 1, 2017.

[306] G. Charalampous, Y. Hardalupas, and A. Taylor, "Structure of the continuous liquid jet core during coaxial air-blast atomisation," *International journal of spray and combustion dynamics*, vol. 1, no. 4, pp. 389–415, 2009.

[307] G. Zhou, J. Zhou, Y. Fang, and X. Yang, "Properties effect of blending fischer-tropsch aviation fuel on spray performances," *Energy*, vol. 179, pp. 1082–1093, 2019.

[308] J. Asibor, K. Pandey, S. Basu, and N. Emekwuru, "Characterization of the spray cone angles of fuels with nanoparticle additives," in *14th Triennial International Conference on Liquid Atomization and Spray Systems*. International Conference on Liquid Atomization and Spray Systems, 2018.

[309] X. Dai, A. Lefebvre, and J. Rollbuhler, "Spray characteristics of a spill-return airblast atomizer," 1989.

[310] J.-S. Gong and W.-B. Fu, "The experimental study on the flow characteristics for a swirling gas–liquid spray atomizer," *Applied thermal engineering*, vol. 27, no. 17-18, pp. 2886–2892, 2007.

[311] M. Shafaee, S. A. Banitabaei, M. Ashjaee, and V. Esfahanian, "Effect of flow conditions on spray cone angle of a two-fluid atomizer," *Journal of mechanical science and technology*, vol. 25, pp. 365–369, 2011.

[312] A. Urbán, B. Katona, M. Malỳ, J. Jedelskỳ, and V. Józsa, "Empirical correlation for spray half cone angle in plain-jet airblast atomizers," *Fuel*, vol. 277, p. 118197, 2020.

[313] S. Poozesh, S. W. Grib, M. W. Renfro, and P. J. Marsac, "Near-field dynamics of high-speed spray dryer coannular two fluid nozzle: Effects of operational conditions and formulations," *Powder technology*, vol. 333, pp. 439–448, 2018.

[314] R. Klein-Douwel, P. Frijters, L. Somers, W. De Boer, and R. Baert, "Macroscopic diesel fuel spray shadowgraphy using high speed digital imaging in a high pressure cell," *Fuel*, vol. 86, no. 12-13, pp. 1994–2007, 2007.

[315] L. Lambosi, A. Khalid, B. Manshoor, S. Hisyam, and L. K. Hao, "Effect of nozzle angle to combustion characteristic in biodiesel burner," *Applied Mechanics and Materials*, vol. 773, pp. 585–589, 2015.

[316] J. Karnawat and A. Kushari, "Controlled atomization using a twin-fluid swirl atomizer," *Experiments in fluids*, vol. 41, no. 4, pp. 649–663, 2006.

[317] H. Gad, I. Ibrahim, M. Abdel-Baky, A. Abd El-samed, and T. Farag, "Experimental study of diesel fuel atomization performance of air blast atomizer," *Experimental Thermal and Fluid Science*, vol. 99, pp. 211–218, 2018.

[318] Y. Zhao, X. He, M. Li, and K. Yao, "Experimental investigation on spray characteristics of aircraft kerosene with an external-mixing atomizer," *Fuel Processing Technology*, vol. 209, p. 106531, 2020.

[319] A. Davanlou, J. D. Lee, S. Basu, and R. Kumar, "Effect of viscosity and surface tension

on breakup and coalescence of bicomponent sprays," *Chemical Engineering Science*, vol. 131, pp. 243–255, 2015.

[320] A. Basak, J. Patra, R. Ganguly, and A. Datta, "Effect of transesterification of vegetable oil on liquid flow number and spray cone angle for pressure and twin fluid atomizers," *Fuel*, vol. 112, pp. 347–354, 2013.

[321] S. Yao, J. Zhang, and T. Fang, "Effect of viscosities on structure and instability of sprays from a swirl atomizer," *Experimental Thermal and Fluid Science*, vol. 39, pp. 158–166, 2012.

[322] T. Müller, A. Sänger, P. Habisreuther, T. Jakobs, D. Trimis, T. Kolb, and N. Zarzalis, "Simulation of the primary breakup of a high-viscosity liquid jet by a coaxial annular gas flow," *International Journal of Multiphase Flow*, vol. 87, pp. 212–228, 2016.

[323] K. Kannaiyan and R. Sadr, "Influence of fuel characteristics on the alternative jet fuel atomization at non-reacting conditions," *Fuel*, vol. 357, p. 129908, 2024.

[324] T. D. Fansler and S. E. Parrish, "Spray measurement technology: a review," *Measurement Science and Technology*, vol. 26, no. 1, p. 012002, 2014.

[325] F. Chang, H. Luo, P. Dong, K. Nishida, Y. Ogata, R. Hara, K. Uchida, and W. Zhang, "Characteristics of droplet behaviors during spray breakup process," *Sustainability*, vol. 15, no. 12, p. 9356, 2023.

[326] H. Wu, F. Zhang, and Z. Zhang, "Fundamental spray characteristics of air-assisted injection system using aviation kerosene," *Fuel*, vol. 286, p. 119420, 2021.

[327] M. O. Panão, A. S. Moita, and A. L. Moreira, "On the statistical characterization of sprays," *Applied Sciences*, vol. 10, no. 17, p. 6122, 2020.

[328] E. Berrocal, "Multiple scattering of light in optical diagnostics of dense sprays and other complex turbid media," Ph.D. dissertation, Cranfield University, 2006.

[329] H. Wu, Z. Zhang, F. Zhang, and W. L. Roberts, "Time-resolved low-pressure air-assisted spray performance and unsteadiness evaluation," *Physics of Fluids*, vol. 35, no. 4, 2023.

[330] Y. N. Mishra, "Droplet size, concentration, and temperature mapping in sprays using slipi-based techniques," Ph.D. dissertation, Lund University, Faculty of Engineering, Department of Physics, 2018.

[331] M. Panão and A. Moreira, "A real-time assessment of measurement uncertainty in

the experimental characterization of sprays," *Measurement Science and Technology*, vol. 19, no. 9, p. 095402, 2008.

[332] M. Roudini and G. Wozniak, "Investigation of the secondary atomization in prefilming air-blast atomizers," *International Journal of Chemical Engineering and Applications*, vol. 10, no. 5, 2019.

[333] Z. Xu, H. Zhao, and H.-F. Liu, "Atomization model based on the ligament-mediated spray mechanism for coaxial two-fluid air-blast nozzle," *Chemical Engineering Journal*, vol. 450, p. 137986, 2022.

[334] J. Karnawat and A. Kushari, "Spray evolution in a twin-fluid swirl atomizer," *Atomization and Sprays*, vol. 18, no. 5, 2008.

[335] C. Pereira, G. Wang, and M. Costa, "Combustion of biodiesel in a large-scale laboratory furnace," *Energy*, vol. 74, pp. 950–955, 2014.

[336] M. Chinnaraj and R. Sadanandan, "The effect of swirling air-to-liquid momentum ratio on the spray and droplet characteristics," *Journal of Applied Fluid Mechanics*, vol. 13, no. 3, pp. 827–837, 2020.

[337] G. Chaussonnet, S. Joshi, S. Wachter, R. Koch, T. Jakobs, T. Kolb, and H.-J. Bauer, "Air-assisted atomization at constant mass and momentum flow rate: Investigation into the ambient pressure influence with the smoothed particle hydrodynamics method," *Journal of Engineering for Gas Turbines and Power*, vol. 142, no. 3, p. 031019, 2020.

[338] Y. Xia, M. Alshehhi, Y. Hardalupas, and L. Khezzar, "Spray characteristics of free air-on-water impinging jets," *International Journal of Multiphase Flow*, vol. 100, pp. 86–103, 2018.

[339] M. Ochowiak, A. Krupińska, S. Włodarczak, M. Matuszak, M. Markowska, M. Janczarek, and T. Szulc, "The two-phase conical swirl atomizers: Spray characteristics," *Energies*, vol. 13, no. 13, p. 3416, 2020.

[340] A. P. Vouros, A. P. Vouros, and T. Panidis, "Spray characteristics of alternative aviation fuel blends," *Aerospace*, vol. 4, no. 2, p. 18, 2017.

[341] K. Kannaiyan and R. Sadr, "The effects of alumina nanoparticles as fuel additives on the spray characteristics of gas-to-liquid jet fuels," *Experimental Thermal and Fluid Science*, vol. 87, pp. 93–103, 2017.

[342] D. Sun, W. Cai, C. Li, and J. Lu, "Experimental study on atomization characteristics

of high-energy-density fuels using a fuel slinger," *Energy*, vol. 234, p. 121222, 2021.

[343] F. R. Westlye, "Experimental study of liquid fuel spray combustion," Ph.D. dissertation, Technical University of Denmark, 2016.

[344] R. A. Alsulami, "The role of physical and chemical properties of single and multicomponent liquid fuels on spray processes, flame stability, and emissions," Ph.D. dissertation, Colorado State University, 2019.

[345] D. Wissmiller, "Pyrolysis oil combustion characteristics and exhaust emissions in a swirl-stabilized combustor," Ph.D. dissertation, Iowa State University, 2009.

[346] Y. Xu, Y. Huang, and G. Ma, "A review on effects of different factors on gas explosions in underground structures," *Underground Space*, vol. 5, no. 4, pp. 298–314, 2020.

[347] A. Li, "Flammability limits of alternative aviation fuels," Master's thesis, Purdue University, 2016.

[348] J. H. Perry, "Chemical engineers' handbook," 1950.

[349] J. Arnaldos, J. Casal, and E. Planas-Cuchi, "Prediction of flammability limits at reduced pressures," *Chemical Engineering Science*, vol. 56, no. 12, pp. 3829–3843, 2001.

[350] P. Coelho and M. Costa, "Combustão," *Edições Orion*, vol. 1, 2007.

[351] L. Silva, "Design of a combustion chamber for liquid fuels," Master's thesis, Lisbon University, 2024.

[352] A. Williams, "Fundamentals of oil combustion," in *Energy and Combustion Science*. Elsevier, 1979, pp. 135–147.

[353] V. Raghavan, *Combustion technology: essentials of flames and burners*. Springer Nature, 2021.

[354] Y. M. Al-Abdeli and A. R. Masri, "Review of laboratory swirl burners and experiments for model validation," *Experimental Thermal and Fluid Science*, vol. 69, pp. 178–196, 2015.

[355] A. Gupta, "Swirl flows," 1984.

[356] J. M. Beér and N. A. Chigier, "Combustion aerodynamics," *Applied Science*, 1972.

[357] W. Bartok and A. F. Sarofim, "Fossil fuel combustion: a source book," 1991.

[358] D. L. Bulzan, "Structure of a swirl-stabilized combusting spray," *Journal of Propulsion and Power*, vol. 11, no. 6, pp. 1093–1102, 1995.

[359] V. McDonell and G. Samuelsen, "An experimental data base for the computational fluid dynamics of reacting and nonreacting methanol sprays," 1995.

[360] C. T. Chong and S. Hochgreb, "Spray and combustion characteristics of biodiesel: Non-reacting and reacting," *International Biodeterioration & Biodegradation*, vol. 102, pp. 353–360, 2015.

[361] ——, "Fundamental spray combustion characteristics of rapeseed biodiesel, diesel and blend," *Energy Procedia*, vol. 75, pp. 2394–2399, 2015.

[362] C. T. Chong, M.-C. Chiong, J.-H. Ng, M. Lim, M.-V. Tran, A. Valera-Medina, and W. W. F. Chong, "Oxygenated sunflower biodiesel: Spectroscopic and emissions quantification under reacting swirl spray conditions," *Energy*, vol. 178, pp. 804–813, 2019.

[363] R. M. El-Zoheiry, A. I. EL-Seesy, A. M. Attia, Z. He, and H. M. El-Batsh, "Combustion and emission characteristics of jojoba biodiesel-jet a1 mixtures applying a lean premixed pre-vaporized combustion techniques: An experimental investigation," *Renewable Energy*, vol. 162, pp. 2227–2245, 2020.

[364] B. Y. Belal, G. Li, Z. Zhang, H. El-Batsh, H. A. Moneib, and A. M. Attia, "The effect of swirl burner design configuration on combustion and emission characteristics of lean pre-vaporized premixed flames," *Energy*, vol. 228, p. 120622, 2021.

[365] M. Kumar and S. Karmakar, "Butyl butyrate, jet a-1 and their blends: Combustion performance in the swirl stabilized burner at different inlet air temperature," *Biomass and Bioenergy*, vol. 168, p. 106651, 2023.

[366] S. Pourhoseini and M. Ghodrat, "Experimental investigation of the effect of al203 nanoparticles as additives to b20 blended biodiesel fuel: Flame characteristics, thermal performance and pollutant emissions," *Case Studies in Thermal Engineering*, vol. 27, p. 101292, 2021.

[367] J. Yang, Z. Xin, K. Corscadden, H. Niu *et al.*, "An overview on performance characteristics of bio-jet fuels," *Fuel*, vol. 237, pp. 916–936, 2019.

[368] S. Richter, M. Braun-Unkhoff, T. Kathrotia, C. Naumann, T. Kick, N. Slavinskaya, and U. Riedel, "Methods and tools for the characterisation of a generic jet fuel," *CEAS Aeronautical Journal*, vol. 10, pp. 925–935, 2019.

[369] T. Rahmes, J. Kinder, G. Crenfeldt, G. LeDuc, Y. Abe, M. McCall, T. Henry, G. Zom-

banakis, D. Lambert, C. Lewis *et al.*, "Sustainable bio-derived synthetic paraffinic kerosene (bio-spk) jet fuel flights and engine tests program results," in *9th AIAA aviation technology, integration, and operations conference (ATIO) and aircraft noise and emissions reduction symposium (ANERS)*, 2009, p. 7002.

[370] J. I. Hileman, H. M. Wong, D. Ortiz, N. Brown, L. Maurice, and M. Rumizen, "The feasibility and potential environmental benefits of alternative fuels for commercial aviation," in *Proceedings of the 26th International Congress of the Aeronautical Sciences*, 2008, pp. 5–8.

[371] N. Corporation, *Neste renewable diesel handbook. Technical report*, October 2020.

[372] Y. Gong, O. Kaario, A. Tilli, M. Larmi, and F. Tanner, "A computational investigation of hydrotreated vegetable oil sprays using rans and a modified version of the rng k-ε model in openfoam," SAE Technical Paper, Tech. Rep., 2010.

[373] M. C. Chiong, C. T. Chong, J.-H. Ng, S. S. Lam, M.-V. Tran, W. W. F. Chong, M. N. M. Jaafar, and A. Valera-Medina, "Liquid biofuels production and emissions performance in gas turbines: A review," *Energy Conversion and Management*, vol. 173, pp. 640–658, 2018.

[374] F. de Sousa Santos, A. S. Soares, M. A. Moret, L. Lefol, and N. Guarieiro, "Hvo production: Concepts and production routes."

[375] J. M. Fernández-Villamil and A. H. de Mendoza Paniagua, "Preliminary design of the green diesel production process by hydrotreatment of vegetable oils," *Student Contest Problem, EURECHA*, p. 115, 2018.

[376] J. Benajes, A. García, J. Monsalve-Serrano, and M. Guzmán-Mendoza, "A review on low carbon fuels for road vehicles: The good, the bad and the energy potential for the transport sector," *Fuel*, vol. 361, p. 130647, 2024.

[377] T. W. Chan, W. A. Chishty, P. Canteenwalla, D. Buote, and C. R. Davison, "Characterization of emissions from the use of alternative aviation fuels," *Journal of Engineering for Gas Turbines and Power*, vol. 138, no. 1, p. 011506, 2016.

[378] C. Klingshirn, M. DeWitt, R. Striebich, D. Anneken, L. Shafer, E. Corporan, M. Wagner, and D. Brigalli, "Hydroprocessed renewable jet fuel evaluation, performance, and emissions in a t63 turbine engine," 2012.

[379] W. A. Chishty, C. R. Davison, J. Bird, T. Chan, K. Cuddihy, M. McCurdy, P. Barton, A. Krasteva, and P. Poitras, "Emissions assessment of alternative aviation fuel at simulated altitudes," in *Turbo Expo: Power for Land, Sea, and Air*, vol. 54617, 2011, pp.

51–61.

[380] R. M. EL-Zohairy, A. S. Attia, A. Huzayyin, and A. I. EL-Seesy, “Improving the biodiesel combustion and emission characteristics in the lean pre-vaporized premixed system using diethyl ether as a fuel additive,” *Fuel*, vol. 356, p. 129614, 2024.

[381] I. K. Reksowardojo, L. H. Duong, R. Zain, F. Hartono, S. Marno, W. Rustyawan, N. Putri, W. Jatiwiramurti, and B. Prabowo, “Performance and exhaust emissions of a gas-turbine engine fueled with biojet/jet a-1 blends for the development of aviation biofuel in tropical regions,” *Energies*, vol. 13, no. 24, p. 6570, 2020.

[382] C. T. Chong and S. Hochgreb, “Spray combustion characteristics of palm biodiesel,” *Combustion science and technology*, vol. 184, no. 7-8, pp. 1093–1107, 2012.

[383] H. Aatola, M. Larmi, T. Sarjovaara, and S. Mikkonen, “Hydrotreated vegetable oil (hvo) as a renewable diesel fuel: trade-off between no□, particulate emission, and fuel consumption of a heavy duty engine,” *SAE International Journal of Engines*, vol. 1, no. 1, pp. 1251–1262, 2009.

[384] M. Lapuerta, J. R. Agudelo, M. Prorok, and A. L. Boehman, “Bulk modulus of compressibility of diesel/biodiesel/hvo blends,” *Energy & fuels*, vol. 26, no. 2, pp. 1336–1343, 2012.

[385] A. Dimitriadis, I. Natsios, A. Dimaratos, D. Katsaounis, Z. Samaras, S. Bezergianni, and K. Lehto, “Evaluation of a hydrotreated vegetable oil (hvo) and effects on emissions of a passenger car diesel engine,” *Frontiers in Mechanical Engineering*, vol. 4, p. 7, 2018.

[386] A. F. Alhikami and W.-C. Wang, “Experimental study of the spray ignition characteristics of hydro-processed renewable jet and petroleum jet fuels in a constant volume combustion chamber,” *Fuel*, vol. 283, p. 119286, 2021.

[387] J. Hunicz, J. Matijošius, A. Rimkus, A. Kilikevičius, P. Kordos, and M. Mikulski, “Efficient hydrotreated vegetable oil combustion under partially premixed conditions with heavy exhaust gas recirculation,” *Fuel*, vol. 268, p. 117350, 2020.

[388] J. Yang, J. Wu, and S. Bi, “Surface tension measurements by pendant drop method of 10 pure long-chain alkanes and alcohols for temperatures up to 573.15 k,” *Journal of Chemical & Engineering Data*, vol. 66, no. 6, pp. 2615–2628, 2021.

[389] P. Simacek, I. Soucek, M. Pospisil, D. Vrtiska, and H. Kittel, “Impact of hydrotreated vegetable oil and biodiesel on properties in blends with mineral diesel fuel,” *Thermal Science*, vol. 23, no. Suppl. 5, pp. 1769–1777, 2019.

[390] W. Pang, Y. Li, L. T. DeLuca, D. Liang, Z. Qin, X. Liu, H. Xu, and X. Fan, "Effect of metal nanopowders on the performance of solid rocket propellants: A review," *Nanomaterials*, vol. 11, no. 10, p. 2749, 2021.

[391] E. Xiu-Tian-Feng, L. Pan, F. Wang, L. Wang, X. Zhang, and J.-J. Zou, "Al-nanoparticle-containing nanofluid fuel: synthesis, stability, properties, and propulsion performance," *Industrial & Engineering Chemistry Research*, vol. 55, no. 10, pp. 2738–2745, 2016.

[392] E. Price and R. Sigman, "Combustion of aluminized solid propellants," *Solid propellant chemistry, combustion, and motor interior ballistics(A 00-36332 09-28), Reston, VA, American Institute of Aeronautics and Astronautics, Inc.(Progress in Astronautics and Aeronautics.*, vol. 185, pp. 663–687, 2000.

[393] Y. Gan, Y. S. Lim, and L. Qiao, "Combustion of nanofluid fuels with the addition of boron and iron particles at dilute and dense concentrations," *Combustion and Flame*, vol. 159, no. 4, pp. 1732–1740, 2012.

[394] L. Wang, H. Chen, and S. Witharana, "Rheology of nanofluids: a review," *Recent patents on nanotechnology*, vol. 7, no. 3, pp. 232–246, 2013.

[395] R. A. Yetter, G. A. Risha, and S. F. Son, "Metal particle combustion and nanotechnology," *Proceedings of the combustion institute*, vol. 32, no. 2, pp. 1819–1838, 2009.

[396] L. L. Schramm, E. N. Stasiuk, and D. G. Marangoni, "2 surfactants and their applications," *Annual Reports Section" C"(Physical Chemistry)*, vol. 99, pp. 3–48, 2003.

[397] P. Kougias, K. Boe, E. Einarsdottir, and I. Angelidaki, "Counteracting foaming caused by lipids or proteins in biogas reactors using rapeseed oil or oleic acid as antifoaming agents," *Water Research*, vol. 79, pp. 119–127, 2015.

[398] S. Kumar, G. Mishra, M. Kumar, A. K. Dwivedi, T. Saud, A. Khan, B. Sapra, S. Kumar, and S. N. Tripathi, "Response of pdpa to optical materials and thickness of test section window," *Measurement*, vol. 197, p. 111317, 2022.

[399] R. Clayton and L. Back, "Physical and chemical characteristics of cenospheres from the combustion of heavy fuel oil," 1989.

[400] L. Jiang, A. M. Elbaz, P. Guida, S. M. Al-Noman, I. A. AlGhamdi, S. Saxena, and W. L. Roberts, "Cenosphere formation during single-droplet combustion of heavy fuel oil," *Energy & fuels*, vol. 33, no. 2, pp. 1570–1581, 2019.

[401] I. Ferrão, M. Mendes, A. Moita, and A. R. Silva, "Experimental investigation of disrup-

tive burning phenomena on nanofuel droplets," in *20th International Symposium on Applications of Laser and Imaging Techniques to Fluid Mechanics*. Center for Innovation, Technology and Policy Research IN+, 2022.

[402] M. Stöhr, S. Ruoff, B. Rauch, W. Meier, and P. Le Clercq, "Droplet vaporization for conventional and alternative jet fuels at realistic temperature conditions: Systematic measurements and numerical modeling," *Proceedings of the Combustion Institute*, vol. 38, no. 2, pp. 3269–3276, 2021.

[403] Y. C. Liu, A. J. Savas, and C. T. Avedisian, "The spherically symmetric droplet burning characteristics of jet-a and biofuels derived from camelina and tallow," *Fuel*, vol. 108, pp. 824–832, 2013.

[404] M. Buffi, A. Valera-Medina, R. Marsh, D. Pugh, A. Giles, J. Runyon, and D. Chiaramonti, "Emissions characterization tests for hydrotreated renewable jet fuel from used cooking oil and its blends," *Applied Energy*, vol. 201, pp. 84–93, 2017.

[405] K. Pandey, S. Basu, V. Gautham, A. Potnis, and K. Chattopadhyay, "Self-tuning and topological transitions in a free-falling nanofuel droplet flame," *Combustion and Flame*, vol. 220, pp. 144–156, 2020.

[406] C. K. Law and F. A. Williams, "Kinetics and convection in the combustion of alkane droplets," *Combustion and Flame*, vol. 19, no. 3, pp. 393–405, 1972.

[407] T. L. Bergman, F. P. Incropera, D. P. DeWitt, and A. S. Lavine, *Fundamentals of heat and mass transfer*. John Wiley & Sons, 2011.

[408] J. Yang, G. Jackson, and C. Avedisian, "Combustion of unsupported methanol/dodecanol mixture droplets at low gravity," in *Symposium (International) on Combustion*, vol. 23, no. 1. Elsevier, 1991, pp. 1619–1625.

[409] F. Takahashi, I. Heilweil, and F. Dryer, "Disruptive burning mechanism of free slurry droplets," *Combustion science and technology*, vol. 65, no. 1-3, pp. 151–165, 1989.

[410] R. Kägo, R. Ilves, A. Küüt, and J. Olt, "A review of the behavior of fuel drops in a fuel spray in the context of biofuels," *Journal of Power Technologies*, vol. 99, no. 3, p. 218, 2019.

[411] K. Sirviö, S. Niemi, S. Heikkilä, E. Hiltunen *et al.*, "Kinematic viscosity studies for medium-speed ci engine fuel blends," 2018.

[412] I. Javed, S. W. Baek, and K. Waheed, "Autoignition and combustion characteristics of kerosene droplets with dilute concentrations of aluminum nanoparticles at elevated

temperatures," *Combustion and flame*, vol. 162, no. 3, pp. 774–787, 2015.

[413] P. M. Guerieri, S. DeCarlo, B. Eichhorn, T. Connell, R. A. Yetter, X. Tang, Z. Hicks, K. H. Bowen, and M. R. Zachariah, "Molecular aluminum additive for burn enhancement of hydrocarbon fuels," *The Journal of Physical Chemistry A*, vol. 119, no. 45, pp. 11 084–11 093, 2015.

[414] J. Wang, X. Qiao, D. Ju, L. Wang, and C. Sun, "Experimental study on the evaporation and micro-explosion characteristics of nanofuel droplet at dilute concentrations," *Energy*, vol. 183, pp. 149–159, 2019.

[415] D. Mei, Y. Fang, D. Zhang, D. Guo, and Z. Chen, "Evaporation and micro-explosion performances of nano-fuel droplets," *Fuel*, vol. 334, p. 126623, 2023.

[416] C. L. Yaws, *Chemical properties handbook*. McGraw-Hill Education, 1999.

[417] T. L. Bergman, A. S. Lavine, F. P. Incropera, and D. P. DeWitt, *Introduction to heat transfer*. John Wiley & Sons, 2011.

[418] G. M. Faeth, "Current status of droplet and liquid combustion," *Progress in Energy and Combustion Science*, vol. 3, no. 4, pp. 191–224, 1977.

[419] E. Boel, R. Koekoekx, S. Dedroog, I. Babkin, M. R. Vetrano, C. Clasen, and G. Van den Mooter, "Unraveling particle formation: From single droplet drying to spray drying and electrospraying," *Pharmaceutics*, vol. 12, no. 7, 2020.

[420] R. de Souza Lima, M.-I. Ré, and P. Arlabosse, "Drying droplet as a template for solid formation: A review," *Powder Technology*, vol. 359, pp. 161–171, 2020.

[421] H. Rumpf, *Particle Technology*, 1st ed. Chapman and Hall, 1990.

[422] D. Megias-Alguacil and L. J. Gauckler, "Capillary and van der waals forces between uncharged colloidal particles linked by a liquid bridge," *Colloid and Polymer Science*, vol. 288, pp. 133–139, 2010.

[423] M. R. O. Panão, "Assessment of measurement efficiency in laser-and phase-doppler techniques: an information theory approach," *Measurement Science and Technology*, vol. 23, no. 12, p. 125304, 2012.

[424] "Measurement principles of pda," DANTEC. [Online]. Available: https://www.dantecdynamics.com/solutions/spray-and-particle/phase-doppler-anemometry-pda/measurement-principles-of-pda/

[425] F. Zhang, T. Zirwes, S. Wachter, T. Jakobs, P. Habisreuther, N. Zarzalis, D. Trimis,

T. Kolb, H. Bockhorn, and D. Stapf, "Numerical simulations of air-assisted primary atomization at different air-to-liquid injection angles," *International Journal of Multiphase Flow*, vol. 158, p. 104304, 2023.

[426] A. P. Kulkarni, T. Megaritis, and L. C. Ganippa, "Insights on the morphology of air-assisted breakup of urea-water-solution sprays for varying surface tension," *International Journal of Multiphase Flow*, vol. 133, p. 103448, 2020.

[427] M. Roudini and G. Wozniak, "Experimental investigation of spray characteristics of pre-filming air-blast atomizers ii–influence of liquid properties," *Journal of Applied Fluid Mechanics*, vol. 13, no. 2, pp. 679–691, 2020.

[428] S. Mahapatra, S. Chatterjee, S. Shannigrahi, A. Mukhopadhyay, and S. Sen, "Experimental investigation and spray characterization of liquid jet atomization of conventional fuels and liquid bio-fuels," in *12th Triennial International Conference on Liquid Atomization and Spray Systems*, 2012.

[429] X. Wang and A. Lefebvre, "Mean drop sizes from pressure-swirl nozzles," *Journal of Propulsion and Power*, vol. 3, no. 1, pp. 11–18, 1987.

[430] J. R. Custer and N. K. Rizk, "Influence of design concept and liquid properties on fuel injector performance," *Journal of Propulsion and Power*, vol. 4, no. 4, pp. 378–384, 1988.

[431] E. Giffen and B. Massey, "B. s., report 1950/5," 1950.

[432] W.-H. Lai, K. Yang, C. Hong, and M.-R. Wang, "Droplet transport in simplex and air-assisted sprays," *Atomization and Sprays*, vol. 6, no. 1, 1996.

[433] P. K. Kirar, S. K. Soni, P. S. Kolhe, and K. C. Sahu, "An experimental investigation of droplet morphology in swirl flow," *Journal of Fluid Mechanics*, vol. 938, p. A6, 2022.

[434] Q. Cheng, H. Tuomo, O. Kaario, and L. Martti, "Hvo, rme, and diesel fuel combustion in an optically accessible compression ignition engine," *Energy & Fuels*, vol. 33, no. 3, pp. 2489–2501, 2019.

[435] V. Tangirala, R. Chen, and J. F. Driscoll, "Effect of heat release and swirl on the recirculation within swirl-stabilized flames," *Combustion science and technology*, vol. 51, no. 1-3, pp. 75–95, 1987.

[436] A. E. Khalil, J. M. Brooks, and A. K. Gupta, "Impact of confinement on flowfield of swirl flow burners," *Fuel*, vol. 184, pp. 1–9, 2016.

[437] L. Ji, J. Wang, W. Zhang, R. Mao, G. Hu, and Z. Huang, "Effect of confinement ratio on flame structure and blow-off characteristics of swirl flames," *Experimental Thermal and Fluid Science*, vol. 135, p. 110630, 2022.

[438] G. Scribano and M.-V. Tran, "Numerical investigation of a confined diffusion flame in a swirl burner," *European Journal of Mechanics-B/Fluids*, vol. 82, pp. 1–10, 2020.

[439] N. Syred and K. Dahman, "Effect of high levels of confinement upon the aerodynamics of swirl burners," *Journal of Energy*, vol. 2, no. 1, pp. 8–15, 1978.

[440] G. Partners, *Safety Data Sheet Kerosene*, 2016. [Online]. Available: https://www.globalp.com/wp-content/uploads/2019/10/SDS_Kerosene_Final1.pdf

[441] R. O. Company, *Material Safety Data Sheet Kerosene*, 2004. [Online]. Available: https://www.ramosoil.com/wp-content/uploads/RAMOS-KEROSENE.pdf

[442] N. Oceanic and A. Administration, *Kerosene*, 1999. [Online]. Available: https://cameochemicals.noaa.gov/chris/KRS.pdf

[443] H. Xing, C. Stuart, S. Spence, and H. Chen, "Alternative fuel options for low carbon maritime transportation: Pathways to 2050," *Journal of Cleaner Production*, vol. 297, p. 126651, 2021.

[444] M. Zabetakis, S. Lambiris, and G. Scott, "Flame temperatures of limit mixtures," in *Symposium (International) on Combustion*, vol. 7, no. 1. Elsevier, 1958, pp. 484–487.

[445] M. G. Zabetakis, "Flammability characteristics of combustible gases and vapors," Bureau of Mines, Pittsburgh, PA (United States), Tech. Rep., 1964.

Appendix A

Biofuels - Conversion Process

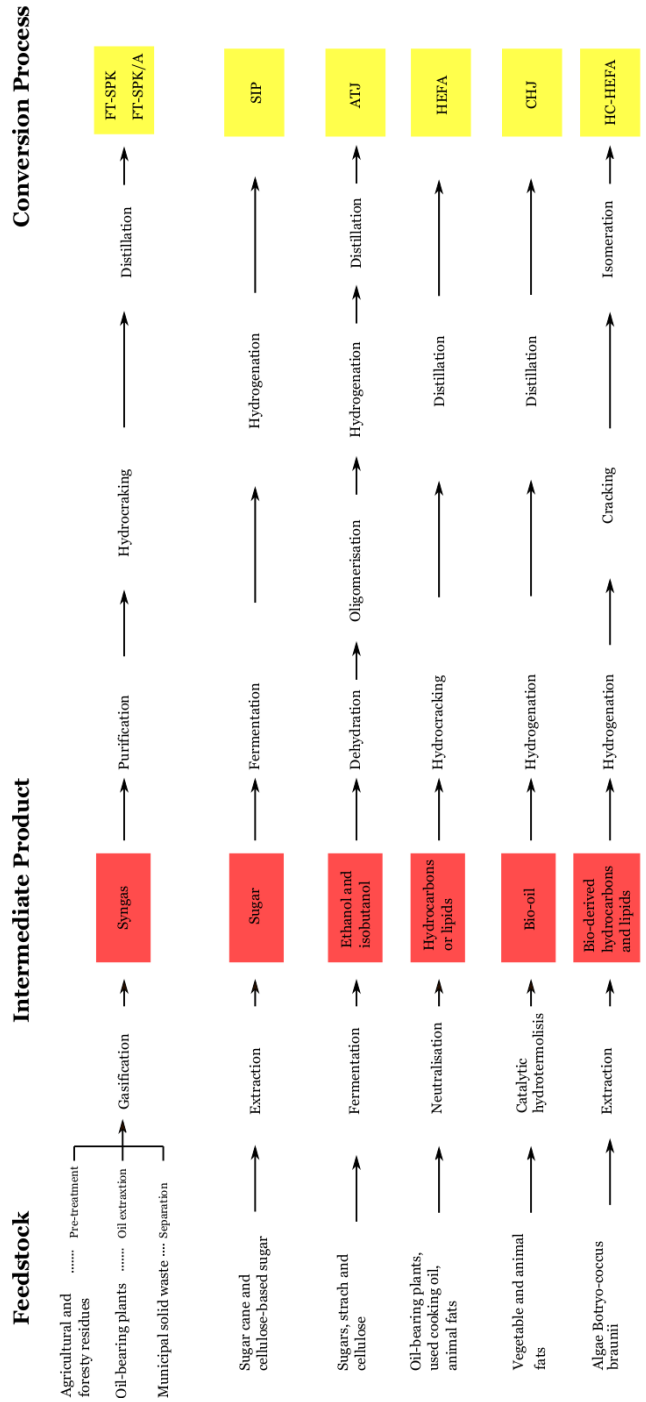

Figure A.1: Biofuels approved conversion processes [86].

Appendix B

Drop Tube Furnace - Injector

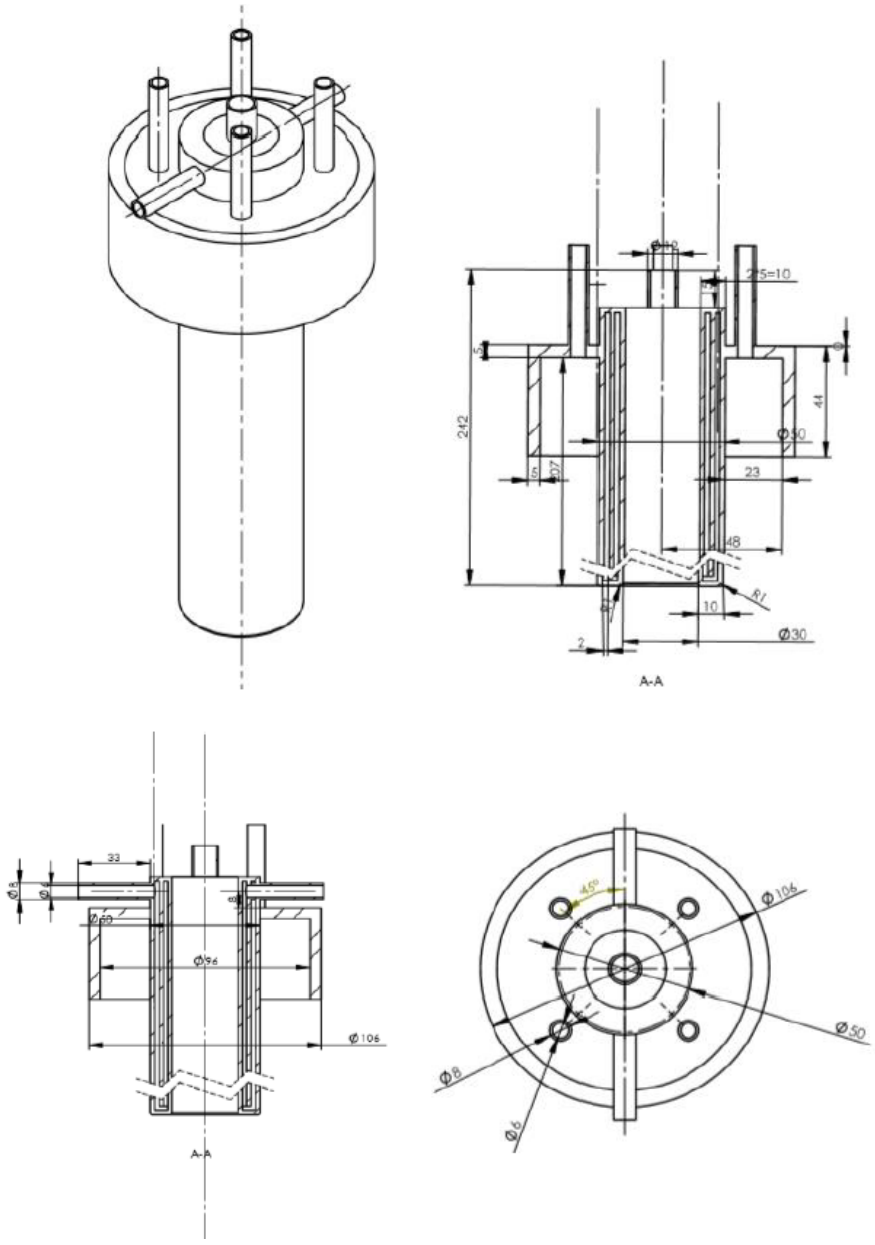

Figure B.1: Injector technical draw (units in mm).

Appendix C

Air Properties

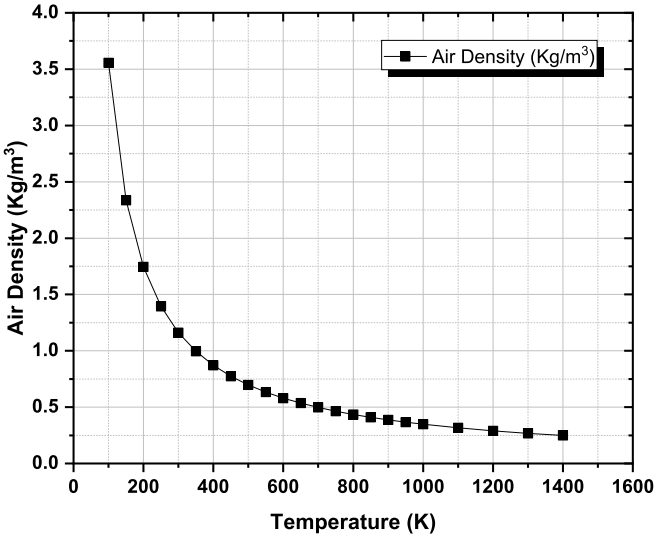

Figure C.1: Air density as a function of temperature.

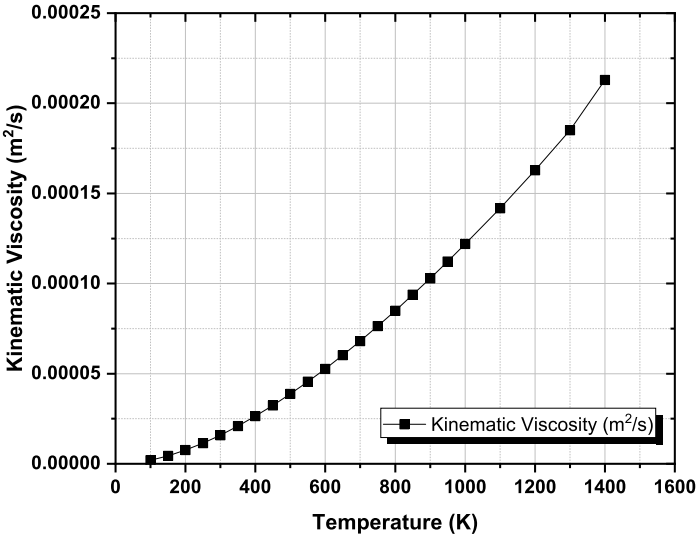

Figure C.2: Air kinematic viscosity as a function of temperature.

Appendix D

SCA - Calibration

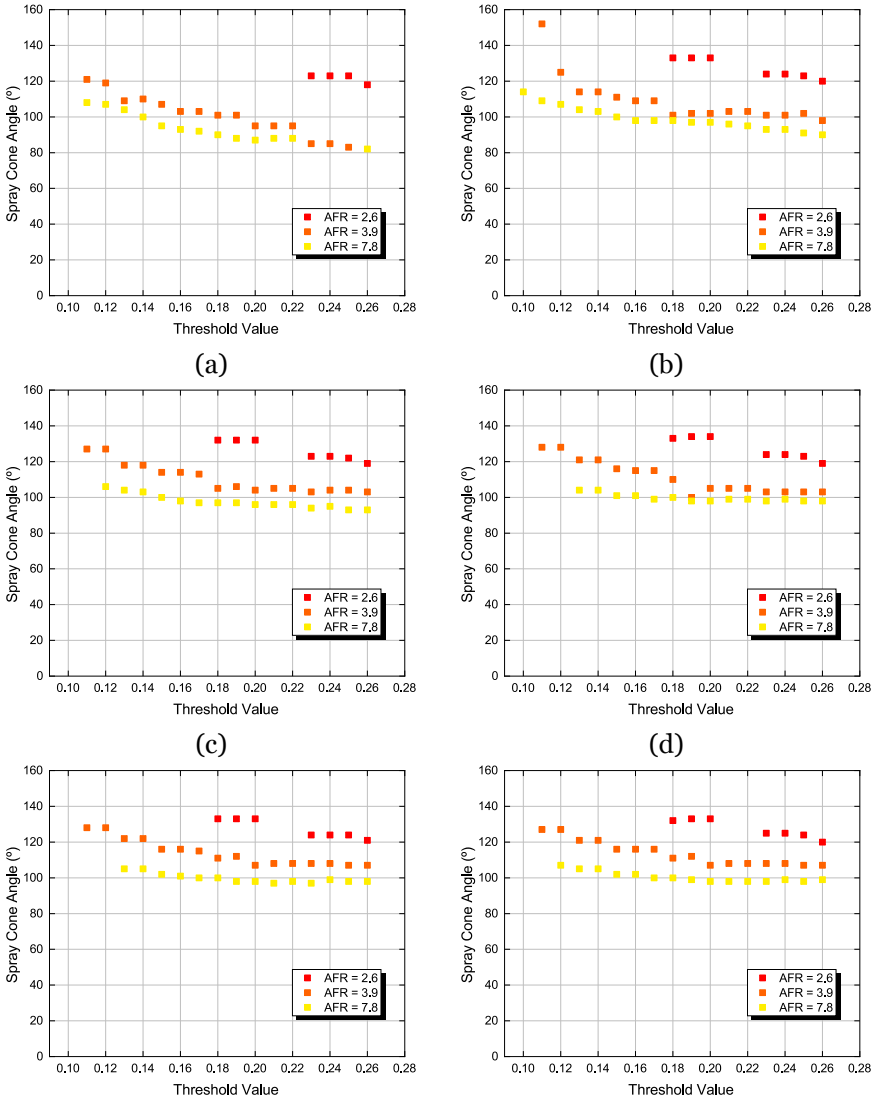

Figure D.1: The influence of frame number on the SCA for Jet A-1 under different AFR conditions: a) 1000 images; b) 2000 images; c) 3000 images; d) 4000 images; e) 5000 images; f) 6000 images.

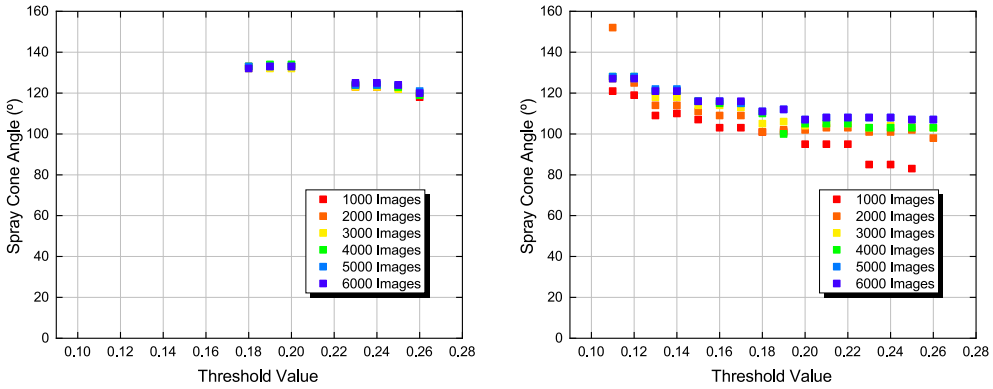

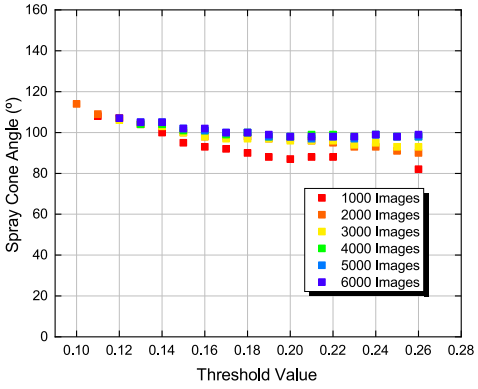

Figure D.2: Comparsion of SCA for Jet A-1, a) AFR = 2.6, b) AFR = 3.9, c) AFR = 7.8.

Appendix E

Spray: Operating Conditions

Table E.1: Fuels operating conditions and the corresponding dimensionless numbers.

	Jet A-1					HVO				HVO + 0.5% Al				HVO + 1.0% Al			
	$\dot{m}_a(g/s)$	Re_l	We_a	M	AFR	Re_l	We_a	M	AFR	Re_l	We_a	M	AFR	Re_l	We_a	M	AFR
1st Condition	0.11	61.0	1.6	5.6	2.6	19.1	1.5	6.0	2.7	18.8	1.5	6.0	2.7				
	0.22	61.0	6.6	22.5	5.2	19.1	6.1	24.2	5.4	18.8	6.1	24.2	5.4				
	0.33	61.0	15.0	50.7	7.9	19.1	13.8	54.4	8.1	18.8	13.8	54.4	8.1	18.3	13.7	57.2	8.3
	0.66	61.0	60.1	202.9	15.7	19.1	55.6	217.8	16.2	18.8	55.6	217.8	16.2	18.3	55.3	228.8	16.6
2nd Condition	0.11	72.2	1.6	4.0	2.2	22.8	1.5	4.2	2.3	22.4	1.5	4.2	2.3				
	0.22	72.2	6.6	16.1	4.4	22.8	6.1	4.1	4.5	22.4	6.1	16.9	4.5				
3rd Condition	0.11	92.4	1.6	2.5	1.7	29.8	1.5	2.5	1.7	29.3	1.5	2.5	1.7				
	0.22	92.4	6.6	9.8	3.5	29.8	6.1	9.9	3.5	29.3	6.1	9.9	3.5				
4th Condition	0.11	122.8	1.6	1.4	1.3	39.2	1.5	1.4	1.3	37.5	1.5	1.5	1.3	38.5	1.4	1.4	1.3
	0.22	122.8	6.5	5.6	2.6	39.2	6.0	5.8	2.6	37.5	6.0	6.0	2.7				
	0.33	122.8	14.8	12.5	3.9	39.2	13.7	13.0	3.9	37.5	13.7	13.6	4.0				
	0.55	122.8	59.8	50.0	7.8	39.2	55.3	51.9	7.9	37.5	55.3	54.4	8.1	38.5	38.1	36.0	6.6
5th Condition	0.11	144.4	1.6	1.0	1.1	55.0	1.4	0.7	0.9	54.0	1.4	0.7	0.9	54.0	1.4	0.7	0.9
	0.22	144.4	6.5	4.0	2.2	55.0	5.9	2.9	1.9	54.0	5.9	2.9	1.9	54.0	5.9	2.9	1.9